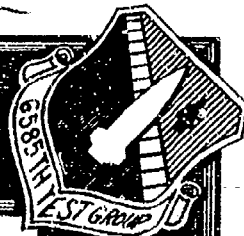


UNCLASSIFIED

AD NUMBER
ADB164018
NEW LIMITATION CHANGE
TO Approved for public release, distribution unlimited
FROM Distribution authorized to DoD and DoD contractors only; Critical Technology; JUL 1991. Other requests shall be referred to Wright Laboratory, Attn: MNAG, Eglin AFB, FL 32542-5434.
AUTHORITY
Hq 6585th Test Gp[AFSC]/ GD via ltr., 1 Apr 1992

THIS PAGE IS UNCLASSIFIED

AD-B164 018



AFDTC-TR-91-06
VOLUME 1

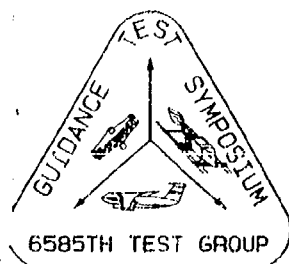
②

L

FIFTEENTH BIENNIAL GUIDANCE TEST SYMPOSIUM

PREPARED BY
CENTRAL INERTIAL GUIDANCE TEST FACILITY
GUIDANCE TEST DIVISION

DTIC
ELECTE
MAY 06 1992
S. D.



6585TH TEST GROUP
HOLLOMAN AFB, NEW MEXICO 88330-5000

24, 25, & 26 SEPTEMBER 1991

Publication of this report does not constitute approval or disapproval of the ideas or findings. It is published in the interest of exchanging scientific and technical information.

[Handwritten signature]
DISTRIBUTION STATEMENT: Approved for public release; distribution is unlimited.

The Public Affairs Office has reviewed this report, and it is releasable to the National Technical Information Service where it will be available to the general public, including foreign nationals.

92-12278





DEPARTMENT OF THE AIR FORCE
HEADQUARTERS 6585TH TEST GROUP (AFSC)
HOLLOMAN AIR FORCE BASE, NEW MEXICO 88330-5000

REPLY TO

ATTN OF: GD

14 February 1992

SUBJECT: Proceedings of Fifteenth Biennial Guidance Test Symposium
- Volume I

TO: TO ALL RECIPIENTS OF VOLUME I

1. The Proceedings of the Fifteenth Biennial Guidance Test Symposium have been shipped by UPS to all who have requested them. This year, for budgetary reasons, we shipped to one address per company location, which was deemed to be the Data Custodian or Librarian. If you have not received your copy(s) of the proceedings, please check with your library. Address labels were on the back of each Volume II. (Volume III was sent to your Security Officer.)

2. PLEASE NOTE -- Effective immediately, Volume I of the Proceedings must be treated as a "Limited Distribution" document due to the inclusion of one paper. Until further notice, this document is no longer approved for public release! Please insure it is handled accordingly.

K. R. HOLLAND
Technical Director
Guidance Test Division

The following notice applies to any unclassified (including originally classified and now declassified) technical reports released to "qualified U.S. contractors" under the provisions of DoD Directive 5230.25, Withholding of Unclassified Technical Data From Public Disclosure.

NOTICE TO ACCOMPANY THE DISSEMINATION OF EXPORT-CONTROLLED TECHNICAL DATA

1. Export of information contained herein, which includes, in some circumstances, release to foreign nationals within the United States, without first obtaining approval or license from the Department of State for items controlled by the International Traffic in Arms Regulations (ITAR), or the Department of Commerce for items controlled by the Export Administration Regulations (EAR), may constitute a violation of law.
2. Under 22 U.S.C. 2778 the penalty for unlawful export of items or information controlled under the ITAR is up to two years imprisonment, or a fine of \$100,000, or both. Under 50 U.S.C., Appendix 2410, the penalty for unlawful export of items or information controlled under the EAR is a fine of up to \$1,000,000, or five times the value of the exports, whichever is greater; or for an individual, imprisonment of up to 10 years, or a fine of up to \$250,000, or both.
3. In accordance with your certification that establishes you as a "qualified U.S. Contractor", unauthorized dissemination of this information is prohibited and may result in disqualification as a qualified U.S. contractor, and may be considered in determining your eligibility for future contracts with the Department of Defense.
4. The U.S. Government assumes no liability for direct patent infringement, or contributory patent infringement or misuse of technical data.
5. The U.S. Government does not warrant the adequacy, accuracy, currency, or completeness of the technical data.
6. The U.S. Government assumes no liability for loss, damage, or injury resulting from manufacture or use for any purpose of any product, article, system, or material involving reliance upon any or all technical data furnished in response to the request for technical data.
7. If the technical data furnished by the Government will be used for commercial manufacturing or other profit potential, a license for such use may be necessary. Any payments made in support of the request for data do not include or involve any license rights.
8. A copy of this notice shall be provided with any partial or complete reproduction of these data that are provided to qualified U.S. contractors.

D E S T R U C T I O N N O T I C E

For classified documents, follow the procedures in DoD 5200.22-M, Industrial Security Manual, Section II-19 or DoD 5200.1-R, Information Security Program Regulation, Chapter IX. For unclassified, limited documents, destroy by any method that will prevent disclosure of contents or reconstruction of the document.

REPORT DOCUMENTATION PAGE

Form Approved
OMB No. 0704-0188

Public reporting burden for this collection of information is estimated to average 1 hour per response, including the time for reviewing instructions, searching existing data sources, gathering and maintaining the data needed, and completing and reviewing the collection of information. Send comments regarding this burden estimate or any other aspect of this collection of information, including suggestions for reducing this burden, to Washington Headquarters Services, Directorate for Information Operations and Reports, 1215 Jefferson Davis Highway, Suite 1204, Arlington, VA 22202-4302, and to the Office of Management and Budget, Paperwork Reduction Project (0704-0188), Washington, DC 20503.

1. AGENCY USE ONLY (Leave blank)		2. REPORT DATE SEPTEMBER 1991	3. REPORT TYPE AND DATES COVERED SYMPOSIUM PAPERS 24-26 SEP 91
4. TITLE AND SUBTITLE FIFTEENTH BIENNIAL GUIDANCE TEST SYMPOSIUM (VOLUME I)			5. FUNDING NUMBERS JON 9993NGTS PE 65708F
6. AUTHOR(S) The authors' names are indicated on the individual papers.			
7. PERFORMING ORGANIZATION NAME(S) AND ADDRESS(ES) 6585th Test Group/GD (AFSC/AFDTC) Holloman AFB NM 88330-5000			8. PERFORMING ORGANIZATION REPORT NUMBER AFDTC-TR-91-06 Volume I
9. SPONSORING/MONITORING AGENCY NAME(S) AND ADDRESS(ES) 6585th Test Group/GD (AFSC/AFDTC) Holloman AFB NM 88330-5000			10. SPONSORING/MONITORING AGENCY REPORT NUMBER AFDTC-TR-91-06 Volume I
11. SUPPLEMENTARY NOTES DISTRIBUTION STATEMENT D: Distribution authorized to the Department of Defense and U.S. DoD contractors only CRITICAL TECHNOLOGY 7 July 91 Other requests shall be referred to WL/MNAG, Eglin AFB, FL 32542-			
12a. DISTRIBUTION/AVAILABILITY STATEMENT Approved for public release; distribution is unlimited			12b. DISTRIBUTION CODE 5434
13. ABSTRACT (Maximum 200 words) These proceedings contain papers which were presented at the Fifteenth Biennial Guidance Test Symposium. This symposium, hosted by the Central Inertial Guidance Test Facility, Holloman Air Force Base, New Mexico, on 24-25-26 September 1991, was directed toward the exchange of information, stimulation of new ideas, and discussion of current techniques associated with the development and evaluation of inertial guidance and navigation systems. The papers presented included such topics as new test and calibration techniques for accelerometers and ring laser gyros, advances in flight reference systems, new test equipment, new software developments, and global positioning system information. Volume I contains papers which are unclassified and have no distribution restriction. Volume II contains the unclassified papers which have a limited distribution restriction, and Volume III contains papers which are classified up to and including SECRET.			
14. SUBJECT TERMS			15. NUMBER OF PAGES 594
			16. PRICE CODE
17. SECURITY CLASSIFICATION OF REPORT UNCLASSIFIED	18. SECURITY CLASSIFICATION OF THIS PAGE UNCLASSIFIED	19. SECURITY CLASSIFICATION OF ABSTRACT UNCLASSIFIED	20. LIMITATION OF ABSTRACT SAME AS REPORT

FOREWORD

The Fifteenth Biennial Guidance Test Symposium was held at Holloman Air Force Base, New Mexico, on 24-25-26 September 1991. This symposium was hosted by the Central Inertial Guidance Test Facility (CIGTF). The purpose of the symposium was to provide a forum for approximately 400 people from industry, universities, foreign governments, Department of Defense, and other Government agencies. The forum provided an exchange of technical information and stimulation of new ideas associated with development, testing, and evaluation of inertial components, aircraft navigation, missile guidance, and global positioning systems.

Many excellent papers were received for presentation at this meeting, but due to the time allotted to this symposium, only a portion of those papers submitted could be included in the program.

The Paper Selection Committee included Darwin Abby, Intermetrics; Lt Col Arnie Alanis, BMO/MVEG; Dave Anderson, Honeywell, Inc; Dominic Brienza, Naval Avionics Center; Richard E. Clark, TASC; Joe Coulter, Northrop ESD; Ron Cox, Litton Guidance & Control; Dirk DeDoes, Intermetrics; Charles Evans, Litton Guidance & Control; Bob Fall, Honeywell, Inc; Samuel George, OC-ALC/LIIRN; Gaylord Green, Stanford University; Richard Greenspan, C. S. Draper Laboratory; Michael Hadfield, Honeywell, Inc; James Hand, C. S. Draper Laboratory; Richard Holdeman, TRWOgden; Gene Hymas, TRW-Ogden; Jack Jankovitz, Naval Air Development Center; Fred Nadeau, WRDC/AAAN; John Niemela, U.S. Army Avionics Lab; Ann Orlando, Synetics; Tom Sanders, Naval Air Development Center; Len Sugerman, Physical Science Laboratory; and Phil Ward, Texas Instruments.

In addition to those mentioned above and the contributing authors, a large number of people contributed to the success of this symposium. I wish to express my appreciation to each of them for their efforts. Special thanks go to our Technical Director, Kenneth R. Holland; to our Technical Managers, Fred Schreiber and Robert Kelher; and to the Symposium Coordinator, Dora Walker.

Publication of this report does not constitute approval or disapproval of the ideas or findings. It is published in the interest of exchanging scientific and technical information.

Kenneth R. Wernle
KENNETH R. WERNLE, Lt Col, USAF
Director, Guidance Test Division

iii



Accession For	
NTIS GRA&I	<input type="checkbox"/>
DTIC TAB	<input checked="" type="checkbox"/>
Unannounced	<input type="checkbox"/>
Justification	
<i>See page 183</i>	
By <i>per letter</i>	
Distribution/	
Availability Codes	
Dist.	Avail and/or Special
<i>D-16</i>	

Partial
TABLE OF CONTENTS ;

VOLUME I

	PAGE
ABSTRACT.....	i
FOREWORD.....	iii
TABLE OF CONTENTS.....	v

SESSION I: UPDATES/STATUS

<i>Global Positioning System (GPS) Program Status.....</i>	3
Commander Allen Burgess, Space Systems Division, Joint Program Office, Los Angeles AFB CA	
<i>Measuring Inertial Space-Gravity Probe B.....</i>	589
Gaylord B. Green, C. W. F. Everitt, Brad Parkinson, J. Turneure, D. Bardas, and the Stanford Relativity Gyroscope Team, Stanford University, Stanford CA	
<i>An Introduction to the GPS Guidance Package (GGP).....</i>	11
William C. Homer, Naval Ocean Systems Center, San Diego CA	

SESSION II-A: ADVANCED GUIDANCE

<i>Strapdown Astro-Inertial Navigation As a Secure Method of Satisfying the Twenty-first Century's Precision Mission Requirements</i>	19
Sy Levine, Northrop ESD, Hawthorne CA; Fred Nadeau, Wright Labs/AAAN-1, Wright-Patterson AFB OH	
<i>A Strapdown ICBM Guidance System With Peacekeeper Accuracy?.....</i>	41
John Lukesh, Northrop ESD, Hawthorne CA; Tom Reed, R. G. Brown Associates, Inc., Charlton MA	
<i>Application of Maximum Likelihood Parameter Identification..... to Test and Evaluation of Inertial Navigation Systems</i>	49
Larry J. Levy, Applied Physics Laboratory, Johns Hopkins University, Laurel MD; David W. Porter, Coleman Research Corporation, Laurel MD	

SESSION II-B: GPS-ATTITUDE/AZIMUTH/TSPT

<i>GPS Derived Azimuth.....</i>	67
Scott D. Michael, U.S. Army Engineer Topographic Laboratories, CEETL-TL-ST, Fort Belvoir VA	

GPS Frequency Translator Tracking Used for ERIS TSPI,.....75
Carl E. Hoefener, Interstate Electronics Corp., Anaheim CA

Advances in GPS Attitude Determining Technology81
as Developed for the Strategic Defense Command
Richard Jurgens and Charles Rodgers,
Adroit Systems, Inc., Alexandria VA

SESSION III-A: INERTIAL INSTRUMENTS

Cryogenic Inertial Instruments,.....97
Lt Col Gerald L. Shaw, Phillips Laboratory (AFSC),
Hanscom AFB MA

Extracting Horizontal and Vertical Components of.....111
Balloon-Borne Gravity Vectors from the Integration
of GPS and Inertial Ring Laser Strapdown System Data
David M. Gleason, GL (AFSC)/LWG, Hanscom AFB MA

Evolution of Miniature Quartz Vibrating Beam.....147
Accelerometer Technology for Navigation and
Flight Control
David P. Jensen, Sundstrand Data Control, Inc., Redmond WA

SESSION III-B: INS/GPS INTEGRATION

INS Alignment Using the RCVR 3A Computed Corrections.....171
Prasun Sinha, Dirk DeDoes, and Kendall Barckley,
Intermetrics, Inc., Huntington Beach CA

Tightly Coupled GPS/INS Integration Using183
an Open Loop Approach
Christopher C. Ross, WL/MNAG, Eglin AFB FL

An Inexpensive PC Based GPS Satellite Signal Simulator.....211
Charles Rodgers, Adroit Systems, Inc., Alexandria VA

SESSION IV-A: INSTRUMENT TESTING

A Practical Three Axis Balancing System225
for Precision Centrifuge Applications
Rex B. Peters, Sundstrand Data Control, Inc., Redmond WA;
R. D. Marquess, Applied Motion Technology, Inc., Concord CA

Determination of Nonlinear Coefficients In237
a Dry Accelerometer by Vibration Testing
Rex B. Peters and S. Foote, Sundstrand Data Control, Inc.,
Redmond WA

<i>Design of Precision Vibration Test Station</i>	259
<i>for High Accuracy Accelerometer Calibration</i>	
R. Alan Burnett and Fred Macary (D. E. Wentzel), Sundstrand Data Control, Inc., Redmond WA	

SESSION IV-B: GPS INTEGRATION - DIGITAL TERRAIN

<i>A Guidance and Control Expert System Shell for</i>	273
<i>Peacekeeper Missile Maintenance Applications</i>	
Ray L. Fischer, Northrop Corp., Hawthorne CA	

SESSION V-B: GPS

<i>Test Report for GPS (Prototype) Antenna</i>	291
<i>on the Cylindrical Construction</i>	
Akiyoshi Yamamoto, Japan Radio Co., Ltd., Tokyo Japan	
<i>Use of Aircraft Facet Models in Determining</i>	309
<i>GPS Signal Availability</i>	
Steven N. Karels, TASC, Reading MA; Edward P. Bradley, ASD/YIEB, Eglin AFB FL	
<i>Real-time Attitude Determination Using the</i>	319
<i>Ashtech Three-Dimensional Direction Finding System</i>	
Mark Kuhl and Kendall Ferguson, Ashtech, Inc., Sunnyvale CA	

SESSION VI-A: INERTIAL INSTRUMENTS

<i>A Case of Flicker Noise</i>	331
Reid G. Reynolds, TRW, Carson CA	
<i>Self Calibration of Q-Flex Sensor Head for</i>	339
<i>Space Shuttle Microgravity Experiments</i>	
Rex Peters, R. S. Anderson, C. R. Wilson, and Byron Scott, Sundstrand Data Control, Redmond WA	
<i>Prototype Fiber Optic Gyro Performance</i>	369
Dr. Edward Kanegsberg, Litton Guidance & Control, Woodland Hills CA	

SESSION VI-B: STELLAR GUIDANCE

<i>Ultra-Precise Azimuth Determination and Azimuth</i>	381
<i>Transfer Using Stellar Optical Interferometry</i>	
James A. Hughes and Donald J. Hutter, U.S. Naval Observatory, Astronomy Department, Washington DC	

SESSION VII-B: TEST TECHNIQUES

- High Accuracy Measurement Techniques for397**
Characterizing an Accelerometer Current Output
D. E. Wentzel, Sundstrand Data Control, Redmond WA
- Methods for Minimizing the Interaction Between423**
Coupled Parallel Control Systems
John Blackburn, Applied Technology
Associates, Inc., Albuquerque NM
- Feasibility of Correcting Gyro Bias Errors While Taxiing.....441**
John Diesel, Robert Buchler, and Robert Grethel,
Litton Aero Products, Moorpark CA

SESSION VIII-B: GPS SIMULATION-INS

- Honeywell's GG1308 Ring Laser Gyro Inertial467**
Measurement Systems - Test Results
Michael G. Secord, John G. Meissier, and Leroy O.
Thielman, Honeywell, Inc., Minneapolis MN
- Approach for the Evaluation of Alternative Cleaning.....475**
Solvents and Techniques to Replace the Use of Ozone
Depleting Solvents in Inertial Instrument Production, 406
John W. Agopovich and Ann L. Hynes,
C. S. Draper Laboratory, Inc., Cambridge MA

SESSION IX-A: PEACEKEEPER INSTRUMENTS

- Litton's Second Generation Laser Gyroscope.....493**
Steve Gillespie, Joe Fischer, and Charles Volk,
Litton Guidance & Control, Woodland Hills CA

SESSION IX-B: GPS USES - TERRAIN SYSTEMS

- ASICs and BIT/Testability in Navigation Systems.....503**
Jacques A. Tazartes, Litton Guidance
& Control, Woodland Hills CA
- INS and GPS Competitive or Synergistic?.....519**
Michael J. Hadfield and Glenn R. Quasius,
Honeywell Military Avionics, Clearwater FL
- Flight Testing a Terrain Referenced Navigation System.....535**
Roger Blasius, 6510th Test Wing/DORN, Edwards AFB CA

Low Cost Navigation and Battlefield Information.....	543
Forward Systems (BIFFS)	
Chris Coles, UK Research & Development, Ltd.,	
Salisbury, Wiltshire, England	

SESSION X: TEST CAPABILITIES

State-of-the-art Vibration Measurements	551
for Spacecraft Applications	

Joel Anspach, Paul Sydney, and Henry Sebesta,
Applied Technology Associates, Albuquerque NM;
Gregg Hendry, Ball Aerospace Systems, Boulder CO

Problems Specifying Precision INS in the 90's.....	565
Regan Lowrey, Honeywell Military Avionics Division, St. Petersburg FL	

Aerial Cable Test Capability Precision	579
Testing in a Controlled Environment	

Robert E. Green, STEWS-ID-P, White Sands Missile Range NM

LIST OF ATTENDEES.....	607
-------------------------------	------------

SESSION I
UPDATES/STATUS

CHAIRMAN
GAYLORD GREEN
STANFORD UNIVERSITY

GLOBAL POSITIONING SYSTEM (GPS)

PROGRAM STATUS

Commander Alan Burgess, Royal Navy
NATO Deputy Program Manager
USAF Space Systems Division, Los Angeles, California

1. ABSTRACT

The Navstar GPS program has now entered the production phase in all three segments of the system: Space, Ground and User. The Space Segment portion of the overall program completed launching the developmental Block I satellites in 1986. The first operational Block II satellite (PRN 14) was launched on 14 February 1989. Program management responsibility for the Operational Control System (OCS) transferred to Falcon AFB at Colorado Springs in 1987 and emphasis has been placed on upgrading the OCS components to full operational status and in developing a status reporting system. The User Equipment (UE) program for the American military is in Limited Rate Initial Production and the decision to proceed to full rate will be made in late 1991. This paper addresses the current status of the GPS program as it is poised to transition into the operational phase and considers some aspects which will be of interest to those concerned with planning its introduction into service.

2. BACKGROUND

As a result of the initial efforts by the USN and the USAF to develop an all weather global radio navigation system, the multi-service GPS program was born in 1973. The Air Force, as executive service, manages the overall program at the GPS Joint Program Office (JPO) located at HQ Space Systems Division in Los Angeles, California. The other US military services, as well as representatives from the Defense Mapping Agency, Department of Transport and NATO maintain active participation in the JPO. The GPS was designed to be a passive, survivable continuous space-based system which will provide any suitably equipped user with three dimensional position, velocity and precise time information. The high levels of accuracy provided by the Precise Positioning Service (PPS) can be denied to unauthorized users, but the Standard Positioning Service (SPS) will be made available free of charge to any user worldwide.

The GPS comprises three segments: Space, Ground and User. The Space segment consists of the constellation of GPS satellites and includes the responsibilities for development, production and launch. The operational constellation is planned to consist of 21 satellites with sufficient spares to ensure maximum global coverage with 98% satellite availability. The Operational Control System (OCS) of the Ground segment consists of three Ground Antenna, five

Monitor Stations (MS), the prelaunch Compatibility Station (PCS) and the Master Control Station (MCS). The MCS, with its co-located monitor station, are resident at the Consolidated Space Operations Centre (CSOC) located at Falcon AFB in Colorado Springs. The OCS is now operational and a planned upgrade to the PCS to realize a full MS capability will enhance the full operational capability of the Operations Segment. The User Segment consists of the families of UE which will provide users with precise positioning and timing data. A limited production contract was awarded to Rockwell-Collins in 1986 for the initial military purchases to ensure maximum compatibility across a wide range of platforms. Full-rate production to supply military equipment to all US Services will depend on the outcome of the Defense Acquisition Boards' decision in 1991.

3. SPACE SEGMENT STATUS

Between 1987 and 1990, a very comprehensive User equipment test program was undertaken by the US military on land, sea and in the air using the early production equipment. Signals from space were provided by the initial prototype Block I satellites and the useable satellites were configured to give a maximum coverage over the US. Of the initial eleven prototype Block I satellites, ten were successfully launched. Of these ten, five still remain useable for GPS test and operational missions. The oldest of these, designated NAVSTAR 3, recently completed its twelfth year of service. The Block I's form the core of the present constellation.

SV NO	PRN	STATUS	LAUNCHED
1	-	Non-operational	Feb 78
2	-	Non-operational	May 78
3	6	Marginal operation	Oct 78
4	-	Non-operational	Dec 78
5	-	Non-operational	Feb 80
6	-	Non-operational	Apr 80
7	-	Booster failed	-----
8	11	Operating	Jun 84
9	13	Operating	Jun 84
10	12	Operating	Sep 84
11	3	Operating	Oct 85

TABLE I. Status of Block I Development Satellites

The Block II, or operational satellite production contract was awarded to Rockwell International, Seal Beach, in 1983. Due to the tragedy of the Shuttle Challenger in 1986 and the subsequent unavailability of the Space Transport System (STS) for the GPS satellite launches, a contract was awarded to McDonald Douglas in

1986 for production of Delta II medium launch vehicles (MLV) which would be used to boost the first Block II satellite into orbit. At that stage, it was intended to retain some launches on the shuttle, but this option has now been removed although the design of the Block II satellites is such that this capability is still available.

On February 14, 1989, the first Block II satellite was launched from Cape Canaveral on a new Delta II rocket. Initial placement of this and successive satellites was to maintain and then extend the test "window". Such a launch and positioning policy during 1989 and 1990 has now achieved 11 operational Block II satellites supporting the original Block I's. Launches will continue at a rate of approximately 5 per year. 3 further launches are planned to take place before the end of 1991.

Launch Date	GPS No	PRN No	Plane
14 Feb 89	14	14	E
10 Jun 89	13	2	B
18 Aug 89	16	16	E
21 Oct 89	15	19	A
11 Dec 89	17	17	D
24 Jan 90	18	18	F
25 Mar 90	20	20	B
2 Aug 90	21	21	E
1 Sep 90	15	15	D
26 Nov 90	23	23	E
4 Jul 90	24	24	D

TABLE II. Block II Satellite Status

Over the years, there has been various projections made over the eventual number of satellites in the constellation. The original plan was for a constellation of 18 with 3 on-orbit spares. This number unfortunately gave areas of degraded coverage where PDOP (a position accuracy factor) was greater than 6 which, from a military standpoint, was unacceptable. The Program Manager has now been directed to achieve a 21 satellite primary constellation as soon as practicable. Such a system is aimed at achieving 100% global coverage for 95% of the time. Spares, be they on orbit or ready-for-launch, are to be available. The funding for satellite and launch vehicles, coupled with the expected satellite life determines that a slower build-up of the constellation will now be achieved. It is likely that full global 2D coverage will be available from Block II satellites late 1991 with full 3D coverage in 1993. Any remaining Block I satellites during the early build-up will be a bonus. GPS does not necessarily have prime launch

priority and it must take its place against other missions being launched from the Cape, which could result in a change to the planned programme. Sufficient satellites have been ordered to form a full constellation of Block IIs with spares available. Eventually there will be a transition to a full 24 SV constellation. During 1990, several satellites were rephased into new positions to ensure that a minimum degraded coverage is seen worldwide when the constellation is complete.

A contract was awarded mid 1990 for the procurement of 20 Block IIR replenishment satellites that will be launched from 1996. These will replace early Block IIs and will have additional features (e.g. enhanced survivability and autonomous on-orbit operations) that will remove in part the dependence of the control system.

4. GROUND SEGMENT STATUS

The Ground Segment was the first portion of GPS to undergo Program Management Responsibility Transfer from the JPO. Transfer occurred in 1988 and program control now rests with the Joint Service System Management Office (JSSMO) located at the Warner Robins Air Logistic Centre. The JPO is still responsible for some residual development tasks including System Level Interface Compatibility (SLIC) testing. The first such test was performed at the Eastern Launch Site (Cape Canaveral) where all GPS satellites are checked upon delivery from the manufacturer. The initial test on the first Block II satellite consisted of end to-end signal flow and command/command/control exercises using satellite signals transmitted from the Telecommunication Simulator (TSM) located at the Cape. The TSM consists of rack mounted Block II GPS satellite components which can implement Selective Availability/Anti-Spoofing (SA/A-S) in the transmitted signal. During one such test, the first satellite (Navstar 14) successfully transmitted signals from Cape Canaveral Centre via a roof mounted antenna. Ephemeris parameters were adjusted so that Navstar 14 appeared to be transmitting from a geostationary orbit. Users from many military and civilian communities tested their receivers for SA/A-S compatibility. During this testing, command and control of the TSM and Navstar 14 was performed by personnel at the MCS at Colorado Springs (Falcon AFB).

Operation of the Ground and Space Segment is now managed by the USAF Space Command at Falcon AFB, Colorado Springs. The Second Space Wing assumes responsibility as each new satellite becomes operational (approximately 3 weeks after launch).

Development of the Operations Reporting and Management System (ORMS) began in 1987 at the MCS. ORMS will provide military commanders and GPS operators worldwide with information on the status and health of the GPS constellation. Only limited progress has so far been made. The exact nature of releasable information has not yet been agreed, neither has the means of transmission been established. In the main, it will be used for the dissemination of classified information to military users worldwide. In the interim, information is passed by message in the form of a

NANU (Navigation Advisory Notice to NAVSTAR User) to US lead commands and to a designated Military Point of Contact in each NATO country which has signed the MOU with the US. For civilian users (and military if they so wish) a Bulletin Board has been established by the US Coast Guard. Individual NATO nations are already establishing their own information systems. Rather than be dependent on (and therefore commit) the US to an extensive and expansive reporting system, thoughts are now being given to the inclusion of more detailed satellite data in an expanded 50 HZ navigation message that can be read by all users whose equipment interfaces with a PC through an instrumentation port on their receiver. Although in its infancy, this facility is gaining increased support. During the constellation build-up, users need to have knowledge of the availability of the satellites. A prediction program has been developed in the US and is now being used by Allied nations worldwide. Similar programs are widely available for civilian users.

5. USER SEGMENT STATUS

The US military is currently procuring Phase III Rockwell-Collins designed family of military receivers. The current procurement program provides funds for an initial purchase of some 4,000 user equipment (UE) spread across land, sea and air applications. The eventual purchase will be for approximately 27,000 receivers, but the numbers are growing as the capabilities of the system are realised. The JPO awarded contracts to Canadian Marconi and SCI to qualify them as potential second-source vendors for the 2 and 5 channel Collins Phase III design whilst a contract was awarded to Texas Instruments for the production of a Non-Developmental Item (NDI) "off the shelf", manpack receiver. It soon became apparent that not all the US military platforms could accept the Rockwell-Collins size equipment whose design is limited to 1984 technology. NDI procurement is now considered an accepted means of procurement for specific applications and contracts were awarded in late 1990 for alternate GPS Fixed Reception Pattern Antennas (FRPAs), Controlled Reception Pattern Antennas (CRPAs) and Control Display Units (CDUs). The JPO has now awarded a contract for an NDI 3/8 ATR 5-channel receiver (MAGR). Two years ago, over 1000 single channel C/A code receivers were purchased from Trimble (the SLGR) for demonstration, familiarization and initial training purposes. The Gulf crises showed a shortage of military receivers available for deployment and the terrain was of such a nature as to make navigation devices a prime requirement. Urgent acquisition of more SLGRs supported by units from Texas Instruments and Magellan was made and Selective Available set at zero to give the Allied Forces navigation superiority. The results from the Gulf War ground campaign adequately justified GPS as a very worthy navigation system and this has resulted in a new acquisition of a P code lightweight GPS Receiver (PLGR). An open competition will be run and the specification will be issued during the Fall of 1991. Substantial numbers will eventually be required.

Over the past 2 years, UE in-plant testing has been underway for performance, environmental and electromagnetic interface/compatibility/pulse qualification. Production equipments have been delivered to the Air Force, Army and Navy for their own specific testing within a coordinated test program whilst other units are provided to the prospective services for inclusion in their integration programs.

With a limited satellite window (some 4 hours per day) in 1987/88, the US recognized that the qualification testing was limited, and Rockwell-Collins equipments were leased to NATO countries. The object was to capture more test data using the window as it crossed Europe and to give Research agencies the opportunities to expand their knowledge with operational equipment. These trials have all been completed, and their results will support US gained evidence at the Defence Acquisition Board (DAB).

6. OTHER ISSUES

The foregoing describes the status of the three main components of the system, but there are a number of aspects that concern both the military and civilian communities to varying degrees and the following will identify the position taken by the Pentagon, NSA and the JPO on these contentious issues. It must be remembered that the GPS is, first and foremost, a military system. GPS will provide highly accurate position, velocity and time information on a continuous, worldwide basis. This information is provided at two accuracy levels; the Standard Positioning Service (SPS) and the Precise Positioning Service (PPS). The SPS is a civil position/navigation (POS/NAV) service providing a lower accuracy available to any user. The SPS horizontal accuracy will be set at an average 100 meters 2drms in peacetime, (The term 2drms [twice the distance root mean square] refers to the radius of a circle that contains 95% of the data points). The PPS is the military PCS/NAV service providing a full system accuracy of 16 meters Spherical Error Probable (SEP - 50% of data points in a sphere of 16 meters radius) and will be restricted to US and allied military forces and, if in the national interest, to selected civil users. Such "authorised users" would include Government Sponsored Geodetic or Mapping Agencies and certain Department of Transport Services whose work is aligned to Government or military needs. To be privileged to the PPS, there needs to be an MOU/MOA between the nation or agency concerned and the US Department of Defense. For the security and key aspects of a PPS system, the agency must have a COMSEC agreement with the National Security Agency (NSA)

7. GPS SYSTEM SECURITY FEATURE

Selective Availability (SA) is the method whereby the MCS at Colorado Springs is able to deny the unauthorised real time use of full GPS accuracy provided by the PPS. SPS users are similarly affected by SA. It is achieved by modifying the satellite's transmission to introduce errors in pseudorange measurements by either altering the navigation message data (i.e. ephemeris) by a

procedure referred to as "Epsilon" or by manipulation of the satellite clock - "Dither". Removal of these errors within a PPS receiver is achieved by receiving encrypted correction data in the navigation message which will negate the imposed errors when the appropriate software or hardware security module has been activated by the use of cryptographic keys through fill devices. An SPS user will not be able to counteract these errors directly. It is the US Government's policy to enable S/A as soon as possible after each Block II satellite is declared healthy. It will normally average 100m (95%) in peacetime, but will be changed as defence conditions dictate. The 100m accuracy (2drms) quoted for the SPS equates to a navigational accuracy of 76m with SA applied. Without SA, an SPS receiver can expect an accuracy of at least 30m. Selected Availability was set at zero throughout the Gulf War and its subsequent "mopping-up" campaign, but it has now been restored.

OPERATING MODE		AUTHORIZED USERS		UNAUTHORIZED USERS	
SA	A-S	P(Y)-code	C/A code	P-code	C/A code
OFF	OFF	16 m	30 m	16 m	30 m
ON	OFF	16 M	30 M	72 M	76 M
OFF	ON	16 M	30 M	30 M	30 M
ON	ON	16 M	30 M	76 M	76 M

TABLE III - Positional Accuracies in SA/A-S Environment

8. DIFFERENTIAL GPS

Differential GPS (DGPS) is now a well proven means of achieving greater position accuracy than provided by PPS, but it is not the current intention of the US military to employ such a technique. Induced biases and system errors are attributable to Selective Availability (up to 100m), Ionospheric Delays (up to 30m), Tropospheric Delays (up to 3m), Ephemeris errors (up to 3m) and Satellite Clock errors (approx 3m). By placing a GPS receiver at a known surveyed point, errors can be determined and by transmission of these errors to other receivers utilising the same satellites at the same time, most of the system errors can be removed. A variety of trials have been conducted in many parts of the world and the accuracy level registered is of the order of 2 - 4 meters. The disadvantage of DGPS in military terms is that the system is no longer passive. DGPS transmitters can only be established on friendly territory, need maintenance, manpower and additional cost if an encrypted data link is required. The user equipment needs to be enhanced with reception and correlation facilities and the reference station is vulnerable in times of

tension. NATO nations are seriously considering DGPS for mine countermeasure activities where a high and repeatable level of accuracy is required and all military nations do recognize its potential in range applications. It is in use with the US Coast Guard and in the civil sector. A chain has been established off Norway and the European Civil Airlines are considering its potential as an approach and landing aid.

9. SUMMARY

As the world community at large realises the potential of GPS, an increasing number of electronic equipment manufacturers in the US, Europe and the Far East will be competing for a share of the market, be it military or commercial. The US have initially committed themselves to a 1984 design of the Rockwell Collins family of equipments but a major Source Selection exercise is now concluding to select the next generation of smaller faster receivers. There is considerable interest within other NATO nations but planned decisions to purchase major outfits have been delayed by the changing political position in Eastern Europe. Only Norway and the Netherlands have made any significant purchases for their military to date.

The civil community, however, is moving rapidly to acquire this equipment. In the US, initiatives which illustrate its potential have already been taken by, for example, the American railway operators and by the postal couriers, and its use in off-shore explorations is already reaping dividends. The FAA and European Marine and Air operators are now more actively discussing its use. GPS will revolutionise navigation and positioning activities and will enable countries to communicate more readily in geodetic, time and position terms through use of reference stations. Whether operating as a stand-alone equipment, or integrated with INS or other navigation systems, GPS will give a navigation accuracy far superior to any system currently in use.

UNCLASSIFIED

An Introduction to the GPS Guidance Package (GGP)

**William C. Homer
Naval Ocean Systems Center (NOSC) Code 765
San Diego, CA 92152-5000
(619) 553-6667, Autovon 553-6667**

UNCLASSIFIED

An Introduction to the GPS Guidance Package (GGP)

William C. Homer
Naval Ocean Systems Center (NOSC) Code 765
San Diego, CA 92152-5000
(619) 553-6667, Autovon 553-6667

Biography

William C. Homer is currently working at the Naval Ocean Systems Center (NOSC) in San Diego, California. He is the Program Manager for the GPS Guidance Package (GGP) Program, that is sponsored by the Defense Advanced Research Projects Agency (DARPA).

Abstract


Under DARPA sponsorship, NOSC has made a dual contract award for advanced development brassboard models of a Global Positioning System Guidance Package (GGP). The approximate \$28 million in contracts were awarded to the contractor teams of Texas Instruments & Honeywell and Litton Systems & Rockwell Collins. The existing 48 month (GGP Phase 1) contracts provide for the advanced development of a strapdown inertial guidance package comprised of a navigation grade Interferometric Fiberoptic Gyro (IFOG) tightly coupled to a miniaturized GPS receiver (MGR). The GGP exploits the synergisms achieved by combining inertially sensed Inertial Measurement Unit (IMU) movement with externally sensed GPS reference signals. The goal is to produce a combined GPS/IMU navigation grade system which will be miniaturized for easy insertion into any host vehicle, and inexpensive for use by expendable vehicles (weapons and platforms). Follow-on Phase 2 contracts will develop preproduction prototype GGP units tailored for specific platforms.

The GGP effort aims to match the navigation performance of the conventional technologies but fit within an envelope of 10 pounds total weight, 20 watts of power, 100 cubic inches of volume, and a per unit cost of \$15,000. The brassboard units being developed under the current Phase 1 contract will fit within an envelope of 20 pounds, 30 to 40 watts, and 300 cubic inches of volume. The GGP builds upon the integrated circuit technology from the existing DARPA mini GPS receiver program combined with the following: (a) solid state linear accelerometers and fiber optic rotation sensors (gyros) for three axes inertial sensing, and (b) a data processor and associated software to implement a Kalman filter to integrate the sensor outputs and provide the



navigation solution as well as filtered velocity, acceleration, and orientation data needed by the host vehicle. Major cost reduction breakthroughs are offered by FOG sensors which employ integrated optic chips for light wave processing along with the polarization preserving fiber optic rotation sensing coil and a broadband optical source. GGP host vehicle insertion is also aided by its packing/customizing achieved through modularity of MGR, IMU, and navigation microprocessor subsystems. Modularity is achieved with standardization of (1) the Kalman filter architecture in the navigation processor and (2) data transfer points (ports) interfacing the MGR and IMU sensors to the navigation processors.

Dual award contracts were issued for GGP Phase 1 because each prime contractor offered a significantly different approach to solving the technical challenges associated with the GGP.



Introduction

	GPS Guidance Package (GGP) Program Overview	NOSC
<ul style="list-style-type: none">DARPA Initiated, NOSC Executed Technology Development And Verification ProgramObjective: Miniature GPS-Based Navigation Guidance System Development<ul style="list-style-type: none">Highly AccurateModularMass ProducingLow Unit Cost / Light WeightBroad Spectrum Mission Area Support<ul style="list-style-type: none">Strike WeaponsUnmanned VehiclesHigh Dynamics AircraftStructure A Well-Ordered Transition Of Technology To The Services		

DARPA initiated the GPS Guidance Package (GGP) program to develop a miniature guidance package based on a combination of a miniature GPS receiver (MGR), a miniature inertial measurement unit (MIMU), and control processors. The emphasis is on developing a small, low-cost, mass producible guidance package that will support a broad spectrum of Department of Defense (DoD) platforms including strike weapons, high dynamic aircraft, and unmanned vehicles. The GGP Program is divided into several developmental phases.

	<p align="center">GPS Guidance Package (GGP) Program Phases</p>	
<p>• Phase 0 (Sep 87 - Sep 88)</p>	<p align="center">GGP Systems Study - Conceptual Design/Systems Analysis of Four Suik Weapon/Unmanned Vehicle Scenarios</p> <p align="center">Output - GGP Performance Requirements Defined</p>	
<p>• Phase 1 (May 90 - May 94)</p>	<p align="center">Design, Fabricate, and Test GGP Brassboard Units</p> <p align="center">Output - Navigation Package with MGR, MEMU, Processing, & Software meeting Mid-to-High Performance Requirements</p>	
<p>• Phase 2 (Jun 94 - Start)</p>	<p align="center">Full Scale Engineering Development</p> <p align="center">Output - Physically Integrated, Fully Qualified GGP Units. Navigation, Flight Management, and Control Functions Operational</p>	

The objective of Phase 1 is to design, fabricate, and test a brassboard demonstration GGP unit consisting of a MGR, a MIMU, and the processors and software for a tightly-coupled integrated navigation package meeting the medium to upper level performance requirements established in Phase 0. Flight management and control are not part of the Phase 1 development model. The Full Scale Engineering Development phase, GGP Phase 2, will provide the miniaturized, fully qualified GGP units for rigorous operational testing and eventual installation into DoD platforms. Phase 1 is scheduled for completion in mid-calendar year 1994, with Phase 2 commencing shortly thereafter.



	<h2 style="text-align: center;">GPS Guidance Package (GGP) Overview</h2>																																				
<h3 style="text-align: center;">Objective</h3> <p>Develop Family of Low Cost, Miniature GPS-Aided, Tightly Coupled New Packages for Variety of DSD Managed and Unmanaged Platforms</p> <table><tr><td></td><td>Phase 1</td><td>Phase 2</td></tr><tr><td>New Accuracy (m)</td><td>20</td><td>16</td></tr><tr><td>Size (in)</td><td>50/100</td><td></td></tr><tr><td>Weight (lbs)</td><td>20</td><td>7</td></tr><tr><td>Power (watts)</td><td>30</td><td>TBD</td></tr></table>		Phase 1	Phase 2	New Accuracy (m)	20	16	Size (in)	50/100		Weight (lbs)	20	7	Power (watts)	30	TBD	<h3 style="text-align: center;">Contractor Teams</h3> <table><tr><td>Test Instruments</td><td>MMR</td></tr><tr><td>Hardware</td><td>MMRU</td></tr><tr><td>Loan Systems</td><td>MMRU</td></tr><tr><td>Rockwell (Cellular)</td><td>MMR</td></tr><tr><td>Bosch</td><td></td></tr></table>	Test Instruments	MMR	Hardware	MMRU	Loan Systems	MMRU	Rockwell (Cellular)	MMR	Bosch												
	Phase 1	Phase 2																																			
New Accuracy (m)	20	16																																			
Size (in)	50/100																																				
Weight (lbs)	20	7																																			
Power (watts)	30	TBD																																			
Test Instruments	MMR																																				
Hardware	MMRU																																				
Loan Systems	MMRU																																				
Rockwell (Cellular)	MMR																																				
Bosch																																					
<h3 style="text-align: center;">Technical Approach</h3> <p>Advance and Exploit Technologies for Affordable Miniatures Integrated Circuits, Fiber Optic Gyros, Solid State Accelerometers, Enhanced Optical Sources and Integrated Optical Circuits.</p>	<h3 style="text-align: center;">GGP System Performance Goals</h3> <table><tr><td></td><td>Phase 1</td><td>Phase 2</td></tr><tr><td>New Accuracy (m)</td><td>20</td><td>16</td></tr><tr><td>Gyro</td><td>1FOG</td><td>1FOG</td></tr><tr><td>Stability (deg/hr)</td><td>.01</td><td>.003</td></tr><tr><td>SF Error (ppm)</td><td>50</td><td>10</td></tr><tr><td>White Noise (deg/hr-1/2)</td><td>.005</td><td>.0015</td></tr><tr><td>Angle Rate (deg/hr)</td><td>500</td><td>1000</td></tr><tr><td>Accelerometers</td><td>Subminiatures</td><td></td></tr><tr><td>Stability (g)</td><td>50</td><td>10</td></tr><tr><td>SF Error (ppm)</td><td>100</td><td>50</td></tr><tr><td>White Noise (g/hr-1/2)</td><td>3</td><td>3</td></tr><tr><td>Acceleration (G)</td><td>70</td><td>100</td></tr></table>		Phase 1	Phase 2	New Accuracy (m)	20	16	Gyro	1FOG	1FOG	Stability (deg/hr)	.01	.003	SF Error (ppm)	50	10	White Noise (deg/hr-1/2)	.005	.0015	Angle Rate (deg/hr)	500	1000	Accelerometers	Subminiatures		Stability (g)	50	10	SF Error (ppm)	100	50	White Noise (g/hr-1/2)	3	3	Acceleration (G)	70	100
	Phase 1	Phase 2																																			
New Accuracy (m)	20	16																																			
Gyro	1FOG	1FOG																																			
Stability (deg/hr)	.01	.003																																			
SF Error (ppm)	50	10																																			
White Noise (deg/hr-1/2)	.005	.0015																																			
Angle Rate (deg/hr)	500	1000																																			
Accelerometers	Subminiatures																																				
Stability (g)	50	10																																			
SF Error (ppm)	100	50																																			
White Noise (g/hr-1/2)	3	3																																			
Acceleration (G)	70	100																																			

The GGP will perform a minimum of three functions: navigation, flight management (including guidance), and flight control. The navigation function provides high accuracy position, velocity, attitude, and time. Flight management contains the mission in the form of a trajectory to be used in the enroute phases of guidance and, using the navigation information, derives guidance commands to minimize the difference. The flight control function will accept the guidance commands and formulate commands to be applied to the vehicle control system. The navigation functions will be performed by the GGP,

but flight management and flight control may be shared between the GGP and the host platform subsystems.

GGP Description

The Phase 1 GGP will meet the requirements of a brassboard demonstration navigation package employing a tightly coupled MGR and MIMU, based upon the use of advanced technologies suitable for miniaturization and capable of low cost in high volume production in subsequent phases of development. The Phase 2 GGP will have to demonstrate the established miniaturization, packaging, performance, and manufacturing goals prior to approval for large scale production.

	GPS Guidance Package (GGP) Basic Requirements																
<p>Develop Family Of Low Cost, Miniature GPS-Aided, Tightly Coupled Nav Packages for Variety of DoD Manned and Unmanned Platforms</p> <table border="1"> <thead> <tr> <th></th><th>Phase 1</th><th>Phase 2</th></tr> </thead> <tbody> <tr> <td>Nav Accuracy (meters)</td><td>20</td><td>16</td></tr> <tr> <td>Size (cubic inches)</td><td>300</td><td>100</td></tr> <tr> <td>Weight (pounds)</td><td>20</td><td>7</td></tr> <tr> <td>Power (watts)</td><td>30</td><td>TBD</td></tr> </tbody> </table>				Phase 1	Phase 2	Nav Accuracy (meters)	20	16	Size (cubic inches)	300	100	Weight (pounds)	20	7	Power (watts)	30	TBD
	Phase 1	Phase 2															
Nav Accuracy (meters)	20	16															
Size (cubic inches)	300	100															
Weight (pounds)	20	7															
Power (watts)	30	TBD															

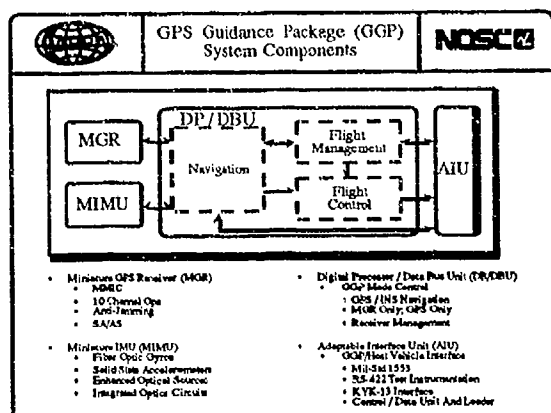
Performance Requirements

MGR positioning accuracy requirements will increase only slightly over existing capabilities, but significant advances must be achieved in the design and production of substantially smaller GPS receiver components. The most difficult challenge in the development of the GGP is the miniaturization and integration of the MIMU components into smaller and smaller packages with increasing accuracy and ruggedness requirements. The smaller volume and lower weight constraints should also expand the number of future vehicles for GGP use.

System Components

The GGP has four major components: the miniature GPS receiver (MGR), the miniature IMU (MIMU), the digital processor and data base unit (DB/DBU), and the adaptable interface unit (AIU). These components provide the primary navigational functions for the GGP with the following characteristics: (a) generation and maintenance of the estimated navigation solution by combining MGR and MIMU sensor data, (b) autonomous GPS or IMU operation when there is a fault in either the MGR or

MIMU, and (c) graceful performance degradation during navigation sensor outages. The MGR will



determine and track the optimal combination of GPS transmitters for maximum performance of the set. Using both P and C/A code, the multi-channel MGR is to provide ionospheric corrected pseudo range and delta range measurements; and complete selective availability and anti-spoofing (SA/AS) protection. The GGP is to accommodate multiple antennas and usage criteria based upon host vehicle attitude, signal quality, GPS transmitter selection, etc.

The MGR will be an integrated chip set consisting of microwave monolithic integrated circuits (MMICs) and application specific integrated circuits (ASICs) to implement the following: the RF/IF front end, analog-to-digital converter (ADC), frequency synthesizer, signal processor, and support/interface.

The MIMU will provide inertial acceleration and attitude rates (or delta velocity and delta angles) from sensed motion. It will also include the acceleration/attitude-rate sensors and associated electronics. The inertial rate sensors are to be of the interferometric fiber optic type and shall use a "long" wavelength (1.3 - 1.55 micron) optical source. The baseline accelerometers will be subminiature units of an advanced design or development based on a technology suitable for low cost volume production and emphasizing solid state techniques. However, currently available units meeting the GGP accelerometer requirements may be used to facilitate achievement of overall program objectives.

The DP/DBU will be based on either a federated or a distributed architecture for system control and initialization, integrated navigation, and MGR and MIMU control. For each DP/DBU processor, whether federated or distributed, at least 50 percent of the total memory and 50 percent of the total processing speed will be in reserve when operating at the required capacity. The design of the DP/DBU is to provide for

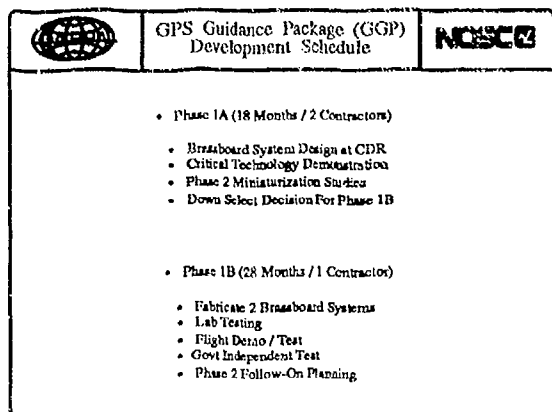
an increase in memory and processing speed capacity such that with the addition of flight management and flight control functions in future phases, the same reserve requirements will be met. The DP/DBU will implement a tightly coupled integrated navigation solution using a single Kalman estimator, with synchronous interfaces to the MGR and the MIMU. Propagation of the solution using inertial measurements will provide "nominal" total state trajectory components and aiding data to the MGR. An extended Kalman filter shall estimate perturbation states, reset total states, and accept as measurements the residuals between MGR measured pseudo range and delta range in each MGR channel and corresponding quantities based on the propagated total state trajectory. The design of the Kalman filter and aiding of the MGR code/carrier tracking will deal with potentially destabilizing correlations between errors in the aiding signals and measurement errors, including the effects of a high jamming environment. An appropriate factorization will be used to implement the Kalman filter to enhance numerical stability and improve computational efficiency. The navigation processing architecture will be capable of incorporating other externally supplied position and/or velocity data (e.g. barometric altimeter altitude). The Kalman filter design for the integrated navigation configuration shall include, as a minimum, seventeen error states; and be subject to additional sensor error states where required to meet the navigational accuracy for a specific host vehicle or mission.

Design of the AIU is to be based on the future need to implement flight management and flight control functions, as well as the host vehicle and instrumentation interfaces needed for operation and test herein. As a minimum, the AIU shall provide a MIL-STD-1553 host vehicle interface, a RS422 test instrumentation interface, a control and display unit (CDU) interface, and a data loader interface. When the GGP is reconfigured by external command to perform the navigation function independent of the MIMU, the instrumentation interface will meet the standard instrumentation port and functionality requirements of ICD-GPS-215. A remote control and data unit will be provided for GGP control and display of data during the test and development phases. The data loader will be used in support of system initialization and startup.

GGP Phase 1 Schedule

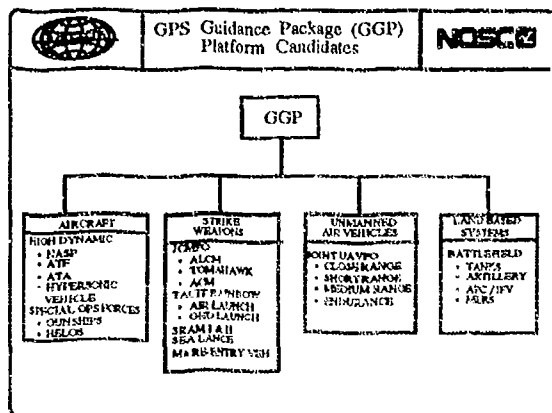
The GGP Program has completed the Preliminary Design Review stage and is enroute to Critical Design Reviews to occur near the end of calendar year 1991. The original contracts specified a "down-select" to a single contractor at the end of Phase 1A, for the

development of the GGP brassboard prototypes. Recent and ongoing efforts to receive additional "non-DARPA" funding from possible GGP users are being conducted to preserve competition and provide GGP units on an advanced delivery schedule.



GGP Applications

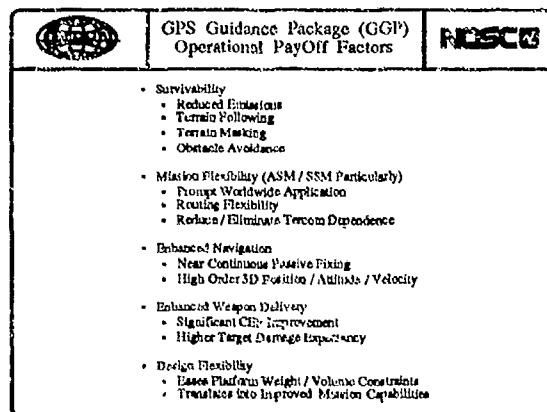
The design goals for the GGP are to service the broad spectrum of DoD missions and platforms for the next few decades. As a "next generation" navigational aid, the GGP will internally incorporate the functions of existing GPS and IMU integrations. This will greatly simplify the installation and integration of this capability into operational platforms and unmanned vehicles. The entire families of autonomous strike weapons, unmanned vehicles, and other platforms with stringent space requirements stand to benefit from the successful development of the GGP.



GGP Operational Payoffs

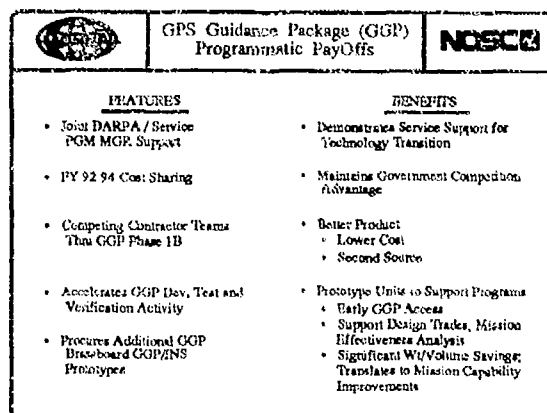
The receive-only nature of the GPS receiver, combined with the real-time positioning accuracies being demonstrated by today's receivers and integrated IMUs provide insight into the operational payoffs to be realized with the GGP. The long recognized

benefits of the complimentary nature of IMU and GPS receiver measurements, when combined into a single small "black-box", overcome many of the existing constraints to today's arsenal of weaponry. The GGP will improve the survivability, increase the mission flexibility, and improve the delivery accuracy of weapons without increasing the vulnerability of the devices.



GGP Programmatic Payoffs

DARPA's continued development of mini-GPS components and miniaturized IMUs could provide the foundation for the infusion of "next generation" integrated navigational equipment for airborne and nautical DoD platforms. The transition of this new and innovative technology, along with the vast utility of its usage, is one of DARPA's primary goals for the GGP program.



The accelerated development of GGP units, through the cooperation and funding assistance from other DoD programs, can insure the rapid infusion of this much needed technology into future systems, which currently exist primarily in a conceptual stage.

SESSION II-A
ADVANCED GUIDANCE

CHAIRMAN
BILL KERCHNER
ASD/VC/SEMCO

**STRAPDOWN ASTRO-INERTIAL NAVIGATION
AS A SECURE METHOD OF SATISFYING THE TWENTY-FIRST
CENTURY'S PRECISION MISSION REQUIREMENTS**

Paper No. 91-32

**CENTRAL INERTIAL GUIDANCE TEST FACILITY
HOLLOMAN AIR FORCE BASE, NEW MEXICO**

AUTHORS

**Seymour Levine, Manager - Navigation and Avionics Programs
NORTHROP ELECTRONICS SYSTEMS DIVISION, HAWTHORNE, CA**

**Fredric R. Nadeau, Manager - WRIGHT LABORATORY/AAAN-1
WRIGHT-PATTERSON AIR FORCE BASE, OHIO**

09 September 1991

**STRAPDOWN ASTRO-INERTIAL NAVIGATION
AS A SECURE METHOD OF SATISFYING THE TWENTY-FIRST
CENTURY'S PRECISION MISSION REQUIREMENTS**

ABSTRACT No. 91-32

Strapdown astro-inertial navigators provide autonomous high precision terrestrial navigation for aircraft, ships, missiles, space and remote piloted vehicles. These systems, which approach GPS accuracy, do not depend upon man-made electromagnetic radiating devices that may be intentionally shut down, destroyed or unreliable in a hostile environment (e.g., jamming, mimicking decoys, anti-satellite weapons, etc.). The U.S. Air Force, Navy, and SDIO, with Northrop, have embarked upon the design and test of the first fully strapdown, low cost, astro-inertial navigation system. The paper covers startracker signal-to-noise ratio and strapdown stellar inertial system performance on a hyper velocity vehicle.

1.0 INTRODUCTION

For several hundred years, man has successfully utilized star positions to reset his long range navigation systems. During his earthly journeys, the stellar augmentation subsystem, namely the sextant, provided updates to minimize the accumulated errors in his continuous dead reckoning (DR) navigation. As he approached his destination or wartime target, he resorted to a relative navigation (RN) solution. His eyes took on the function of a terminal seeker. They focused on the terminus of his mission (e.g., dock, etc.) or onto the position of his enemy. Thus nineteenth century man had an autonomous, precision navigation suite that utilized DR, stellar updating, and terminal seeking to achieve a circular error probable (CEP) measured in feet.

Although the present autonomous navigation suites bear little physical resemblance to those of their predecessors, the system elements are the same (see Table I, Autonomous Navigation Suite Chronology). They consist of a DR continuous navigator, i.e., inertial navigation system, (INS), periodically updated or reset by a DR reference system, such as a stellar tracker and altimeter. Finally, after the navigation system guides the vehicle into an operational area or basket of the terminal seeker, the seeker provides precise closure for docking, landing, or interdiction of fixed and maneuvering targets. This autonomous suite is free from radio aids, which may be unreliable, jammable, or unavailable during a twenty-first century wartime encounter.

TABLE I AUTONOMOUS NAVIGATION SUITE CHRONOLOGY

ELEMENT	YEAR	NAVIGATION COMPONENTS									
	1800	1940	1950	1960	1970	1980	1990	2000			
DEAD RECKONING	MAGNETIC COMPASS	FLUX VALVE									
		GYROCOMPASS		MAGNETOMETER	GIMBALED INERTIAL NAVIGATION		STRAPDOWN INERTIAL NAVIGATION				
					DOPPLER RADAR						
	LOG	PITOT TUBE/EM LOG									
	INCREMENTAL CLOCK										
STELLAR TRACKER	SEXTANT										
	CHRONOMETER										
TERMINAL SEEKER	VISUAL/OPTICAL AIDS										
PROCESSOR	MANUAL	MECHANICAL			ANALOG	DIGITAL					

From the 1950s and on, inertial systems have been the dominant DR navigators aboard ships and air vehicles. During the fifties, these devices were made with gyroscopes and accelerometers mounted on one gimbal and surrounded by two or three other gimbals in order to isolate the inertial sensors from the vehicle's angular rates. The inertial element assembly was usually called the stable member, or yaw gimbal. In order to provide high precision, a narrow field of view (FOV) startracker embedded in train and elevation pointing gimbals were mounted on top of the yaw gimbal. In this configuration, there were usually five gimbals, multiple gimbal resolver angular readouts, servo-mechanism, and associated electronics. A limited quantity of two-gimbal versions, the minimum number of gimbals necessary to point a telescope at any point in three-dimensional space, were also developed. These gimballed astro-inertial navigators were successfully used as the navigation reference for reconnaissance, precision rendezvous, and for indirect, coordinate firing of munitions. The applications not only used the precision position data, but also made use of the accurate velocity and attitude outputs for synthetic aperture radars (SAR). Although this complement of hardware did achieve high accuracy autonomous navigation, its million-dollar-per-copy cost prevented it from being widely deployed. In the early 1980s, low-cost digital computers and inertial instruments specifically designed to perform moderate accuracy navigation in gimbal-less, or strapdown environments were developed. By the late 1980s, these strapdown INS dominated the Air Force's moderate accuracy "Standard Navigator" and the Navy's "Carrier Aircraft Inertial Navigation System" (CAINS) procurements. These strapdown INS, not only provided position and the roll, pitch, and heading Euler angles, but were also capable of supplying the timely accurate angular rates required for the vehicle's flight control and autopilot. The angular rate data, flight-critical to dynamically unstable vehicle control systems, is relatively simple to obtain in a strapdown INS, as compared to the gimballed INS process, which required the costly and noisy differentiation of the gimbal resolver readouts. Unfortunately, the startracker technology had not kept pace with the strapdown INS development, and high precision autonomous strapdown navigation systems remained unavailable to the hypervelocity, strategic, ballistic, and reconnaissance users.

On present manned aircraft, the stellar augmentation system bounds the INS gyroscopic induced navigation errors accumulated over hours of flight during long distance missions. In the future, Mach 10 manned hyper-velocity vehicles (HVV) will perform similar long-distance missions in reduced flight times with stringent target CEP requirements. These stringent CEP requirements are driven not only by reconnaissance issues but also by the limited search area capability of the terminal seekers. The area of search for a seeker becomes even more critical for an HVV, due to the high Mach numbers. Stellar sensors augmenting precision strapdown inertial navigators in high Mach, endo- and exo-atmospheric environments will face additional technology and engineering challenges as high temperature, plasmas, and shock waves occur on or near the skin of the HVV.

The Air Force's Wright Laboratory and Ballistic Missile Office and the Navy's Naval Air Development Center embarked upon a Strapdown Stellar Sensor/Inertial System (SS/IS) program with Northrop to develop a high-precision Strapdown Astro-Inertial Navigator (SAIN). The high accuracy SAIN, unlike its gimballed counterpart, provides timely accurate angular rate data, along with enhanced reliability, smaller package size, at a more affordable price (\$50K to \$300K per unit, dependent upon the unaided inertial sensors accuracy). The substantial cost reduction for a strapdown vs. gimballed stellar inertial system is primarily due to the elimination of all precision mechanical servo-mechanisms and the concurrent

calibration of the strapdown inertial system and the telescope. Concurrent strapdown calibration provides only a small increase in computation workload and test time for the SAIN over a basic INS. The computational load, both from a processing and a memory point of view, has been reduced by the substantial advances in high-speed computer technology. This computational revolution has also reduced the size and cost of navigation processing to less than ten percent of the total system's size and cost. Furthermore, focal plane arrays (FPAs), which serve as the retina of the strapdown telescope, have also gone through a similar revolution, so that now video cameras are available for a few hundreds of dollars. Thus the stellar update option to an INS represents an affordable performance enhancement to a navigation system.

A block diagram showing a cadre of sensors and processing functions that could be present in an autonomous navigation system are shown in Figure 1. Since the terminal seeker may only be utilized during the final phase of the mission, the data processing could be shared with the stellar computation. Similarly, an autonomous velocity sensor may also have its processing functions interwoven with stellar observations, further reducing the cost of the stellar option. In addition, by having SAIN accuracy, the seeker acquisition and data processing, which will be elaborated upon in Section 3.0 of this paper, are also simplified. Thus SAIN provides a synergistic catalyst that enhances the whole navigation suite. A cost and size reduction is also taking place in the manufacture of GPS receivers. Therefore, a radio option could be integrated into the navigation suite. The integrated precision navigation complement would not only provide a critical level of redundancy, but would also increase the probability of the mission's success by maintaining a surgical strike capability during periods of radio outage.

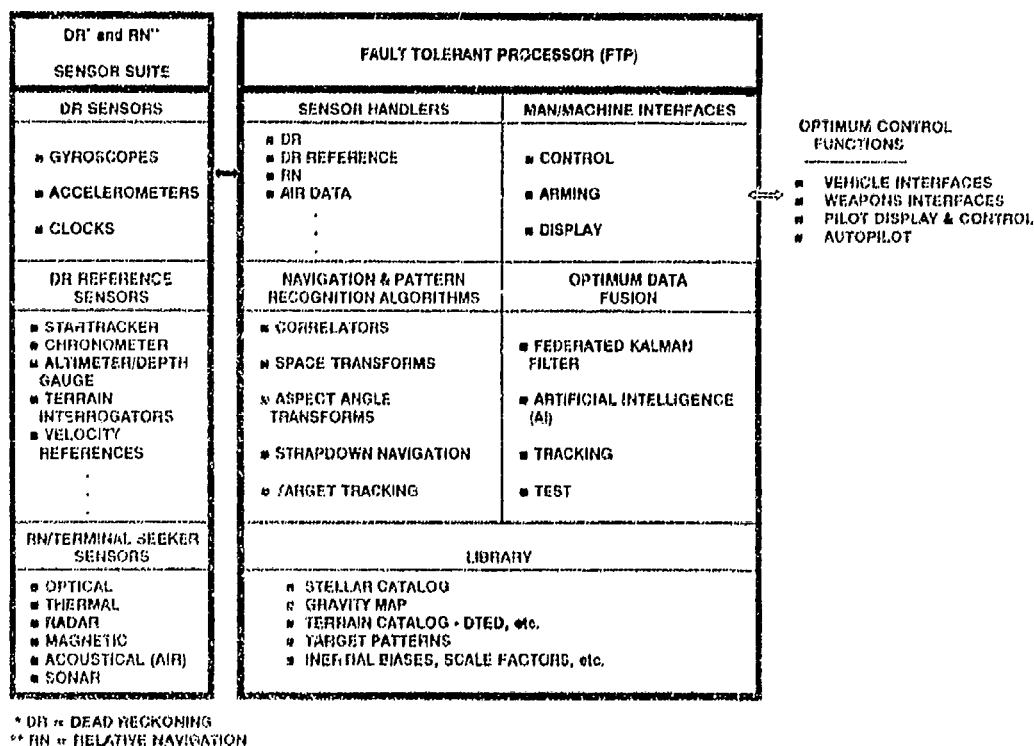


FIGURE 1 BLOCK DIAGRAM OF STRAPDOWN AUTONOMOUS NAVIGATION SYSTEM, SHOWING A CADRE OF SENSOR AND PROCESSING FUNCTIONS

2.0 SYSTEM PERFORMANCE FOR AN HVV

Figure 2 is a heuristic astro-inertial navigator error model of a vertical Schuller loop. The stellar tracker essentially observes the difference between the INS position error and the tilt of the platform. The INS azimuth error can essentially be observed directly. This direct observation of azimuth bounds its error and provides one of the major attributes of a stellar inertial system.

A generic HVV mission scenario was developed for the purpose of defining the SS/IS program performance requirements. During the 65,000 foot altitude portion of the mission, the star visibility is high. The stellar visibility vs. altitude equation is:

WORLD WIDE AVERAGE STELLAR VISIBILITY (SV) vs. ALTITUDE (A) in FEET:

$$\begin{array}{ll} \text{SV} \approx 50\% + 10\% \times A/9000 & A \leq 45,000 \text{ FEET} \\ \text{SV} = 100\% & A > 45,000 \text{ FEET} \end{array}$$

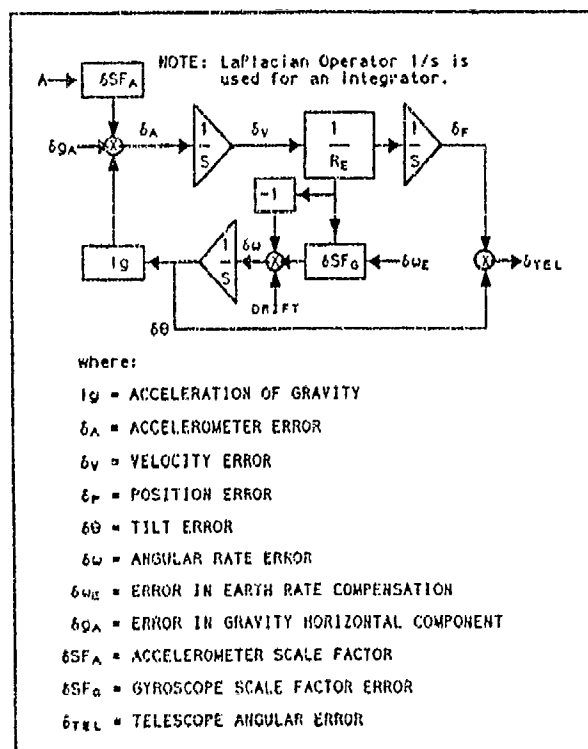


FIGURE 2 HEURISTIC STELLAR INERTIAL ERROR MODEL

Figure 3 shows the position error of a 12,000 ft/sec (Mach 12) HVV cruising at 65,000 feet on a strategic weapon delivery scenario. The figure is a trade matrix of stellar-inertial vs. free inertial performance for four classes of optical gyroscopes (i.e., 40 cm, 30 cm, 20 cm, and 10 cm ring laser gyroscopes, RLGs, where the low performance 10 cm RLG random drift characteristics are similar to those of the finest of the fiber optical gyroscopes, FOGs, in the present stage of their development).

The simulations show the dramatic reduction in position error when stellar augmentation is utilized. An expanded view of the stellar inertial error propagation (Figure 4) illustrates that the 600-foot terminal error is almost independent of the intrinsic gyroscope performance for 20-cm or greater perimeter RLGs. The reason for independence from gyroscopic drift is that the stellar tracker can observe the attitude error, tilt, and azimuth errors of the inertial platform, due to gyroscopic drift, prior to its propagation into position errors (e.g., one integrator from drift to tilt vs. three integrators from drift to position errors). The Kalman filter utilizes the stellar tracker's observation of inertial error and optimally corrects the platform attitude error and gyroscopic drift terms.

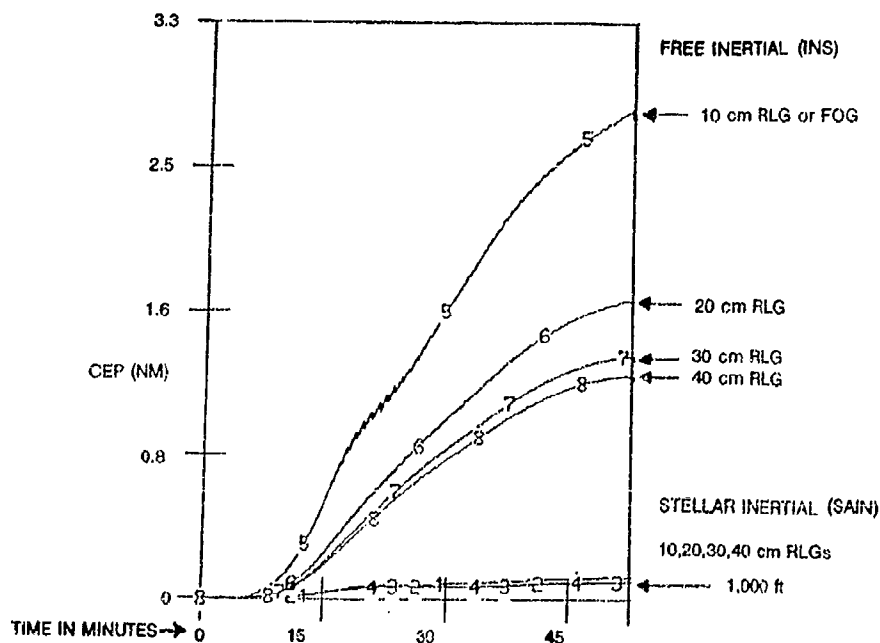


FIGURE 3 HVV POSITION CEP vs. TIME SUMMARY

SAIN 1-10 cm, 2-20 cm, 3-30 cm, 4-40 cm RLGs; INS 5-10 cm, 6-20 cm, 7-30 cm, 8-40 cm RLGs

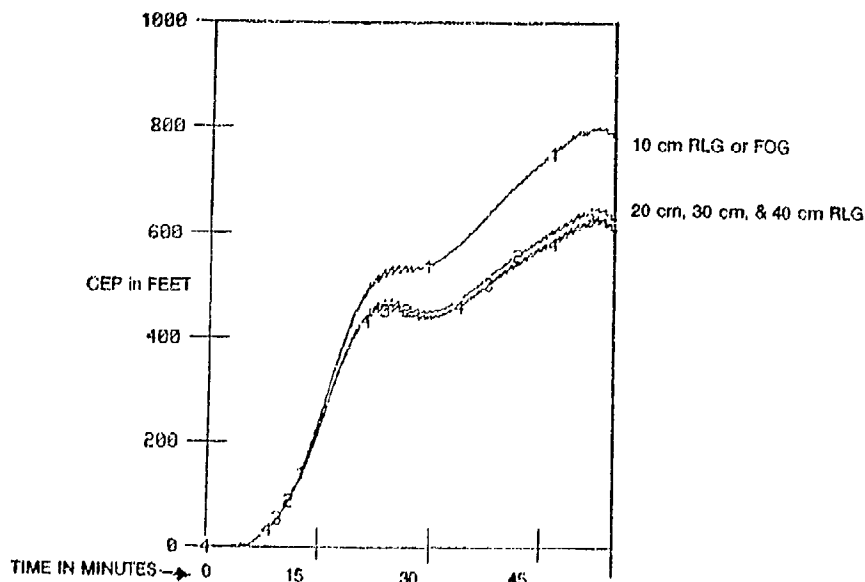


FIGURE 4 HVV SAIN POSITION ERROR CEP vs. TIME SUMMARY

1-10 cm, 2-20 cm, 3-30 cm, 4-40 cm RLGs

A feature of the stellar inertial systems, as opposed to pure inertial systems, is their ability to perform a precise in-air alignment when radio navigation aids, such as GPS or LORAN, are the "only" aids available. The reason for this is that an inertial navigator travelling west at 450 knots at 60 degrees latitude has its east-west component of horizontal earth rate exactly equal to the vehicle's westerly velocity. Under this vehicle profile, the horizontal component of earth rate cancels the effects of the vehicle's longitude rate and thereby eliminates the pure INS azimuth error to vertical tilt response. Thus the vertical or position INS channels cannot sense azimuth errors. Therefore, even with radio navigation position aids, there exists no gyro-compassing signal for vehicles travelling in this westerly trajectory at a speed close to earth rate. Stellar-inertial systems, on the other hand, by virtue of their direct azimuth stellar observations, can correct azimuth error with no restrictions on the vehicle's flight path. This in-air alignment scenario can occur during the early phases of a mission where radio navigation aids are only available in the Continental United States (CONUS) or Ocean region, but not in the battle theater. SAIN thus provides a high precision mission quick escape option for strategic vehicles with only a pre-selected segment of radio navigation aids. By utilizing this feature, radio navigation aids can be deliberately shut down and denied to our adversaries while a fast escape capability is maintained.

3.0 AUTONOMOUS NAVIGATION IN THE TERMINAL PHASE OF AN HVV MISSION

The SAIN, with autonomous augmentation aids, can provide ultra-precision mission accuracy. In a mission scenario, where the HVV proceeds to its target area at an altitude with high ground visibility, it can interrogate the ground with an optical position correlator or SAR as an update reference. The interrogator periodically recognizes pre-surveyed salient terrain features to update the accumulated errors. Figure 5 shows the effect of four resets spaced twenty minutes apart. Under these conditions, a 100 foot CEP is realized with a terminal velocity error of less than a tenth of a foot per second.

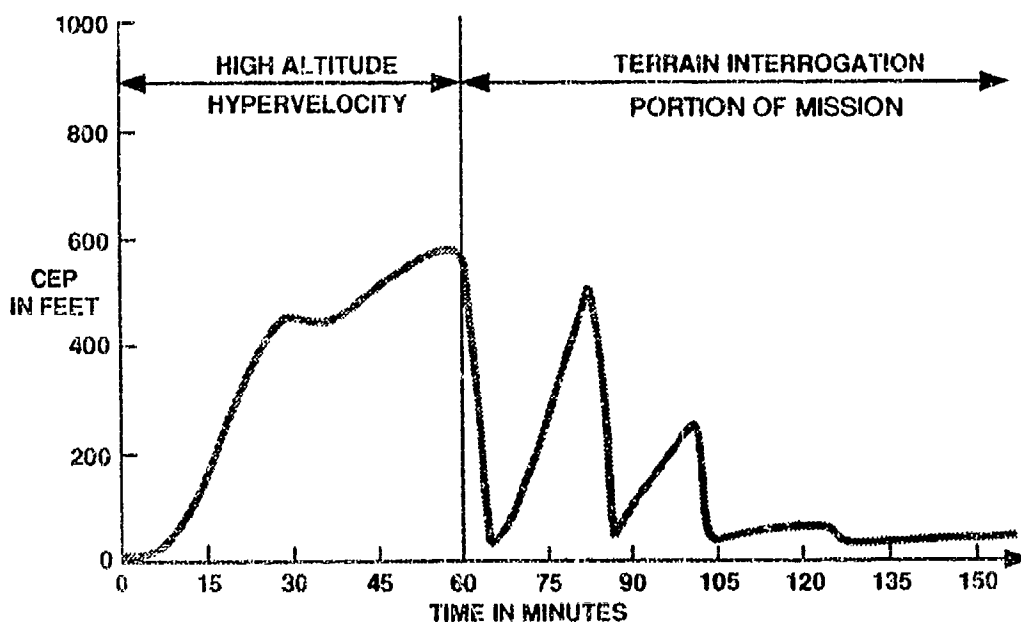
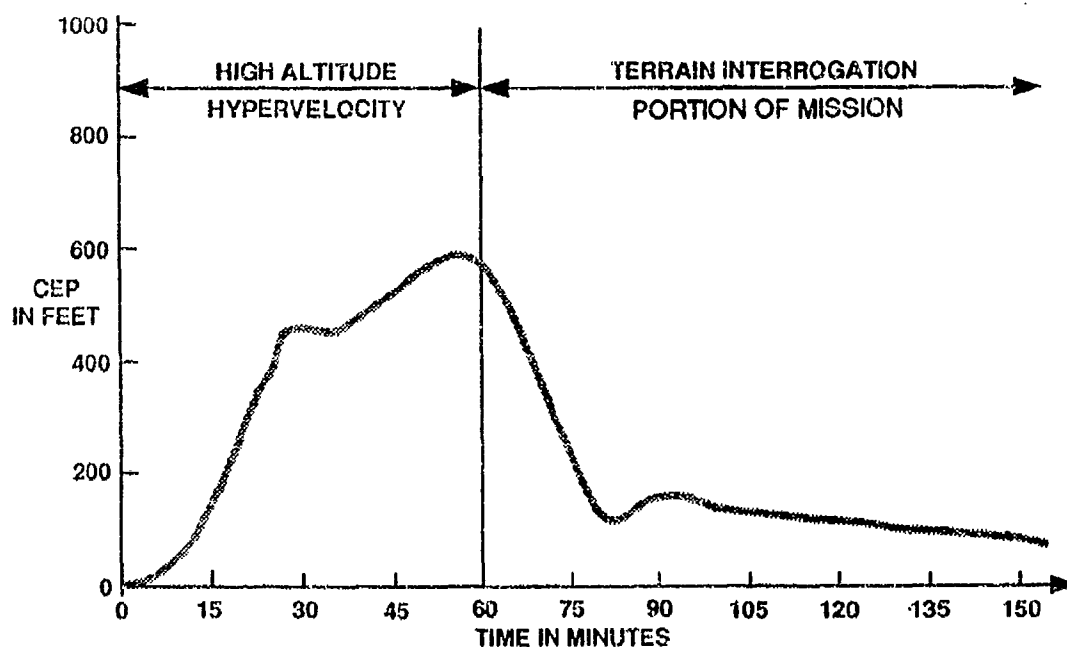


FIGURE 5 HVV SAIN POSITION ERROR CEP vs. TIME
EFFECT OF FOUR RESETS SPACED 20 MINUTES APART DURING
THE TERRAIN INTERROGATION PORTION OF A MISSION

Another autonomous method of enhancing SAIN accuracy when a vehicle is operated at an altitude with high ground visibility, is to differentiate optical or SAR terrain images or snapshots in order to derive vehicle along track and cross track velocities. By the generation of stereoscopic images and processing of the data along with the SAIN chronometer as a time reference, a velocity reference with respect to the vehicle can be generated. When these image-generated along track and cross track velocities are resolved around the SAIN azimuth and then optimally mixed, an autonomous CEP of less than 200 feet is achieved. Figure 6 shows the result of this optical velocity correlator augmentation system. Furthermore, similar results can be obtained when SAIN information is mixed with other autonomous aids (e.g., Digital Terrain Elevation Data, DTED, etc.). An autonomous surgical strike capability of less than ten feet on both fixed and mobile targets can be obtained by the addition of a terminal seeker to the navigation suite. This system mimics nature's autonomous navigation system in predatory creatures, where millions of years of evolution have optimized their navigation into a DR and RN solution. The key to the system is to have the DR precision of sufficient accuracy to minimize the search area requirements for the seeker. A 0.1 nautical mile CEP SAIN requires 0.01 square miles (0.1 NM times 0.1 NM) of terminal seeker search area. This greatly reduces the pattern recognition requirements of a seeker when compared to a High Accuracy Inertial Navigation System (HAINS) after a four hour flight. The HAINS, with a 0.25 mile per hour capability would have a 1 NM CEP and thus a one square mile search area. As a result, SAIN requires one hundredth the search area and therefore substantially reduces memory and registration time requirements. The 100 to 1 reduction in search area is only one of the benefits of the SAIN system. The required range and power of the seeker is also greatly



**FIGURE 6 HVV SAIN POSITION ERROR CEP vs. TIME SUMMARY
OPTICAL VELOCITY CORRELATOR AUGMENTATION RESULTS DURING
THE TERRAIN INTERROGATION PORTION OF A MISSION**

reduced by the SAIN augmentation system as opposed to INS. For example, a ten to one reduction in seeker range requirements results in at least a 100 to one reduction in seeker illumination power (it could be as much as a 10,000 to one reduction). This greatly simplifies and minimizes the size, power, and cost of the terminal aid. In addition, the seeker's pattern recognition computational algorithms could simply be added to the SAIN processor, since during the terminal seeker portion of the mission, the stellar processing functions are no longer utilized. By the transfer of similar processing functions from star tracking to seeker, there is concomitant reduction in both cost and size of the autonomous navigator. Thus SAIN provides the key element to the autonomous navigation suite.

4.0 STELLAR TRACKER PERFORMANCE PARAMETERS

The driving factor in the design of shipboard and airborne stellar trackers that augment inertial systems is its capability to accurately measure star positions in daylight at sea level. For the HVV missions simulated, the signal-to-noise ratio (SNR) improves by a factor of 2.5 (one star magnitude) as the vehicle ascends from sea level to a 20,000 foot altitude. This is primarily due to the effects of the atmosphere. As the air density decreases, the sky darkens because of a decrease in the light scattering. Figure 7 shows the sky background as a function of wavelength for sea level and at a 100,000 foot altitude.

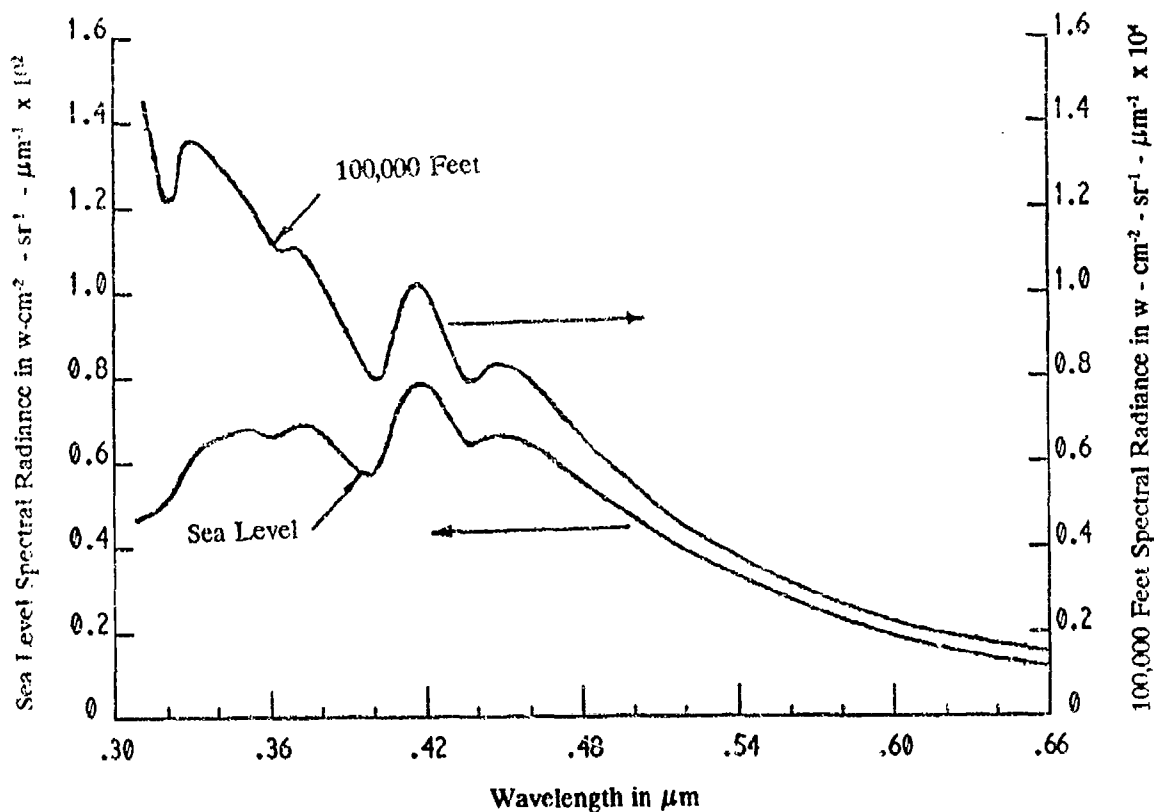


Figure 7 A Typical Sky Background at Sea Level and 100,000 ft
(Sun Zenith Angle 53°, Observer Angle 58°, Sun-to-Observer Azimuth 90°)
SEYRAY Electro-Optical System Analysis, Page 139, Pub. "EO RESEARCH CO."
(AFAL Report of NEMD)

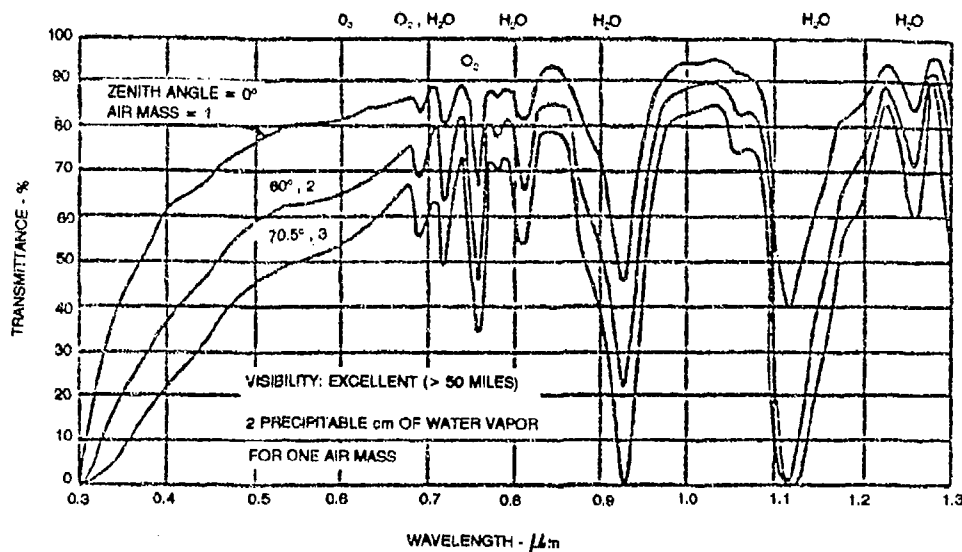


Figure 8 ATMOSPHERIC TRANSMISSION FOR VARIOUS AIR MASSES, OR EQUIVALENTLY, FROM THE GROUND TO SPACE AT VARIOUS ANGLES FROM THE NORMAL; ONE AIR MASS CORRESPONDS TO THE AMOUNT OF AIR THROUGH WHICH A BEAM MUST PASS WHEN GOING STRAIGHT UP TO SPACE. (COURTESY RCA)

The spectral radiance is a hundred times brighter at sea level than at the 100,000 foot altitude. In addition, atmospheric molecular absorption degradation factors decrease at higher altitudes. Figure 8 shows the optical atmospheric transmittance as a function of wavelength and zenith angle. The atmospheric transmission is attenuated at wavelengths where there is O_2 , O_3 , and H_2O molecular absorption. For an astrotracker that utilizes a focal-plane array (FPA) as its photon detector, the SNR can be approximated by the following expression:

SIGNAL-TO-NOISE RATIO (SNR)

$$Q_{SP} = q \cdot \phi_s \cdot \Delta\lambda \cdot A_T \cdot A_a \cdot T_T \cdot \eta \cdot I_t \cdot N_f / N_s$$

where:

- Q_{SP} = STAR SIGNAL CHARGES PER PIXEL
- q = ELECTRONIC CHARGE
- ϕ_s = STELLAR SPECTRAL RADIANCE
- $\Delta\lambda$ = WAVELENGTH BANDWIDTH OF TELESCOPE SYSTEM
- A_T = ATMOSPHERE TRANSMISSION
- A_a = APERTURE AREA
- T_T = TELESCOPE TRANSMISSION
- η = QUANTUM EFFICIENCY
- I_t = INTEGRATION TIME OF A FRAME (STELLAR SNAPSHOT)
- N_f = NUMBER OF FRAME SNAPSHOTS UTILIZED
- N_s = NUMBER OF PIXELS CONTAINING THE STAR IMAGE (STAR BLUR FACTOR)

$$Q_{BP} = \frac{q \cdot \phi_B \cdot \Delta\lambda \cdot A_s \cdot T_T \cdot FOV \cdot \eta \cdot I_i \cdot N_f}{N \cdot O_F}$$

where:

- Q_{BP} = BACKGROUND PHOTO CHARGES PER PIXEL
 ϕ_B = SKY BACKGROUND SPECTRAL RADIANCE
 FOV = FIELD OF VIEW
 N = TOTAL NUMBER OF PIXELS IN SENSOR ARRAY
 O_F = SKY BACKGROUND ATTENUATION OF OPTICAL FILTER

$$Q_{DP} = q \cdot ni/\tau \cdot V_B \cdot I_i \cdot N_f$$

where:

- Q_{DP} = DETECTOR DARK CURRENT CHARGES PER PIXEL
 n = DETECTOR INTRINSIC CARRIER CONCENTRATION
 τ = DETECTOR DARK CURRENT CHARGE GENERATION TIME
 V_B = DETECTOR CHARGE GENERATION BUCKET VOLUME

$$Q_{NP} = \sqrt{(Q_{SP} + Q_{BP} + Q_{DP}) Q_{ES}}$$

where:

- Q_{NP} = NOISE CHARGES PER PIXEL
 Q_{SP} = STAR PHOTO CHARGES PER PIXEL
 Q_{BP} = BACKGROUND PHOTO CHARGES PER PIXEL
 Q_{DP} = DARK DETECTOR CHARGES PER PIXEL
 Q_{ES} = ELECTRONIC SYSTEM BANDWIDTH NOISE COEFFICIENT

$$SNR = \frac{Q_{SP}}{\sqrt{(Q_{SP} + Q_{BP} + Q_{DP}) Q_{ES}}}$$

FOR SEA LEVEL DAYTIME TRACKING IN A NON-NUCLEAR EVENT ENVIRONMENT, THE SNR EQUATION SIMPLIFIES TO:

$$Q_{BP} \gg Q_{SP} + Q_{DP}$$

$$SNR = \frac{Q_{SP}}{\sqrt{Q_{BP} \cdot Q_{ES}}}$$

$$SNR \approx \frac{\phi_S \cdot A_T}{N_S} \cdot \sqrt{\frac{q \cdot \Delta\lambda \cdot A_s \cdot T_T \cdot \eta \cdot I_i \cdot N_f \cdot N \cdot O_F}{\phi_B \cdot FOV \cdot Q_{ES}}}$$

TABLE II COMPARISON OF STELLAR DENSITIES FOR THE R & B BAND
STELLAR WAVELENGTHS

NUMBER OF STARS EQUAL TO OR BRIGHTER THAN MAGNITUDE M_r		
M_r	B BAND $0.4 \pm 0.049\mu$	R BAND $0.70 \pm 0.11\mu$
	DENSITY PER DEG ²	
1	0.0002	0.0006
2	0.0006	0.0022
3	0.0022	0.0077
4	0.0075	0.0250
5	0.0240	0.0750
6	0.0710	0.2300

Unfortunately, the tracker's SNR provides only a part of the insight necessary for the design of a stellar inertial system. Knowledge of the stellar density is also of major importance. For example, the number of stars brighter than a given magnitude, M_r , is a function of the spectral contents of the stars. Stars radiate in a similar fashion to a blackbody at different maximum temperatures based on their age and composition. Table II is a comparison of the stellar densities for the R band (red) stars and that of B band (blue) stars. A few simple terms dominate the astro-tracker design thought process. The SNR is proportional to the square root of the tracker's aperture and the star photon integration time (stellar exposure time). The reason for only a square-root improvement in the SNR as a function of aperture is that the expansion of the aperture not only increases the star signal photon collection but also has an associated increase in the collection of sky background noise flux. Therefore, a 6.25 times increase in aperture area is required in order to observe a single magnitude increase (i.e., 2.5) in dimmer stars. Similarly, the 6.25 increase factor holds for the stellar exposure time, since extension of the integration increases the collection of both the star photons and the sky background noise flux. In the opposite direction, a wide FOV detracts from the stellar observation by allowing more sky brightness background noise flux into the optical system. For example, when the FOV is very small, as when looking at the sky from the bottom of a deep mine shaft (illustrated in Figure 9), the unaided eye can observe stars in the daytime. The sky brightness noise increases as the inverse of the square root of the FOV. In order to achieve satisfactory performance, a balance is struck between the benefit of a wide FOV increasing the number of bright stars observed in the tracker at a given time vs. the deteriorative effects of the sky brightness noise. Figure 10 summarizes some of these considerations for a silicon FPA and a three degree FOV optical wide-angle lens startracker (OWLS). It is a plot of star magnitude capability vs. altitude. A space satellite startracker with only a 0.72 square inch aperture and a one-millisecond exposure time has the same capability as the much larger sea-level tracker with a 36 square inch aperture utilizing a 100 millisecond exposure time. Figure 11 shows a system size comparison for both gimballed and strapdown astro-inertial navigators that have the same daytime, sea level tracking capability. The dramatic disparity shown in Figures 10 and 11 illustrates how the tracker technology and application dictate the physical startracker design.

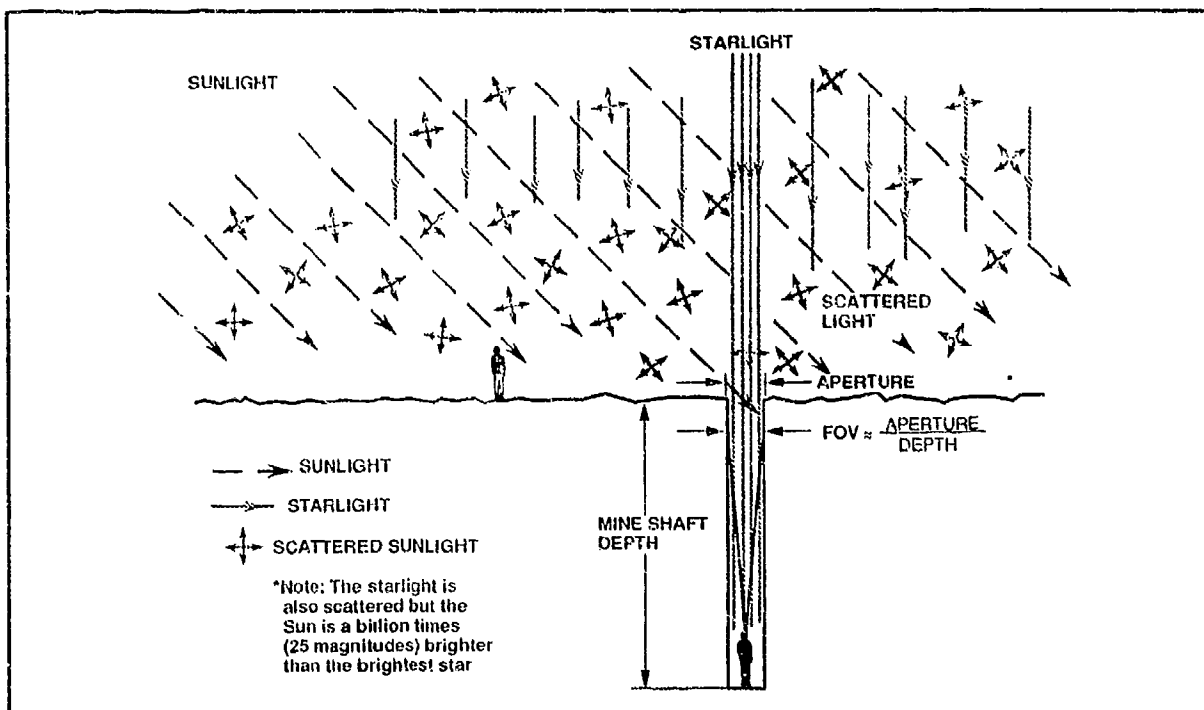


FIGURE 9 MINER OBSERVING STARLIGHT IN THE DAYTIME

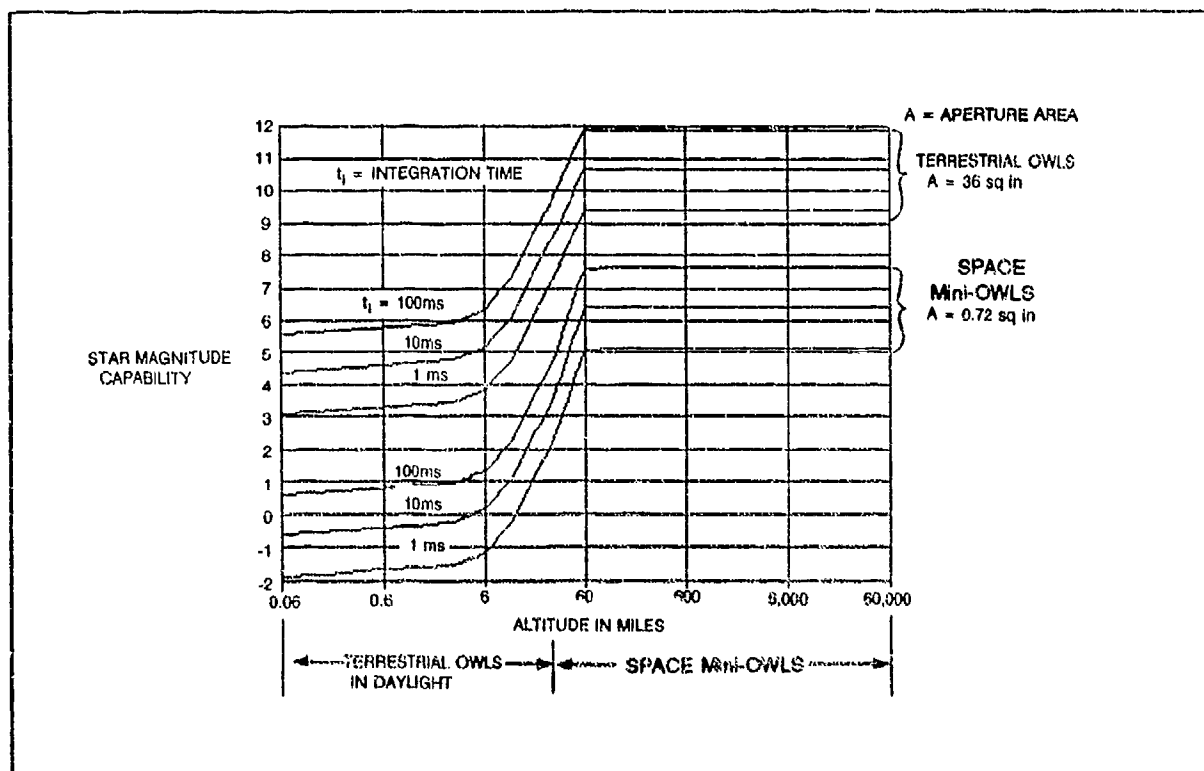
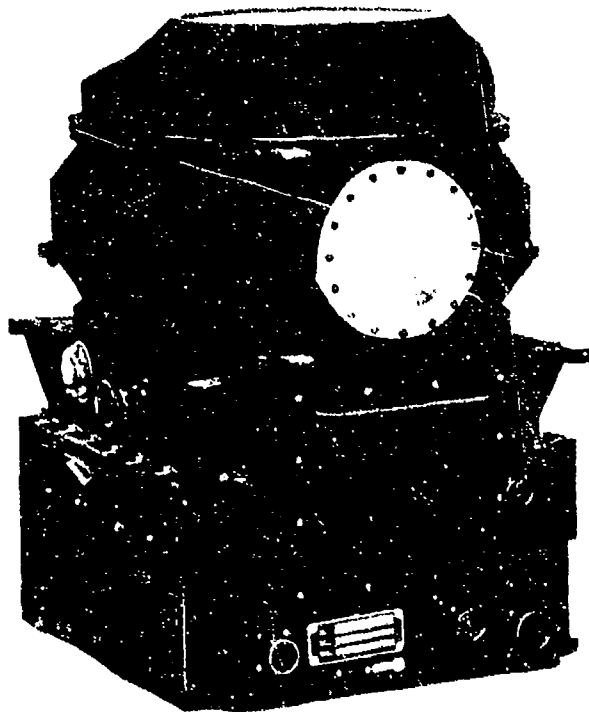


FIGURE 10 STAKTRACKER SENSED MAGNITUDE vs. ALTITUDE FOR A SILICON DETECTOR AND A 3 DEGREE FOV

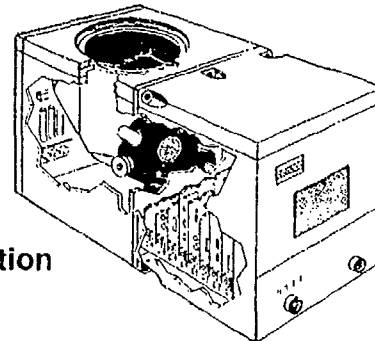
Today - 1991 - Gimballed



14"W x 15"D x 20"H

Including Power Supply & Processor (165 lb)

Tomorrow - 1996 - Strapdown
Including Power Supply & Processor



4:1
Reduction

$7\frac{1}{2}$ "W x $7\frac{1}{2}$ "H x 20"D
45 lb

FIGURE 11 COMPARISON OF GIMBALED AND STRAPDOWN STELLAR INERTIAL NAVIGATORS

5.0 STELLAR PERFORMANCE IN IONIZED PLASMA FIELD

Optical navigation aids in the high Mach HVV environment are affected by the standing bow and secondary shock waves, or Mach lines, and the plasma sheath surrounding the vehicle. The effect of the plasma varies with the Mach number and altitude, as shown in Figure 12, with the most severe region (within the isobar marked region) between 75,000 feet altitude at 10-15,000 feet/second (Mach 10-15) and 150,000 feet altitude at 20-22,000 feet/second (Mach 20-22).

The HVV profile used in this study remained outside the severe plasma region; however, boundary layer and shock wave effects are still evident in the HVV profile region and must be considered in the performance of a high accuracy stellar-inertial system. Standing shock wave in front of the stellar sensor window causes optical refractions that vary with the viewing angle to the celestial body, the heat flux and temperature gradients across the window cause scintillations in star imagery. Small refraction errors, less than one arc-second, on such a high accuracy sensor can be intolerable. Plasma fields between the viscous boundary layer and the shock wave also cause scintillation of the star image and cause blurring on the FPA as well as adding to the sky background noise. The result to the centroiding algorithm and the background noise processing can be computationally intensive.

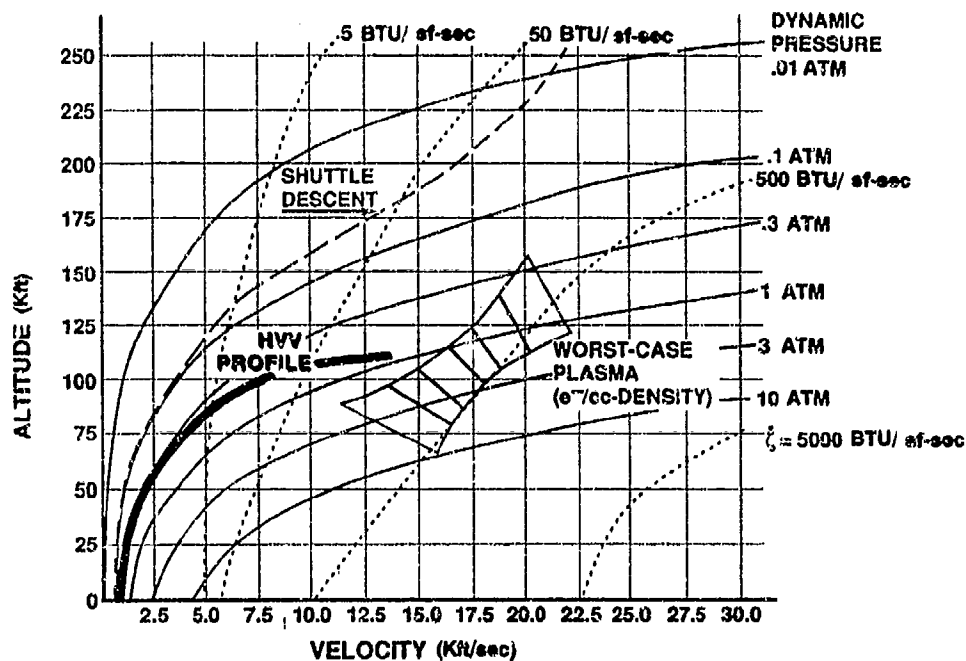


FIGURE 12 HVV AEROTHERMAL ENVELOPE
(Courtesy, McDonnell-Douglas Missile Systems Co.)

Computational fluid dynamics (CFD) studies and analyses performed by Northrop Electronics Systems and McDonnell-Douglas under contract to Wright Laboratory have provided validated plasma field characterizations permitting the design of compensation algorithms for such optical sensors. Various HVV shapes have been studied. Figure 13 portrays a generic manned HVV configuration, for which a plasma flow field has been determined using a full parabolized modified Navier-Stokes with non-equilibrium formulation (courtesy of McDonnell-Douglas Missile Systems Co.).

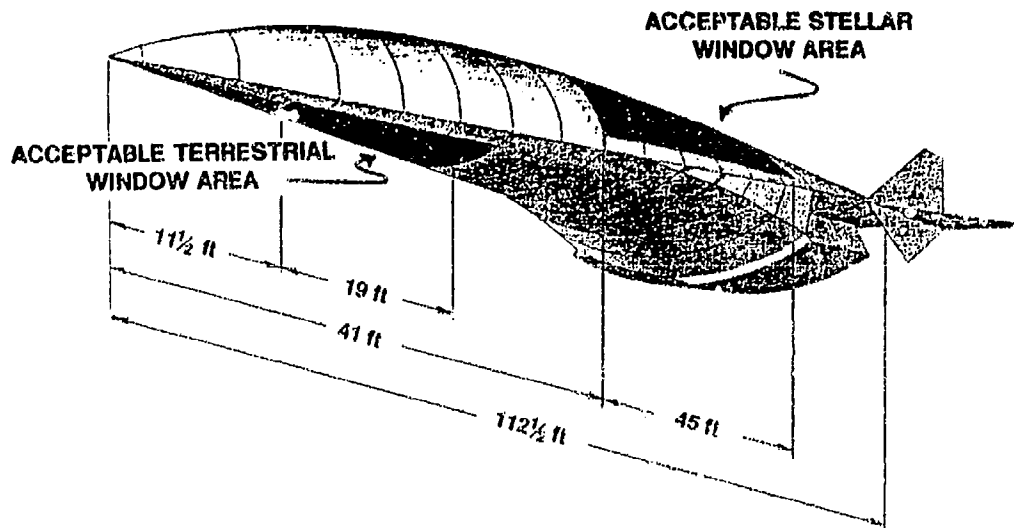


FIGURE 13 CONCEPTUAL MANNED HVV CONFIGURATION
(Courtesy, McDonnell-Douglas Missile Systems Co.)

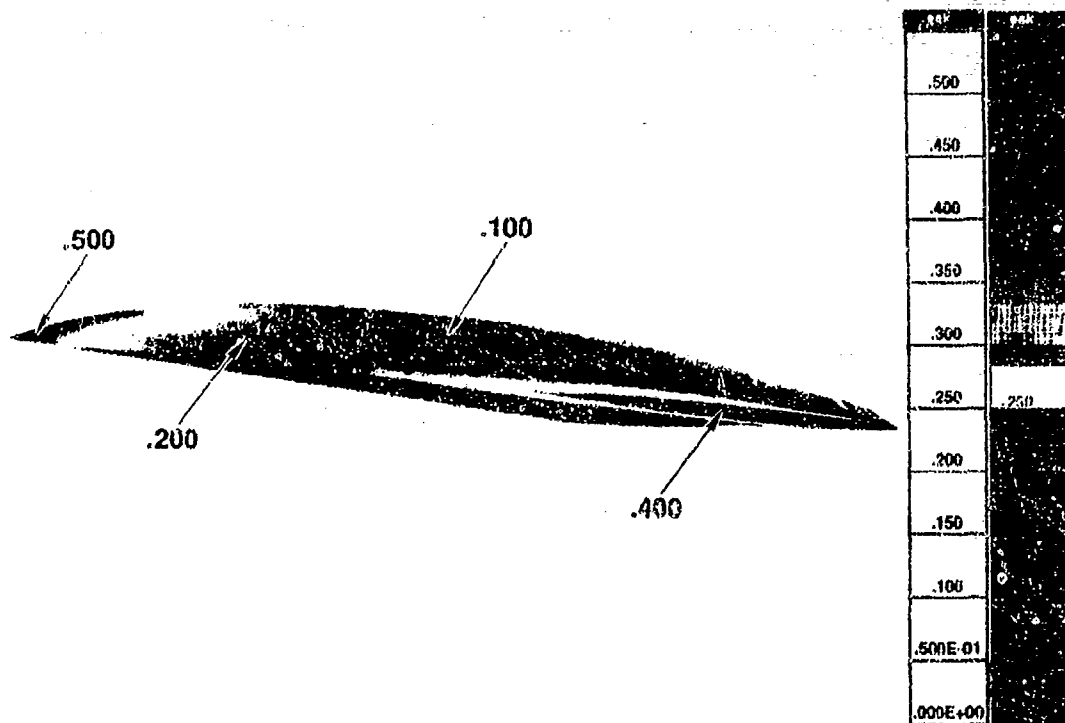


FIGURE 14 M17 135 K& JETS-ON SURFACE HEAT (BTU/sf-sec)

The stellar sensor window (fused silica with potentially carbon-carbon coatings) aft of the stagnation region (located between the shock wave and the viscous boundary layer) and ahead of the wake region (where electron ion recombination occurs) caused in part by the vertical fins and engine nacelles, appears to be the most suitable location to maximize stellar system performance. As shown in Figures 14 and 15, heat flux (BTU/sq ft-sec) at Mach 17, 135,000 feet altitude, reaches levels of 0.20 BTU/sq ft-sec at equilibrium and surface temperatures of 1,040-1,240 degrees Fahrenheit.

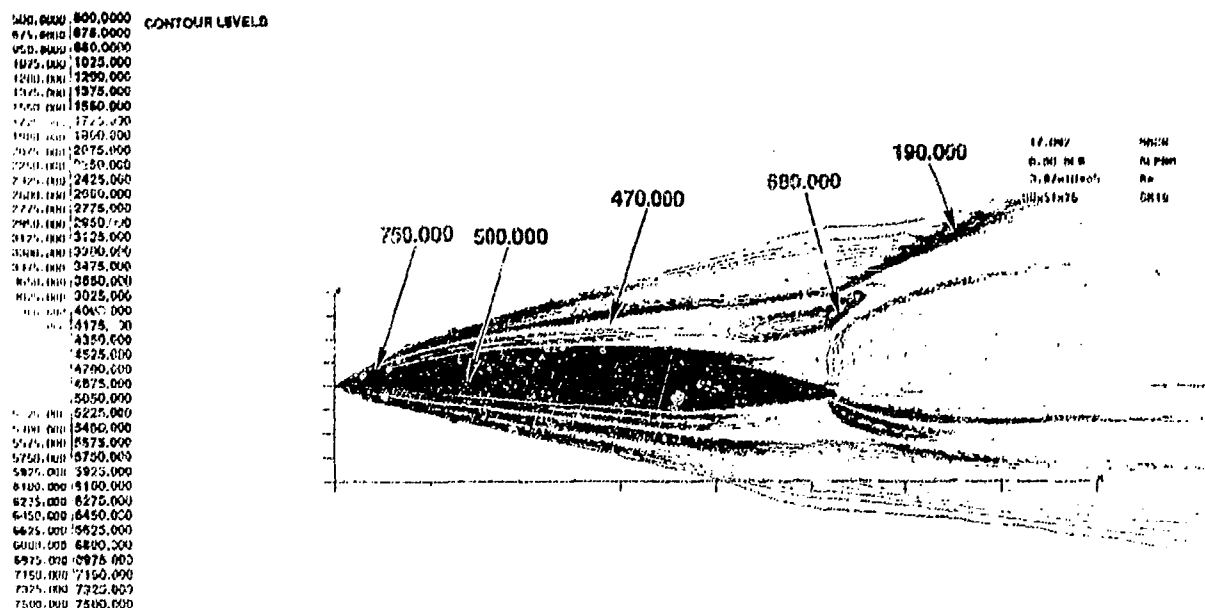


FIGURE 15 M17 135 K& JETS ON SURFACE TEMPERATURE (R)

Refraction of the star image caused by changes in densities from the viscous boundary layer and the shock waves are shown in Figure 16 for three Mach number conditions. The values represent the angular refraction of the starlight at the preferred or acceptable window location on the HVV test body. Using an OWLS with three telescopes spaced 120 deg apart in azimuth and 30 deg in elevation off the zenith yields a maximum refraction of 0.6 arc-sec at Mach 15 and 115,000 foot altitude. Looking aft affects only one lens and is considered inconsequential. At higher altitudes, the loss from refraction produces even less effect. The higher the altitude and the higher the viewing angle, i.e., approaching zenith position, the less the severity of the refraction. Figure 17 illustrates the impact of plasma induced errors on star viewing angle. Compensation algorithms can be developed for specific conditions; however, an adaptive filter development is required to satisfy all portions of an HVV mission profile. The diffraction and refraction problems caused by the plasma sheath are compensated by the lack of cloud cover and reduced sky background noise at altitudes of 65,000 feet or higher. This lack of cloud cover and the low sky background irradiance reduce the processing time necessary for centroiding a star's location after it is derived from the stellar irradiance absorbed by the OWLS FPA.

Window thin film cooling by means of water glycol compounds is a consideration; however, these induce turbulent flow and boundary layer separation over the stellar sensor window and cause additional optical distortion, background noise, and refraction. Cooling the window surface increases the heat flux, causing temperature gradients over the viewing surface and adding to the scintillation problem. Additional studies are being conducted by Wright Laboratory to further determine the effects of window cooling as well as various mitigation techniques. Figures 17 and 18 illustrate primary and secondary shock waves in a plasma field through which a stellar sensor must be capable of accurately determining star location. The irradiance transmission losses at the stellar window station locations for high Mach numbers (with rockets on) has been calculated to be nearly one decibel, or approximately one-quarter star magnitude. The HVV OWLS can easily compensate this transmission loss.

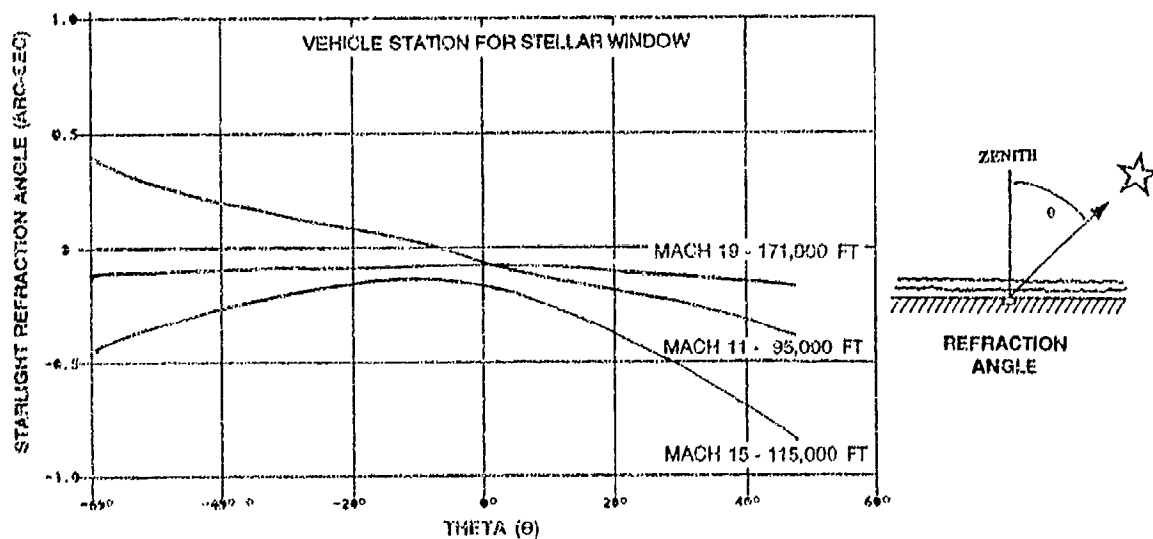


FIGURE 16 STARTRACKER ELEVATION ANGLE THETA OFF ZENITH (DEGREES) vs. STARLIGHT REFRACTION ANGLE

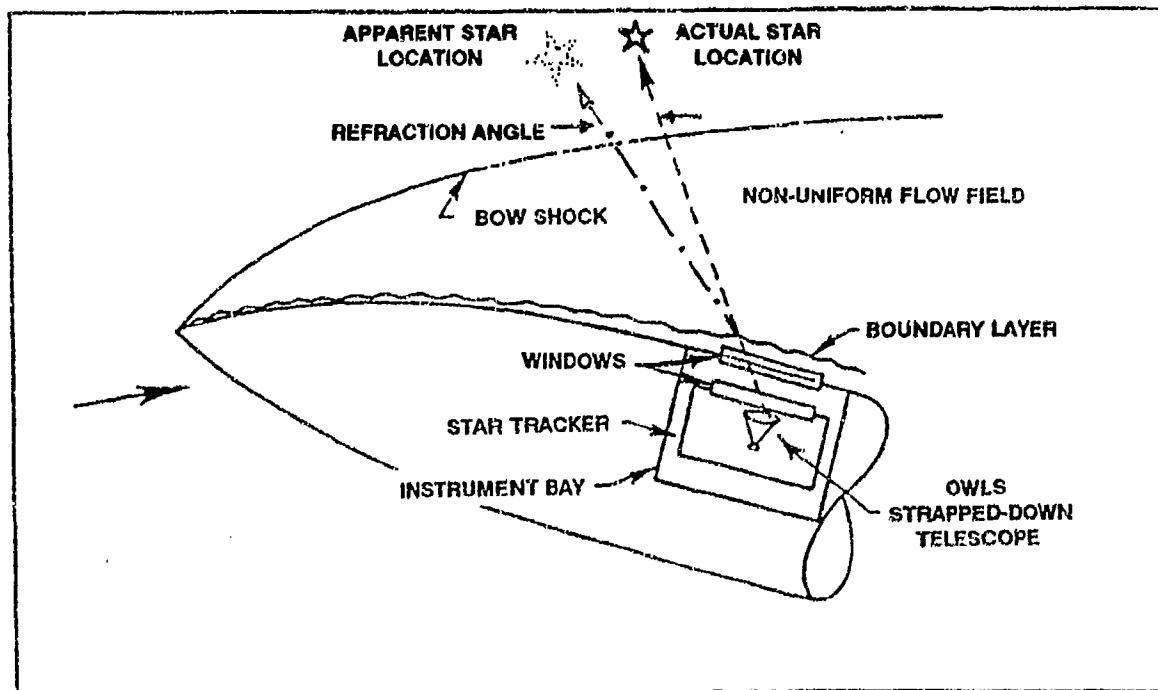


FIGURE 17 TYPICAL VEHICLE STELLAR REFRACTIVE BOUNDARY AIR FLOW

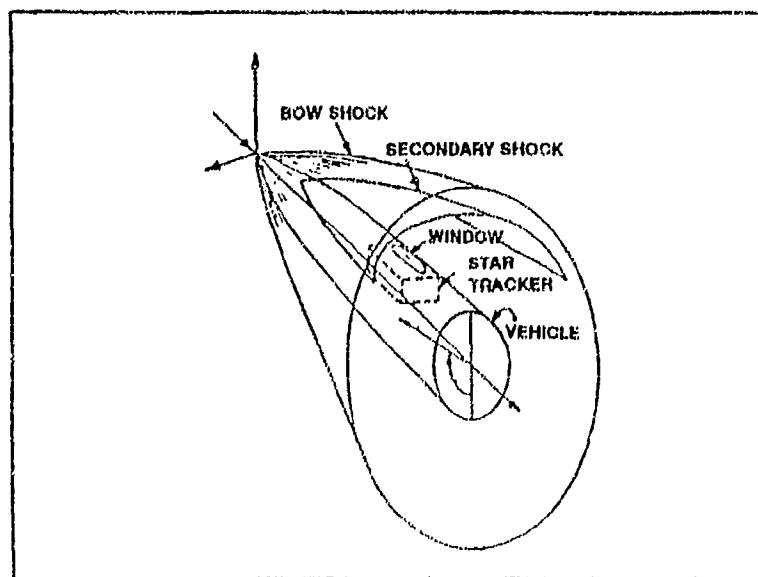


FIGURE 18 HVV FLOW FIELD SCHEMATIC

6.0 SAIN FAULT TOLERANCE AND SOFT DEGRADATION MODE

The stellar sensor complements the inertial sensors by providing a level of fault identification and navigation redundancy. For example, the INS portion of SAIN, just like all basic INS cannot detect an operator error in the initial or update of vehicle longitude. In fact, when a potentially catastrophic erroneous initial longitude is inserted into an unaided INS, it will produce the identical velocity, latitude, and azimuth responses as if the correct longitude were inserted. The reason for this lack of longitude error observability is that none of the earth rate INS compensation and driving functions are longitude dependent. This lack of longitude dependent responses when only an unaided INS provides the vehicle's guidance, has led to many critical problems. The stellar augmentation removes this longitude ambiguity, since the observed position should closely match the INS star latitude and longitude position when they are both functioning correctly. If there is a lack of good correlation between the INS and the OWLS position, the navigation processor can issue a built-in-test alert.

Furthermore, during the low acceleration portion of a mission, the OWLS, with the aid of the accelerometers, can provide a reasonable position fix. This is similar to an aircraft sextant where the accelerometers function as high quality bubble levels. Although this automated strapdown sextant feature, which is not dependent on the gyroscopes, is not presently implemented in the SS/IS program software, it remains as a future enhancement. Thus the strapdown OWLS with accelerometer augmentation may provide a highly reliable position reference and a soft degradation mode when gyroscopes fail.

7.0 CONCLUSIONS

Stellar-inertial capability is a precision autonomous navigation national asset. The technology encompasses our gravity compensation techniques, stellar catalog, telescope design, and inertial navigator capability. The U.S. is the world leader in strategic autonomous navigation critical technology. Furthermore, besides the USSR, UK, France, Italy, and Germany, there are no other countries that possess any capability in this area. This unique advantage allows the U.S. to have a surgical strike capability in an area where, for a host of reasons, radio navigation has been eliminated or temporarily denied.

The SS/IS program allows the cost, size, and reliability penalty for precision strike capability to be reduced to an affordable option in future vehicles. When sensor fusion is taken into account, the low cost stellar option provides in-air alignment regardless of the vehicle's flight path or speed, and a level of navigation redundancy to enhance mission success.

Thus, as in the past, modern man should depend on the stars for navigation.

BIBLIOGRAPHY

- 1) Joseph F. Caligiuri, "The Navigation System for the Polaris Submarine", Navigation Journal of the Institute of Navigation, p. 3, Spring 1960.
- 2) Vern A. Blumhagen, "Stellar Inertial Navigation Applied to Cruise Vehicles", IEEE Transactions of Aerospace and Navigation Electronics, p. 235, September 1963.
- 3) Kenton L. Bachman, Ronald Dennis, and Seymour Levine, "Strapdown Astro-Inertial Navigation (SAIN) - An Idea That Has Come of Age", Central Inertial Guidance Test Facility (CIGTF) - Fourteenth Biennial Guidance Test Symposium, p. 181, October 1989.
- 4) Kenton L. Bachman, Ronald Dennis, and Seymour Levine, "Strapdown Astro-Inertial Navigation Utilizing the Optical Wide-angle Lens Startracker", Navigation, Journal of the Institute of Navigation, p. 347, Winter, 1990-91.
- 5) John McCale, "Foreign Technology Assessment", Institute for Defense Analysis, IDA, Technical Review Group 5, 10 June 1991.
- 6) Thomas J. Seavoy and Sue-Lynn K. Yim, "Hypervelocity Vehicle Technology Development Requirements", Boeing Advanced Systems, October 1988, AFWL-TR-88-1084.

ACKNOWLEDGEMENT

- The authors wish to thank Thomas Cranor, of McDonnell-Douglas Missile Systems Company for his contributions to the Hyper-Velocity Vehicle plasma analysis.

A STRAPDOWN ICBM GUIDANCE SYSTEM

WITH

PEACEKEEPER ACCURACY?

**TOM REED
R. G. BROWN ASSOCIATES, INC.**

**JOHN LUKESH
NORTHROP ELECTRONICS SYSTEMS DIVISION**

PRESENTED TO:

**FIFTEENTH BIENNIAL GUIDANCE SYMPOSIUM
DEPARTMENT OF THE AIR FORCE
HEADQUARTERS 6585TH TEST GROUP (AFSC)
HOLLOMAN AIR FORCE BASE, NEW MEXICO 88330-5000**

ABSTRACT

The Air Force has indicated that the goal of the next ICBM guidance system program will be to achieve a dramatic reduction in cost without loss of accuracy. The ultimate method for achieving this goal is a small fully strapdown system. This system would not only reduce the complexity, which is synonymous with cost, but would also reduce weight and power requirements. It may be achievable with today's technology. A study has been completed that addresses the advantages of the strapdown system, the specific risks and the direction of research and development needed to reduce or eliminate these risks. The study assumes a stellar-inertial system using significantly lower cost instruments than the present AIRS type systems.

This study has also shown that it is possible to begin the design of a lower risk non-strapdown system which can then be simplified later, if and when the cited risks are mitigated, to the strapdown configuration with a minimum amount of redesign.

Toward the future, this study indicates that this smaller, less costly system could be a major component in the design of a small non-nuclear intercontinental missile. This missile could give to the Air Force an essentially instantaneous, extremely invulnerable strike capability against high priority targets any place in the world, with truly surgical precision (i.e. zero CEP). It could be more cost effective than the short range cruise missiles with their high cost delivery systems. This lower cost could be realized by using lower cost instruments, GPS, simpler C³ and softer basing.

INTRODUCTION

The term "strapdown" to most guidance people brings out descriptive words like small, inexpensive, low maintenance and inaccuracy. The thought of designing a strapdown guidance system for an ICBM has always been a dream of both designers and their sponsors, but the inaccuracy from the inherent inability to perform preflight instrument calibration has kept that dream from being a reality.

The realization of an adequate strapdown would not only reduce the cost of each missile but would open the door for broader applications of present ICBMs. Two examples come to mind. The first is the use of boost through reentry guidance in multiple warhead missiles allowing reentry evasion and the second, more radical application, would be the building of inexpensive non-nuclear ICBMs for almost instantaneous use anywhere in the world.

A strapdown IMU cannot be calibrated preflight in the usual sense, as this requires tumbling of the instrument cluster to provide observability of individual error sources. For this reason, no current precision ICBM guidance system is strapdown, nor are any of the developments systems proposed for the Air Force's Advanced Guidance Program. A strapdown IMU cannot be rotated preflight, but it can be postflight along with the entire post-boost vehicle once the booster has put the package into a nominal ballistic trajectory. With stellar aiding at this point, and the assumption of close to zero specific force on the inertial instruments, an alternative calibration concept becomes feasible. It may be possible to achieve Peacekeeper accuracy with a considerable savings in cost, weight and complexity.

ADVANTAGES

The overall advantages were stated previously but it might be in order to show in more detail the many simplifications that a strapdown design can produce.

The first simplification that comes to mind is the elimination of gimbals, or the complication of the floated ball concept (viz. AIRS). This eliminates not only the following mechanical entities but also the complexity, power and size of the support electronics.

Gimbal System		AIRS
1.	Bearings	Flotation Pads. w/Pump
2.	Torquers	Jets w/Pump
3.	Resolvers	"Belly" Bands
4.	Slip Rings	Two Wire I/O
5 ¹	Balancing	Balancing

One major design problem in gimballed systems is the ability to dissipate the internal heat while maintaining adequate temperature control. This is further complicated by the changing heat load from the torquers and their electronics that tends to be g-sensitive. This problem is solved in most gimballed systems by introducing forced convection with an internal or external fan, which have relatively high failure rates and introduce added vibrations. Other systems rely, in varying degrees, on heat dissipation by natural convection, which can introduce g-sensitive performance changes, while others use small air gap "thermal slippings", which require close build tolerances.

As the strapdown platform is, in itself, a homogeneous mass it inherently approaches an isothermal mass and, assuming a constant heat load, need only control the interfering external heat flow. This can be done at the convenient interface found at the vibration and shock isolator tie points. Perhaps an adequate control concept would use passive variable thermal resistance units built into these isolators coupled with some very small range internal thermal controllers. This combination of inherently smaller power requirements, controlled thermal resistance and smaller control heat should allow, at best, the elimination of ground coolant, and, at worst, longer non-coolant flight times.

The post boost calibration process, which replaces preflight calibration, is simpler, and there is another advantage - the reduction in some instrument parameter stability requirements. At present, systems are either calibrated periodically or continuously. The periodical calibrations require instrument stabilities over the periods between calibrations, which could be as long as 30 days. The continuous calibration method, as used in the Peacekeeper, requires closure times of days - again requiring long term instrument parameter stabilities. The strapdown system, on the other hand, requires that the parameters remain stable for a very short period before flight, during boost and then for the short post-boost calibration period - a period measured in minutes, not days. This significantly shorter stability time requirement could allow the introduction of less expensive instruments that were previously unacceptable.

The reduction in internal IMU power is multiplied by factors up to seven for the entire weapon system when power conversion inefficiencies and coolant requirements are taken into account. In other words, a reduction of one watt internally will reduce the total wattage requirement by up to seven watts. This in turn will reduce total weight as the batteries become smaller and with the elimination of all coolant umbilicals, tubes and heat exchanges.

¹All types of systems require some control over their center of gravity in order not to translate linear accelerations into rotational accelerations, but this is not as critical as gimbal or ball balance requirements.

This smaller weight, both of the IMU and its flight support equipment can directly result in heavier RVs, increased range or smaller total weight. Note, a reduction in throw weight of 100# can reduce the missile liftoff weight by approximately one ton!

The fact that the instruments will be tied to missile axes will allow the use of more inexpensive accelerometers in the non-thrust or low acceleration plane.

The reduction in parts count and parts complexity will significantly reduce the development and procurement costs. This reduction added to the decrease in removal and repair time will dramatically reduce the number of pipeline units thereby reducing the number of required spares. All of the above will result in a significant reduction in total weapon system life cycle cost.

PROBLEMS

Before listing these problems some assumptions need to be made. First, the goal is a totally strapdown system with essentially no moving parts. Second, the system will be stellar-inertial, it will contain a star tracker. And third, launch point gravity is adequately known. It will also be assumed that the guidance system cannot be used as an effective land navigator.

This study shows that the following problems must be solved to make a feasible strapdown system:

1. The alignment of the three gyro axes with the three accelerometer axes must be calibrated at the factory and be adequately stable for the field life of the system and have either negligible or stable acceleration sensitivities (i.e. unbalances, compliances)
2. Post boost (i.e. free fall) acceleration must be negligible or known to sufficient accuracy.
3. The cross axis accelerometers, nominally horizontal at launch, have scale factors with long term stable within requirements.
4. The initial prelaunch alignment places the post boost attitude knowledge within the acquisition range of the star tracker.
5. The system would most likely not have sufficient navigational accuracy for mobile operation.
5. There is sufficient proof to convince the sponsors that solutions to the above problems have been found.

SOLUTIONS

The above problems have not all been solved, as yet, but the means to define their difficulty and work for a solution can be outlined. The following are suggestions toward that end.

INSTRUMENT AXIS STABILITY

Reviewing data from a Peacekeeper system that has been in the field for over three years, indicate that when properly designed the long term stability of instrument axes is not a problem.

The compliance values of the three gyros are presently calibrated in the field but there is no indication that they are not stable. The flight sensitivity to compliance is very much a function of the flight environment, primarily roll rates. The missile might be required to have some form of roll control.

This sensitivity to compliance might preclude the use of dithered RLGs, unless they can be produced with sufficient rigidity. The sensitivity to unbalance terms will probable preclude the use of gyroscopic gyros.

POST BOOST ACCELERATION.

There are three causes for non-zero acceleration after engine cutoff:

1. Atmospheric drag. The missile is essentially out of the atmosphere and this drag is know to be negligible.
2. Solar pressure. This has been calculated and is negligible.
3. Attitude control jet asymmetries. This can be neglected if the jets are turned off during accelerometer bias calibration. Shutoff leakage could be a problem.
4. PBV outgassing. There undoubtedly will be some outgassing, the quantity is yet unknown. This should be made negligible, if not already, by PBV design.

The miss sensitivity to these unwanted accelerations, since they directly influence scale factor calibration, is approximately 92 feet per μg .

CROSS-AXIS ACCELEROMETER SCALE FACTOR

Before a specification can be set for the required long term cross-axis accelerometer scale factor, a miss sensitivity must be determined. The miss sensitivity to cross-axis accelerometer scale factors becomes a function of the following:

1. Preflight alignment to the horizontal plane. This is a procedural problem that should not be a major problem, except it may dramatically complicate mobile missile application. Assume a 5 milliradian error, this will result in a knowledge of tilt alignment error of 0.005 μ radians/ppm error in scale factor.
2. Flight alignment to the thrust plane. This becomes a mechanical tolerance problem but its magnitude should not exceed 5 milliradians, yielding a maximum velocity component of 120 feet/second.
3. Distance of the system from the pitch axis and the magnitude of the pitch. It is estimated that this tangential acceleration integral should not exceed 160 feet/second
4. The angle of attack during atmospheric flight. This angle of attack, or lift angle, is a function of speed, lift coefficient and atmospheric density. Assuming 3 degrees for 30 seconds at 5 g's will produce a total of 246 ft/sec along the "yaw" axis.

All of the above yield an RMS miss of approximately 0.68 feet/ppm error. Relatively inexpensive instruments are presently available with long term scale factor stability in the 100 to 200 ppm region.

INITIAL ALIGNMENT

The alignment to the vertical has been covered earlier, leaving only the azimuth alignment problem. The azimuth uncertainty is determined by the bias uncertainty of the "east" gyro. The field of view of the star tracker must be larger than 0.6 degrees per degree/hour of long term gyro bias uncertainty. Present star tracker and gyro technology should be able to meet these criteria.

MOBILE NAVIGATION

Perhaps the only way to solve this problem would be to have a separate navigator on board the mobile launcher. This navigator would most likely be an off-the-shelf military avionics unit, requiring no major development or procurement costs.

SELLING THE SPONSORS

This, perhaps, is the most difficult problem, at least the most non-technical. Our suggestion is the development of this system be coincident with the development of more conventional non-strapdown system; a system that would have one or more degrees of freedom preflight, using some form of gimbaling. The strapdown development would spin-off the main development program sometime after the preliminary design review as a separate high payoff parallel effort. It would use the same inner member and the majority of the development costs would have been prepaid by the parent program. This has the advantage of early development and a late decision when the majority of the aforementioned problems are solved.

CALIBRATION

Prior to launch the six instrument outputs are stored, this assumes a static environment. After boost the three accelerometer outputs are read yielding their bias values, if you can assume a zero g environment. This in turn determines the preflight vertical erection errors and, with the knowledge of launch site gravity, the scale factor of the thrust accelerometer.

Next the PBV is aimed at the first star and information is taken on two attitude errors. This produces the value of two gyro biases. The PBV is now slewed about a single axis to the second star, approximately 90 degrees away. This star tracker reading now defines the other attitude error and the third gyro bias as well as the scale factor for the gyro whose input axis was along the slew axis. The PBV is then rotated about its line of sight by 90 degrees and then slewed back to the original star. This star tracker reading now produces complete information about the scale factor of the gyro on which the 90 degree rotation was effected as well as the scale factor of the other cross-axis gyro and the alignment of the star tracker to the gyro triad.

The system is now calibrated and sufficient information is obtained to correct the ballistic flight trajectory.

FUTURE USES

The obvious use would be the replacement of older systems whose maintenance problems have started to increase. This would require some alterations in the PBV but this cost could be easily offset by the LCC of the new units.

Perhaps the most exciting use for this system would be to give the country, specifically the Air Force, a non-nuclear, nearly invulnerable, world-wide strategic alternative to the cruise

missiles. It could use GPS aids to produce an essentially zero CEP. While it is not suggested that this missile would cost less than a cruise missile on a one-on-one basis, but it should compete favorably with the total weapon system costs. This would rely on the simpler softer launch facilities and C³ as well as the reduction in design hardness requirements. They would be less vulnerable to conventional defenses, yielding a higher kill ratio and they would have a shorter flight time, allowing the targeting of high priority volatile targets. All of this in contrast to the for the present cruise missiles need for extremely expensive launch platforms (viz. large naval ships or transcontinental aircraft).

CONCLUSION

The present ICBM guidance systems are one of the most expensive units in the weapon system, in both procurement costs, maintenance costs and missile downtime. The successful development of a strapdown system would dramatically reduce all of these cost factors.

The development of this system is not without risk, but we believe that these risks can be mitigated within a period that would make its development timely and highly competitive.

As the price of guidance systems are reduced the applications will grow. The development of a world wide strike capability that is practically instantaneous, almost invulnerable and with the capability of having absolute accuracy could be a major deterrent to world-wide aggression.

**Application of
Maximum Likelihood Parameter Identification to
Test and Evaluation of
Inertial Navigation Systems**

**Larry J. Levy
Johns Hopkins University Applied Physics Laboratory
Laurel, MD**

**David W. Porter
Coleman Research Corporation
Laurel, MD**

**Presented at the
Fifteenth Biennial Guidance Test Symposium
Holloman Air Force Base, New Mexico
24-26 September 1991**

ABSTRACT

System performance prediction has relied on system testing using either "brute force" empirical methods or "validation" of a few engineering model test predictions. The former tends to be too costly while the latter provides no quantifiable confidence over untested conditions. Both neglect the rich source of detailed model information in each test. Confident and cost effective system performance prediction requires the effective use of all types of information to develop a reliable detailed model that can be extrapolated to untested conditions. Maximum likelihood parameter identification techniques have now been developed that will: (1) extract the maximum model information from each test, (2) optimally combine diverse factory, subsystem, and system tests, and (3) provide an identification uncertainty along with the identified model to numerically quantify model confidence. This also enables test planning tradeoffs to be conducted in terms of sizing, instrumentation requirements, and types of tests to achieve a desired numerical confidence in system performance prediction over untested scenarios. Recent dramatic improvements in computational efficiency and reliability have made these parameter identification tools accessible for large scale system evaluation in a technical workstation environment.

Specific application of the technology to a simplified example of missile inertial guidance test and evaluation will be shown. The example will illustrate how a combination of diverse system tests (sled, special aircraft, and operational missile tests) can be combined for confident guidance performance prediction over tactical scenarios.

1. Introduction

System performance prediction has relied on either empirical methods based on extensive repetitive system testing over the entire range of possible operational conditions or "validating" complex engineering model predictions by a "limited" set of system tests. The former is usually too costly and yields minimal insight into system understanding. The latter gives a "warm feeling" but cannot predict system performance over untested conditions with quantified confidence. Test planning and requirements are difficult to numerically predict from system performance requirements. Both approaches neglect the rich source of detailed model information provided by each system test.

For example, inertial navigation system performance requires accurate statistical error models that are useable over the entire operational environment. Traditionally, inertial navigation system (INS) error models have been developed by fitting well known (from first principles) structural models to factory component and subsystem test data for component parameter estimation. These tests must be tightly controlled and repeatable so that, hopefully, all the relevant parameters are repeatedly observed for a good statistical sample. Operational testing on the range or in the field is used to more or less validate that the factory derived model is "good" in the actual system environment. When "mismatches" occur, attempts are made to modify the factory model to match the operational system test data. Generally, however, no systematic approach is used to extract the error model parameter information from the operational tests for comparison and/or combination with

the factory derived model. The traditional methodologies could not handle the nonrepeatable and complex nature of these tests, neglecting the rich source of model information contained therein. Also, it was difficult to quantify the test requirements (type, size, instrumentation) and numerically relate them to some high level system performance requirement. Consequently, justification of test requirements was usually by the "seat of the pants" type reasoning.

The methodology described in this paper provides a practical computational technique for estimating the system model from all types of test data. It extracts the maximum model information from each test and provides its own estimation uncertainty to enable quantifiable confidence statements to be attached to model predictions. This also allows test planning requirements analyses to be conducted prior to any test program by numerically relating system performance confidence statements to specific test characteristics. Section 2 defines the generic state space model applicable to this methodology. Section 3 describes the overall operation of the maximum likelihood identification methodology. (The theoretical derivation and the detailed algorithms are presented in [1].) Section 4 defines the simplified missile inertial guidance test and evaluation example with Section 5 discussing the numerical results, contrasting this method with a more traditional approach.

2. Definition of the Identification Problem

The identification methodology presumes that the model for the system consists of a known structure and a set of unknown parameters. The structure is a nonlinear (or linearized) simulation that transforms the parameters into system performance such as target accuracy, CEP, for a missile guidance system. It is assumed that the structure can be known confidently from first principles and laboratory subsystem testing. If the unknown parameters are independent of scenario (i.e., all scenario dependence is in the structure), diverse tests can be combined for statistical leverage in the model identification process.

Mathematically, the system under test is assumed to be defined by the following discrete-time linear state space model for each test (realization) j ($j = 1, \dots, N$),

$$x_{k+1}^j = \Phi_k^j(\theta)x_k^j + w_k^j ; k=0,1,\dots,n(j)-1 \quad (1)$$

$$z_k^j = H_k^j(\theta)x_k^j + v_k^j ; k=0,1,\dots,n(j) \quad (2)$$

where x_o^j, w_k^j, v_k^j are mutually independent for all k, j with dimensions $p(j), p(j)$ and $m(j)$, respectively. w_k^j and v_k^j are white noise sequences in each realization with $x_o^j \sim N(\mu_o^j(\theta), \Sigma_o^j(\theta))$, $v_k^j \sim N(0, R_k^j(\theta))$ and $w_k^j \sim N(0, Q_k^j(\theta))$. The unknown $qx1$ parameter vector θ has elements that are generally common across most realizations. Essentially, a number of realizations will be needed to estimate elements in $\mu_o^j(\theta)$ and $\Sigma_o^j(\theta)$ but only one realization may be sufficient for elements in $\Phi_k^j(\theta), H_k^j(\theta), Q_k^j(\theta)$ and $R_k^j(\theta)$. This generality of the model description allows for multiple but dissimilar (same system under test with different test environments and different instrumentation) tests to be used in the identification process. Given N realizations (tests) of the random process (system) represented by the model in (1) & (2), our objective is to determine compact and computationally efficient algorithms for calculating the maximum likelihood estimate (MLE), $\hat{\theta}_{ML}$.

In inertial system testing, the model must be linearized about a nominal trajectory in order to fit the form of (1) and (2). Typical INS elements in θ will be the 1-sigma values in $\Sigma_o^j(\theta)$ of the accelerometer, gyro, and misalignment biases, time constants in $\Phi_k^j(\theta)$ for the markov processes, spectral density values in $Q_k^j(\theta)$ for the markov and random walk processes, and residual mean errors (in the factory calibrations) in $\mu_o^j(\theta)$. Occasionally, instrumentation measurement noise covariances may be unknown in $R_k^j(\theta)$. For detailed INS models one could easily expect the number of unknown elements to be in the 30's or more (some possibly in the 100's). In other applications, such as evaluation of aircraft aerodynamic characteristics, the model must be linearized about an estimated trajectory. Here the unknown elements in θ are stability and control coefficients along with parameters characterizing the atmospheric turbulence.

The method of maximum likelihood essentially uses the known structure of the model to calculate the analytical form of how the unknown parameters, θ , influence the probability of observing a set of measurement data from an ensemble of N tests. When a specific set

of measurement data is obtained from the tests, the best estimate, $\hat{\theta}_{ML}$, is the value of θ that maximizes the probability of obtaining that data. Thus, $\hat{\theta}_{ML}$ is the value that makes the actual measurements "most likely." It can be shown that as more and more data are gathered, the estimate will be unbiased with a Gaussian distribution having a computable covariance (uncertainty) that is the inverse of the so-called Fisher Information matrix [2]. Thus, for a missile inertial system, the estimate $\hat{\theta}_{ML}$ can be propagated to target impact to obtain an accuracy estimate, \hat{CEP} , while the inverse Fisher Information matrix, $\mathcal{F}_{\theta\theta}^{-1}$, can be propagated to target impact to calculate confidence intervals about \hat{CEP} . The maximum-likelihood method was chosen over other criteria for estimating θ because:

1. The most likely model (to have caused the observed test measurements) is an intuitively pleasing criterion.
2. It is also asymptotically (as the number of test samples gets large enough) an unbiased and minimum mean-square-error estimate.
3. It provides a computationally practical estimate, $\hat{\theta}_{ML}$, and estimation uncertainty, $\mathcal{F}_{\theta\theta}^{-1}$, to calculate confidence intervals.
4. The estimation uncertainty, $\mathcal{F}_{\theta\theta}^{-1}$, is due solely to the quality (observability) and quantity (sample size) of the test data. If needed, apriori information based on engineering judgment can be blended in to reduce the estimation uncertainty.
5. Even if the assumed model structure is wrong, the resulting estimate yields a fitted model that is as near to the truth as possible [3].

Other criteria required more prior information about θ , were too difficult to compute, or yielded poorer estimates (in the mean-square-error sense).

3. Maximum Likelihood Identification Algorithms

The MLE is obtained by maximizing the log likelihood function, $\log L(\hat{\theta}) \triangleq \log p(Z^1, \dots, Z^N / \hat{\theta})$, where $p(\cdot / \theta)$ is the conditional probability density function and $Z^j \triangleq [z_o^j, \dots, z_{n(t)}^j]^T$ is the data from each realization j . The traditional MLE approach [2,3] to the above state space problem reformulates the log likelihood function in

terms of the Kalman filter innovations with the resulting Scoring (Gauss-Newton) algorithm requiring a Kalman filter plus q "differentiated Kalman filters" for each realization per iteration to calculate the log likelihood gradient and Fisher information matrix. This exploding computational burden plus the known slow and erratic numerical convergence character of Scoring under poor starting values [4] has limited its usage in practical applications.

Some of these problems were alleviated in [5, 6] by reformulating the MLE around the log likelihood of the "complete" data, $\log L^c(\theta) \triangleq \log p(Z^1, X^1, \dots, Z^N, X^N/\theta)$, where

$X^j \triangleq [x_o^j, \dots, x_{n(j)}^j]^T$ and Z^j, X^j is termed the "complete" data from the realization j .

This resulted in an EM algorithm with the $i+1$ iteration given by

Expectation (E) step:

$$G(\theta; \theta^i) \triangleq E\{\log L^c(\theta)/Z^1, \dots, Z^N, \theta^i\} \quad (3)$$

Maximization (M) step:

$$\theta^{i+1} = \arg \max_{\theta} G(\theta; \theta^i) \quad (4)$$

The EM idea is to maximize the "complete" data log likelihood, $\log L^c(\theta)$, which results in relatively simple solutions for the maximum. However, since the "complete" data is not available, the next best thing is to maximize its average value, given the measurements. It is proved in [4] that whenever a value of θ satisfies

$G(\theta; \theta^i) > G(\theta^i; \theta^i)$, then $\log L(\theta) > \log L(\theta^i)$ and the algorithm will converge to a stationary point of the $\log L(\theta)$ under mild regularity conditions [7]. The E step only required a single Kalman filter and fixed interval smoother for each realization per iteration regardless of the size of q . The M step is achieved by setting $\partial G(\theta; \theta^i)/\partial \theta = 0$ and solving for θ . The case where everything is constant (across $k \& j$) $\mu_o, \Sigma_o, Q, R, \Phi, H$

is unknown results in simple analytical solutions for θ^{i+1} . The more realistic partially known model cases were solved in [1]. The EM algorithm has good starting characteristics

but slows down as the iterate nears a stationary point of the $\log L(\theta)$ [6]. Also, no Fisher information calculation is required.

The well known Scoring algorithm is another numerical technique for finding the maximum of $\log L(\theta)$ and is given by

$$\theta^{i+1} = \theta^i + \mathcal{F}_{\theta\theta'}(\theta^i)^{-1} \left. \frac{\partial \log L(\theta)}{\partial \theta} \right|_{\theta^i} \quad (5)$$

with the Fisher information matrix given by

$$\mathcal{F}_{\theta\theta'}(\theta^i) = E \left\{ \left(\left. \frac{\partial \log L(\theta)}{\partial \theta} \right|_{\theta^i} \right) \left(\left. \frac{\partial \log L(\theta)}{\partial \theta} \right|_{\theta^i} \right)' / \theta^i \right\} \quad (6)$$

It was already mentioned that the traditional approach in computing the gradient and the Fisher Information matrix resulted in the exploding dimensionality problem of q in [2,3]. It was shown in [8] that Scoring is related to EM by Fisher's Identity,

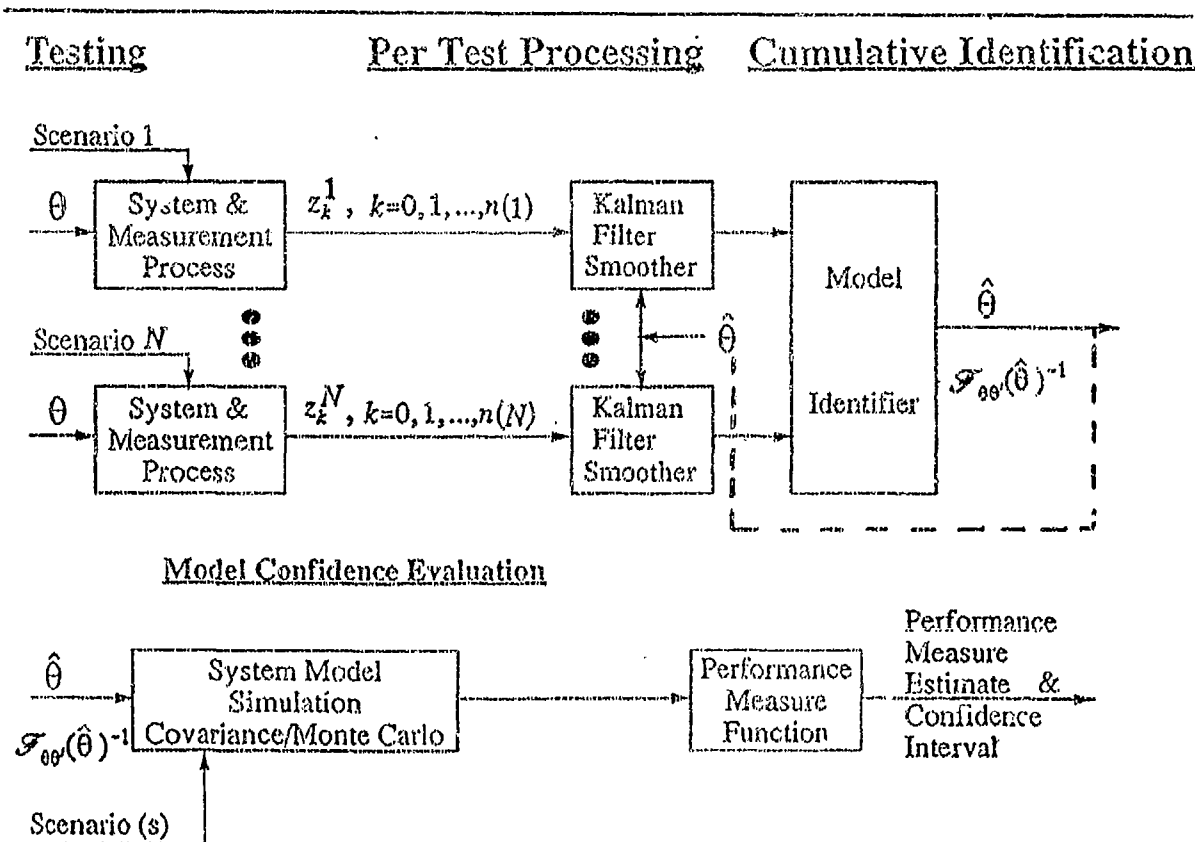
$$\left. \frac{\partial G(\theta; \theta^i)}{\partial \theta} \right|_{\theta^i} = \left. \frac{\partial \log L(\theta)}{\partial \theta} \right|_{\theta^i} \quad (7)$$

Thus, the same Kalman filters and fixed interval smoothers used in EM in [6] could also be used in Scoring [8], obviating the exploding dimensionality problem of q . The practical algorithm to accomplish this was developed in [1].

The complementary characteristics of the EM and Scoring algorithms (EM - good starting convergence, poor finish, and no Fisher; Scoring - poor starting convergence, good finish, with Fisher calculation) plus their common Kalman filter/fixed interval smoother computations provided a unified algorithm that starts out with EM and finishes with Scoring, exploiting the desirable convergence characteristics of each procedure. Consequently, computational reliability and efficiency are dramatically improved. A block diagram of the overall procedure is shown in Figure 1. When the algorithm is in the EM mode, the bank of Kalman filter-smoothers provides the "E" step and the "M" step is accomplished in the Model Identifier. The model uncertainty, $\mathcal{F}_{\theta\theta'}^{-1}$, is only calculated when the algorithm is in

the Scoring mode. After the identification algorithm has converged, the identified model and its uncertainty may be projected into some system performance measure estimate with an associated confidence interval.

Figure 1 - System Identification Flow



It must be noted that the distribution of the estimate, $\hat{\theta}_{ML} \sim N(\theta, \mathcal{F}_{\theta\theta}^{-1})$, is an asymptotic property. Actually, for finite data, $\mathcal{F}_{\theta\theta}^{-1}$ is a lower bound on the estimation error covariance. Consequently, care must be exercised in using this quantity in data poor situations or when the observability of a particular parameter or group of parameters is poor from the set of tests. Experience [9] has shown that even if some parameters are poorly observable, their combined projection into some higher level performance quantity such as trajectory uncertainty or target uncertainty (CEP) may still be reasonably approximated by the asymptotic property. In any event, the calculation of $\mathcal{F}_{\theta\theta}^{-1}$ (or its inverse) will indicate which components are poorly observable so that the tests can be modified (more data, better instrumentation, different type of tests). Since $\mathcal{F}_{\theta\theta}^{-1}$ can be calculated from covariance simulations of the tests (and not real data), this provides the basis for test

planning and design. Required confidence intervals in a high level system performance criterion can be translated into test requirements by iteratively simulating various combinations of test types, test sizes, and instrumentation until the confidence interval criterion is satisfied.

4. Simplified Missile Inertial Guidance Example

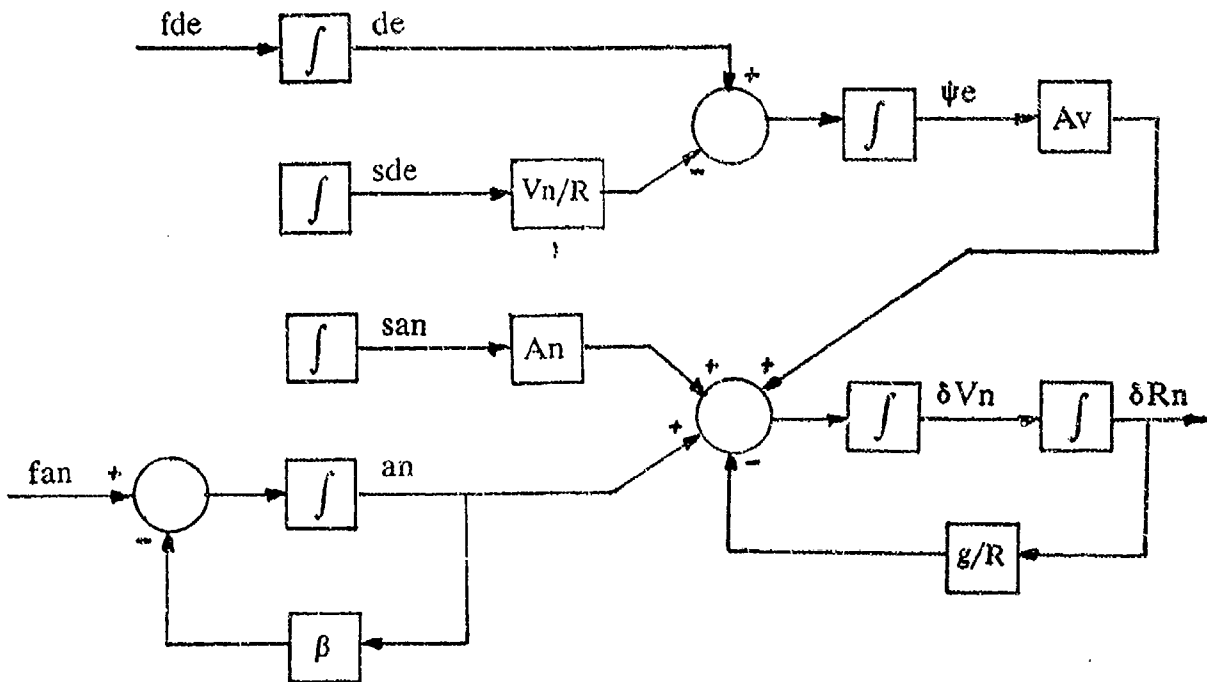
To illustrate the efficacy of the identification technique, a very simplified missile inertial system test and evaluation problem will be considered. The performance of the inertial system is based on its error model which is derived from first principles and factory tests and is shown in Figure 2. This assumes the inertial instruments are on a local level stabilized platform with vehicle motion constrained in two dimensions (north-vertical) on a nonrotating earth using a very good altimeter and where

A_n, A_v	=	north and vertical specific force (f/s^2)
V_n	=	north velocity (f/s)
R	=	earth radius
g	=	earth gravity magnitude
$\delta V_n, \delta R_n$	=	errors in north velocity (f/s) and position (ft)
ψ_e	=	"computer to platform" misalignment about east (μrad)
d_e	=	east gyro drift random walk ($mrad/hr$)
f_{de}	=	east gyro drift rate white noise
s_{de}	=	east gyro torque scale factor bias (ppm)
a_n	=	north accelerometer offset markov process (μg)
f_{an}	=	north accelerometer offset rate white noise
$1/\beta$	=	north accelerometer offset markov time constant (sec)
s_{an}	=	north accelerometer scale factor bias (ppm)

It is desired to estimate the statistical parameters in this inertial model from system test data to validate the predicted performance from the manufacturer. The initial errors δV_n and δR_n are assumed to be zero with no uncertainty since the missile is to be launched from a fixed and surveyed land site. The unknowns in the system model are the initial means and variances of d_e , s_{de} , s_{an} , a_n ; the spectral amplitude of the white noises f_{de} and f_{an} ; and the time constant $1/\beta$. The initial value in ψ_e will be assumed to be $-a_n/g$ due to the levelling process prior to launch.

The tactical missile scenario is a 8000 nm flight with a 150 sec constant 5.5g boost at a thrust angle of 29° from the local horizon. The inertial system is used to control a

Figure 2 - Simplified Inertial System Error Model



reentry body deployment (negligible deployment error) at 600 sec. This tactical scenario can never be tested so a combination of other system tests will be used to extract the scenario independent parameters (the unknowns described above) which will then be projected via a covariance simulation of the tactical scenario into an estimate of tactical system performance (impact error RMS). Three types of system tests will be used: (1) sled testing with $\pm 5g$ horizontal thrusts for 10 sec each and sampled measurements of position error at .1 sec intervals with .01 ft ($1-\sigma$) uncorrelated measurement noise. (2) high performance aircraft testing of the missile INS on a test pallet using a GPS precision post flight track (integrated doppler) of sampled measurements of position error at 10 sec intervals for 1/4 hr with equivalent .1 ft ($1-\sigma$) uncorrelated measurement noise. The assumed trajectory of the aircraft is a horizontal figure eight in the north-vertical plane with 25 nm between foci and each turn of radius 30 kft at a constant speed of 1000 kts. (3) missile flight tests over a 6000 nm range with a 150 sec constant 5.5g boost at a thrust angle of 42° . A GPS precision post flight track of the same quality and sample rate as in the aircraft tests is assumed for 600 sec worth of tracking.

The model in Figure 2 for each test and the tactical scenario can be expressed as a linear continuous dynamics state space model, given by (suppressing j superscript)

$$\dot{x}_t = A_t x_t + \omega_t ; \quad 0 \leq t \leq t_n \quad (8)$$

with ω_t a 7 dimensional white noise vector with spectral density matrix Ω_t . The measurements from the system tests are discrete time as in (2). The appropriate EM and Scoring algorithms can be easily obtained by running the discrete time Kalman filter and smoother at a high enough recursion rate (possibly higher than the measurement rate) so that

$$\Phi_k \approx I + A_k \Delta t_k \quad (9)$$

$$Q_k \approx \Omega_k \Delta t_k \quad (10)$$

In this case

$$x_t = \begin{bmatrix} \psi e \\ \delta V n \\ \delta R n \\ de \\ sde \\ an \\ san \end{bmatrix}; \quad A_t = \begin{bmatrix} 0 & 0 & 0 & 1 & -Vn/R & 0 & 0 \\ Av & 0 & -g/R & 0 & 0 & 1 & An \\ 0 & 1 & 0 & 0 & 0 & 0 & 0 \\ 0 & 0 & 0 & 0 & 0 & 0 & 0 \\ 0 & 0 & 0 & 0 & 0 & 0 & 0 \\ 0 & 0 & 0 & 0 & 0 & -\beta & 0 \\ 0 & 0 & 0 & 0 & 0 & 0 & 0 \end{bmatrix} \quad (11)$$

$$\omega_t = \begin{bmatrix} 0 \\ 0 \\ 0 \\ fde \\ 0 \\ fan \\ 0 \end{bmatrix}; \quad \Omega_t = \begin{bmatrix} 0 & 0 & 0 & 0 & 0 & 0 & 0 \\ 0 & 0 & 0 & 0 & 0 & 0 & 0 \\ 0 & 0 & 0 & 0 & 0 & 0 & 0 \\ 0 & 0 & 0 & \sigma_{fde}^2 & 0 & 0 & 0 \\ 0 & 0 & 0 & 0 & 0 & 0 & 0 \\ 0 & 0 & 0 & 0 & 0 & \sigma_{fan}^2 & 0 \\ 0 & 0 & 0 & 0 & 0 & 0 & 0 \end{bmatrix} \quad (12)$$

$$\mu_o = \begin{bmatrix} -\mu_{an} \\ 0 \\ 0 \\ \mu_{de} \\ \mu_{sde} \\ \mu_{an} \\ \mu_{san} \end{bmatrix} ; \Sigma_o = \begin{bmatrix} \sigma_{an}^2 & 0 & 0 & 0 & 0 & -\sigma_{an}^2 & 0 \\ 0 & 0 & 0 & 0 & 0 & 0 & 0 \\ 0 & 0 & 0 & 0 & 0 & 0 & 0 \\ 0 & 0 & 0 & \sigma_{de}^2 & 0 & 0 & 0 \\ 0 & 0 & 0 & 0 & \sigma_{sde}^2 & 0 & 0 \\ -\sigma_{an}^2 & 0 & 0 & 0 & 0 & \sigma_{an}^2 & 0 \\ 0 & 0 & 0 & 0 & 0 & 0 & \sigma_{san}^2 \end{bmatrix} \quad (13)$$

with the associated discrete time measurement given by (2) where

$$H_k = [0 \quad 0 \quad 1 \quad 0 \quad 0 \quad 0 \quad 0] \quad (14)$$

and $R_k = (.01)^2$ for sled testing and $(.1)^2$ for aircraft and missile testing.

In this example, θ is the vector of unknown parameters.

$$\theta = [\mu_{de} \quad \mu_{sde} \quad \mu_{an} \quad \mu_{san} \quad \sigma_{de}^2 \quad \sigma_{sde}^2 \quad \sigma_{an}^2 \quad \sigma_{san}^2 \quad \beta \quad \sigma_{fde}^2 \quad \sigma_{fan}^2]^T \quad (15)$$

The true values of θ , shown in Table 1, are such as to cause a tactical impact error of 1200 feet RMS. The objective is to process combinations of sled, aircraft, and missile test flights to estimate θ and project the model in (8) - (13) with $\hat{\theta}_{ML}$ into tactical impact RMS along with a confidence interval derived from the asymptotic distribution of $\hat{\theta}_{ML}$. The nominal values of θ (our best guess from factory tests and other information) are also shown in Table 1 and cause a tactical impact error of 1900 feet RMS.

5. Numerical Results

First of all, a "test planning" analysis was conducted to determine the appropriate combinations and sizes of different tests to achieve a required confidence requirement. The requirement was that the true tactical RMS was to be within $\pm 15\%$ of the estimated tactical RMS with 90% confidence. To achieve this confidence by only impact scoring of test trajectories (not a tactical estimate) would require about 35 repeatable test flights with perfect impact location instrumentation. Obviously, we hope to require a significantly less number of missile tests by extracting more information per test and by using information from other test types such as aircraft or sled tests. The test planning analysis follows from Figure 1 where a Kalman filter smoother covariance analysis is run for each generic type of test with θ set to the nominal model (our best guess). The model identifier is then run in a "covariance only" mode to produce a Fisher Information matrix for each type of test. Various combinations and numbers of tests can be combined by simply adding the appropriate Fisher Information matrices. The inverse of the combined Fisher matrix along with the nominal θ define a Gaussian distribution from which sampled values of $\hat{\theta}$ can be propagated into impact means and covariances via a tactical inertial model covariance simulation. A distribution of RMS's is then obtained from the distribution of impact means and covariances yielding the appropriate confidence intervals.

The analysis showed that 29 test missiles would be needed to achieve the tactical confidence requirement if the model was truly at the nominal values. The aircraft tests provided more information per test as only 18 tests yielded acceptable confidence intervals. Sled tests provided much less information than either of the other two types except for the accelerometer scale factor terms μ_{san} and σ_{san}^2 . Since there was virtually no information on μ_{an} and σ_{an}^2 , sled testing alone could not provide a confident tactical model. However, combining 16 sled and 15 aircraft tests satisfied the requirement, so that 16 sled tests essentially made up for the loss of 3 aircraft tests. Combining all three types of tests and recognizing the relatively high cost of missile testing, a test program of 4 missile tests (to exercise and test other missile subsystems) plus 13 aircraft tests plus 13 sled tests was found to satisfy the tactical requirement. Obviously many other combinations could be used to satisfy the test requirements. In fact, the tests themselves could be modified to produce more information per test. For example, by lengthening the aircraft tests to 1 hour, a combination of 4 missile plus 4 aircraft plus 13 sled tests satisfied the requirement.

In test planning analysis, one has to literally guess at the range of possible "true" values that the model could take on so as to provide enough tests of adequate information. As the "true" values get smaller with constant test instrumentation quality and number of tests, the percentage confidence intervals will grow. In other words, achieving the confidence requirement on a better guidance system will require more or better test resources. In this case, we chose a conservative test program of 4 missile tests, 16 aircraft tests (1/4 hr long) and 16 sled tests which would have produced $\pm 13\%$ confidence intervals at the nominal model. This test program was then simulated to exercise the parameter estimation software shown in Figure 1. The results are shown in Table 1 with θ (nominal)

Table 1 - Test and Evaluation Results for Missile Guidance Example

θ	Units	$\theta(\text{nominal})$	$\theta(\text{true})$	90% Confidence	
				$\hat{\theta}_{ML}$	Int. About $\hat{\theta}_{ML}$
μ_{dc}	mrad/hr	0	.4	.46	± 1
μ_{sdc}	ppm	0	0	153	± 158
μ_{an}	μg	0	0	.32	± 3.5
μ_{san}	ppm	0	0	-.30	± 1.3
σ_{dc}^2	(mrad/hr) ²	.16	.09	.069	$\pm .04$
σ_{sdc}^2	(ppm) ²	40000	90000	142700	± 95290
σ_{an}^2	(μg) ²	400	100	85.1	± 48.4
σ_{san}^2	(ppm) ²	50	16	21.5	± 8.76
β	1/sec	.001	.0025	.004	$\pm .0013$
σ_{fde}^2	(mrad/hr) ² /sec	.0009	.0001	.00005	$\pm .000024$
σ_{fan}^2	(μg) ² /sec	1.0	.25	.29	$\pm .07$
<hr/>					
Tactical Impact RMS	feet	1900	1200	1186	± 192 ($\pm 16.2\%$)

being the starting value in the parameter estimation iterative process and $\hat{\theta}_{ML}$ being the final estimate of the θ (true). The 90% confidence intervals were generated from the Fisher Information matrix inverse evaluated at $\hat{\theta}_{ML}$. Note that the 90% confidence intervals cover the true values for all parameters except for β and σ_{fde}^2 . Here, the asymptotic distribution is somewhat optimistic at the individual component level. The overall RMS estimate for the tactical trajectory is very good and well within the confidence intervals. Note that the % confidence intervals are slightly outside the requirement due to the fairly drastic improvement of the model from nominal to $\hat{\theta}_{ML}$. An extra 3 aircraft tests would have brought the % confidence intervals within specifications.

The example presented here is illustrative but not truly representative of the potential of this methodology. Realistic guidance models are much more complex with more dynamic acceleration profiles. This should enable more detailed model information to be extracted per test, producing an even wider disparity between traditional impact scoring and this methodology.

6. Conclusions

A new approach to system test and evaluation has been presented and demonstrated that utilizes detailed test data to estimate the underlying ensemble system model which can then be extrapolated to untested scenarios for tactical system performance estimates. In addition, it provides its own estimation error distribution which allows confidence statements to be made for the model estimates and extrapolations. Furthermore, this also enables test planning analysis to be conducted prior to the test program for more efficient utilization of test facilities.

References

- [1] Levy, L. J., and D. W. Porter, "Unified EM/Scoring Identification Algorithms for Linear State Space Models," Proceedings of the 25th Annual Conference on Information Sciences and Systems, March 20-22, 1991, pp. 91-101.
- [2] Gupta, N. K. and R.K. Mehra, "Computational Aspects of Maximum Likelihood Estimation and Reduction in Sensitivity Function Calculations," IEEE Transactions on Automatic Control, vol. AC-19, no. 6, pp. 774-783, December 1974.
- [3] Goodrich, R. L., and P. E. Caines, "Linear System Identification for Nonstationary Cross-Sectional Data," IEEE Transactions on Automatic Control, vol. AC-24, no. 3, pp. 403-411, June 1979.
- [4] Meilijson, I., "A Fast Improvement to the EM Algorithm on Its Own Terms," Journal of the Royal Statistical Society, Series B, vol. 51, No. 1, pp. 127-138, 1989.
- [5] Shumway, R. H., D. E. Olsen, and L. J. Levy, "Estimation and Tests of Hypothesis for the Initial Mean and Covariance in the Kalman Filter Model," Communications in Statistics - Theory and Methods, A10 [16], pp. 1625-1641, 1981.
- [6] Shumway, R. H., and D. S. Stoffer, "An Approach to Time Series Smoothing and Forecasting Using the EM Algorithm," Journal of Time Series Analysis, vol. 3, no. 4, pp. 253-254, 1982.
- [7] Wu, C.F.J., "On the Convergence Properties of the EM Algorithm," The Annals of Statistics, vol. 11, no. 1, pp. 95-103, 1983.

- [8] Segal, M., and E. Weinstein, "A New Method for Evaluating the Log-Likelihood Gradient, the Hessian, and the Fisher Information Matrix for Linear Dynamics Systems," IEEE Transactions on Information Theory, vol. 35, no. 3, May 1989.
- [9] Haley, D.R., "Validation of Asymptotic Fisher Theory by Monte Carlo Simulation," Proceedings of the 1987 Summer Computer Simulation Conference, July 27-30, 1987, pp 185-190.

SESSION II-B
GPS-ATTITUDE/AZIMUTH/TSPI

CHAIRMAN
RICHARD GREENSPAN
C. S. DRAPER LABORATORY, INC.

GPS DERIVED AZIMUTH

**Scott D. Michael
U.S. Army Engineer Topographic Laboratories
Fort Belvoir, Virginia 22060-5546**

ABSTRACT

In the summer of 1990, the U.S. Army Engineer Topographic Laboratories (USAETL) took delivery of three Global Positioning System Azimuth Determining Systems (GPS ADS). This paper is an introduction to the GPS ADS research and development efforts currently underway at ETL, and a presentation of the results of testing completed thus far.

INTRODUCTION

Contracts funded largely by the Army Space Technology Research Organization were issued by the Engineer Topographic Laboratories (ETL) to investigate the technical feasibility of GPS derived azimuth. Except for the specifications outlined below, the contractors were permitted to pursue any method they chose for an Azimuth Determining System (ADS).

To determine an azimuth, the phase difference of the GPS signal between two antennas is measured. However, this always results in a number of phase ambiguities. The methods of resolving the phase ambiguities differ between the three contractors.

The requirements for the ADS are that it be a portable field system capable of real time azimuth determination. The system must be capable of acquiring an azimuth within 10 minutes of turn on, and 30 seconds after moving the ADS. The receiver must retain its positioning capability, and deliver an accuracy of 3.0 mils (0.17 degree), with a goal of 0.5 mil (0.03 degree). (The mil is the unit of measure of an angle used by artillery. $360 \text{ degrees} = 6283 \text{ milliradians} = 6400 \text{ artillery mils}$, a 1.862 % difference.)

A demonstration of the three systems was given at the U.S. Army Field Artillery School (USAFAS) at Fort Sill, Oklahoma, in September 1990. All three receivers performed within the goals stated below. Results of this demonstration are presented.

DESCRIPTION OF SYSTEMS

1. Magnavox

Two dual frequency microstrip antennas with preamplifiers are mounted on a baseline of one meter. A test signal generator inside the antenna assembly is used to calibrate the receivers and remove differential phase shifts. The user sights on distant targets with a telescope mounted under the antenna baseline.

Two Wild/Magnavox (WM) 102 receivers are used. The receivers share the same reference oscillator and local oscillator (LO). Each receiver contains five L1 channels and a L1/L2 channel pair. The test signal generator sends a low level L-band signal into two antenna feed lines for phase calibration. Receivers are kept phase coherent by using a common reference oscillator and common LO frequency synthesizer.

Both receivers have two intermediate frequency (IF) signal processor modules: one for the five L1 Course Acquisition (C/A) code channels, and one for the one L2 C/A and L2 P code channel. The six channel module is used for initial phase measurements. The L1/L2 channel is for L1-L2 "wide lane" phase measurements [1].

In the wide lane approach, the longer L1-L2 wavelength (84 cm) provides a very rough solution, but with few ambiguities. Then, the L1 carrier is used to obtain the precise azimuth. Hatch [1] explains that with a L1 wavelength of 19 centimeters, there are 11 different possible solutions for an azimuth. With a one meter baseline, this problem is equivalent to locating one antenna with respect to the other on a sphere of one meter radius.

Phase ambiguities are resolved by evaluating the phase residuals of all possible solutions. A minimum of three satellites are needed; five are desired for quicker ambiguity resolution. The ADS is operated through a Grid laptop computer connected to the receiver. Azimuths and the status of the ADS are displayed on the computer's screen. Data is recorded to a file on a floppy disk.

2. Texas Instruments (T.I.)

The T.I. ADS employs a one meter baseline of two antennas. The L1 carrier phase received at each antenna is mixed with the LO frequency at the antenna, creating the IF signal which is sent to the RF board of the receiver.

One T.I. ADS uses a 420 GPS receiver. The standard 420 includes the T.I. developed "channel on a chip" (COAC) technology, whereby a single channel is placed on each of five chips, with the capability of adding another channel to each chip. The modification made was to dedicate one channel to antenna A and the other channel on the chip to antenna B, each chip tracking the same satellite. The receiver can therefore track no more than five satellites.

An azimuth is calculated by first taking the single path difference between the baseline and each satellite, resulting in four single difference calculations if four satellites are tracked. Double path differences are then computed from the single differences. This results in three equations in three unknowns, from which the vector of the baseline can be calculated [2]. Like the Magnavox ADS, all software for the computation of azimuth is executed on a Grid laptop computer, and data is written to a file on disk.

3. Adroit

The Adroit ADS uses a 0.84 meter, three antenna baseline. Antennas A and B are 0.14 meter apart, and antennas A and C are 0.84 meter apart. Antennas are collinear microstrip. The software calculates a double difference of the phase measurements from the AB and AC baselines. First, the receiver computes an azimuth from the short baseline. This is a rough starting point from which to calculate the more accurate final solution. Preamplifiers attached to each antenna and a telescope complete the antenna array.

Adroit sub-contracted to Ashtech, Inc. for the receiver part of the ADS. It is a modified L-XII commercial receiver. Ashtech placed two 12 channel boards into one box, and divided the 24 channels into three RF sections of eight channels each (i.e. one RF section for each antenna). The receiver requires 12 volts to operate.

A satellite must be tracked by all three RF sections to be used in the azimuth determination. All RF sections use a common local oscillator. The software for determining azimuth is inside the receiver. Position and azimuth is given on the receiver display. However, the data recording capabilities of the Ashtech XII were not modified to record the azimuth solutions in a data file.

ADS DEMONSTRATION DATA

Upon delivery of all systems, a demonstration was given at the U.S. Army Field Artillery School. Each ADS was set up over a surveyed point, and data collected for about a three hour period. Contractor personnel operated the equipment, with an ETL representative acting as data recorder and witness.

Delta is the difference between the averaged ADS azimuths and the known surveyed azimuth. Sigma is the standard deviation for that group of data. Before comparing data between systems, consideration should be given as to how the data was collected.

With the Magnavox and T.I. systems, the ADS was pointed at a target and an average azimuth was recorded after about 15 minutes. This was only repeated about twice for each target. With the Adroit ADS, however, at least 10 azimuths were recorded for each target, recorded over a period of 3 hours. Therefore, when averaging together a group of data for each target, much atmospheric and multipath effects are averaged out. The Magnavox and T.I. data were averaged over a much shorter period of time.

MAGNAVOX		
Target	Delta	Sigma
MB-4	-2.15	1.87
MB-2	-4.22	2.69
ART	-0.56	2.18
SIGNAL	-7.38	2.95
WATER TOWER	-5.36	1.72
TEXAS INSTRUMENTS		
Target	Delta	Sigma
MB-4	3.43	2.96
MB-2	2.20	9.10
ART	-12.10	5.82
SIGNAL	0.54	6.49
WATER TOWER	No Measurement	
ADROIT		
Target	Delta	Sigma
MB-4	0.93	4.61
MB-2	0.83	4.93
ART	0.05	7.19
SIGNAL	4.39	5.35
WATER TOWER	-0.08	5.52

Table 1. ADS demonstration data.

Additional data was recorded with the Adroit ADS in October 1990. A test range was established by surveying in azimuths with a ring laser gyro inertial navigation system. The data presented is for a HDOP of less than 2.0. Table 2 shows the results of what is called the "single azimuth" test. The ADS is pointed at a target and one

number is recorded. Then the ADS is moved to a new target and the process repeated. The Adroit displays both a "quickazimuth" updated every second, and an average of 25 azimuths. This average is also updated every second, as a new quick azimuth is calculated. The average is the number that was recorded.

The Delta figure is the difference between the average of all 22 data samples recorded and the reference azimuth. The RMS value is the root mean square error of all data samples for that target. RMS and standard deviation are calculated as follows:

$$\Delta = \frac{(\sum q_i)}{N} - q_r$$

$$RMS = \sqrt{\frac{(\sum (q_i - q_r)^2)}{N}}$$

where q_i = data sample, q_r = reference azimuth, and N = number of samples.

Target	Delta	Std Dev	RMS
1	-0.23	2.65	2.65
2	-1.10	4.15	4.30
3	-0.55	4.50	4.53
4	5.06	5.34	7.35
5	3.94	1.82	4.34

Table 2. Single azimuth data (mils).

To see how the Adroit ADS azimuths vary over a short time period on a single target, the average azimuth was recorded every 30 seconds for ten minutes. (A total of 20 samples were recorded for each target.) This data is presented in Table 3.

Target	Delta	Std Dev	RMS
1	0.17	3.60	3.60
2	1.49	2.21	2.66
3	3.31	4.39	5.50
4	7.48	3.14	8.11
5	6.48	1.50	6.47

Table 3. Data over 10 min. (mils).

Note that in both cases, the data for the first three targets appears much better than the last two. Targets 4 and 5 were very close to the instrument; only a few hundred yards. The first three were about 2 to 3 miles away. Such errors as parallax would have less effect at these longer distances. (The scope on the Adroit and T.I. systems is mounted on the side of the antenna assembly.)

The data is presented in this manner to make an important point. The Delta figure shown is simply a difference of all average azimuths (recorded over a five day period) to the reference azimuth. But the RMS is calculated from a difference of each data point and the reference azimuth.

The Delta is almost always a more impressive figure than the RMS. These systems perform best when single azimuths over a large time frame are averaged, thereby eliminating most multipath and atmospheric effects. If one has three hours to determine an azimuth, a good figure can be attained.

Also of interest is how the data varies over an extended period of time. The graphs below (Figures 1 through 3) are plots covering a one hour period, while pointed in an arbitrary direction. The azimuths are plotted as a difference from the mean azimuth over the whole data collection time.

The high peaks in the Magnavox ADS data occurred at a time when the satellite constellation was changing. The gaps in this graph correspond to fewer than four satellites. In general, both the T.I. and Magnavox systems show more stability in their data.

FUTURE DEVELOPMENTS

Piraeus are underway to mount the Adroit ADS onto the top of a Multiple Launch Rocket System (MLRS). The short baseline will be kept the same, but the long baseline can be varied to find an optimal length. The azimuth data will be compared to the azimuths reported by the inertial navigation system of the MLRS. Static performance tests will be conducted at a variety of launcher elevations. Also to be investigated will be multipath reflections from the vehicle.

The next generation of GPS ADS will probably incorporate multiple baselines and require a 1 mil accuracy. Multipath and antenna phase center migration may be the largest problems to be overcome in the search for this high accuracy.

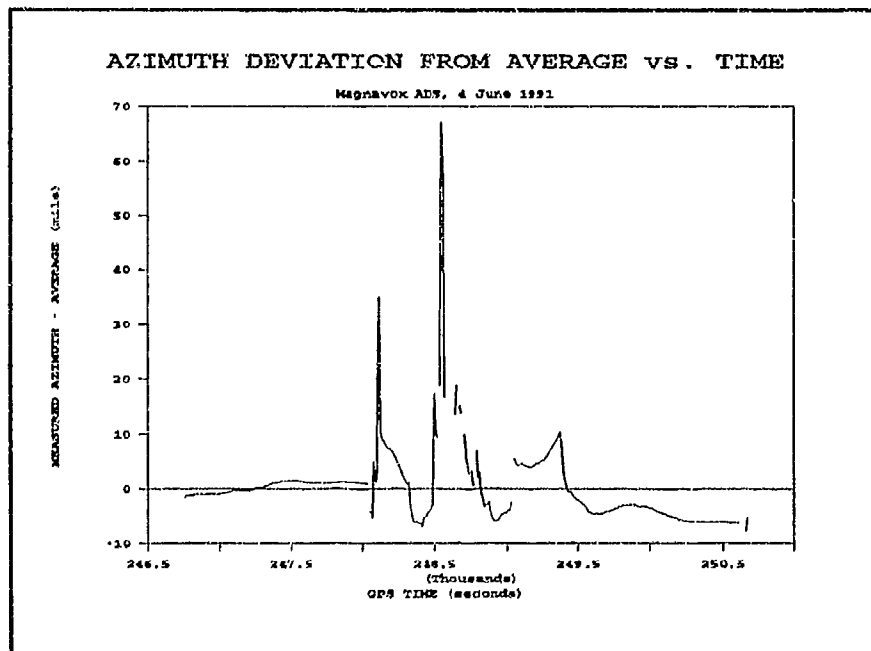


Figure 1 Magnavox azimuth variation over 1 hour.

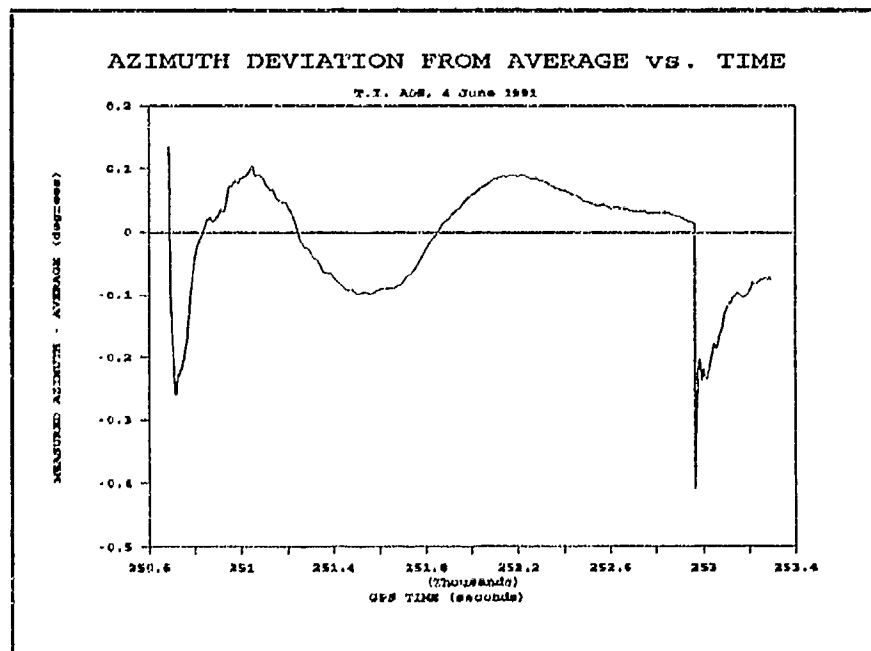


Figure 2 T.I. ADS azimuth variation over 45 minutes.

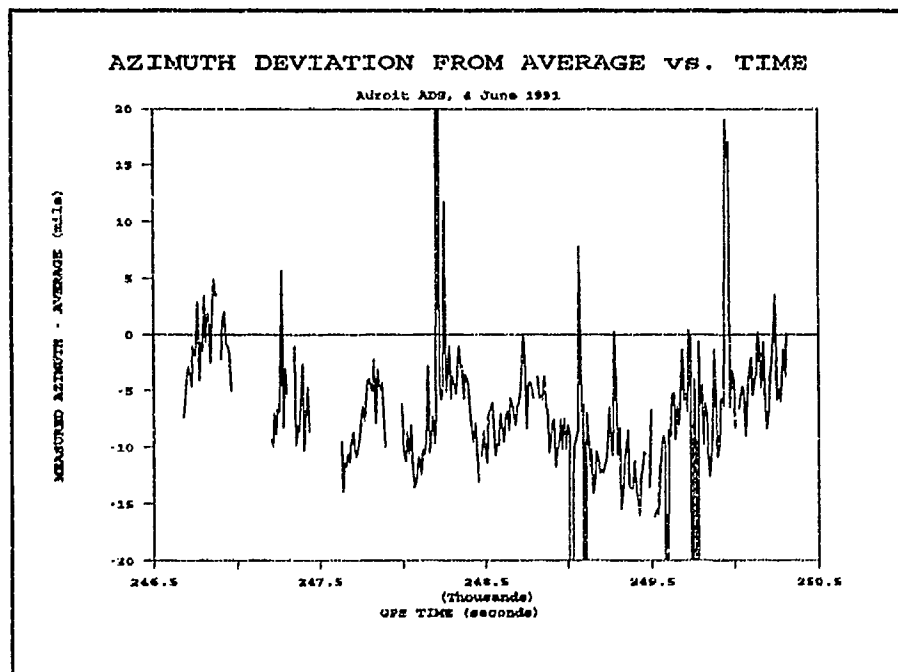


Figure 3 Adroit ADS azimuth variation over 1 hour.

CONCLUSIONS

The GPS ADS "proof of technical feasibility" study resulted in a successful demonstration of the interferometric approach to azimuth determination. As a result, there is interest within the U.S. Army toward using GPS for attitude determination. Finally, these contracts have led to the arrival of new receivers incorporating these concepts.

REFERENCES

1. Hatch, Ron, "Ambiguity Resolution in the Fast Lane," ION GPS-89, Second International Technical Meeting, Sept. 1989, Colorado Springs, CO.
2. Rath, J. and P. Ward, "Attitude Estimation Using GPS," ION National Technical Meeting, Jan. 1989, San Mateo, CA.

**INTERSTATE
ELECTRONICS
CORPORATION**
A Figgie International Company

1001 East Ball Road
Post Office Box 3117
Anaheim, California 92803

Telephone (714) 758-0500
TWX U.S.A. 910-591-1197 TELEX ITT 4722046

GPS FREQUENCY TRANSLATOR TRACKING USED FOR ERIS TSPI

By

CARL E. HOEFENER
Interstate Electronics Corporation

Prepared for Presentation at

FIFTEENTH BIENNIAL GUIDANCE TEST SYMPOSIUM
Holloman AFB, New Mexico
24-26 September 1991

GPS FREQUENCY TRANSLATOR TRACKING USED FOR ERIS TSPI

**By
Carl E. Hoefener
Interstate Electronics Corporation**

The Exoatmospheric Reentry-Vehicle Intercept Subsystem (ERIS) program presented some interesting guidance system evaluation problems. A unique tracking system was required to verify system performance. This paper defines the tracking requirements and the system developed to satisfy these severe tracking requirements.

WEAPON SYSTEM DESCRIPTION

The Strategic Defense Initiative (SDI) program is dedicated to the defense of the United States during a ballistic missile attack. The intent of the program is to detect and destroy enemy missiles or reentry bodies in the boost, midcourse, or terminal phase of flight. The two techniques selected for the destruction of these incoming vehicles are directed energy weapons and kinetic energy weapons. The kinetic energy weapons will be both space based and ground based. The Air Force is responsible for developing space-based weapons while the Army develops ground-based kinetic energy weapons. This paper deals with the flight test tracking requirements of the ERIS, a ground-based kinetic energy interceptor being developed by the U.S. Army Strategic Defense Command. The ERIS is designed to destroy vehicles during the midcourse portion of flight while still outside the atmosphere. It depends upon kinetic energy to destroy its target rather than conventional or nuclear warheads and must make a direct hit on the target.

THE SYSTEM TEST SCENARIO

The system test involves the launching of a target from Vandenberg AFB, California. The target is a reentry vehicle launched on a Minuteman I missile and is aimed for Kwajalein Missile Range in the mid-Pacific. The ERIS is launched from Meck Island in the Kwajalein Atoll. It is targeted to intercept the reentry-vehicle target before it reenters the atmosphere approaching Kwajalein. This test scenario presents some interesting time and space-position information (TSPI) problems. The reentry vehicle must be tracked from the time it passes over Hawaii, about 2,500 miles out from Kwajalein. The ERIS interceptor must be tracked from launch to intercept. The intercept takes place at an altitude of about 60 miles over the Kwajalein area before the reentry vehicle enters the atmosphere.

TRACKING PROBLEMS EXPERIENCED

Because of the large area over which the test takes place and the severe dynamics of the interceptor, many serious tracking problems are experienced. Also, because of the extreme range at which the reentry vehicle must be precisely tracked, conventional tracking techniques such as radars or ground-based trilateration systems are not effective. Therefore, a GPS system was selected for target tracking. Tracking of the interceptor presented a whole new set of problems because of its severe dynamics. Not only does the vehicle experience 10 g acceleration during its boost phase, it experiences jerk of about 50 g/sec during staging. Precise tracking is required throughout the entire flight of the interceptor for range safety and guidance system evaluation purposes. Even though GPS tracking technology was selected for the test tracking technique, normal GPS receivers are incapable of maintaining lock throughout the dynamics of these magnitudes. In addition, because of the size constraints of both the reentry vehicle and the ERIS interceptor, space was not available for GPS instrumentation receiver installation. The tracking solution clearly called for the use of a GPS frequency translator, both on the target and the interceptor.

A GPS frequency translator tracking system requires a broadband frequency translator located in the vehicle to be tracked. This frequency translator receives the broadband L1 GPS signal, translates the entire spectrum to S-band, and retransmits it to a ground-based translator processing system (TPS). The TPS contains a GPS reference receiver, which is a multichannel P-code receiver used to locate the TPS and provide initialization and aiding for the translator receivers. The mission control rack, besides containing the reference receiver, also contains a computer to provide control for the entire TPS. The translator receivers are GPS C/A-code receivers with an S-band RF front end. Because the received signal strength of the translators is relatively low, particularly at extended ranges from the target, directional dish antennas are generally used. Polarization diversity combiners are, therefore, required as part of the translator receivers. Each translator receiving system occupies a single equipment rack. A block diagram of a GPS frequency translator tracking system is shown in figure 1.

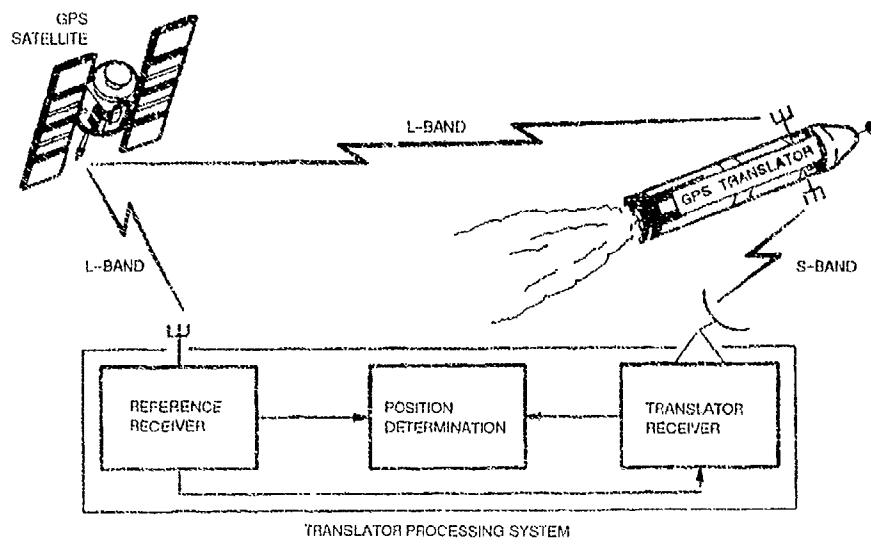


Figure 1. Translator Processing System

Although the GPS frequency translator is much smaller than a GPS instrumentation receiver, the size difference alone is not the major advantage of its use for this application. The two major advantages of the GPS frequency translator are the 6-dB signal tracking advantage of the translator over a GPS receiver, and most important that all signal processing takes place at the ground station. Because of the extreme dynamics of the interceptor, normal GPS instrumentation receivers cannot track through the severe changes in rate of acceleration owing to the characteristics of their tracking filters. Special filters using fast Fourier tracking technology have been developed that are capable of tracking the translated GPS signals even though the translator on the interceptor is experiencing jerk up to 50 g/sec. These special translator tracking receivers are relatively large. The size of the special filters they contain makes it impractical to incorporate them in an airborne GPS instrumentation receiver. Therefore the only practical approach to the ERIS tracking problems was the use of a GPS frequency translator tracking system. This was not the first application of a tracking system of this type. The GPS frequency translator tracking concept was proven in the testing of the U.S. Navy's Trident ballistic missile program.

THE GPS FREQUENCY TRANSLATOR TRACKING SYSTEM USED

Although the tracking concept had been proven, a whole new system design was required for the ERIS program because of its unique characteristics. A smaller GPS frequency translator was required than that used on the Trident program. Special high-dynamics GPS frequency translator tracking receivers were required. This tracking system was developed by Interstate Electronics under contract to the U.S. Air Force, who in turn provided the system to the U.S. Army Strategic Defense Command. The system has been installed and tested and is in operation at the U.S. Army's Kwajalein Missile Range (USAKA).

Since the only translators in use were the 180-cubic-inch dual-channel translators used on the Trident program, a new translator development program was needed for the ERIS program. A 40-cubic-inch single-channel C/A-code unit was developed and is in use on the ERIS program for both the target and interceptor. See figure 2. The ground-based TPS was also developed for the program. The TPS required two translator receivers and a reference receiver. (Actually four

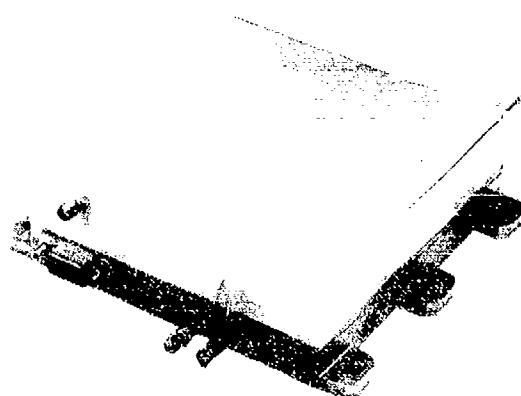


Figure 2. GPS Frequency Translator

051188-10

translator receivers were provided for redundancy and future growth.) In addition a signal simulator was available for premission system test, and a two-channel predetect recording system was on hand to accommodate postflight mission analysis. Figure 3 shows the entire ERS TPS.

SATELLITE COVERAGE FOR ERS TESTS

By far the most significant determinant of GPS tracking system accuracy is geometric dilution of precision (GDOP), or the position of the satellites in relation to the location of the vehicles containing the GPS frequency translators. Each vehicle must "see" at least four satellites. For maximum position accuracy determination, the satellites should be fairly well spread out. Since the original schedule for the ERS program called for flight tests before the complete GPS constellation would be deployed, several pseudosatellites, or ground transmitters, were planned to support the operation. The original test plan called for seven pseudosatellites located on islands around the Kwajalein area. See figure 4. When the original flight tests took place in early 1991, however, there were sufficient satellites in the GPS constellation that only two pseudosatellites were used.

The initial ERS flight test was a resounding success, and the GPS translator tracking system was the major factor in verifying system performance.

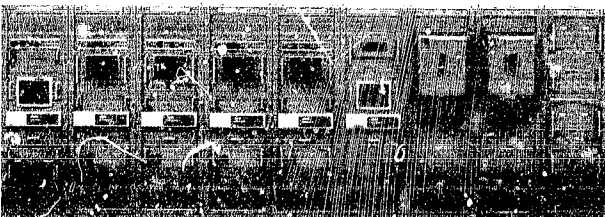


Figure 3. ERS Translator Processing System

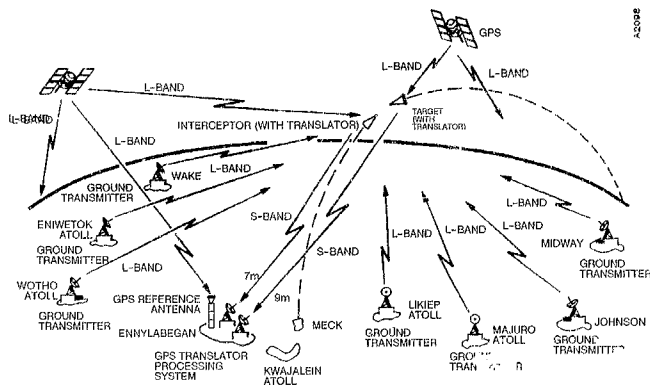


Figure 4. Originally Planned Global Positioning System Support for ERS

ADVANCES IN GPS ATTITUDE DETERMINING TECHNOLOGY AS DEVELOPED
FOR THE STRATEGIC DEFENSE COMMAND

Richard Jurgens
Charles Rodgers
Adroit Systems, Inc.
809 N. Royal St.
Alexandria, VA 22314

ABSTRACT

Under a contract from the Strategic Defense Command (SDC), Adroit Systems, Inc. has developed and tested an Attitude Determining System (ADS) based on GPS satellite signal interferometry. The relative phase difference of the GPS carrier is measured between a pair of antennas spaced about 1 meter apart to determine the antenna baseline pointing vector. The system requires only three satellites to operate once the position of the antenna is ascertained. Double differencing is used to eliminate RF bias and drift between antennas.

The original SDC ADS used only two antennas and a single baseline. To solve the integer cycle ambiguity problem more efficiently, Adroit has implemented a method to use three antennas to form two baselines. This modified system uses a GPS receiver that has only two antenna ports. Having only two antenna ports avoids the expense of adding a third RF module to the receiver. The three antennas form a short and a long baseline. The short baseline is used to obtain a rough baseline pointing vector. This rough vector is then refined using the long baseline measurements to obtain an accurate baseline vector.

The second generation of this ADS was designed and delivered in 1990 to the US Army's Engineer Topographic Laboratories (ETL) for evaluation along side two other systems submitted by other contractors. Test results are presented for all systems. The Adroit ADS can calculate and update pointing information each second. Accuracy was demonstrated to approximately 10 milliradians in one second, and below 1 milliradian with a 300 second sample time.

INTRODUCTION

Adroit Systems, Inc., the first company to produce a successful GPS ADS, is working under a new contract from the Strategic Defense Initiative Organization (SDIO) to further enhance the performance of the system. This paper will briefly recap the theory, history, and present performance of the GPS ADS. Then it will discuss some of the methods we are using to improve the system. Test results for these new methods are not yet available.

However, we anticipate some results will be available for the oral presentation of this paper.

ADS THEORY

The ADS is an instrument that is used to measure azimuth and elevation of a desired baseline for pointing or navigation applications. The instrument is a type of electronic compass and theodolite that is immune to local variations of magnetism and gravity. Its attitude solution does not drift as inertial sensors do. It measures azimuth and elevation from the point of the instrument to a point that the instrument is sighted to. It uses Global Positioning System (GPS) C/A signals to determine position, azimuth and elevation.

The system is comprised of three GPS antennas that are mounted on a baseline whose length is about a meter (Fig. 1). Two of the antennas are mounted at each end of the baseline, the third is mounted about 14 centimeters from one of the first two. These antennas feed into a modified GPS receiver that has enough RF sections to measure simultaneously carrier phase received on each antenna. A normal GPS receiver has only one antenna and one RF section. The receiver also contains the real-time software to

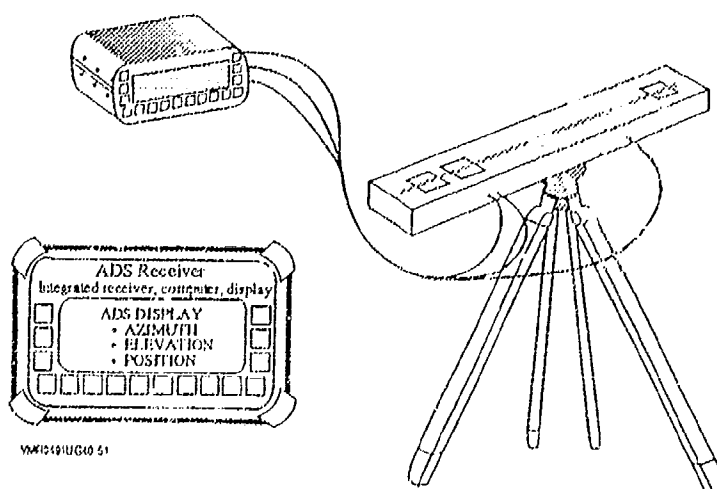
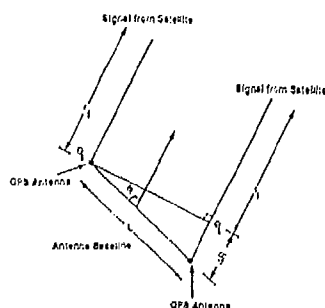


Figure 1: System Design

process the phase measurements into an attitude solution, as well as the standard GPS positioning software.

The carrier phase measurement made at each antenna includes the effects of receiver measurement error, antenna phase center migration, and multipath errors. The receiver uses the difference between the carrier phase measurement made at each antenna to determine an angle to each satellite (Fig. 2). This phase difference retains some of phase errors mentioned above, although

ATTITUDE DETERMINATION



WITH DIFFERENTIAL PHASE ΔR MEASURED BY RECEIVER THE ANGLE BETWEEN THE BASELINE VECTOR, X , AND THE VECTOR TO SATELLITE 1, I_1 , IS

$$\theta_1 = \cos^{-1}(\Delta R_{(1)} / L_1)$$

$$\text{DEFINE } Y = \begin{bmatrix} \cos(\theta_1) \\ \vdots \\ \cos(\theta_{N_{SAT}}) \end{bmatrix} \quad \text{AND } R = \begin{bmatrix} I_1 \\ \vdots \\ I_{N_{SAT}} \end{bmatrix} \quad \text{THEN } R X = Y$$

AND BASELINE VECTOR CAN BE CALCULATED AS $X = (R^T R)^{-1} R^T Y$

VH1451UG40 52

Figure 2: Software Design

the common components of the errors are eliminated. The receiver can only measure the truncated fractional part of the full carrier phase difference, not the number of full carrier cycles between the antennas. This unmeasured integer is called the cycle ambiguity, and it was the most difficult and time consuming calculation.

Adroit has developed software to determine the cycle ambiguity, and has configured the hardware to speed up the determination process. The three antenna configuration, first developed by Adroit, allows the system to take advantage of dual baselines. The antenna pair A-B is spaced less than a wavelength apart, and constitutes the short baseline. Antenna pair A-C constitutes the long baseline. The long baseline solution is

desirable because the accuracy of the attitude measurement is proportional to the baseline length. The system is capable of calculating the attitude of both baselines. However, the algorithm first determines the attitude of the short baseline because it has no integer carrier cycle ambiguity. This coarse attitude solution provides an initial attitude approximation for the long baseline. This approximate attitude limits the possible solution space of integer cycles between the antennas on the long baseline. With fewer integer cycle possibilities, the software rapidly converges to the actual integer count.

When the cycle ambiguity integer is added to the measured fractional phase, this total phase difference can be used with the known baseline length to calculate a satellite pointing angle. This satellite pointing angle is calculated in the local reference frame of the antenna baseline. Using three of these satellite pointing angles and the known satellite positions, we can transform from the baseline reference frame to the Earth Centered Earth Fixed (ECEF) reference frame. This transformation results in the azimuth and elevation, or attitude, of the baseline in the ECEF reference frame. Knowledge of the user's position can be used to transform the attitude results into any local reference frame..

SYSTEM DEVELOPMENT AND TEST

Adroit Systems began development of a GPS ADS in 1988 under a contract with SDIO. Our initial laboratory prototype used a TI-420 receiver modified to have two RF sections to process the phase measurements from two antennas. This prototype used a personal computer (PC) for data processing, and was not a real-time system. However, it did prove the feasibility of the concept. Adroit built on the knowledge gained under that contract to develop a second generation ADS for the ETL.

The ETL system was designed to be used a free standing instrument to point artillery (Fig. 1). The system uses a receiver with three RF sections to process the signal from the three antennas. All the software is resident in the receiver, and the solution is indicated on the receiver display. The system operation is very simple. Turn the receiver on, let it lock on to four satellites, point the baseline, and then read the baseline attitude. This ADS works in real-time with attitude updates each second. The system has demonstrated azimuth accuracy to about 1 mil (1 mil = 0.982 mrad). Table 1 summarizes the performance of Adroit's ADS system, and gives its design specifications.

The ADS was delivered to ETL in June 1990. Texas Instruments (TI) and Magnavox also built systems for ETL.

A comparative demonstration of all three systems was held on September 27, 1990 at the U.S. Army Field Artillery School at Ft. Sill. The participants were to use their ADS to find the azimuths

Table 1: System Performance

PARAMETER	PERFORMANCE	SPECIFICATION
AZIMUTH		
accuracy:		
80% avg (360 seconds)	0.5 mils	n/a
100% avg (360 seconds)	1.2 mils	n/a
1 sigma (30 seconds)	5.7 mils	+/-3 mils
1 second sample	10.0 mils	n/a
ELEVATION		
accuracy:		
1 sigma (30 seconds)	10.0 mils	+/-3 mils
RESPONSE TIME		
Initialization time	120.0 seconds	300 secs
realignment recovery	1.0 second	30 secs
POSITION		
UTM coordinate offsets		
North	-8.1 meters	10 meters
East	-3.5 meters	10 meters
Altitude	0.0 meters	10 meters

from a central point to five previously surveyed targets. The participants were given approximately one hour of operating time to arrive at their final azimuths. The Adroit system was operational in less than two minutes. The operator pointed the baseline at the first target, waited 30 seconds for the averaged azimuth reading, and recorded the data. He then took data similarly for the other four targets. This procedure was repeated until the allotted time expired. The operator was able to take 68 measurements in 53 minutes. The readings for each target were then averaged to arrive at the final azimuths. Table 2 contains Adroit's results. Tables 3 and 4 contain Magnavox's and TI's results.

The Adroit ADS's average error for all five targets combined was 1.2 mils, with a standard deviation of 5.7 mils. The error for the Signal Mountain target was the worst at 4.4 mils. The next highest azimuth error for one target was 0.9 mils at target MB-4. The lowest average error for one target was 0.08 mils at the post water tank. Note that all three systems measured Signal Mountain's azimuth poorly. If the Signal Mountain measurements are disregarded, the average error for the remaining four targets is 0.52 mils.

Adroit's average azimuth error was three times better than the next best system. One factor in that result is that Adroit was able to take and average nearly twice as many measurements as the other two systems. We achieved this efficiency because our three antenna system allowed us to solve the integer cycle ambiguity faster than the other two antenna systems. Also, our system is simple to operate. The Adroit ADS required no operator

Table 2: Ft. Sill Data Summary

STATION TARGET	ADROIT DAVIS AZIMUTH (MIL)			
	TRUE	MEASURED	Δ	σ
MB-4	6323.009	6322.08	0.93	4.61
MB-2	1000.269	999.44	0.83	4.93
ART	5014.67	5014.62	0.05	7.19
SIGNAL MTN	4733.951	4729.56	4.37	5.35
WATER TOWER	2431.887	2431.97	-0.08	5.52
AVERAGE ERROR			1.2	5.7
POSITION	TRUE	MEASURED	DELTA	
N	553065.711	553057.6	-8.11	
E	3837262.031	3837258.5	-3.53	
ELEV	363.955	364.0	0.05	

 Δ = TRUE AZIMUTH - MEASURED AZIMUTH σ = STANDARD DEVIATION ABOUT THE MEAN

VJA179110036-15

Table 3: Ft. Sill Data Summary

STATION TARGET	MAGNAVOX DAVIS - 1 AZIMUTH (MIL)			
	TRUE	MEASURED	Δ	σ
MB-4	6294.142	6296.29	-2.15	1.87
MB-2	972.41	976.63	-4.22	2.69
ART	5022.815	5023.38	-0.56	2.18
SIGNAL MTN	4736.629	4744.01	-7.38	2.95
WATER TOWER	2434.569	2429.42	-5.36	1.72
AVERAGE ERROR			3.9	3.8
POSITION	TRUE	MEASURED	DELTA	
N	553093.37	553086	-7.37	
E	3837246.96	3837238	-7.04	
ELEV	363.955	416	52.05	

 Δ = TRUE AZIMUTH - MEASURED AZIMUTH σ = STANDARD DEVIATION ABOUT THE MEAN

VJA179111038-16

Table 4: Ft. Sill Data Summary

STATION TARGET		TEXAS INSTRUMENTS DAVIS - 2 AZIMUTH (MIL)		
		TRUE	MEASURED	Δ
MB-4		6340.992	6337.56	3.43
MB-2		986.871	984.67	2.20
ART		5042.057	5054.16	-12.10
SIGNAL MTN		4738.046	4737.51	0.54
WATER TOWER		NO MEASUREMENT		
ALTN. WAT TOWER		1907.36	1903.44	3.92
AVERAGE ERROR				4.4
POSITION		TRUE	MEASURED	DELTA
N		553051.06	553044.40	-6.61
E		3837235.46	3837228.00	-7.46
ELEV		353.955	371.60	7.65

Δ = TRUE AZIMUTH - MEASURED AZIMUTH
YIA1701UC38-17

σ = STANDARD DEVIATION ABOUT THE MEAN

intervention except pointing the baseline and recording the attitude.

The Adroit ADS's standard deviation is slightly higher than Magnavox's system. This is probably due to the way the two teams took data. Magnavox took a set of data at each target during a short period. Adroit spread out the data collection at each target over the full test time. By taking the data for each target all at once, Magnavox did not get the measurement variation caused by the changing satellite geometry. Adroit's data collection method allowed the measurements to be taken under a variety of satellite geometries. This variation can cause geometrical biases to be averaged out improving the average error but giving us a larger deviation. We will discuss satellite geometry's contribution to attitude error later in this paper.

SYSTEM IMPROVEMENTS

As stated earlier, Adroit is under contract to SDIO to develop methods to improve the ADS. Figure 3 gives some idea of the accuracy improvement we expect if all our methods are implemented. The figure also lists factors that affect the attitude accuracy. As the contract is not complete, we will not discuss all our new methods in this article.

One of the improvements we are working on for the next generation ADS is satellite selection algorithms. The satellite selection algorithms will reduce the errors due to less than optimum satellite geometry.

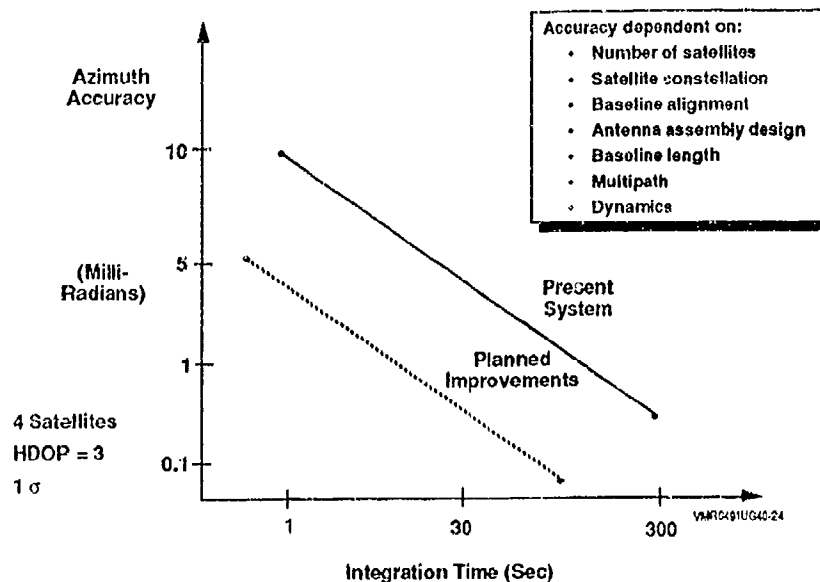


Figure 3: ADS Accuracy
1 Meter Baseline

In addition, we have developed a simple way to get the benefits of a three antenna ADS from a receiver that has only two RF modules. These benefits include faster solution convergence and fewer attitude errors. Also, a receiver that has only two RF sections is less expensive than a three RF section receiver.

SATELLITE SELECTION

As in GPS positioning, satellite geometry plays a significant role in determining the accuracy of the measurement. During the Ft. Sill tests, Adroit ADS's measurements made with the best satellite constellations were twice as accurate as the overall average. They were seven times as accurate as the measurements made during the worst satellite geometry periods.

To get an intuitive grasp of the satellite geometry problem, we can simplify the problem by looking at it in two dimensions. It can be shown that, in two dimensions, the relationship between the angle of the vector to the satellite and the measured differential phase is described by the equation:

$$\Delta\phi = L * \sin(\alpha)$$

where

$\Delta\phi$ = the differential phase between the baseline antennas [mm]

L = the baseline length [mm]

α = the angle to the satellite as defined in Figure 4

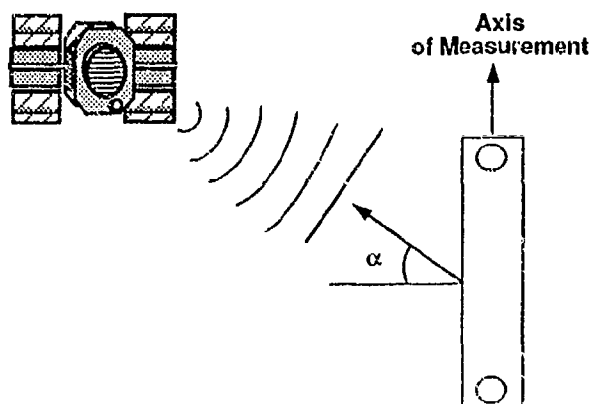


Figure 4: Definition of Satellite Angle

WM7071UG40.1

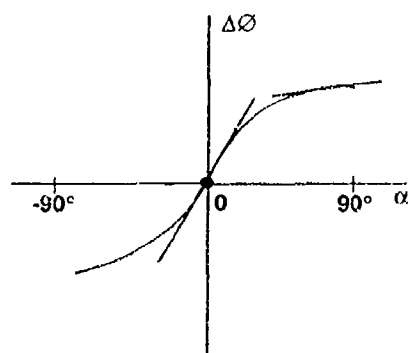


Figure 5: Measured Differential Phase
vs.
Angle to Satellite

WM7071UG40.1

This sine relationship causes greater errors in calculating the angle to the satellite when the satellites angle α is large. This can be seen from Figure 5 which shows the sine relationship. There is always a few millimeters worth of uncertainty in the phase measurement due to the receiver and antenna errors. This

uncertainty means there is always a range of alphas that are possible solutions. For satellites with an alpha angle near 0, the small measurement uncertainty yields an equally small alpha uncertainty because the slope is nearly one. However, for satellites at alpha angles near 90 degrees this small measurement uncertainty causes a large angular uncertainty because the slope approaches zero in that region. Therefore, the closer the satellites are to being lined up with the axis of measurement the less accurate the attitude can be determined.

The problem is how do we evaluate the "goodness" of a satellite constellation's geometry. In normal GPS positioning, satellite geometry is rated by the standard figures of merit GDOP, HDOP and VDOP. GDOP, HDOP, and VDOP stand for Geometric, Horizontal and Vertical Dilution of Precision. All three of these figures of merit are based on the same method of rating satellite geometry for positioning accuracy. Adroit has found that, although there is some correlation between good positioning geometry and good attitude geometry, GDOP is not the best method of choosing the satellite constellation for attitude measurement.

To demonstrate this, Adroit has run simulations in which the attitude solution was determined from satellites chosen according to HDOP. We have then run the same simulations again, but with the satellites chosen according AZDOP. AZDOP (azimuthal dilution of precision) is Adroit's figure of merit (modified from earlier work¹) that considers the positions of the satellites relative to the baseline vector. AZDOP is determined from the following formula:

$$AZDOP = \sqrt{\cos^2(AZ) * D_{11} + \sin^2(AZ) * D_{22}}$$

where the matrix

$$D = (RA^TAR^T)^{-1}$$

and

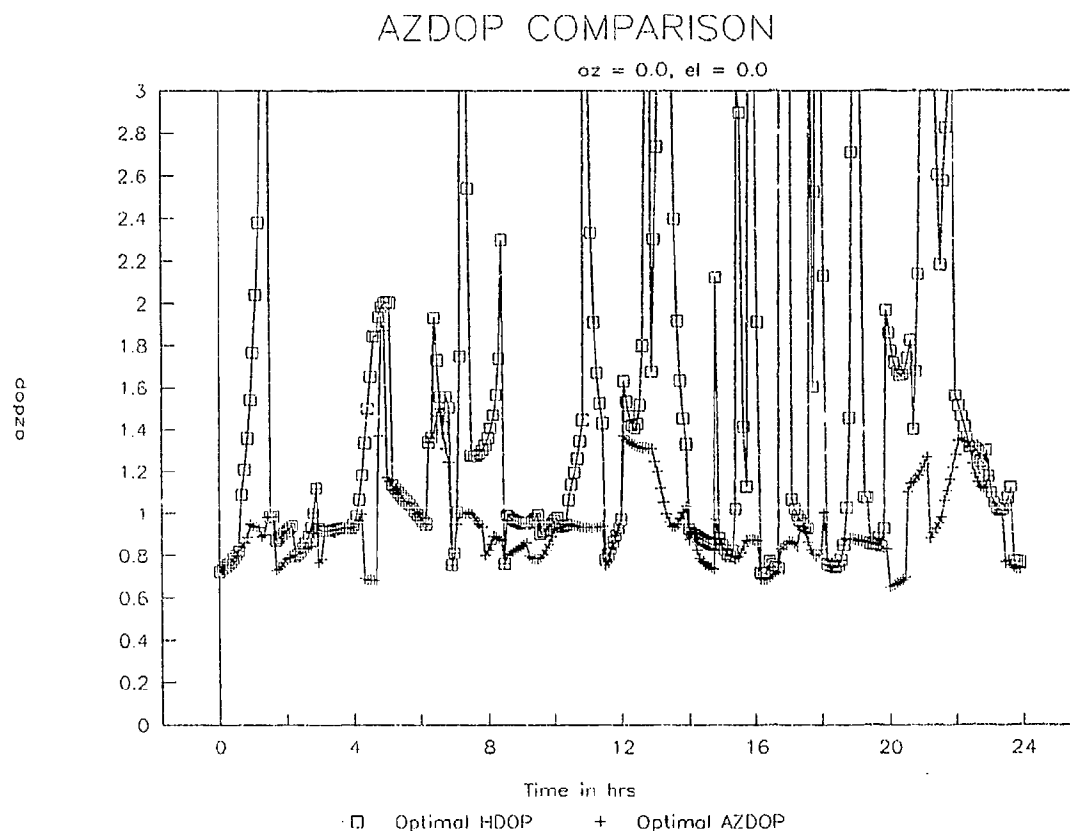
az = azimuth angle

D_{ii} = the i th element of the D matrix

A = double difference matrix operator which ensures

independence in R
 R = matrix of receiver to satellite vectors.

Figure 6 shows the results of these simulations. If AZDOP is an indicator of good attitude geometry, as Adroit believes, it can be seen from this plot that HDOP is not an optimum method of selecting constellations for attitude measurement. Although it is cut off in figure, selecting by HDOP sometimes yields an attitude dilution of precision 35 times worse than selecting by AZDOP.



The overall accuracy of the azimuth measurement can be predicted by using AZDOP combined with baseline length and carrier phase measurement noise. The equation for the azimuthal accuracy is:

$$AZIMUTHACCURACY = AZDOP * \frac{1}{L} * PE$$

where L = length of the baseline and PE = phase error.

Similar equations can be defined to predict elevation and roll accuracy from their DOP figures of merit. Note that the optimum set of satellites will be different for roll, elevation, and azimuth measurements.

The next generation ADS will incorporate software that selects satellite constellation according to AZDOP. The coarse attitude solution from the short baseline will be used as the baseline vector to choose the satellites. The software will then use that constellation to solve for the long baseline attitude. The system will check to see if the best constellation was used for that attitude. If not, a new constellation will be chosen, and the process will be repeated. The algorithms for this enhancement have been written, and are now being tested.

ALTERNATE SYSTEM CONFIGURATION

Adroit has discovered a simple way to reduce the ADS system cost for static applications. Adroit's first ADS prototype was a TI-420 receiver with only two RF sections. With two antennas, it was enough to demonstrate the system's potential to SDIO. However, two antenna systems have slower solution convergence, and the solution integrity is much poorer.

The system that uses the TI-420 requires a PC to process the data the receiver collects. We have been using a commercial digital Input/Output (I/O) expansion board in the PC for the data transfer. As this is a serial transfer, there are extra lines on the board that are not used. We determined we could use these lines to control a two state mechanical microwave switch.

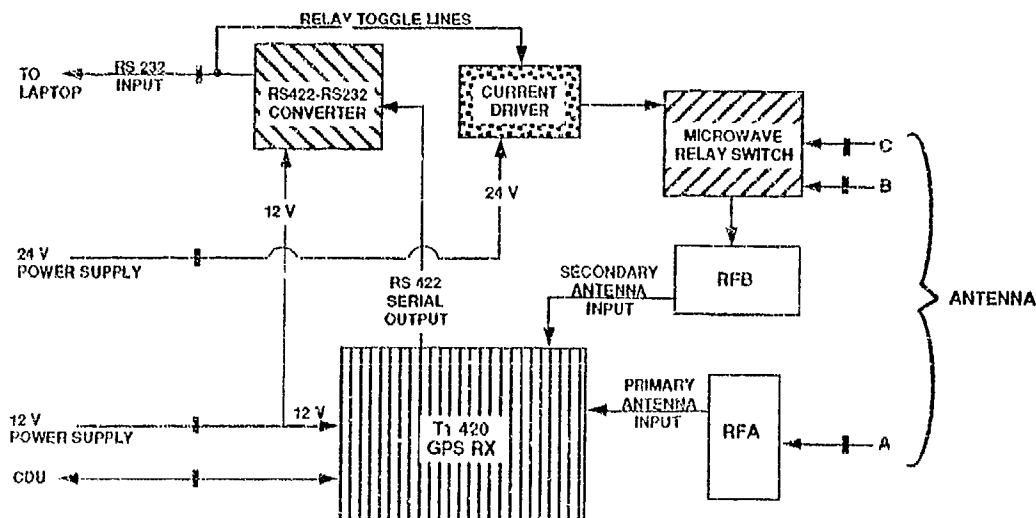


Figure 7: 2 RF Section System Configuration

VAX001UG30

Therefore, we connected the three antenna leads for our dual baseline system to the switch. We then modified the ETL dual baseline software to control the switch through the I/C board. The modified system first connects the short baseline antenna leads to the PC, collects phase data, and solves for the coarse attitude. Then it switches to the long baseline and solves for the precise attitude. Figure 7 is a schematic of the design.

The modification works well. Solution integrity is as good as the ETL system. However, the time to solution is longer, mainly due to delays in the transfer of the serial data. Also, the PC we are using in this prototype is slower than the processor in the ETL ADS receiver. Whereas a single attitude solution takes about one second on the ETL machine, it takes 8 to 12 seconds on the modified prototype. It takes 3 - 5 seconds to get each baseline's attitude solution because of the slow transfer of phase data. The switching takes about 2 seconds. This time includes a period during which the data coming to the PC is intentionally disregarded. The system is programmed to do this because of the data errors caused by the bounce of the mechanical switch.

We intend to speed up the system by either implementing a debouncing circuit or using a solid state switch. Also, a faster PC would speed up the processing. Unfortunately, because of the data format of the present TI-420 receiver, there is no way to speed up the data transfer. However, if a receiver manufacturer were designing an ADS receiver, they could incorporate the faster processor and solid state switch into the new design. The receiver could then use the dual baseline system with two RF sections. The time to solution for such a system should be as good as our ETL ADS because there would be no data transfer bottleneck.

ACKNOWLEDGEMENTS

The authors would like to thank SDIO and Dr. David Lukins, Dr. John Phillips, and Dr. John Johnson of the US Army Strategic Defense Command in Huntsville for their continued support and funding. Also, the support of the US Army Engineer Topographic Laboratories and Mr. Toney Hawker, Mr. Richard Marth, and Pete Cervarich has made this research possible.

REFERENCES

1. Brown, R. and Evans, A., "GPS Pointing System Performance," Proceedings of ION GPS-90, Third International Technical Meeting Of the Satellite Division of The Institute of Navigation, Colorado Springs, Colorado, Sept. 1990.
2. Jurgens, R., "Realtime GPS Azimuth Determining System," Proceedings of the National Technical Meeting, The Institute of Navigation, San Diego, CA., Jan. 1990.

SESSION III-A
INERTIAL INSTRUMENTS

CHAIRMAN
RON COX
LITTON GUIDANCE & CONTROL

Cryogenic Inertial Instruments
LtCol Gerald L. Shaw
Phillips Laboratory Hanscom AFB, MA

Abstract

Current inertial navigation and guidance systems use relatively mature technologies. These systems depend on the availability of pre-mapped gravity information and they require periodic external updates to account for instrument drift. Our goal for the twenty-first century is a compact, autonomous, non-jammable and virtually drift-free inertial system for precise navigation, guidance and pointing. This goal demands revolutionary rather than evolutionary inertial technologies. A long range research program is investigating such technologies, with an emphasis on highly promising cryogenic techniques that exploit unique properties of superconductors and superfluids.

The Air Force and NASA are supporting the development of a family of niobium based superconducting instruments at the University of Maryland. The superconducting six-axis accelerometer senses the rigid body motion in all six degrees-of-freedom of a single levitated niobium proof mass, and constitutes a complete inertial measurement unit by itself. Superconducting tensor and linear gravity gradiometers are being developed to support a space mission to obtain dense, precise, and direct global measurements of gravity. These gradiometers also have application as real time gravity measurement aids for autonomous inertial navigation. In another effort, the Air Force and NOAA are supporting development of a superfluid helium gyroscope at the University of California at Berkeley. This development is in the very early stages and poses several practical limitations. However it does promise unprecedented sensitivity to rotation and may find application in attitude determination and control of large Earth-based platforms. Status and projected performance of the superconducting six-axis accelerometer and the superfluid helium interference gyro will be discussed.

Cryogenic Inertial Instruments
LtCol Gerald L. Shaw
Phillips Laboratory, Hanscom AFB, MA

The Earth Sciences Division of the Phillips Laboratory performs research in seismology, geodynamics, geology, geodesy and gravity. The aims of the geodesy and gravity programs include improving the fundamental knowledge of the earth's size, shape and gravity field and improving the techniques used for determining position, distance and direction on the earth's surface. To help achieve these goals part of the program is devoted to develop new instrumentation to measure geophysical phenomena at ever increasing levels of accuracy and precision. Since geodetic and gravimetric parameters for the earth are fundamental inputs for inertial guidance systems, this instrumentation has direct application to guidance navigation and control.

Two such instruments are the Superconducting Six-axis Accelerometer (SSA), under development at the University of Maryland and the Superfluid Helium Interference Gyroscope (SHIG) being developed by the University of California at Berkeley. The SSA grew out of geophysics requirements to develop moving base gravity gradiometers and fundamental physics research efforts to perform a test of the Gravitational Inverse Square Law. This test is first to be performed in the laboratory and then on a polar orbiting spacecraft using a spaceborne gravity gradiometer. The SHIG grew out of geophysics requirements to measure the rotation vector of the solid earth to better than 0.1 milli-arc second with a temporal frequency of at least several cycles per day, and scientific efforts to investigate both the general relativistic effect associated with the earth's rotation (i.e. the Lense-Thirring effect) and the fundamental physics of macroscopic quantum phase coherence in superfluid helium. In both development efforts, to meet science and applications requirements, a revolutionary improvement in performance over conventional inertial sensing technologies was demanded.

Superconducting technologies afford several unique advantages, which, when exploited properly, offset the complications associated with cryogenic technology. In particular, beyond the obvious reduction in thermal noise, superconductivity affords the opportunity for near perfect magnetic shielding (Meissner effect), a high degree of mechanical and electrical stability, virtual elimination of thermal gradients and unprecedented measurement sensitivity using SQUIDs (Superconducting Quantum Interference Devices). For these reasons the Earth Sciences Division has been pursuing a program to develop superconducting inertial instruments since 1985.

SUPERCONDUCTING SIX-AXIS ACCELEROMETER (SSA)

DESCRIPTION ¹

An exploded view of the SSA is shown in Figure 1. The proof mass is constructed from four plates of pure niobium to form an inverted cube, 2.784 cm on a side. These plates are polished to a thickness of 2.39 mm with orthogonality and flatness maintained to a part in 10^3 . Eight titanium alloy, (Ti-6Al-4V), cubic coil forms surround the proof mass. The three cube surfaces that face the proof mass contain a recessed flat circular region which holds the Nb-48Ti levitation/sensing coils. The three opposite faces are held in place by a set of six cylindrical niobium coil form holders which come together to form a niobium cube inside the titanium cube. The resulting gap between the coil forms and the proof mass is 0.15mm. The 10.16 cm precision titanium cube, which houses the SSA, has surfaces machined and polished flat and mutually orthogonal to better than 2 parts in 10^5 . The entire assembly weighs less than 5 kg.

LEVITATION

The proof mass is suspended in quantized magnetic flux generated by persistent supercurrents in the levitation coils. Being superconducting itself, the proof mass excludes magnetic flux and thus its motion within the cavity forces the magnetic flux to redistribute within the superconducting circuitry. The transfer of energy to redistribute the magnetic flux produces reaction forces opposing the change which in effect act as "magnetic springs" having stiffnesses proportional to the corresponding levitation supercurrents. The ability to adjust these supercurrents allows each degree of freedom (three translational and three rotational) to be constrained and controlled by an independent superconducting circuit made up of four levitation coils. Levitation in the x axis is accomplished by the four coils beneath the yz plane (Figure 2). Three letter subscripts uniquely specify the position of each coil. The first two refer to the plane and the third to the normal axis. Bars over the subscripts indicate the negative direction. Thus $L_{\bar{y}z\bar{x}}$ is the coil in the yz plane (negative y , positive z quadrant) facing the negative x side of the proof mass. The superconducting circuit is shown in Figure 3. The resistive element indicated is a shielded heat switch made from a 1/8 watt, 500 ohm carbon resistor. When the device is initially cooled there is no current flow in the levitation circuit. To store the desired persistent supercurrent in the loop requires several iterations. First the circuit is driven with a constant current I_1 from an external source. Then the heat switch is pulsed on, driving the path between the superconducting joints normal and forcing the current to flow through the four superconducting coils in the direction indicated. When the heat switch is turned off the short path becomes superconducting, trapping the current I_1 in the levitation/feedback loop. This procedure is repeated with successively larger currents until the desired levitation force is obtained. Also included in the loop is a feedback transformer which

permits a feedback controller to adjust the persistent current.

Rotational levitation about the x axis is accomplished with four coils above the xy plane (Figure 4). The circuitry to accomplish this is shown in Figure 5. Here two external current sources and two heat switches are required. The procedure is to first input I_2 with hs_3 on and hs_2 cycled storing identical currents, I_2 , in all the coils and putting a force on the proof mass in the negative z direction. Next, with I_3 on and hs_3 cycled the effect is to add $I_3/2$ to the right half branch and to subtract $I_3/2$ from the left half branch. The resulting current difference produces a torque about the x axis.

SENSING

Another consequence of the redistribution of flux allows detection of the motion. Each degree of freedom is monitored by four coils connected together to form a superconducting bridge. In the latest model these are the same coils used to constrain and control the corresponding motion. Detection is possible due to the fact that the coil inductance will change in proportion to the displacement of the superconducting proof mass.²

Figure 6 depicts a simplified version of the detection scheme for a single degree of freedom. As the proof mass is displaced in the positive x direction, the sensing inductances L_2 and L_4 decrease while L_1 and L_3 increase. This unbalances the bridge and generates an oscillating current in the output coil. This current is converted to a voltage by the SQUID amplifier. Figure 7 shows how this is actually implemented to sense x axis translation in the SSA. Here L_2 and L_4 correspond to L_{yzx} and $L_{\bar{y}z\bar{x}}$ and L_1 and L_3 correspond to $L_{y\bar{z}\bar{x}}$ and $L_{\bar{y}z\bar{x}}$. Clearly rotation about x or translation along either the y or z will not alter any of the gaps. A careful look will also reveal that, while rotations about y and z change the gaps, the inductances are altered such that adjacent arms of the bridge change together and the bridge is indeed only sensitive to translation along the x axis. Figure 8 depicts the sensing circuit for a rotation about x . Similar strategies are employed to detect the remaining translational and rotational motions.

TEST RESULTS³

Extensive tests were run on the Model I SSA to verify parameters, measure transfer functions and determine noise levels. All of these tests were run in an open loop mode, with small DC current sources connected to the feedback lines. Calibration inputs were supplied by a shaker which can translate in three degrees of freedom and rotate about a single axis. The amplitude of the rotation was measured optically and the linear motions were monitored by a triad of Sundstrand Q-flex 1000 accelerometers. In this manner the scale factors for each of the six degrees of freedom were determined. These are shown in Table 1 in terms of fluxoids at the SQUID loop per unit input. Also

shown is the calculated total acceleration white noise.

AXIS	MEASURED RESPONSE	ACCELERATION WHITE NOISE
X	$3.1 \times 10^5 \Phi_0/g$	$4.0 \times 10^{-10} g/Hz^{1/2}$
Y	$9.9 \times 10^3 \Phi_0/g$	$1.6 \times 10^{-8} g/Hz^{1/2}$
Z	$1.6 \times 10^5 \Phi_0/g$	$5.9 \times 10^{-10} g/Hz^{1/2}$
θ_x	$2.1 \times 10^3 \Phi_0/rad/sec^2$	$6.7 \times 10^{-8} rad/sec^2/Hz^{1/2}$
θ_y	$6.0 \times 10^2 \Phi_0/rad/sec^2$	$2.2 \times 10^{-7} rad/sec^2/Hz^{1/2}$
θ_z	$4.7 \times 10^2 \Phi_0/rad/sec^2$	$3.5 \times 10^{-7} rad/sec^2/Hz^{1/2}$

Table 1. Test results for Model I SSA

This first test of the SSA successfully verified performance in agreement with predictions and demonstrated good sensitivity. However it also pointed to some areas where immediate and substantial improvements could be realized. Thus the Model II SSA has incorporated several changes. First of all the dual coil scheme (one levitation, one sensing) was redesigned such that a single coil serves both functions. This requires six SQUIDs versus only one for Model I, but that is more than offset by the increased reliability, better coil matching capability and better coupling of the sensing circuits to the SQUIDs. The new coils are made of pure niobium, which allows operation in the Type-I superconducting region, reducing flux creep and hence low frequency noise. Use of high quality DC SQUIDs will even further reduce the inherent instrument noise. The Model II SSA is in test at the time of this writing and is expected to show two orders of magnitude improvement in noise level. The Model I instrument will also be upgraded to the Model II design.

SUPERFLUID HELIUM INTERFERENCE GYRO (SHIG)

DESCRIPTION⁴

The second cryogenic instrument being developed is the SHIG. The particular device described here is based on superfluid 3He although an alternative implementation based on 4He is also being investigated. 3He , when cooled below 2mK, condenses to a state characterized by a macroscopic wavefunction, the phase of which is directly related to the velocity flow of the liquid. The phase of the superfluid wavefunction can be treated like that of a deBroglie matter wave. Thus a velocity field produces a gradient in the quantum phase, and for a uniform velocity in the z direction the phase ϕ is given by

$$(1) \quad \phi = \frac{m^*}{\hbar} v z.$$

where m^* is twice the mass of the ^3He atom (i.e. the Cooper pair mass). To see how this phenomenon can be exploited to develop a rotation sensor consider the case of a blocked torus (Figure 9). The phase shift across the blockage can be determined by integrating the gradient around the torus,

$$(2) \quad \delta = \Delta\phi = \int_0^{2\pi R} \frac{m^*}{\hbar} v \, dl = 2\pi R \frac{m^* \omega R}{\hbar}.$$

The similarity to the Sagnac interferometer can be seen from rewriting equation (2) as

$$(3) \quad \delta = \frac{2m^* A}{\hbar} \omega;$$

then, making use of the deBroglie wavelength relation

$$(4) \quad \delta = \frac{4\pi A}{\lambda c} \omega$$

which is the equivalent of the Sagnac equation. The important feature here is that since the deBroglie wavelength of the ^3He pairs is 10^9 times shorter than that of a photon, the potential sensitivity of the device is much greater. However, the inability to detect this phase difference has, until recently, frustrated all attempts to develop a rotation sensor based on this principle. Experiments by Avenel and Varoquaux⁵ in France have shown that the ^3He supercurrent I through a small orifice is related to the phase difference across the orifice by a relation analogous to the DC Josephson equation,

$$(5) \quad I = I_c \sin\delta.$$

Now if one modifies the blocked torus such that there are orifices obstructing each leg, Equation (5) shows that the total supercurrent I_t through the torus is

$$(6) \quad I_t = I_c \sin\delta_1 + I_c \sin\delta_2 = I_{\max} \sin\frac{\delta_1 + \delta_2}{2}.$$

Since the magnitude of the macroscopic wavefunction must be single valued, the maximum supercurrent can be shown to be a simple cosine function of the rotation,

$$(7) \quad I_{\max} = 2I_c \cos\left(\frac{2m^* \pi R^2 \omega}{\hbar}\right).$$

Small changes in rotation of the torus will produce large changes in I_{\max} . The challenge now becomes developing a technique to precisely measure I_{\max} . Packard⁴ has proposed coupling the torus to a chamber containing a metalized diaphragm (Figure 11). The diaphragm can be moved by applying an electric field. The impedance of the orifices to the flow of normal ^3He is so large as to guarantee the flow to be I_{\max} even when a finite pressure is applied across the orifice. Thus if a step voltage is applied to the diaphragm and the subsequent displacement of the diaphragm is monitored (e.g. with a SQUID) the velocity of the diaphragm can be related to the rotation by

$$(8) \quad V_d = \left\{ 2 \left(\frac{\rho_s}{\rho} \right) v_c \left(\frac{a}{A_d} \right) \right\} \cos\left(\frac{2\omega m^* \pi R^2}{\hbar}\right)$$

where a is the orifice area, A_d is the diaphragm area, ρ_s/ρ is the superfluid fraction, and v_c is the average superfluid velocity corresponding to I_c through the orifice. Analyses of noise limitations in this device ($R = 4$ cm) indicates a potential to detect variations of as little as one part per billion of earth rate ($<10^{-13}$ rad/sec) with a 100 second integration time.

STATUS

The SHIG, in its second year of development at Berkeley, has passed several milestones. First of all a number of critical components have been fabricated, including a 250 mK refrigerator, a DC SQUID detected displacement transducer, a vibration isolation stage, a rotating dewar and a variety of micro-slits and holes. A phase slip (Helmholtz) oscillator was constructed and operated, demonstrating the ability to produce good superfluid weak links (micro-orifices) and demonstrating the displacement noise in the diaphragm to be less than 10^{-12} m RMS.⁶ The noise level appears to be environmental rather than intrinsic SQUID noise. The SHIG component development will continue as more is learned about the behavior of superfluid helium flow through micro-orifices.

CONCLUSION

Of the two projects described the SSA is by far the more advanced. As a low T_c instrument it is the baseline inertial measurement unit for integration with the NASA Superconducting Gravity Gradiometer (SGG) for a potential gravity mission post 2000. It is also a candidate sensor for integration with GPS to demonstrate a moving base gravity gradiometry on a balloon or an aircraft as part of a Phillips Lab in-house program. The SSA has been integrated with the NASA SGG for testing and will be used this year to perform a laboratory null test of the Gravitational Inverse Square Law.

There are no aspects of the SSA design that would preclude its implementation in high T_c technology. This would sacrifice thermal noise and mechanical stability but still provide a means of fabricating a single device inertial measurement unit that could be attractive from both size and performance points of view. The Josephson Junction Gyro (JJG), under development by the Navy, is the only high T_c analog to the SHIG. In this case however the sacrifice involves more than thermal noise and mechanical stability. Since the superfluid for the JJG is Cooper pairs of electrons, the m^* is twice the mass of an electron and the respective deBroglie wavelength is correspondingly larger. Thus it is not yet clear that the SHIG will have any practical applications in inertial navigation systems. However the low T_c SSA as well as the SHIG, in addition to serving a role as geophysical and scientific sensors, should serve as excellent sensors for stabilizing large platforms for precision pointing or testing of other precision inertial instruments.

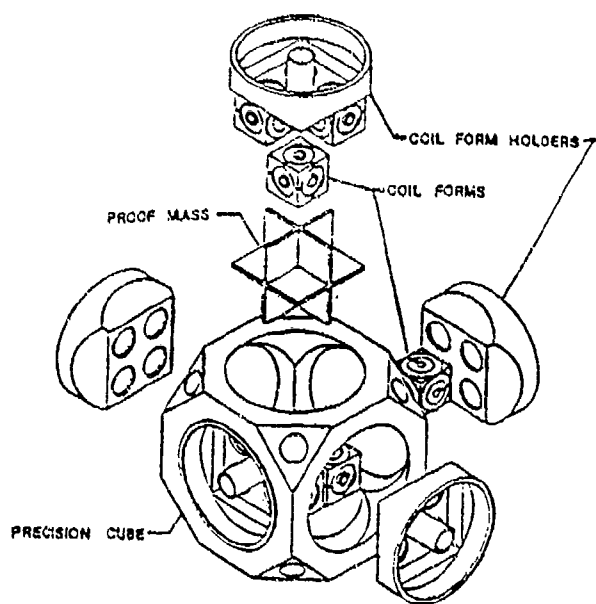


Figure 1. An exploded view of the SSA

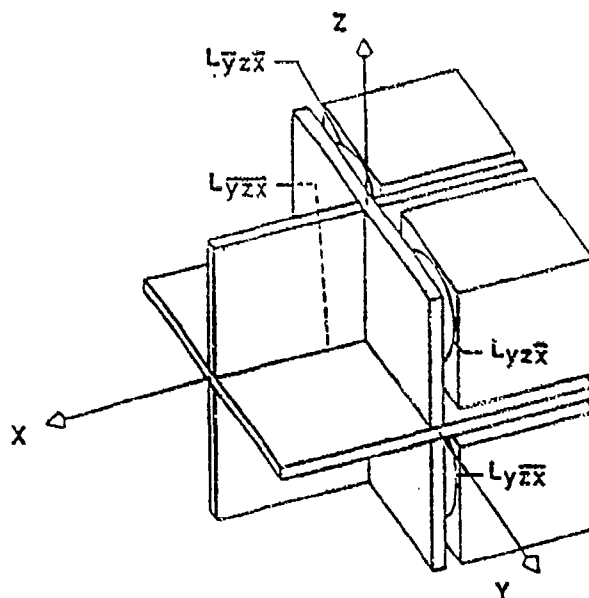


Figure 2. X axis levitation

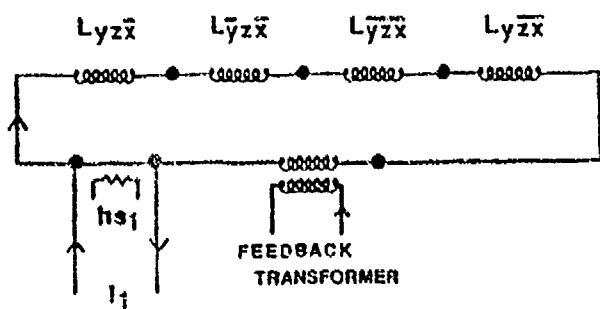


Figure 3. X axis levitation circuit

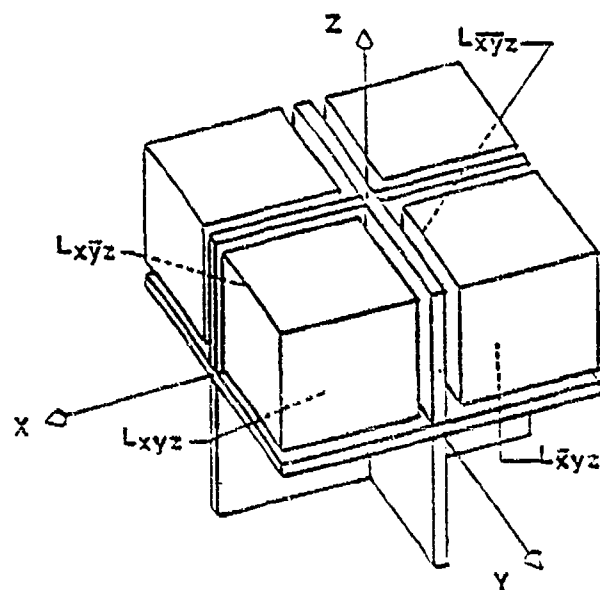


Figure 4. θ_x levitation

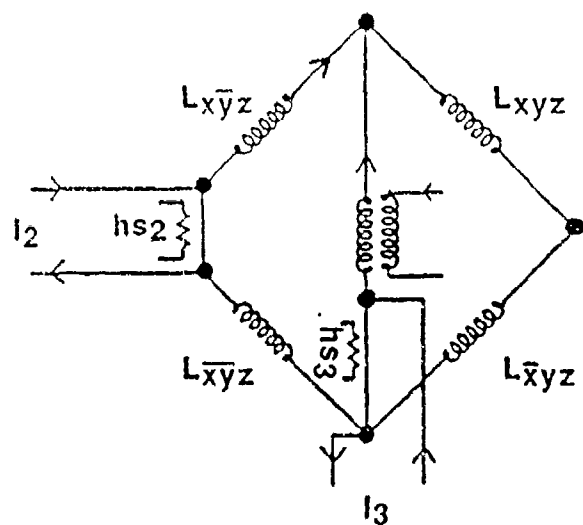


Figure 5. θ_x levitation circuit

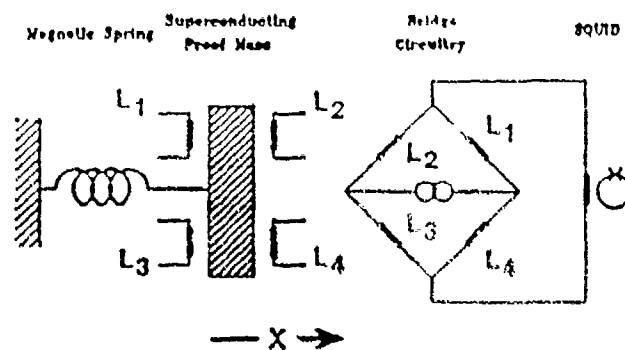


Figure 6. Simplified superconducting bridge acceleration sensor

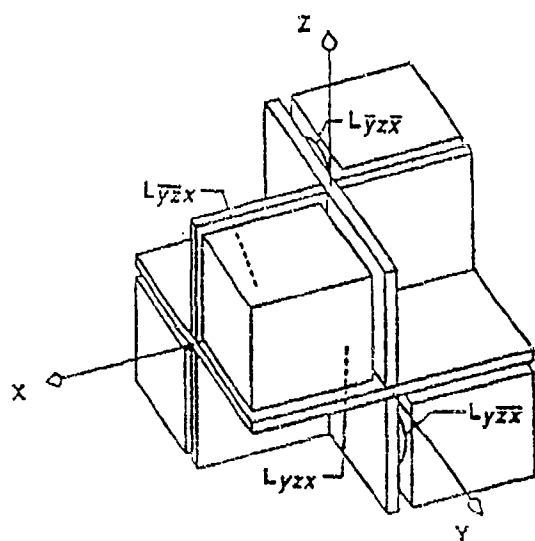
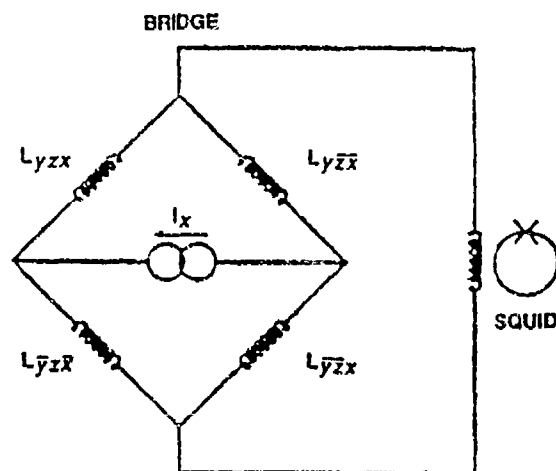


Figure 7. X axis translation sensing



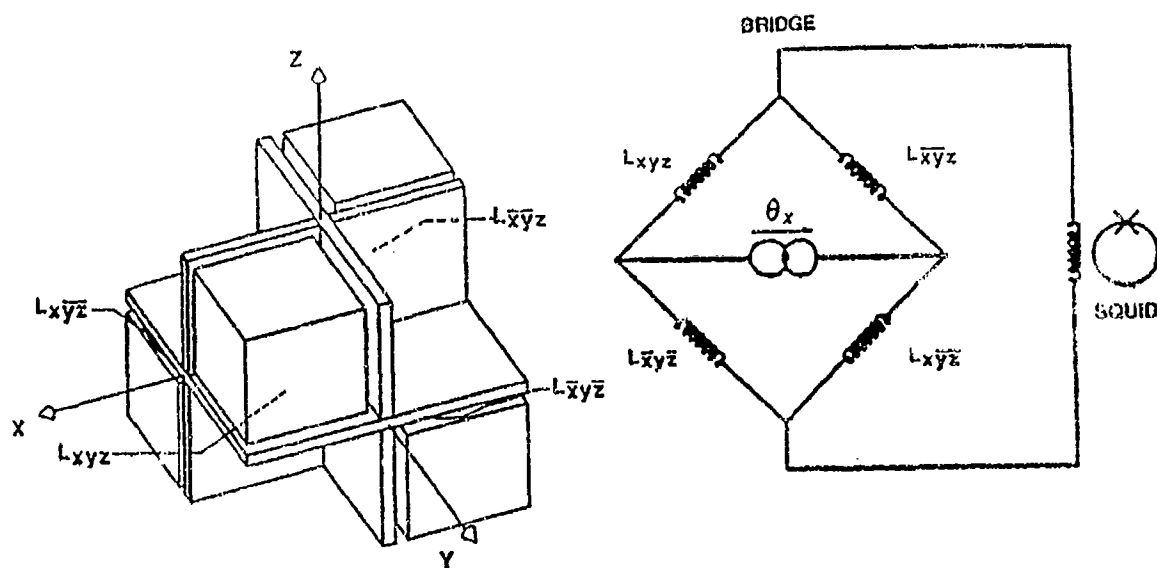


Figure 8. X axis rotation sensing

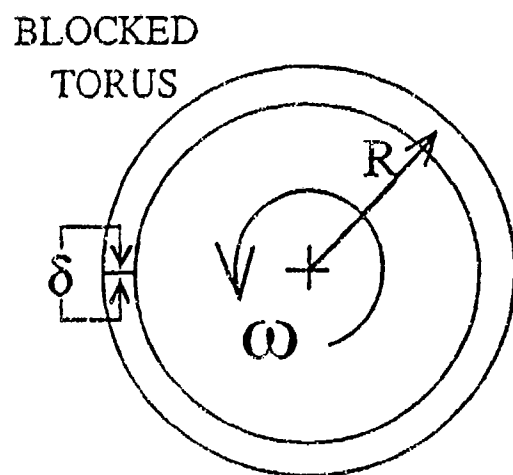


Figure 9. Blocked torus

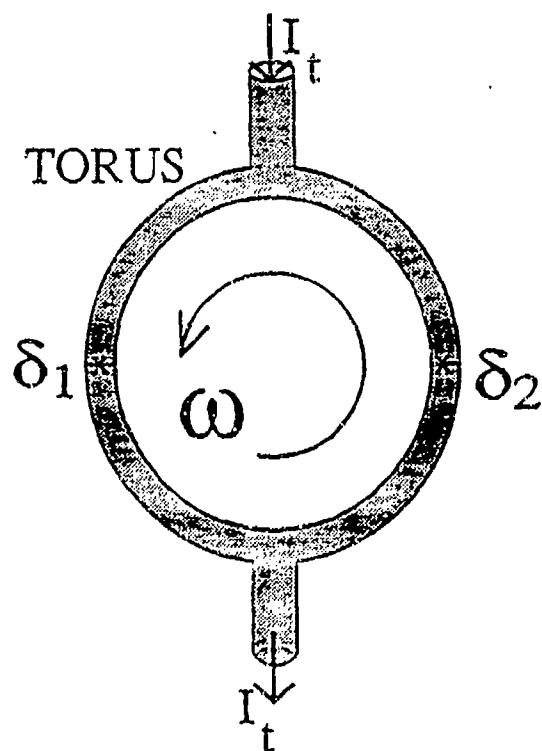


Figure 10. Torus with two superfluid weak links

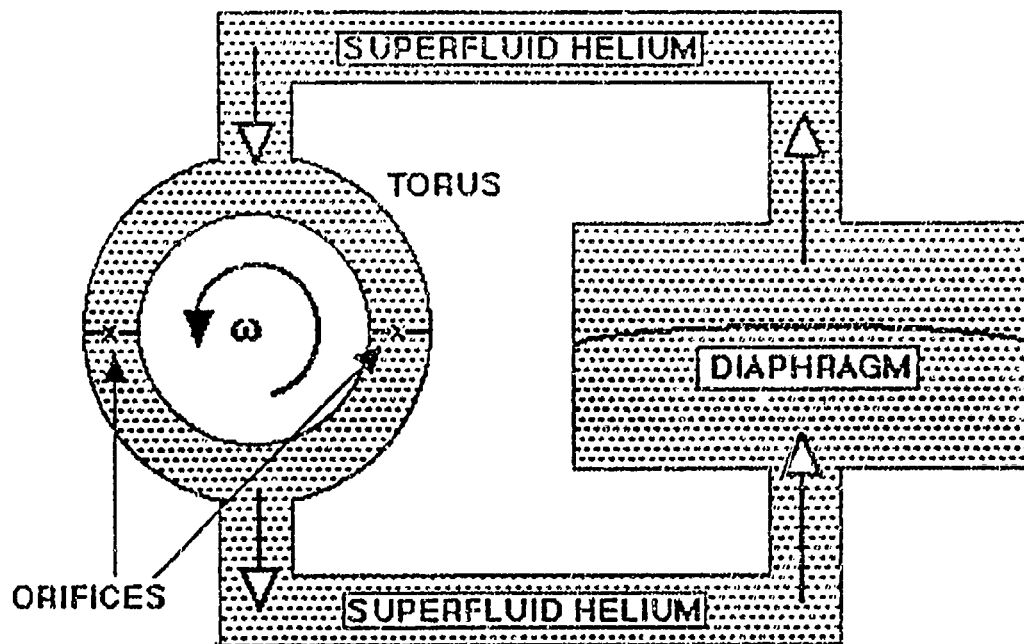


Figure 11. SHIG concept

SYMBOLS

A, a	area
c	velocity of light
g	Earth's gravitational acceleration
h	Planck's constant
\hbar	$h/2\pi$
I	electrical current
I	superfluid supercurrent
I_c	critical superfluid supercurrent
L	inductance
m^*	twice the mass of ^3He atom
R	radius
T_c	critical temperature
v	superfluid velocity
$\delta, \Delta\phi$	superfluid wavefunction phase shift
$\theta_x, \theta_y, \theta_z$	displacement angle of proof mass about x, y and z axes respectively
λ	deBroglie wavelength
ρ	density
Φ_0	fluxoid (flux quantum), 2.07×10^{-7} gauss-cm ²
ϕ	phase of the superfluid wavefunction (rad)
ω	angular rate (rad/sec)

BIBLIOGRAPHY

1. H.J. Paik, J.W. Parke, E.R. Canavan, "Development of a Superconducting Six-Axis Accelerometer", GL-TR-89-0181, July 1989, Approved for public release; distribution unlimited.
2. H.J. Paik, "Analysis and Development of a Very Sensitive Low Temperature Gravitational Radiation Detector", PhD Thesis, Stanford University, Stanford, CA, 1974, (unpublished).
3. J.W. Parke, "Null Test of the Gravitational Inverse Square Law and the Development of a Superconducting Six-Axis Accelerometer", PhD Thesis, University of Maryland, College Park, MD, 1990, (unpublished).
4. R.E. Packard, "The Development of a Superfluid Helium Interference Gyroscope", Research Proposal, 1989, (unpublished).
5. O. Avenal, E. Varoquaux, "", *Physical Review Letters*, Vol. 60, pg. 416, 1988.
6. R.E. Packard, private correspondence.

EXTRACTING HORIZONTAL AND VERTICAL COMPONENTS OF BALLOON-BORNE GRAVITY VECTORS FROM THE INTEGRATION OF GPS AND INERTIAL RING LASER STRAPDOWN SYSTEM DATA

D M Gleason (Geophysics Directorate, Phillips Laboratory (AFSC), Hanscom AFB, MA 01731-5000)

***** UNCLASSIFIED *****

ABSTRACT: Consulting records of a past flight, 1 HZ trajectory and (roll,pitch,yaw) motion profiles were adopted for a simulated 7.5 hour balloon flight over New Mexico. The assumed payload of the balloon was an inertial ring laser strapdown system and a GPS receiver. The adopted trajectory was assumed to be GPS-determined and interferometric in nature reflecting a second, ground-fixed receiver. Due to the strapdown INS, a corresponding 1 HZ profile of accelerometer specific force outputs [total (GPS sensitive) inertially referenced accelerations less gravitational accelerations present] was also required to conduct an error analysis. The gravitational accelerations were computed by a spherical harmonic expansion through $n=m=360$. A 36 state, 40 noise process, open-loop Kalman filter integrating GPS and INS data was constructed. A full constellation of 18 GPS satellites was simulated. Related to the two receivers, external GPS updating observation types used were pseudorange differences, single differenced carrier phases and single differenced phase rates. A fourth type of updating observation used was the error in the INS's estimation of phase differences between GPS antenna pairs (a three antenna equilateral triangle balloon-borne configuration was assumed with 1 meter baselines). The filter cycle and update frequency were both set at 1 HZ. A post mission covariance analysis based Kalman filter mechanization was simulated, taking into account the major initial INS and GPS error sources. Hybrid alignment errors were reduced to 0.4 arc secs about the north and east axes (levelling errors) and to 0.7 arc secs about the down axis (heading error). Hybrid positioning and velocity errors were held to the 1 to 2 cm and 1 to 2 mm/s range respectively and were highly correlated to the corresponding PDOP satellite geometry. The benign motions of the balloon allowed for a smooth time behavior of the states. Assuming the accelerometer errors are essentially bias states that can be calibrated in-flight based on very accurate GPS observations, the levelling uncertainties are the main error sources in obtaining the 3 components of the balloon-borne gravity vector. The filter's alignment errors mentioned above contribute a 2.5 mGal error to the computed horizontal components and a 0.05 mGal error to the vertical. Limiting the misalignment contributions to the deflection-error budgets to 1 mGal will require levelling errors of 0.2 arc secs. The Air Force is planning an actual balloon launch in 1992. Gravity components obtained from a hybrid system can be compared to upward continued (from extensive ground gravity data) components to validate continuation models and to establish instrumental proof of concept. A successful balloon experiment would be a strong argument for a "high-low" satellite to satellite tracking mission involving the GPS constellation and a dedicated, polar orbit, low satellite [altitude ϵ (160 km, 300 km)] possessing the same payload. Such a spaceborne mission would allow for a downward continued gravity mapping over all heretofore inaccessible earth surface regions.

1. INTRODUCTION.

Well-established gravitational potential theories, and approximations thereof, allow for upward

and downward continuations (to any desired altitude) of the information content inherent to **measured** horizontal and/or vertical gravity vector components. Such continuations allow for the estimation of any subset of the three components of the gravity **disturbance** vector, i.e., $g_{\text{observed}}(\text{at } P) - \gamma_{\text{computed}}(\text{at } P)$ per ellipsoidal gravity formula, at altitudes of interest (cf. Heiskanen and Moritz, 1967). Thus if densely gridded and accurate data sets of vertical (e.g.) disturbance components were available everywhere on the earth's surface, then one could straight-forwardly and efficiently (due to the applicability of flat earth 2D and 3D Fast Fourier Transform methods) estimate grids of all three disturbance components at selected altitudes. Possessing accurate and pre-determined grids of airborne deflections of the vertical (i.e. the horizontal disturbances) would greatly assist passive or autonomous inertial navigation systems (cf., Jordan and Center, 1986).

Due to unfavorable political and environmental conditions, gravity data is lacking over large areas of the Earth's surface. Global digital terrain elevation models however do exist at resolutions as fine as 2 arc secs (≈ 60 m). Employing available density models (even one as crude as a nominal value of $\rho = 2.67 \text{ g cm}^{-3}$) to all masses above some adopted reference surface, such as the ellipsoid, allow for similar FFT implementations of the classical potential theories. The elevation/density based estimations clearly will not be as accurate as the gravity data based predictions due to imperfections in the density modelling. Regardless of the type of regional input data used, the estimation process accounts for long wavelength gravitational effects with a truncated set of low harmonic degree geopotential coefficients (e.g. WGS84) and attempts to account for the middle to short wavelength effects with the data itself.

For scientific and navigational reasons it would be most interesting to compare such mathematically estimated gravity disturbance components to actual and accurate at-altitude measurements. Agreement at the 5 mGal level ($1 \text{ mGal} = 10^{-5} \text{ ms}^{-2}$) would result in two meaningful accomplishments: a) validation of the continuation models and b) establishment of "proof of concept" for the hardware devices yielding the gravity measurements. If these two goals can be met with measuring devices that can also be used on a low orbiting satellite, then one opens the door to a downward continued gravity mapping over all heretofore inaccessible regions of the Earth. A hybrid system consisting of a GPS receiver and an inertial measuring unit contains such devices. GPS-determined accelerations are sensitive to all inertially referenced accelerations while the specific force outputs of an INS reflect such accelerations less the gravitational accelerations present. The benign motions of a helium-filled balloon make it an ideal vehicle to perform a gravity vector measurement experiment on, using a GPS/INS payload.

This paper will describe, and detail the results of, a feasibility study wherein a post mission Kalman mechanization error analysis was performed under the assumption that a ring laser gyro strapdown INS accompanied a dual frequency GPS receiver on a simulated balloon flight. It was further assumed that a second GPS receiver was at a centrally located fixed position on the ground. One is intuitively tempted to avoid modelling the gravity disturbances as state variables and instead concentrate on minimizing the body frame to local (n,e,d) navigation frame orientation errors and on performing in-flight calibration of the accelerometers and gyros. A final simple difference between GPS-determined navigation frame acceleration components and the corresponding INS values would thus yield the gravity vector components from which the desired gravity disturbances are obtained using the ellipsoidal formulae. As will be shown in a later section, the horizontal gravity disturbances (i.e. the deflections of the vertical) unfortunately cross couple into the two levelling navigation error states. Thus the total absence of gravity disturbance state variables leads to unjustified, overly optimistic orientation error estimates. For this initial error analysis, the gravity disturbance components are modelled as simple bias states. While such modelling is well-suited for a hovering type of vehicle or for flights over a region

possessing a benign gravity field, a more elaborate model will be required for flights over rugged terrain and/or over areas containing significant crustal density variations. A second ordered Gauss-Markov process is presented by Knickmeyer (1990) but it is unable to adjust for vehicle azimuth changes.

2. OBTAINING ALL REQUIRED INPUT DATA TO PERFORM AN ERROR ANALYSIS FOR A GPS/STRAPDOWN INS PAYLOAD.

Since the sensors of a strapdown inertial system are mounted directly on the vehicle, the sensor outputs now represent specific force and angular rate with respect to inertial space coordinatized in the vehicle's ($b_1^{\text{roll}}, b_2^{\text{pitch}}, b_3^{\text{yaw}}$) body frame axes. As presented by Eissfeller and Spietz (1989), the signal flow in a ring laser gyro strapdown system can essentially be described as a three step process. In the first step the sensor outputs (data rates $\cong 50$ to 250 Hz) are usually compensated by calibration models. In the second step, a digitally computed (at 50 to 150 Hz) $[C_b^n]$ body frame to local (n,e,d) navigation frame transformation matrix is obtained. In the final step, the specific force components, measured in the vehicle's body coordinates, are transformed to the local navigation frame (at 25 to 100 Hz).

The planned balloon experiment's trajectory would be differentially (or interferometrically) determined at 1 Hz with the two GPS receivers involved. Such a tracking should be accurate to a decimeter (cf. Goad, (1990)). Eissfeller and Spietz (ibid) show that a hybrid GPS/INS(strapdown) navigation approach can provide high frequency position and velocity signals (at 8 to 50 Hz) between the 1 Hz GPS updates without degrading accuracies. They also show how this high frequency navigation data can be used to detect GPS cycle slips and to bound cycle slip-induced position error rates to ± 0.5 m per minute of loss of lock and to reduce them to 10 cm after the GPS signal returns. The INS based velocity and position signals are of course obtained by integrating (wrt time) the navigation frame components of the specific force outputs (after they've been compensated for ellipsoidal gravity field, centrifical force and Coriolis effects, cf. Britting (1971), p. 113).

Now the $[C_b^n]$ transformation matrix clearly depends on the vehicle's motion and can not be specified in advance. Thus to conduct any Kalman filter error analysis involving a strapdown INS, vehicle trajectory and (roll,pitch,yaw) attitude profiles must be supplied at the filter's cycle (which will equal the GPS external updating frequency of 1 Hz in this study). As will be shown in the next section, navigation-frame [local (n,e,d)] and body-frame (roll,pitch,yaw) 1 Hz profiles of the accelerometer specific force outputs are also required to build the system dynamics $[F]$ and disturbance input $[G]$ matrices.

Lazarewicz et al (1985) describe an actual 7.5 hour balloon flight which was flown over southeastern New Mexico. The trajectory of the flight was determined by a network of ground radar stations with the frequency of the raw tracking data being 20 Hz. Figures 1 and 2 plot smoothed ground and altitude profiles [in geodetic (ϕ, λ, h) coordinates] of the flight. Altitude control was maintained through remote gas valving commands and ballast pouring. Balloon velocities ranged from 30 to 100 km/hr, depending on ascending, floating or descending stages as well as on local wind conditions. A separable gondola-parachute recovery train was used to insure a soft payload landing with low g impact. Consulting these records, 1 Hz (ϕ, λ, h), ($\dot{\phi}, \dot{\lambda}, \dot{h}$) and ($\ddot{\phi}, \ddot{\lambda}, \ddot{h}$) profiles were adopted (the velocities and accelerations were obtained by numerical differentiations). Using well-known procedures, the (ϕ, λ, h) based profiles were then

transformed to global Earth-fixed (x,y,z) , $(\dot{x},\dot{y},\dot{z})$ and $(\ddot{x},\ddot{y},\ddot{z})$ profiles which in turn were transformed to inertially-referenced (X,Y,Z) , $(\dot{X},\dot{Y},\dot{Z})$ and $(\ddot{X},\ddot{Y},\ddot{Z})$ profiles (again compensating for Coriolis-type effects).

As shown in an exaggerated (for visual effects) Figure 3, taken from Lazarewicz et al (ibid), the kinematic motions of a balloon are largely accounted for by fairly benign rotations (typical period of 2 hours), bobbings and pendulum-like swayings (typical period of 15 secs and maximum angular distance around 0.01°). Movements of this type can be easily modelled as simple harmonic motions (SHM). Attitudinal 1 Hz (roll,pitch,yaw) profiles were obtained from such SHM modelling. **Inertially-referenced** gravitational acceleration components were next computed at the 1 Hz (X,Y,Z) balloon positions through a spherical harmonic expansion through degree and order $n=m=360$, using the OSU86F geopotential coefficient set. **Specific force** components, in the inertial (X,Y,Z) system, were obtained by subtracting the gravitational accelerations from the $(\ddot{X},\ddot{Y},\ddot{Z})$ accelerations related to the radar ground tracking records. Again using well-known procedures, the inertially-referenced specific force components were transformed to local (n,e,d) components which, in turn, were transformed to body-frame components via $[C_n^b] = [C_b^n]^{-1} = [C_b^n]^T$ due to the orthogonality properties of $[C_b^n]$.

NOTE: As shown in Stieler and Winter (1982), at each time epoch t

$$[C_b^n(t)] = [R_3(\text{yaw}_t)]^T [R_2(\text{pitch}_t)]^T [R_1(\text{roll}_t)]^T \quad (1)$$

where $[R_i(\theta)]$ denotes the 3 by 3 orthogonal rotation matrix used to rotate the system by an angle of θ about the i^{th} axis (cf. Mueller, 1969).

The final type of simulated information needed to perform the error analysis is a 1 Hz set of global earth-fixed state vectors of all GPS satellites "in view" from the balloon. This data is used to construct the $[H]$ (external) measurement matrix in the Kalman filter. Using Hamming's predictor/corrector multi-step method [see chapter 6 of Carnahan et al (1969) for a thorough description], 1 second stepsize inertially-referenced orbits were generated for a full constellation of 18 GPS satellites. To minimize CPU concerns, the orbit determinations allowed only for the J_2 gravimetric perturbations. Considering the high altitude of the GPS satellites ($\approx 20,000$ km), such a simplification is acceptable for this study's needs. The inertial $(X,Y,Z,\dot{X},\dot{Y},\dot{Z})$ state vectors were then transformed to their earth-fixed $(x,y,z,\dot{x},\dot{y},\dot{z})$ counterparts. For each time epoch t_k , the state vectors of all satellites "in view" from the balloon were time-tagged for use in subsequent processing.

3. PRESENTING THE 36 STATE, 40 NOISE PROCESS, OPEN-LOOP KALMAN FILTER DESIGN.

The discrete form Kalman algorithm used in the covariance analysis of this paper is presented in Gelb (1974). A listing of the covariance propagation equations follow. The well-known discrete Kalman recursive equations are of the form

$$\begin{bmatrix} \tilde{P}_k \end{bmatrix} = \begin{bmatrix} \Phi_{k-1} \end{bmatrix} \begin{bmatrix} \hat{P}_{k-1} \end{bmatrix} \begin{bmatrix} \Phi_{k-1} \end{bmatrix}^T + \begin{bmatrix} \Gamma_{k-1} \end{bmatrix} \begin{bmatrix} Q_{k-1} \end{bmatrix} \begin{bmatrix} \Gamma_{k-1} \end{bmatrix}^T \quad (2)$$

$$\begin{bmatrix} \hat{P}_k \end{bmatrix} = \left[\begin{bmatrix} I \end{bmatrix} - \begin{bmatrix} K_k \end{bmatrix} \begin{bmatrix} H_k \end{bmatrix} \right] \begin{bmatrix} \tilde{P}_k \end{bmatrix} \quad (3)$$

$$\begin{bmatrix} K_k \end{bmatrix} = \begin{bmatrix} \tilde{P}_k \end{bmatrix} \begin{bmatrix} H_k \end{bmatrix}^T \left[\begin{bmatrix} R_k \end{bmatrix} + \begin{bmatrix} H_k \end{bmatrix} \begin{bmatrix} \tilde{P}_k \end{bmatrix} \begin{bmatrix} H_k \end{bmatrix}^T \right]^{-1} \quad (4)$$

$$\begin{bmatrix} \Phi_{k-1} \end{bmatrix} \cong \begin{bmatrix} I \end{bmatrix} + \begin{bmatrix} F(t_{k-1}) \end{bmatrix} \Delta t + (1/2) \begin{bmatrix} F(t_{k-1}) \end{bmatrix}^2 \Delta t^2 \quad (5)$$

$$\begin{bmatrix} \Gamma_{k-1} \end{bmatrix} \cong \begin{bmatrix} G(t_{k-1}) \end{bmatrix} + \begin{bmatrix} F(t_{k-1}) \end{bmatrix} \begin{bmatrix} G(t_{k-1}) \end{bmatrix} \Delta t \quad (6)$$

where (hereafter the number of states is denoted by NSTATES, the number of noise disturbing processes by NDISTS and the number of external updating observations by NOBS)

$\begin{bmatrix} \tilde{P} \end{bmatrix}$ is the NSTATES by NSTATES variance/covariance matrix of the **predicted** error states,

$\begin{bmatrix} \hat{P} \end{bmatrix}$ is the NSTATES by NSTATES variance/covariance matrix of the **updated** error states (initial $\begin{bmatrix} \hat{P}_0 \end{bmatrix}$ matrix to be defined below),

$\begin{bmatrix} \Phi \end{bmatrix}$ is the NSTATES by NSTATES transition matrix,

$\begin{bmatrix} \Gamma \end{bmatrix}$ is the NSTATES by NDISTS discrete disturbance (noise) input matrix,

$\begin{bmatrix} Q \end{bmatrix}$ is the NDISTS by NDISTS covariance matrix of the discrete input noise processes (to be defined below)

$\begin{bmatrix} K \end{bmatrix}$ is the NSTATES by NOBS Kalman gain matrix,

$\begin{bmatrix} R \end{bmatrix}$ is the NOBS by NOBS covariance matrix of the external GPS observational noise (to be defined below),

$\begin{bmatrix} H \end{bmatrix}$ is the NOBS by NSTATES measurement matrix (to be defined below),

$\begin{bmatrix} F \end{bmatrix}$ is the NSTATES by NSTATES system dynamics matrix (to be defined below),

$\begin{bmatrix} G \end{bmatrix}$ is the NSTATES by NDISTS disturbance (noise) input matrix (to be defined below) and

$\Delta t = 1$ second = time between successive external GPS updates (and also the filter's cycle).

A 30 state **linear** GPS/strapdown INS integrated navigational model, which constitutes the foundation of the 36 state model used in this study, is admirably developed by Eissfeller and Spietz (ibid). Due to the meticulous nature of the subject matter and the presence of a few typographical errors in the Eissfeller et al paper, their model is summarized here. An added emphasis is placed on clarity in presenting both the 30 and 36 state models to allow for immediate implementations by any reader so disposed. The Eissfeller and Spietz model possesses the familiar $\dot{\underline{x}} = [F] \cdot \underline{x} + [G] \cdot \underline{u}$ form, where the vector \underline{x} contains 30 error states and \underline{u} contains 43 input noise processes, and is given by

$$\dot{\underline{x}} = \begin{bmatrix} \dot{\underline{x}}_1 \\ \dot{\underline{x}}_2 \\ \dot{\underline{x}}_3 \\ \dot{\underline{x}}_4 \end{bmatrix} = \begin{bmatrix} [F^{free}] & [F^{rw}] & [F^{bias}] & [0] \\ [0] & [0] & [0] & [0] \\ [0] & [0] & [0] & [0] \\ [0] & [0] & [0] & [F^{GPS}] \end{bmatrix} \begin{bmatrix} \underline{x}_1 \\ \underline{x}_2 \\ \underline{x}_3 \\ \underline{x}_4 \end{bmatrix} + \begin{bmatrix} [G_1] & [0] & [0] \\ [0] & [G_2] & [0] \\ [0] & [0] & [0] \\ [0] & [0] & [G_4] \end{bmatrix} \begin{bmatrix} \underline{u}_1 \\ \underline{u}_2 \\ \underline{u}_4 \end{bmatrix} \quad (7)$$

where the 9 by 1 vector $\underline{x}_1 = (\delta\epsilon_N, \delta\epsilon_E, \delta\epsilon_D, \delta\dot{\phi}, \delta\dot{\lambda}, \delta\dot{h}, \delta\phi, \delta\lambda, \delta h)^T$ contains the orientation, velocity and position **navigation-frame** errors,

the 3 by 1 vector $\underline{x}_2 = (\epsilon_{rw}^{roll}, \epsilon_{rw}^{pitch}, \epsilon_{rw}^{yaw})^T$ contains the gyro random walk **body-frame** errors,

the 12 by 1 vector $\underline{x}_3 = (d^{roll}, d^{pitch}, d^{yaw}, \kappa^{roll}, \kappa^{pitch}, \kappa^{yaw}, b^{roll}, b^{pitch}, b^{yaw}, \epsilon_0^{roll}, \epsilon_0^{pitch}, \epsilon_0^{yaw})^T$ contains the **body-frame** d fixed gyro bias drift errors, κ gyro scale factor errors, b accelerometer bias errors and the ϵ_0 accelerometer scale factor errors and

the 6 by 1 vector $\underline{x}_4 = (\eta_0, \eta_1, m_1, m_2, m_3, m_4)^T$ contains the η_0 balloon-borne GPS receiver clock offset, the η_1 balloon-borne GPS receiver clock drift and the m integer valued ambiguities of the GPS phase data observations related to the assumed four satellites "in view"

from the balloon (in actuality > 4 satellites are possible).

The 43 noise forcing inputs are contained in u_1 , u_2 and u_4 where

the 39 by 1 vector $u_1 = (\Delta\tau^{\text{roll}}, \Delta\tau^{\text{pitch}}, \Delta\tau^{\text{yaw}}, h^{\text{roll}}, h^{\text{pitch}}, h^{\text{yaw}}, \beta_1, \beta_2, \beta_3, \beta_4, \beta_5, \beta_6, \epsilon_1^{\text{roll}}, \epsilon_1^{\text{pitch}}, \epsilon_1^{\text{yaw}}, \epsilon_2^{\text{roll}}, \epsilon_2^{\text{pitch}}, \epsilon_2^{\text{yaw}}, \epsilon_3^{\text{roll}}, \epsilon_3^{\text{pitch}}, \epsilon_3^{\text{yaw}}, \alpha_1, \alpha_2, \alpha_3, \alpha_4, \alpha_5, \alpha_6, c^{\text{roll}}, c^{\text{pitch}}, c^{\text{yaw}}, w^{\text{roll}}, w^{\text{pitch}}, w^{\text{yaw}}, \epsilon_f^{\text{roll}}, \epsilon_f^{\text{pitch}}, \epsilon_f^{\text{yaw}}, \delta g^{\text{north}}, \delta g^{\text{east}}, \delta g^{\text{down}})^T$ contains the $\Delta\tau$ temperature uncertainties, the h magnetic field uncertainties, the six β gyro axes misalignments (see section 3.8 of Britting (ibid) for detailed account), the ϵ_1, ϵ_2 and ϵ_3 accelerometer asymmetry, quadratic and cubic scale factor errors, the six α accelerometer axes misalignments (again see section 3.8 of Britting), the c accelerometer cross-coupling errors, the w accelerometer crossrate sensitivities (wrt products of input gyro angular rates), the ϵ_f acceleration white noise levels and the δg gravity field uncertainties;

the 3 by 1 vector $u_2 = (\epsilon_{\text{rw}}^{\text{roll}}, \epsilon_{\text{rw}}^{\text{pitch}}, \epsilon_{\text{rw}}^{\text{yaw}})$ again contains the gyro random walk errors

and the scalar u_4 denotes the η_1 GPS receiver clock drift error.

The four non-zero sub-matrices contained in the overall 30 by 30 $[F]$ system dynamics matrix in (7) are 1) the 9 by 9 navigational error dynamics matrix $[F^{\text{free}}]$ which is listed in detail by Schmidt ('978), 2) the 9 by 3 matrix $[F^{\text{rw}}]$ whose upper 3 by 3 section is given by $(-1/t)[C_b^n]$ where t denotes the time elapsed since the initial time epoch t_0 and whose remaining elements are zero, 3) the 9 by 12 matrix $[F^{\text{bias}}]$ given by

$$[F^{\text{bias}}] = \begin{bmatrix} -[C_b^n] & [C_b^n] \cdot [W_K] & [0] & [0] \\ [0] & [0] & [D] \cdot [C_b^n] & [D] \cdot [C_b^n] \cdot [F_\epsilon] \\ [0] & [0] & [0] & [0] \end{bmatrix} \quad (8)$$

and 4) the 6 by 6 matrix $[F^{\text{GPS}}]$ whose only non-zero element is given by $F_{22}^{\text{GPS}} = -1/T_{\eta_1}$ where $T_{\eta_1} = 72000$ seconds = the correlation time of the $u_4 = \eta_1$ GPS receiver clock drift which, as described below, will be modelled as a 1st order Gauss-Markov random process.

In (8) the 3 by 3 matrix $[W_K] = \text{Diag}(\omega^b_1, \omega^b_2, \omega^b_3)$ where the gyroscopically measured angular rate vector of the **body-frame** with respect to the **inertial frame**, is given by (cf.

Britting (ibid)

$$\underline{\omega}_{ib}^b = \begin{bmatrix} \omega_1^b \\ \omega_2^b \\ \omega_3^b \end{bmatrix} = \begin{bmatrix} C_b^n \end{bmatrix} \cdot \begin{bmatrix} \dot{\lambda} \cos \phi \\ -\dot{\phi} \\ -\dot{\lambda} \sin \phi \end{bmatrix} + \underline{\omega}_{nb}^b \quad (9)$$

where the **inertial** longitude rate $\dot{\lambda} = \dot{\lambda} +$ the Earth's spin rate (7.2921×10^{-5}) and the $\underline{\omega}_{nb}^b$ angular rate vector of the body-frame with respect to the **navigation frame** is given by (see Stieler and Winter (ibid), p.143)

$$\underline{\omega}_{nb}^b = \begin{bmatrix} \dot{\zeta} - \sin \theta \dot{\alpha} \\ \sin \zeta \cos \theta \dot{\alpha} + \cos \zeta \dot{\theta} \\ \cos \zeta \cos \theta \dot{\alpha} - \sin \zeta \dot{\theta} \end{bmatrix} \quad (10)$$

where $(\zeta, \theta, \alpha)_t = (\text{roll}, \text{pitch}, \text{yaw})_t$. Also appearing in (8) is the 3 by 3 matrix relating **linear** velocity errors to latitude and longitude **radian** rate errors, viz, $[D] = \text{Diag}(1/r, 1/(r \cos \phi), -1)$ and the 3 by 3 matrix $[F_e] = \text{Diag}(f_{\text{roll}}, f_{\text{pitch}}, f_{\text{yaw}})$ which contain the three body-frame components of the inertially-referenced specific force outputs of the accelerometers.

The three non-zero submatrices contained in the overall 30 by 43 disturbance input $[G]$ matrix in (7) are 1) the 9 by 39 $[G_1]$ given by

$$[G_1] = \begin{bmatrix} -[C_b^n][D_e] & -[C_b^n][D_h] & -[C_b^n][W_\beta] & [0] \dots \dots \dots \\ [0] & [0] & [0] & [D][C_b^n] \text{sgn}[F_e][F_e] \dots \dots \dots \\ [0] & [0] & [0] & [0] \dots \dots \dots \\ \dots \dots \dots [0] & [0] & [0] & [0] \dots \dots \dots \\ \dots \dots \dots [D][C_b^n][F_e]^2 & [D][C_b^n][F_e]^3 & [D][C_b^n][F_\alpha] & [D][C_b^n][F_e] \dots \dots \dots \\ \dots \dots \dots [0] & [0] & [0] & [0] \dots \dots \dots \end{bmatrix}$$

$$\begin{bmatrix} \dots\dots\dots[0] & [0] & [0] \\ \dots\dots\dots[D][C_b^a][W_f] & [D][C_b^a] & [D] \\ \dots\dots\dots[0] & [0] & [0] \end{bmatrix} \quad (11)$$

2) the 3 by 3 $[G_2] = [I]$ and 3) the 6 by 1 matrix $[G_4] = (0,1,0,0,0,0)^T$.

In (11) the 3 by 3 $[D_\tau]$ is a diagonal matrix containing the 3 body-frame gyro bias drift temperature sensitivities $[\approx 0.002^\circ/(\text{hr}^\circ\text{C})]$ per Stieler and Winter (ibid), the 3 by 3 $[D_h]$ is a diagonal matrix containing the 3 gyro magnetic field sensitivities $[\approx 0.025^\circ/(\text{hr} \cdot \text{Gauss})]$, $[W_\beta]$ is a 3 by 6 matrix, related to the six β gyro misalignment angles, and is given by

$$[W_\beta] = \begin{bmatrix} \omega_2^b & \omega_3^b & 0 & 0 & 0 & 0 \\ 0 & 0 & \omega_1^b & \omega_3^b & 0 & 0 \\ 0 & 0 & 0 & 0 & \omega_1^b & \omega_2^b \end{bmatrix}$$

$[F_\alpha]$ is the α accelerometer misalignment counterpart, also 3 by 6, and is given by

$$[F_\alpha] = \begin{bmatrix} f^{\text{yaw}} & f^{\text{pitch}} & 0 & 0 & 0 & 0 \\ 0 & 0 & f^{\text{yaw}} & f^{\text{roll}} & 0 & 0 \\ 0 & 0 & 0 & 0 & f^{\text{roll}} & f^{\text{pitch}} \end{bmatrix}$$

$[F_c]$ is a 3 by 3 matrix given by $\text{Diag}(f^{\text{roll}}, f^{\text{yaw}}, f^{\text{pitch}}, f^{\text{yaw}}, f^{\text{yaw}}, f^{\text{roll}})$ accounting for accelerometer crosscoupling errors and $[W_f]$ is a 3 by 3 matrix given by $\text{Diag}(\omega_1^b \cdot \omega_3^b, \omega_2^b \cdot \omega_3^b, \omega_3^b \cdot \omega_1^b)$ which reflects accelerometer sensitivities related to products of the input gyro rates.

The only matrices still to be defined to implement equations (2) - (6) for the 30 state model are $[Q]$, $[H]$ and $[R]$. With the exception of the η_1 GPS receiver clock drift error, all input

disturbing forces will be treated as white noise. Thus the 43 by 43 [Q] will be diagonal and denote the covariance matrix of discrete white noise processes. Under this treatment, Moritz and Wei (1987) show the covariance $q_{ii} \cong (\text{PSD of } i^{\text{th}} \text{ noise process}) \cdot \Delta t \cong 2\sigma_i^2(\Delta t)^2$ where $\sigma_i^2 =$ the variance of the i^{th} disturbing process and again $\Delta t = t_k - t_{k-1} = 1$ second in this simulation. The η_1 clock drift error is modelled as a first order Gauss-Markov process and its diagonal element in [Q] is given by (cf. Gelb (ibid)) $q_{43,43} = 2(\sigma_{\eta_1}^2/T_{\eta_1})\Delta t$ where again $T_{\eta_1} = 72000$ seconds.

The well-known **linear external (GPS) observation model** possesses the form

$$\delta \underline{L}(t) = \underline{L}^{\text{GPS}}(t) - \underline{L}^{\text{INS}}(t) = [H(t)] \cdot \underline{x}(t) + \underline{\epsilon}^{\text{GPS}}(t) \quad (12)$$

where the vectors $\delta \underline{L}$, $\underline{L}^{\text{GPS}}$, $\underline{L}^{\text{INS}}$ and $\underline{\epsilon}^{\text{GPS}}$ are all $3 \cdot \text{NSATS}$ by 1 (NSATS denotes the number of satellites "in view") with $\underline{L}^{\text{GPS}}$ denoting the observational values related to external GPS data, $\underline{L}^{\text{INS}}$ the same values related to the INS; and $\underline{\epsilon}^{\text{GPS}}$ the error in the GPS measurements. Eissfeller and Spietz (ibid) linked each satellite j "in view" to three external GPS observations: 1) ΔS_j range differences, 2) $\Delta \psi_j$ single phase differences and 3) $\Delta \dot{\psi}_j$ single phase difference rates. All three observation types refer to both the GPS receiver on the balloon and a ground-fixed receiver. Assuming $\text{NSATS} = 4$, the non-zero elements of the overall 12 by 30 [H(t)] matrix related to satellite j can be taken straight from the $\underline{L}^{\text{GPS}} - \underline{L}^{\text{INS}}$ equations (cf. Cannon et al (1986))

$$\delta(\Delta S_j) = \begin{bmatrix} \underline{Q}_3^T & \underline{Q}_3^T & \frac{(\underline{r}_{\text{balloon}}^e - \underline{r}_j^e)^T}{S_j} [C_n^e] [D]^{-1} \end{bmatrix} \underline{x}_1 + \begin{bmatrix} 1 & (t-t_0) & \underline{Q}_4^T \end{bmatrix} \underline{x}_4 + \epsilon_s \quad (13)$$

$$\delta(\Delta \psi_j) = \begin{bmatrix} \underline{Q}_3^T & \underline{Q}_3^T & \frac{(\underline{r}_{\text{balloon}}^e - \underline{r}_j^e)^T}{S_j} [C_n^e] [D]^{-1} \end{bmatrix} \underline{x}_1 + \begin{bmatrix} 1 & (t-t_0) & \underline{\lambda}_4^T \end{bmatrix} \underline{x}_4 + \epsilon_{\psi} \quad (14)$$

$$\delta(\Delta\psi_j) = \left[\begin{array}{c} \underline{Q}_3^T \frac{(\underline{r}_{\text{balloon}}^e - \underline{r}_j^e)^T}{S_j} [C_n^e] [D]^{-1} \left[\frac{(\dot{\underline{r}}_{\text{balloon}}^e - \dot{\underline{r}}_j^e)^T}{S_j} + \frac{\dot{S}_j (\underline{r}_{\text{balloon}}^e - \underline{r}_j^e)^T}{S_j^2} \right] [C_n^e] [D]^{-1} \end{array} \right] \underline{x}_1 + \left[\begin{array}{ccc} 0 & 1 & \delta_4^T(t - t_j) \end{array} \right] \underline{x}_4 + \varepsilon_{\psi_j} \quad (15)$$

where \underline{Q}_3 and \underline{Q}_4 are 3 by 1 and 4 by 1 zero vectors, $\underline{r}_{\text{balloon}}^e$ and \underline{r}_j^e are earth-fixed geocentric position vectors of the balloon and GPS satellite j , $S_j = \|\underline{r}_j^e - \underline{r}_{\text{balloon}}^e\|$ (i.e. the scalar magnitude range between the balloon and satellite j),

$\Delta S_j = \|\underline{r}_j^e - \underline{r}_{\text{balloon}}^e\| - \|\underline{r}_j^e - \underline{r}_{\text{ground fixed}}^e\|$ is the range difference observation,

$\dot{S}_j = [(\underline{r}_j^e - \underline{r}_{\text{balloon}}^e)^T \cdot (\dot{\underline{r}}_j^e - \dot{\underline{r}}_{\text{balloon}}^e)] / S_j$, $\underline{\lambda}_4$ is a 4 by 1 vector containing the GPS carrier wave lengths for the assumed 4 satellites "in view", $\delta_4(t - t_j)$ is a 4 by 1 Dirac delta function vector where t_j denotes a time when a cycle-slip occurs with satellite j , and the navigation frame to global earth-fixed transformation matrix is given by

$$\left[\begin{array}{c} C_n^e \end{array} \right] = \left[\begin{array}{ccc} -\sin\phi\cos\lambda & -\sin\lambda & -\cos\phi\cos\lambda \\ -\sin\phi\sin\lambda & \cos\lambda & -\cos\phi\sin\lambda \\ \cos\phi & 0 & -\sin\phi \end{array} \right].$$

Again assuming NSATS = 4, the 12 by 12 covariance matrix $[R]$ of the external GPS observational noise is assumed to be diagonal. The standard deviations related to $[R]$ are given in Table 1.

Table 1.
Standard deviations related to the $[R]$ matrix.

<u>observation type</u>	<u>1σ</u>	<u>Reference</u>
range difference	± 1 m	Aggarwal (1987)
single phase difference	± 2 cm	Hein et al (1988)
single phase difference rate	± 2 cm/sec	Wells et al (1987)

Table 2 lists the initial $[P_0]$ diagonal covariance matrix adopted along with some pertinent comments. Not only will it be assumed that all GPS cycle slips are fixed and removed prior to the balloon's liftoff but also that they remain fixed for the duration of the simulation. All angular quantities must be converted to radians, all linear quantities to meters and all time references to seconds in the actual computer execution. The $\delta\dot{\phi}$, $\delta\dot{\lambda}$, $\delta\phi$ and $\delta\lambda$ states **must** be converted to radian/second and radian units to insure compatibility with the $[F_{\text{free}}]$ elements given by Schmidt (ibid).

Recall the diagonal elements of $[Q]$ are given by $q_{ii} \equiv 2\sigma_i^2 \Delta t^2$. Table 3 lists the σ_i standard deviations adopted for this study. For the random walk-related diagonal elements of $[Q]$, Stieler and Winter (ibid) show that $(\text{PSD}_{\text{rw}})^{1/2}$ is typically $0.003^\circ / \sqrt{\text{hr}}$. Thus one has $q_{40,40} = q_{41,41} = q_{42,42} = (\text{PSD}_{\text{rw}}) \cdot \Delta t$ which again will be converted to radian units.

4. SIMULATION RESULTS.

Since the chief priority of the simulation was to minimize the body frame to navigation frame orientation errors and to perform in-flight calibrations of the gyro and accelerometer sensor biases and scale factor errors, both the INS and GPS devices were activated (and thus the Kalman filter as well) a full eight hours before the balloon's liftoff. This warmup period commenced after the assumed INS analytical alignments and pre-filter GPS solutions, referred to in Table 2, were complete. Such a warmup period impressively reduces the north and east (levelling) alignment errors prior to liftoff and appreciably lowers the down (heading) misalignment. Once flight has begun, the heading errors drop much faster if a warmup period is used, allowing for a greater portion of the flight to possess accurate heading orientations.

It was decided to classify a GPS satellite as "in view" if its zenith angle with respect to the balloon's position was $\leq 80^\circ$. Using the simulated full constellation of 18 satellites, the number of satellites "in view" at any given epoch ranged from 4 to 8. Executions of the Kalman filter described in the previous section led to numerical instability problems, viz. round-off errors, if five or more satellites were utilized whenever $\text{NSATS} > 4$. The round-off errors inevitably led to the filter's collapse by generating negative diagonal elements in $[P]$. Such unwanted behavior is well chronicled in Brown (1983). This author was able to significantly delay the filter's collapse by switching from FORTRAN double precision to quadruple precision but was never able to reach the balloon's touchdown epoch (even if the preflight warmup period was omitted). Brown (ibid) suggests using the Joseph-form update equation for $[P]$ for added stability but it had no effect in this simulation. One can also raise the $[Q]$ input noise process levels to help stabilize such a situation (albeit at a cost in optimality). It was determined that limiting the number of selected satellites at each epoch to four, viz. the quartet possessing the minimum PDOP (position dilution of precision) value from all possible combinations of four "in view" satellites, suppressed all round-off concerns (even if extended warmup periods are used). In addition, except for periods of high four-satellite PDOP values, the error state outputs of the filter were more or less comparable in magnitude to those obtained using more than four satellites before the (>4) filter collapsed. Finding remedies for $\text{NSATS} > 4$ round-off problem is left for future numerical investigations. Figure 4 is a plot of the (best 4 satellite) PDOP curve. Recall the liftoff epoch occurs at $t = 8 \text{ hr} = 28800$ seconds.

Initial ^{Table 2.} \hat{P}_0 matrix adopted.

<u>states</u>	<u>1 σ</u>	<u>Comments</u>
$(\delta\epsilon_n, \delta\epsilon_e, \delta\epsilon_d)$	$(\pm 8'', \pm 8'', \pm 130'')$	An initial 1 hr. analytical alignment is assumed.
$(\delta\dot{\phi}, \delta\dot{\lambda}, \delta\dot{h})$	$(\pm 3 \text{ mm/s}, \pm 3 \text{ mm/s}, \pm 3 \text{ mm/s})$	Assuming a static differential GPS solution
$(\delta\phi, \delta\lambda, \delta h)$	$(\pm 3 \text{ cm}, \pm 3 \text{ cm}, \pm 3 \text{ cm})$	performed during analytical alignment of INS.
ϵ_{rw}	0	
d	$\pm 0.007^\circ/\text{hr}$	Reference: Stieler and Winter (ibid)
k	$\pm 5 \text{ ppm}$	" "
b	$\pm 3.5 \mu\text{g} (\pm 3.4 \text{ mGals})$	" "
ϵ_0	$\pm 10 \text{ ppm}$	" "
η_0	$\pm 10 \text{ m}$	Assumed GPS Pseudo-range solution performed during the INS's analytical alignment period.
η_1	$\pm 2.5 \text{ m/s}$	As determined by Wong et al (1987).
m	$\pm 0 \text{ cycles}$	Assumed that a static differential GPS solution performed during analytical alignment of INS fixing the values of the ambiguities.

Table 3.
Standard deviations adopted in the construction of the $[Q]$ matrix.

<u>noise process</u>	<u>1 σ</u>	<u>reference</u>
ΔT	$\pm 0.5^\circ\text{C}$	Eissfeller and Spietz (ibid)
h	$\pm 0.2 \text{ Gauss}$	"
β	5 arc secs	Stieler and Winter (ibid)
ϵ_1	10 ppm	"
ϵ_2	10 ppm/g	"
ϵ_3	10 ppm/g ²	"
α	6.5 arc secs	"
c	10 ppm/g	"
w	4 mm	"
ϵ_f	0.1 μg ($\approx 0.1 \text{ mGal}$)	Sundstrand memo.
δg	15 mGal ($\approx 15\text{E-}5\text{m/s}^2$)	Eissfeller and Spietz

Figure 5 is a plot of the GPS/INS hybrid 1σ position errors as determined by the 30 state filter. As expected, a high correlation exists between Figures 4 and 5. One can note that the general position error seems to stay in the 1 to 2 cm range. Figure 6 is a plot of the hybrid velocity errors. The spike occurs at the $t = 28800$ second liftoff epoch. Although less exaggerated, there still exists visible correlations between the satellite PDOP geometry and the velocity errors. Figure 7 plots all 3 hybrid alignment errors during the entire 15 1/2 hour period while Figure 8 plots only the levelling errors. By the liftoff epoch the levelling errors had been reduced from 8 arc secs to ≈ 1 arc sec. During flight the levelling errors take on a cyclical behavior ≈ 2 hours which is the simulated yaw rotation rate. During the 8 hour warmup period the heading errors were reduced from 130 arc secs to ≈ 90 arc secs. At the liftoff epoch the balloon's azimuth heading changes and thus the orientation of the gyro and accelerometer sensors changes with respect to the navigation axes. As described in Schmidt (1978), changes in vehicle heading introduce **observable** acceleration errors in a strapdown INS. This fact, in conjunction with the external GPS updates, allow for in-flight calibrations of the sensor biases and scale factor errors as well as dramatic improvement in the heading alignment. As the flight progresses, the heading errors decline more gradually, reaching a level of around 2.8 arc secs at the landing epoch. As alluded to earlier, if one does not adopt the 8 hour warmup period, then the launch drop in heading errors is less dramatic [one also has to wait for the **more important** (for the purpose of recovering gravity vector components... see applicable remarks below) levelling errors to drop to the 1 arc sec level]. The appearance and magnitudes of Figures 5, 6 and 7 generally agree with corresponding plots in Eissfeller and Spietz (ibid). The latter plots refer to a simulation involving a Ferranti Inertial Land Surveyor. The main difference between the two plot sets is the smoother time behavior of the balloon-related states. This is clearly due to the fact that the body-frame motions of the balloon were much more benign than those of the land vehicle.

Close examination of the navigation state-related dynamics submatrix $[F^{\text{free}}]$, cf. Schmidt (ibid), reveals cross couplings between the levelling error $\delta\epsilon_N$ and the f_E east component of the specific force and also between $\delta\epsilon_E$ and f_N . Thus Eissfeller and Spietz' treatment of the $(\delta g_N, \delta g_E, \delta g_D)$ gravity disturbances as (non-state) white noise processes is too crude. Their 30 state, 43 noise process model was transformed into the 33 state, 40 noise process model given by

$$\begin{bmatrix} \dot{x}_1 \\ \dot{x}_2 \\ \dot{x}_3 \\ \dot{x}_4 \\ \dot{\delta g} \end{bmatrix} = \begin{bmatrix} [F^{\text{old}}]_{30 \text{ by } 30} & [F^{\text{new}}]_{30 \text{ by } 3} \\ [0]_{3 \text{ by } 30} & [0]_{3 \text{ by } 3} \end{bmatrix} \cdot \begin{bmatrix} x_1 \\ x_2 \\ x_3 \\ x_4 \\ \delta g \end{bmatrix} + \begin{bmatrix} [G_1^*]_{9 \text{ by } 36} & [0]_{9 \text{ by } 3} & [0]_{9 \text{ by } 1} \\ [0] & [G_2] & [0] \\ [0] & [0] & [0] \\ [0] & [0] & [G_4] \\ [0]_{3 \text{ by } 36} & [0]_{3 \text{ by } 3} & [0]_{3 \text{ by } 1} \end{bmatrix} \cdot \begin{bmatrix} u_1^* \\ u_2 \\ u_4 \end{bmatrix} \quad (16)$$

where $[F^{old}]$ is the overall $[F]$ dynamics matrix listed in (7), $[G_1^*]$ is the left-most 9 by 36 portion of the 9 by 39 $[G_1]$ given by (11), u_1^* is the previous u_1 less the three δg 's and

$$[F^{new}] = \begin{bmatrix} [0]_{3 \text{ by } 3} \\ [D]_{3 \text{ by } 3} \\ [0]_{24 \text{ by } 3} \end{bmatrix}.$$

Therefore, the δg 's are now in x and out of u and are treated as bias states. The 15 mGal standard deviations for the three gravity disturbances were taken out of $[Q]$ (now reduced to dimension 40 by 40) and inserted into $[P_0]$ (now extended to 33 by 33). As alluded to above, including the three gravity disturbances as bias states appreciably changed the behavior of only 3 original states: the two levelling errors and the yaw (\cong "down" for a balloon flight) accelerometer scale factor error (a summarizing Table 4 appears below). Figure 9 is the 33 state counterpart to Figure 8. Figure 10 plots the estimated errors of the gravity disturbances. The aforementioned cross couplings can be seen by comparing Figures 9 and 10 (1 arc sec \cong 5 mGal) and the necessity of including the δg 's as states (even if modelled only as biases) is confirmed. To bring the levelling errors back to sub arc second levels (and thus the error estimates of the horizontal gravity disturbances to under 5 mGals) a fourth type of external observation, related to a three GPS antenna balloon-borne configuration, will be employed. The configuration assumed is an equilateral triangle having baselines Δr_I , Δr_{II} and Δr_{III} of 1 meter.

Brown (1981) shows that such a multi-antenna GPS receiver measures the $\delta(\Delta\Psi) = \Delta\Psi_{TRUE} - \Delta\Psi_{ESTIMATED \text{ BY INS}}$ error in the INS's estimate of the $\Delta\Psi$ phase difference between any two antennae. Such a measurement, corresponding e.g. to baseline Δr_I and satellite j , is related to the $(\delta\epsilon_N, \delta\epsilon_E, \delta\epsilon_D)$ attitude (recall they reside in x_1) and (the new)

$x_5 = \Delta r_{I,II,III}^{TRUE} - \Delta r_{I,II,III}^{PRE-FLIGHT \text{ ESTIMATED}}$ baseline length errors by (cf. Brown (1981))

$$\delta(\Delta\Psi_j^I) = \left[\frac{2\pi}{\lambda} (\hat{\Delta r}_I^n \times \underline{1}_j^n)^T \quad Q_3^T \quad Q_3^T \right] x_1 + \left[\frac{2\pi}{\lambda} (\hat{\underline{1}}_I^n \cdot \underline{1}_j^n) \quad 0 \quad 0 \right] x_5 \quad (17)$$

where $\lambda = .19m$ is the GPS carrier wavelength, $\hat{\Delta r}_I^n = [\hat{C}_b^n(t)] \cdot \Delta r_I^b$ contains the " \wedge " INS-estimated navigation frame components of the Δr_I baseline vector, $\underline{1}_j^n$ is the unitized navigation frame balloon to satellite j line-of-sight vector and $\hat{\underline{1}}_I^n$ is the unitized version of $\hat{\Delta r}_I^n$. Again assuming NSATS = 4, the merger of the 12 possible $\delta(\Delta\Psi)$ combinations with the previous $\delta(\Delta S)$, $\delta(\Delta\psi)$ and $\delta(\Delta\dot{\psi})$ raises the number of external updating measurements (NOBS) at each epoch t_k to 24. Adding the x_5 baseline length uncertainties to the overall state vector thus

raises the dimensions of $[H]$ to 24 by 36. The new $[R]$ matrix will be 24 by 24 and is given by

$$[R^{new}] = \begin{bmatrix} [R^{old}]_{12 \text{ by } 12} & [0] \\ [0] & [R^*]_{12 \text{ by } 12} \end{bmatrix}$$

where

$$[R^*] = \begin{bmatrix} [R_{j=1}] & [0] & [0] & [0] \\ [0] & [R_{j=2}] & [0] & [0] \\ [0] & [0] & [R_{j=3}] & [0] \\ [0] & [0] & [0] & [R_{j=4}] \end{bmatrix}$$

where each 3 by 3 $[R_j]$ denotes the covariance matrix for the three baseline phase difference measurements from a single satellite j and is given by

$$[R_j] = \begin{bmatrix} r & c & c \\ c & r & c \\ c & c & r \end{bmatrix}$$

where the measurements are **not** independent of each other as thermal noise from each antenna corrupts two measurements. The numerical values used for r and c were (cf. Brown (1981)) $\sqrt{r} \cong 13$ mrad or 0.75° and $\sqrt{c} \cong 9$ mrad or 0.5° . The 36 state, 40 noise process model is finally given by

$$\begin{bmatrix} \dot{x}_1 \\ \dot{x}_2 \\ \dot{x}_3 \\ \dot{x}_4 \\ \dot{\delta g} \\ \dot{x}_5 \end{bmatrix} = \begin{bmatrix} [F^{eqn. 16}]_{33 \text{ by } 33} & [0]_{33 \text{ by } 3} \\ [0]_{3 \text{ by } 33} & [0]_{3 \text{ by } 3} \end{bmatrix} \cdot \begin{bmatrix} x_1 \\ x_2 \\ x_3 \\ x_4 \\ \delta g \\ x_5 \end{bmatrix} + \begin{bmatrix} [G^{eqn. 16}]_{33 \text{ by } 40} \\ [0]_{3 \text{ by } 40} \end{bmatrix} \cdot \begin{bmatrix} u_1^* \\ u_2 \\ u_4 \end{bmatrix} \quad (18)$$

wherein the \underline{x}_5 baseline length uncertainties have been modelled as simple biases. The initial \underline{x}_5 error estimates in the $[\hat{P}_0]$ covariance matrix were set at 1 mm each.

Figure 11 plots the 36 state/ 3 antennae alignment errors. Comparing Figures 9 and 11 reveals the dramatic contributions of the $\delta(\Delta\Psi)$ updates. Moreover, the heading errors now plummet to roughly the same values as the levelling errors during the warmup period. Figure 12 plots the 36 state/ 3 antenna estimated errors of the gravity disturbances. Table 4 summarizes the final 1 σ accuracies of all the states for the three models presented herein.

Table 4.

Final 1 σ error estimates for the three models studied.

<u>States</u>	<u>Model</u>		
	<u>30 state</u>	<u>33 state</u>	<u>36 state, 3 antennae</u>
$(\delta\epsilon_N, \delta\epsilon_E, \delta\epsilon_D)$	(0.5, 0.5, 2.8) arc sec	(3.0, 1.8, 3.3) arc sec	(0.4, 0.4, 0.7) arc sec
$(\delta\dot{\phi}, \delta\dot{\lambda}, \delta\dot{h})$	(1.7, 1.5, 1.5) mm/s	(1.6, 1.4, 1.2) mm/s	(1.6, 1.4, 1.2) mm/s
$(\delta\phi, \delta\lambda, \delta h)$	(1.2, 0.8, 1.6) cm	(1.1, 0.8, 1.5) cm	(1.1, 0.8, 1.5) cm
$(roll, pitch, yaw)_{rw}$	(42, 42, 42) arc sec	(42, 42, 42) arc sec	(42, 42, 42) arc sec
(d^r, d^p, d^y)	(9E-4, 9E-4, 12E-4) °/hr	(8E-4, 8E-4, 12E-4) °/hr	(8E-4, 8E-4, 12E-4) °/hr
$(\kappa^r, \kappa^p, \kappa^y)$	(4.43, 4.46, 4.96) ppm	(4.69, 4.70, 4.96) ppm	(4.38, 4.43, 4.96) ppm
(b^r, b^p, b^y)	(2.0, 2.1, 3.2) mGal	(2.0, 2.1, 3.4) mGal	(0.9, 0.9, 3.4) mGal
$(\epsilon_0^r, \epsilon_0^p, \epsilon_0^y)$	(9.94, 9.85, 3.31) ppm	(9.93, 9.83, 7.98) ppm	(9.93, 9.83, 7.98) ppm
$(\delta g_N, \delta g_E, \delta g_D)$	-----	(7.8, 13.6, 8.1) mGal	(0.9, 0.9, 8.1) mGal
(baseline lengths)	-----	-----	(1E-3, 1E-3, 1E-3) mm

Table 4 reveals that the inclusion of the 3 GPS antennae significantly reduced the b^{roll} and b^{pitch} accelerometer bias errors. Unfortunately, the ϵ_0^{yaw} accelerometer scale factor error still remained at a troublesome 7.98 ppm level. This translates into an error of around 8 mGal in the strong yaw (\cong "down") balloon-borne specific force signal of approximately 970,000 mGal. For an actual flight, highly accurate astrogeodetic measurements will be taken at the launch site and the initial error estimates for all three gravity disturbances will be 1 mGal or less. Changing the initial entries in $[\hat{P}_0]$ from 15 mGal to 1 mGal reduced the final b accelerometer bias error estimates from (0.9, 0.9, 3.4) to (0.8, 0.8, 3.2) mGal, the critical yaw accelerometer s.f. error from 7.98 to 3.41 ppm and the error estimates in the final δg 's from (0.9, 0.9, 8.1) to

(0.7, 0.7, 1.0) mGal. All other final state values were unchanged (including the attitude errors). Figure 13 plots the error estimates of the gravity disturbance using initial 1 mGal uncertainties. One could of course supplement a GPS/INS payload with a single axis airborne gravimeter possessing a much lower scale factor error to further insure accurate determinations of the vertical gravity components. The reader is **strongly** reminded that it is assumed that no cycle slips occurred during the entire 15 1/2 hour period. Again, the detection and fixing of cycle slips from integrated GPS/INS data is discussed in Eissfeller and Spietz (ibid).

Modelling the gravity disturbances as first order Gauss-Markov processes requires minimum editing of equation (18). Adopting a correlation distance of 40 km and a representative balloon speed of 70 km/hr yields a corresponding correlation time T_g of 2057 seconds. Since the three

δg states are in positions 31,32 and 33 in the overall 36 by 1 state vector \underline{x} in (18), one edits [F] eqn 18 by setting the elements $f_{31,31} = f_{32,32} = f_{33,33} = -1/T_g$. For a first order Gauss-Markov process, the driving white noise processes in an extended 43 by 43 [Q] matrix (recall the dimension of [Q] was reduced to 40 by 40 when the gravity disturbances were modelled as bias states) are given by $q_{41,41} = q_{42,42} = q_{43,43} = 2\sigma_g^2 / T_g$ where it is assumed that $\sigma_g^2 = 900 \text{ mGal}^2$. The edits to [G] eqn 18 are limited to setting $g_{31,41} = g_{32,42} = g_{33,43} = 1$. Figure 14 plots error estimates of the gravity disturbances when they are modelled as bias states during the 8 hour warmup period and as first order G-M processes during flight. After the launch epoch the error estimates jump to the 6 to 8 mGal level but thereafter hold more or less steady with $\delta(\delta g_D)$ strongly correlated to the δh profile of Figure 6. Figure 15 plots the corresponding alignment errors. Figures 13 and 14 yield strikingly different estimates of the errors in the gravity disturbances. It is **strongly** emphasized here that neither a bias nor 1st order G-M model for the δg 's is very realistic for an actual flight. By contrast, Figures 11 and 15 both yield alignment error estimates well below 1 arc sec. If one can bound (e.g. using an n^{th} order Gauss Markov model.... recall as $n \rightarrow \infty$ one reaches the bias state model) the **actual** alignment errors in an **actual** flight to under 1 arc sec and **successfully** calibrate the accelerometer errors "in-flight" to under 1 mGal, then a final simple difference between GPS and INS determined acceleration components (in the navigation frame) would back out the gravity disturbance components to an accuracy near the desired 5 mGal level. The simulation results herein reveal the necessity to include the δg 's as states even if they are not modelled optimally. It is hoped for an actual flight that the **other** states can be estimated to an accuracy level allowing for the ultimate determination of the gravity disturbances through the aforementioned differencing.

5. FROM BALLOON-BORNE TO SPACEBORNE EXPERIMENTS.

A successful balloon mission would be a strong argument for a "high-low" satellite to satellite tracking experiment wherein a single "low" [polar orbiting, altitude ϵ (160 km,300km)] satellite possessing a GPS/IMU payload would be tracked by the multiple "high" GPS constellation (altitude \cong 20189 km). The fundamental observable would be **gravitational** intersatellite line-of-sight (l.o.s.) accelerations. Non-gravitational accelerations of the GPS satellites can be accurately modelled while those of the "low" satellite would be measured by an IMU. Jekeli and Upadhyay (1990), citing current GPS receiver, orbit determination and IMU capabilities, report that the expected accuracy of "arc mean" (over some averaging time period τ) l.o.s. gravitational accelerations is between 0.1 and 0.3 mGals. New generation GPS receivers are being developed which should yield such accuracies at 1 Hz. Gleason (1991) shows that the gravity information

obtained from simulated 1 Hz, $\sigma = 0.1$ mGal, intersatellite l.o.s. acceleration data, related to a "low" satellite with an altitude of 300 km, can be downward continued to the Earth's surface at a resolution of 100 km to an accuracy of about 6 mGals. This essentially matches the anticipated accuracies of the more costly spaceborne gradiometry proposal known as ARISTOTELES (see Benz et al (1988) for description) which would fly at an altitude of ≈ 200 km. If one is willing to digest the added satellite design cost to lower a GPS/IMU payload down to 200 km, the aforementioned 6 mGal accuracies would be significantly enhanced. Thus a spaceborne GPS/INS data integration project would allow for an accurate gravity mapping of all heretofore inaccessible areas of the Earth's surface.

CONCLUDING REMARKS. The results of this simulation suggest one can recover the three components of balloon-borne gravity vectors, to an accuracy of 5 mGal or better, if the balloon is flown over an area where the gravity disturbances can adequately be modelled as simple biases. For flights over rugged terrain or over areas containing significant crustal density variations, the big challenge is to develop an **optimal** (quite possibly non-linear) gravity disturbance model. A possible alternative is to adopt a non-optimal (possibly involving higher order Gauss-Markov processes) linear δg model which can limit the **actual** levelling errors to 1 arc sec (≈ 5 mGal) or better. An ultimate, simple subtraction could then take place between corresponding GPS and INS determined acceleration components. Hehl et al (1990) demonstrate that 20 second mean GPS-determined accelerations can be determined to accuracies of 0.5 mGals. Clearly before an ultimate subtraction occurs, care must be taken to insure that 1) proper GPS/INS time synchronization is established and 2) compatible GPS/INS bandwidths and sampling rates are employed. The bounding of the misalignment-induced errors in the horizontal δg components is the main task at hand since the **computed** $[\hat{C}_b^n]$ and **true** $[C_b^n]$ transformation matrices are related by (cf. Britting (ibid))

$$\begin{bmatrix} \hat{C}_b^n \end{bmatrix} = \begin{bmatrix} 1 & \delta\epsilon_D & -\delta\epsilon_E \\ -\delta\epsilon_D & 1 & \delta\epsilon_N \\ \delta\epsilon_E & -\delta\epsilon_N & 1 \end{bmatrix} \begin{bmatrix} C_b^n \end{bmatrix}_{\text{TRUE}}$$

and the approximate magnitude of the (n,e,d) components of the sensed accelerometer signals (from typical balloon-borne Coriolis, centrifugal force and g values) are $(f_n, f_e, f_d) \approx (4500, 200, 970,000)$ mGals. This paper has demonstrated the ability to satisfactorily calibrate in-flight accelerometer bias and scale factor errors. The gyro and accelerometer related initial error estimates adopted for this simulation's $[P_0]$ and $[Q]$ matrices were taken from references that are nearly 10 years old. Using state of the art accuracies may well enhance the results of the Kalman filter presented herein. In the same vein, new generation GPS receivers should make the data integration even more appealing. It is hoped that a successful balloon experiment will stimulate serious interest in a subsequent spaceborne mission possessing the same payload possibly augmented with a startracker. Such a project would yield gravity information over heretofore inaccessible regions.

REFERENCES:

Aggarwal, A.K., "Integration of Differential GPS with INS for Precise Position, Altitude and Azimuth Determination", presented at the Institute of Navigation, Satellite Division, First Technical Meeting, Colorado Springs, September, 1987.

Benz, R., Faulks, H. and Langemann, M., "ARISTOTELES - A European Approach for an Earth Gravity Field Recovery Mission", Proceedings of the Chapman Conference on Gravity Field Determination, Ft. Lauderdale, Fla., 1988.

Britting, K.R., Inertial Navigation Systems Analysis, Wiley-Interscience, New York, 1971.

Brown, A.K., Interferometric Attitude Determination Using the Global Positioning System, M.S. thesis, Massachusetts Institute of Technology, Dept. of Aeronautical and Astronautical Engineering, August, 1981.

Brown, G., Introduction to Random Signal Analysis and Kalman Filtering, John Wiley and Sons, New York, 1983.

Cannon, M.E., Schwarz, K.P. and Wong, R.V.C., "Kinematic Positioning with GPS: An Analysis of Road Tests", Proceedings of the Fourth International Geodetic Symposium on Satellite Positioning, Austin, Tx., April, 1986.

Carnahan, B., Luther, H.A. and Wilkes, J.O., Applied Numerical Methods, John Wiley and Sons, 1969.

Eissfeller B. and Spietz, P., "Basic Filter Concepts for the Integration of GPS and an Inertial Ring Laser Gyro Strapdown System", Manuscripta Geodaetica, Vol. 14, pp.166-182, 1989.

Gelb, A. (editor), Applied Optimal Estimation, M.I.T. Press, Cambridge, Ma., 1974.

Gleason, D.M., "Obtaining Earth Surface Gravity Disturbances from a GPS-Based "High-Low" Satellite to Satellite Tracking Experiment", Geophysical Journal International, in press, 1991.

Goad, C., "Determination of Precise Position on a Moving Vehicle with GPS", Proceedings of IEEE PLANS, Las Vegas, NV., March, 1990.

Hehl, K., Hein, G.W., Landau, M., Eotel, M., Fritsch, J., Kewitsch P., "An Integrated Precise Airborne Navigation and Gravity Recovery System", Proceedings of the International Symposium on Kinematic Systems in Geodesy, Surveying and Remote Sensing, Banff, Canada, 1990.

Hein, G.W., Landau, H. and Baustert G., "Terrestrial and Aircraft Differential Kinematic Positioning", International GPS Workshop, Darmstadt, Germany, April, 1988.

Heiskanen, W. and Moritz, H., Physical Geodesy, W.H. Freeman and Son, San Francisco, 1967.

Jekeli, C. and Upadhyay, T., "Gravity Estimation from Multiple-High Single-Low Satellite to Satellite Tracking", Journal of Geophysical Research, Vol. 95, No. B7, pp. 10973-10985, 1990.

Jordan, S. and Center, J., "Establishing Requirements for Gravity Surveys for Very Accurate Inertial Navigation", Navigation Journal of the Institute of Navigation, Vol. 33, No. 2, pp. 90-108, 1986.

Knickmeyer, E., Vector Gravimetry by a Combination of Inertial and GPS Satellite Measurements, Ph. D. Thesis, University of Calgary, 1990.

Lazarewicz, A.R., Schilinski, B.J., Cowie, R.J., Rice, C.L., Moss, P. and Carter, L.N., "Balloon-Borne, High Altitude Gravimetry: The Flight of DUCKY Ia", Air Force Geophysics Laboratory Technical Report No. TR-85-0342, Hanscom AFB, Ma., December, 1985.

Moritz, H. and Wei, M., "A Simple Error Study for the Gradiometer-Accelerometer Equation", Manuscripta Geodaetica, Vol. 12, No. 2, pp. 113-127, 1987.

Mueller, I.I., Spherical and Practical Astronomy, Frederick Ungar, New York, 1969.

Schmidt, G.T., "Strapdown Inertial Systems - Theory and Applications, Introduction and Overview", In: Strapdown Inertial Systems, AGARD Lecture Series No. 95, NATO, 7 Rue Ancelle, 92200 Neuilly-sur-Seine, France, 1978.

Stieler B. and Winter, H., "Gyroscopic Instruments and their Application to Flight Testing", AGARD Flight Test Instrumentation Series, Vol. 15, AGARDograph No. 160, NATO, 7 Rue Ancelle, 92200 Neuilly-sur-Seine, France, 1982.

Wells, D. Beck, N., Delikaraoglu, D., Kleusberg, A., Krakiwsky E., Lachapelle, G., Langley, R., Nakiboglu M., Schwarz, K.P., Tranquilla, J. and Vanicek, P., "Guide to GPS Positioning", Canadian GPS Associates, Fredericton, New Brunswick, Canada, 1986.

Wong, R.V.C., Schwarz, K.P. and Cannon, M.E., "High Accuracy Kinematic Positioning by GPS-INS", Presented at the XIX General Assembly of the IUGG, Vancouver, August, 1987.

Figure 1.

Ground profile of 7.5 hour balloon flight of Lazarewicz et al (1985).

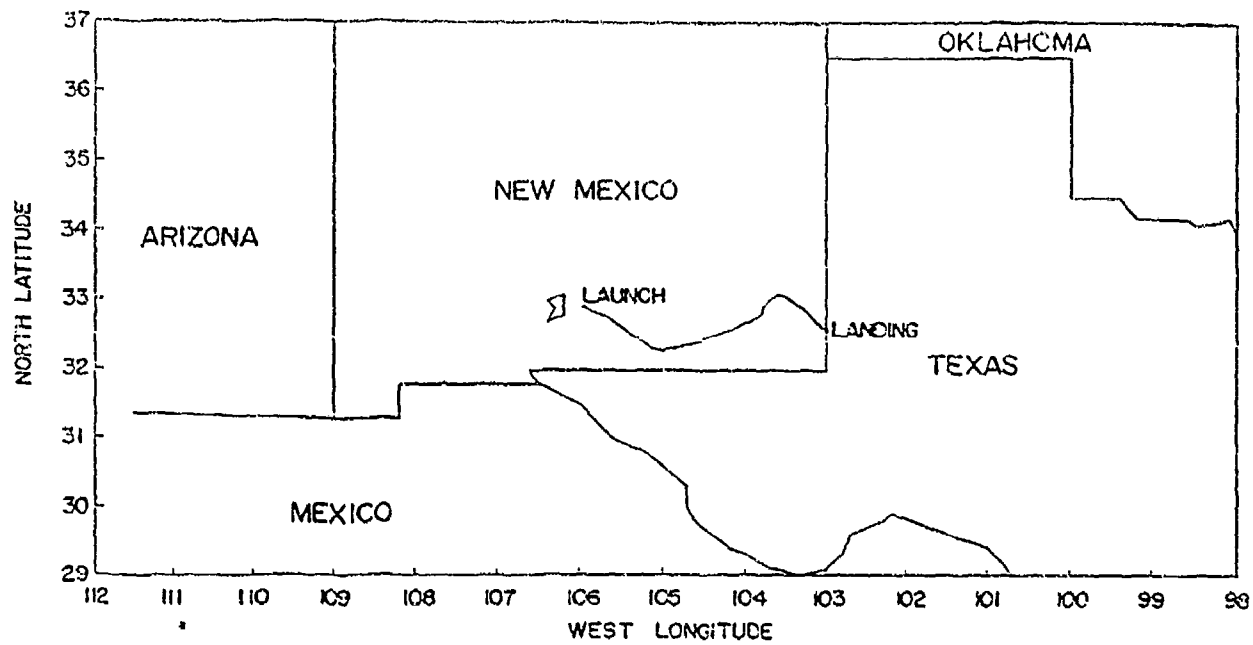


Figure 2.

Altitude profile of 7.5 hour balloon flight of Lazarewicz et al (1985).

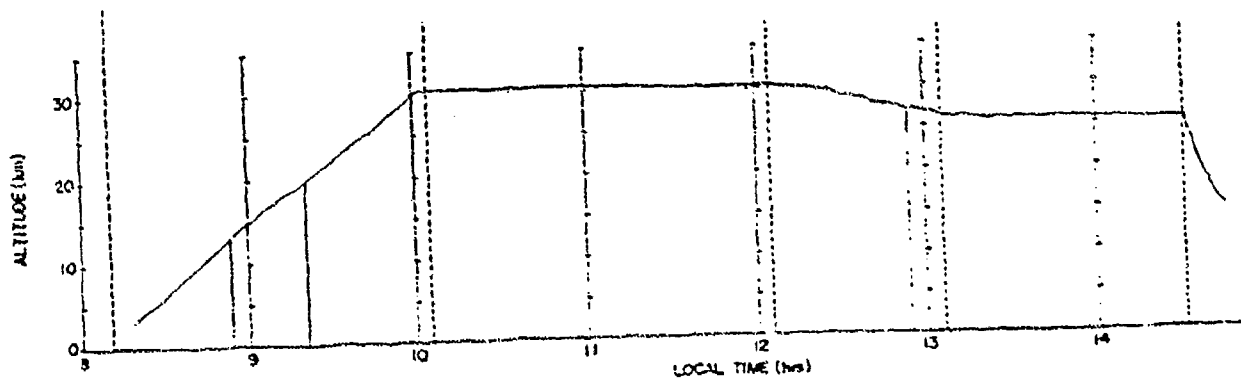


Figure 3.

Exaggerated kinematic motions of a balloon in flight [taken from Lazarewicz et al (1985)].

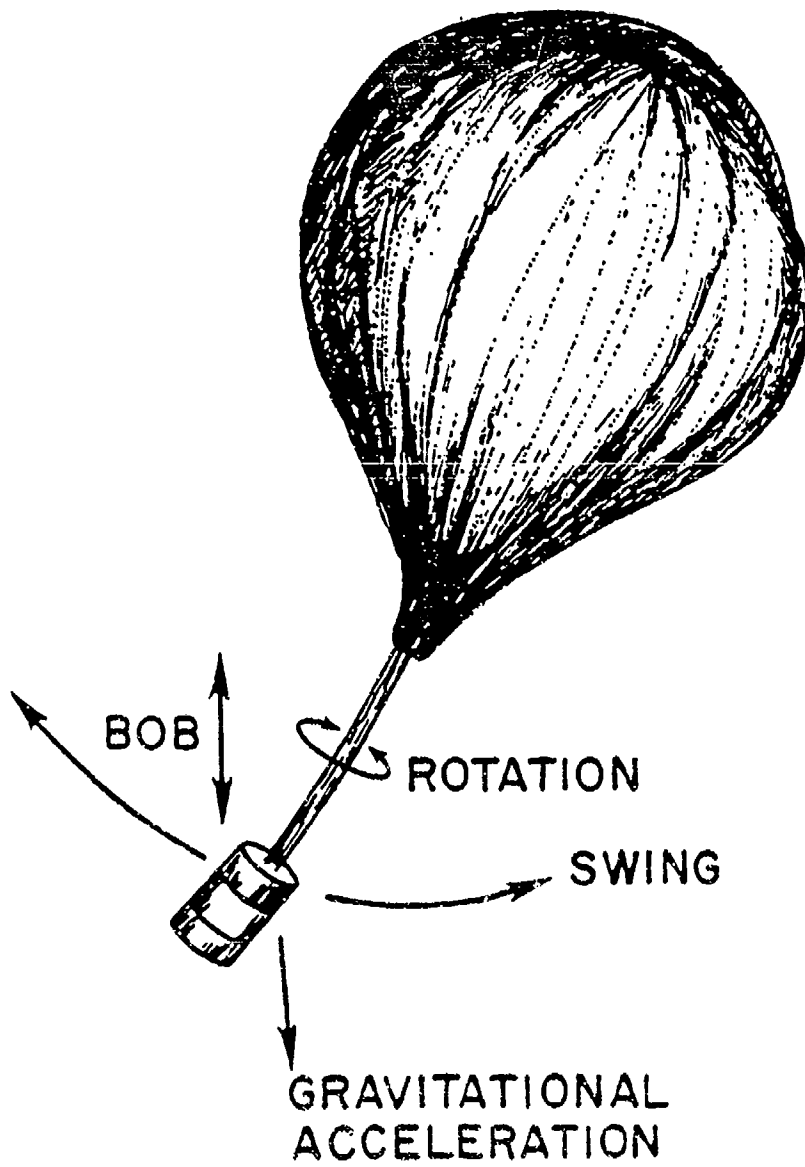


Figure 4 .

Note: Launch occurs at $t = 8 \text{ hour} = 28800 \text{ second epoch}$.

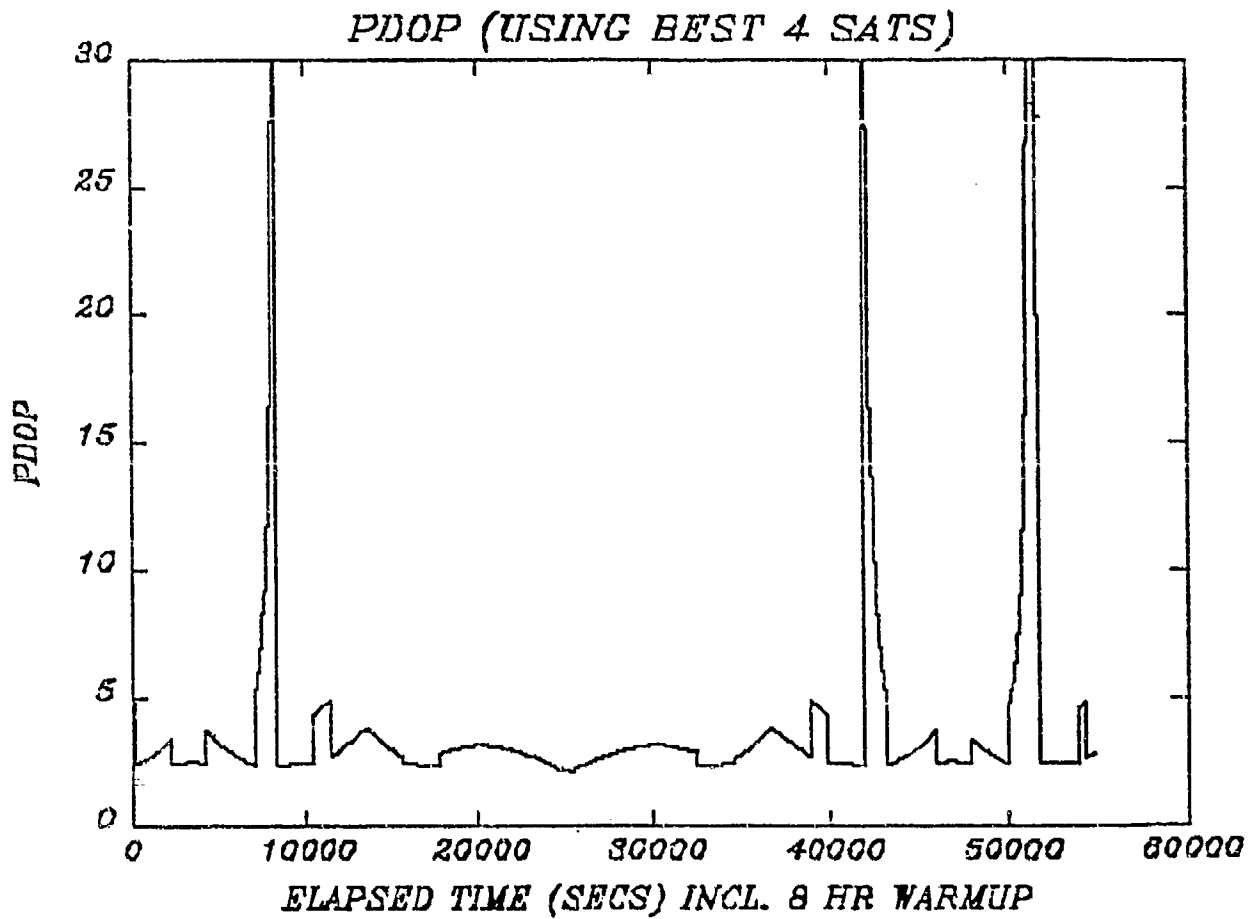
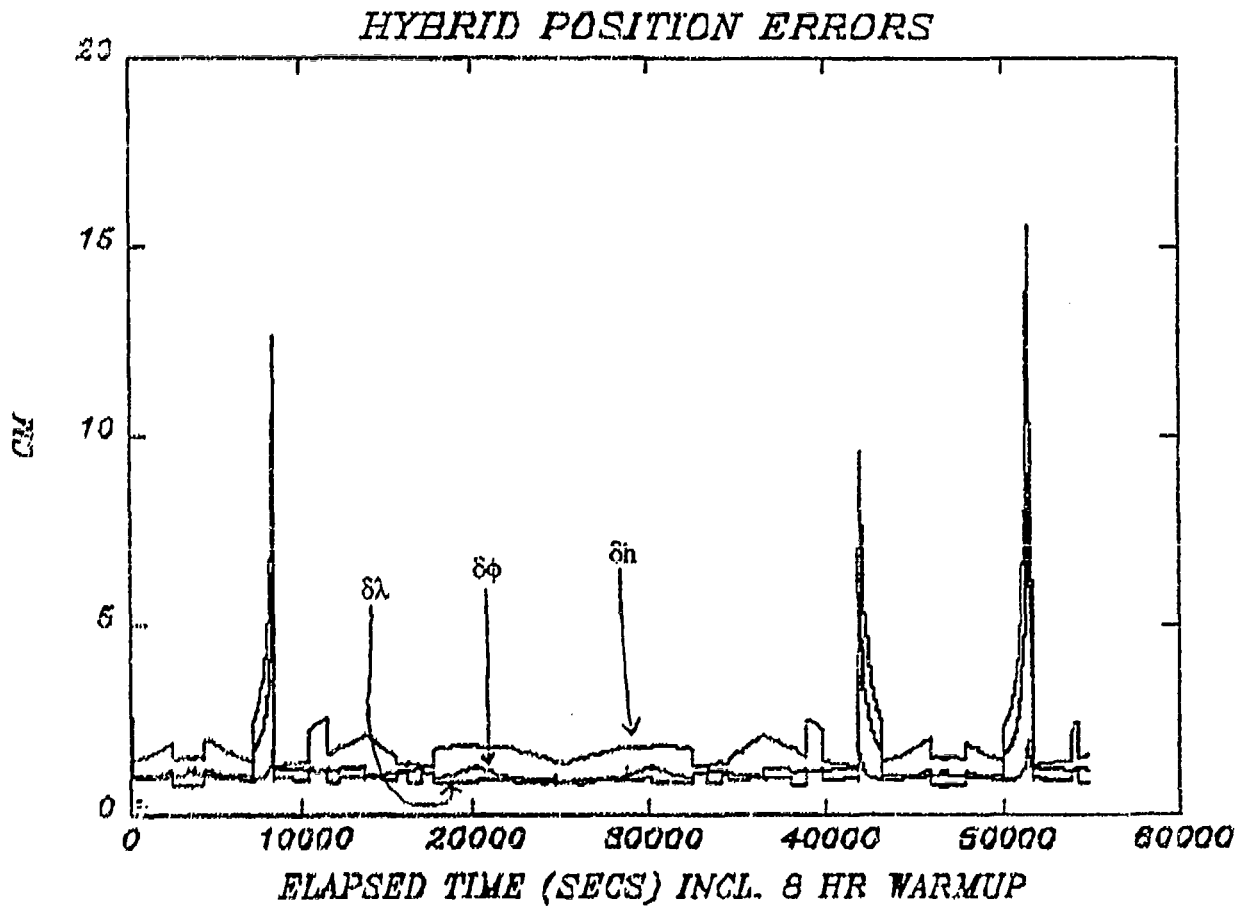


Figure 5.

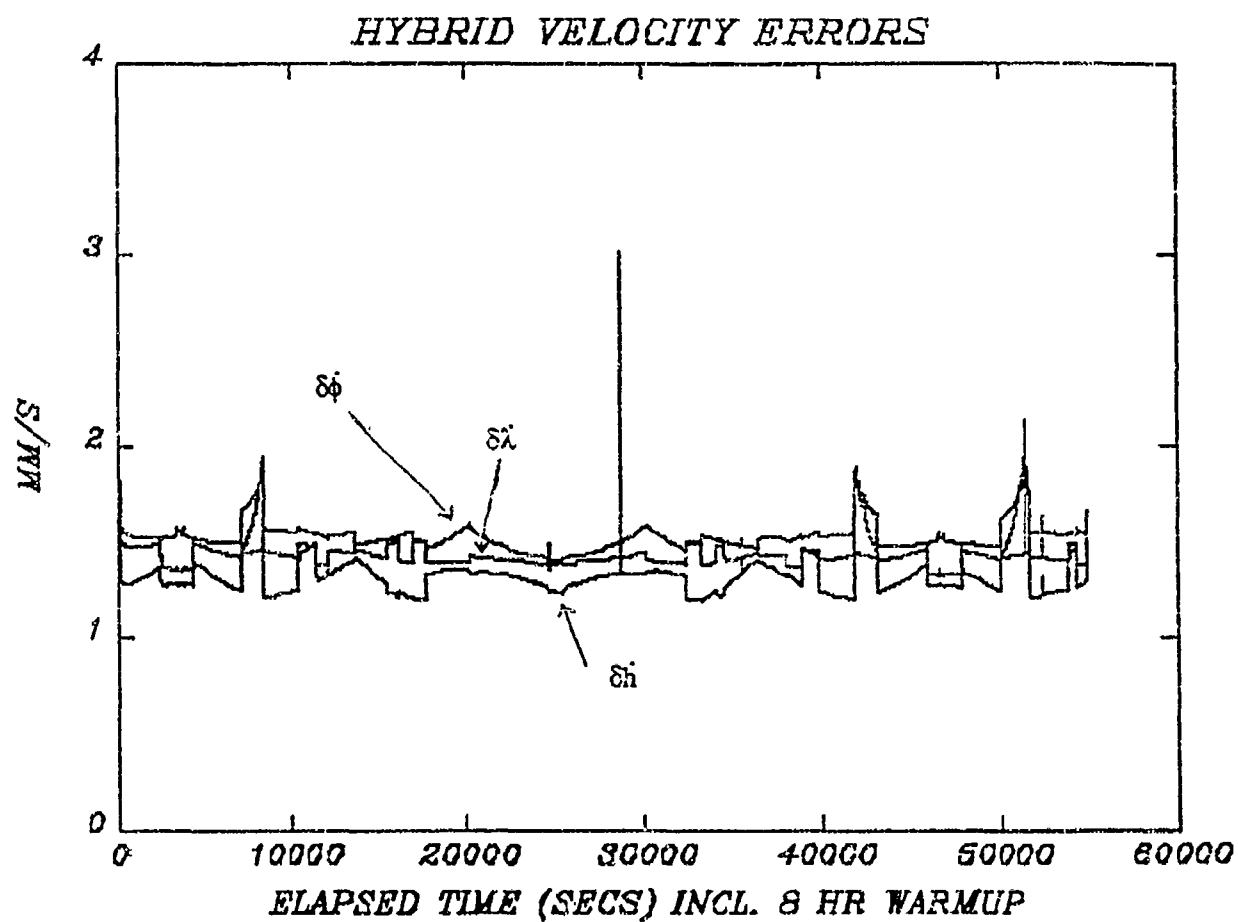
Note: Launch occurs at $t = 8$ hour = 28800 second epoch.



	Initial Errors	Final Errors
$\delta\phi$	3 cm	1.2 cm
$\delta\lambda$	3 cm	0.8 cm
δh	3 cm	1.6 cm

Figure 6.

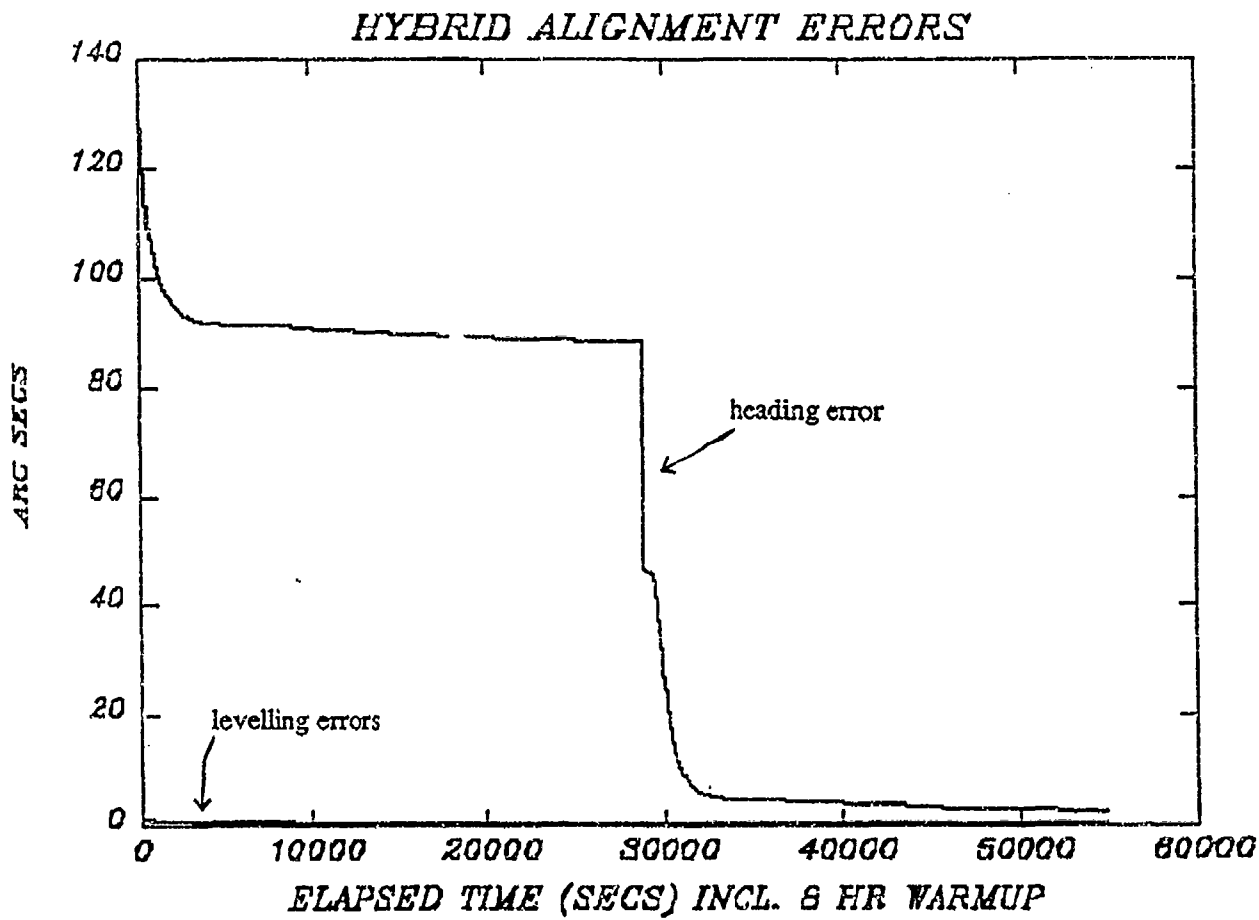
Note: Launch occurs at $t = 8 \text{ hour} = 28800 \text{ second epoch}$.



	<u>Initial Errors</u>	<u>Final Errors</u>
$\delta\phi$	3 mm/s	1.7 mm/s
$\delta\lambda$	3 mm/s	1.5 mm/s
δh	3 mm/s	1.5 mm/s

Figure 7.

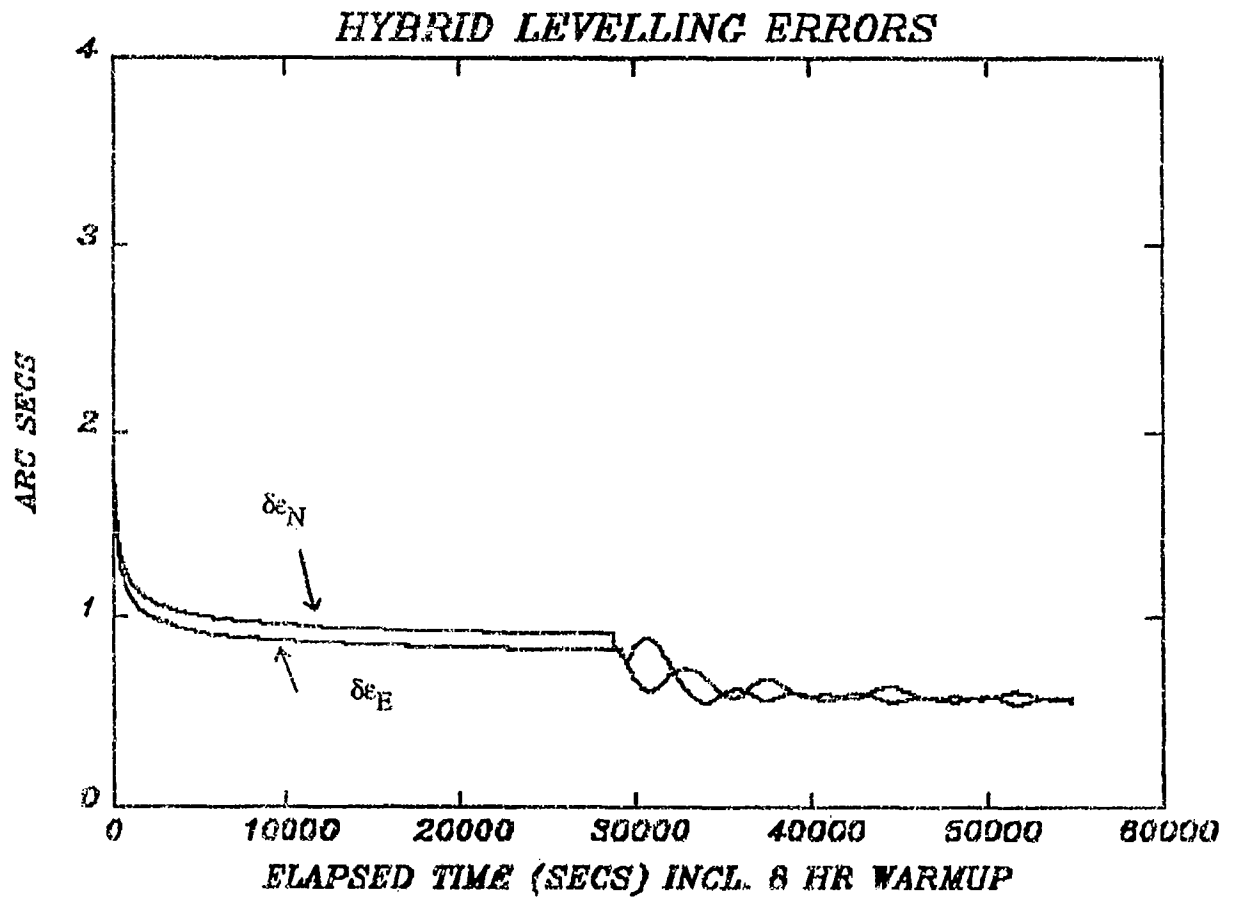
Note: Launch occurs at $t = 8$ hour = 28800 second epoch.



	<u>Initial Errors</u>	<u>Final Errors</u>
$\delta\epsilon_N$	8 arc secs	0.5 arc secs
$\delta\epsilon_E$	8 arc secs	0.5 arc secs
$\delta\epsilon_D$	130 arc secs	2.8 arc secs

Figure 8 .

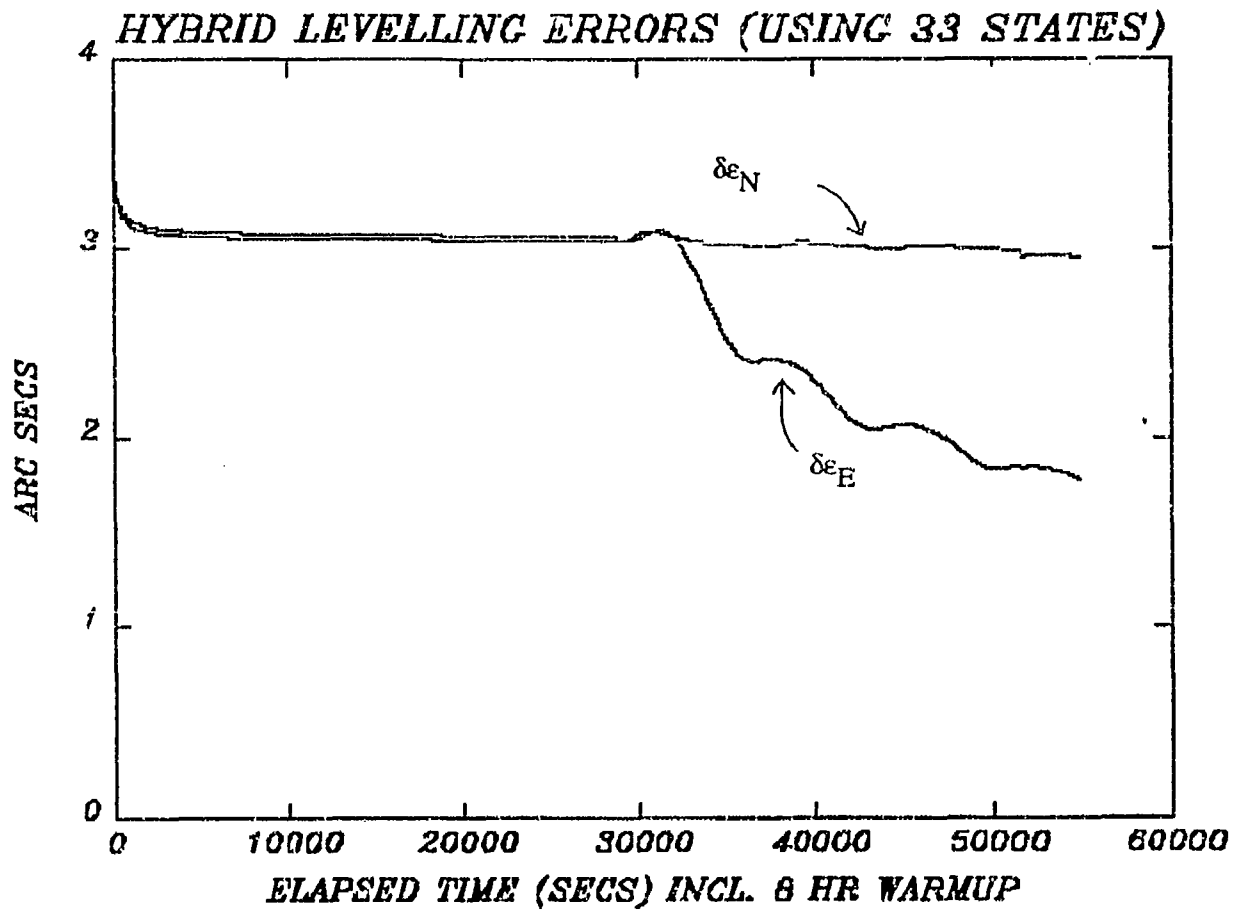
Note: Launch occurs at $t = 8 \text{ hour} = 28800 \text{ second epoch}$.



	<u>Initial Errors</u>	<u>Final Errors</u>
δe_N	8 arc secs	0.5 arc secs
δe_E	8 arc secs	0.5 arc secs

Figure 9.

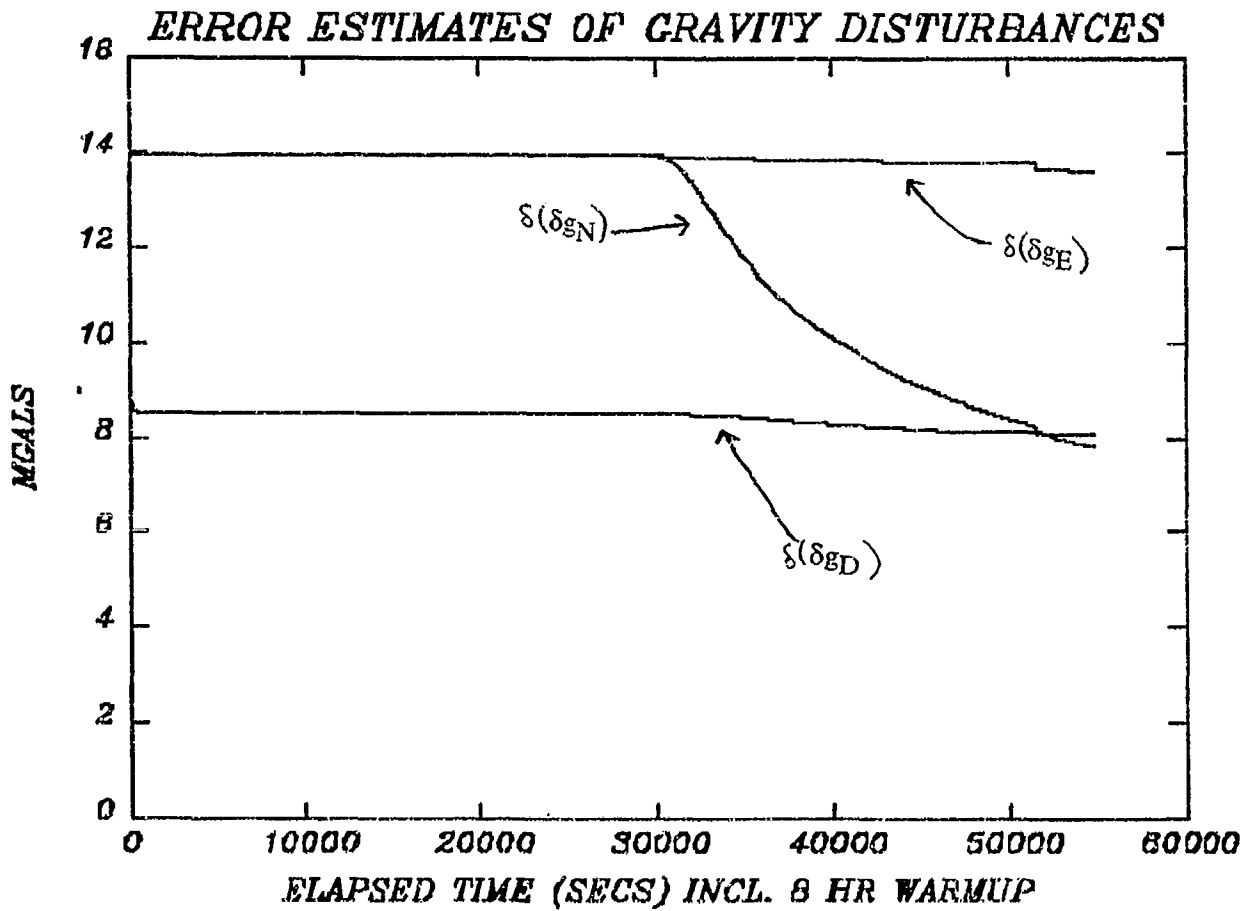
Note: Launch occurs at $t = 8 \text{ hour} = 28800 \text{ second epoch}$.



	<u>Initial Errors</u>	<u>Final Errors</u>
$\delta\epsilon_N$	8 arc secs	3.0 arc secs
$\delta\epsilon_E$	8 arc secs	1.8 arc secs

Figure 10.

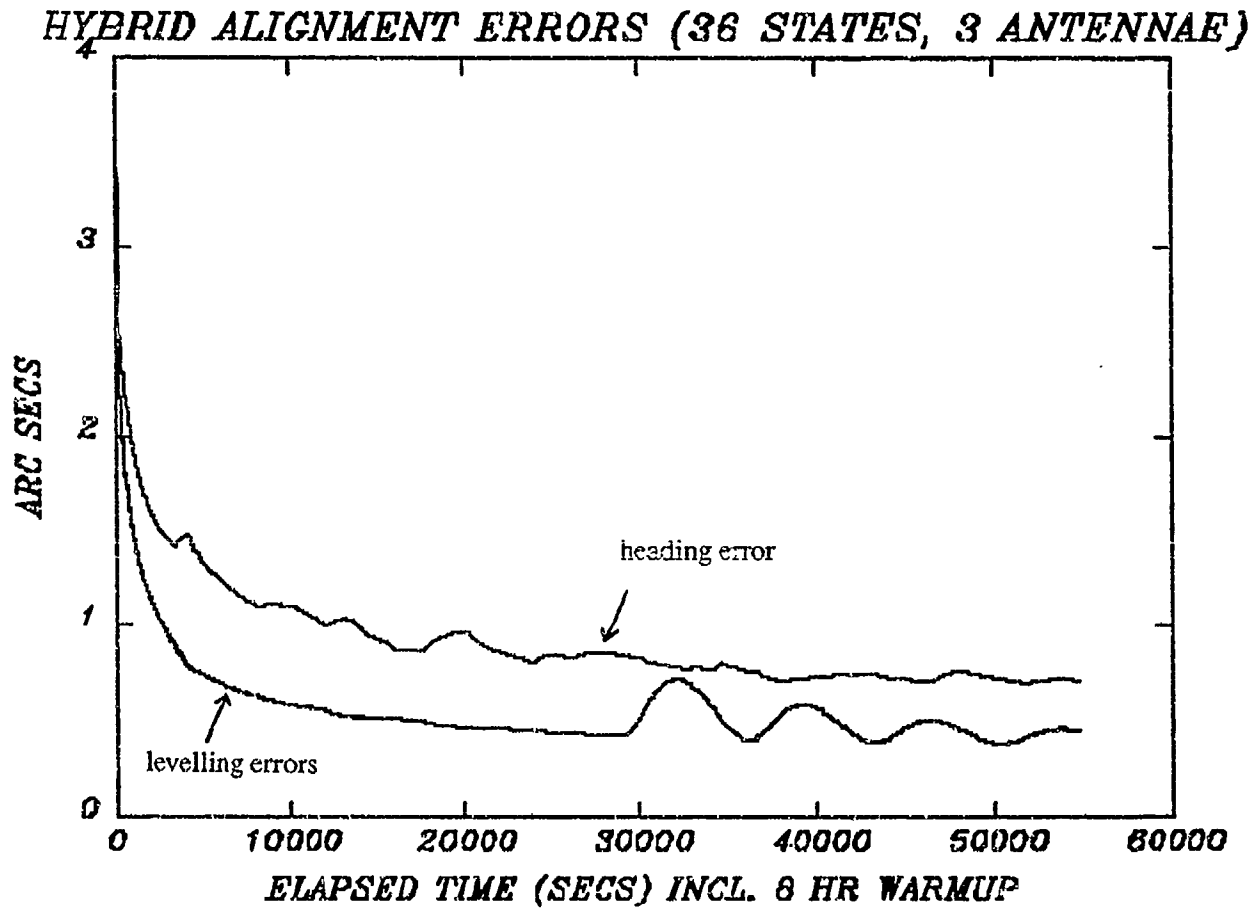
Note: Launch occurs at $t = 8 \text{ hour} = 28800 \text{ second epoch}$.



	<u>Initial Errors</u>	<u>Final Errors</u>
$\delta(\delta_{gN})$	15 mGal	7.8 mGal
$\delta(\delta_{gE})$	15 mGal	13.6 mGal
$\delta(\delta_{gD})$	15 mGal	8.1 mGal

Figure 11.

Note: Launch occurs at $t = 8$ hour = 28800 second epoch.

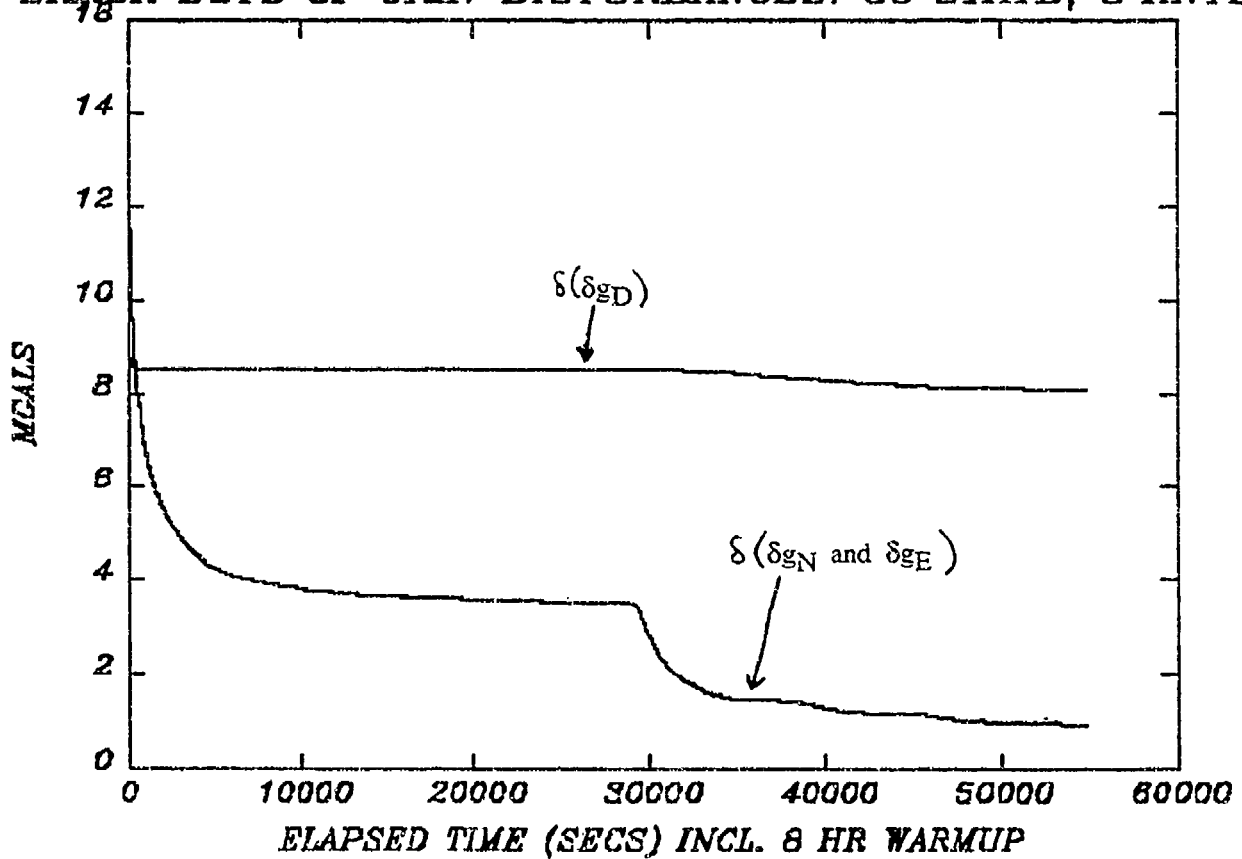


	<u>Initial Errors</u>	<u>Final Errors</u>
$\delta\epsilon_N$	8 arc secs	0.4 arc secs
$\delta\epsilon_E$	8 arc secs	0.4 arc secs
$\delta\epsilon_D$	130 arc secs	0.7 arc secs

Figure 12.

Note: Launch occurs at $t = 8 \text{ hour} = 28800 \text{ second epoch}$.

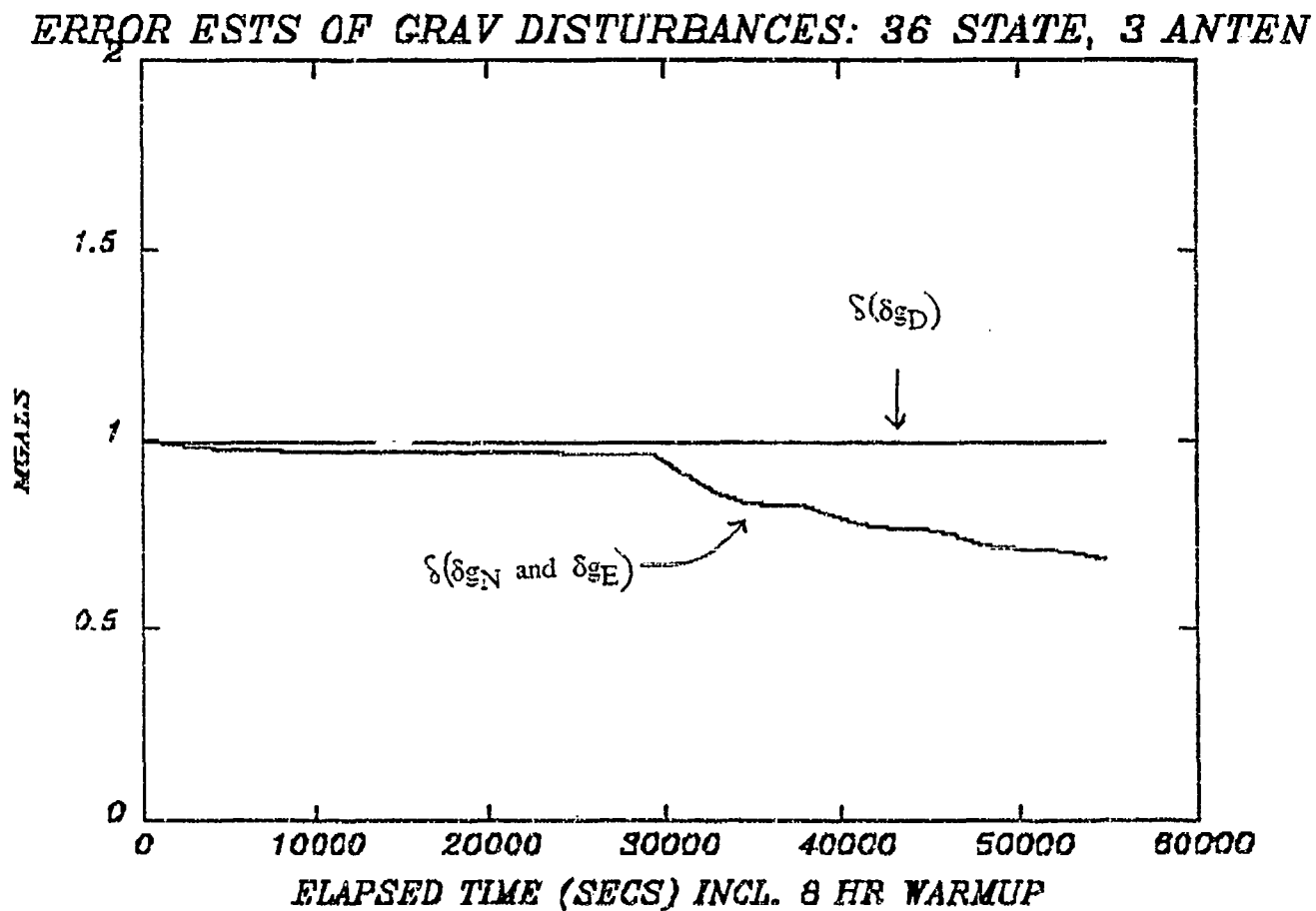
ERROR ESTS OF GRAV DISTURBANCES: 36 STATE, 3 ANTEN



	Initial Errors	Final Errors
$\delta(\delta g_N)$	15 mGal	0.9 mGal
$\delta(\delta g_E)$	15 mGal	0.9 mGal
$\delta(\delta g_D)$	15 mGal	8.1 mGal

Figure 13.

Note: Launch occurs at $t = 8 \text{ hour} = 28800 \text{ second epoch}$.



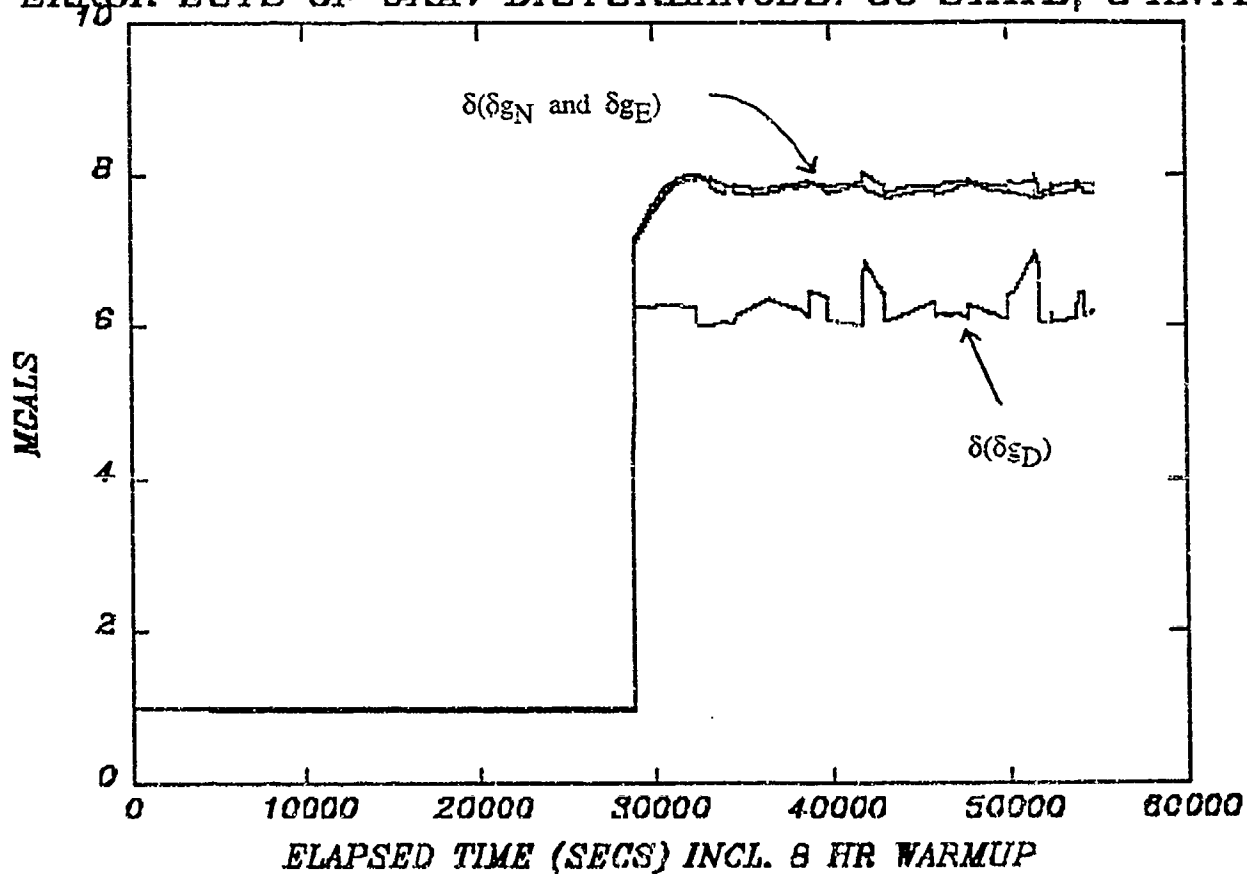
	Initial Errors	Final Errors
$\delta(\delta g_N)$	1 mGal	0.7 mGal
$\delta(\delta g_E)$	1 mGal	0.7 mGal
$\delta(\delta g_D)$	1 mGal	1.0 mGal

Figure 14 .

Gravity disturbances modelled as biases during the warmup period and as first order Gauss-Markov processes during flight.

Note: Launch occurs at $t = 8 \text{ hour} = 28800 \text{ second epoch}$.

ERROR ESTS OF GRAV DISTURBANCES: 36 STATE, 3 ANTEN

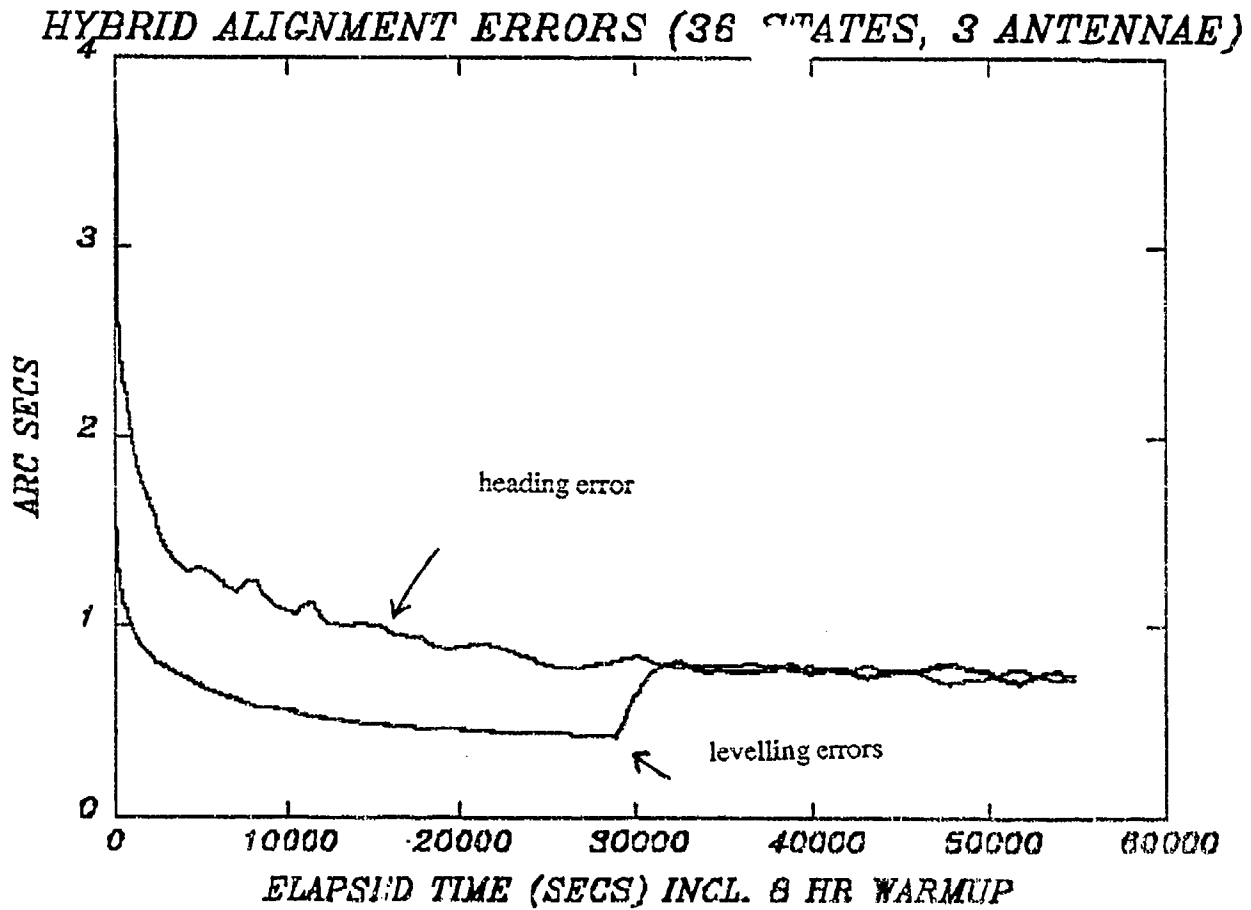


	<u>Initial Errors</u>	<u>Final Errors</u>
$\delta(\delta g_N)$	1 mGal	7.9 mGal
$\delta(\delta g_E)$	1 mGal	7.8 mGal
$\delta(\delta g_D)$	1 mGal	6.2 mGal

Figure 15.

Alignment errors corresponding to Figure 14.

Note: Launch occurs at $t = 8$ hour = 28800 second epoch.



	Initial Errors	Final Errors
$\delta\epsilon_N$	8 arc secs	0.8 arc secs
$\delta\epsilon_E$	8 arc secs	0.8 arc secs
$\delta\epsilon_D$	130 arc secs	0.7 arc secs

**EVOLUTION OF MINIATURE QUARTZ VIBRATING
BEAM ACCELEROMETER TECHNOLOGY
FOR NAVIGATION AND FLIGHT CONTROL**

By

David P. Jensen
Advanced Technology Engineering
Sundstrand Data Control
15001 N.E. 36th Street
Redmond, WA 98073

**Evolution of Miniature Quartz Vibrating
Beam Accelerometer Technology
for Navigation and Flight Control
at Sundstrand Data Control**

ABSTRACT

Over the years, a number of techniques for designing vibrating beams in accelerometers have been developed in the industry. As these accelerometers have evolved, they have begun to contribute to the state-of-the-art in acceleration measurements. Some of the advantages offered by vibrating beam technology include the inherently digital output, ease of signal processing and the ability to digitally remove errors using supplier-furnished algorithms and calibration constants. Vibrating beam accelerometers also offer the small size, lower power and high-g ranges necessary for navigational and flight control applications in today's aircraft and missiles.

Sundstrand Data Control has been developing its Accelerex® vibrating beam accelerometer technology since 1981. Its designs utilize a dual-tine quartz crystal resonator similar to a double-ended tuning fork. This configuration has the advantage of providing dynamic balance which results in the elimination of coupling and energy loss to the crystal support structure. Crystalline quartz is used for the resonator material because of its inherent stability. The no-load frequency is dependent almost entirely on the beam dimensions and the physical properties of the quartz, which are very stable.

Sundstrand has developed a series of vibrating beam accelerometers that utilize a flexure constrained proofmass which converts the input acceleration into applied force on the quartz crystals. Two crystals are used in each accelerometer and are configured in a "push-pull" orientation. For a given input acceleration, one crystal is placed in tension with a resultant increase in the frequency, and the other crystal is placed in compression with a corresponding decrease in frequency. The acceleration output signal is derived from the difference in frequency of the two crystal frequencies. The "push-pull" crystal configuration cancels out many of the common mode errors that would be present in a single crystal design.

This paper provides an overview of vibrating beam accelerometer theory; a discussion of evolution and maturity of different designs and performance; the system implementation for the use of the accelerometer; and test data for the different configurations.

INTRODUCTION

Quartz resonators have been used to control frequency for communication equipment since the 1920s. During World War II, quartz resonators were used to measure physical quantities when they were applied for use in sonar. More recently, quartz resonators have been used as sensing elements for measuring other physical parameters, such as pressure, temperature and acceleration. Quartz sensing elements used in accelerometers have been developed using two different operating principles.

The first type uses the piezoelectric charge producing capabilities of quartz to produce an output that is a function of input acceleration. Because these accelerometers have limited capability to measure DC or steady state acceleration, they are used mostly for dynamic measurements.

The other type of accelerometer uses quartz vibrating beams to measure acceleration. In these devices, the piezoelectric qualities of quartz are used to drive the beam and pick off the signal of the resonating beam. The beam operates at its resonant frequency which changes as a function of acceleration, as a result of the internal mechanism of the beam to proofmass structure. This allows the accelerometer to measure not only dynamic acceleration, but also DC and steady state acceleration, because the beam is providing an output signal at its no load resonant frequency when no acceleration forces are acting on it.

Although the use of quartz vibrating beams in accelerometers is not necessarily new, lower cost, medium to higher accuracy accelerometers are. Crystalline quartz is used for the resonator material because of its ability to carry both compression and tension loads, its inherent stability and the fact that the no load frequency is almost entirely dependent on the beam dimensions and the physical properties of quartz.

The accelerometers being discussed both use dual tine quartz resonators which have virtually eliminated the larger isolators used in single tine beam resonators. This results in a smaller, simpler design which assists in smaller, lower-cost accelerometers.

Some of the advantages offered by vibrating beam technology include the inherently digital output which eliminates the costs and inaccuracies of A to D conversion. It also allows for signal processing using supplier-supplied algorithms and the on-board storage of accelerometer unique correction coefficients that can be used for error corrections.

Dual-tine quartz resonators, used in a number of accelerometer designs at Sundstrand, support performance requirements from low to high accuracies. This paper discusses two models of Accelerex vibrating beam accelerometers developed by Sundstrand Data Control. These accelerometers are called the Resonating Beam Accelerometer (RBA) Model RBA-500, and Precision RBA, respectively. The RBA-500 is designed for tactical missile, flight control, and AHRS navigation requirements. The PRBA is designed for precision inertial navigation on future digital systems. It is exceptionally good for skewed axis navigation systems because of the inherent excellence of scale factor in RBAs.

The performance specifications for the two accelerometers are shown in Table 1.

TABLE 1: PERFORMANCE SPECIFICATIONS

	<u>RBA-500</u>	<u>PRBA</u>
Input Range	$\pm 70g's$	$\pm 25g's$
Bias (Composite Error)	$< 5\text{ mg}$	$< 150\text{ }\mu g$
Scale Factor ($F_1 - F_2$)	$\sim 75\text{ Hz/g}$	$\sim 140\text{ Hz/g}$
Scale Factor (Composite Error)	$< 350\text{ ppm}$	$< 50\text{ ppm}$
Axis Misalignment (Initial)	$< 12\text{ mradian}$	$< 7\text{ mradian}$
AA (Composite Error)	$< 400\text{ }\mu\text{radian}$	$< 50\text{ }\mu\text{radian}$
Linearity (to full scale)	$< 65\text{ }\mu g/g^2$	$< 20\text{ }\mu g/g^2$
VRC	$50\text{ }\mu g/g^2$	$32\text{ }\mu g/g^2$
Input Voltage (VDC)	+9 to 16	+15 $\pm 5\%$
Input Current	$< 5\text{ mA}$	$< 20\text{ mA}$
Weight	$< 10\text{ grams}$	$< 59\text{ grams}$
Volume	$< 2\text{ cm}^3$	$< 11\text{ cm}^3$
Integral Temperature Sensor	No	Yes
Integral E ² PROM	No	Yes

THEORY OF OPERATION

Both designs discussed are open loop accelerometers which have the proofmass constrained by a pendulum with a pair of dual beam crystalline quartz force crystals mounted in a push-pull orientation. The flexure constraint of the proofmass provides a single degree of freedom and a single axis sensitive to input acceleration. The quartz crystals are mounted so that (for a given input acceleration) one crystal is placed in tension with a resultant increase in its resonant frequency, and the other is placed in compression with a corresponding decrease in its resonant frequency. Each force crystal operates with an integral hybrid electronics oscillator, where the oscillator frequency is dependent on the resonant frequency of the force crystal. The frequency outputs, as a function of acceleration, are a pair of buffered square wave frequencies suitable for signal processing. The RBA-500 furnishes no integral temperature signal and shares a single block mounted temperature sensor, whereas the PRBA (Precision Resonating Beam Accelerometer) has an internal temperature sensor. The temperature sensor output is also a frequency signal developed from a vibrating beam temperature sensor.

Other important features of quartz vibrating beam accelerometers are:

- Small Size
 - Low Power Consumption--independent of input gs
 - Low Cost
 - High Reliability
 - Fast Turn-on
 - Frequency Outputs suitable for digital signal processing
 - Correction Coefficients furnished for thermal modeling
 - High Scale Factor Frequency
- Change: $\pm 10\%$ of nominal frequency

VIBRATING BEAM CRYSTALS

Each accelerometer uses two quartz vibrating beam force crystals. The crystals constrain the flexure proofmass and provide the mechanism to convert the acceleration force to an output frequency. The crystals are the frequency determining elements for the internal hybrid oscillators. The frequency of oscillation of each crystal is a nominal 35 KHz when there are no acceleration forces applied.

The choice of quartz vibrating beams for the force crystals is twofold. First, the mechanical and physical properties of quartz are very stable, as demonstrated by its use over the years as a precision frequency standard. Secondly, quartz is piezoelectric, which allows the implementation of the closed loop hybrid oscillator and frequency determining quartz force crystal.

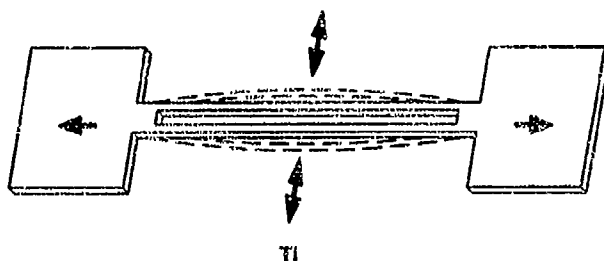
In operation, the quartz crystal behaves like a string in tension. As the tension increases the frequency of a vibrating string will also increase. However, unlike a string, the quartz crystal also works well in compression which makes it ideal for bidirectional accelerometers.

Sundstrand's proprietary beam geometry allows for a wide operating frequency change as a function of input acceleration, up to 10% of the nominal no load frequency. The geometry of the crystal, as shown in Figure 1 is a double-ended tuning fork which has the advantage of dynamic balance which negates the use of large isolator masses. The tines of tuning forks vibrate 180° out of phase. The dynamic forces of the resonating tines are equal and opposite, and cancel one another at the mounting base. This type of crystal design with its inherently low energy loss to its mounting structure provides for high crystal "Q" without operating in a vacuum.

The vibrating beam force crystals are etched from crystalline quartz wafers using semiconductor industry photolithographic processes. Many force crystals are etched from the same wafer because of the crystal's small size. The orientation of the crystallographic axis is controlled to give the least sensitivity to temperatures, and the best piezoelectric properties.

The piezoelectric drive and pickoff of the beam resonance are controlled by precise conductive patterns that are located on the crystal tines. Batch fabrication in the wafer results in low cost crystals, which match each other extremely well for rejection of common mode errors.

FIGURE 1: VIBRATING FORCE CRYSTAL



MECHANISM CONFIGURATION

Both accelerometers discussed are similar in design features, but slightly different in size. Figure 2 shows the internal mechanism of the accelerometers which consists of a single pendulum which is used as a seismic mass. It is pendulously constrained by a single flexure to provide a single degree-of-freedom motion resulting in a single axis sensitive to input acceleration. The pendulum assembly is mounted between two damping plates which establish the damping gaps above and below the pendulum to provide squeeze film damping. Shock caging is also provided to prevent the pendulum from over-travel during over-range shock events.

The pendulum is constrained by the force crystals. The constraint and the damping are the same for both the powered and unpowered conditions of the accelerometer; unlike a servo constrained accelerometer, which allows the pendulum to travel completely to the stops when it is unpowered. When stored in a 1g position, the pendulum displaces a very small percentage of the total travel which lends to the low stress on the flexure and overall bias stability.

The force crystal constraint of the pendulum is shown schematically in Figure 3, which provides the push-pull operation of the force crystals. For any input acceleration, one crystal is placed in tension and one is placed in compression, producing one increasing and one decreasing output frequency.

The difference between the increasing and decreasing frequencies is proportional to input acceleration. The benefits of doing this are the common mode rejection of the effects of temperature sensitivities, reference clock variations, aging, and even order nonlinearities.

FIGURE 2: ACCELEROMETER MECHANISM

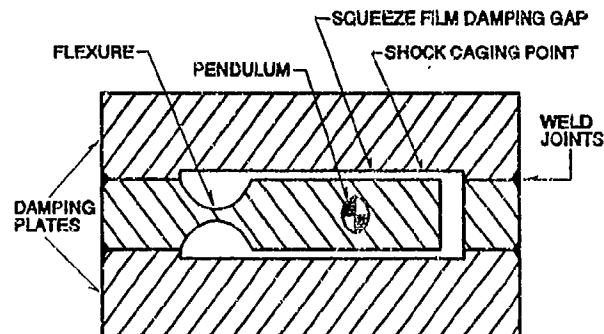
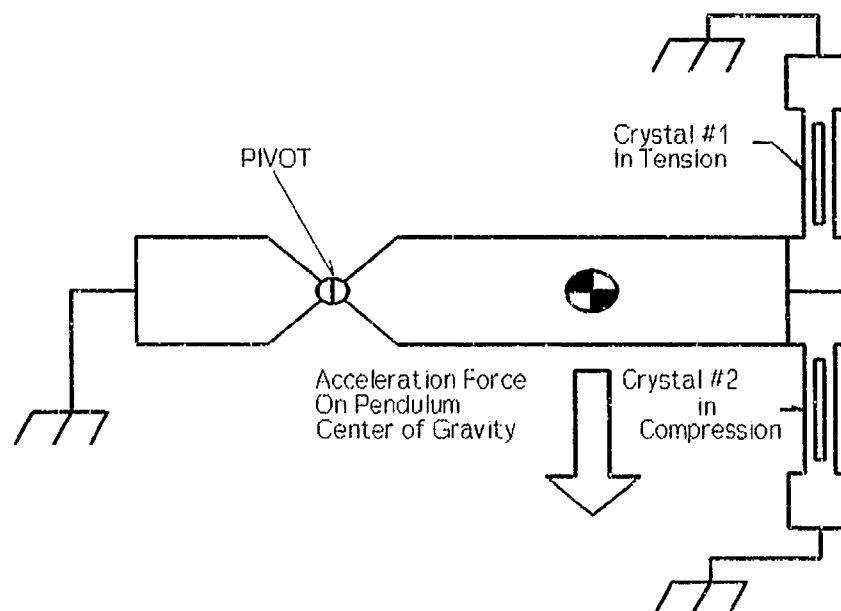


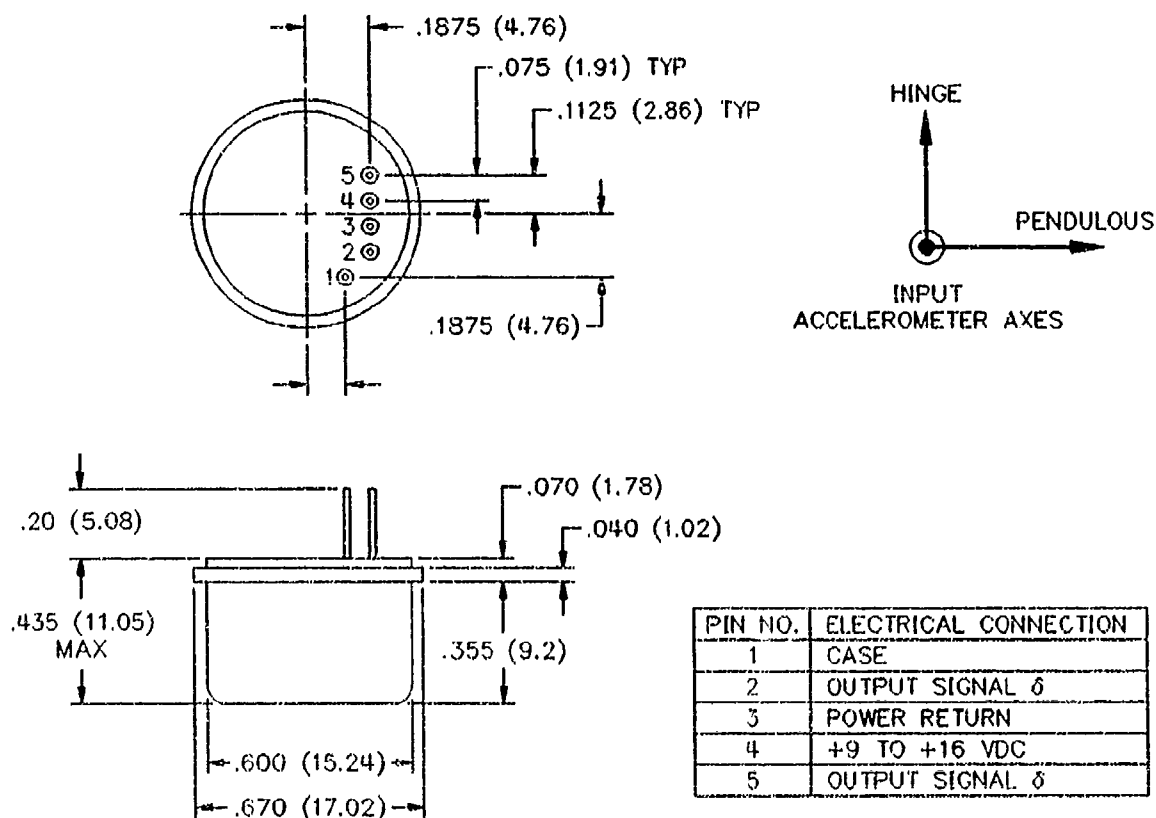
FIGURE 3: PUSH-PULL CONSTRAINT



PACKAGING

The outline drawings of the RBA-500 and the PRBA accelerometers are shown in Figures 4 and 5. Both designs utilize welded seams and glass insulated header pins that provide a hermetic package. The RBA-500 header has the same pin configuration as a 16-pin TO-8 header, so standard connectors can be used for testing. The stainless steel case and concentric mounting flange provide corrosion resistance. Internally, the sensor assembly is welded to the mounting flange, thus providing good axis alignment stability and mounting repeatability. The PRBA is packaged in a slightly larger hermetic package, and has a traditional three-point mounting flange. The header pins are in a circular configuration suitable for a connector or soldered connections. The internal construction of the PRBA is similar to the RBA-500.

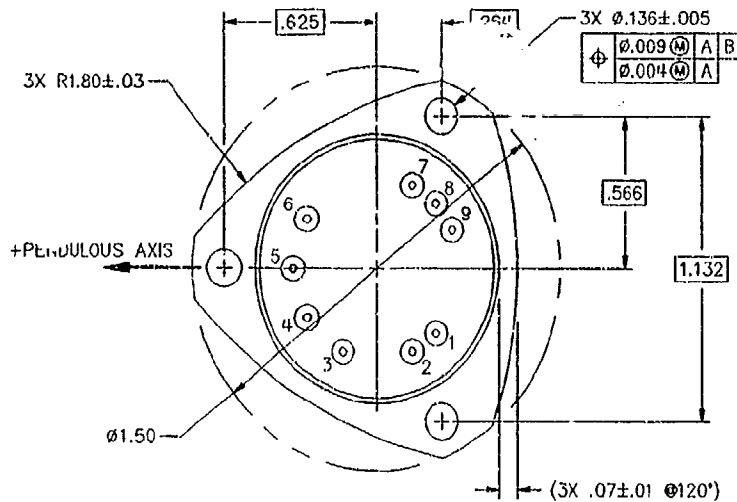
FIGURE 4: RBA-500 OUTLINE



Both accelerometer designs have the hybrid electronics mounted inside the hermetic housing. They are mounted against the underside of the header to furnish a heat transfer path from the hybrid to the outside environment. Both hybrid electronics utilize CMOS circuitry to provide low power consumption to minimize any thermal effects. The RBA-500 accelerometer hybrid contains two oscillators: one for each force crystal. The PRBA hybrid contains

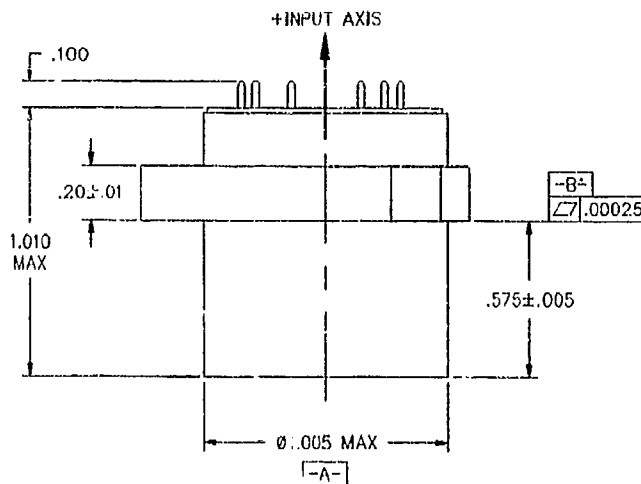
three oscillators: two for the force crystals, and one for an internal vibrating beam temperature sensor. In addition, the PRBA hybrid contains a memory for the storage and readout of the modeled compensation coefficients used for error correction.

FIGURE 5: PRBA OUTLINE



PIN OUT:

1. FT.
2. CASE
3. F1
4. V_s
5. GND
6. F2
7. SDL SERIAL DATA
8. SCL SERIAL CLOCK
9. WRITE CONTROL



RBA-500 PERFORMANCE TEST RESULTS

The RBA-500 Accelerometer, which is currently in production at Sundstrand, was initially designed in 1988. Design verification testing was performed on eight accelerometers in 1989, and qualification testing was completed in August 1991.

PERFORMANCE OVER TEMPERATURE

The RBA-500 is designed to operate over the temperature range of -54°C to $+105^{\circ}\text{C}$. Each accelerometer receives a preconditioning which includes temperature cycling and burn-in. Then the units are temperature tested and modeled over the operating temperature range.

At each of eleven temperature points, bias and scale factor are derived from two-point $\pm 1g$ tumbles on a dividing head. During the temperature testing, a complete thermal loop is made by starting at room temperature, stepping up to $+105^{\circ}\text{C}$, then down to -54°C , and returning to room temperature. From these measurements a third order compensation model is derived, and the residual errors between the model and actual data are calculated.

Misalignment data is developed by rotating the input axis in a zero "g" position and taking data with the pendulous and output axis positioned at various angular positions on a dividing head. This test is performed over the same temperature range and steps that the bias and scale factor performance are determined.

Figure 6 shows the composite bias, scale factor, and misalignment errors of a group of production RBA-500 accelerometers, approximately thirty units. Maximum compensated bias and scale factor residuals over the entire temperature range are well within the 3σ performance specifications of 2 millig's for bias and 125 ppm for scale factor. The initial misalignment of the accelerometer as built is also well within the 3σ specification of 12 milliradians. Axis misalignment stability over temperature is very good because of the welded internal construction of the accelerometer and the force crystal constraints of the pendulum. Total misalignment (output and pendulous) error as a function of temperature is specified to be less than 350μ radians, and test results show values to be one-third of that: 120-150 μ radians.

FIGURE 6: PRODUCTION STATISTICS FOR CRITICAL PARAMETERS

	MEAN	STANDARD DEVIATION	SPEC 3σ
Max Bias Modeling Residual from Thermal Model, -54°C to $+105^{\circ}\text{C}$.93	.57 mg	2 mg
Max Scale Factor Residual from Thermal Model, -54°C to $+105^{\circ}\text{C}$	22 PPM	22 μ pm	125 ppm
Absolute Axis Misalignment	3.4 mRad	2.0 mRad	12 mRad

LONG-TERM REPEATABILITY

Long-term repeatability data taken on the design verification units over a period of 610 days show excellent stability for seismic and thermal environments. Six (6) units were tested. During the first 420 days, the units were subjected to 260g shock, 20g sine vibration,

more than 30 thermal cycles between -61°C to +121°C, and a 7-day thermal soak at 105°C. Since that time, they have been in a benign environment. Figure 7 shows that, of the six units, the worst case bias nonrepeatability was 0.3 mg. Figure 8 shows that, of the six units, the worst case scale factor nonrepeatability was -9 ppm.

FIGURE 7: RBA-500 LONG-TERM BIAS REPEATABILITY

S/N	BIAS (mg)		
	AT LAST MEASUREMENT	CHANGE FROM 420 DAYS	1 σ DEVIATION OVER 610 DAYS
101	.5	$\Delta = .2$.7
103	2.2	$\Delta = .0$	1.1
104	2.9	$\Delta = -.3$	1.5
107	.6	$\Delta = -.1$.5
108	1.0	$\Delta = -.1$.6
113	.4	$\Delta = .2$.2

FIGURE 8: RBA-500 LONG-TERM SCALE FACTOR REPEATABILITY

S/N	SCALE FACTOR ERROR (ppm)		
	AT LAST MEASUREMENT	CHANGE FROM 420 DAYS	1 σ DEVIATION OVER 610 DAYS
101	2	$\Delta = -3$	19
103	4	$\Delta = -6$	20
104	9	$\Delta = 2$	50
107	20	$\Delta = 5$	17
108	1	$\Delta = -9$	18
113	18	$\Delta = 0$	11

LONG-TERM STABILITY

The DVT test units were subjected to various seismic and thermal tests earlier in the development program, including 250 g's shock, more than 30 thermal cycles between -61°C to 121°C, 20 g sine vibration, 7-day high temperature soak at 105°C, and multiple temperature tumble tests between -55°C to +105°C. In between tests, they are stored in a 1g

position. Looking at S/N 113, which has the best repeatability during the testing for long-term stability, the bias and scale factor stabilities are shown in Figures 9 and 10. The overall bias stability over a period of 610 days is within $\pm 400 \mu g's$, and the scale factor stability is within ± 30 ppm.

FIGURE 9: S/N 113 BIAS STABILITY

AVERAGE = -85 S.D. = 202
Data File: STAB_TG113

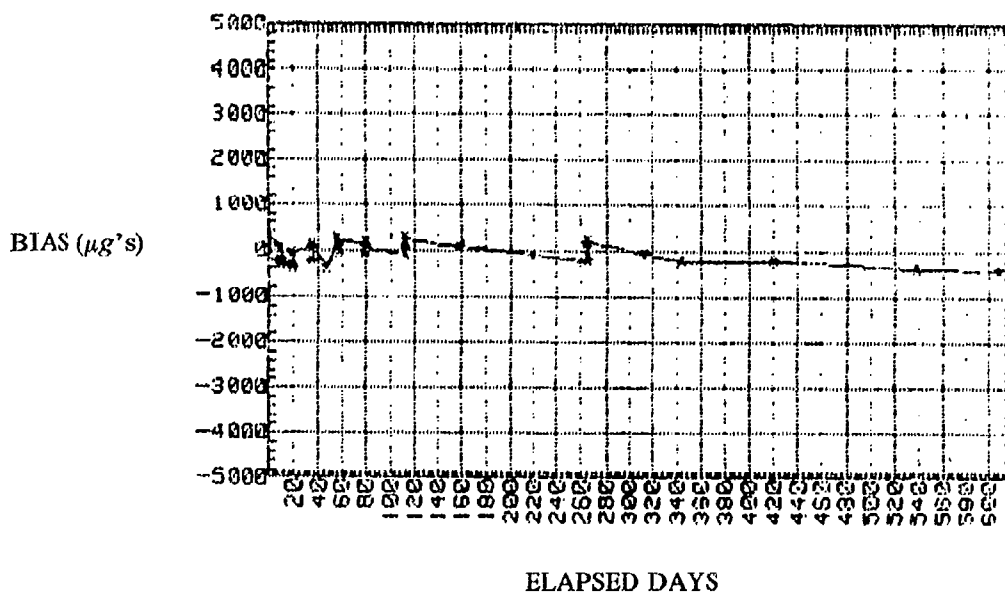
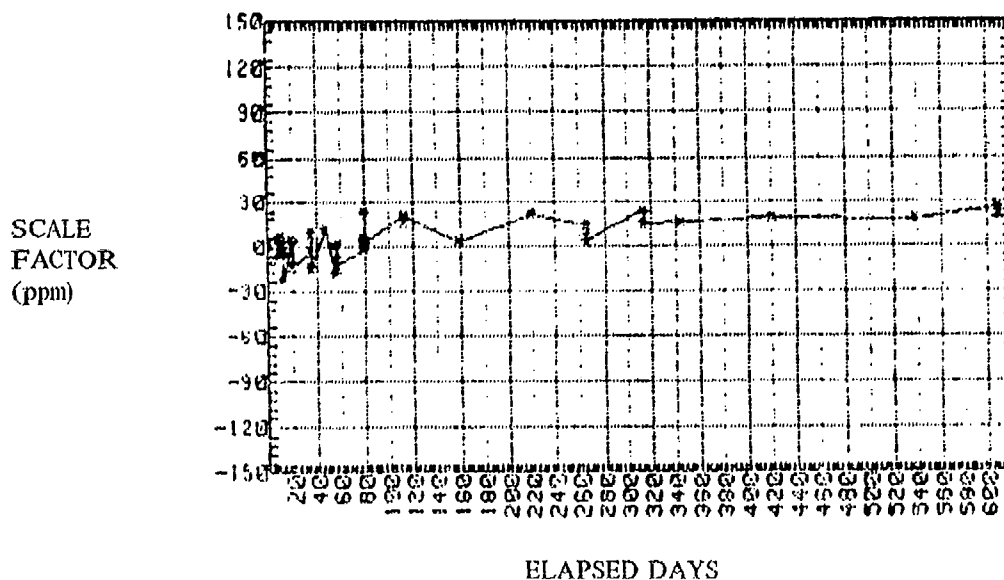


FIGURE 10: S/N 113 SCALE FACTOR STABILITY

AVERAGE = 5 S.D. = 11
Data File: STAB_TG113



ERRORS DUE TO TEMPERATURE RATE-OF-CHANGE

The RBA-500 is constructed to minimize the effects of external temperature inputs. Heat conduction into the internal sensor assembly is designed to produce the minimum possible errors by isolating the sensor assembly from uneven temperature effects. Figure 11 shows the input temperature ramp starting at 30°C, ramping at 5°C/min. to 70°C. It then soaks at 70°C before decreasing back to 30°C.

FIGURE 11: INPUT TEMPERATURE RAMP

AD590 PLOT

5DEGC/MIN, 1HR DWELL, 30 SEC SAMPLE FILE

"*" = Datapoint, Line connects the data points

AD590
TEMP °C

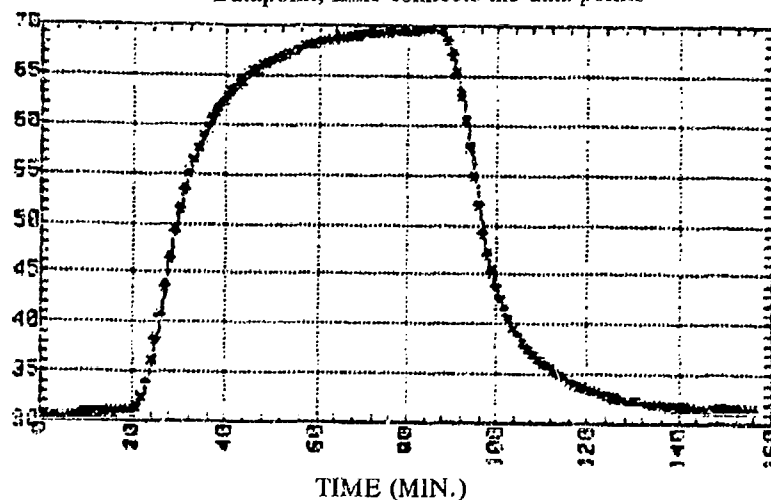


FIGURE 12: ACCELEROMETER RESPONSE TO THERMAL RAMP

ACCELEREX DUAL G LEVEL PLOT

5DEGC/MIN, 1HR DWELL, 30 SEC SAMPLE FILE:

"*" = Datapoint, Line connects the data points

TEMP
CORRECTED
G's

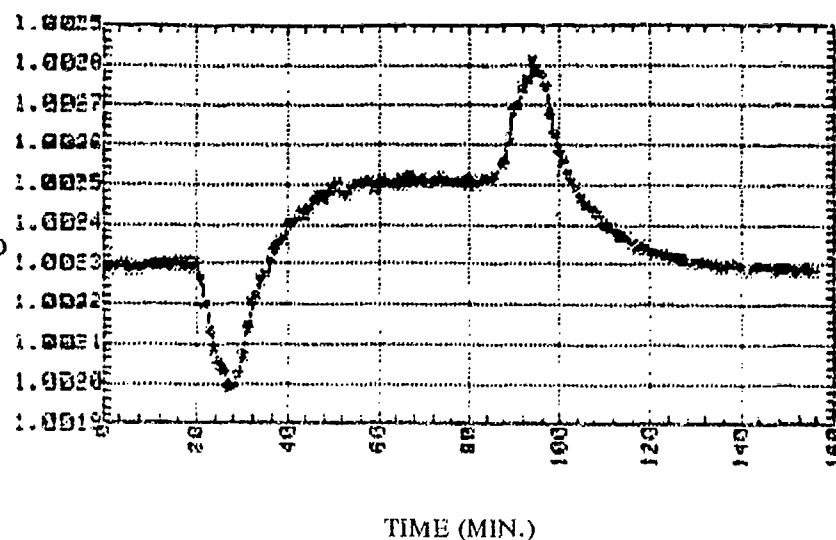


Figure 12 shows the response of the accelerometer, which is mounted in a mounting block in a 1g orientation, to the temperature ramp. On the increasing ramp, the output of the accelerometer decreases $300\ \mu\text{g}$ s, then returns to within $200\ \mu\text{g}$'s of the initial reading during the temperature soak. When the temperature ramp starts to decrease, the accelerometer output increases $300\ \mu\text{g}$'s, and then returns to the original reading. The total excursion is $800\ \mu\text{g}$'s.

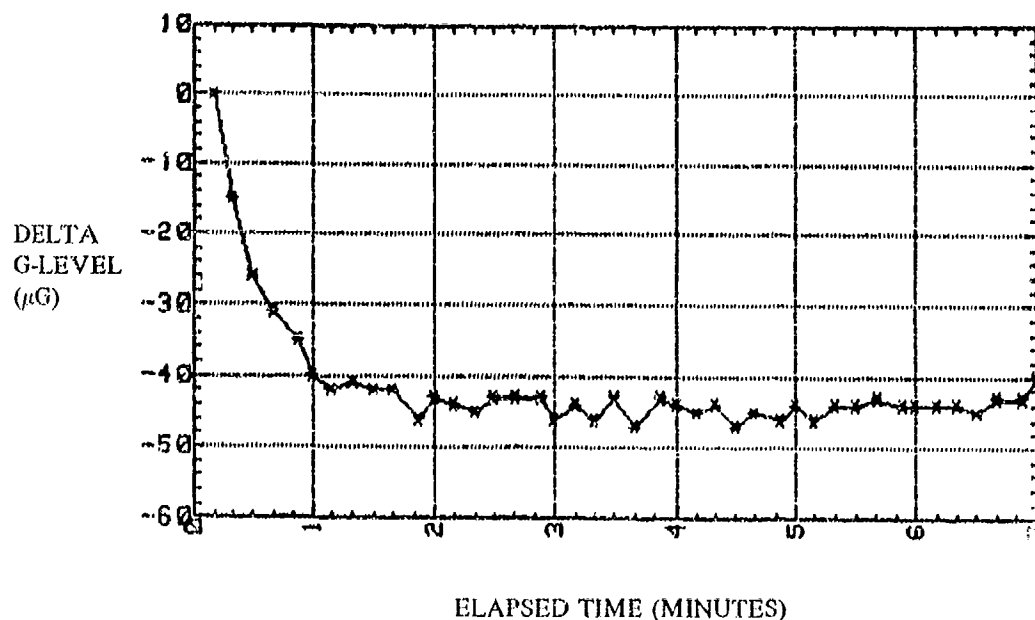
TURN-ON/WARM-UP TEST

The RBA-500 is designed for rapid turn-on and warm-up after periods of prolonged storage. The hybrid electronics and resonating force crystal starts and provides a stabilized output in less than one second.

The amount of power dissipated in the hybrid electronics is less than 100MW, and this heat is directed into the header and mounting ring. As a result, the warm-up error, due to the electronics, is small (see Figure 13). A large portion of the warm-up error is due to the fact that the RBA-500 does not have an internal temperature sensor, and uses an external block mounted sensor, which causes a small temperature gradient.

Warm-up error is less than $50\ \mu\text{g}$'s, and equilibrium is achieved in approximately one minute.

FIGURE 13: RBA-500 WARM-UP, TURN-ON RESPONSE
15 VDC TURN-ON WARM-UP TEST
S/N TG101



PRECISION RESONATING BEAM ACCELEROMETER (PRBA) PERFORMANCE TEST RESULTS

The PRBA Accelerometer was started in development midyear 1990, with the first development units becoming available in early 1991. Because it was designed to use many of the design features of the RBA-500, the development time was quite short. The major differences between the RBA-500 and the PRBA are shown in Table 1 on page 4.

The PRBA has an internal vibrating beam temperature sensor. The hybrid contains the additional oscillator for the temperature sensor, and it also contains the E²PROM which is used for compensation coefficient storage. Seven development units have been built and are still being tested. Some additional units are currently being fabricated for testing; and they will incorporate design improvements suggested by the initial testing.

PERFORMANCE OVER TEMPERATURE

The PRBA is designed to operate over the temperature range of -54°C to +105°C. Prior to testing, each accelerometer received a preconditioning, including temperature cycling and burn-in. The units are then temperature tested and modeled over the operating temperature range.

At each of eleven temperature points, bias and scale factors are derived from 2-point $\pm 1g$ tumbles on a dividing head. The eleven temperatures are run so a complete thermal loop is completed. A third order compensation model is derived, and the residual errors calculated.

Figure 14 shows the composite bias for the seven test units. As can be seen, all but one of these units meets the specification limit of 150 μg 's over the temperature range tested.

**FIGURE 14: PRBA BIAS PERFORMANCE
OVER TEMPERATURE -54°C TO 105°C**

S/N	PRBA BIAS (μg)		
	MAXIMUM RESIDUAL	STANDARD DEVIATION	BTC MAX
1	- 80	42	-573
2	121	68	-221
3	-218	115	-192
4	- 71	47	152
5	- 98	46	157
7	- 28	18	-217
8	84	51	143
SPEC	150	---	---

Figure 15 shows the bias performance of S/N 8 PRBA over a more narrow temperature range of -15°C to $+75^{\circ}\text{C}$. As would be expected, the bias residual performance shows improvement proportional to the temperature range reduction. The residual bias on S/N 8 is a maximum of $+10$ to $-20\mu\text{g}'\text{s}$. The hysteresis is $5\mu\text{g}'\text{s}$; and the repeatability is $4\mu\text{g}'\text{s}$, which also includes the repeatability of the temperature points in the chamber, and the accelerometer's internal temperature sensor. An accelerometer with this compensated performance is well suited for 1 NMPH or less navigational and flight control applications.

FIGURE 15: BIAS RESIDUAL ERRORS

S/N #MB008 Dual Bias Residuals

Test Date May 22, 1991

Square Model (Modeled against Ft)

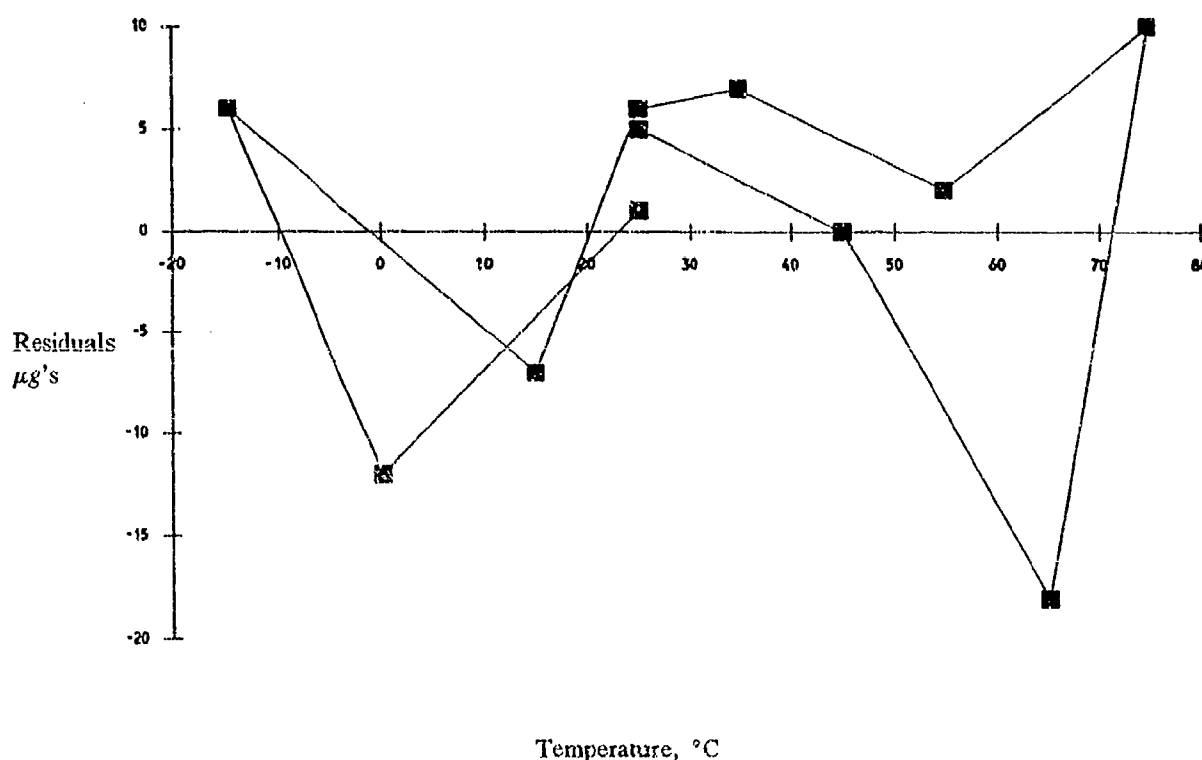


Figure 16 shows the excellent scale factor performance of the seven test units. Scale factor performance with temperature and time is controlled to a large extent by the stable physical properties of the quartz resonating beam. As can be seen, all but one of these units meets the specification limit of 50ppm over the temperature range tested.

Figure 17 shows the scale factor performance of S/N 3 PRBA over a narrower temperature range. Again, as one might expect, the residual scale factor error shows improvement proportional for the reduced temperature range. The residual scale factor on S/N 3 is a maximum of $+12$ to -8ppm with almost no hysteresis or repeatability errors.

**FIGURE 16: PRBA SCALE FACTOR PERFORMANCE
OVER TEMPERATURE 54°C TO +105°C**

S/N	PRBA SCALE FACTOR (ppm)		
	MAXIMUM RESIDUAL	STANDARD DEVIATION	SFTC MAX
1	-49	21	9
2	-11	6	11
3	39	17	11
4	54	24	11
5	14	6	10
7	12	7	11
8	34	12	12
	50 MAX	---	---

FIGURE 17: SCALE FACTOR RESIDUAL ERRORS

S/N #MB003 Dual Scale Factor Residuals

Test Date May 22, 1991

Square Model (modeled against Ft)

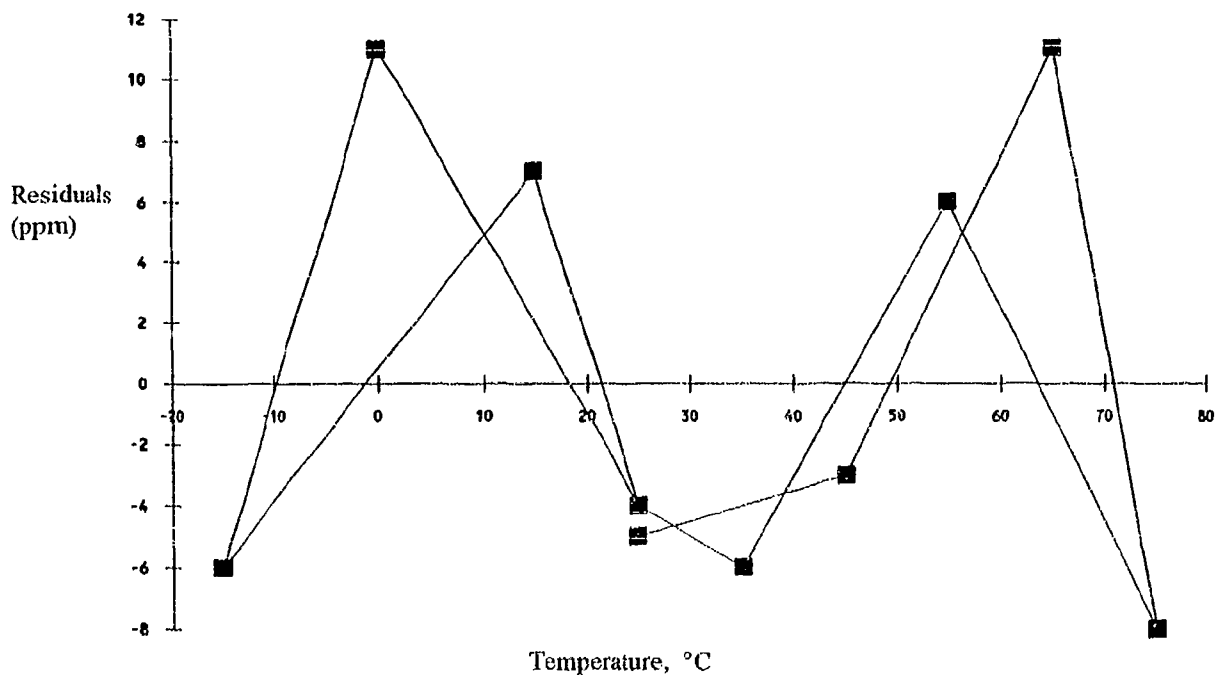


Figure 18 shows the misalignment errors on three of the seven test units over the temperature range of -54°C to +105°C. One of the units had an as-built tilt axis misalignment

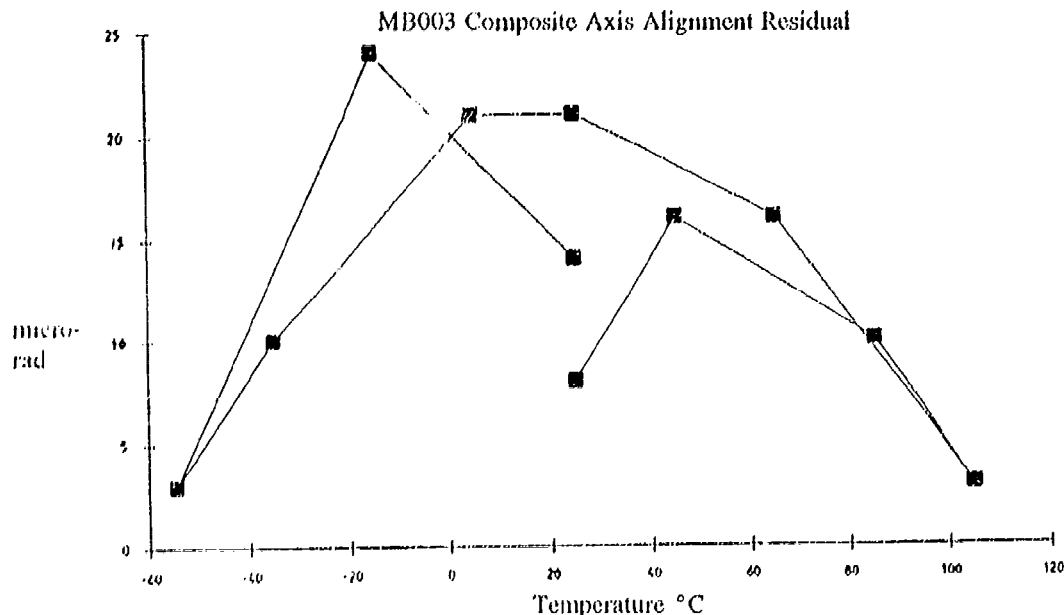
greater than the 7 milliradians allowed. That particular unit also had a pendulous axis residual error greater than the 50 μ rad allowed. The other two units showed excellent misalignment performance. In fact, the average temperature sensitivity of all three units showed less than .25 μ rad per $^{\circ}$ C change, and the two showed less than 0.1 μ rad/ $^{\circ}$ C.

FIGURE 18: PRBA AXIS ALIGNMENT

S/N	Initial Axis Misalignment (mRad)	Output Axis Max Residual (μ Rad)	Output Axis Std Deviation (μ Rad)	Pendulous Axis Max Residual (μ Rad)	Pendulous Axis Std Deviation (μ Rad)	Avg. Temp. Sensitivity (μ Rad/ $^{\circ}$ C)
3	0.86	-17	11	-18	11	.05
7	9.61	-9	5	66	29	.24
8	4.53	-22	13	5	3	.09
SPEC	7 MAX	50 MAX	---	50 MAX	---	---

Figure 19 shows a plot versus temperature of the residual composite axis alignment error for PRBA S/N 3 over the temperature range -55° C to $+105^{\circ}$ C. The overall composite error of 25 μ rad is well within the 50 μ rad allowed. The hysteresis is approximately 5 μ rad and the repeatability of the measurement including the test equipment is approximately 11 μ rad. This type of performance can be attributed to the all-welded construction of the accelerometer and the pendulum/quartz crystal mounting construction. In the PRBA testing, the misalignment errors are modeled against temperature using a third order equation, and the compensation coefficients are calculated and available to be stored in the E²PROM for use for error correction by the accelerometer user.

FIGURE 19: PRBA S/N 3 COMPOSITE AXIS MISALIGNMENT RESIDUAL



VIBRATION TESTING

To date, the PRBAs have been tested in vibration up to 10g's sine. This testing is ongoing and, thus far, no problems have developed. Vibration rectification is, of course, a key parameter of interest. By using a single pendulum constrained by dual quartz force crystals, certain benefits are realized. The crystals are selected from a common wafer which assures a high degree of matched properties. As an individual crystal has second order nonlinearities, by using a matched pair in Sundstrand's push-pull configuration, the even-ordered nonlinearities cancel. The single pendulum produces almost identical performance in both crystals. Figure 20 shows the vibration rectification of three of the test units when tested at 10g's sine. All three units demonstrated VRCs less than the $32 \mu\text{gs/g}^2$ allowed by our specification.

**FIGURE 20: VIBRATION
RECTIFICATION COEFFICIENT**

S/N	VRC @50Hz $\mu\text{g/g}^2$
3	20
7	25
8	6
SPEC	32

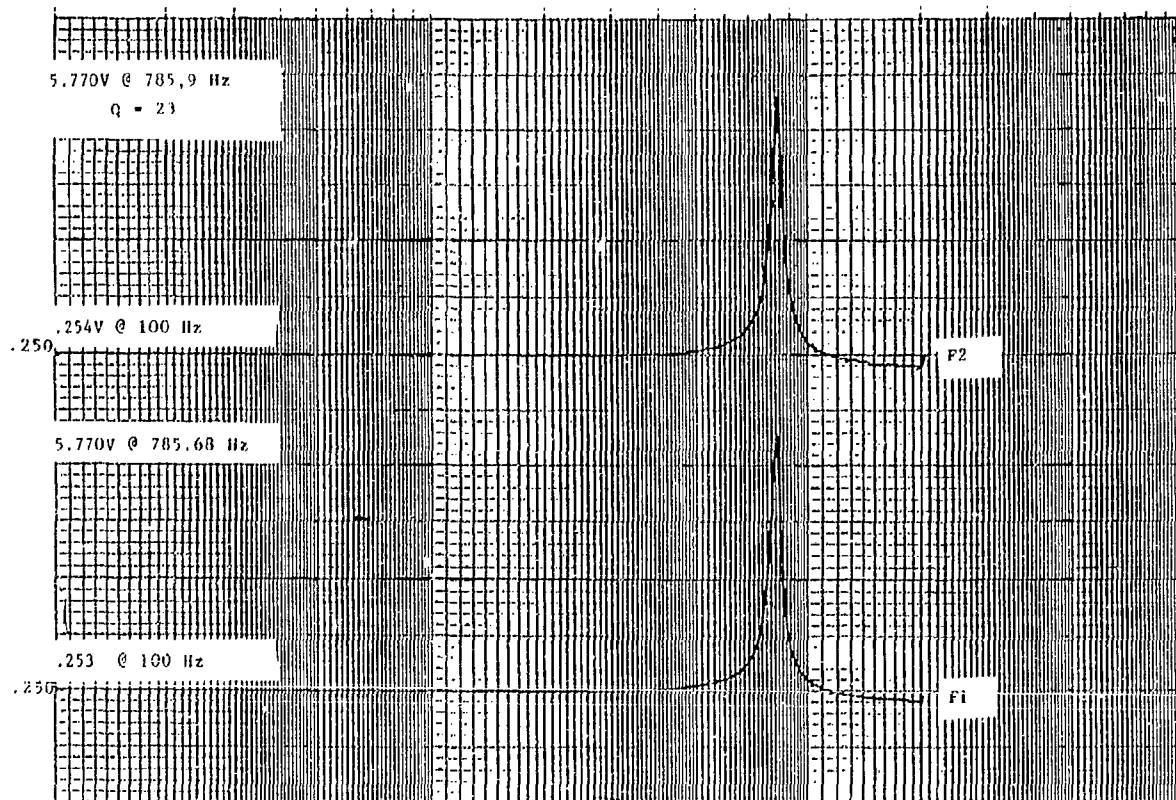
FREQUENCY RESPONSE

The pendulum of the PRBA is constrained by the high spring rate of the quartz resonating beam crystals, and the damping is achieved by squeeze film gas damping. Similar to the RBA-500, this results in a second order dynamic frequency response. This is shown in Figures 21 and 22. Figure 21 shows the frequency response and transmissibility of three of the test units. The response resonance is approximately at 780Hz, with the output flat at 100Hz to within .15db. Figure 22 shows the plotted frequency response of S/N 3 Accelerometer and the two individual force crystals, with their responses being almost identical.

FIGURE 21: VRC SUMMARY FOR 3 PRBA TEST UNITS

S/N	RESONANT FREQUENCY	TRANSMISSIBILITY DB	DB AT 100 Hz
3	785.90	27.3	.138
7	778.61	27.3	.104
8	773.46	27.3	.138

FIGURE 22: S/N 3 FREQUENCY RESPONSE
@ 1g/10 Hz - 2000Hz

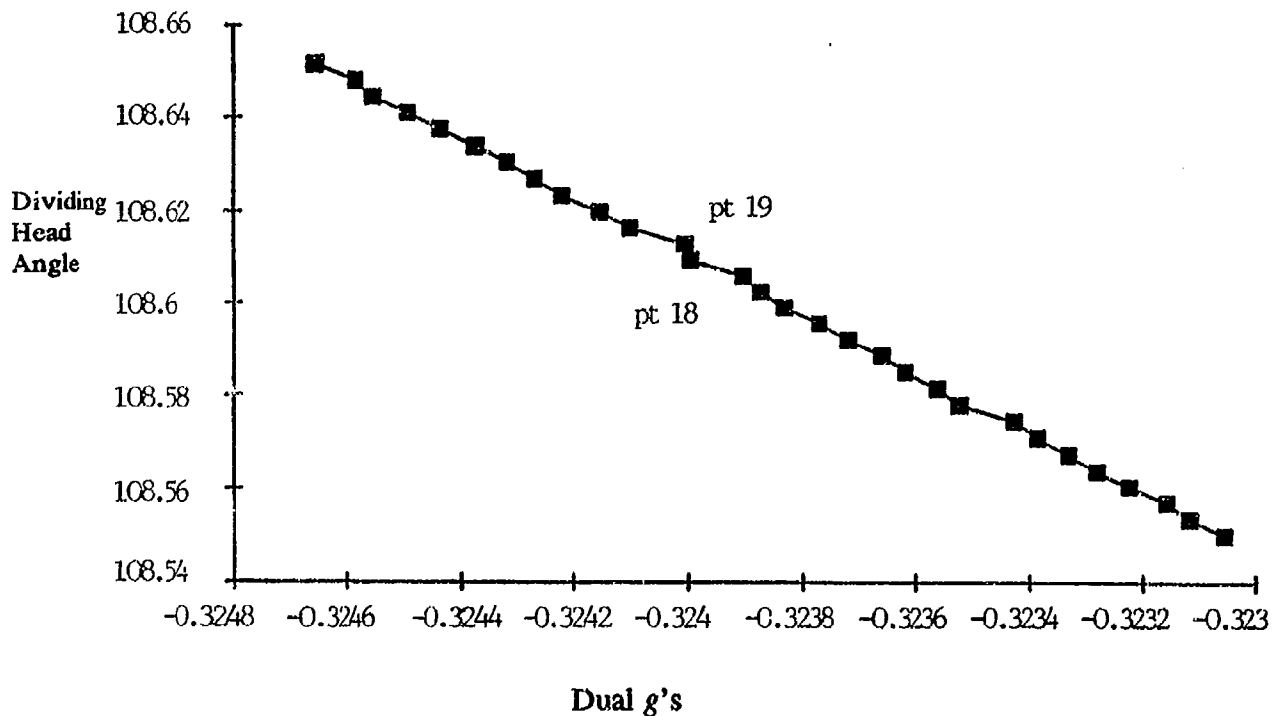


FREQUENCY CROSSOVER

Using a dual crystal, push-pull difference frequency configuration for the accelerometer results in a point where the two crystal frequencies will match each other. This is usually picked to be at a high enough g range (outside the $\pm 1g$ range) where the effect is not noticeable or detectable because the ambient dynamic vibration and g levels are high and varied enough that the two crystals cannot acquire the same frequency and stay at that point. Only by using a precision dividing head isolated from seismic inputs, and moving it through very small increments of angle could the crossover frequency on the PRBA be found. The error associated with this crossover was found to be $46 \mu g$'s. This information is shown in Figure 23.

FIGURE 23: CROSSOVER FREQUENCY PLOT

Angle vs. dual g's



SENSITIVITY TO OTHER EXTERNAL INPUTS

Other tests have been performed thus far on the PRBAs. The effects of other external inputs have been evaluated in terms of performance errors, and nothing adverse has been found. The following tests and limits are shown below:

PARAMETER	SPECIFICATION	TEST RESULTS
Magnetic Sensitivity	< 10 μ g/gauss for fields up to 5 gauss	< 5 μ g for 5 gauss
Voltage Sensitivity	< 5 μ g/volt for $\pm 5\%$ of input voltage	No effect measured
Mounting Sensitivity	< 50 μ g	< 10 μ g

SUMMARY

With the introduction of the RBA-500 accelerometer and the development of the Precision Resonating Beam Accelerometer (PRBA), new technology alternatives are now available for flight control and navigational systems. The advantages of a frequency output, digitally compatible signal with self-contained compensation correction coefficients to further improve the overall accuracy are readily apparent. Vibrating Beam Accelerometer technology is a major advance in the state-of-the-art in accelerometer measurements, and will continue to impact the navigation, guidance, and control industry in the years to come.

ACKNOWLEDGEMENTS

The author would like to acknowledge the help of Peter LaFond, Paul Collins and Brian Norling at Sundstrand Data Control for help in getting the information for preparing this paper.

BIOGRAPHY

Mr. Jensen is currently Project Manager in the Advanced Technology Engineering Department at Sundstrand. His current assignment consists of the development of new accelerometers for inertial measurements which include the PRBA. Prior to joining Sundstrand, Mr. Jensen worked as Manager of Engineering Operations at Bell Aerospace Textron in Buffalo, New York; and has over twenty years of experience in the design and development of precision instruments.

SESSION III-B
INS/GSP INTEGRATION

CHAIRMAN
DR. PHIL WARD
TEXAS INSTRUMENTS

INS ALIGNMENT USING THE RCVR 3A COMPUTED CORRECTIONS

Prasun K. Sinha, Dirk deDoes, Kendall Barckley
Intermetrics, Inc.
Huntington Beach, California

ABSTRACT

Phase III Global Position System (GPS) user equipment (RCVR 3A) is being integrated into Host Vehicle (HV) platforms whose avionics suites include a Mission Computer (MC) and an Inertial Navigation System (INS). In those platforms where memory and through-put constraints prohibit the mechanization of a Kalman filter in the MC to estimate INS corrections, INS errors estimated by the RCVR 3A provide an alternate means of performing INS alignment. This paper presents navigation performance results obtained from laboratory simulations (with hardware in the loop), and flight tests to demonstrate the utility of the RCVR 3A computed corrections in performing INS alignment.

INTRODUCTION

The Phase III airborne GPS receiver (RCVR3A), implements a Kalman filter to estimate errors in the INS position, velocity, and attitude. These estimates are provided in the UE 1553 G-7 message [1]. The design and tuning of the filter was constrained by a number of factors such as the requirement to accommodate a variety of INSs, and computer through-put and memory limitations which restrict the number of INS errors that can be modelled. Because of these constraints the tuning parameters were selected to produce a filter generally tuned to the worst case. Consequently, the performance of this filter will not

be as good as that of a filter tuned to a given INS, particularly with regard to the accuracy of the velocity and alignment error estimates. The question thus arose as to whether or not the quality of the corrections - and in particular that of the attitude corrections - was adequate to provide an alternative means of performing INS alignment. Laboratory and flight tests were conducted to address this issue. This paper describes the test program and discusses the results.

The laboratory test was conducted on a 003 version of the RCVR3A using the Nav Central Engineering Activity (CEA) test facility at the Navy Air Development Center (NADC). This test represented the case of an INS that had undergone an initial alignment procedure which resulted in alignment errors of 2 arc-minutes about each horizontal axis, and 8.5 arc-minutes about azimuth, prior to the start of alignment refinement using the RCVR3A computed corrections.

The flight tests were conducted on-board the T-39 avionics test platform operated by the USAF Instrument Flight Center at Randolph AFB, Texas. Results are presented for the case where in-flight alignment was conducted following a degraded gyro-compass alignment.

LABORATORY TEST

EQUIPMENT CONFIGURATION

The CEA consists of facilities developed by the NADC to provide a test and evaluation environment for GPS UE [2]. This environment permits GPS UE to be exercised dynamically under laboratory conditions by a real time simulation of both GPS satellite signals and HV communications.

A functional block diagram of the equipment configuration used is shown in Figure 1. Simulated satellite RF signals were provided to the UE Under Test (UEUT) by the Satellite Signal Simulator (SSS) hardware in the Integrated Satellite Signal Generator (ISSG). The ISSG also computed platform motion parameters and provided them to the User Equipment Test Facility (UETF) via the Shared Memory Unit (SMU). The UETF in turn used these data to derive HV navigation subsystem sensor data which was sent to the UEUT via the Host Vehicle Interface Emulator (HVIE).

Data was logged on two tapes: one recorded data collected by the Smart Buffer Box (SBB) from the UE instrumentation port, while the other recorded data from the UETF and ISSG.

SCENARIO DESCRIPTION

The scenario consisted of a 5 minute stationary period, followed by a 3 minute take-off sequence, followed by 8.5 laps of a medium dynamics race track profile. The race track was comprised of east-west and west-east straight segments of 300s duration, and flat 2g turns. The scenario was traversed at a constant speed of 350m/s and a constant altitude of 100m. The duration of the scenario was 2.5 hours. Four Space Vehicle (SV), State 5 tracking obtained for the first 2 hours of the scenario. Tracking of all SVs was suspended during the last 15 minutes to permit assessment of the inertial navigation extrapolation capability of the RCVR3A. The PDOP for the optimum 4 SV group ranged between 2.4 and 3.2.

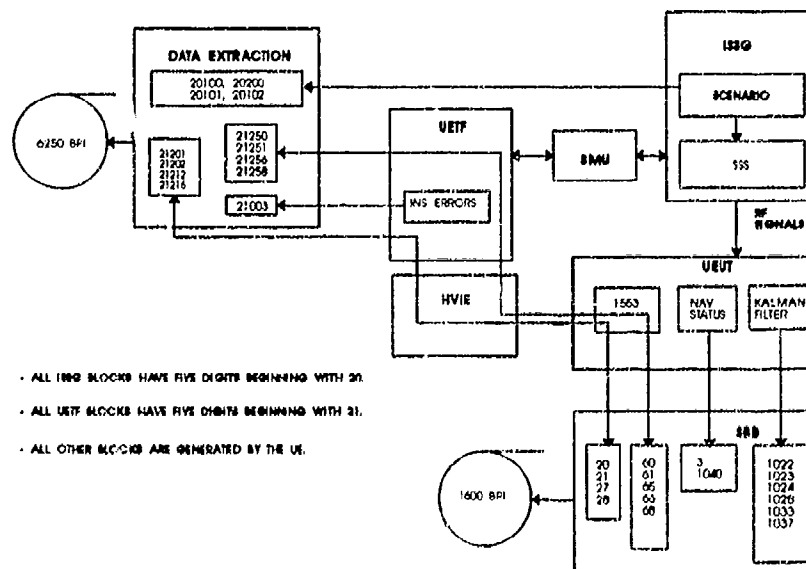


Figure 1. Functional Block Diagram of Equipment Configuration

INS MODEL

The inertial navigation system model contained in the UETF software was used to produce the INS error profiles used in this study. The INS modelled was a three-axes, gimbaled, wander azimuth platform which produced outputs of three dimensional position, velocity, and tilts in the local level, wander azimuth (UVZ) frame shown in Figure 2.

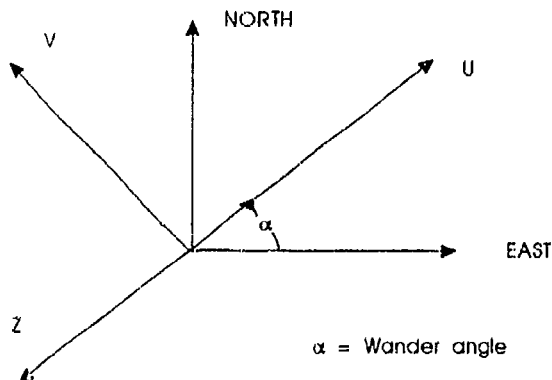


Figure 2. Definition of Wander Azimuth Frame

Fifteen INS error states were modelled. These are defined in Table 1. The accelerometer and gyro errors were modelled as constant bias; and gravity deflection and gravity anomaly errors were not included.

Error State	Definition
δRu	Position error along U axis
δRv	Position error along V axis
δRz	Position error along Z axis
δVu	Velocity error along U axis
δVv	Velocity error along V axis
δVz	Velocity error along Z axis
ϕu	Attitude error about U axis
ϕv	Attitude error about V axis
ϕz	Attitude error about Z axis
ϵau	U axis accelerometer bias
ϵav	V axis accelerometer bias
ϵaz	Z axis accelerometer bias
$\epsilon \dot{\phi} u$	U axis gyro drift bias
$\epsilon \dot{\phi} v$	V axis gyro drift bias
$\epsilon \dot{\phi} z$	Z axis gyro drift bias

INS error budget

The INS errors used in this study are presented in Table 2. The initial errors were representative of a nominal 1 nmi/hr INS which had been operating for a period of time necessary to produce the initial position errors shown in Table 2.

INS resets were simulated by reinitializing the errors at 30, 60, and 90 minutes into the scenario. The values of the errors following the resets at 30 and 60 minutes are shown in Table 2. At 90 minutes, all INS errors were set to 0.

Error State	Units	Initial Value	Value Following Resets	
			30 Min.	60 Min.
δRu	km	-9.1428	1.0	0.1
δRv	km	-10.0	1.0	0.1
δRz	m	121.92	100	10.0
δVu	m/s	-0.33	1.0	0.1
δVv	m/s	-0.65	1.0	0.1
δVz	m/s	0.0027	0.5	0.5
ϕu	rad	1.351×10^{-4}	5.818×10^{-4}	2.909×10^{-4}
ϕv	rad	-2.144×10^{-4}	5.818×10^{-4}	2.909×10^{-4}
ϕz	rad	2.458×10^{-4}	5.818×10^{-4}	2.909×10^{-4}
ϵau	μg	50	50	50
ϵav	μg	50	50	50
ϵaz	μg	50	50	50
$\epsilon \dot{\phi} u$	rad/s	3.636×10^{-6}	3.636×10^{-6}	3.636×10^{-6}
$\epsilon \dot{\phi} v$	rad/s	3.636×10^{-6}	3.636×10^{-6}	3.636×10^{-6}
$\epsilon \dot{\phi} z$	rad/s	7.272×10^{-6}	7.272×10^{-6}	7.272×10^{-6}

The value reset policy was implemented to report the INS resets to the RCVR3A. The values of the resets were provided to the UE over the 1553 data bus via the I-9 message [1].

True INS error state histories

Figures 3 to 7 show the true INS position and attitude errors produced by the INS error budgets defined in Table 2. The resets are evident in these figures as the step discontinuities at 17:24:00, 17:54:00, and 18:24:00 hours.

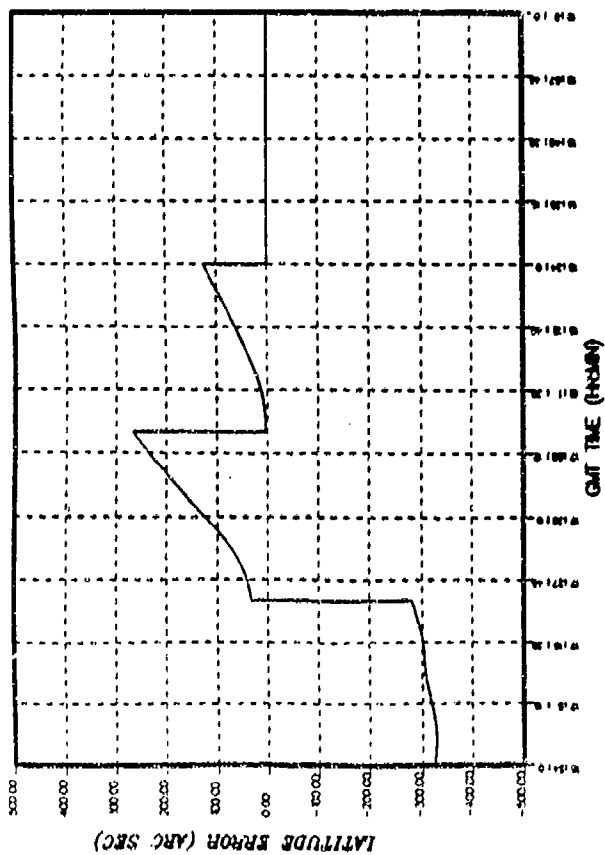


Figure 3 True error in INS indicated latitude.

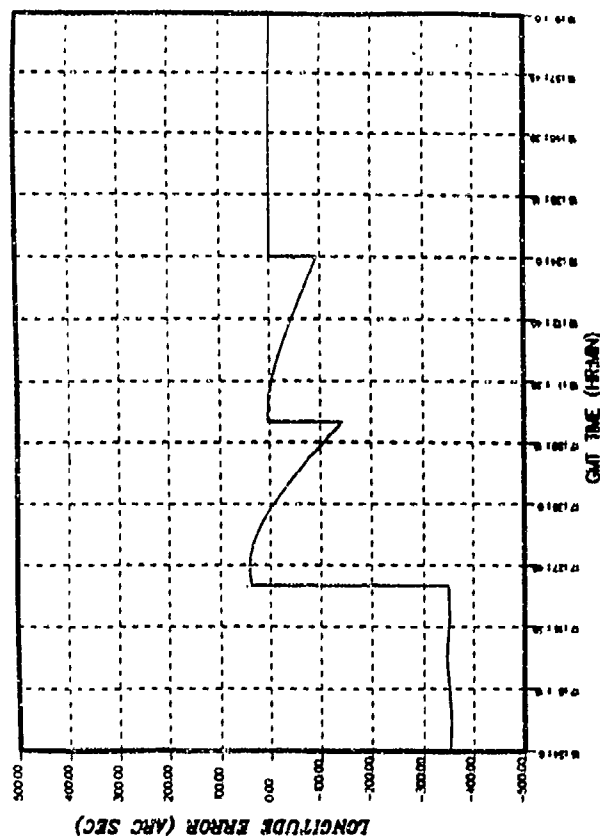


Figure 4 True error in INS indicated longitude.

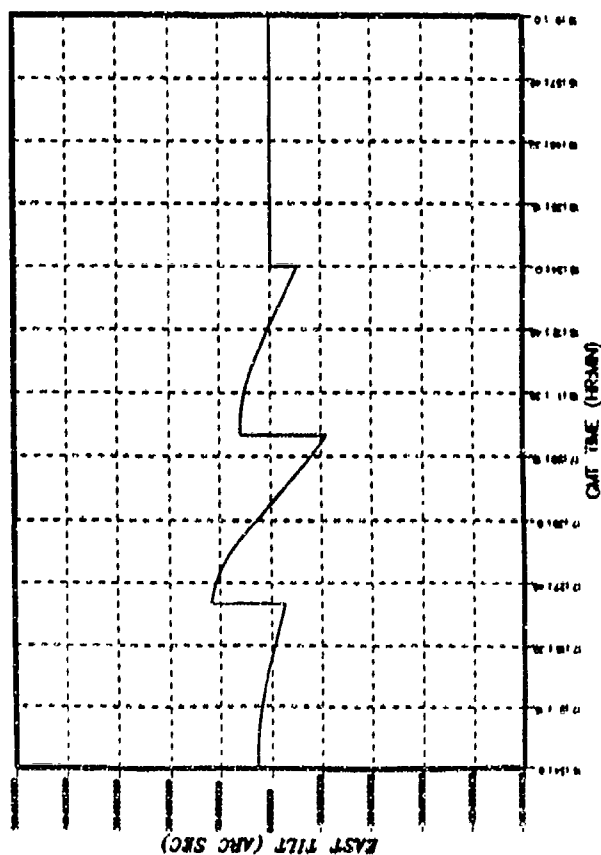


Figure 5 True platform tilt about east axis.

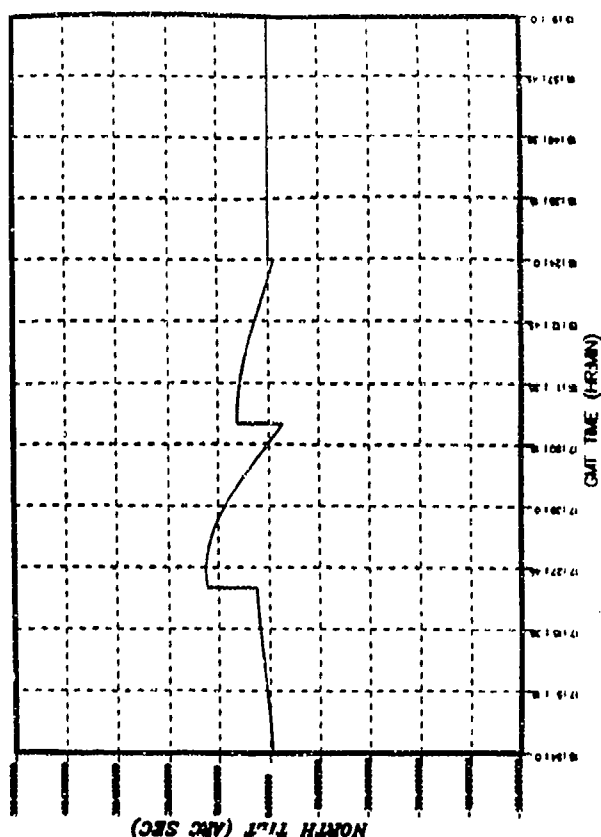


Figure 6 True platform tilt about north axis.

ACCURACY OF THE G-7 TILT ESTIMATES

The true INS tilt errors shown in Figures 5, 6, and 7 were compared with their RCVR3A estimated counterparts, derived from the data provided in the G-7 message.

Figures 8, 9, and 10 are the plots of the differences between the RCVR3A estimated tilts about east, north and vertical and their truth counterparts shown in Figures 5, 6, and 7.

Figures 8 and 9 show that during steady flight conditions, the error in the estimate of east component of tilt was about 10 arc-secs, and that in the north component was about -17 arc-secs. These errors were consistent with the accelerometer biases of 50 micro-gs along the platform's U and V axes. Manoeuvres caused transient shifts away from these steady state error values. The largest transient peak errors during a turn were 85 arc-seconds for the east component and -65 arc-seconds for the north component, and occurred when the true platform azimuth error was largest (510 arc-sec). Figures 8 and 9 also show that the RCVR3A tilt estimates were virtually zero following the reset at 18:24:00 hours, when all INS errors were set to 0.

Figure 10 shows that prior to the linear acceleration at 16:59:00 hours, the RCVR3A was unable to estimate the INS tilt error about the Z (vertical) axis. However, following the linear acceleration which provided observability of the INS azimuth error, the RCVR3A was able to rapidly estimate this component. The horizontal turns caused shifts in the estimate of azimuth attitude error, but the error was generally less than 45 arc-secs. Unlike the east and north tilt error estimates which

converged to virtually 0 following the reset at 18:24:00 hours, the azimuth component displayed a bias error of about 25 arc-secs.

Figures 8 and 9 also show that the estimates of east and north components of tilt error underwent large transients at each of the resets. These transients were the result of misreporting to the UE, via the (I-9) INS reset message, the amounts by which the east and north components of tilt were reset. Figure 10, on the other hand, shows that the azimuth component did not undergo similar transients. The spikes in the plot of azimuth error at the reset times are artifacts of the difference computations during post test data processing. Spikes due to difference computations are also evident in Figures 8 and 9.

FLIGHT TEST

AIRBORNE TEST FACILITY

The airborne testbed for evaluating use of the RCVR3A G-7 block for INS in-flight alignment is a T-39 aircraft operated by the USAF Instrument Flight Center, Randolph AFB, TX. This T-39 has been specially modified with an advanced avionics system and is engaged in a flight test program to develop procedures for and evaluate use of GPS for flying in the National Airspace System. The T-39 Advanced Avionics System (AAS) is shown in Figure 11.

The T-39 software integration was performed by Intermetrics. The Canadian Marconi Company (CMC) CMA-882 control display unit (CDU) functions as the bus controller for the MIL-STD-1553 multiplex data bus that interconnects the systems shown. Intermetrics developed the CDU software to control and manage each of the subsystems, perform the INS in-flight

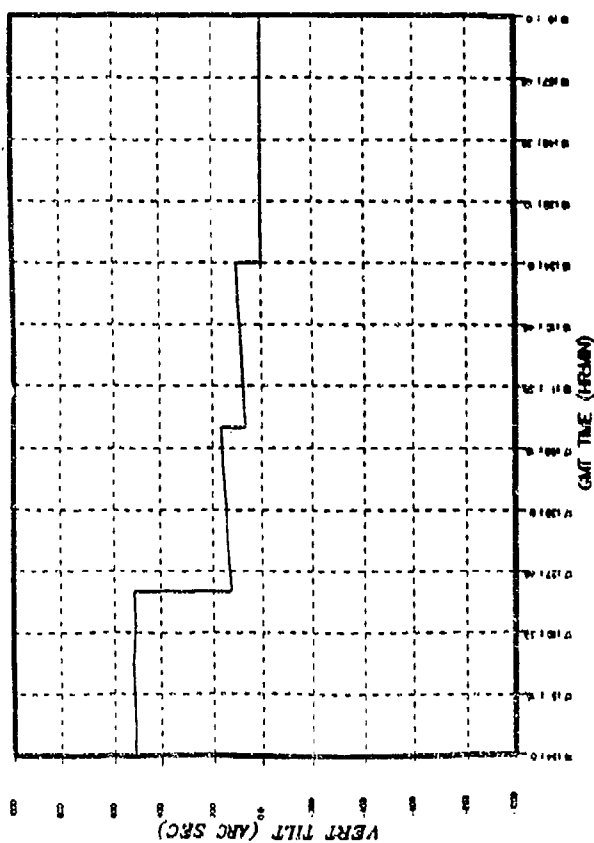


Figure 7 True platform tilt about vertical axis.

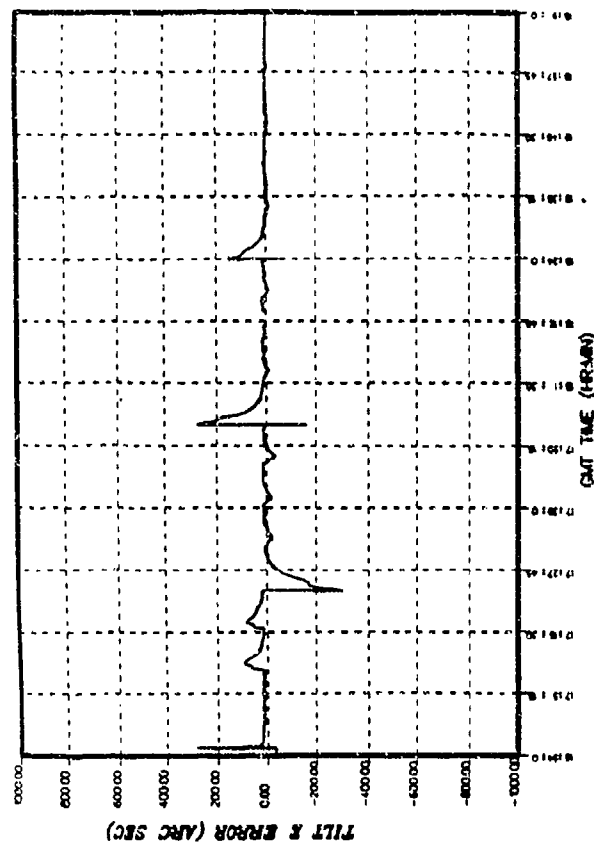


Figure 8 Error in estimate of tilt about east axis.

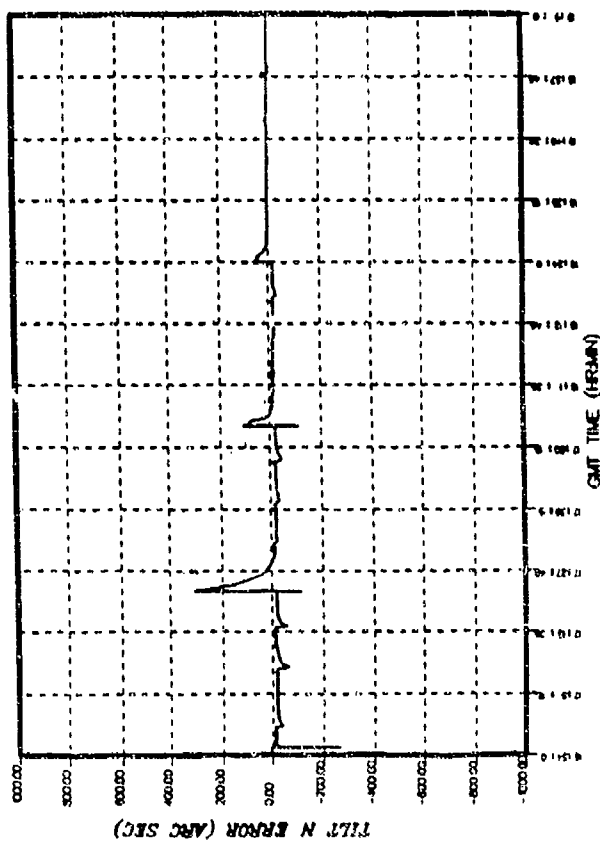


Figure 9 Error in estimate of tilt about north axis.

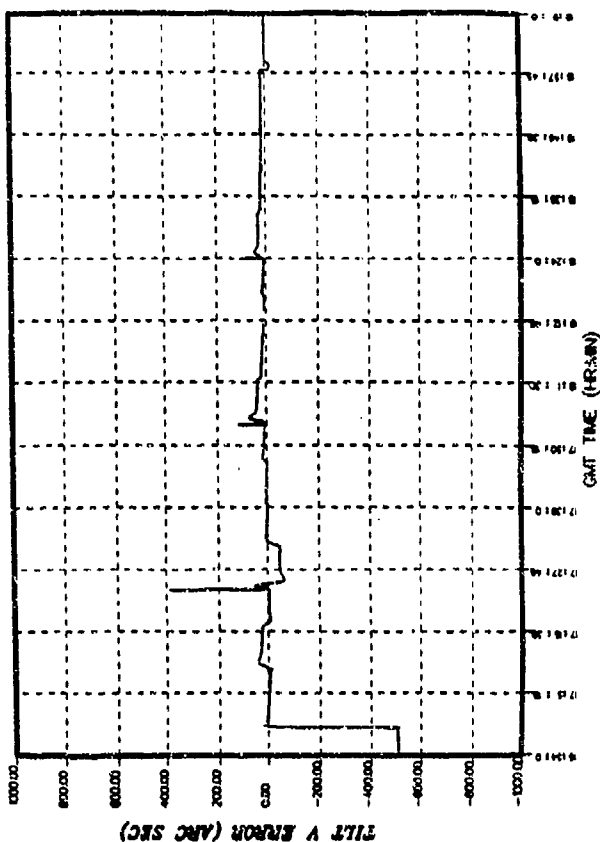


Figure 10 Error in estimate of tilt about vertical axis.

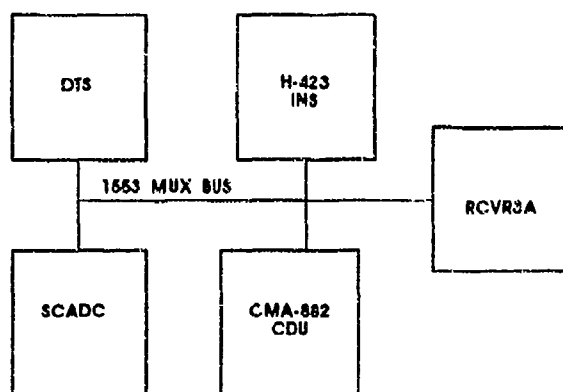


Figure 11. T-39 Advanced Avionics System

alignment, control mux bus data transfers and integrate it with core CDU software from CMC. The INS is a Honeywell H-423 laser strapdown system built to SNU 84-1, the USAF specification for a moderate accuracy inertial navigation system [3]. The GPS receiver is a Rockwell-Collins R-2332/AR, the five channel high dynamic receiver familiarly referred to as a RCVR3A. The Standard Central Air Data Computer (SCADC) is produced by GEC and is specially programmed with the specific T-39 static source error corrections. A prototype Sundstrand data transfer system (DTS) consisting of a ruggedized 3 1/2 inch floppy disk drive with a MIL-STD-1553 interface completes the system. The DTS is used to load mission flight plans along with navigation waypoint and GPS satellite almanac databases.

The avionics suite is instrumented by an Intermetrics developed Personal Computer Buffer Box (PCBB) that interfaces with the RCVR3A instrumentation port (IP). The PCBB provides a real-time display of IP data and records the data in a disk file. Data recorded includes the INS state vector (I01 block) supplied to the RCVR3A, the GPS state vector (G-6 block), and SV measurement data that is post-processed

with Satellite Reference Station data to obtain TSPI of the same order of accuracy as laser tracking.

The IFA-related data transfers are shown in Figure 12. The IFA process begins with the CDU commanding the INS to the air align mode (automatic updates) via the D01 data block. A position update based on the GPS G-6 and INS I01 blocks is computed and supplied to the INS via the F02 message. Five seconds later, a position and velocity update is computed (also based on I01 and G-6) and the second F02 reset is sent. A third F02 reset, correcting platform azimuth based on manual inputs or GPS ground track, is sent if the INS has not previously completed a full gyrocompass or degraded navigation alignment. After the INS Nav Data Valid bit is set with the last F02 message the RCVR3A will begin using the INS aiding data and estimating the INS error for the G-7 output message. The first F02 reset with position, velocity and tilt corrections based on the RCVR3A G-7 estimates is sent 200 seconds after the INS data is set valid and then every 240 seconds thereafter. The INS resets are indicated to the RCVR3A using the "default reset" technique described in ICD-GPS-059 whereby the INS data is briefly indicated to be invalid so as to force the receiver to re-estimate the INS error when the INS data becomes valid.

IFA-2 Navigation Performance Results

This section presents INS navigation performance that resulted following a degraded navigation alignment (IFA-2). The INS was placed in the Gyro-compass (GC) align mode for about 45 seconds when a steady "NAV READY" message was displayed on the CDU indicating that a valid, albeit degraded, navigation solution is available. The INS was then placed in the NAV mode. A normal taxi, take off, and

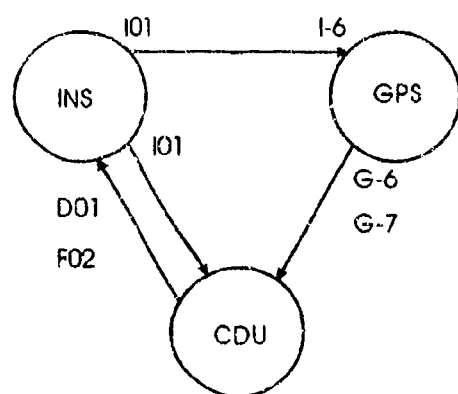


Figure 12. IFA-Related Data Transfers

departure sequence was then conducted. To allow comparison of navigation performance following degraded navigation alignment with that following IFA, the INS was allowed to run autonomously for about 27 minutes before IFA resets using GPS data were applied. The resets described in the previous section were applied for a period of about 30 minutes, following which the INS again navigated autonomously for about an hour and 10 minutes until the end of the flight.

Figure 13 shows the error in the horizontal components of the INS indicated position. Following the degraded navigation alignment, the Root Sum Square (RSS) horizontal position error grew to about 1900m in about 27 minutes. The first reset occurred at about 20:03 hrs, and the IFA was terminated at about 20:34 hours. The INS then ran autonomously for approximately 1 hour and 10 minutes. The plots show that the growth rate of the INS position error following IFA was significantly lower than that following the degraded navigation alignment. The horizontal position error 1 hour after IFA was terminated was about 300m.

The error in the horizontal components of the INS indicated velocity are shown in Figure 14. In the 27 minute interval following the degraded navigation alignment, the RSS horizontal velocity grew to about 2 m/s. By contrast it remained below 0.25 m/s in the one hour following the end of IFA.

SUMMARY

Laboratory and flight tests were conducted to assess INS alignment and navigation performance following alignment using error estimates provided in the G-7 message.

Results from the laboratory test showed that for an INS with medium accuracy instrument characteristics, the level axes tilt components were estimated to an accuracy of better than 20 arc-secs during steady flight conditions. The azimuth component was estimated to an accuracy of better than 45 arc-secs.

Manoeuvres caused transients in the estimates of the level axes components, with the size of the transient depending on the size of the true platform azimuth error existing at the time and the acceleration level. Two-g turns coupled with a true INS azimuth error of 510 arc-seconds caused transient errors of 85 and 63 arc-seconds, respectively, in the estimates of the east and north components of tilt.

The results from the flight test showed that INS navigation performance following a degraded navigation alignment can be substantially improved by performing in-flight alignment using GPS data. RSS horizontal position and velocity errors at the

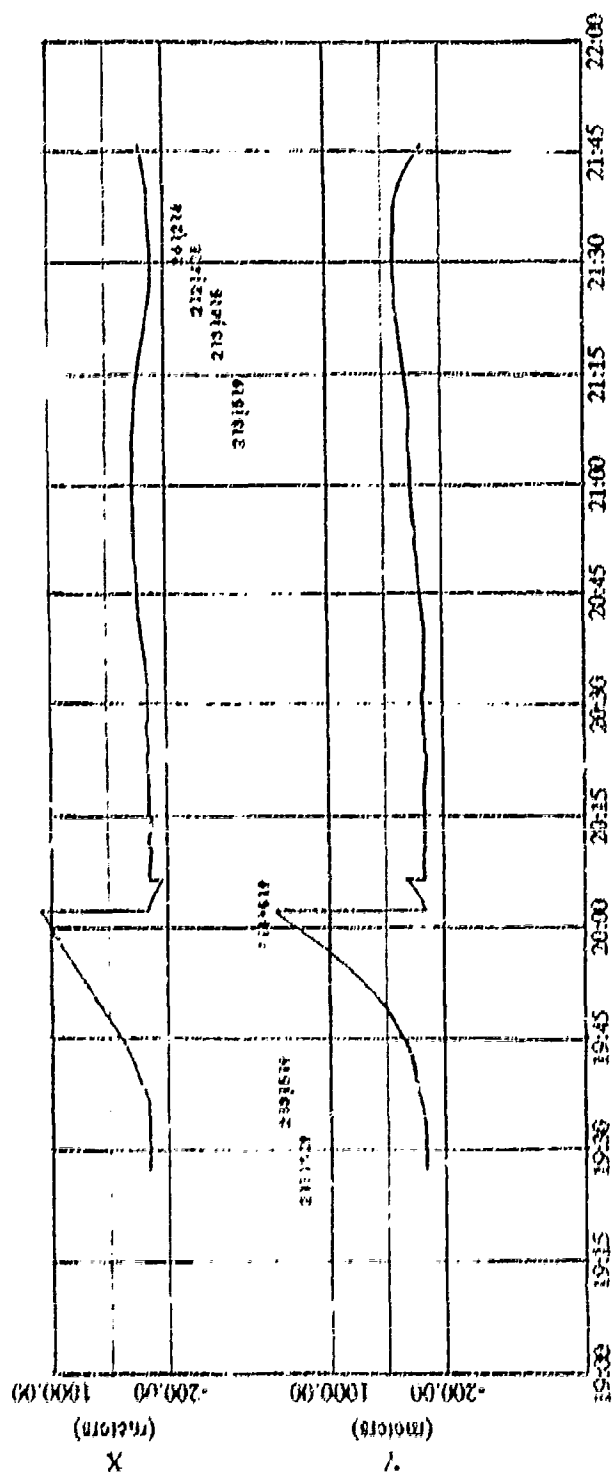


Figure 13 Errors in INS indicated horizontal position components.

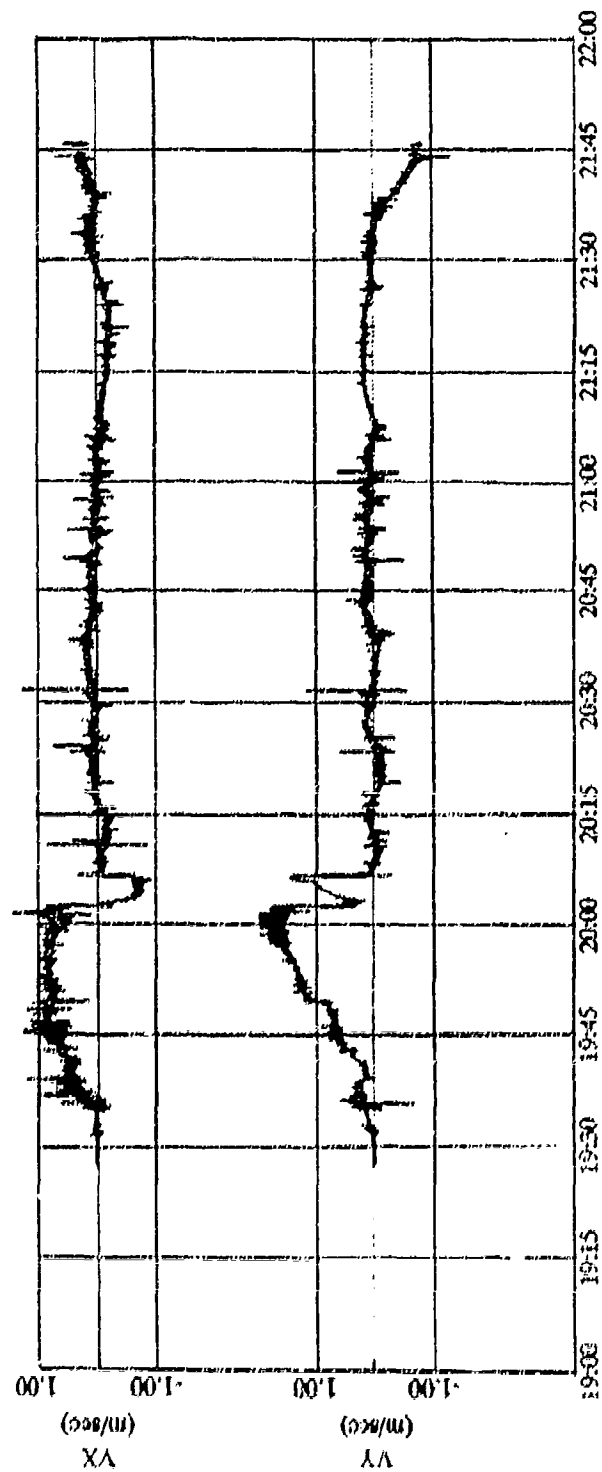


Figure 14 Errors in INS indicated horizontal velocity components.

end of one hour following the end of in-flight alignment were less than 300 m and 0.25 m/s, respectively.

In summary, the results presented in this paper have demonstrated that the RCVR3A is properly able to estimate INS alignment errors, and that the G-7 message provides a viable option for performing INS alignment.

REFERENCES

- [1] Anon., "GPS User Equipment MIL-STD-1553 Multiplex Bus Interface, Revision B," Navstar GPS Phase III Document No. GPS-89-11132-025, February 1989.
- [2] Anon., "Naval Air Development Center GPS Central Engineering Activity Laboratory Simulation Capabilities Description," Navstar GPS Document No. GPS-90-13921-03, 13 October 1989.
- [3] Anon., "Specification for the USAF Standard Form, Fit and Function Medium Accuracy Inertial Navigation Unit," Aeronautical Systems Division, Air Force Systems Command, Wright-Patterson AFB, Ohio; 28 February 1986.

TIGHTLY COUPLED GPS/INS INTEGRATION USING AN OPEN LOOP APPROACH

BY CHRISTOPHER C. ROSS

WRIGHT LABORATORY
ARMAMENT DIRECTORATE
INERTIAL TECHNOLOGY SECTION
OFFICE SYMBOL: WL/MNAG
EGLIN AFB, FLORIDA

WARNING: This document contains technical data whose export is restricted by the Arms Export Control Act (Title 22, USC, Sec 2753, et seq) or the Export Administration Act of 1979, as amended (Title 50, USC, App. 2401, et seq). Violations of these export laws are subject to severe criminal penalties. Dissemination in accordance with the provisions of DoD Directive 5230.25.

"Distribution authorized to the Department of Defense and DoD contractors only to protect information and technical data that describe new technology in an area of significant or potentially significant military application or that relate to a specific military deficiency of a potential adversary (07 July, 1991). Other requests for this document shall be referred to WL/MNAG, Eglin AFB, FL, 32542-5434."

"For unclassified, limited documents, destroy by any method that will prevent disclosure of contents or reconstruction of the document."

ABSTRACT:

GPS/INS open loop integration is subject to cascaded filter problems, such as increased time correlation, when the GPS receiver provides pre-filtered navigation data. If the GPS receiver provides raw pseudorange and pseudorange-rate data, a tightly coupled open loop integration is made possible. The tight coupling design reported in this paper details an extended suboptimal Kalman filter which processes the difference between the GPS and INS information. The Kalman filter processes an eleven state error vector which includes position, velocity, tilts, GPS clock phase, and GPS clock frequency errors.

Simulation results for a low dynamic and high dynamic trajectory are provided in this paper which suggest that position and velocity errors are bounded even when pseudorange and pseudorange-rate data is available from only two satellites. The simulation utilized models of the Honeywell H-423 INS and the Magnavox MX4400 GPS receiver.

Introduction

Since the advent of the Global Positioning System (GPS) receiver, various integration schemes [1,2,3,4,5] have been developed for integrating GPS with Inertial Navigation System (INS) data using a Kalman Filter [6,7,8]. Most of the integration schemes involve updating the INS position and velocity measurements with the corresponding GPS estimates in the geodetic coordinate frame (see Figures 1 and 2.)

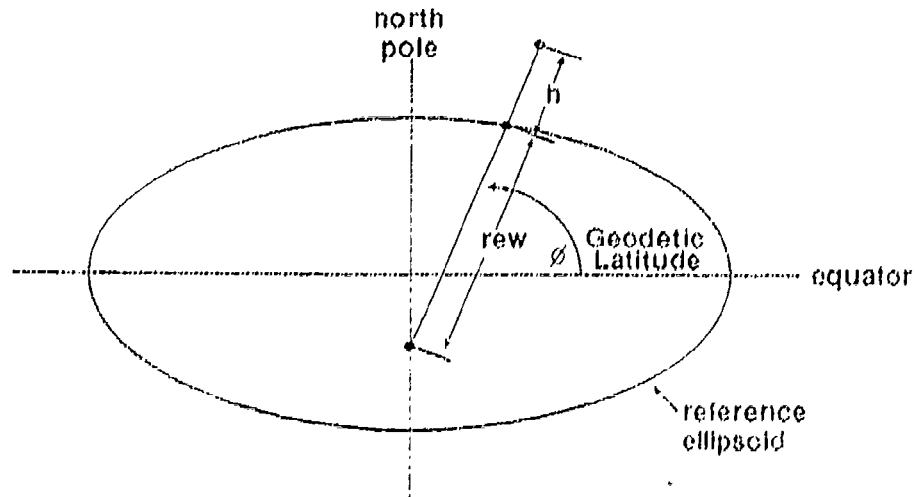


Figure 1. Geodetic Latitude.

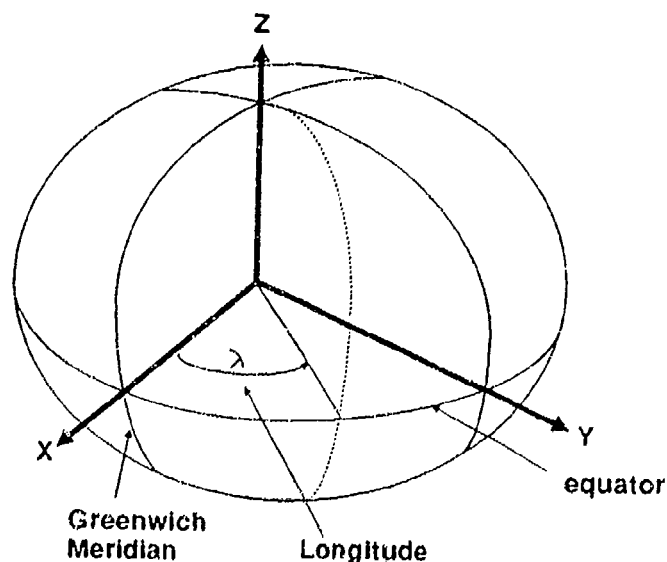


Figure 2. Geodetic Longitude.

There is a problem with using GPS updates in the geodetic coordinate frame in that the GPS receiver must be tracking at least four satellites to provide a complete navigation solution for position and velocity. D.A. Tzartas and J.G. Mark [1] suggest that this problem may be limited if the raw data is available from the GPS receiver. The raw data from a GPS receiver are the measurements of range and range-rate to each of the satellites it is tracking. When range and range-rate data are available from four different satellites, the GPS receiver uses its knowledge of the satellite orbital ephemeris data to compute position in the ECEF coordinate system [9]. The data is normally converted to and output in geodetic coordinates. This paper investigates a GPS/INS integration technique for optimally using the raw data from the GPS receiver so that GPS updates can be provided to the integration filter even when only three or two satellites are being tracked.

GPS/INS Integration Technique

The method of simulation suggested by Tzartas and Mark involves processing Kalman filter error estimates in the ECEF coordinate frame (see Figure 3) and processing the error measurements in the GPS Line of Sight (LOS) reference frame (see Figure 4.) A GPS LOS frame position measurement is a scalar estimate of the distance from the user to one of the four satellites being tracked. The GPS LOS frame velocity measurement is the time rate of change of the distance from the user to each satellite. A position error measurement for the integration filter is found by taking the difference between the GPS receiver measurement

of the range to a satellite and the INS estimate of the range to a satellite. The INS estimate is calculated using the satellite ephemeris data provided by the GPS receiver. The GPS LOS velocity error measurement is the time rate of change of the difference between the GPS and INS range to satellite estimates.

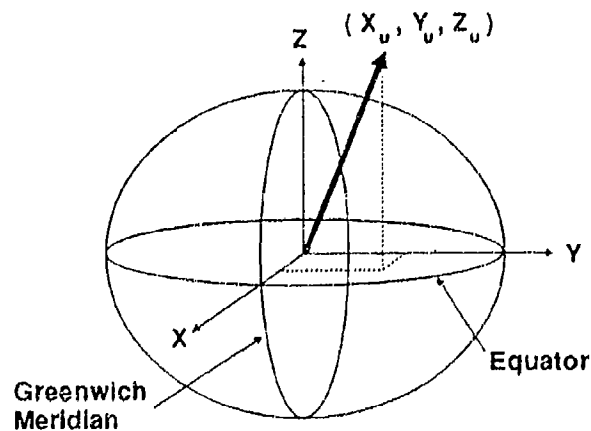


Figure 3. The ECEF Coordinate System.

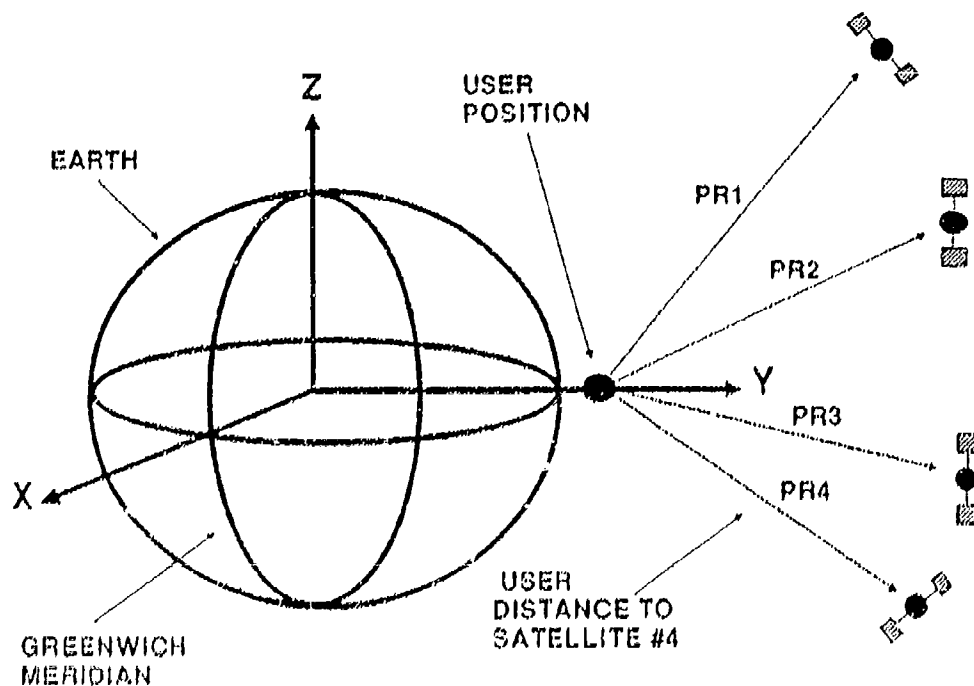


Figure 4. The GPS LOS Coordinate Frame.

The GPS/INS integration technique involves converting the INS position, velocity, and tilt estimates into the GPS LOG frame so that the INS data can be differenced with the GPS receiver position and velocity estimates to provide measurements of INS error to the integration Kalman filter. The first nine states of the Kalman filter are the error estimates of the INS data based on GPS receiver measurements. The remaining two states are the estimates of the GPS receiver clock phase and clock frequency errors. The Kalman filter INS error estimates can be used to correct the INS data.

The Kalman filter implemented in this study was designed to process the measurements of the INS error estimates of the range and range-rate to the four satellites sequentially (one satellite at a time.) Processing the measurements sequentially allows the implementer to easily neglect information from one or more satellites to simulate a condition where the GPS receiver is unable to provide measurement data from one or two of the four satellites normally tracked.

Simulation Characteristics

In order to evaluate the GPS/INS simulation, a low dynamic and high dynamic trajectory was generated using a profile generator. The low dynamic trajectory simulates a land vehicle class of maneuvers while the high dynamic trajectory simulates an aircraft class of maneuvers. The low dynamic trajectory information is provided in Table 1 while the high dynamic trajectory information is given in Table 2.

Table 1. Low Dynamic Trajectory Information.

INITIAL CONDITIONS		
VELOCITY	0.0	meters/sec
HEADING	45.0	degrees from North
PITCH	0.0	degrees
LATITUDE	31.15	degrees North of equator
LONGITUDE	86.15	degrees West of Greenwich Meridian
ALTITUDE	5.2	meters
TRAJECTORY INFORMATION		
1. Accelerate to 9.2 meters/sec in 20 seconds.		
2. Maintain velocity and heading for 45 seconds.		
3. Change heading 39 degrees in 10 seconds.		
4. Reduce velocity to 0.97 meters/sec in 20 seconds.		
5. Change heading 45 degrees in 5 seconds.		
6. Increase velocity to 6.2 meters/sec in 10 seconds.		
7. Maintain velocity for 590 seconds.		

Table 2. High Dynamic Trajectory Information.

INITIAL CONDITIONS		
VELOCITY	183.0	meters/sec
LATITUDE	31.15	degrees North of the equator
HEADING	45.0	degrees
PITCH	0.0	degrees
LONGITUDE	86.15	degrees West of the Greenwich Meridian
ALTITUDE	9144.0	meters above reference ellipsoid
TRAJECTORY MANEUVERS		
<ol style="list-style-type: none"> 1. Maintain velocity and heading for 120 seconds. 2. Change heading 45.0 degrees in 20 seconds. 3. Maintain velocity and heading for 320 seconds. 4. Change heading 45 degrees in 5 seconds. 5. Change pitch -45 degrees in 5 seconds. 6. Maintain velocity and heading for 30 seconds. 7. Change pitch 45 degrees in 5 seconds. 8. Maintain velocity and heading for 300 seconds. 		

The two trajectories were simulated using a generalized covariance analysis software package [10] called "INERCA" (pronounced inertia.) The software was used to generate trajectory data files, error histories for the INS, and satellite trajectory files for GPS modeling.

The position, velocity, and tilt errors, generated through covariance analysis, were added to the generated trajectory data to simulate INS measurements. The GPS measurements were simulated by first generating the range to each of the four satellites through differencing user position (from the vehicle trajectory file) and satellite position (from a generated satellite trajectory file.) Once the range had been calculated, simulated white noise with a normal distribution was added to the range to simulate a GPS pseudorange measurement. The GPS pseudorange-rate measurements were obtained by simply taking the derivative of the range measurements and adding an appropriate amount of normally distributed white noise.

After generating simulated GPS and INS measurements, the INS measurements were transformed into the GPS LOS frame. In the LOS frame, the INS data could be differenced with the GPS pseudorange and pseudorange-rate measurements to provide the input measurements to the Kalman filter. The Kalman filter was designed to process those measurements and estimate the INS error state vector in the ECEF coordinate frame. Finally, the data was transformed back into the

navigation frame for output. A block diagram of the simulation process is given in Figure 5. The blocks with the shaded background region were functions performed using INERCA software.

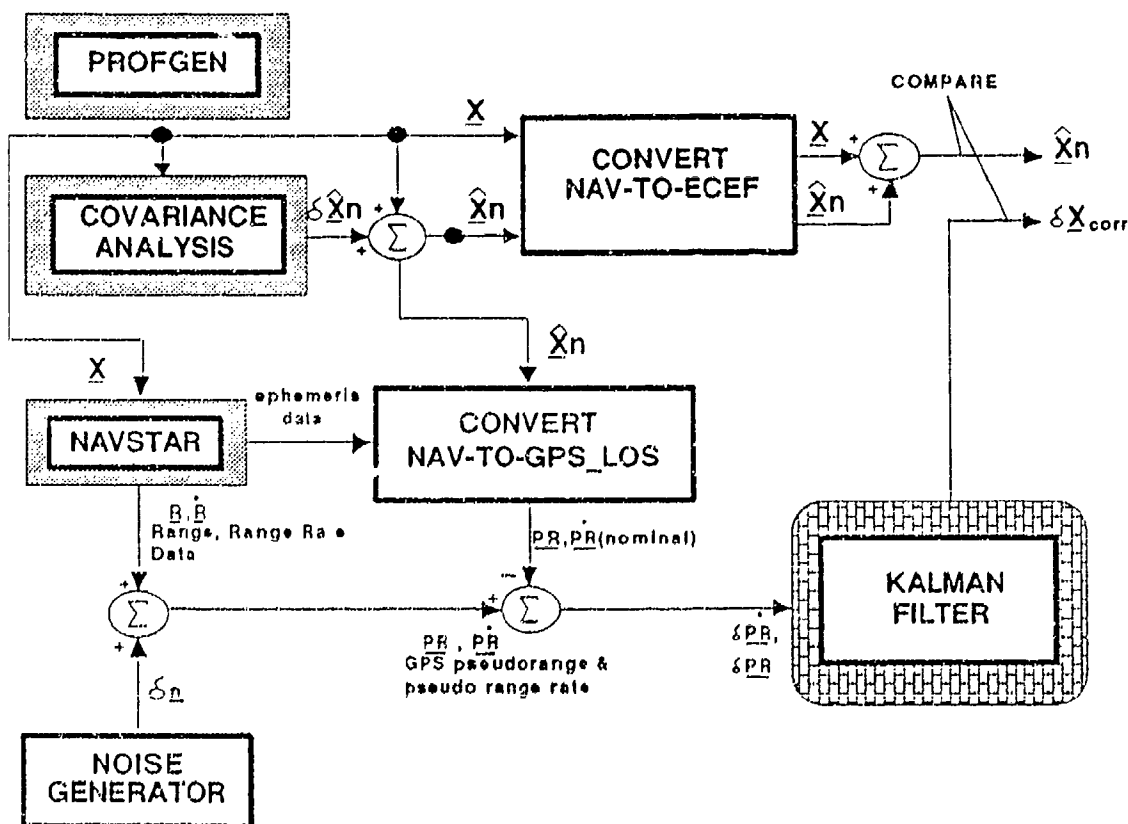


Figure 5. Simulation Block Diagram.

Low Dynamic Error Estimate Results

Figures 6 through 8 illustrate the filter's performance in estimating the INS position errors for the low dynamic trajectory. The solid lines represent the actual INS errors generated by the covariance simulation. The dashed lines are the filter estimates using measurements from all four of the simulated satellites. The dash-dot-dash lines represent the filter estimate using three satellites and the dotted lines represent the filter estimates using only two satellites. The legend for all the simulation graphs is given in Figure 6.

Figure 7 and 8 are the graphs of the north and east position error estimates for the low dynamic simulation. The four and three satellite error estimates track the actual error within eight meters. It is interesting to note that no significant degradation results from ignoring information from one of the four satellites. The two satellite simulation error estimates appears to be unable to track the INS errors

until approximately 300 seconds when it begins to track the errors within 80 meters for the north and east error estimates. The INS down position error shown in Figure 9 is bounded to five meters due to baro-altimeter updates to the INS. Since the GPS data is not as accurate as the baro-altimeter updates, the filter does not observe the errors.

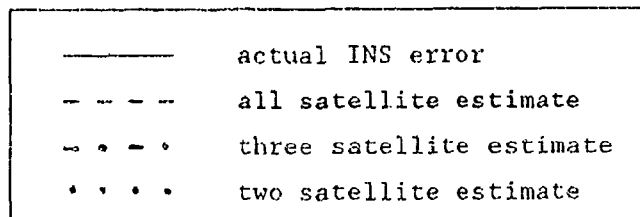


Figure 6. Legend for Output Graphs.

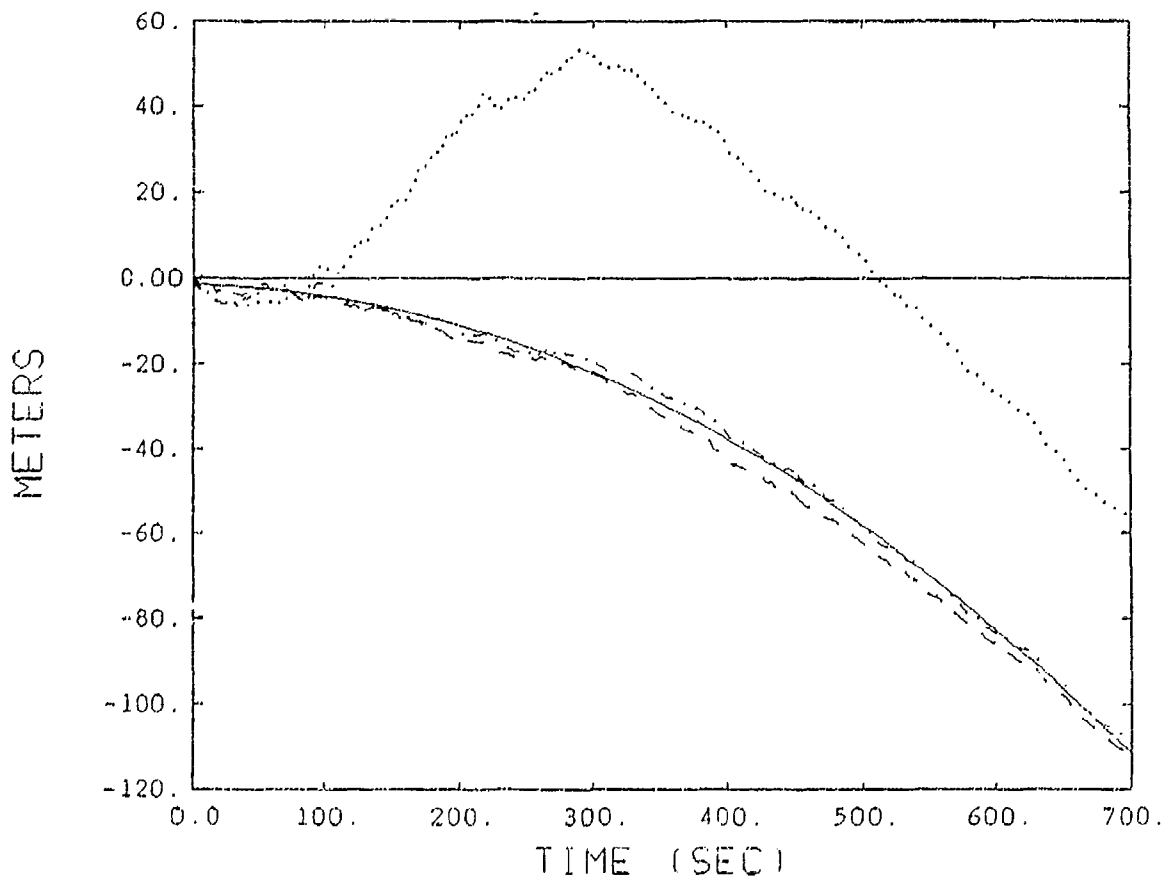


Figure 7. North Position Error Estimates.

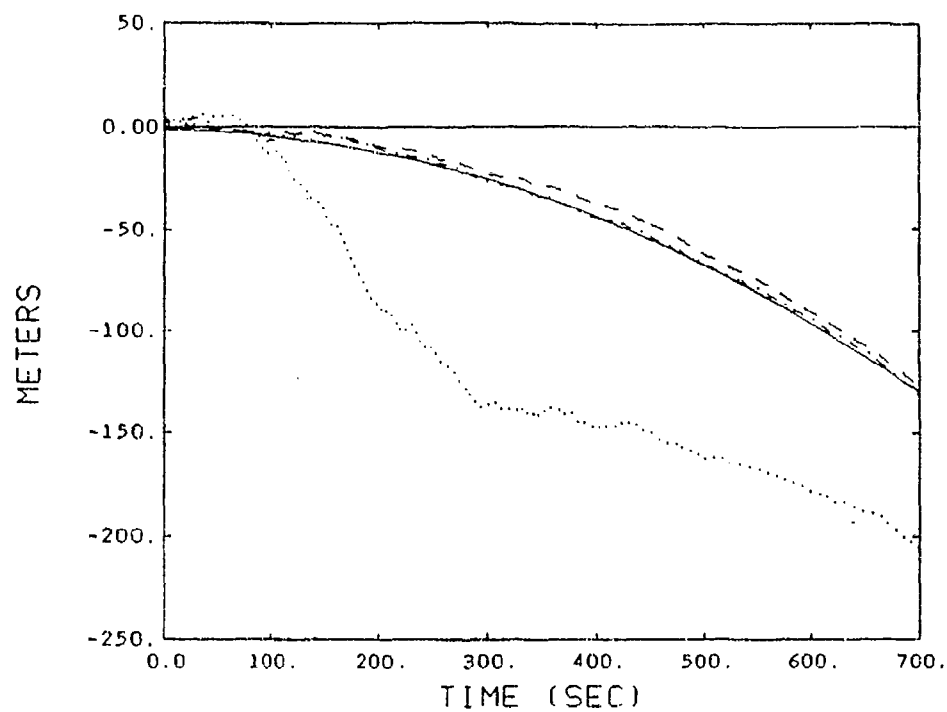


Figure 8. East Position Error Estimates.

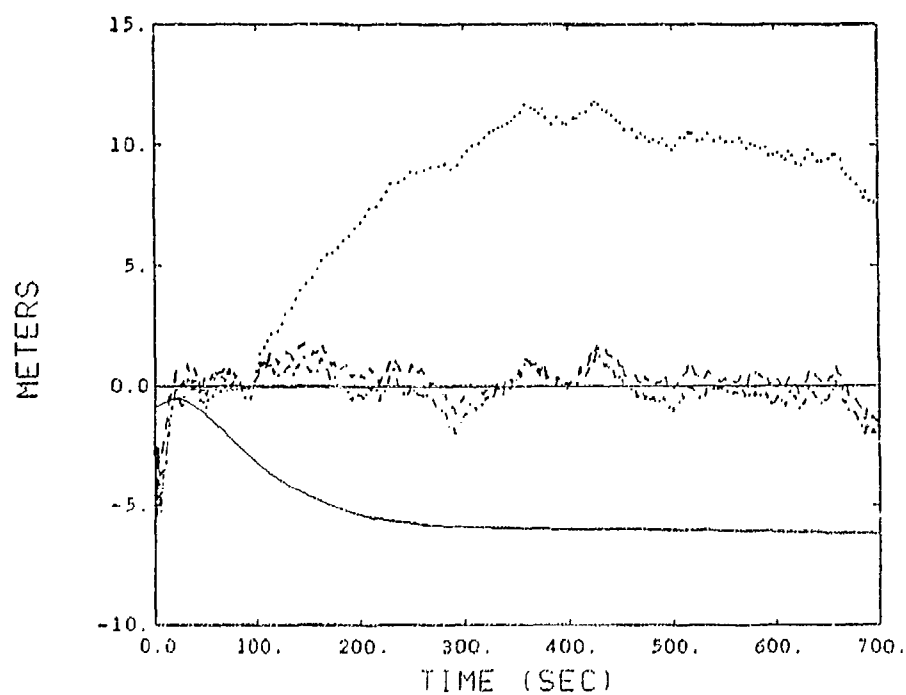


Figure 9. Down Position Error Estimates

Figures 10, 11, and 12 illustrate the filter's estimates of the north, east, and down velocity errors. The four and three satellite error estimates track the INS velocity errors within 0.1 meters/sec (one sigma) of the north, east, and down error estimates. The two satellite estimate degrades marginally for the north and east estimates while the down error estimate is corrupted to a maximum of 0.35 meters/sec deviation.

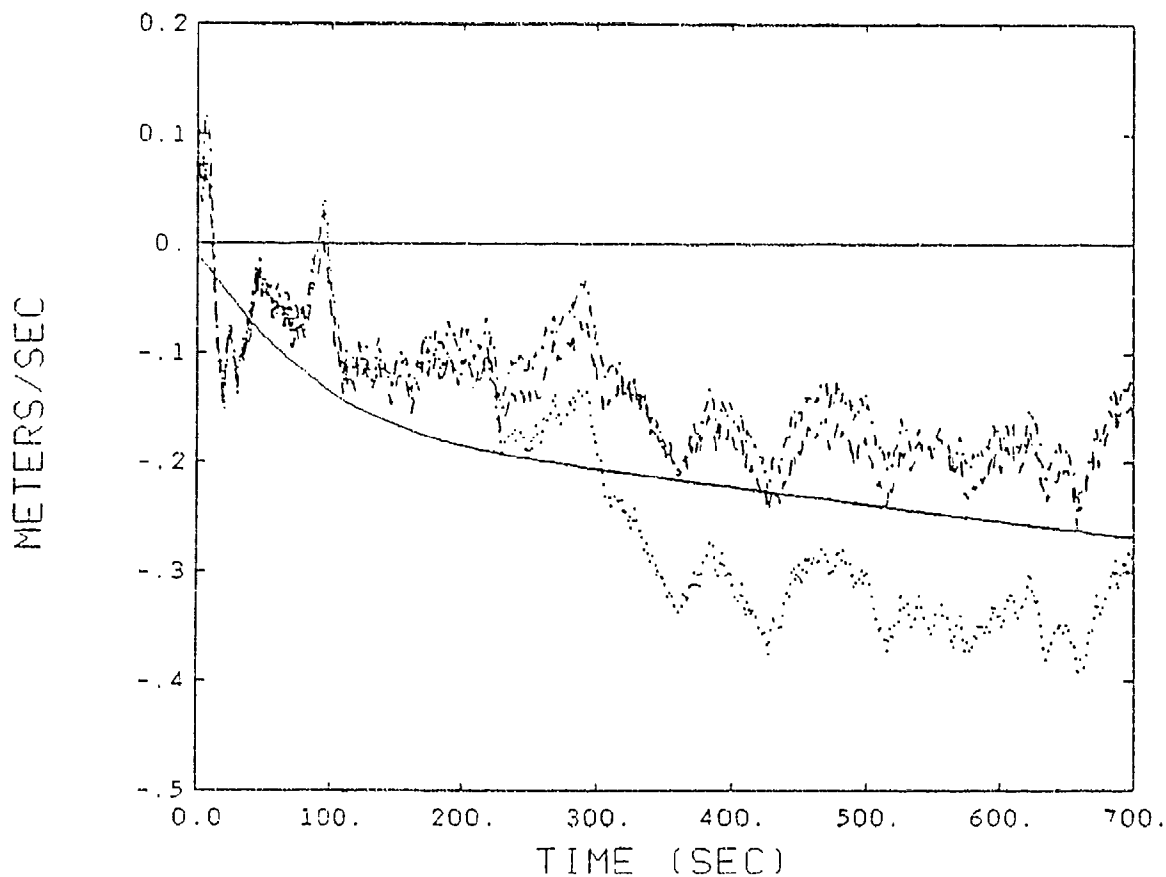


Figure 10. North Velocity Error Estimates.

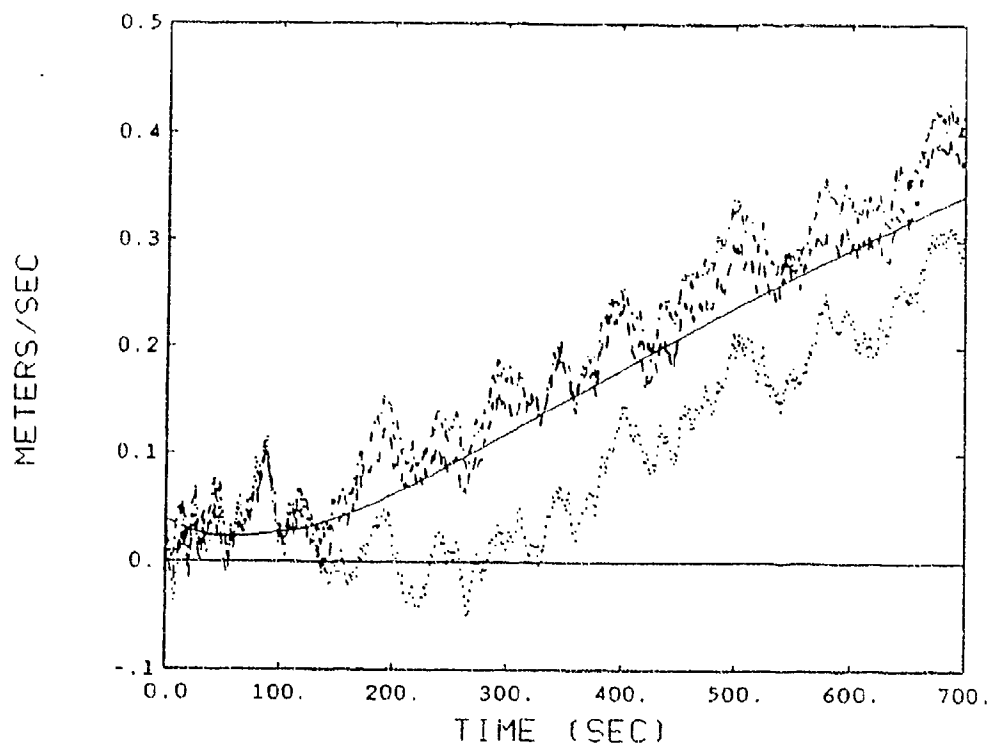


Figure 11. East Velocity Error Estimates.

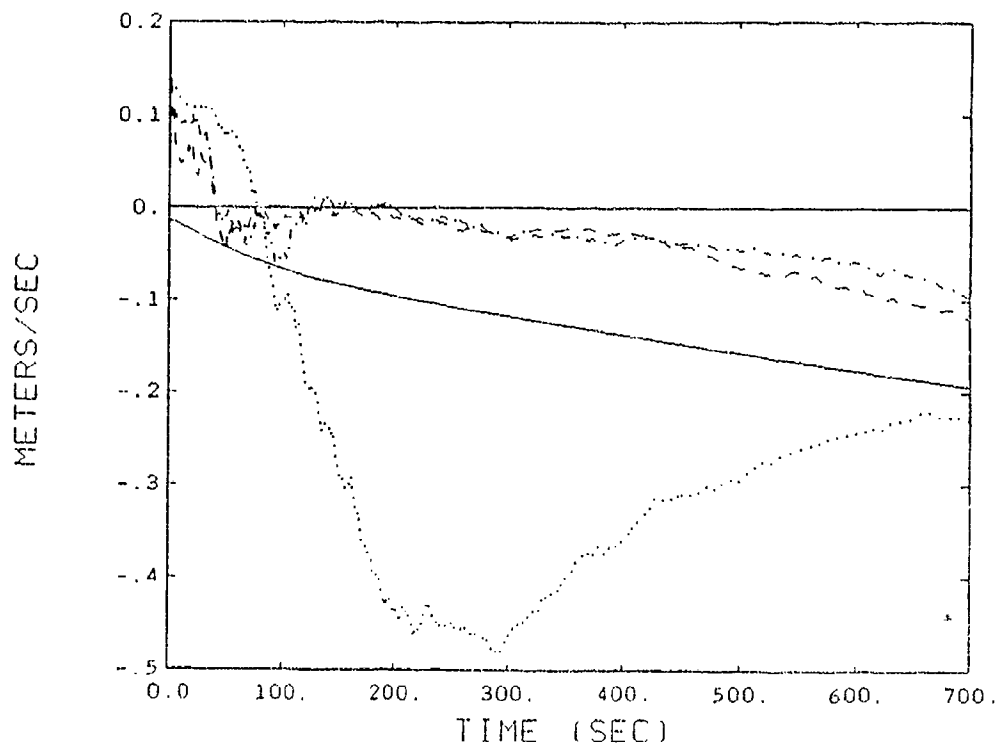


Figure 12. Down Velocity Error Estimates.

Figures 13, 14, and 15 display the north, east, and down tilt error estimates for the Kalman filter. Vehicle tilt error measurements cannot be processed by the OPB/INS Kalman filter because the OPB receiver simulated does not estimate vehicle tilt. Tilt information is coupled into the state dynamics through the gravity vector matrix to account for Coriolis effects in position and velocity calculations. The north and east tilt error estimates are bounded to within 0.5 milliradians. The down tilt error estimate levels off at 5.5 milliradians.

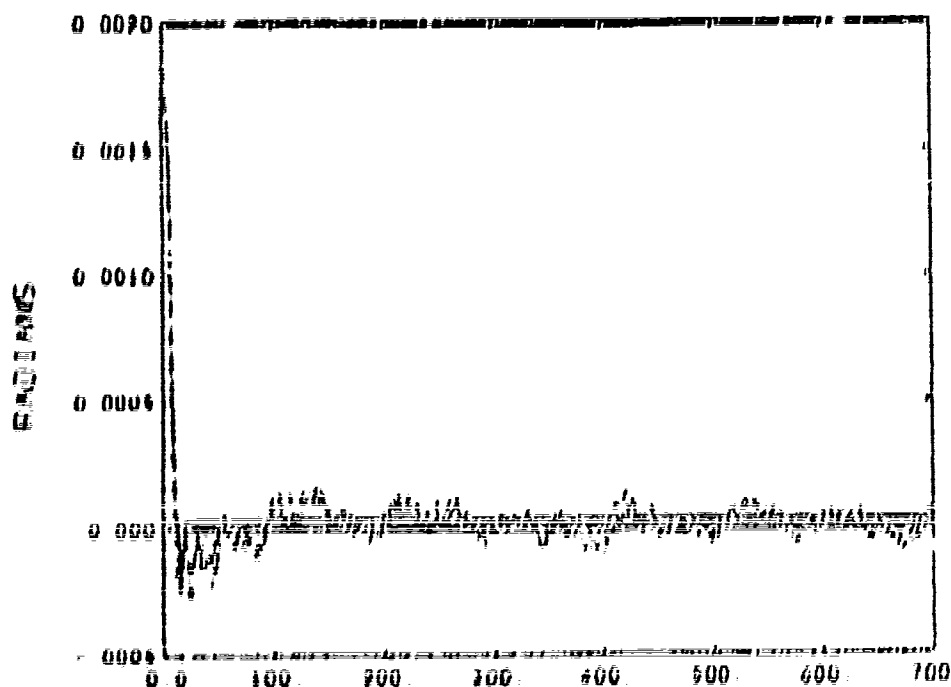


Figure 13. North Tilt Error Estimates.

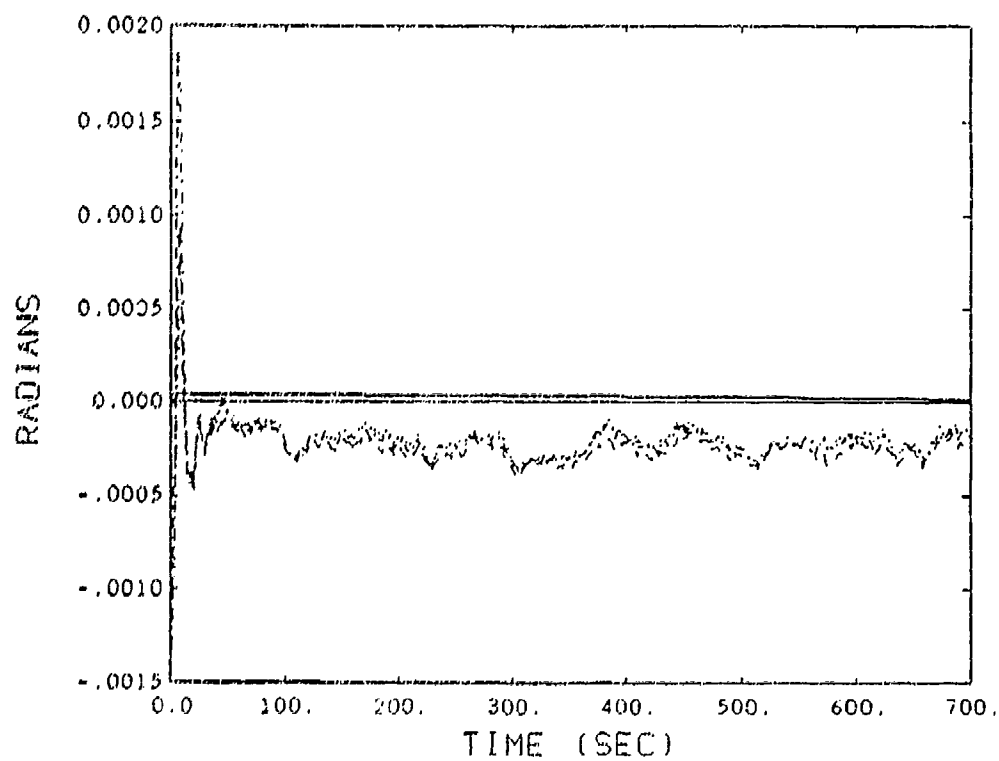


Figure 14. East Tilt Error Estimates.

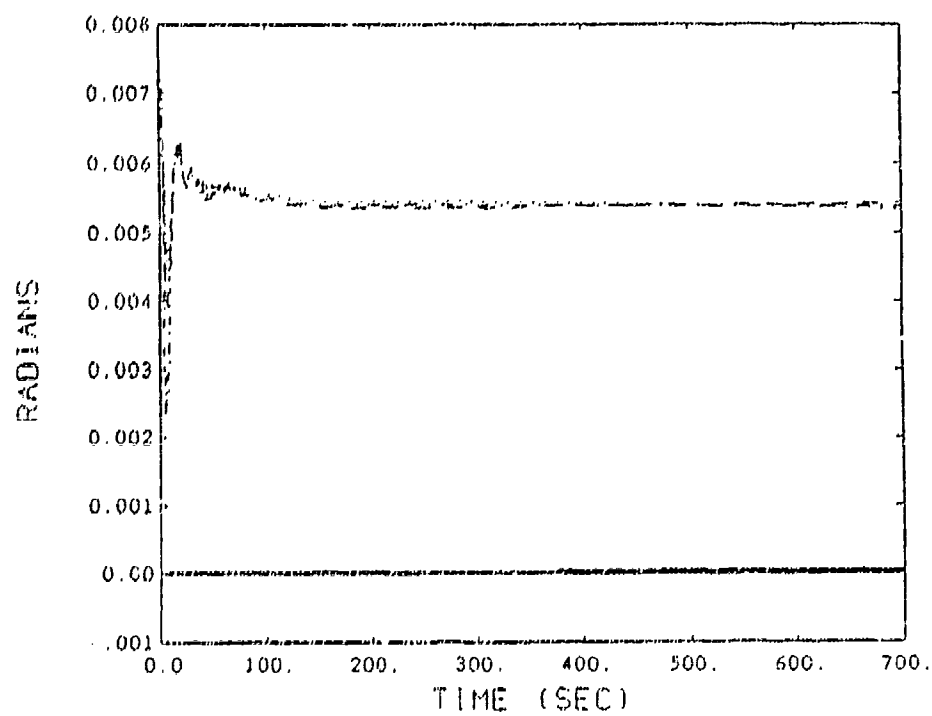


Figure 15. Down Tilt Error Estimates.

High Dynamic Error Estimate Results

Figures 16 through 18 present the extended Kalman filter's ability to estimate INS position error for a trajectory with a high dynamic profile. The north, east, and down error estimation data is very similar to the low dynamic profile results. The only significant difference is seen in the down position INS error shown in Figure 18. A jump in the data occurs at 460 seconds which is the result of a rapid change in the altitude trajectory occurring at that time.

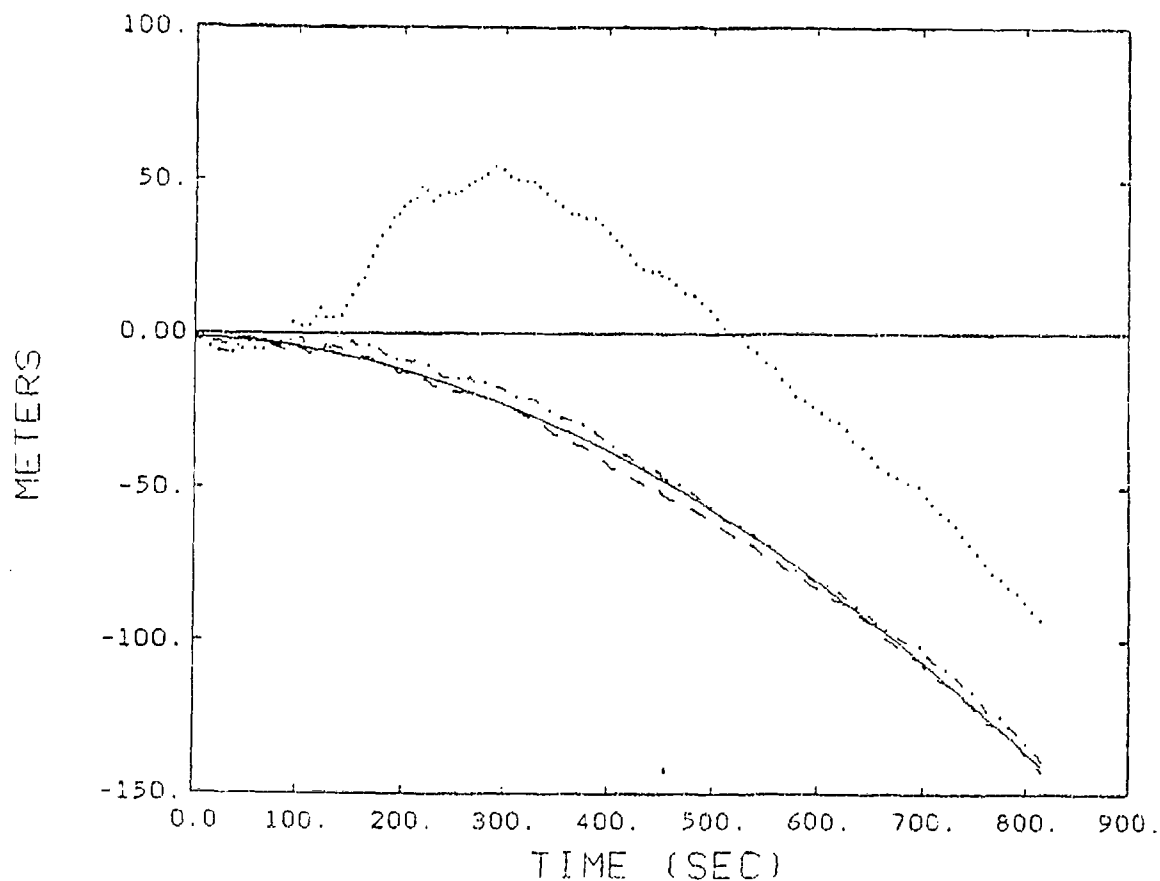


Figure 16. High Dynamic North Position Error Estimates.

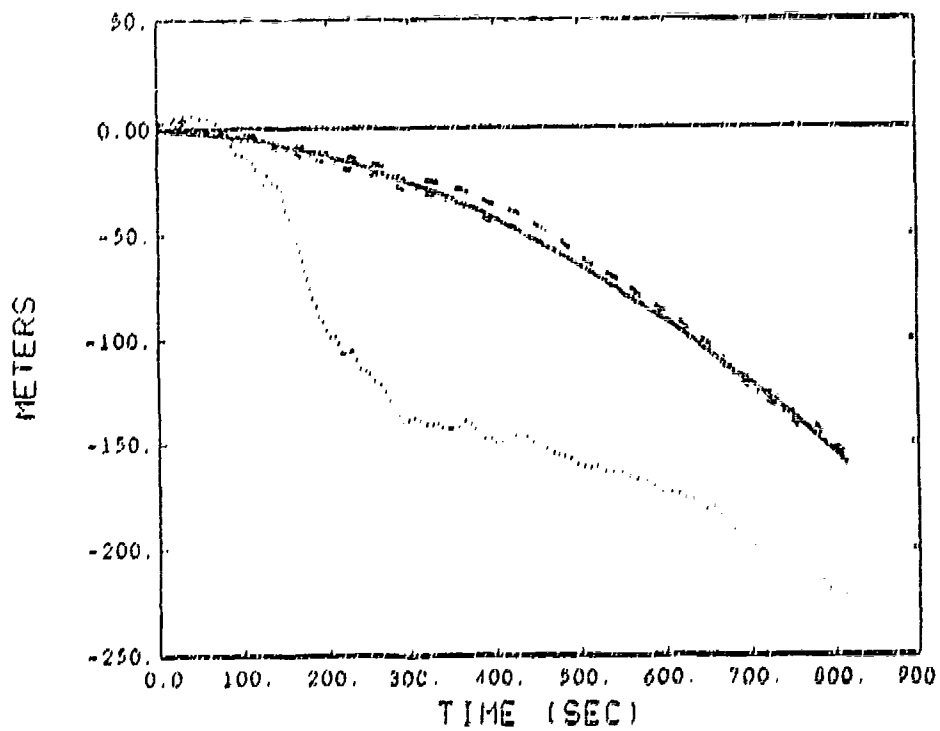


Figure 20. High Dynamic East Position Error Estimates.

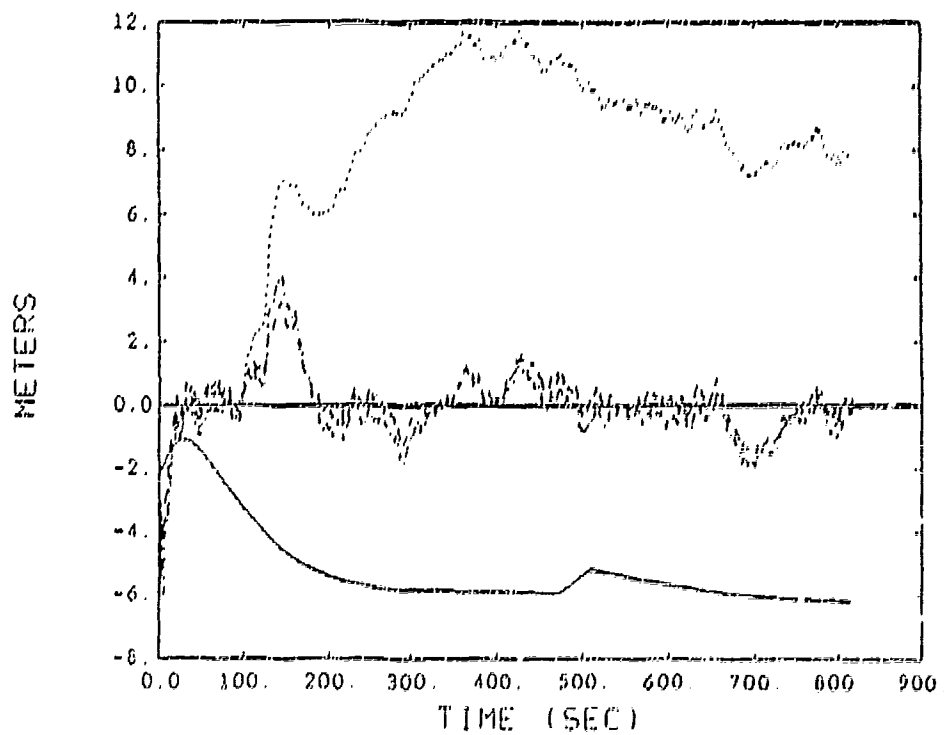


Figure 21. High Dynamic Down Position Error Estimates.

Figures 19 through 21 provide the high dynamic error estimates for the north, east, and down velocity errors of the INS. In Figure 19, the north velocity error estimates exhibit major excursions at 120 and 460 seconds corresponding to two high dynamic maneuvers performed. Such excursions are typical of an extended Kalman filter which is characteristically sensitive to dynamic changes in the filter states. The steady state estimates for the deviations of the results were between 0.1 and 0.2 meters/second. The excursions reached one meter/second of error at the 120 second maneuver and 0.2 meters/second at the 460 second maneuver. The east and south velocity errors are less affected by the maneuvers as is seen in figures 20 and 21.

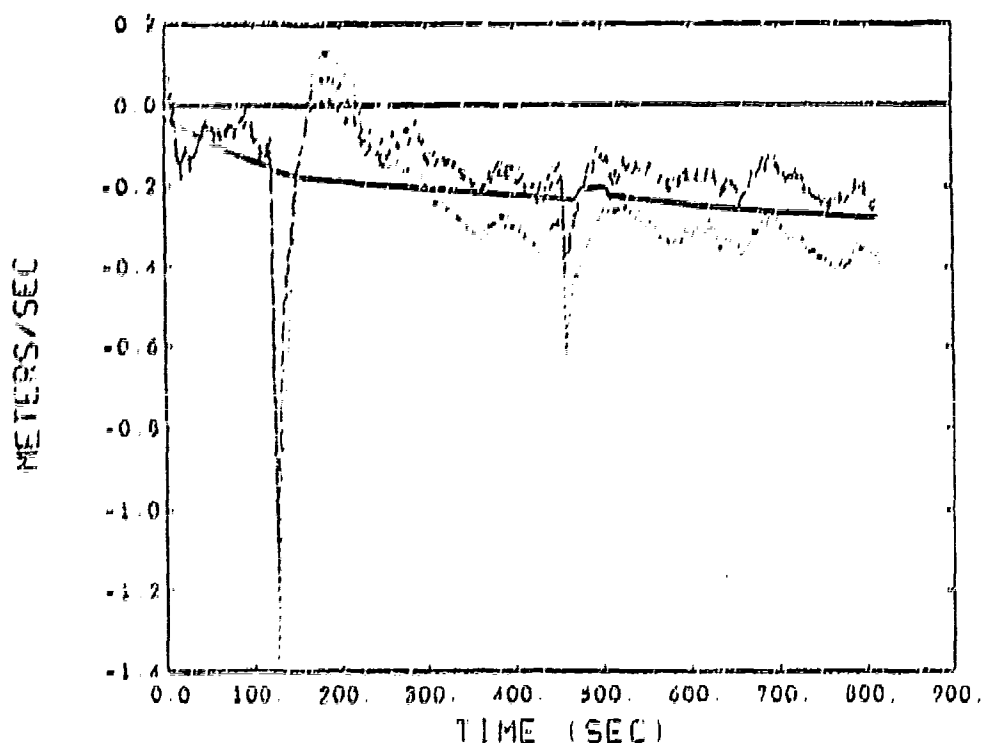


Figure 19. High Dynamic North Velocity Error Estimates.

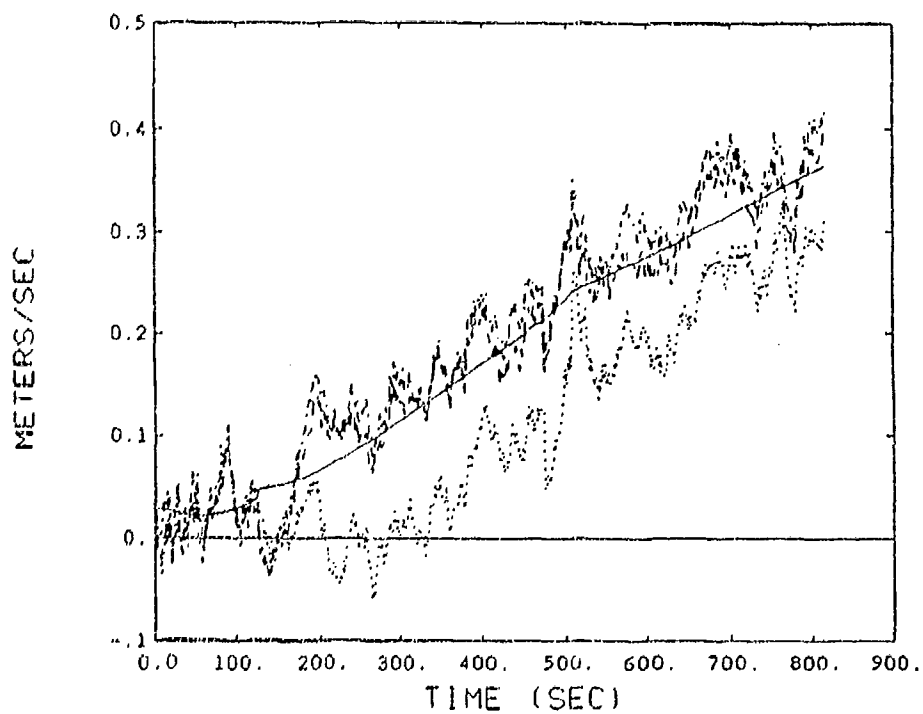


Figure 20 High Dynamic East Velocity Error Estimates.

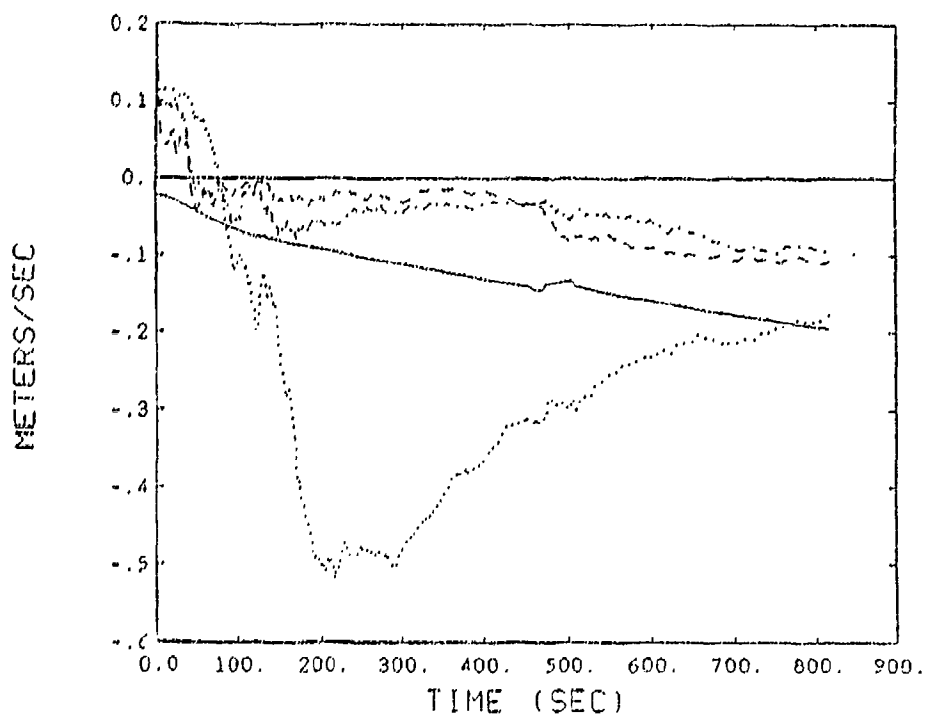


Figure 21. High Dynamic Down Velocity Error Estimates.

The north, east, and down tilt error estimates for the high dynamic profile are given in Figures 22, 23, and 24. The north tilt error estimate is almost identical to the low dynamics north tilt error estimate while the east tilt error estimate exhibits large excursions at the 120 and 460 second points due to the maneuvers. The excursions are due to the coupling between the east tilt estimates and the north velocity error estimates. Figure 24 shows how the filter gains observability on the down tilt-error estimate when the high dynamic maneuvers are performed. The filter's down tilt error estimate is reduced from six milliradians to less than one milliradian after the second maneuver.

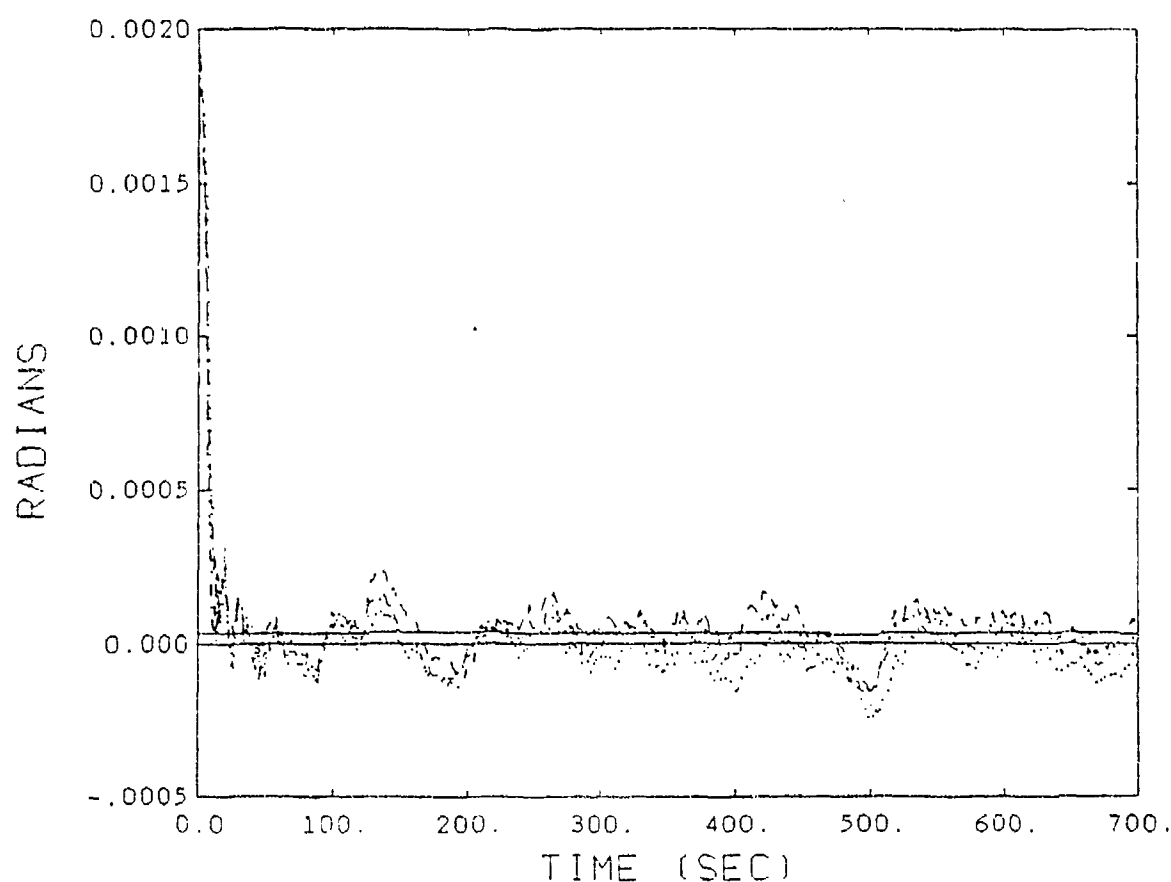


Figure 22. High Dynamic North Tilt Error

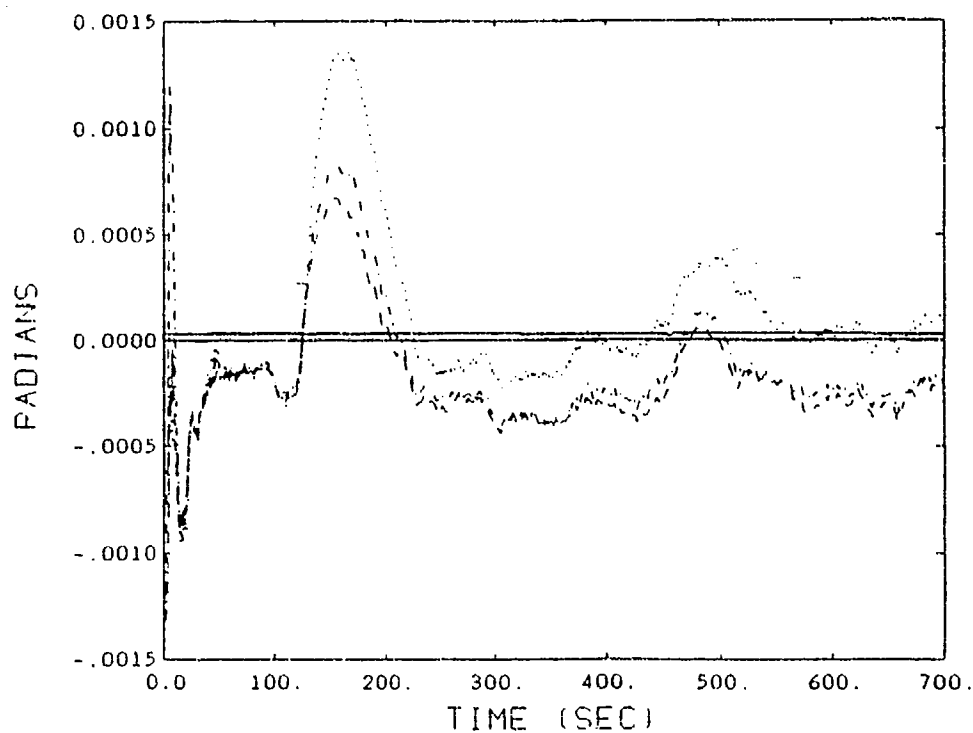


Figure 26. High Dynamics East Tilt Error

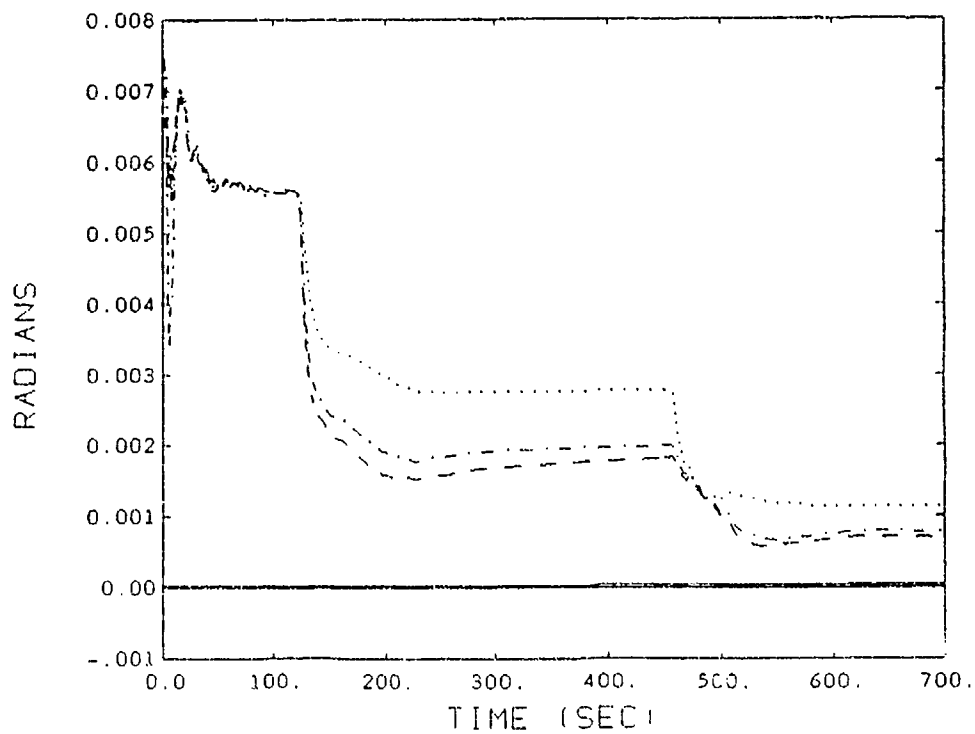


Figure 27. High Dynamics Down Tilt Error

Conclusions

Based on the results provided on the previous pages, if a GPS/INS integration is being designed for an environment in which data is not available from the four satellites normally used for GPS navigation, then the integration scheme investigated in this paper is a possible design for obtaining bounded measurements from the raw GPS data even under degraded conditions. More work is necessary, however, to further verify the potential benefits of the design. First, a more detailed simulation should be performed to better characterize GPS measurement errors. Second, a hardware simulation should be performed to validate the robustness of the design and whether or not the design is implementable using today's INSs and GPS receivers.

The Kalman Filter Design Parameters and Equations

The primary discrete Kalman filter equations used to generate the data in this paper are given in Table 3. The filter implemented is an extended Kalman filter due to the time varying nature of the system dynamics matrix which is given by equations 1 through 9.

Table 3. Recursive Discrete Kalman Filter Equations.

STATE ESTIMATE PROPAGATION	$\hat{\underline{x}}_k(-) = \Phi_{k-1} \hat{\underline{x}}_{k-1}(+)$
ERROR COVARIANCE PROPAGATION	$P_k(-) = \Phi_{k-1} P_{k-1}(+) \Phi_{k-1}^T + Q_{k-1}$
KALMAN GAIN MATRIX	$K_k = P_k(-) H_k^T [H_k P_k(-) H_k^T + R_k]^{-1}$
STATE ESTIMATE UPDATE	$\hat{\underline{x}}_k(+) = \hat{\underline{x}}_k(-) + K_k [Z_k - H_k \hat{\underline{x}}_k(-)]$
ERROR COVARIANCE MATRIX UPDATE	$P_k(+) = [I - K_k H_k] P_k(-) [I - K_k H_k]^T + K_k R_k K_k^T$
APPROXIMATION	$\Phi_k = I + F \Delta t$

where,

$\hat{\underline{x}}_k(-)$ = State estimate vector before an update

$\hat{\underline{x}}_k(+)$ = State estimate vector after an update

Φ_k = State propagation matrix approximation

Q = Process noise of the system

R = Measurement noise

K_k = Kalman gain matrix

F = State dynamics matrix

I = Identity matrix

The state dynamics matrix, F, is given in equation 1.

$$F = \begin{bmatrix} M1_{3 \times 3} & I_{3 \times 3} & 0_{3 \times 3} & 0_{3 \times 2} \\ M2_{3 \times 3} & M3_{3 \times 3} & M4_{3 \times 3} & 0_{3 \times 2} \\ 0_{3 \times 3} & 0_{3 \times 3} & M5_{3 \times 3} & 0_{3 \times 2} \\ 0_{2 \times 3} & 0_{2 \times 3} & 0_{2 \times 3} & M6_{2 \times 3} \end{bmatrix} \quad (1)$$

The individual element sub-matrices M1 through M6 are unique and require separate discussions. The $0_{3 \times 3}$ matrix is simply a 3x3 matrix of all zeros. The $I_{3 \times 3}$ matrix is a 3x3 identity matrix. Matrix M1 is given by

$$M1 = -k_1 \Pi \quad (2)$$

where k_1 is a vertical state aiding parameter which is introduced to dampen transient conditions in the vertical states which are a problem in a typical INS [5,7,and 8]. The Π symbol is a 3x3 matrix given by

$$\Pi = (e)(e)^T \quad (3)$$

where e is a unit position vector in ECEF coordinates given by equation 4.

$$e = \frac{x_u u_x + y_u u_y + z_u u_z}{\sqrt{x_u^2 + y_u^2 + z_u^2}} \quad (4)$$

Matrix M2 is given by

$$M2 = -\omega_s^2 I_{3 \times 3} - (k_2 - 3\omega_s^2) x \Pi \quad (5)$$

where ω_s is the Schuler period, which is approximately 84 minutes, that takes into account the pendulous nature of accelerometer based data that is influenced by earth gravity. The parameter k_2 is another vertical state damping coefficient. Matrix M3 is given in equation 6.

$$M3 = \begin{bmatrix} 0.0 & 2\Omega & 0.0 \\ -2\Omega & 0.0 & 0.0 \\ 0.0 & 0.0 & 0.0 \end{bmatrix} \quad (6)$$

The parameter Ω is the angular velocity of the earth which is approximately 15 degrees per hour. Matrix M4 couples in the specific force vector through the influence of the tilt angles and is given by

$$M4 = \begin{pmatrix} 0.0 & -f_z & f_y \\ f_z & 0.0 & -f_x \\ -f_y & f_x & 0.0 \end{pmatrix} \quad (7)$$

where (f_x, f_y, f_z) are the components of gravity in the ECEF coordinate frame. Matrix M5 is the matrix which couples earth rate data into the tilt states and is given by equation 8.

$$M5 = \begin{pmatrix} 0.0 & \Omega & 0.0 \\ \Omega & 0.0 & 0.0 \\ 0.0 & 0.0 & 0.0 \end{pmatrix} \quad (8)$$

Sub-matrices M1, M2, and M4 are time varying and contain variables that introduce non-linearities into the filter equations. The effects of non-linearities are due to rapid changes in the states.

The final matrix, M6, is the matrix which relates the clock phase and clock frequency errors and is given by equation 9.

$$M6 = \begin{pmatrix} 0.0 & 0.0 & 1.0 \\ 0.0 & 0.0 & 0.0 \end{pmatrix} \quad (9)$$

The state dynamics matrix is used to calculate the discrete state transition matrix using a truncated Taylor Series expansion given in equation 10. The state transition matrix is used to propagate the covariance matrix and the state matrix.

$$\Phi = I + F\Delta t \quad (10)$$

The eleven states estimated in the Kalman filter along with the initial values are given in Table 4. All states are referenced in the ECEF coordinate frame. The initial diagonal values of the covariance matrix are given in Table 5. The off-diagonal elements are all initially set to zero. The initial measurement noise matrix diagonal elements are given in Table 6. Finally, the process noise matrix is given in Table 7.

Table 4. Filter States and Initial Values.

Filter State	Units	Initial Value
X Position Error	meters	3.0
Y Position Error	meters	3.0
Z Position Error	meters	3.0
X Velocity Error	meters/sec	0.1
Y Velocity Error	meters/sec	0.1
Z Velocity Error	meters/sec	0.1
X Tilt Error	radians	0.007
Y Tilt Error	radians	0.002
Z Tilt Error	radians	0.00284
Clock Phase Error	seconds	2.032e-11
CLK Frequency Error	seconds	1.02e-13

Table 5. Initial Covariance Matrix Diagonals

element	scale	value	units
P(1,1)	x	9.0	meters ²
P(2,2)	y	9.0	meters ²
P(3,3)	z	9.0	meters ²
P(4,4)	v _x	0.01	(meters/sec) ²
P(5,5)	v _y	0.01	(meters/sec) ²
P(6,6)	v _z	0.01	(meters/sec) ²
P(7,7)	ψ _x	4.0e-9	degrees ²
P(8,8)	ψ _y	4e-6	degrees ²
P(9,9)	ψ _z	8e-6	degrees ²
P(10,10)	σ _p	2e-10	degrees ²
P(11,11)	σ _f	1e-12	degrees ²

Table 6. Measurement Noise Values

element	value	units
R(1,1)	33.0	meters ²
R(2,2)	33.0	meters ²
R(3,3)	33.0	meters ²
R(4,4)	33.0	meters ²
R(5,5)	0.01	(meters/sec) ²
R(6,6)	0.01	(meters/sec) ²
R(7,7)	0.01	(meters/sec) ²
R(8,8)	0.01	(meters/sec) ²

Table 7: Process Noise Matrix Diagonals

element	state	value	units
$Q(1,1)$	x	0.0	m^2/sec
$Q(2,2)$	y	0.0	m^2/sec
$Q(3,3)$	z	0.0	m^2/sec
$Q(4,4)$	v_x	$1e-7$	$(m/sec)^2/sec$
$Q(5,5)$	v_y	$1e-7$	$(m/sec)^2/sec$
$Q(6,6)$	v_z	$1e-7$	$(m/sec)^2/sec$
$Q(7,7)$	ψ_x	$1e-10$	$radians^2/sec$
$Q(8,8)$	ψ_y	$1e-10$	$radians^2/sec^2$
$Q(9,9)$	ψ_z	$1e-10$	$radians^2/sec$
$Q(11,11)$	a_p	$1e-10$	$radians^2$
$Q(12,12)$	a_f	$1e-12$	$radians^2$

The final information to be presented is the error model which was used to generate the corrupted trajectory files. The IJB error model information input into the INERCA covariance analysis run is given in Table 8.

Table 8. INS Error Model.

Performance Parameter	Units	1 Sigma Value
Gyro		
Bias	Deg/Hr	0.0035
Temperature Markov Bias	Deg/Hr	0.002 (1 Hr time constant)
Scale Factor Uncertainty	PPM	2.0
Orthogonality	Arc-Sec	1.0
Random Noise	Deg/ $\sqrt{\text{Hr}}$	0.002
Misalignment	Arc-Sec	1.0
Accelerometer		
Turn-on Transient	μg	7 (7 Min. time constant)
Bias	μg	30.0
Scale Factor Uncertainty	PPM	175.0
Scale Factor Asymmetry	PPM	20.0
Orthogonality	Arc-Sec	5.0
Random Noise	FPS/ $\sqrt{\text{Hr}}$	5 (25nm correlation distance)

REFERENCES

- [1] D.A. Tazartes and J.G. Mark, "Integration of GPS Receivers into Existing Inertial Navigation Systems," *Journal of The Institute of Navigation*, vol. 35, No. 1, pp. 105-119, Spring 1988.
- [2] Joseph K. Solomon, Capt. USAF, *Development of the Extended Kalman Filter for the Advanced Completely Integrated Reference Instrumentation System (CIRIS)*, Master's Thesis, Air Force Institute of Technology, Wright Patterson AFB, Ohio, March 1989.
- [3] Prasun K. Singa, Dirk Dedoes, Marvin May, "INS Alignment Using GPS Phase III User Equipment Computed Corrections," *Proceedings of ION GPS-90 Third International Technical Meeting of the Satellite Division of The Institute of Navigation*, September 1990.
- [4] F.R. Bletzacker, D.H. Eller, T.M. Forgette, G.L. Seibert, J.L. Vavrus, and M.D. Wade, "Kalman Filter Design For Integration of Phase III GPS with an Inertial Navigation System," *Proceedings of the National Technical Meeting of the Institute of Navigation*, January 1988.
- [5] Mark A. Sturza, Alison K. Brown, and Joseph C. Kemp, "GPS/AHRS: A Synergistic Mix," *NAECON Proceedings*, May 1984.
- [6] A. Gelb, Technical Staff, The Analytical Sciences Corporation, *Applied Optimal Estimation*, Cambridge and London: The MIT Press, 1988.
- [7] R.E. Kalman, "A New Approach to Linear Filtering and Prediction Problems," *J. Basic Eng.*, pp. 35-46, March 1960.
- [8] R.E. Kalman and R.S. Bucy, "New Results In Linear Filtering and Prediction Theory," *J. Basic Eng.*, pp. 95-108, March 1961.
- [9] Gregory V. Fountain and Gary A. Matchett, *GPS Applications to Conventional Weapons Guidance*, The Analytical Sciences Corp., Reading, Mass., June 1989, Technical Report TR-5486-1, April, 1989.
- [10] John Shearer, users manual, *Inertial Navigation Error Covariance Analysis (INERCA)*, Fort Walton Beach, Fla.: General Research Corporation, February 1989.

AN INEXPENSIVE PC BASED GPS SATELLITE SIGNAL SIMULATOR

Charles Rodgers
Adroit Systems, Inc.
809 N. Royal St.
Alexandria, VA 22314

ABSTRACT

Under a contract with the Strategic Defense Command, Adroit Systems, Inc. has developed and prototyped an inexpensive GPS satellite signal simulator. The signal simulator produces the L1 C/A code signal. GPS signal simulators are used in GPS equipment testing, and for GPS applications research. The signal simulator is designed for use with the user's personal computer (PC). The PC is used to generate the 50 Hz. navigation data and to program the C/A code generating microchip. Generating the navigation data in the PC allows for complete flexibility in setting different constellation scenarios, unlike other low priced simulators that use a fixed navigation message contained on a ROM. The PC accomplishes its tasks through a digital I/O board and with proprietary software. The C/A code is generated by a C/A coder microchip. This chip also provides the timing signal that controls the computer output. The coder, mixer, carrier oscillator and support chips are located externally. The prototype has been tested with several GPS receivers.

Adroit Systems has also written additional proprietary software for the simulator that aids in the positioning of simulated GPS constellations and in scaling and encoding the navigation data.

INTRODUCTION

There are numerous GPS satellite signal simulators on the market. They range in price from about \$10,000 to \$300,000. The most expensive systems can simulate simultaneously most of the satellites that are currently active. They produce both P and C/A code, and both the L1 and L2 carrier frequencies. The navigation message can be modified to position the constellation as the user desires. It also can be programmed to have built in ephemeris errors. The carrier frequency's doppler shift can be controlled to simulate not only the satellites' movement relative to the earth, but to simulate a receiver's dynamics as well. At the low end of the scale, the simulators produce a single satellite's C/A code signal on the L1 band. The navigation message containing the orbital parameters and the constellation almanac are fixed in Read Only Memory (ROM) chips. This fixed message usually repeats every

thirty seconds.

Adroit Systems, Inc. needed a satellite signal simulator for tests we were performing on GPS receivers. The tests were part of an effort funded by the Strategic Defense Initiative Organization (SDIO) to develop a GPS Attitude Determining System (ADS). We looked over the simulator market and determined that we needed more flexibility than was available from the lower priced models, and something much less expensive than the premium models. After doing some research, we came up with an original and economical idea for a simulator design that would meet our needs. It would utilize the HP 8660 microwave signal generator and IBM XT clone we already had, and about \$1000.00 in new equipment.

REQUIREMENTS

Adroit needed a stable, clean satellite signal to use for the receiver differential phase measurement tests. These tests were to quantify the accuracy of GPS receivers' measurements of differential carrier phase. Differential carrier phase measurements are used to determine attitude from GPS signals.

As an accurate signal carrier source and phase modulator was already available, the first prototype of the simulator had only to produce the navigational data and C/A code. Therefore, the prime requirements were that the digital portion of the signal have the correct format, content, and signal quality. The simulator was to be designed to produce C/A code for all possible satellites. It also would have a navigation message that could be changed for any desired satellite constellation or nario. Software was to be written to place and move the satellites, and to calculate and encode the navigation data parameters. The simulator also was to be designed modularly, so additional channels could be added as needed. These types of flexible features are not available on lower cost commercial GPS signal simulators.

GPS SATELLITE SIGNAL STRUCTURE

The L1 GPS satellite signal is spread spectrum, and is composed of two digital code streams and a digital navigation message that modulate the 1.57542 GHz carrier. The precise or P code is a pseudo-random binary code with a chip rate of 10.23 Mbps. The clear access or C/A code is a binary Gold code with a chip rate of 1.023 Mbps and a period of 1 millisecond. Gold codes have the property that any two codes have a very low cross correlation.

Figure 1 shows how the C/A code for satellite 2 may be generated. G1 and G2 are two ten stage tapped shift registers. At each time increment, the data in each register shifts. The now empty first register is filled by the binary addition of various tapped registers. The registers to be tapped to fill the first register for G1 and G2 are indicated in the figure. These taps

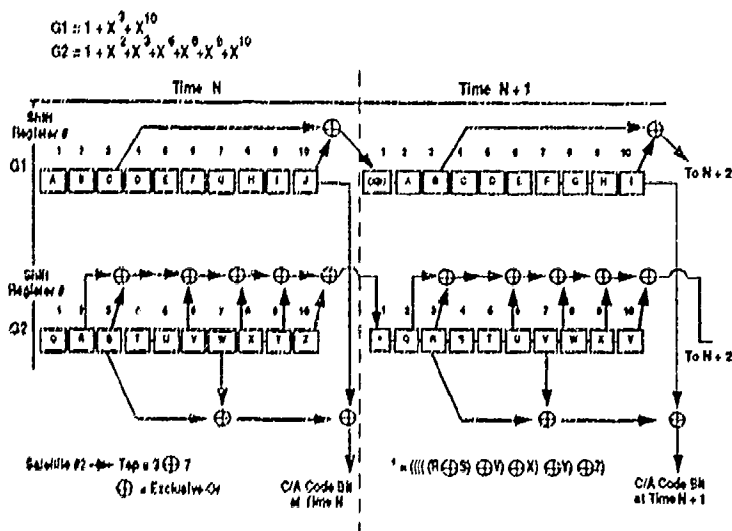


Figure 1: C/A Code Generation-Satellite #2

NAVJAGUS-4

are the same for all the C/A codes. The difference in the codes from satellite to satellite is determined by the way G2 is tapped to produce the bit that is binary added to the last register of G1 to produce the C/A code bit. The G2 taps are different for each satellite. The complete set of taps for all the GPS satellites can be found in the GPS Interface Control Document-200 (ICD-GPS-200).

The navigation message consists of a 50 bps, 1500 bit binary data stream. The navigation message contains information about the satellite time, position, and health. The orbital parameters are scaled, and the entire message is parity encoded. The details of the message format can be found in the ICD-GPS-200. Before it can calculate its own position, the receiver must decode this message to calculate the satellites' positions accurately.

The L1 carrier is split into two signals, orthogonal in phase. Each orthogonal version of the carrier is modulated by one of the codes, and both versions have the navigation message. To determine the distance to a satellite, a GPS receiver compares an internally generated code to the actual received code. The offset between these two versions of the code is a measure of the time it takes for the signal to travel from the satellite to the receiver. The receiver then multiplies the time by the speed of light to obtain the distance.

Figure 2 shows the spectra of the complete L1 signal². The equation for the complete L1 signal is:

$$S(t) = XP(t)D(t)\cos(\omega t + b) + XG(t)D(t)\sin(\omega t + b)$$

where

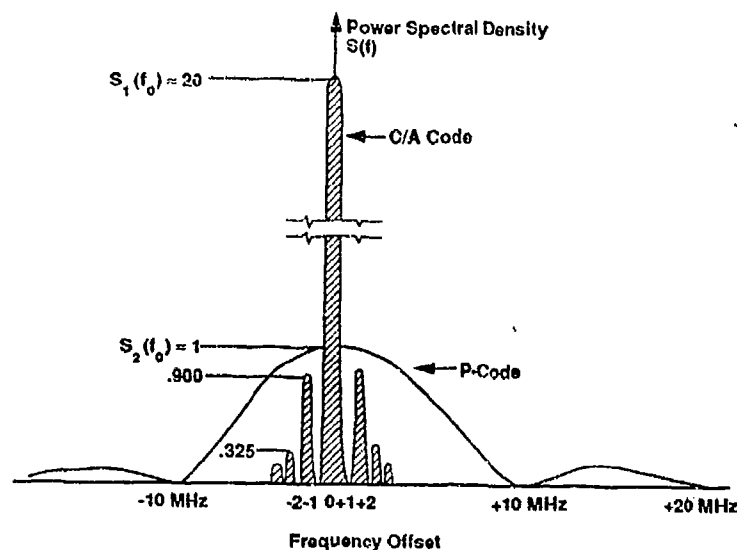


Figure 2: Spectra of L1 Signal

VU1781UG558

$XP(t)$ = the P code
 $XG(t)$ = the C/A code
 $D(t)$ = the navigation data
 w = L1 carrier frequency (radians/sec)
 b = phase noise.

The GPS receivers we were using for our ADS development were L1 C/A code receivers. They do not utilize the P code. Therefore, the equation for the signal we would be simulating could be simplified to:

$$S(t) = XG(t)D(t)\sin(wt + b).$$

HARDWARE DESIGN

Figure 3 is a functional diagram of the prototype GPS signal simulator. The Numerically Controlled Oscillator (NCO) is programmed to produce the master clock signal for the C/A coder. An alternate, lower priced, design uses a fixed frequency source in place of this NCO. This is the design used in the testing we have done to date. The C/A coder generates the selected C/A code, the computer outputs the navigation data. The two data streams are synchronized, then combined in an exclusive-or gate. A phase modulator uses the data stream to modulate the L1 carrier. The major components are discussed in the sections that follow.

The PC and the Digital I/O Board

The key to keeping the hardware costs down and still maintaining the desired flexibility over the test scenarios was our laboratory personal computer (PC). It was used to generate the navigation data and to control the other components. To do this,

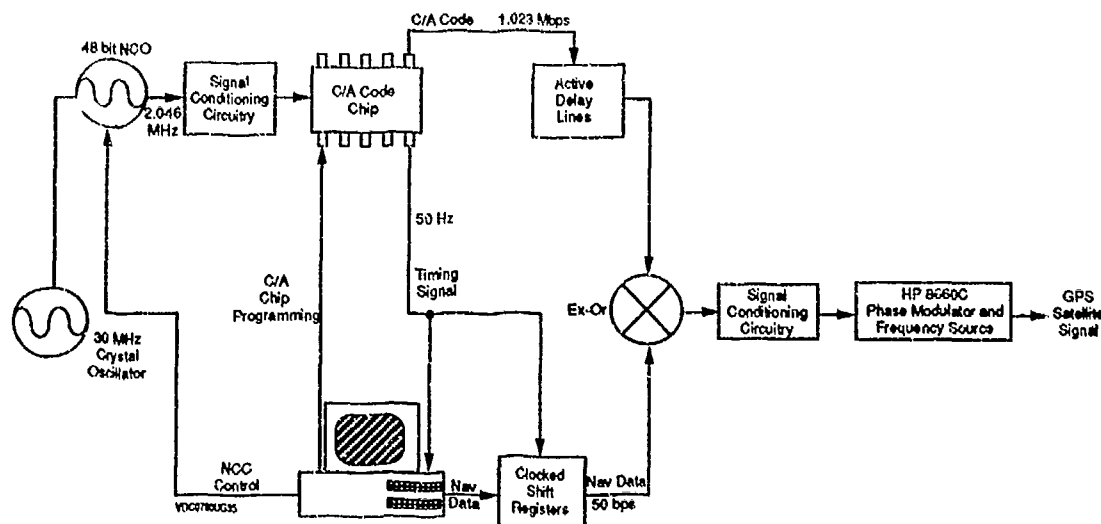


Figure 3: Prototype GPS Satellite Signal Simulator Functional Diagram

I equipped it with a commercially available, digital input/output (I/O) expansion board. The board was a MetraByte PIO12 24 bit parallel interface. This board has three separately addressable, eight bit ports that can be configured for either input or output. In addition it contains a line for handshaking the data transfer with an external timing signal. The data exchange is controlled by programs written in C, resident on the PC.

To program the NCO, six eight bit data registers are sequentially filled. The address of the active register requires three other bits, and the write enable, reset, and load data lines require three more. A single eight bit port was configured for output, and used to program the NCO data registers. Another port was used to manipulate the control lines. In the prototype, the NCO programming was done before the simulator began producing the GPS signal.

The I/O board ports are then reconfigured to program the C/A coder chip and to output the navigation data. The coder chip has six six bit data registers, three address lines, and a write enable line. Two ports are used for this. The last eight bit port is available for the navigation data.

The navigation data is stored in a data file on the PC's hard drive. The data in the file is generated and encoded before the simulation begins by proprietary software. The I/O board has an interrupt circuit that, upon receiving an activating pulse from the C/A code chip, addresses the PC interrupt handler. Unless the PC is executing a higher priority interrupt, it immediately stops what it was doing and goes to the real-time program designated by the

interrupt handler. This program accesses the data file and outputs the appropriate data bits. A single port of the I/O board can, potentially, generate the navigation data for eight satellites.

C/A CODER

Neither the board nor an 80286 equipped PC is fast enough to output the C/A code because of its 1.023 MHz chip rate. The STEL 1023 C/A coder chip was located to generate the C/A code and to provide the timing signals for synchronizing the two data streams. The coder requires a master clock frequency double the C/A code chip rate. It can be programmed to produce any of the planned satellites' code. It also provides timing outputs at the chip rate, the C/A epoch rate (1 KHz), the navigation data rate (50 Hz), and the X1 epoch rate (2/3 Hz). In the simulator design, the 50 Hz timing signal is used to initiate the navigation data interrupt. It also controls the state change of the flip-flops that make up the shift register.

Clocking Circuits

Another major component of the simulator was an accurate, stable clocking circuit to provide the precise timing necessary. The heart of this circuit was a 48 bit numerically controlled oscillator. The 48 bit resolution over the 15 MHz oscillator range gave us the microradian accuracy necessary to match the code chip rate to the simulated carrier doppler shifts. A 30 MHz crystal is used as the master oscillator for the NCO. The PC utilizes an interactive program written by Adroit to program the NCO for the desired clocking frequency. The normal clocking frequency without doppler is 2.046 MHz.

The alternate design that uses the fixed frequency source is not as flexible as the NCO design. The C/A coder master clock frequency can not be adjusted to match the doppler of the carrier. This causes problems for some receivers. See the test results section for a more complete discussion.

Synchronization and Signal Conditioning Circuits

The computer navigation data signal had an intolerable jitter of several microseconds due to the variable processing steps in the computer. To alleviate this problem the navigation data is stored in a clocked shift register after leaving the computer. This shift register is just a clocked flip-flop stage, controlled by the timing signal from the C/A coder. The 20 millisecond delay allows ample time for the bit to become stable before it was passed to the ex-or gate. It does not matter that the data is delayed one bit because during that 20 milliseconds the C/A code repeats 20 times. The important thing is if the beginning bit of the C/A code starts at the beginning edge of the navigation bit.

The C/A code bit and the timing signal that releases the navigation data leave the chip at the same time. However, the delays in the lines and shift register cause the two data streams to be out of synchronization. The period of a C/A code bit is about 977 nanoseconds. Therefore, we wanted the data streams to be synchronized to a maximum of 10 nanoseconds difference between the beginning of the bits for each data stream. To do this, active tap delay lines were used.

The synchronized data streams are combined in an exclusive-or gate. The signal is then conditioned through a level shifting circuit (Fig. 4). This level shifting circuit provides variable signal levels and DC offset to produce the optimum signal for phase modulating the carrier.

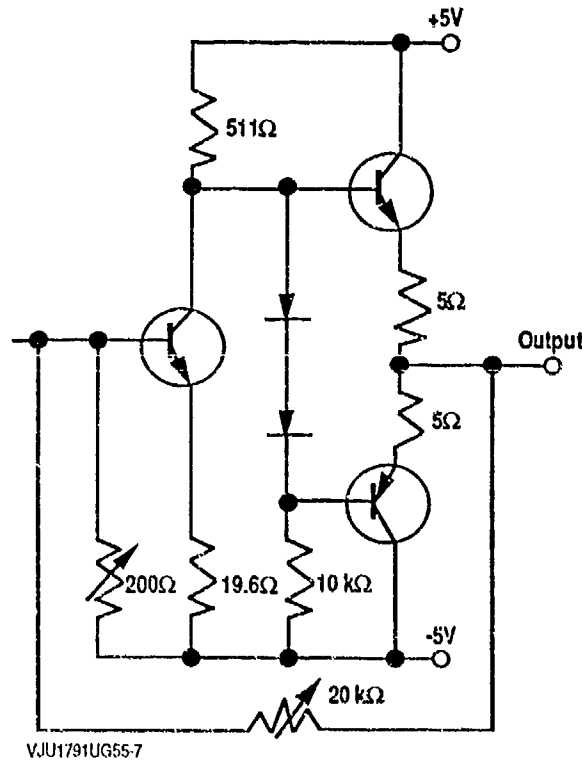


Figure 4: Level Shifting Circuit

The Phase Modulator and L1 Frequency Source

The data stream is used to phase modulate the carrier. For our laboratory prototype, a HP 8660C signal generator and plug in phase modulator was used for the carrier modulation. In place of that in future generations, a separate frequency source and modulator will be used. Preliminary investigation of these additions has indicated that even after these components are added, the cost is still less than half of the lowest priced

commercial model.

SOFTWARE

To make the simulator work some custom programs had to be written. All programs were written in Microsoft C except Satpos. It was written in Microsoft Fortran. A list of the programs and a brief synopsis of each follows.

- Bintio - This program sets up the PC interrupt handler to output the navigation data. It also configures the digital I/O board. After each bit of the message is transferred, it clears the interrupt, and resets the computer to its previous state.
- Cacode - This program reconfigures the digital I/O board, then programs the C/A coder chip by writing sequentially to six data registers of six bits each. Cacode is interactive and prompts the user for the desired satellite.
- Cagen - Cagen generates the complete C/A code for all satellites. It was used to locate C/A code strings during simulator testing. For the method see figure 1.
- Clk - This program controls the output of a variable frequency simulated clock signal from the PC. It was used in testing.
- Nco - This program first reconfigures the digital I/O board. Then it prompts for the master oscillator frequency and the desired output frequency. The NCO is then programmed by filling six eight-bit data registers on the NCO board.
- Parity - Parity takes raw navigation data, already in two's compliment form and then parity encodes it for the GPS navigation message. This program prompts the user for the blocks of binary data.
- Constel - This program uses GPS almanac data to calculate the orbital movement of a GPS satellite. This program is used to position the desired simulated GPS constellation.
- Ephcalc - Ephcalc uses GPS ephemeris data to calculate a satellite's position in three dimensional, fixed, earth centered coordinates (x, y, z). It is useful in setting up test scenarios.
- Satpos - Satpos is the only program written in Fortran. It was written in Fortran because it calls another routine written for Fortran calls only. It converts an orbit specified in one of four coordinate systems to the other

three coordinate system parameters. The coordinate systems used are geocentric classical, cartesian, spherical, or geographic. In addition, the user may center the output coordinate systems about the user's position. As it is used in positioning the simulator's

satellites, it scales the classical parameters according to the scale factors used in the navigation message. It then converts them to binary two's complement form.

TEST RESULTS

During this testing the NCO was replaced by a fixed frequency source at 2.046 MHz. The data stream production for the satellite signal worked well. A data analyzer confirmed that the navigation data and the C/A code were consistently synchronized to less than 10 nanoseconds. The analyzer was also used to compare the C/A code being generated by the simulator to the C/A code produced by the software routine Cagen. The simulator was able to produce all 32 satellite C/A codes. The pulse shape and level out of the ex-or gate were nearly optimum. To determine the optimum voltage and polarity level of the data being used to drive the phase modulator, we experimented with shifting a positive voltage data stream to bipolar, and then negative voltage data. We found that the best phase modulation could be obtained with a signal of about 1.25 volts peak to peak, and a "0" level of -0.25 volts. Using this signal level and a square wave to calibrate the modulator, we achieved greater than -40 dBs of carrier suppression. The greater the carrier suppression, the closer to a perfect 180 degree phase reversal there is from a "1" to a "0," or vice versa.

The resultant simulated signal was tested on three GPS receivers, two different versions of the Ashtech XII and one TI-420. The signal was both radiated from an antenna, and fed by cable directly into the antenna ports. The Ashtech machine immediately locked on to the signal and recognized the C/A code as belonging to the satellite we had selected for simulation. It then decoded the navigation message, which caused it to reset its internal time to match the time we had implanted in the navigation message. Finally, the Ashtech receiver began making differential phase measurements between the split signal. Numerous subsequent tests demonstrated that the Ashtech receiver worked 100% of the time with the simulated signal.

The TI-420 receiver only was able to lock to the simulated signal twice during these tests. At those times it did decode the navigation message, and change its on board time. Adroit is convinced that the problem is due to the different tracking loops in the two machines. The TI machine employs a dual aided tracking loop, the Ashtech machine uses a single input tracking loop. The TI machine attempts to track both the C/A code and the carrier separately. It uses a code tracking loop and a carrier tracking

loop that issue separate error corrections to the tracking electronics. If the code chip frequency does not exactly match the carrier doppler frequency, the two loops issue conflicting instructions to the tracking electronics. This causes oscillation in the tracking loop, and as a result the machine cannot lock onto the signal. The Ashtech machine does not have this problem because it only tracks the C/A code to lock onto the signal.

This difference between the code and carrier doppler could have been eliminated if the NCO had been available as the design called for. The NCO could have been adjusted to microradian accuracy to match the C/A code rate to the carrier doppler.

In summary, the low cost GPS satellite signal simulator performs as it was designed. Many GPS receivers have the single tracking loop design so they can use the simulator even without the NCO. The design with the NCO will work with all receivers. Without the NCO, our hardware cost for the simulator, excluding the lab PC and signal generator, was about \$350.00. If the NCO had been included in that version, the cost would be \$700 more, still much less than commercial simulators.

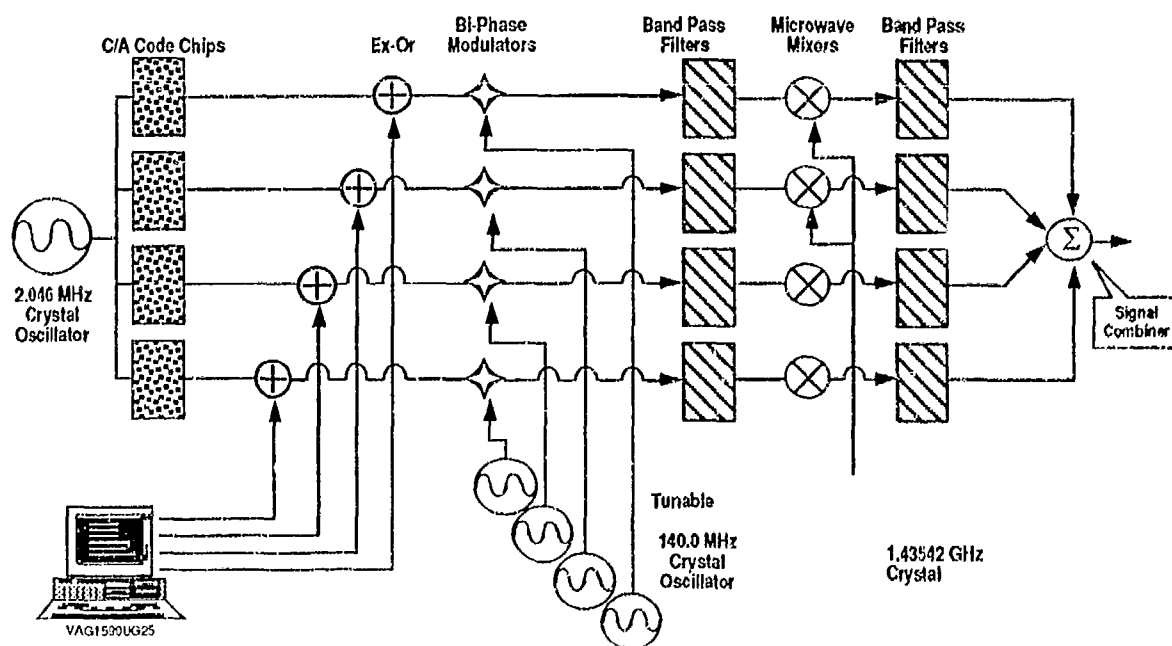


Figure 5: Proposed GPS Simulator Block Diagram
4 Channel

THE NEXT GENERATION

For the simulator to have commercial applications, a bi-phase modulator and microwave frequency source and mixer need to be integrated into the simulator. The simulator was designed to be easily expanded into a multichannel device. Figure 5 shows a proposed multichannel version. For each additional channel, a C/A chip, ex-or gate, and biphasic modulator would have to be added. We expect that the PC and the single digital I/O board could function for up to eight satellite channels. We estimate the cost to be about \$1000.00 for each channel.

In addition to the hardware refinement, the software needs to be integrated under a single, interactive shell program. The user would enter the scenario that is desired. The PC would automatically calculate the needed orbital and time parameters, then scale and parity encode the navigation data for the data file. The PC also would proceed with the programming of the components, and begin the signal generation.

ACKNOWLEDGMENTS

I would like to thank SDIO for the support, Rick Jurgens for turning me loose, Pat McCarthy for helping me tinker, and Leo Van for the interrupt program.

REFERENCES

1. System Specifications for Navstar GPS Space Segment / Navigation Users Interface, Interface Control Document - Global Positioning System - 300 (ICD-GPS-300), Nov. 30, 1987.
2. Spilker, Jr., J., "GPS Signal Structure and Performance Characteristics," Global Positioning System Papers, Vol. 1, The Institute of Navigation, 1980, pp. 20-54.
3. Van Dierendonck, A., et al, "The GPS Navigation Message," Global Positioning System Papers, Vol. 1, The Institute of Navigation, 1980, pp. 55 - 73.
4. Wells, D. et al, "Guide to GPS Positioning," University of New Brunswick Graphic Services, Fredericton, New Brunswick, 1987, pp. 6.1 - 6.8.

SECTION IV-A
INSTRUMENT TESTING

CHAIRMAN
JOHN H. BARNES
U.S. ARMY AVIONICS

ABSTRACT

A Practical Three Axis Autobalance Mechanism for Precision Centrifuge Applications

R.D. Marquess
Applied Motion Technology, Inc.
Concord, California

Rex B. Peters
Sundstrand Data Control, Inc.
Redmond, Washington

Laboratory test centrifuges are large rotating machines in which balanced operation presents special problems. They are normally operated with large user supplied masses attached, consisting of test items, fixture, ovens, cables, etc. Manual balancing techniques are imprecise, time consuming, and often bypassed. This situation commonly results in erroneous data, but can easily lead even to destruction of the centrifuge and portions of the laboratory. The effect is subtle. A centrifuge which is used to calibrate accelerometers can produce large errors in apparent linearity due to imbalanced shaking which is imperceptible to most operators. Imbalance forces also increase rapidly with increasing rotational speed, and can reach destructive levels surprisingly quickly.

The paper describes a practical solution to these problems. It is a three axis mechanism capable of canceling dynamic imbalance, as well as balancing errors along and across the arm. It uses a closed loop servo to position three sets of balance masses in response to two Sundstrand Q-FLEX® accelerometers mounted on the frame. The accelerometers provide a high signal-to-noise ratio motion reference which requires no external attachments. Synchronous demodulation of the two signals with appropriate phase and weighting functions provides signals for all three degrees of freedom. Nulling of this motion assures that the imbalanced forcing function has been nulled.

Operation is automatic and occurs under computer control during the centrifuge's acceleration time. Automatic shut-down occurs if the initial imbalance is out of range. The process of balancing to null during acceleration to speed is unique, and not only saves time, but also minimizes the effect of changes in the dynamics of the centrifuge as a result of installation or the way it is loaded.

The paper describes the initial application of this mechanism, to a large centrifuge delivered to Kelly Air Force Base in Texas. This centrifuge is designed to test a 150 pound package at a nominal radius of 48 inches up to 150g, and will autobalance mismatches up to 2 inches vertically, 1 inch horizontally, and 10 pounds end to end. The mechanism itself is described in detail: the hardware, the theory of operation, the performance expected, and experimental data to support the performance actually achieved.

1.0 INTRODUCTION

The Precision Centrifuge System (PCS) which was delivered to Kelly AFB in San Antonio, Texas in April, 1990, was designed to test a wide variety of test packages to a wide variety of requirements. Its payloads range from relatively fragile components with acceleration limits as low as 10 g, to 150 pound packages which must be tested at 150 g. Many of these packages contain inertial components which require greater precision than would be required for purely environmental testing.

Accurate balancing is necessary for the safe operation of a high g-pound centrifuge, and it is crucial to the accurate operation of a precision centrifuge. Maintenance of accurate static and dynamic balance on a centrifuge is best guaranteed by always testing with symmetrical loads. The logistics of the items to be tested on the PCS, as well as the expected diversity of test instrumentation, make that approach impractical. Accordingly, a key requirement was that the PCS should contain an automatic system for nulling out the effects of test item imbalance. Applied Motion Technology, Inc., had already developed a system which senses and servo balances centrifuge arm imbalance in three degrees of freedom: end to end, side to side, and up and down. This system was adapted to the needs of the Air Force.

With test loads not to exceed 150 pounds located at a nominal 48 inch test radius, the PCS has been designed to servo balance mismatches in excess of 1 inch side to side CG mismatch, 2 inch up and down CG mismatch, and 10 pounds end to end weight mismatch. A unique balancing sequence which autobalances continually as the centrifuge is accelerated from rest allows the centrifuge to balance a worst case load without tripping the 10 millig fail safe imbalance shut-down system.

After completion of the autobalance routine at 10 g, the centrifuge will not exceed 3 millig shake at 150 g. This limit corresponds to a linearity error less than 0.13 microg/g^2 squared, and the PCS routinely balances to better than 0.10 microg/g^2 . This performance meets the needs of the Air Force, but does not yet represent the full performance potential of the system.

2.0 SYSTEM DESCRIPTION

The Centrifuge consists of a Test Stand which encloses the rotating Arm, spindle, test connectors and slip rings, 50 HP DC motor and mechanical drive. A separate Control Console is used to operate/control all aspects of the Precision Centrifuge System (PCS), including the door latches. The rotating Arm houses the three motor driven moving mass mechanisms used to dynamically balance the Arm and test objects. Cables are used to connect the Control Console to the Test Stand and via a second set of slip rings, to the Arm. The principal part of the PCS discussed in this paper is the AUTOBALANCE System: the MODEL AMT-11.0-SP-1-SSAB Automatic Balancing System.

Functionally, the system can be separated into two sections: Acceleration Profile Generation and the Moving Mass Servos. The Moving Mass servos are in turn composed of the moving masses themselves, the motion sensing devices, and the analog electro-mechanical system which connects them. The moving masses provide the means to physically reconfigure an unbalanced arm, while the motion sensing devices provide the means to measure the physical motion that is being controlled.

2.1 Moving Masses

The general configuration of the moving balance weights is shown in Figure 1. The weights are in pairs so that the center of the arm is left open for the slip ring assembly. The

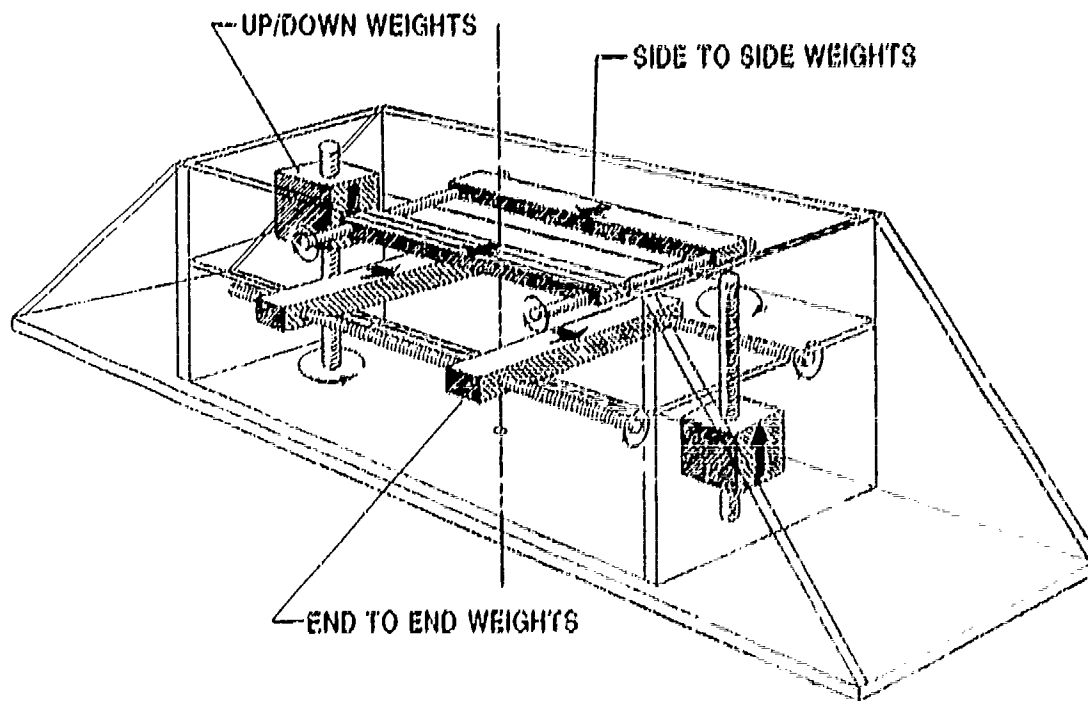


FIGURE 1: Balance Weight Configuration

weights are moved by threaded rods which in turn are driven by worm gear assemblies. The end-to-end and side-to-side balance weights are geared to move together in the same direction. The up/down balance weights move differentially, one up and the other down. The use of worm drives produces a system which cannot be back-driven. Once balance is achieved, the autobalance system can be electrically disconnected, and will function passively. This feature contributes to system safety since it is physically impossible for electrical faults, even massive power transients, to cause the system to run away while the centrifuge is rotating at high acceleration.

2.2 Motion Sensing

The motion sensors employed are a pair of Sundstrand Data Control Q-FLEX® Accelerometers. These accelerometers are hard-mounted to the Test Stand, actually to the spindle support structure. One of the sensitive axes is aligned with the length, and the other crosswise with the Test Stand frame. The accelerometers are scaled in the hundreds of volts per g range and the outputs are AC coupled. The operating frequency band is in the quietest part of the Q-Flex spectrum; self-generated noise is approximately $1/\mu g$ RMS (Reference 1). The locations of the two accelerometers are shown in Figure 2.

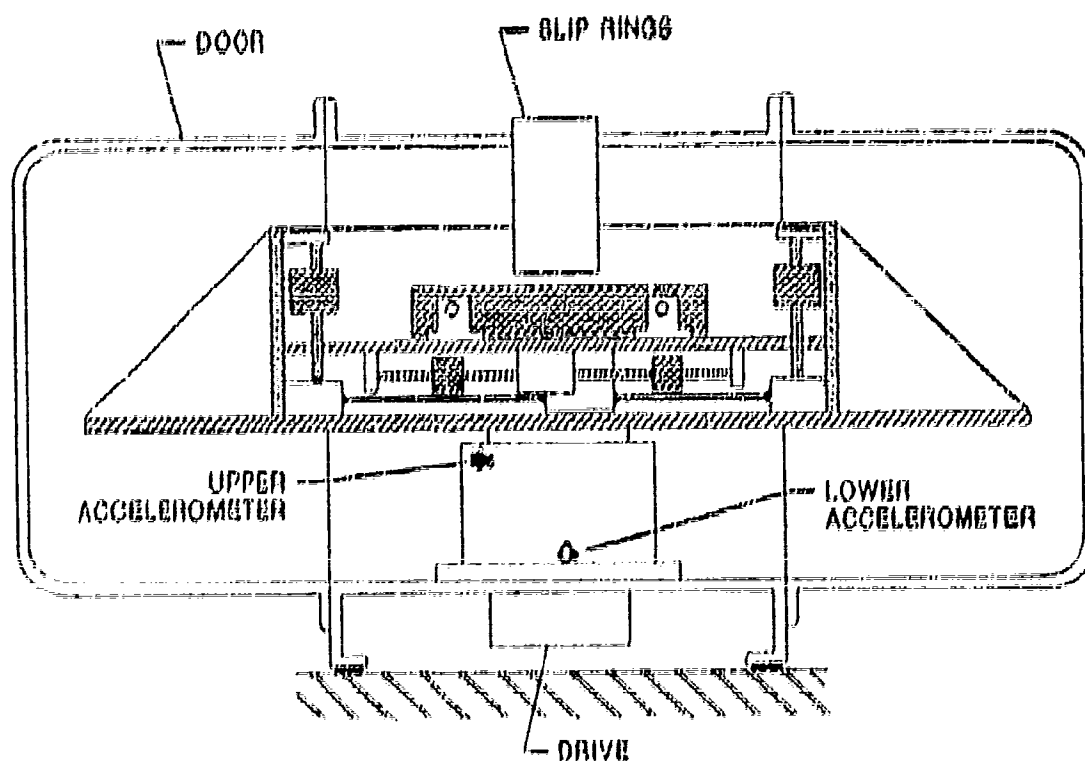


FIGURE 2: Autobalance Physical Layout

2.3 Autobalance Profile

The Centrifuge generated acceleration is a low level (nominally 10 g peak) profile which is computer controlled. As previously described, the accelerometer scaling allows this mild environment in which to accomplish the dynamic balance. This is a tradeoff area, if the balancing routine were raised to say 40 g, the increased imbalance motion would provide a larger signal to noise ratio and increased performance might result. Balancing at 10g provides better performance than is required for most applications, and is compatible with the testing of instruments that will not tolerate higher accelerations.

2.4 Control Console

The Control Console includes the low level accelerometer signal processing circuitry. The outputs from this section are the inputs to three linear amplifiers (Electrocraft LA 5600 DC Motor Drives). Also located in the Control Console are the main Computer (IBM PS/2 Model 60), the "watchdog" computer (Microsys ECX-188), and all other necessary electronic hardware for operation of the Centrifuge.

The system operating software CENTCON was developed initially in 1985 by Applied Motion Technology and has been continuously upgraded. The AUTOBALANCE sequence is an option on the MAIN MENU of CENTCON. When this routine is selected, the computer operates the machine and the acceleration profile is of 120 seconds duration. The 10 g peak level of the profile is based on the nominal 48 inch Test Radius. This profile is used regardless of the Test Radius specified by the operator when entering the data in the CHECKLIST.

2.5 Signal Processing

The signals from the two accelerometers are demodulated with respect to the position of the rotating Arm by using a one pulse per revolution output signal to determine the "reference end". By counting pulses from a 600 pulse per revolution output, the signals are sampled synchronously with the motion of the Test Stand due to an Arm imbalance. These signals will track, one 90 degrees later than the other, if the motion is caused by the center of the rotating mass being located off center towards either end or side.

If the Arm including the test fixtures and device being tested was very thin, a reasonable degree of balance would be obtained with only end to end and side to side compensation. Centrifuge Arms that are relatively thin have another problem however, that is very detrimental when precision testing is required, the phenomenon is known as "arm droop".

The real world of Centrifuge Testing usually involves quite substantial fixtures, especially when testing larger assemblies at higher g levels. Many times the center of mass of the test object (fixture, unit under test and cables) is up to 12 inches above the mounting

platform surface. It is also a fairly rare occurrence to find a dummy unit with a matching fixture being used as a counterweight. All these facts of life cause the vertical displacement of the centers of mass to differ considerably.

To accommodate this problem, the Applied Motion Technology AUTOBALANCE System also incorporates another degree of mass movement, that being the "up/down" compensation. The demodulation process for this axis involves the properly phased and tailored difference of the two accelerometer signals. The "end to end" mass servo uses the sum of the two signals also properly phased and weighted. The "side to side" only requires the properly processed signal from one of the accelerometers. The level of performance required of this system does not require an "up/down" compensation along the cross or "side to side" axis, but some improvement could probably be made in performance if this capability was included.

A block diagram of the present 3 degree of freedom system is shown in Figure 3.

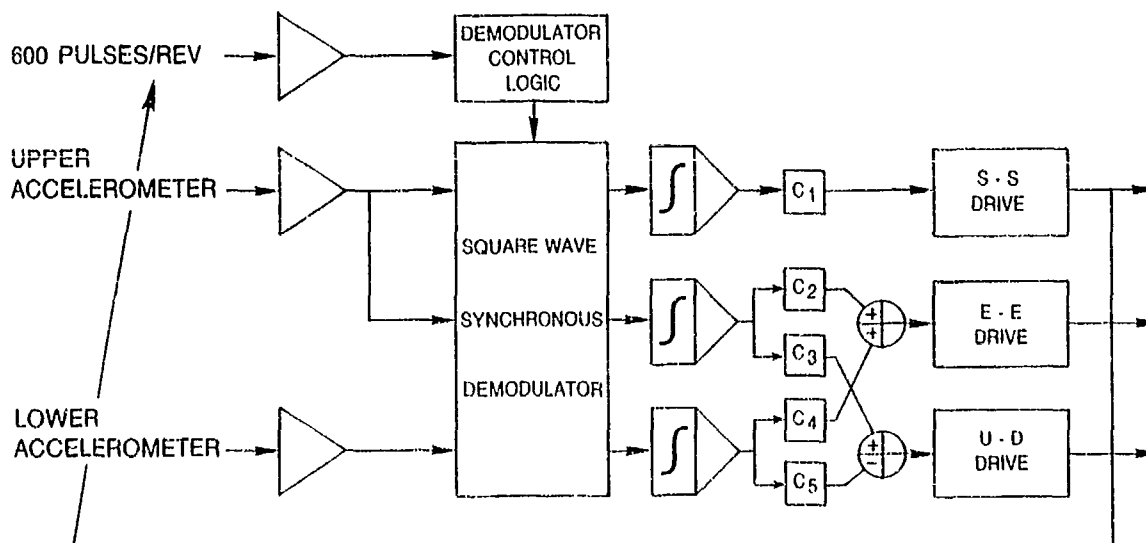


FIGURE 3: Autobalance Block Diagram

2.6 Servo Amplifiers

The outputs of the demodulation process are inputs to the DC motor drive amplifiers. These three units are capable of a continuous 22 Amp output, and with feedback from the tachometers, are set to control the maximum speed of the servo motors. We limit the motor speed to 1800 RPM due to worm gear manufacturer recommendations.

The other input signals to the servo amplifiers come from D/A converters in the IBM when "preset" positions are used.

2.7 Weight Position Readouts and Storage

There are three panel meters labeled SIDE TO SIDE, END TO END and UP / DOWN on the Equipment Rack on the right side of the Control Console. These meters are configured to be centered when the movable masses are at the centers of their respective travel. The CHECKLIST subroutine in CENTCON asks for and must receive an affirmative answer that the operator has completed "gross balancing". In this context, "gross balancing" would mean a difference of not more than 5 lb. end to end at the nominal 48 inch radius. If this is the case, the needle on the "end to end" weight meter will not indicate more than 50% of scale in either direction from center at the completion of the AUTOBALANCE routine. If in fact, any meter moves to beyond 60% of scale, the setup was not "gross balanced" carefully and the Operator's Manual suggests the routine be repeated. This involves performing a "fine tune" by using the positions of the weights at the end of the first routine as an indication of the magnitude and direction of the gross imbalance. If this procedure is followed, the System will properly balance a 10 lb. difference end to end at the nominal radius.

At the completion of the AUTOBALANCE routine, the position of the three mass sets is shown on the panel meters. This information can also be stored in the computer's memory as "presets". If the same setup is to be used at a later date, these stored positions can be called up to pre-position the weights without actually running the AUTOBALANCE routine. Each channel utilizes an 8 bit A/D with corresponding D/A for position storage and pre-positioning. The travel limits are also controlled by the computer since limit switches are thought to be an unreliable complication.

2.8 Interconnections

The electrical connections between the accelerometers and the Control Console are through cables (with shielded leads) between the two assemblies. The connections between the servo amplifiers and the DC Motor-tachometers and Position Readout Potentiometer are also through shielded cables and, within the Test Stand, slip rings are required. There are also spare rings on the lower set to allow Arm temperature monitoring.

2.9 Rotating Arm Configuration

The design of the Arm was driven by two main requirements. First, the stress margin would be at least 4:1 under any worst case condition imagined. With this design, that margin is exceeded with a test object weight of 150 lbs. and the effective center of mass 18 inches above the mounting platform with a Centrifugal Acceleration of 150 g. This condition also assumes a fixture that has a zero area footprint or none inboard from the 48 inch radius. Under more realistic conditions, the stress margin is in excess of 60:1. This was not a safety requirement, rather the lower limit necessary to maintain an "Arm stretch coefficient" of less than 0.5 ppm/g @ 22,500 g lbs.

The second in house requirement of the Arm design was that it must incorporate the AUTOBALANCE mechanisms within and as a part of the structure. Since our customers want their individual requirements incorporated in the Centrifuge, considerable effort was expended to include provisions for RF and liquid rotary joints, plumbing capability for Temperature Chambers and in general a versatile design with good access for service.

One of the main requirements our customers usually have is a high "onset rate". This machine will attain 150 g within 13 seconds from a dead stop with 150 lbs. on each end of the Arm. We therefore use high strength Aluminum Alloy for the Arm material. Applied Motion Technology does not use any welding on any part of the Arm. Material properties after welding are difficult to be certain about and the risks are thought to be unacceptably high. The construction techniques utilized are that of dowel pins and threaded fasteners (all with certs). This allows a structure that exhibits the same sort of rigidity as a weldment and it can be disassembled for service.

The general configuration of the Arm interior is that of a full length platform with an "H" Section resting on the top surface, both of which are directly mounted to the drive hub. The hub is mounted on the Spindle and keyed in place. The "H" Section is comprised of two bulkheads (the vertical members) with a horizontal center plate connecting the two. All centrifugal loads of the AUTOBALANCE mechanisms and masses are born by the "H" Section itself, which requires substantial gusseting and bracketry. The "H" Section and the mounting platform are both dowel pinned to full length and full height (25.5 inch) sideplates to form an extremely stiff structure. Sheet Aluminum covers close the interior "box section" and provide a barrier to keep personnel from coming in contact with the gears or any high voltages that may be present during a test. The covers also make a slight reduction in the air drag during high g testing. 8 Horsepower is expended in aerodynamic drag at 150 g at the 48 inch radius.

3.0 AUTOBALANCE MECHANISM DETAILS

The mechanisms are all three similar in that they use the same DC motor-tachometer, position feedback potentiometer and all operate worm gear and wheel driven threaded shafts to position the weights. Worm gear drives and threaded shafts are used to prevent the possibility of "back driving" any of the moveable masses.

3.1 Motor-tachometers & Feedback Potentiometer

The AUTOBALANCE mechanisms all utilize Electrocraft Model 0588-33-500 motor-tach assemblies. The continuous torque rating for these motors is 13 inch lbs. With the ratio chosen for the worm drives and the pitch of the leadscrews, 1800 turns each way from center are required for full travel in either direction. Thirty turn potentiometers are used to provide position information for each of the three axes.

3.2 Mechanism details

The basic form of the "End to End" and the "Side to Side" moving masses are two each 40 lb. weights with internal threads per axis. The two weights in each set are located on opposite sides of the Spindle Axis. For both of these mechanisms, the threaded shafts are geared to turn in parallel which results in the weights moving in tandem.

The "End to End" set travel is limited to 6 inches either way from center which results in the capability to compensate for 10 lbs. at the nominal 48 inch Test Radius.

The "Side to Side" set has effectively 2 inches travel either way from center. This allows a generous horizontal difference in c.g. location. The ratio of the Arm width (25 inches) to length (120 inches) results in a lesser mass-length requirement for this axis.

The "Up-Down" weight set is similar only in that the two weights are again 40 lbs. each with internal threads. For this set, rollers are required to carry the centrifugal load and the leadscrews are only used to move the weights up and down. The motor driven worm gear mechanism in this case drives a differential which results in opposite rotation of the two output shafts. These shafts drive another set of worm gears with the leadscrews attached. The travel limit of the two weights is 6 inches either up or down from center.

The capacity to compensate for vertical displacement of the centers of mass of the test objects is not as straight forward as it might at first seem. The overall weight of the bare Arm becomes an important consideration. The ratio of the weight of the test objects to that of the bare Arm (1200 lbs.) is proportional to the effect of the couple produced by a vertical separation of the centers of mass of the two objects. This system will achieve the listed performance with a 2.5 inch vertical difference in the location of the c.g. of two nominally 150 lb. objects. This is not exclusive of the 10 lb. difference (one weighing 140 lbs. and the other 150 lbs.) that can be simultaneously compensated for by the "End to End" set.

4.0 PERFORMANCE ACHIEVED

4.1 Performance to the Present Specification

The system described was delivered to Kelly Air Force Base in San Antonio, Texas in April 1990. The "summarized" specifications for the AUTOBALANCE System were that the Test Stand motion would be limited to 3 milli-g peak acceleration when at 150 g using the nominal 48 inch test radius with a 10 lb. difference (150 lbs. on one mounting platform and 140 lbs. on the other). This specification was met and the ability to compensate for asymmetry in the vertical and horizontal locations of the centers of mass was demonstrated. The means of verification was visual inspection of Test Stand motion as evidenced by placing a dial indicator on an isolated stand and reading the total indicated runout (T.I.R.) of the Test Stand enclosure at Arm height. The peak to peak displacement was within 0.002 inches

under the above mentioned conditions at a rotational rate of 331.70 RPM. This appears to be about the limit for this configuration and can be considered a 3 sigma value. The range of actual peak to peak displacement readings in a series of five AUTOBALANCE routines started with the weights centered was from less than 0.001 inch to 0.002 inches.

The PCS was operated manually with the Arm at the limit of compensation capacity without performing the AUTOBALANCE routine. There was excellent correlation between the 10 milli-g IMBALANCE SHUTDOWN and the observed peak to peak displacement dial indicator readings.

The AUTOBALANCE routine requires 120 seconds to complete and the Test Stand motion is reduced to on the order of tens of micro-g during the profile in order to result in the degree of balance required at the 150 g PCS limit. This level was not determined by using the dial indicator but instead was measured by Oscilloscope voltage readings and the known scale factor of the accelerometers.

During all operations of the Centrifuge System, the IMBALANCE SHUTDOWN function is active. This Shutdown will occur if the output from the accelerometer in the most sensitive position exceeds 10 milli-g. The attack time of the Imbalance Switch comparator is about 5 seconds. The outputs from the two accelerometers are also continuously monitored for relative amplitude comparison to result in a means to detect a possible sensor fault. Both accelerometers would have to fail simultaneously in order to defeat this safety device. The probability of that happening is considered to be very remote.

4.2 Projected Performance for Other Applications

For a high precision centrifuge, the definitive application is modeling of the non-linear coefficients of a high performance accelerometer. For rotational speeds smaller than the lowest structural resonance of the mounted centrifuge, the foundation deflections caused by imbalance produce an error in applied acceleration which approximates the effect of a quadratic non-linearity (K_2). See references 2 and 3. The PCS balances to .003 g, 3 sigma, at 150g. That corresponds to a quadratic nonlinearity equal to 0.13 microg/g^2 . This level of performance is near state of the art, even with final balancing taking place at only 10g. The implied balancing accuracy at 10g is 4 microg rms.

If the present system is noise limited, raising the final balancing speed to 40g would improve this error by 16 to 1, to less than 10 nanog/g^2 . If side to side dynamic imbalance is significant, smaller gains would occur without the addition of a fourth axis of balancing, as noted in 2.5; but even a factor of 2 to 4 improvement would yield balancing compatible with the best centrifuges now operating.

5.0 SUMMARY

High acceleration testing requirements of the Air Force at Kelly Air Force Base have defined a need for a large centrifuge with an unprecedented combination of capacity (up to 22,500 g-pounds), accuracy, and operating convenience. The answer to those requirements was an automatic balancing system developed by Applied Motion Technology, Inc., using low noise accelerometers as imbalance sensors, to make a robust, self-contained system. In operation the system has proved itself reliable and convenient to use. A bonus may be expected in operating safety, since its convenience eliminates most incentives to short-cut procedures or bypass built-in safeguards.

Applications of this new technology to environmental testing are obvious; but the level of precision obtained suggests many other applications, as well. The Sundstrand Q-Flex accelerometers selected as monitors are operated in their quietest frequency range, and permit balancing down to several microg in the presence of normal operating vibration. Imbalance can be reduced to a negligible error even in very high precision installations. This is not an inexpensive way to build a centrifuge; but the system costs, including development costs, have been defined now by actual operating experience. It should be considered as a cost-effective component of new centrifuge designs.

ACKNOWLEDGEMENTS

The authors wish to express their thanks to J. Curdy and J. Hegstrom for their support in the publication of this paper. Without their effort, dedication, and expertise this paper would not have been possible.

REFERENCES

Reference 1: Peters, R. B. "Noise PSD Measurement of a High-Performance Accelerometer with Motion Cancellation"; Proceedings of the 30th International Instrumentation Symposium; Denver, Colorado, 1984 (ISA Instrumentation in the Aerospace Industry - Volume 30; ISA Advances in Test Measurement - Volume 21).

Reference 2: Peters, R. B. "Use of Multiple Acceleration References to Obtain High Precision Centrifuge Data at Low Cost"; Proceedings of the Institution of Mechanical Engineers, International Conference on Mechanical Technology of Inertial Devices, The University of Newcastle Upon Tyne, Newcastle, England, 1987.

Reference 3: Members of the IEEE/AESS Gyro and Accelerometer Panel "P836: Recommended Practice for Precision Centrifuge Testing of Linear Accelerometers"; document in work, expected to be published as an IEEE Standard in 1992.

ABSTRACT

Determination of Nonlinear Coefficients in a Dry Accelerometer by Vibration Testing

R. Peters, S. Foote

Sundstrand Data Control, Inc.
Redmond, Washington

The traditional technique for determining non-linear coefficients in high performance accelerometers is by means of a precision centrifuge. Centrifuges capable of precision in the area of several parts per million are costly to procure and time consuming to maintain and operate, and consequently are found in only a few key installations. With the introduction of the Q-FLEX® Model QA3000 accelerometer used on Advanced Centaur, Sundstrand finds itself in the position of having to run such tests on an accelerometer which may be produced at the rate of a few hundred per month. Apart from the obvious cost and time lag of precision centrifuge testing, it is clearly undesirable to have an entire production line dependent on the status of a single test apparatus. Sundstrand has, therefore, been motivated to find an alternate means to perform these tests.

The paper describes a technique which has been developed to evaluate K_2 within $0.2 \mu g/g^2$ one sigma and K_3 within less than $0.1 \mu g/g^2$, one sigma, using a vibration exciter. It is more than a factor of ten less time consuming than testing to comparable accuracy on a centrifuge, and uses widely available test equipment. It also can be used to evaluate cross-coupling coefficients, such as K_{IP} , with similar advantages.

The paper provides background information on the physical sources of non-linearity in force-balance accelerometers. It uses this brief study both as part of an error analysis and to provide a rule of thumb for identifying accelerometer designs which may not be suitable for testing by vibration methods. The background theory of the vibration test itself is developed to the point of providing algorithms for its application, including compensation for temperature effect. A thorough error study of effects from both accelerometer physics and shaker dynamics provides an estimate of accuracy to be expected, and also suggests methods of validating the use of a specific shaker.

The paper concludes with the presentation of data taken on a total of thirteen accelerometers at two different shaker installations and on two different centrifuges. The shakers are two Unholtz-Dickie models of different mechanical design, rated 6000 and 7000 force pounds, respectively, both located at Sundstrand. The centrifuge data were mostly taken on the 260 inch centrifuge at CIGTF, but some accelerometers were also run on the 100 inch CIGTF centrifuge. The test data were consistent with the error estimates presented, and validate this new technique as a means of production nonlinearity testing. Excellent agreement between two different shaker installations indicates that it may have other uses, as well.

DETERMINATION OF NONLINEAR COEFFICIENTS IN A DRY ACCELEROMETER BY VIBRATION TESTING

1.0 INTRODUCTION

This report describes the theory and documents the results of using vibration testing to evaluate the K_2 and K_3 coefficients of a dry torque-to-balance servo accelerometer. The methods of test and analysis described are generally applicable to other nonlinear coefficients such as K_{1p} and K_{1H} , but only K_2 and K_3 are discussed in detail.

For reasons that are described in the text, vibration test methods are not generally useful for evaluating static nonlinearly coefficients in liquid filled accelerometers, but they can provide excellent results with gas filled, or "dry", accelerometers such as Sundstrand Q-Flex.

The motivation for such testing lies in the ease of use and availability of vibration test equipment as opposed to precision centrifuges. Only a handful of test laboratories have centrifuge installations capable of sufficient precision to evaluate K_2 and K_3 with accuracy better than $1 \mu g/g^2$ and $0.5 \mu g/g^3$, respectively, but most aerospace companies, as well as their counterpart government laboratories, have suitable vibration test facilities in use; furthermore, precision centrifuges are time consuming to operate and subject to a long list of subtle error sources which must be compensated each time the equipment is used. In testing for nonlinear coefficients such as K_2 and K_3 , these compensations must be applied with great care, since the nonlinear components of the output of inertial grade accelerometer are typically only a few parts per million of the total signal.

Vibration testing, by comparison, is quicker and easier. Shakers are also subject to subtle error sources which must be understood and accommodated to get good results, but the list of sources is much shorter, and they tend to have the character of being avoidable simply by avoiding certain operating areas; e.g., frequencies near resonances of the test table suspension. Finally, testing based on rectification effect permits direct measurement of errors due to nonlinearity, with the million times larger linear signals suppressed by noncritical analog filters. High precision testing is never simple or routine, but once a vibration test setup has been determined to be functioning correctly, its repeated use entails minimal compensation and minimal pitfalls, making it well suited to production testing.

2.0 PHYSICAL SOURCES OF K_2 AND K_3 IN SERVO ACCELEROMETERS

To understand the characteristics and limitations of the alternative methods of measuring the nonlinearities of a servo accelerometer, it helps to know something about the physical sources of nonlinearity in the instruments to be tested.

The mechanisms which operate to produce nonlinearity in the transfer function of an accelerometer may be broadly classified as static sources and dynamic sources. Static sources are those which operate in the presence of an unchanging or static acceleration input. Most

static sources are quasi-static as well; that is, that they operate in the same way and with the same magnitude for slowly changing acceleration inputs up to and including the useful bandwidth of the accelerometer. Dynamic sources, on the other hand, are dynamic only. They produce no effect whatsoever at zero frequency. Static sources in a force balanced servo accelerometer are primarily associated with the magnetic torquer. Dynamic sources are associated with viscous damping.

2.1 Static Sources

Static sources include:

1. Modulation of the permanent magnet field by torque coil currents.
2. Interaction of the torque coil with the structure of the magnetic return path.
3. Torque coil deflection in the presence of gradients in the permanent magnet field.
4. Self heating.

Dynamic sources are generally related to viscous damping in an accelerometer, and specifically to squeeze film damping effects. The most common sources are:

5. The Bernoulli effect (fluid inertia)
6. Compressibility effects combined with modulation of the damping coefficient as a result of changes in the damping gap.

Sources 1 and 2 are usually considered separately, but in reality, they are two different ways of looking at the same phenomenon. In the accelerometer cross section of Figure 1 it can be seen that the torque coil, in a typical "voice coil" type of torquer, is coaxial with the permanent magnet and essentially surrounds one end of it. The usual explanation of the source of nonlinearity in this arrangement is that the field due to currents in the torque coil adds a little to or subtracts a little from the permanent magnet field so that the torque constant varies somewhat with torquer current:

$$\begin{aligned} \text{Torque} &= MLg &= K_T I_C \\ & &= K_{T0} (1 + \alpha I_C) I_C \\ & &= K_{T0} (I_C + \beta I_C^2) \end{aligned}$$

The inverse of this relationship is

$$\begin{aligned} \hat{g} &= \frac{K_{T0} I_C}{ML} = \frac{K_{T0}}{ML} \cdot \frac{ML}{K_{T0}} (g + \beta MLg^2) \\ &= g + \beta \frac{ML}{K_{T0}} g^2 \end{aligned}$$

Clearly, in this relationship

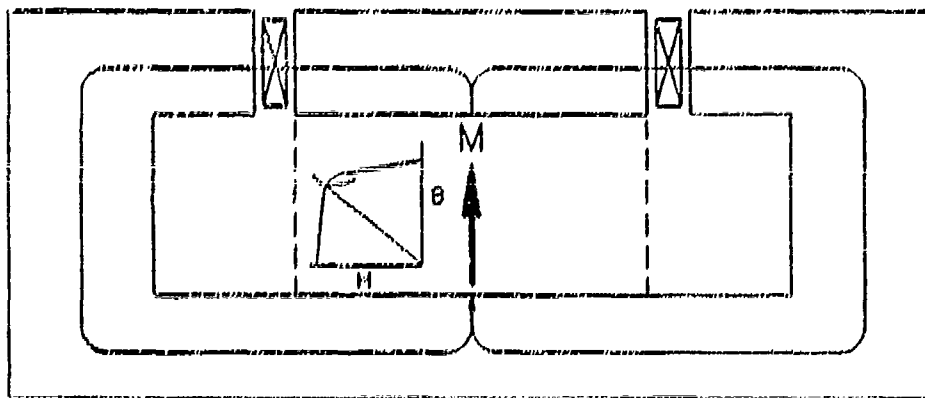
$$K_1 = \frac{ML}{K_{TO}}$$

$$K_2 = \beta ML$$

If α is not truly constant, but varies a small amount with I_C (not uncommon with magnetic materials), it is easy to see how an additional term representing K_3 could arise.

The conclusion commonly drawn from this analysis is that the only way to get a small K_2 with voice coil torquers is to use two coils and two magnetic assemblies facing each other, so that torque coil current increases the field on one side and decreases it on the other, giving a first-order cancellation of the two changes.

FIGURE 1: Coil interaction with magnetic structure.



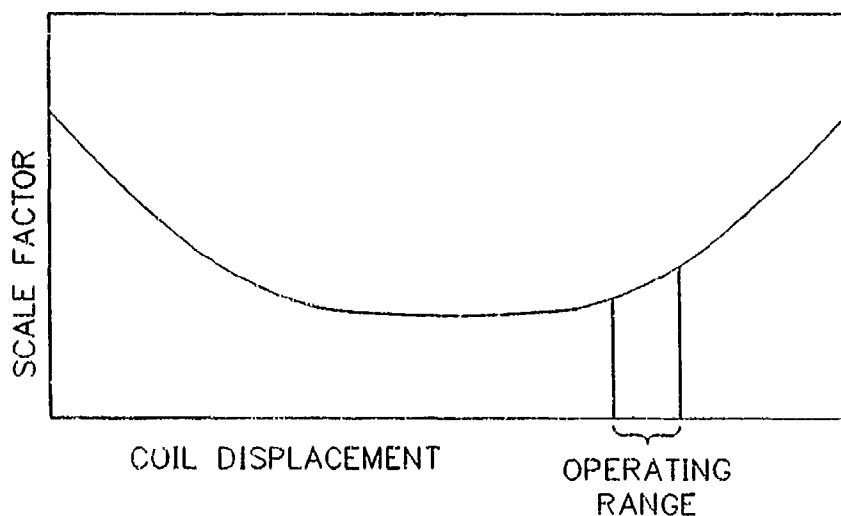
There is another way of viewing the phenomenon though. Also in Figure 1 is shown a typical second quadrant demagnetization curve for a permanent magnet. The variation in B for small variations in H as shown by the minor loop inside the major loop. It is generally observed that these minor loops or "recoil" loops are very narrow and essentially parallel to the upper part of the BH curve and that they have a slope not much larger than unity (in CGS units). For purposes of small field variations, therefore, the structure can be considered as a coil in the middle of a high permeability structure (the return path) having a large air gap in its center. Since current carrying coils are known to exhibit a square law attraction to high permeability materials, the basic torquer forces will be supplemented by a small current squared contribution:

$$\text{Torque} = K_{TO}I_C + \phi I_C^2$$

If $\phi = \beta K_{TO}$, this is clearly the same phenomenon as source 1, but with cause and effect interchanged. The important conceptual difference is that the coil, viewed from the point of view of source 2 will always be drawn toward a point near the center of the magnetic gap, so that even with a single coil and magnet it is possible for K_2 to be positive, negative, or nearly zero, depending on its nominal position in the gap. This possibility has been verified experimentally, showing that symmetric structures are not essential for good linearity, though they do make that achievement significantly easier.

Figure 2 shows a typical plot of scale factor vs. coil position in the magnetic field. The torque constant, and hence, the scale factor varies a little because the magnetic field is not quite perfectly uniform. If the coil moves a bit under acceleration, which it typically will due to finite loop gain and elastic compliances in the constraint structure, the torque constant will be modulated in a manner quite similar to source 1. For a given stiffness, the modulation will be large or small depending on the slope of the scale factor curve near the point of operation. The apparent K_2 is proportional to the slope of the curve, and the apparent K_3 to the curvature. Nonlinearity due to source 1 and 2 can be excited by torquer currents only; e.g., by ac current torquing, but source 3 requires a true acceleration input.

FIGURE 2: Scale factor modulation due to magnetic gradient



Self heating produces apparent nonlinearity primarily because of the scale factor temperature coefficient, which is of the order of 100 ppm/°C for Alnico IX magnets, and may be 300-400 ppm/°C for undoped S_mC_o magnets. If the dominant heat source is coil dissipation, then:

$$\hat{g} = g (1 + \alpha \delta T)$$

where α = scale factor TC
 δT = temperature change

If, in addition:

$$\delta T = \frac{I_C^2 R_C}{R_T}$$

where I_C = coil current
 R_C = coil resistance
 R_T = thermal resistance

$$\delta T = \frac{R_C}{R_T} K_1^2 g^2$$

$$\hat{g} = g + \frac{(\alpha R_C K_1^2)}{R_T} g^3$$

The effect, if not corrected, is an apparent K_3 .

2.2 Dynamic Sources

The classic and obvious source of rectification error in a squeeze film damper, applicable to either gas or liquid damping, is the Bernoulli effect. In 1838 Daniel Bernoulli observed that pressure head and velocity in an ideal fluid are related by:

$$\frac{P}{\rho g} + \frac{V^2}{2g} = \text{constant}$$

where P = pressure
 ρ = density
 V = velocity

This result can be derived from consideration of potential and kinetic energy, or by noting that a pressure gradient is required to accelerate a fluid particle to velocity V . Either way, we are led to the conclusion that an increase in mean square velocity must be accompanied by a decrease in pressure.

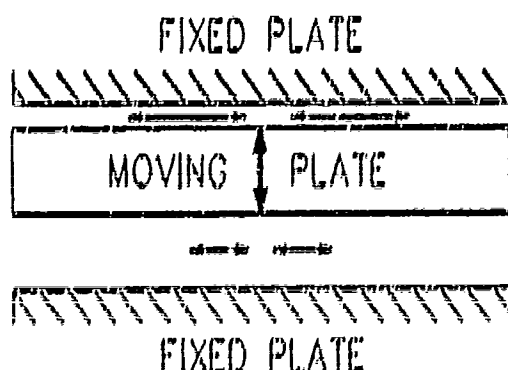
In Figure 3, a balanced squeeze film damper is shown in schematic cross section. When the center plate moves upward, fluid is forced out of the upper cavity and drawn into the lower one. The volumetric flow rate is determined by the center plate area and velocity and is the same for both cavities, but if the height of the upper cavity is less than the height of the lower one, then the fluid will traverse that cavity with a smaller cross sectional area and so at higher velocity. Higher mean square velocity produces lower average pressure, so that the middle plate is pushed toward the upper one. In the presence of vibration, the damping force averages to zero over each cycle, but the Bernoulli effect produces a net force tending to move the center plate toward the nearer side plate. For sinusoidal vibration, the effect is proportional to velocity squared, so that the vibration rectification coefficient (VRC) takes the form:

$$K_R = [\text{geometric factor}] \frac{A^2 \Lambda_s^2 \Omega^2}{h} \frac{\delta_{static}}{h} \frac{\delta_s}{h}$$

where:

K_R	= VRC
A	= plate area
Λ_s	= amplitude response ($\Lambda_s = 1$ if $\Omega = 0$)
Ω	= vibration frequency
δ_{static}	= deflection under 1 g static
δ_s	= average offset from centered condition
h	= mean plate spacing

FIGURE 3: Bernoulli effect in squeeze film damper.



The other source of damper VRC which has been predicted theoretically and observed experimentally is that due to compressibility effects when the damping fluid is a gas. A linear model of a damped second-order system with compressibility effects in the damper is shown in Figure 4.

The compressibility of the gas gives the same physical effect as a spring in series with the damper. At low frequencies, the spring is stiff compared to the dash pot and normal damping is produced. As frequency increases, the dashpot force for a given amplitude of motion increases so that more of the deflection occurs across the spring and less across the dash pot; at frequency $\Omega_c = k/c$ the two deflections are equal, and at higher frequencies the "damper" behaves more like a spring than a dash pot.

At frequencies much less than Ω_c the principal effect of compressibility is to introduce a small phase shift in the damping force. The force lags behind what it would be if the spring were not present. That would

FIGURE 4: Damper model with compressibility.



have little effect if the dashpot damping coefficient were truly constant, but in a squeeze film damper, the value of C varies as $1/h^3$. When the moving plate is moving away from a fixed plate and the C value is decreasing, the lag reduces the average value of C slightly. Conversely, when the plates are moving closer together, the lag increases the average C value slightly. The net result is an average force which tends to push the center plate away from whichever side plate is nearer. This force can be related directly to the magnitude of the damping and to the phase shift, both of which are calculable. For two damping gaps as shown in Figure 3:

$$K_R \approx 6 \frac{C}{C_C} \frac{n}{n_n} \frac{n}{n_C} A_s^2 \frac{\delta_{static}}{h} \frac{\delta_s}{h}$$

This equation has exactly the same form as the one for the Bernoulli effect, but has a different magnitude and opposite sign.

2.3 Static vs. Dynamic K_2 and K_3

Clearly, there are many sources of K_2 and K_3 nonlinearity present in real accelerometers, with different effects at different frequencies. For navigational purposes, the static values are the ones of greatest interest, and so classically they have been measured by means of static instrumentation, primarily precision centrifuges. Since high precision centrifuges are few in number and difficult in operation, an alternate technique is desirable. This paper proposes that the alternate technique be a vibration test. A prerequisite for such an alternate to be viable is that the K_2 and K_3 of the instruments to be tested be the same or nearly the same at some easily accessible vibration frequency as they are at dc.

For dry sensors in which the damping is principally by phase lead in the servo electronics and only partially due to gas squeeze film damping, this criterion is easily met. Shakers are readily available which operate in the range of 20 Hz to a few hundred Hz with only one or two localized problem frequencies due to suspension resonances. At these low frequencies the true dynamic sources can be neglected. The Bernoulli effect tends to be small with gas damping because the gas density is low, and both dynamic effects are small at frequencies much less than the useful bandwidth of the sensor because of the Ω^2 frequency characteristic. The static magnetic sources are theoretically and experimentally seen to be usefully quasi-static in that they are essentially constant to at least several hundred Hz in typical sensors. The effect of magnetic gradients combined with coil deflection could be a problem in some dry accelerometers, but the total effect is typically less than one $\mu g/g^2$ in well designed torquers, and remains essentially constant up to the first zero in the servo loop or the first mechanical resonance. In Q-Flex accelerometers, both of these frequencies are above 200 Hz.

In liquid filled sensors, the Bernoulli effect is potentially quite large due to the high density of the fill fluid, and mechanical effects may be appreciable at low frequencies due to the generally limited bandwidth for which these sensors are designed. Vibration testing for static coefficients of liquid filled sensors must be carefully evaluated on a case by case basis, and is not generally recommended.

Self heating effects pose a difficult problem in any nonlinearity test since thermal time constants tend to fall in a critical area: shorter than the times required for high precision centrifuge measurements; longer than the cycle time associated with vibration testing; and often right in the middle of the actual use spectrum. This error source is probably best handled by use of temperature modeling, as used in all high performance models of the Q-Flex. Vibration testing may have a useful edge in such a case, since the temperature corrections are only one third as large as in a comparable centrifuge test.

3.0 CENTRIFUGE METHOD AND ERROR SOURCES

3.1 Basic Technique and Simplified Data Analysis

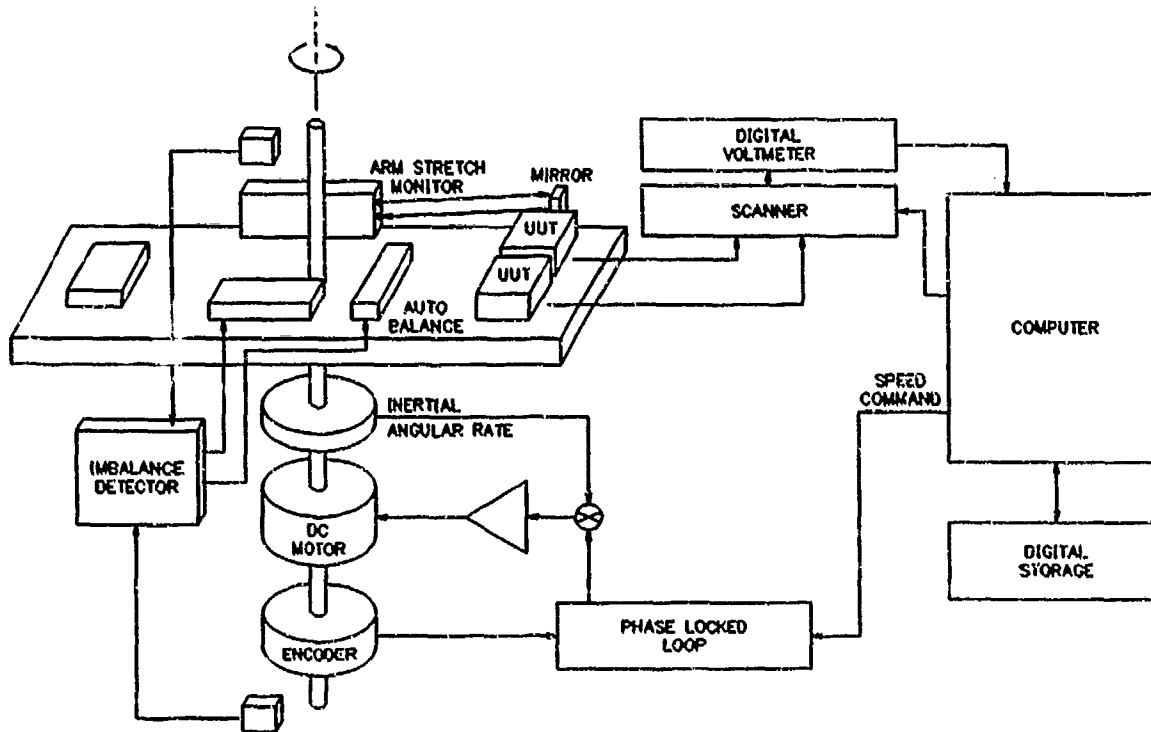
A typical precision centrifuge installation is shown diagrammatically in Figure 5. In concept, the test is fairly simple. A test accelerometer is attached near the end of the arm, with its input axis alignment radially (for K_2 and K_3 ... other orientations may be used for other coefficients). See reference 1. The output of the test accelerometer is measured with the centrifuge stationary and at several rotational speeds corresponding to points in the g range of interest. The applied centripetal acceleration is calculated at each point from the simple relationship $a_c = \Omega^2 R$. Coefficients are calculated by making a least squares polynomial fit to the array of input vs. output data. Negative inputs are obtained by reversing the test accelerometer on the arm and repeating the test sequence.

A complication arises because of the fact that Ω^2 is measurable to great precision, but R is not. Errors in R introduce errors in each centrifuge run individually, and the unknown change in R when the test accelerometer is reversed introduces an even order error which makes it difficult to separate even order coefficients from odd order coefficients. This error is minimized by using the test accelerometer's scale factor as determined from a $\pm 1 g$ tumble to estimate the radius. For medium precision testing (e.g., when K_2 must be known to within ± 20 percent) this method may take the form of establishing a reference baseline which passes through the zero speed point and a reference point in the low g part of the curve. For high precision testing, more rigorous statistical techniques are used to estimate the radius for each polarity from all of the data taken. See reference 2.

3.2 Error Sources

The basic technique describes an idealized situation in which rotational speeds are constant and arm length may be unknown but can be estimated accurately because it doesn't change. The centrifuge geometry is fixed for each test. In reality, numerous subtle error sources arise from speed variations, elastic compliances, and so on. Compensation for these error sources is crucial to the determination of nonlinear coefficients since they are obtained

FIGURE 5: Typical Precision Centrifuge



by examining the difference between the ideal accelerometer output and the actual output; i.e., by looking at small differences between large numbers. The principal error sources are:

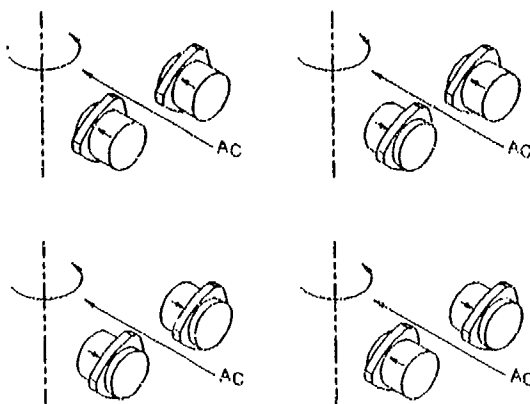
- Radius uncertainties
 - Arm stretch (elasticity)
 - Imbalance (changes in center of rotation)
 - Thermal expansion
 - Rotation of tall fixtures
- Rate uncertainties
 - Revolution to revolution drift
 - Wow and flutter (periodic variations)
 - Measurement simultaneity
- Alignment uncertainties
 - Fixture rotation
 - Centrifuge leveling
- Temperature effects including sensor and load resistor self-heating

These error sources must be measured and corrected for to avoid introducing errors in the determination of coefficients. Uncompensated elastic arm stretch, for example, mimics K_2 in a single polarity test, though it appears mostly as an odd quadratic in dual polarity testing. Imbalance effects which cause the center of rotation to change by as little as a few thousandths of an inch can introduce errors in K_2 , erroneous odd quadratic coefficients, and errors in K_3 . Periodic speed variations ("wow") that would not show in measurements that average speed over a revolution have been observed to cause errors in K_3 if the data are mostly at low g ; e.g., 1-10 g . Speed variations and tilts can cause errors that may take many forms if the speed measurements and the output measurements are not accurately synchronized. Many of these errors are discussed in Reference 3.

3.3 Error Compensation

Organizations that engage in high-precision centrifuge testing typically have test beds which are instrumented to measure and compensate for all of the errors listed above. On-board laser interferometers are used to measure arm stretch and fixture rotations at a point near the test accelerometers. Enclosure wall-mounted proximity detectors provide a back-up measurement. Speed stability is checked both by analysis of the built-in rate measurement signals and by means of tangentially mounted accelerometers which are synchronously demodulated to characterize wow and flutter by measuring angular acceleration. Motion sensors mounted on the frame are monitored for signals which could indicate an out-of-balance condition. Finally, for an additional increment of accuracy, test accelerometers are mounted in pairs and tested in parallel/ antiparallel configurations as illustrated in Figure 6 to separate common mode signals that can be attributed to residual test bed errors. This method does an excellent job of separating even order test accelerometer coefficients, such as K_2 , from even order test bed errors, such as δK_{0Q} , and has revealed previously unsuspected errors of the order of $1 \mu g/g^2$ in carefully instrumented installations even after best effort compensation. Unfortunately, dual sensor testing cannot separate odd order errors such as K_3 .

FIGURE 6: Dual sensor test configurations



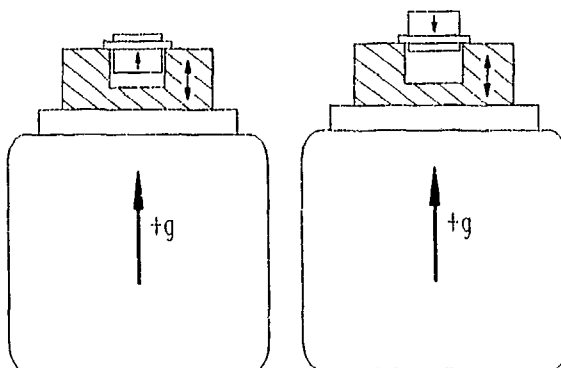
4.0 SHAKER METHOD AND ERROR SOURCES

4.1 Basic Technique and Simplified Data Reduction

The shaker method of K_2 and K_3 determination is based on the phenomenon of rectification during sine vibration. When the transfer function of the accelerometer under test exhibits a net curvature over the range of input acceleration, the average output will be biased; i.e., a zero mean input acceleration will produce a non-zero mean output current.

The test is conducted by mounting a test accelerometer so that it will be vibrated along its input axis (IA) and then orienting the IA upward so that the accelerometer also experiences 1 g along its input axis. DC measurements are taken with and without vibration applied, and the dc offset due to vibration recorded. The test is then repeated with the accelerometer inverted. The nonlinearity represented by K_2 has a constant curvature over the accelerometer range, so it produces the same offset in either position. The non-linearity represented by K_3 , on the other hand, has no net curvature when the average acceleration input is zero, but it adds to K_2 , on the average, near +1 g and subtracts near -1 g. By combining suitable sums and differences of the outputs, it is possible to separate the K_2 and K_3 . The dc measurements taken represent the nonlinear terms directly, with the linear components removed by low pass filtering, so measurement precision is much less critical than centrifuge testing.

FIGURE 7: Shaker test configurations



To be more specific, consider the case of an accelerometer with the following transfer function:

$$A_{\text{ind}} = \frac{I}{K_1} = K_0 + a + K_2 a^2 + K_3 a^3$$

where a = input acceleration in g
 I = output current in mA
 K_1 = scale factor in mA/g

Assume now case 1 in which $a = +1 g$

$$A_{ind1} = K_0 + 1 + K_2 + K_3$$

Then case 2 in which $a = +1 g + A \sin \Omega t$

$$A_{ind2} = K_0 + 1 + A \sin \Omega t + K_2 (1 + 2A \sin \Omega t + A^2 \sin^2 \Omega t) + K_3 (1 + 3A \sin \Omega t + 3A^2 \sin^2 \Omega t + A^3 \sin^3 \Omega t)$$

By trigonometric expansion the average value of A_{ind2} can be found to be:

$$\overline{A_{ind2}} = K_0 + 1 + K_2 \left(1 + \frac{A^2}{2}\right) + K_3 \left(1 + \frac{3A^2}{2}\right)$$

Similarly, for the negative $1 g$ measurements,

$$\overline{A_{ind3}} = K_0 - 1 + K_2 - K_3$$

$$\overline{A_{ind4}} = K_0 - 1 + K_2 \left(1 + \frac{A^2}{2}\right) + K_3 \left(-1 - \frac{A^2}{2}\right)$$

It can then be seen that

$$K_2 = \frac{1}{A^2} (\overline{A_{ind2}} - \overline{A_{ind1}} + (\overline{A_{ind4}} - \overline{A_{ind3}}))$$

$$K_3 = \frac{1}{3A^2} (\overline{A_{ind2}} - \overline{A_{ind1}} - (\overline{A_{ind4}} - \overline{A_{ind3}}))$$

4.2 Error Sources

This measurement technique is subject to subtle error sources too, but the list is shorter than for the centrifuge and the effects generally less critical. The principal error sources are:

- Motional irregularities
 - Waveform distortion
 - Cross axis motion
 - Sculling error
- Magnetic field effects
- Self-heating effects

Waveform distortion is not a significant problem. There can be no first-order effect, since the input acceleration must be identically zero mean. The second-order effects on which this measurement is based are proportional to the square of vibration amplitude, so the effects of harmonics simple RSS in the same way that the harmonics themselves RSS to contribute to the mean square value of applied vibration, as long as the rectification coefficient at the higher frequency is comparable to the one being measured at the fundamental. Swept sine VRC test of Q-Flex accelerometers show that for waveform distortion of several percent, there is no significant error.

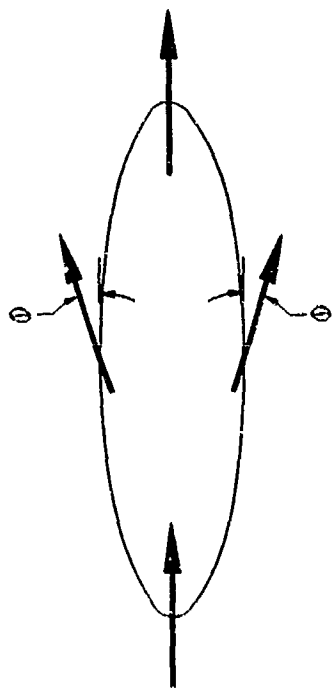
Cross axis motion due to misalignment or to elliptical motion of the shaker head can also be neglected, as long as the test is not conducted at a shaker resonance point. When the accelerometer is inverted by rotation about the hinge axis, misalignment effects coupled through K_{IP} will contribute to an error in K_2 :

$$\delta K_2 = \alpha K_{IP}$$

where K_{IP} = cross coupling coefficient
 α = misalignment or normalized cross-g

For K_{IP} , typically $10 \mu g/g^2$ or less and $\alpha = 0.005$
 (a reasonable nonresonant value),
 $\delta K_2 < (0.005)(1 \times 10^{-5}) = 0.05 \mu g/g^2$

FIGURE 8: Shaker sculling motion



Elliptical motion produces accelerations which are in quadrature and produce no rectification errors.

Sculling errors can occur only near a shaker resonance, since they require a synchronous oscillation of the input axis combined with elliptical motion, as illustrated in Figure 8. Such a combination can contribute directly to an error in K_3 , but its magnitude will typically be small:

$$\delta K_3 = \frac{\theta \alpha}{3A}$$

where θ = peak angular motion

For nonresonant operation, reasonable limits are $\theta = 0.001$ and $\alpha = 0.001$ at 12 g peak:

$$\delta K_3 = \frac{(0.001)(0.001)}{(3)(12)} = 0.03 \mu g/g^3$$

These estimates are compatible with the observed repeatability of the test from setup to setup.

Magnetic effects could contribute to K_2 and K_3 error if the ac magnetic field from the shaker were able to modulate the test sensor scale factor. Static magnetic sensitivity measurements show coefficients of less than 1ppm/gauss for axial fields. The ac magnetic field in the vicinity of the test sensor has been measured as 25 gauss (peak) with a vertical gradient of 5 gauss/inch. If these combined directly, the result would be an error of $1 \mu g/g^2$ in K_2 and $0.02 \mu g/g^3$ in K_3 . Analysis of the test data in the next section indicates that the error in K_2 does not exceed 20 percent of that value. In fact, the calculated skin depth of Invar at the test frequency of 85Hz is less than 15%, which is $1/8$ of the return structure wall thickness, and about equal to the thickness of the belly band that covers the only gap. Twenty percent should be a highly conservative estimate for magnetic leakage.

Self heating effects are significant in this testing, as they are in centrifuge testing, and require compensation for accurate results, but the correction required for K_3 is only one third as large for the same peak g input. For example, if temperature rise is assumed proportional to power dissipated in the torque coil; i.e., $I_C^2 R_C$, then the rise is proportional to acceleration squared. If the proportionality constant, in $^{\circ}C/g^2$, is P , then the uncompensated algorithms will yield.

$$\hat{K}_2 = K_2 + \beta P$$

$$\hat{K}_3 = K_3 + \alpha P$$

by centrifuge

$$\hat{K}_2 = K_2 + \beta P$$

$$\hat{K}_3 = K_3 + \frac{\alpha}{3} P$$

by shaker

where α = scale factor temperature coefficient
 β = bias temperature coefficient

4.3 Data Reduction With Error Correction

The only error that needs correction in this test is temperature error due to self-heating effects or due to environmental changes during the test. Magnetic effects are well shielded and motional effects can be made vanishingly small by identifying shaker resonances and choosing a test frequency safely removed from them.

Temperature compensation can be cast in the notation of the ATP (reference 5), as follows, with temperature compensation:

$$\overline{A_{ind1}} = \frac{N_+}{K_1} (1 - \alpha \delta T_1) - \beta \delta T_1$$

$$\overline{A_{ind2}} = \frac{D_1}{K_1} (1 - \alpha \delta T_2) - \beta \delta T_2$$

$$\overline{A_{ind3}} = \frac{N_+}{K_1} (1 - \alpha \delta T_3) - \beta \delta T_3$$

$$\overline{A_{ind4}} = \frac{D_2}{K_1} (1 - \alpha \delta T_4) - \beta \delta T_4$$

Substituting the notation of the ATP,

$$\alpha = \frac{1}{K_1} \frac{\partial K_1}{\partial T} = \frac{R}{K_1} C_1$$

$$\beta = \frac{K_0}{T} = B_1$$

$$\delta T_1 = \frac{T_1 + T_3}{2}$$

$$\delta T_2 = T_2$$

$$\delta T_3 = \frac{T_4 + T_6}{2}$$

$$\delta T_4 = T_5$$

$$K_1 = \frac{N_+ + N_-}{2}$$

R = Load resistance, $K\Omega$

B_1 = first-order bias coefficient from the temperature model sheet

C_1 = first-order scale factor coefficient from the temperature model sheet

$$T_B = \delta T_2 - \delta T_1 + \delta T_4 - \delta T_3$$

$$= 1/2(2T_2 - T_1 - T_3 + 2T_5 - T_4 - T_6)$$

$$T_d = \delta T_2 - \delta T_1 - (\delta T_4 - \delta T_3)$$

$$= 1/2(2T_2 - 2T_5 - T_1 - T_3 + T_4 + T_6)$$

$$K_2 = \frac{2}{\Lambda^2(N_+ + N_-)} [D_1 + D_2 + N_+ + N_- + RC_1 T_d] + \frac{B_1 T_B}{\Lambda^2}$$

$$K_3 = \frac{2}{3\Lambda^2(N_+ + N_-)} [D_1 + D_2 + N_+ + N_- + RC_1 T_d] + \frac{B_1 T_d}{3\Lambda^2}$$

4.0 TEST DATA

In the first three months of 1989, the Central Inertial Guidance Test Facility (CIGTF) performed a series of tests on four Sundstrand QA-2000 accelerometers to evaluate their nonlinearity coefficients K_2 and K_3 . The accelerometers were run on the CIGTF 100 inch centrifuge as parallel/antiparallel pairs for common mode rejection. The data were analyzed using recently developed software which incorporates an optimal statistical estimate of the test radius for each run. (See Reference 2.) The results of these tests were published in Reference 4 in May 1989.

In July and August of 1990, CIGTF ran a similar series of tests on a larger sample of 12 Advanced Centaur QA-2000 accelerometers, this time using the 200 inch centrifuge. The larger centrifuge was instrumented with dual interferometers so that flexure tilt as well as arm stretch could be monitored. The results of these tests were reported in Reference 6, published in February 1991.

All of these accelerometers were also evaluated for K_2 and K_3 at Sundstrand Data Control in Redmond, Washington. These data are compared in Tables 1 and 2.

Three accelerometers were omitted from these tables. QA-2000 H/N YAN99 was omitted because it showed anomalous behavior at 20g or higher, and appeared to be a significant outlier in the 12g range required by its specification, as well. QA-2000 accelerometers, S/N R87 and S/N C00D9W were inadvertently tested at Sundstrand using a load resistor with a temperature coefficient of resistance of 50ppm/°C. This high T.C. resistor introduced errors in K_3 which were of the order of $0.4\mu g/g^3$. Unfortunately, they were semi-random and appeared as much due to room environment as to self heating. By the time the error was detected, and corrected by substituting a Vishay 2ppm/°C resistor, R87 and C00D9W were no longer available for retest.

All Sundstrand data reported in Tables 1 and 2 were taken with the Vishay resistor, with sensor temperature effects compensated by means of Sundstrand calibration models derived from a -55°C to +95°C test. CIGTF reported coefficients for both the Sundstrand correction model and for a lower residual model which was derived by correlating sensor output with observed temperature during testing, over a smaller temperature range. The difference in coefficients fitted was generally insignificant compared to the scatter in the data, but the Sundstrand modeled data are reported for consistency.

A more significant observation with regard to the CIGTF data reported in this paper is that the data are corrected for the average effect of the temperature coefficients of the load resistors employed. Even with Vishay resistors, self heating could not be neglected. The CIGTF test was more sensitive to self heating, partly because it was a centrifuge test, and partly because it used a higher voltage scale factor to minimize quantization errors. Tests were run to calibrate the effect and model it out of the data. An initial test set, taken during the time that the centrifuge tests were running, gave repeatable corrections, consistent with

theoretical expectations. In three subsequent tests, something seemed to go progressively out of control, with the standard error of measurement growing progressively to 100 times greater than it was in the initial test. CIGTF chose not to use the data in reporting its results, which is the conservative approach. The authors of this paper felt that the results of the first test were significant and should be considered. The result of applying this correction was to reduce the average difference between the K_3 values from the 260 inch centrifuge and those from the vibration test by 40%, and also to bring the 260-inch test results substantially in line with the 100-inch test results.

Tables 1 and 2 show the K_2 and K_3 coefficients, respectively, obtained by the Sundstrand Engineering shaker with Vishay resistor, then the change in coefficients for the production shaker with Vishay resistor, both shakers with the most recently used high T.C. resistor, then the 260-inch centrifuge, and finally the 100-inch centrifuge.

The K_2 values show little variation with test method employed, which is consistent with physical models of the Q-Flex accelerometers and of the tests themselves. The average values for all the methods agree with one another within $0.1 \mu\text{g}/\text{g}^2$, except for the 260-inch centrifuge results which differ from the others by $0.7 \mu\text{g}/\text{g}^2$. If the 100-inch data agreed with the 260-inch data, this might be evidence of a small AC field sensitivity; the fact that it does not, supports the shielding calculation. In the worst case, the effect on K_3 would still be negligible.

The K_3 comparisons show excellent agreement between the two different shakers, with only $.03 \text{ microg}/\text{g}^3$ one sigma scatter over eleven accelerometers, and an average difference that is not significantly different from zero. The tests with an RN55C resistor show that up to $\pm 0.25 \text{ microg}/\text{g}^3$ error can be introduced by not paying careful attention to that error source, and that the result is not exclusively self heating, since that would be the same for all shakers.

The difference between the average of the shaker K_3 values and the 260-inch centrifuge K_3 value is $0.12 \mu\text{g}/\text{g}^3$, with an average correction of $0.07 \mu\text{g}/\text{g}^3$ for load resistor self heating. The 100-inch centrifuge provides a small additional sample, but one which agrees with the corrected 260-inch data.

6.0 ERROR BUDGET FOR THE VIBRATION METHOD

The principal error sources for the vibration method are summarized in Table 3. All numbers listed are one sigma. Errors listed as systematic may be fixed for a particular accelerometer or test condition, but are otherwise random.

The one sigma accuracy calculated for K_2 is $0.3 \text{ microg}/\text{g}^2$ and for K_3 $0.05 \text{ microg}/\text{g}^3$. These estimates are compatible with the scatter in the vibration measurements and generally compatible with the CIGTF centrifuge data.

TABLE 1: K_2 COMPARISONS

SERIAL NUMBER	ENGINEER- ING SHAKER W/ VISHAY	PRODUCTION SHAKER W/VISHAY		ENGINEER- ING SHAKER W/RN55C		PRODUCTION W/SHAKER RN55C		PRODUC- TION SHAKER, FIRST SET-UP	CIGTF 260" CENTRI- FUGE W/ MODELED RESISTORS		CIGTF 100" CEN- TRIFUGE	
		K_2	ΔK_2	ΔK_2	ΔK_2	ΔK_2	ΔK_2		K_2	ΔK_2	K_2	ΔK_2
YAPWC	- 0.5542	- 0.9290	0.2329	0.1199	0.35	0.9042	0.35	0.9042	0.35	0.9042	-7.420	-0.505
YAW16	2.5695	- 0.0452	- 0.1013	- 0.2050	- 0.2050	0.2050	0.2050	0.2050	3.82	1.2505	3.080	+0.435
YAE3H	- 4.3959	- 0.0473	0.0441	0.4599	0.4599	0.4599	0.4599	0.4599	- 3.61	0.7859		
YAPV8	5.6264	- 0.4025	- 0.2085	- 0.2840	- 0.2840	0.2840	0.2840	0.2840	5.69	0.0636		
YAV27	0.7566	0.1040	0.0941	0.1200	0.1200	0.1200	0.1200	0.1200	1.80	1.0434		
YAW8U	- 6.8950	- 0.0679	0.1092	- 0.1213	- 0.1213	0.1213	0.1213	0.1213	- 7.07	- 0.1750		
YAHDD	1.5532	- 0.2830	- 0.1296	- 0.6369	- 0.6369	0.6369	0.6369	0.6369	1.83	0.2768		
YAV5Y	1.9853	0.3950	- 0.1872	0.1095	0.1095	0.1095	0.1095	0.1095	3.27	1.2847		
YA7E8	0.9509	- 0.0974	- 0.1876	- 0.2085	- 0.2085	0.2085	0.2085	0.2085	1.28	0.3291		
YAFYD	2.5583	- 0.1134	- 0.0636	0.2352	0.2352	0.2352	0.2352	0.2352	3.38	0.8217		
YAW23	- 0.1104	- 0.1142	- 0.2087	0.0423	0.0423	0.0423	0.0423	0.0423	0.92	1.0304		
RS6	- 6.9154							- 0.3150				
YAX7M	2.6440							0.2460				
AVERAGE $\Delta K_2 \pm 10$		- 0.1091 ± 0.1491	- 0.055 ± 0.152	- 0.0335 ± 0.297	- 0.0345 ± 0.397	+ 0.6923 ± 0.4922	- 0.035 ± 0.665					

TABLE 2: K_3 COMPARISONS

SERIAL NUMBER	ENGINEER- ING SHAKER W/ VISHAY	K_3	PRODUC- TION SHAKER W/VISHAY	ENGINEER- ING SHAKER W/RN55C	ΔK_3	PRODUC- TION W/SHAKER RN55C	ΔK_3	PRODUCTION SHAKER, FIRST SET-UP	CIGTF 260" CEN- TRIFUGE W/ MOD- ELED RESISTORS		CIGTF 100" CEN- TRIFUGE	
									K_3	ΔK_3	K_3	ΔK_3
YAPWC	-	0.466	0.0087	-	0.2648	0.0275	0.0275		0.0552	0.1018		
YAW16	-	0.1113	0.0187	-	0.1113	0.1248	0.1248		0.0472	0.1		
YAE3H	-	0.1055	0.0469	-	0.1011	0.2182	0.2182		0.0276	0		
YAPV8	-	0.0277	-	0.0519	-	0.0054	0.0054		0.0136	0.0413		
YAV27	-	0.0862	-	0.0323	-	0.0323	0.0323		0.0628	0.1490		
YAWSJ	-	0.0410	-	0.0378	-	0.0141	0.0141		0.0633	0.1043		
YAHDD	-	0.1035	0.0437	-	0.1050	0.2	0.2		0.0258	0.1293		
YAV5Y	-	0.0368	-	0.0770	-	0.0986	0.0986		0.0096	0.0464		
YA7EB	-	0.1332	-	0.0056	-	0.1042	0.1042		0.0445	0.1797		
YAPYD	-	0.0550	-	0.0017	-	0.0179	0.0179		0.0629	0.1179		
YAW28	-	0.0642	-	0.0054	-	0.0638	0.0638		0.0706	0.1348		
RS6		0.0672						- 0.2832			0.118	0.0508
YAX7M	-	0.0137						- 0.2173			0.192	0.2057
AVERAGE $\Delta K_3 \pm 10^\circ$			0.0012 ± 0.0039	- 0.183 ± 0.072	+ 0.086 ± 0.034	- 0.250 ± 0.047	0.1178 ± 0.0525				+ 0.127 ± 0.110	

TABLE 3: VIBRATION RECTIFICATION ERROR BUDGET

ERROR SOURCE	SYSTEMATIC			RANDOM			NOTE: All values are one sigma
	K_1	K_2	K_3	K_1	K_2	K_3	
Dynamic $K_1 = static K_1$	0.2	0.01	0.01	0	0	0	Estimated from sensor frequency
Temperature Error	0	0	0	0.05	0.05	0.02	Estimated from test data
Measurement Error	0	0	0	0	0.10	0.05	Estimated from test data
Misalignments and Cross-Coupling	0.05	0.02	0.02	0.05	0.05	0.02	Estimated from sensor output variations
Scaling Error	0.10	0.05	0.05	0	0	0	Estimated from manufacturer error and output range
Vibration Scaling	0	0	0	0.01	0.01	0.06	Estimated from test data and sensor range
• Differential	0.05	0.02	0.02	0	0	0	
• Common Mode	0	0	0	0	0	0	
Waveform Distortion	0	0	0	0	0	0	Less than 1% THD at base RMS value
TDS	0.02	0.01	0.01	0	0	0	Estimated from minimum value and output coupling
Measurement Errors	0.2	0.05	0.05	0	0	0	Estimated from test data
Total	0.51	0.05	0.05	0.10	0.10	0.04	

7.0 CONCLUSIONS

Vibration testing for K_2 and K_3 has been established as a viable and advantageous alternative to centrifuge testing. For analog accelerometers, the accuracies achieved in this comparison appear comparable, but a test that can be run in an afternoon by vibration may require four to six weeks on a precision centrifuge.

8.0 ACKNOWLEDGEMENTS

The authors wish to express their thanks to J. Curdy and T. Luxon for their support in the publication of this paper. Without their effort, dedication and expertise this paper would not have been possible.

9.0 REFERENCES

1. "Precision Centrifuge Testing of an Accelerometer", G. H. Neugebauer, 16 May 1972, the Aerospace Corporation, San Bernardino Operations, Report No. APP-72 (52970-11)-1

Published in the Proceedings of the sixth Guidance Test Symposium, Holloman Air Force Base, New Mexico, October, 1972
2. "An Improved Data Reduction Procedure for Accelerometer Centrifuge Data", G.H. Neugebauer, Proceedings of the Thirteenth Guidance Test Symposium, Holloman Air Force Base, New Mexico, October, 1987
3. "Use of Multiple Acceleration References to Obtain High Precision Centrifuge Data at Low Cost", R. B. Peters, Proceedings of the First International Symposium on Inertial Components, Institute of Mechanical Engineers, New Castle upon Tyne, April 1987
4. "Sundstrand QA2000 Centrifuge Test", prepared by Guidance Test Division, 6585th Test Group, Holloman AFB, New Mexico, May 1989 Report No. DP-PY-89-02
5. "Acceptance Test Procedure, Sundstrand Data Control Accelerometer 979-3001-001" Drawing No. 979-3001-701 Rev B
6. "Sundstrand QA-3000 Accelerometer Centrifuge Tests", prepared by Guidance Test Division 6585th Test Group, Holloman Air Force Base, New Mexico, February 1991, Report No. AFDTC-TR-91-08.

**Design of a Precision Vibration Test Station for High
Accuracy Accelerometer Calibration**

By

R. Alan Burnett and Fred Macary

*SUNDSTRAND INSTRUMENT SYSTEMS
TEST ENGINEERING*

INTRODUCTION

Characterization of navigation grade accelerometers is highly dependent on the accuracy of the test instrumentation. This would be a simple task if the output of the test device were perfectly linear, that is, if its transfer function was $y=mx$ and the test equipment faithfully measured it as such. Similarly, an offset due to bias which by definition is an output with no input, or $y=mx+b$, is also a linear transfer function with the constant 'b' being the offset due to bias. A real device, however, never exhibits these linear responses. Its output over a range of acceleration is likely to be a non-linear curve which can be approximated by a polynomial of high order terms.

If the measured output is non-linear, the question immediately arises, how much of the non-linearity is due to the test specimen and how much is induced by the test equipment?

A simplified model of accelerometer output is:

$$a_s = E/K_1 = K_0 + a_i + K_2 a_i^2 + K_3 a_i^3 + \text{higher order terms}$$

where; a_s = indicated output (output units)

a_i = acceleration along the input axis

K_0 = bias (g)

K_1 = scale factor (output units/g)

K_2 = second order non-linearity coefficient (g/g^2)

K_3 = third order non-linearity coefficient (g/g^3)

The accuracy of this approximation in representing the output of the test device depends on the determination of the coefficients (K's).

The centrifuge acceleration source is prone to errors by virtue of arm stretch, bending moments, fixture height, wow and flutter, variations in speed control, imbalance, radius uncertainty, thermal expansion and leveling. The determination of the non-linearity coefficients (K_2 and K_3) are subject to variances in these parameters. Consequently, if error sources could be controlled or minimized, a better determination of non-linearity coefficients would be realized.

Vibration shakers which generate sinusoidal inputs are not subjected to the same errors as the centrifuge. Although the shaker indeed has its own list of errors which cause non-linear motion, namely, waveform distortion, cross-axis motion, sculling, together with magnetic field and heating effects, the list is shorter than that of the centrifuge and more manageable. If a shaker system were designed to minimize those errors unique to the vibratory input acceleration, it may be possible to measure the non-linear coefficients as accurately as those made using a centrifuge, but in a much shorter timeframe.¹

The vibration test station design objective was to produce a linear motion in a single plane with minimal roll, pitch and yaw about the desired line of motion. A vibration system with a shaker

coupled to a slip-plate may produce cross-axis movement up to 15%. Reaction from the shaker and slip-plate movement also induces a rolling, pitching, and or yawing motion to the entire test bed. This motion is superpositioned on top of the forementioned non-linear motion. Causes of each of these problems were analyzed, and a station design was developed to minimize their effects.

INITIAL DESIGN IDEAS

The first order of action was the determination of the features of precision shaker systems which minimize the cross-axis movement, pitching, rolling, and yawing normally associated with a slip-plate arrangement. Shaker systems at facilities which perform work similar to Sundstrand were researched, and complete system solutions from various vendors were evaluated. While touring Charles S. Draper Labs, Boston, Mass., Sundstrand Engineers observed a precision shaker system in operation. Further meetings were held to analyze the design of this shaker. The Draper shaker incorporates the use of a Team Corporation 3-beam hydrostatic table, with the shaker pot coupled to a large reaction mass. The design locates the center of gravity of the entire system coincident with the shaker pot trunnion axis. This minimizes pitching moments.

Complete solutions from several vendors were additionally reviewed. Several of these concepts were very similar to the design of the Draper system. One design involved the use of multiple Team tables, which, in theory, absolutely minimizes any pitching moment induced about the reaction mass. These complete solutions were expensive, when compared to the total of the individual part costs.

The use of a hydrostatic table was viewed as a system must. This type of table has very precisely machined beams and ways, and uses pressurized hydraulic fluid both as a lubricant and for bearing pre-load. The Team table uses two "T" shaped sections, which control vertical movements, and one "V" shaped section, which constrains motion to a straight line. The linear tolerance provided for the bearings is on the order of a couple tenths per inch, which makes for a very linear motion. A check with shaker head manufacturers confirmed that a Team 3-beam table would be the optimum solution for producing linear motion.

The basic concept behind the Draper design is very sound. The use of a large reaction mass, whose centroid is located coincident to the shaker trunnion, and the use of a hydrostatic table is an excellent approach. Sundstrand engineers believed that system enhancements could improve the total system accuracy. The Draper system has a fixed trunnion, which is rigidly mounted in the reaction mass (see Figure 1). Since the shaker pot is directly coupled to the reaction mass any translational forces produced by the shaker will induce an equal and opposite reaction force through the trunnion mount to the entire reaction base. The magnitude of the movement caused by these forces will be very small, but it will exist, causing the entire system to oscillate about the air bag suspension system. Since the air bags handle loads in all directions equally, there is the likelihood of not only a translational motion, but eventually a combined pitching, rolling, and yawing motion as well. Although not obvious, a kinematic model of the system confirmed this hypothesis. The system was modeled using SDRS Ideas software, simulating the approximate mass, shape, and rigidity of the reaction base. To simulate the behavior of the air bags, orthogonal spring elements were used, with the spring rate coefficients matching the air bag manufacturers applications engineer's recommendation. A forced response element was used to simulate the reactive force which occurs during a low frequency shaker test. A modal analysis run was conducted and the results reviewed.

Several modes of oscillation at different frequencies resulted, including translation, pitching, rolling, and yawing.

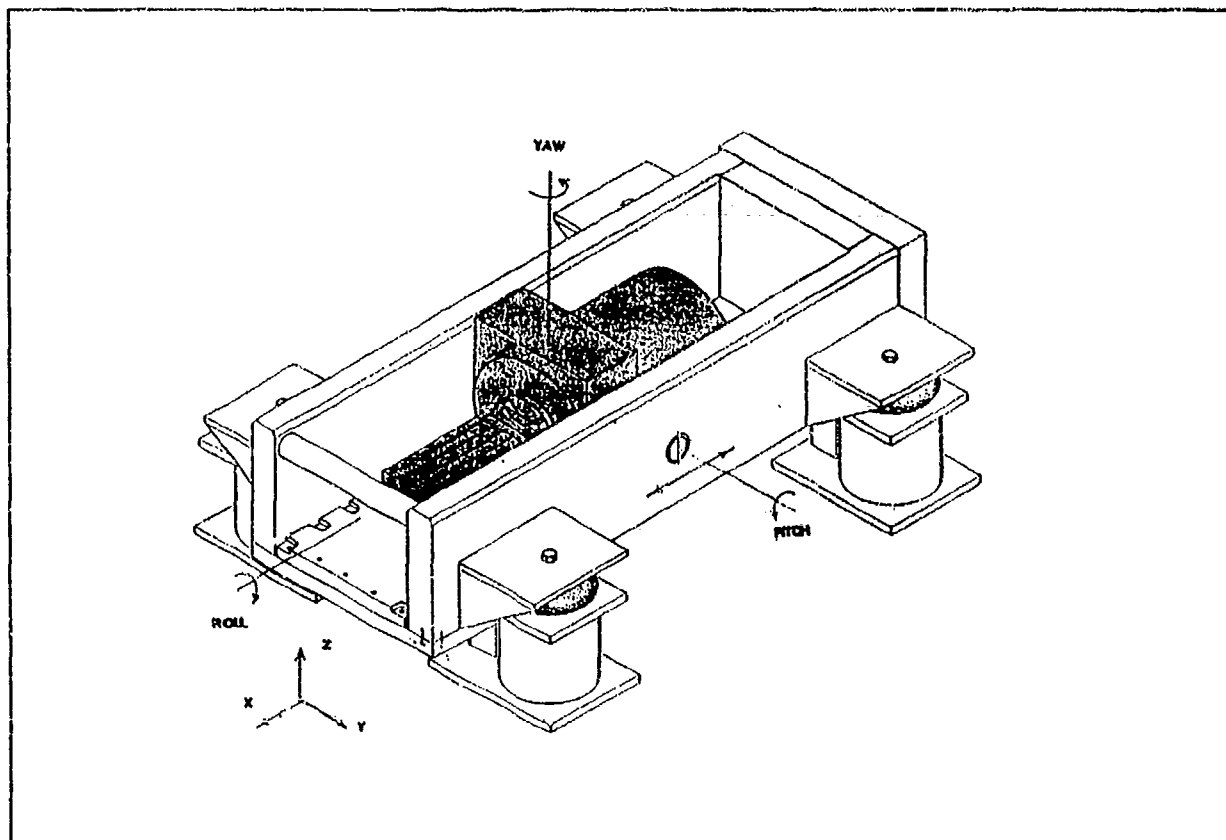


Figure 1. Draper Labs Short Stroke Precision Vibration Station.

It was desired to minimize any of these extraneous movements. Discussion with the Unholtz-Dickie Company, who supplied Sundstrand with the Shaker pot, led to the use of an isolation system Unholtz-Dickie calls "Align-Lock". This system incorporates the use of four leaf-type springs, which are composed of alternating laminations of beryllium copper spring material and rubber, which is used as a dampener. This system is common on some of Unholtz-Dickie's larger shakers, but had never been used on a 6000 lb-force shaker. As illustrated in Figure 2, the align-lock system permits motion in the XY plane (see Figure 1 notation), with a small amount of resistance offered in the X direction, and a much larger amount of resistance in the Y direction. The resistance offered is large enough to enable the shaker to induce adequate g levels at the test specimen, and since the closed-loop accelerometer is mounted at the specimen the control of g-level and frequency is unaltered. Another model of the system was created using the previous components and then adding a dampened spring connection at each of the leaf spring locations. The results from this model revealed a significant reduction in the extraneous oscillations. Another advantage of this system is that it adds another smaller four air-bag isolation system when the shaker is operated in the vertical direction, effectively double isolating the shaker pot from the surrounding lab area, by using two independent air bag isolation systems.

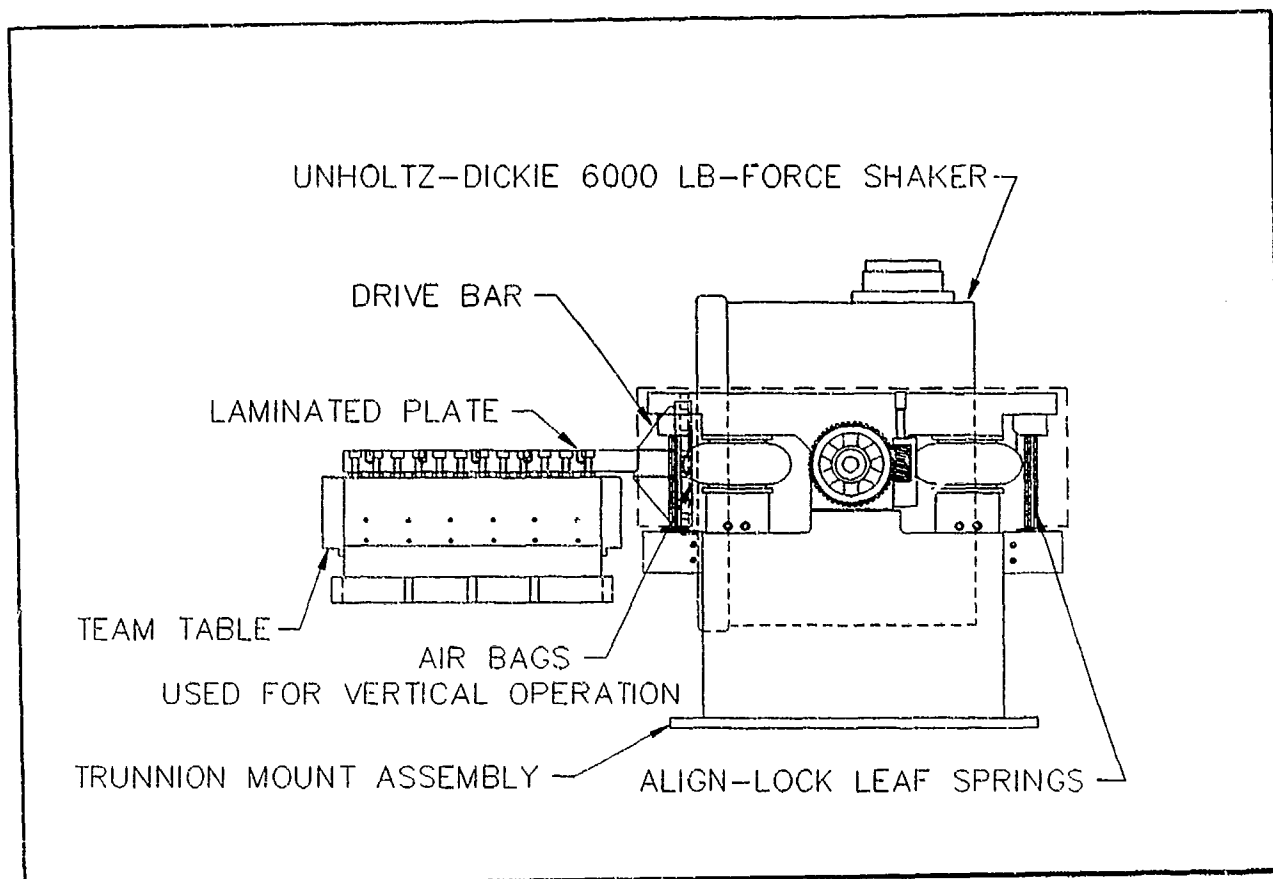


Figure 2. Align-Lock System on Sundstrand Precision Vibration System.

DESIGN OF THE SUNDSTRAND REACTION MASS

The first objective in designing the reaction mass for the Sundstrand precision vibration station was to determine vital parameters, including mass, overall size, and wall thicknesses. The ultimate solution would be to couple a shaker head to a Team table, with both of these components mounted to an infinite mass. Since this is not possible, the next best thing is to design in a reaction mass that weighs as much as practical. A total system weight of approximately 36,000 lbs. was chosen, and the reaction base for such a system was calculated to be about 28,000 lbs. The combined centroid location of the primary subassembly components (the shaker pot, Team table, drive bar, and common test fixturing), was calculated. The initial reaction mass design was completed using SDRC Ideas solid modeling software. Ideas not only performs accurate solid modeling, but allows the user to enter material properties for each part that is used in the system design. The design engineer was able to calculate the overall mass and centroid location as soon as any design changes were made. The design could then easily be modified to locate the center of mass of the combined assembly at the desired location. It was decided to locate the system centroid coincident with the centroid of the combined moving parts during a vibration test. To determine the location of the moving parts another solid model was created which included just the moving parts. After a series of design modifications the initial design was completed. This design had some similarities to the Draper system, but also had some substantial differences. To facilitate the centroid requirement, two large masses were added to the top of the structure. In addition to moving the centroid upward, these steel slabs greatly increased the rigidity of the structure.

The second phase of the design process involved running an FEA model of the initial design. A finite element model composed of more than 4000 brick elements was created. An analysis was conducted using SDRC Supertab to determine the modal response of the system. From this analysis the designer determined areas of high stress, and the natural frequency response of the system. The first run revealed areas of stress, which the designers wanted to minimize. From this information, gusset plates were added in strategic locations to stiffen the struction. A second finite element model incorporated the changes, and new results were obtained. The modal response data for the reaction mass indicated the system would have a natural frequency at 82 hz. Testing on the actual station indicates that the natural frequency resides at 67.5 hz.

The final layout of the reaction base design was constructed using AutoCAD software. A detailed layout of the entire system was completed. A final design of the reaction base was sent out for manufacture. Proper alignment of the assembled components is critical, especially the alignment between the shaker pot drive bar and the Team table. To facilitate this effort, the Team table is mounted on eight adjustable precision leveling blocks, which can easily be positioned to align the two components to the required accuracy.

The final assembly of the major components was conducted at the facility which manufactured the reaction base. This involved lowering the shaker pot into the reaction base and putting the Team table onto the leveling blocks, with the help of a forklift. The drive bar was attached to the shaker head and the Team table was aligned and attached to the drive bar. The shaker pot was welded in place with all pieces properly aligned.

Additional steps were taken to further isolate the shaker base from the outside environment. The reaction base rests on four Barry Controls STABL-LEVL pneumatic spring mounts (air bags), with an automatic leveling valve located at three of the mounts to maintain a level system over time. The air bags are mounted on four large steel bases, which are located on an 83 ton concrete slab, with dimensions of 16 feet long by 10 feet long by 9 feet deep. A large pit was dug, with the bottom filled with sand three feet deep. The top foot of the sides of the pit were lined with a felt vibration dampening material, and the concrete slab was then poured.

Figure 3 contains an illustration of the complete system. In addition to the layout shown, an oven on rails has been added near the top of the reaction base to enable vertical vibration testing under variable temperature conditions.

SYSTEM CONTROLS

The shaker pot is controlled through an amplifier and software control system developed by Unholtz-Dickie Corp. This system allows for pre-programmed vibration sequences, and also permits manual control of frequency and g level. Ramping, and random vibration are additional built-in options. The system provides a real-time graphic display of control parameters, and the vibration profile itself. The system can also provide a hard-copy output of the screen information.

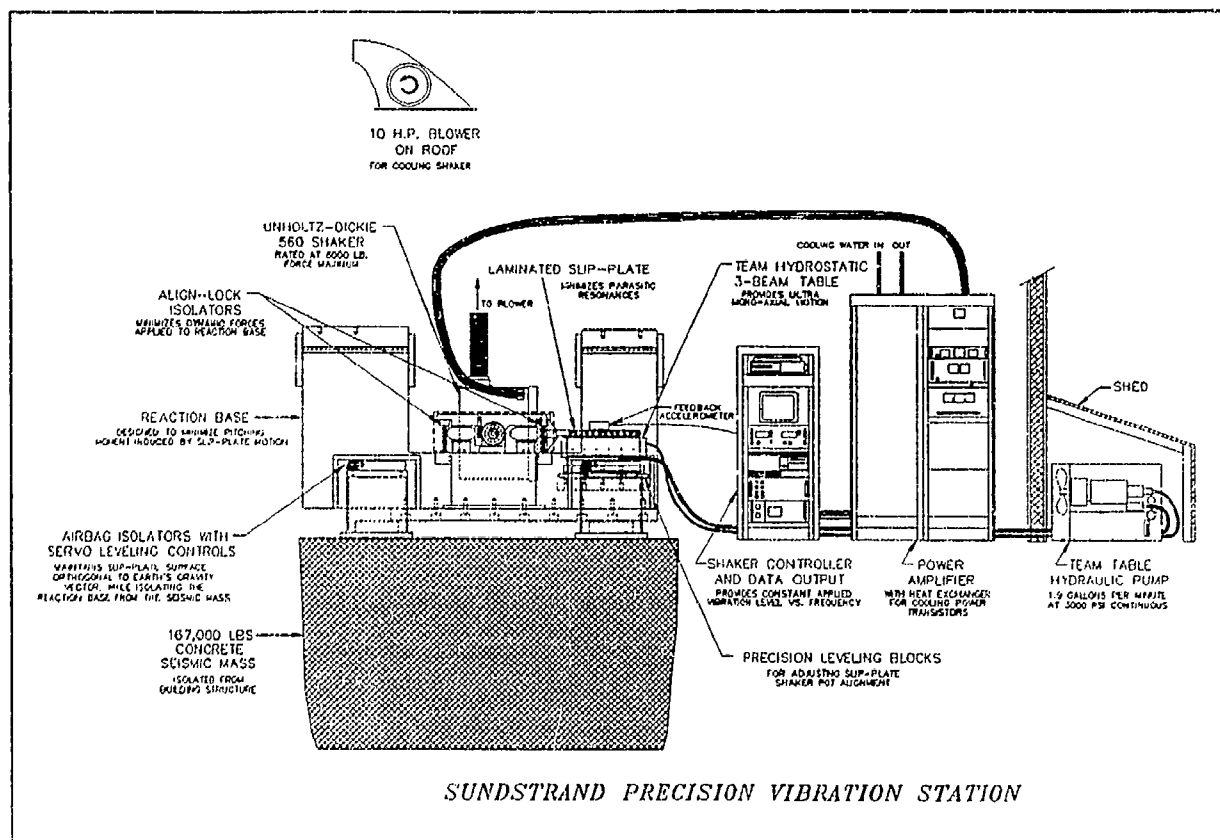


Figure 3. Sundstrand Precision Vibration Station.

SYSTEM PERFORMANCE

The overall performance of the precision vibration system is very good. Several tests, conducted at various frequency and g levels, indicated significant extraneous motions only occur at frequencies below 40 hz. Even at these frequencies, acceleration levels measured at several locations on the station are at worst case less than 1% of acceleration provided to the test specimen. Effects associated with specific higher frequencies warrant investigation. The natural frequency of the station appears to be 67.5 hz. Harmonics are noticeable at 135 and 270 hz, respectively. Effects at higher harmonics are much less noticeable. Fluid pumped through the hydrostatic table also creates an undesired vibration at 230hz, which is related to motor speed and the pump impellers.

The automatic leveling system on the air bags that keeps the shaker base level provides an inadequate response to small air bag height deviations. There appears to be too much play in the valves before they direct air in or out of each air bag. This means an individual air bag could lose air (and thus height) before the valve adjusts the height back. A more sensitive, faster responding leveling system, such as on made by Barry Controls is under consideration.

The following three graphs illustrate the relative cross-axis motion of the system at several frequencies and g levels. Figure 4 results were obtained using a 1 g input to the test table, with a Sundstrand QA-2000 accelerometer located near the front center of the shaker base. Data was taken in the x direction (parallel to the shaker input axis), and the z or vertical direction over a frequency range of 5-35 Hz. The results of a second 1 g input test are compiled in Figure 5. In this test the accelerometer was located just above the center of the right front airbag. Data was taken in the x and z directions as before, and also in the y direction, which is perpendicular to the input axis. The results obtained from the analysis of the data reveals that the airbags are equally compliant in all directions. There is near-equal amplitude of motion in all three planes, even though the input direction is only in the x direction. This result was predicted by the SDRC Idema model. Figure 6 contains data from a third test with a QA-2000 accelerometer located on the top front center of the shaker and varying the g input level from 1 to 5 g's over a frequency range of 20-40 Hz. Note that even at 5 g's the motion measured at 40 Hz is almost non-existent. Above this frequency, the motion becomes even less, except at the forementioned natural frequency, harmonics, and at 230 Hz.

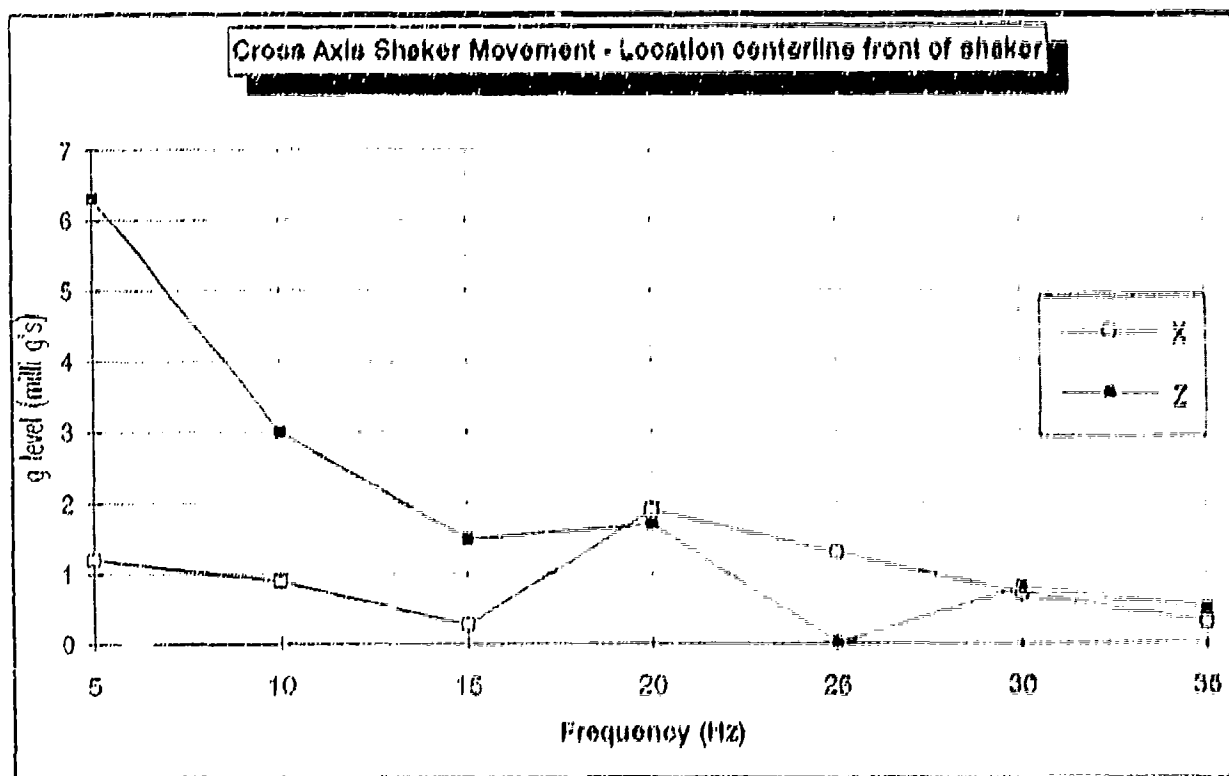
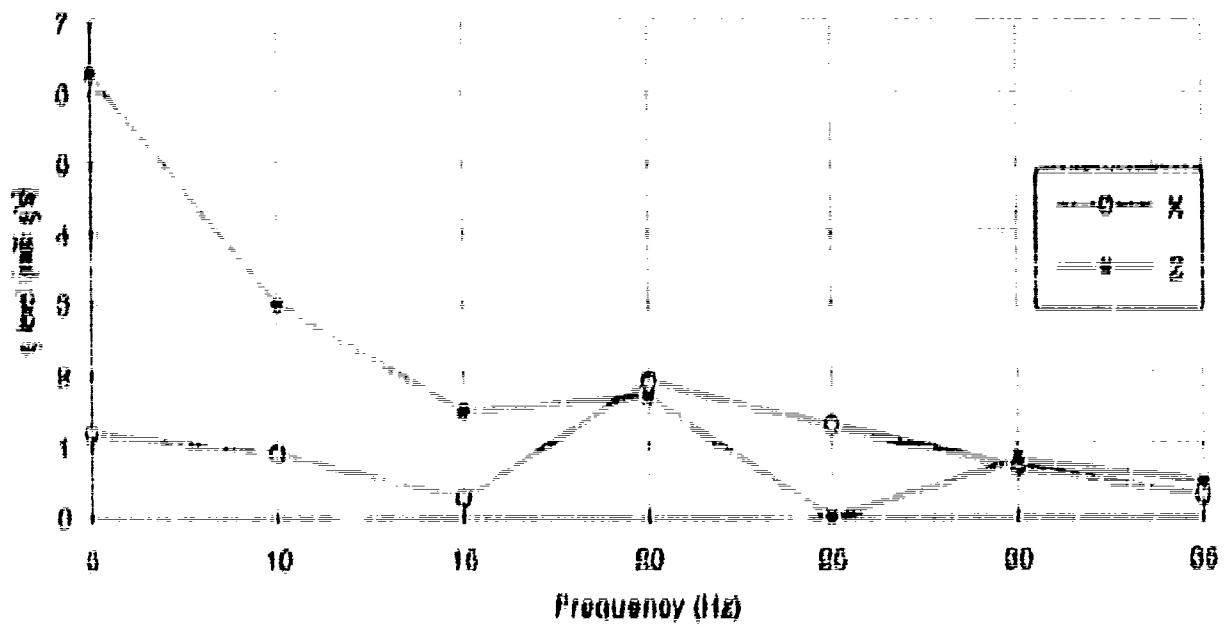


Figure 4. Cross Axis Shaker Movement with a 1 g Input - at Center Front of Shaker.

Gross Axis Shaker Movement - Location centerline front of shaker



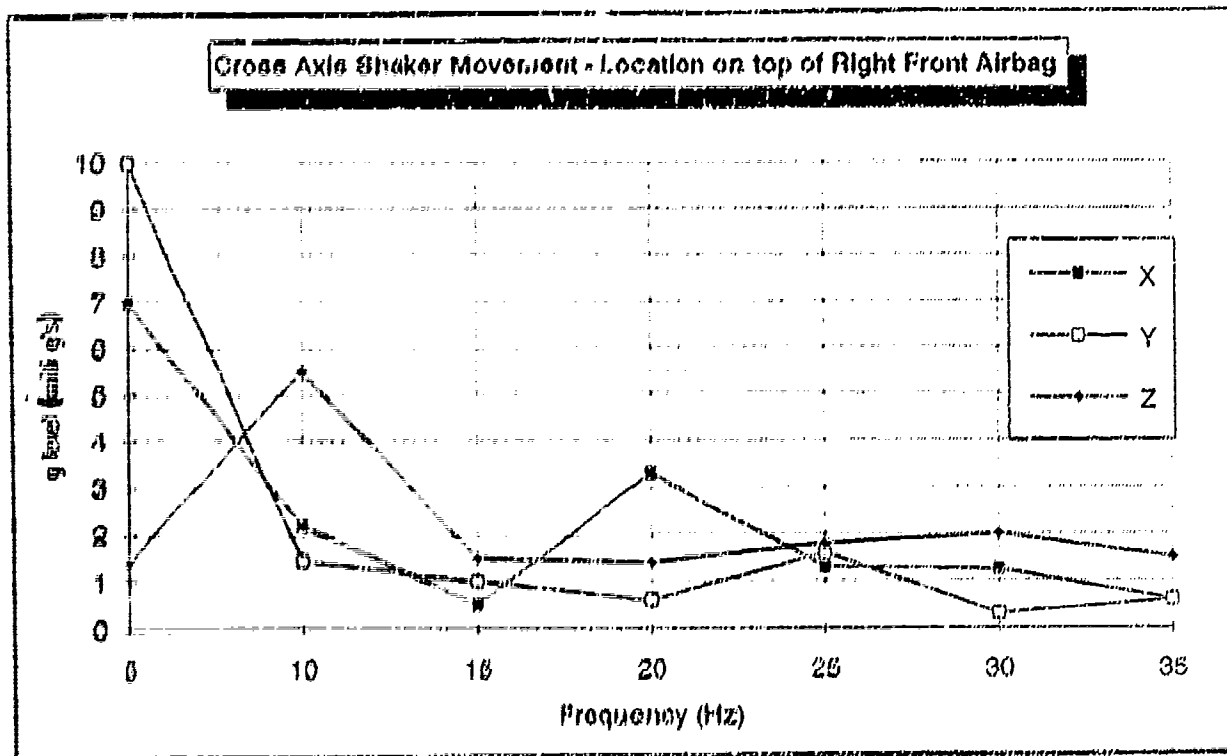


Figure 5. Cross Axis Shaker Movement at 1 g Input - Location on top of Right Front Airbag.

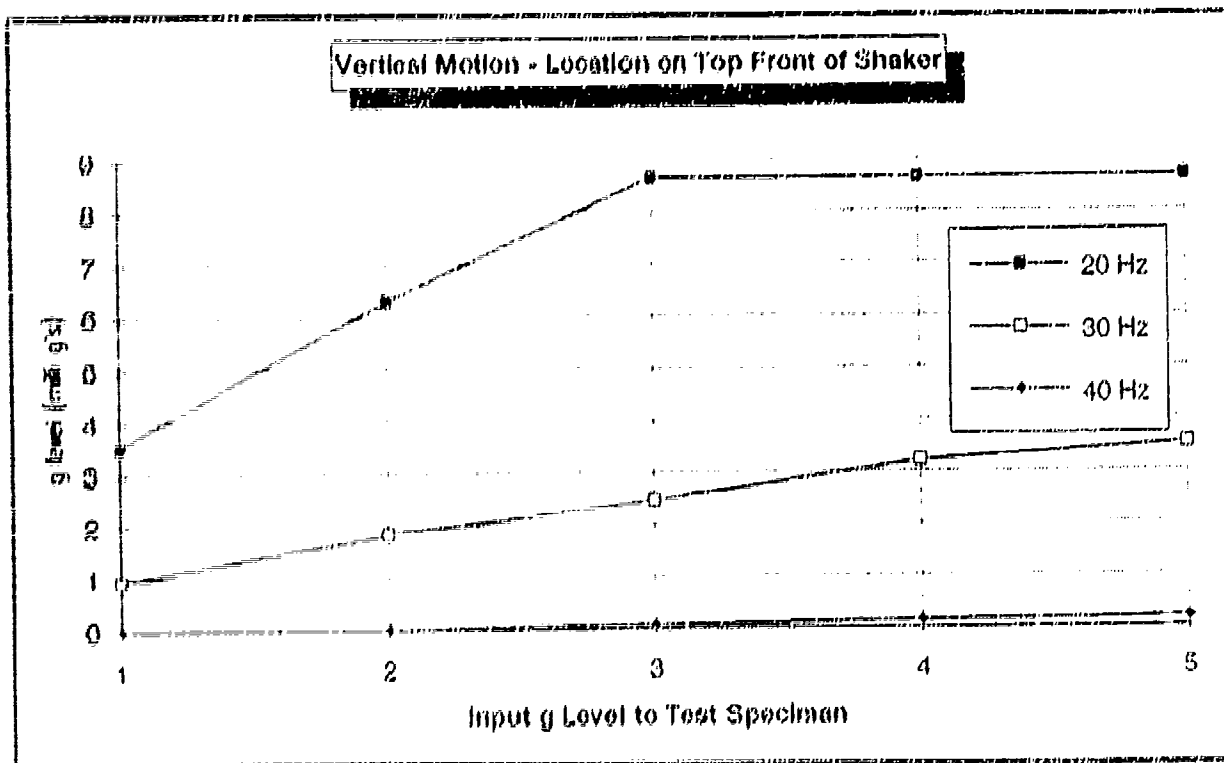


Figure 6. Vertical Motion with a 1-5 g Input - Location on Top Front Center of Shaker.

CONCLUSION

Sundstrand has designed and constructed a state-of-the-art vibration test station. Preliminary test results indicate that several design goals were achieved, including the reduction of extraneous cross-axis motions to a fractional percentage of the desired linear motion. Results closely tracked kinematic and finite element modal analyses. Further system enhancements have been studied, including the use of an improved airbag leveling system, which would provide better test repeatability. The shaker system will help facilitate more accurate modeling of accelerometer coefficients, enabling Sundstrand's customers to deliver higher precision navigation systems. This station will be used in the near future for evaluation test of extremely accurate accelerometers under development at Sundstrand for the U.S. Air Force.

REFERENCES

1. "Determination of nonlinear coefficients in a dry Accelerometer by Vibration testing", R. Peters, and S. Foote, Proceedings of the Fifteenth Biennial Guidance Test Symposium, Holloman AFB, New Mexico, September, 1991.

ACKNOWLEDGEMENTS

We would like to thank the fine people at Charles S. Draper Labs for the technical support they provided during the design phase of this project.

ABOUT THE AUTHORS

R. Alan Burnett has been a Sr. Design Engineer, Instruments Systems, Test Engineering, for two years. He has been involved with instrument test, qualification, and certification throughout his career, including work at several medical companies and the Boeing Co. He also has a strong background in avionics and inertial guidance systems for commercial aircraft. He holds a BSME from Washington State University (1984), and a MSME from the University of Washington (1987).

Frederick S. Macary has been a Principal Engineer, Instruments Systems, Test Engineering, for three years. Prior to joining Sundstrand, he was with the Boeing Co., Commercial Airplane Group. He has been with Northrop Corp., Precision Products, Electronics and B2 Divisions, also Litton Guidance and Control Systems. He has participated in the guidance programs of the C5A, F-14, T-43 and Peacekeeper. He holds a BEE, Villanova University (1967), and an MS (Physics), University of Washington (1987). He is also a member of the Mathematics Dept. of Cogswell College, Kirkland, WA.

SESSION IV-B
GPS INTEGRATION - DIGITAL TERRAIN

CHAIRMAN
JOE COULTER
NORTHROP BOD

**A Guidance and Control Expert System Shell
For Peacekeeper Missile Maintenance Applications**

Raymond L. Fischer

**Northrop Corporation
Electronics Systems Division
Hawthorne, California 90250**

20 June 1991

Unclassified

ABSTRACT

The design and development approach to a diagnostic application-independent expert system shell is presented. The shell will be used by all Peacekeeper Missile Guidance and Control associate contractors to build knowledge bases of expert diagnostic strategies that will increase the efficiency of the maintenance function at the repair depot.

PROJECT BACKGROUND AND MAINTENANCE PROBLEMS

The Aerospace Guidance and Metrology Center (AGMC) in Newark, Ohio, is responsible for diagnosing and repairing faults in the Guidance and Control (G&C) equipment used in the Peacekeeper Missile. Diagnostic and repair support are provided to AGMC by four major G&C associate contractors (ASCONs): Northrop Corporation (Inertial Measurement Unit and gyros), Rockwell International (Guidance Computer and Ordinance), Honeywell Inc. (gyros and accelerometers), and Litton Industries (accelerometers). The support provided to AGMC by the ASCONs includes custom-designed software programs to diagnose faults in both airborne and ground support equipment. These programs are uniquely designed and maintained for different levels of diagnostic support from the major assembly to the circuit card.

Two fundamental problems are being experienced with this approach to the G&C maintenance task. The first problem is the high ongoing cost of maintaining the variety of diagnostic software that has been developed by the ASCONs using conventional software development methods. Different high-level languages, diagnostic architecture, and user interfaces have required extensive involvement of experienced computer programming personnel to improve software diagnostic accuracy and coverage and to make it more user friendly to AGMC personnel. The second problem is the continuing involvement of ASCON experts who are still required to help AGMC to diagnose the causes of G&C equipment faults. It has become evident that the troubleshooting methods employed by the experts have not been sufficiently mechanized within the presently deployed diagnostic software programs. This overdependence on the experts has resulted in higher costs to the USAF and potentially longer repair cycle times when key experts are unavailable.

POTENTIAL SOLUTION AND OBJECTIVES

Expert-system solutions to these problems are being pursued. At the core of the solutions is ART-IM (Automatic Reasoning Tool for Information Management), an expert-system shell that has been developed by Inference Corporation of El Segundo, California. An application-independent program of ART-IM is being developed with the goal of resolving the problems that have been identified with the present ASCON approach to providing diagnostic support to AGMC. This program is GCESS (Guidance and Control Expert System Shell). It will enable nonprogramming personnel from each ASCON to enter a knowledge base of expert-derived diagnostic strategy into a PC platform. The project was started with the development of a prototype GCESS that used the Velocity Subsystem of the Inertial Measurement Unit (IMU) as a diagnostic test case. The main prototype objective was to develop a paradigm suitable for IMU diagnostics (the most difficult G&C diagnostic task) and to demonstrate paradigm operation to the other ASCONs to determine general applicability.

The project's next phase is to build GCESS to accommodate all ASCON requirements that may have differed from the prototype capabilities and to incorporate a diagnostic knowledge base for all IMU subsystems. The remainder of this paper describes the design and development approach to the prototype GCESS and provides a synopsis of the follow-on effort in progress at Northrop and Inference Corporation.

SHELL SELECTION CRITERIA AND FUNCTIONAL DESCRIPTION

ART-IM was chosen as the expert-system shell upon which to build GCESS because it provides a number of integrated facilities that were believed to be important to GCESS, as well as containing a rich development environment. It provides a powerful pattern-matching rule language that uses both facts and schemas, a procedural language component that can define functions to be used on the right side of rules, and a facility for importing arbitrary C functions and packaging them as ART-IM procedural language functions. The rule system provides logical dependency, which can be used to implement truth maintenance systems. ART-IM provides procedural access to the schema system for rapid processing when pattern matching is unnecessary. Its graphical schema browser could be easily incorporated into GCESS, and its user-defined hypertext system and User Interface Toolkit could be used in the development of GCESS. GCESS was to be designed to accommodate a large number of diagnostic rules, but many rule systems will experience almost exponential degradation as the number of rules and/or facts grow. ART-IM, however, typically experiences only sublinear degradation.

ART-IM is also available in both development and deployment versions on the PC platform. The development version provides an incremental compilation environment facilitating rapid development, as well as many other browsing and debugging features, while the deployment version produces executables that are both efficient and not capable of modifying their rules. While the development version was to be used to support maintainability by the diagnostic engineer, the deployed executable helps ensure that the AGMC technician will not be able to modify the production version of the diagnostic system. Figure 1 identifies the integrated facilities of ART-IM and the relationship to GCESS as an application program.

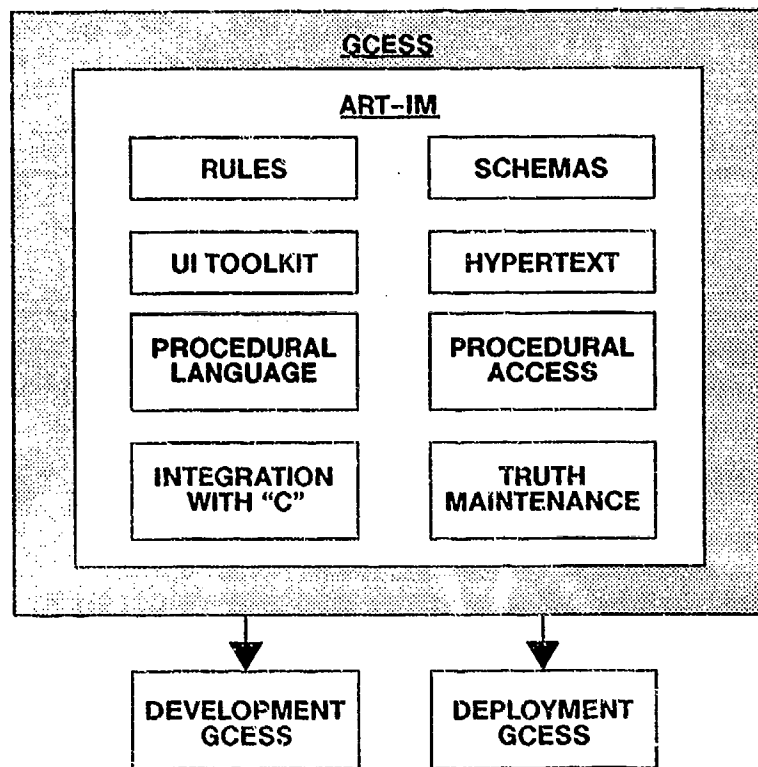


Figure 1. Shell Building Blocks

VELOCITY SUBSYSTEM PROTOTYPE APPROACH

A 22-week prototype development effort was started with a one-week training course, given by Inference Corporation to Northrop personnel, in the use and capabilities of ART-IM's features. During the course, a basic design approach to the prototype GCESS was selected based upon an evaluation of ART-IM capabilities and the features needed to diagnose Velocity Subsystem faults derived from Northrop's design source contractor experience. The first basic approach selected was to use schemas to represent the basic objects germane to the IMU diagnostic process. Schemas and the slots they each contain allow procedural access and easy object modification and facilitate parent-child relationships within a symptom-driven fault tree. The second basic approach selected was to use an explicit agenda, often referred to in the expert-system community as a Blackboard, to implement diagnostic steps, facilitate top-level rule-based control, and support multiple paradigms (as needed by the Peacekeeper ASCONs). A data preprocessor to provide a G&C equipment data server interface with GCESS was the third basic approach selected.

FUNCTIONAL BUILDING BLOCKS

A consideration of these basic approaches led to the functional building blocks, identified in Figure 2, that became the principal design drivers for GCESS. Four modes of operation were believed to be necessary:

1. Single Step -- To support development debugging
2. Automatic -- The principal end-use mode at AGMC
3. Automatic For Symptom -- An option to AGMC to diagnose a single selected symptom.
4. Tutorial -- To support training of AGMC personnel

DATA PREPROCESSOR

The Data Preprocessor's role was envisioned to consist of organizing and formatting the IMU data containing the failure symptoms in a manner precoordinated with the design of the GCESS shell. An IEEE-488 communications link was selected to bring in the IMU data from the test station's mainframe computer (a SEL/Encore 6780). IMU symptoms were grouped and prioritized into four major categories: (1) Test Aborts, (2) Power Down Automatic (PDA), (3) Functional Test Failures, and (4) Calibration and Alignment Failures. The prototype would be limited to Velocity Subsystem faults within these four groups. A data server would provide the necessary intrinsic functions to enable GCESS to measure, test, categorize, and perform prespecified operations on the data that was organized and formatted by the Data Preprocessor. The initial intrinsic functions established to accommodate the Velocity Subsystem were the following:

1. GET -- Measurements
2. GET -- Symptoms
3. GET -- Peak to Peak
4. GET -- Rate of Change
5. GET -- Minimum Value
6. GET -- Maximum Value

Both the Data Preprocessor and Data Server would reside in memory outside of GCESS since it was believed these functions would be slightly different for each G&C ASCON; they would therefore be responsible for tailoring these functions to accommodate the GCESS capabilities and characteristics.

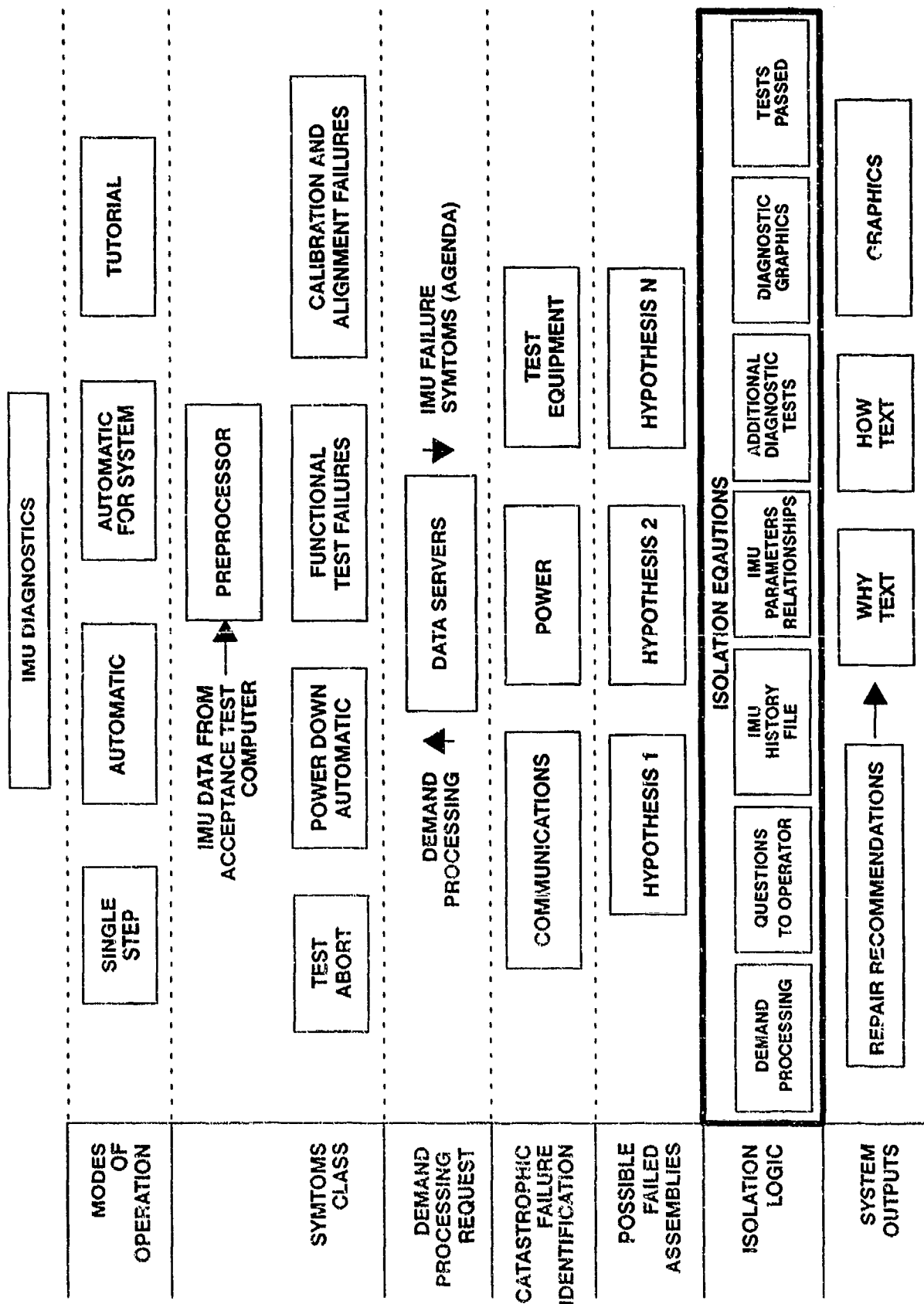


Figure 2. Prototype Functional Building Blocks

DIAGNOSTIC STRATEGY

With the modes of operation, Data Preprocessor function, and Data Server function roughly defined, detailed discussions ensued with Inference Corporation relative to the diagnostic strategy to be employed in identifying the cause of IMU failure symptoms.

It was believed that the first step in this process should be to identify any catastrophic failure that might have occurred that would preclude operating on any specific IMU symptom since it might be a secondary or tertiary symptom resulting from the catastrophic failure. Communications, Power, and Test Equipment tests were placed in this category. This first step was stubbed for the prototype.

The second step in any IMU diagnostic strategy was believed to be the identification of possible failed assemblies within the IMU that could be the cause of the current symptom that GCESS was processing. Possible failed assemblies (e.g., an accelerometer) were identified as hypotheses which would be classified as most probable to least probable based upon IMU failure mode history in the operational silos and the opinions of Northrop's Subsystem experts.

The third step in the diagnostic strategy, to be structured within GCESS, would be to validate that one or more of the hypotheses was correct; this would lead to a recommendation that one or more assemblies within the IMU should be replaced to clear the failure symptom(s).

This hypothesis validation was structured in the form of an isolation equation that could contain one or more of the following elements:

1. Demand Processing
2. Question to Operator
3. IMU Operational History File Results
4. IMU Parameter Relationships
5. Additional Diagnostic Tests Requested and their results
6. Diagnostic Graphics
7. Tests passed in the most recent malfunction verification session at AGMC.

If the isolation equation were satisfied, a repair recommendation would be made (the principal output of GCESS), and the logic behind why it was made would also be available to the test operator at AGMC. This explanation would also be supplemented with text and graphics describing how the repair should be performed.

FAULT TREE PARADIGM

From these initial design approaches and desired building block characteristics, a fault tree paradigm was developed consisting of the following major elements:

1. Each IMU symptom will be mapped to an initial Fault Class.
2. A Fault Class will be defined as a diagnostic rule that may hypothesize other fault classes or make either a repair recommendation or an additional test recommendation.
3. The diagnostic fault classes may be viewed as a Fault Tree where the links are the hypotheses.
4. The nodes in the Fault Tree will all be uniquely defined with an ART-IM schema.
5. The tree will be searched in a depth-first, left-to-right manner.

Figure 3 is a graphic representation of a small section of a fault tree. A Velocity Subsystem symptom is shown mapped to an initial fault class which is a Power Down Automatic (PDA) class that becomes the top node in the tree. This node is linked by ART-IM schemas to all possible IMU parameters that could cause the IMU to be powered off due to the detection of an unsafe condition related to failure of a critical component. Three of the parameters in the Velocity Subsystem that could cause an IMU PDA are temperatures in any one of the accelerometers (SFIR in Figure 3) exceeding pre-established safety limits. These temperatures become the intermediate nodes of this tree subsection; GCESS will validate, via a request to the Data Server, which instrument temperatures exceeded safety limits. Hypotheses have been preestablished for the most probable cause of high instrument temperatures. In the Figure 3 example, it is the SFIR itself as most probable cause and the electronics stack of circuit cards associated with the SFIR as the next most probable cause. This is the terminal mode in the example. A repair recommendation will be made by GCESS if the isolation equation associated with the SFIR, its electronics, or both are satisfied.

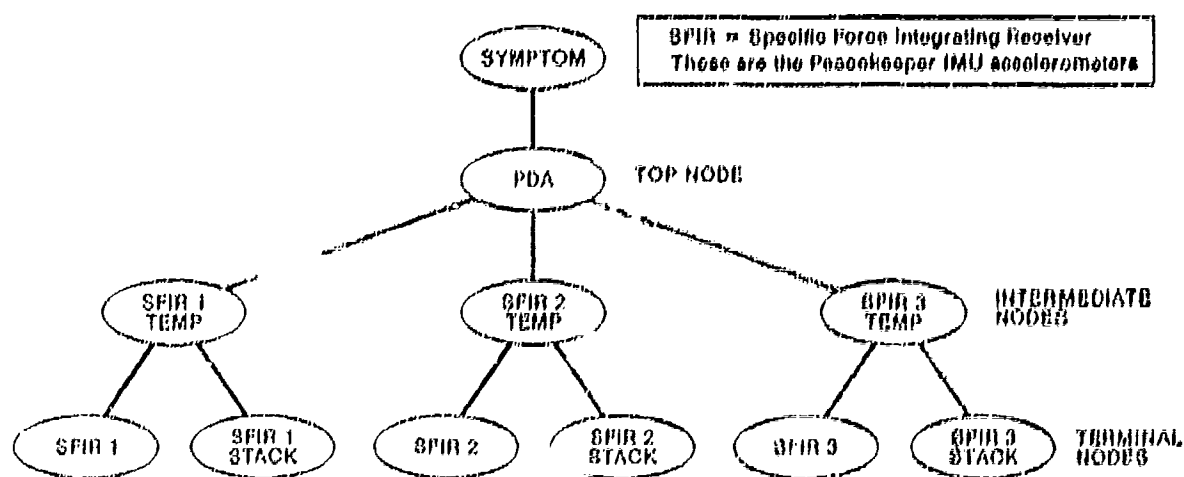


Figure 3. Fault Tree Section

The search for additional terminal node recommendations will be made in a left-to-right manner until all symptoms identified in the Symptoms Queue by the Data Preprocessor have been processed by OCBBB.

ART-IM SCHEMA FORMATS

Top Node

All nodes will contain a unique Fault Class (FC) name that allows OCBBB to establish the parent-descendent relationships in the tree. The top node will always contain all possible failure symptoms within a given IMU FC. These top node symptoms are referred to as a Hypotheses slot in the schema. A Velocity Subsystem example of a top node schema would then be:

Name	(Def Schema PIDA)
Hypothesis	(SPIRN TEMP, RATIN, SPIR WHIRL POWER)

Intermediate Node

This node, in addition to containing a unique FC name (a Hypothesis link from the top node) contains a precondition; it is a OCBBB command to retrieve the PIDA symptom from the Data Preprocessor Symptom Queue and compare it to the FC currently being explored. If the comparison succeeds (i.e., SPIRN TEMP was a valid symptom), one or more hypotheses will be explored as being the symptom root cause. A Velocity Subsystem example of an intermediate node schema would then be:

Name	(Def Schema PIDA SPIRN TEMP)
Precondition	(Symptom Search Command)
Hypothesis	(FC SPIRN, FC SPIRN STACK)

The hypothesis in the example specifies the SPIR or its associated control electronics (the STACK) as the possible root cause of the TEMP symptom.

Terminal (Leaf) Node

The FC names assigned to this terminal node schema are the Hypothesis from the intermediate node. The Precondition slot would contain the isolation equation, expressed in the terms identified in Figure 2; if satisfied, this would validate the FC as the root cause of the current symptom. A Repair and Test slot is reserved to recommend specific repair or additional diagnostic tests, respectively. Three additional slots are designated for use as an information facility to assist the test operator. The final slot contains a list of signals that may have been corrupted due to the root cause of the primary failure symptom. These signals would not be processed further.

A Velocity Subsystem example of a terminal node schema would then be:

Name	(Def Schema PC SFIRN)
Precondition	(Isolation Equation)
Repair	(Replace SFIRN)
Test	(Test Recommendation)
Why	(Explanation for Repair or Test)
How	(Repair or Test Instruction)
Graphics	(PCX File Identification)
Associated Measurements	(SFIR 1 Heater Power)

Figure 4 illustrates the PC processing flow architecture that has been mechanized using ART-IM schemas. Figure 5 identifies the relationship to the symptom agenda, symptom to PC mapping, isolation data, and fault tree.

GCESS PROTOTYPE DEVELOPMENT SUMMARY

Figure 6 illustrates the final GCESS architecture that was developed for the prototype using an AST 386 platform and standard peripherals. The view, edit, and browsing features were mostly standard ART-IM products that greatly enhanced the efficiency of the development process. The report generation feature was customized for the IMU application. The use of Hypertext and the capability to save and restore the diagnostic state were deferred for later implementation. The graphics package initially utilized was Essential Graphics. This was replaced with PCXSHOW due to implementation difficulties. Graphic images were still slow in appearing following the command (several seconds). A user interface was built with the standard UI Toolkit features of ART-IM.

The operation of the prototype was demonstrated to USAF and Peacekeeper G&C ASCON personnel at the end of the 22-week development period (February 1991). All ASCONs were in agreement that the GCESS implementation of the fault tree paradigm would satisfy their diagnostic requirements, and that the tailoring of the data preprocessor and data server functions to comply with their specific applications would be a minor effort.

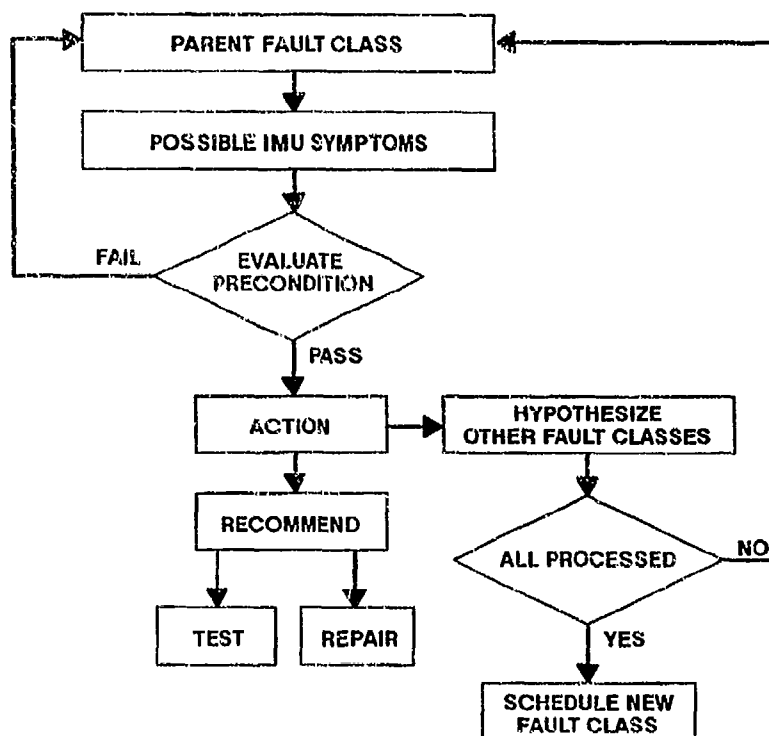


Figure 4. Fault Class Process Flow

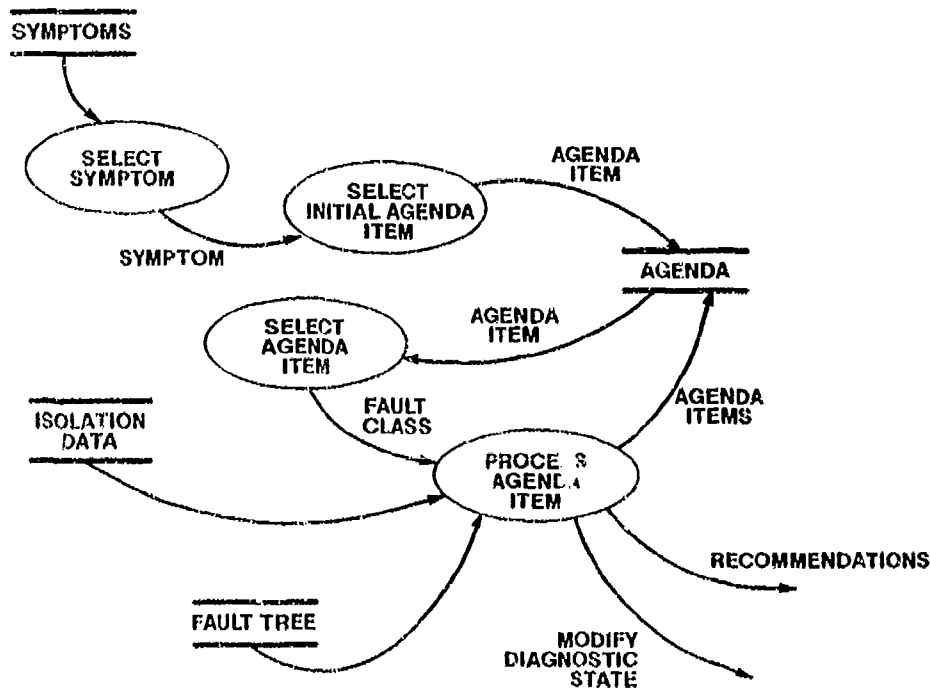


Figure 5. Diagnose Problem

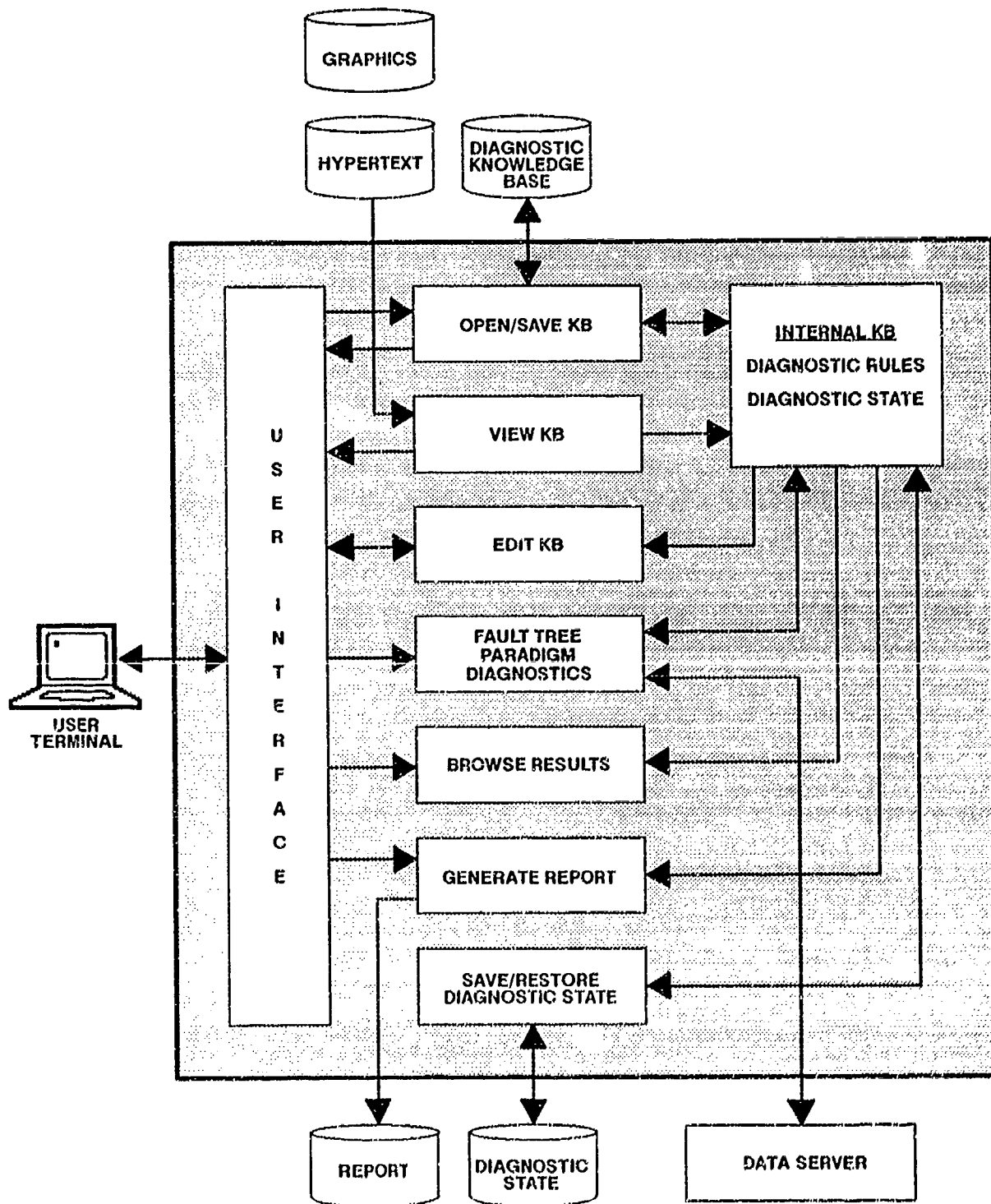


Figure 6. GCESS Architecture

There was one exception. Rockwell International said the fault tree paradigm would satisfy their requirements to diagnose problems in the Guidance Computer but would not be suitable to troubleshoot their test equipment that interfaces with all airborne equipment in the Peacekeeper G&C drawer (Computer, IMU, and Ordnance). Rockwell proposed that GCESS should have the capability to utilize a circuit diagnosis paradigm in addition to the fault tree paradigm. This proposal was adopted by the USAF, and the circuit diagnose paradigm is now under development at Rockwell; Inference Corporation is developing the GCESS features necessary to implement it.

FULL-SCALE GCESS

Northrop is working under a USAF contract to design and develop GCESS to provide the capability to diagnose faults in all IMU subsystems. This development is being coordinated with the other Peacekeeper G&C ASCONs to ensure that the final GCESS product will accommodate their diagnostic application requirements as well as those for the IMU. Several design changes to the prototype GCESS are now in the process of being implemented. The G&C community believes they will enhance the quality of the final GCESS product, scheduled for delivery to AGMC and the other G&C ASCONs in June of 1992. The following is a list of the major enhancements:

1. The Prototype User Interface, which was built with the UI Toolkit features of ART-IM, will be replaced with an interface designed to use the Windows 3.0 environment. Windows has not only that common user feel but also the capability to run concurrent programs that will significantly enhance efficiency in diagnosing IMU calibration and alignment problems; i.e., an application program external to GCESS and designed to evaluate IMU performance data can be running while GCESS is processing the fault tree paradigm.
2. The capability to add weighting factors to each element of an isolation equation will be provided. Elements will be further classified as required or optional to accommodate a variable confidence factor approach to the repair recommendation based on IMU signal behavior and the relative importance to the fault isolation strategy.
3. The capability to enable each ASCON to tailor an output report at the end of a diagnostic session will be provided.
4. Links to Hypertext files outside of GCESS will be added to incorporate IMU theory of operation and diagnostic and repair information that should be useful to AGMC test personnel.
5. The slow display of PCX files problem will be resolved with the selection of a new graphics package interface compatible with the Windows environment.
6. The capability for GCESS to use either the fault tree paradigm or the circuit diagnose paradigm will be provided.

SUMMARY AND CONCLUSIONS

The prototype GCESS was developed by a three-man team (two Northrop and one Inference) over a 22-week period. It provided the means to enable each (Peacekeeper G&C) ASCON to evaluate its suitability to satisfy individual diagnostic application requirements, and to fulfill contractual commitments to support the G&C maintenance functions at AGMC.

The final GCESS product is under development at Northrop and Inference Corporation, which is a subcontractor to Northrop. It is believed that GCESS will provide AGMC test laboratory personnel with one diagnostic software package containing the strategies devised by experts to diagnose all Peacekeeper G&C equipment faults. The maintenance of the GCESS knowledge bases can be performed by nonprogramming personnel.

SESSION V-B

GPS

CHAIRMAN
MICHAEL HADFIELD
HONEYWELL MILITARY AVIONICS

Test Report for GPS (Prototype) Antenna on the Cylindrical Construction

By

Akiyoshi Yamamoto[†]
Japan Radio Co., Ltd.
Tokyo Japan

1. Introduction

The test report describes the prototype antenna for C/A code differential GPS position measurement system proposed, trially manufactured and measured to be mounted on the cylindrical construction.

2. Purpose

The structure is of cylindrical construction shown in Fig. 1, and the directivity in the roll direction and in the pitch direction in case the microstrip antenna is mounted to this was measured.

While the antenna is normally mounted on the ground plane of the plane-plate, in case this is mounted on the cylindrical ground plane of relatively small diameter, that's why there is a fear that the radiation pattern on the hemisphere is deformed.

3. Outline of Microstrip Antenna

3.1 Basic Construction of Back-Feed Type Circularly-Polarized

Microstrip Disk Antenna by one Point Feed.

The basic construction is shown in Fig. 2.

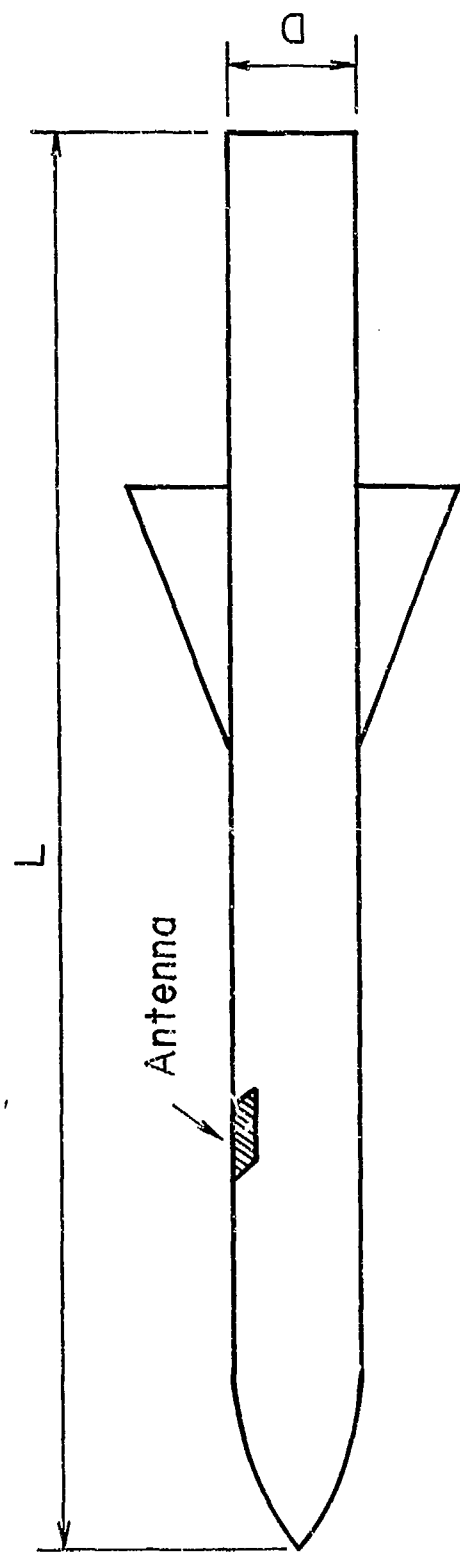
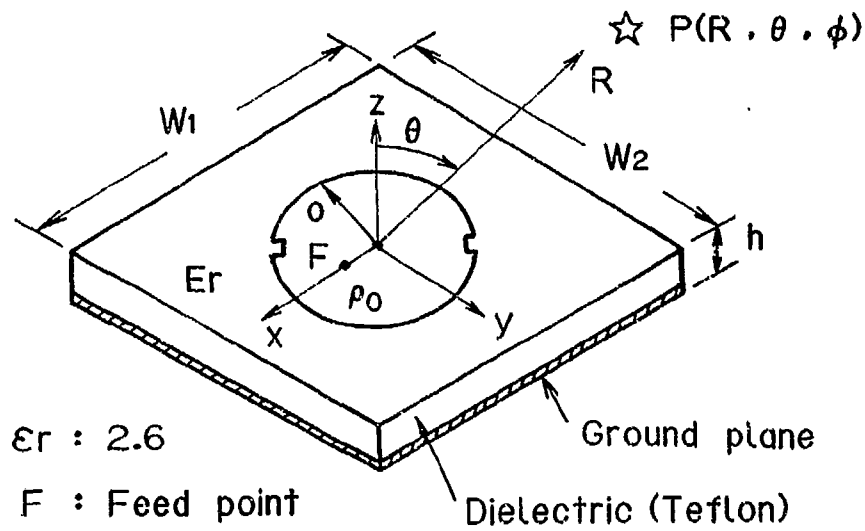
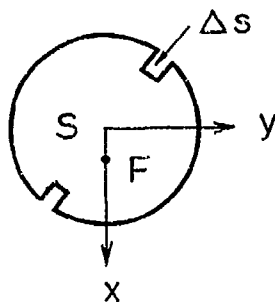


Fig. 1 EXTERNAL VIEW OF
CYLINDRICAL CONSTRUCTION

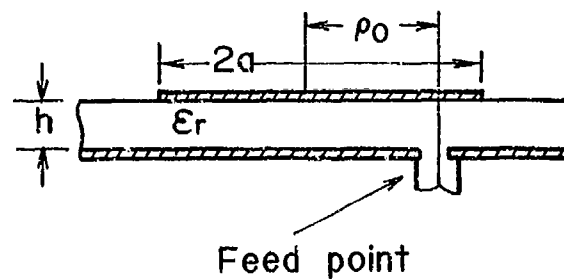


(a) Disk Antenna

ΔS : Separation of generate modes



(b) Disk shape



(c) Feeding

Fig. 2 Back-feed type microstrip disk antenna by one-point feed

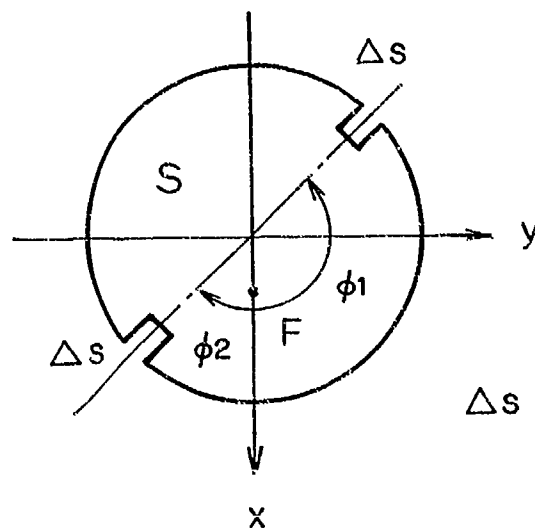
This antenna is fed by one point from the antenna section circuit board, utilizes the amplitude characteristic and phase characteristic in the dipole mode that orthogonalizes in the form of two spaces to remove and to generate in the direction of $\phi_1=+135^\circ$, $\phi_2=-45^\circ$, by adding the separation of generate modes Δs like slit, etc. to the disk element as shown in Fig. 3 in the direction of $\phi_1=+135^\circ$, $\phi_2=-45^\circ$, and releasing the degeneracy of dipole mode TM_{11} degenerated double, resulting in operating as the circularly-polarized antenna.

The shape of the separation of generate modes Δs can be considered in various ways, and in the sample machine the disk element in Fig. 3 was used.

As the sample circuit board, a Teflon circuit board of $\epsilon_r = 2.6$ was used, and as the sample antenna the disk antenna of $2a = 67$ mm of disk diameter was used.

3.2 Radiation Characteristic

The back-feed type circularly-polarized microstrip disk antenna by one point feed is to generate circularly-polarized waves by loading the separation of generate modes Δs by the slit, etc. in the direction of $\phi_1=135^\circ$ or $\phi_2=-45^\circ$ to the disk element of linearly polarized wave disk antenna fed to the position being $F(\rho_0, 0^\circ)$ in Fig. 3, releasing the degeneracy of dipole mode TM_{11} degenerated double, and utilizing the amplitude



Δs : Separation of generate modes

$$\phi_1 = 135^\circ \quad \phi_2 = -45^\circ$$

$$F(\rho_0, \phi_F) \quad , \quad \phi_F = 0^\circ$$

Fig. 3 Back-feed circularly polarized microstrip disk antenna

characteristic and phase characteristic in dipole modes ϕ'_{11a} and ϕ'_{11b} which orthogonalize in the form of two spaces to remove and to generate in the direction of $\phi_1=+135^\circ$, $\phi_2=-45^\circ$. The resonance frequency f_{or} of disk antenna was determined by taking into account the equivalent radius \bar{a} and employing $f_{or} = 1.841 \times \frac{c}{2\pi\bar{a}\sqrt{\epsilon_r}}$, Where, c is the velocity of light. $\bar{a} = a + \Delta\omega$ and $\Delta\omega = (\lambda/\pi)^2 \ln 2$. The feeding point is determined by obtaining the position where the matching can be taken by the experiment. The directional pattern is shown in attached Fig. 5

4. Experimental Method

4.1 Cylindrical ground plane

An aluminum cylinder of 350 mm of diameter and 1,280 mm of length is manufactured as shown in Fig. 4, and a hole for antenna mounting is installed in the shell plate of this center section. The antenna shall be of construction that the radiator can be installed in the position of 25 mm and 15 mm of depth from the shell plate of the cylinder. The antenna of 25 mm of depth for the radiator in Fig. 5 (a) has an opening of 110 mm in the circumferential direction.

4.2 Pattern Measuring Equipment

The pattern measurement was performed in a anechoic chamber for 1.5 GHz band of 4 m \times 7 m of floor area and 2.5 m of

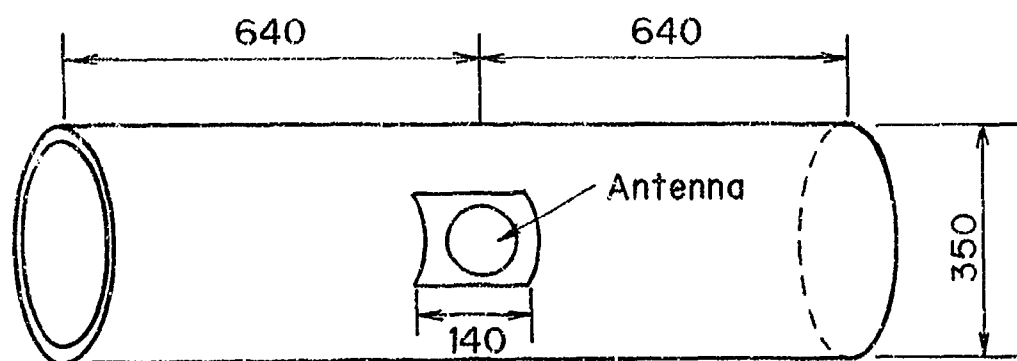
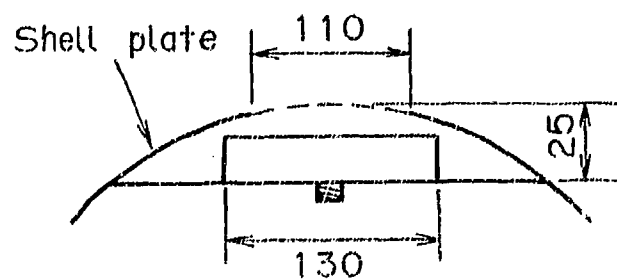
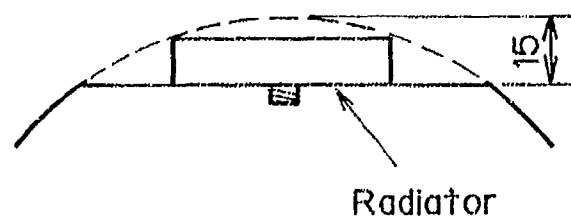


Fig. 4 CYLINDRICAL GROUND PLANE



(a) depths of 25mm



(b) depths of 15mm

Fig. 5 Antenna installation

ceiling height. In this, the pattern measuring equipment shown in Fig. 6 has been installed, and the distance between the transmitting antenna and the sample antenna is 3 m. The transmitting antenna is a dipole with passive reflector, this rotates at the speed of approximately 180 RPM, and it has been designed that the axial ratio of sample pattern can simultaneously be measured with the directivity pattern.

4.3 Measuring Procedure

- (1) The directivity in the direction of roll is measured by placing the sample mounted with the antenna to the mock-up in the standing state to the pedestal as shown in Photo 1 and rotating in the direction of AZ (azimuth).
- (2) This test is conducted for that of 25 mm from the shell plate of the radiator position of sample antenna (Photo 3) and that of 15 mm (Photo 4).
- (3) The directivity in the direction of pitch is measured by electrically floating on the pedestal and horizontally placing as shown in Photo 2, and measuring the directivity rotating in the direction of AZ (azimuth).
- (4) Also in relation to this, those of 25 mm of depth and of 15 mm are measured.

5. Experimental Result

5.1 The measurement result is as per Table 1 and attached Figures 1

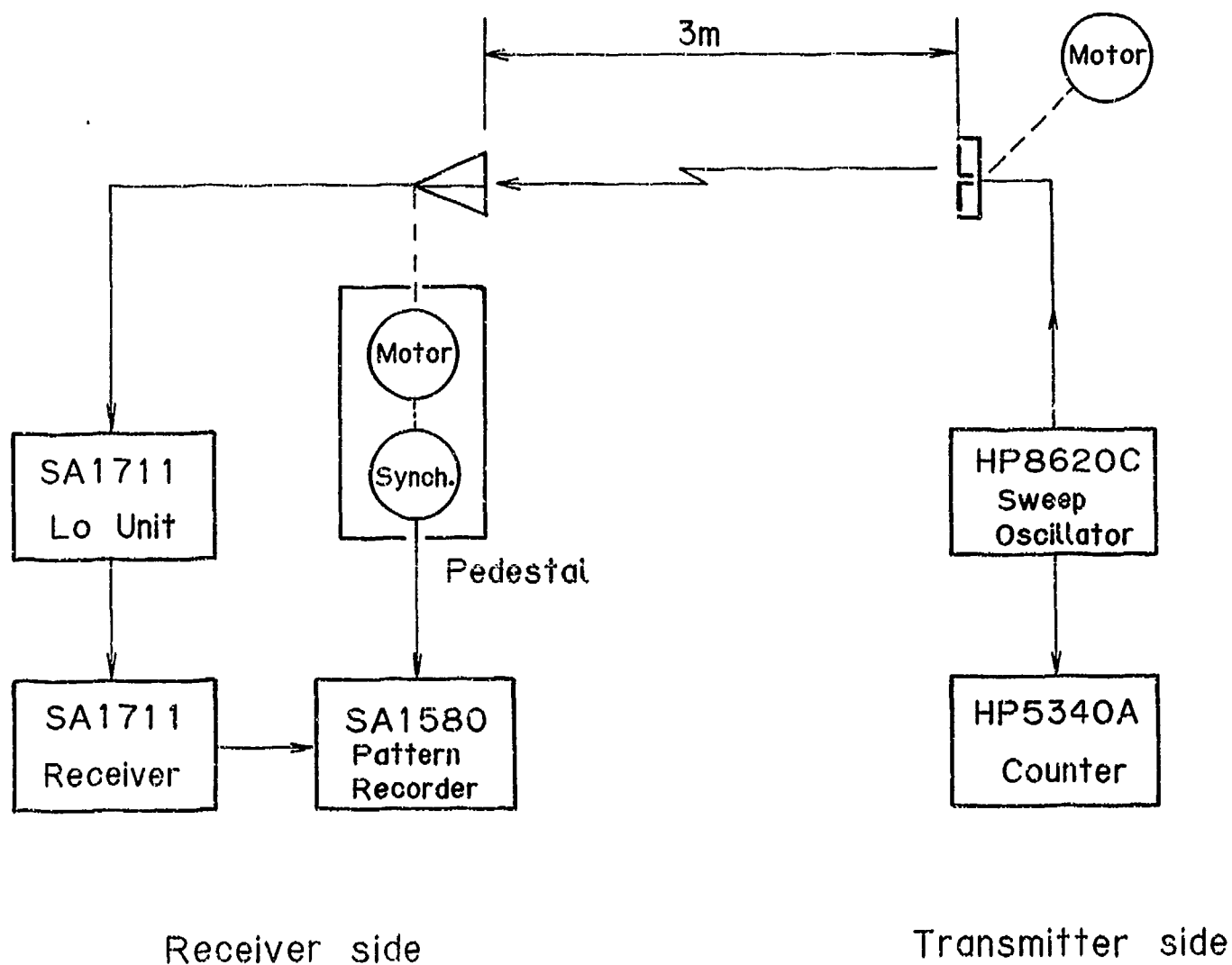


Fig.6 Measuring Instrument

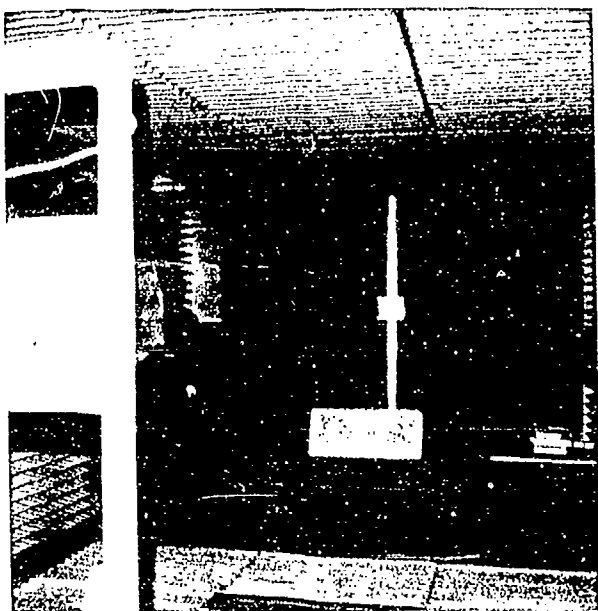


PHOTO 1.

ROLL DIRECTIVITY MEASUREMENT

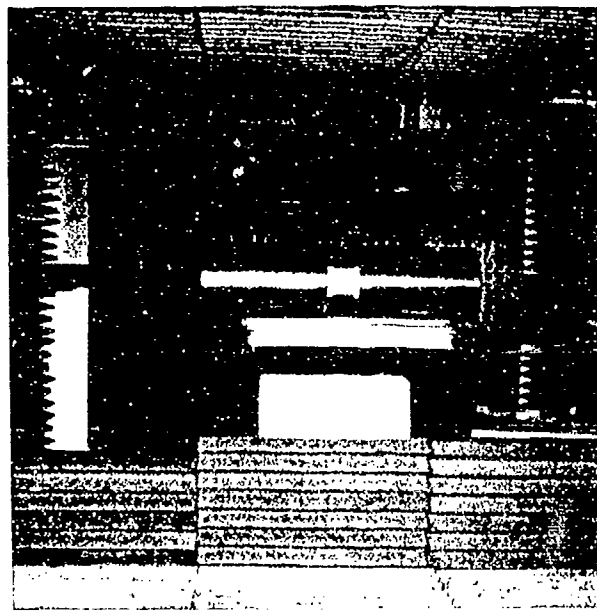


PHOTO 2.

PITCH DIRECTIVITY MEASUREMENT

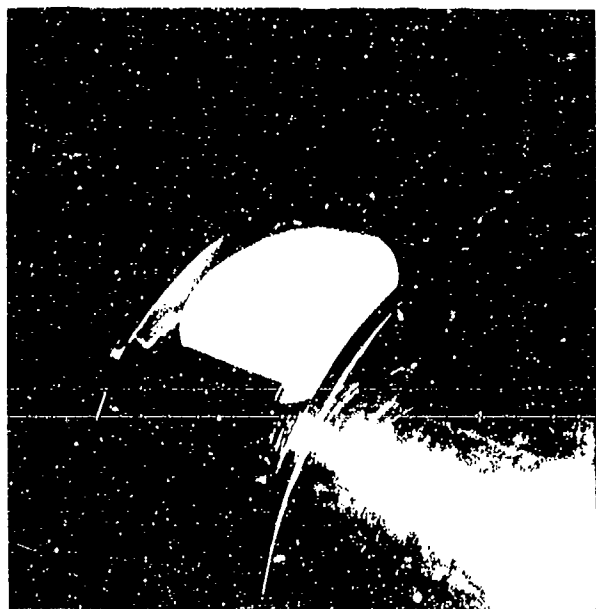


PHOTO 3, DEPTH 25mm

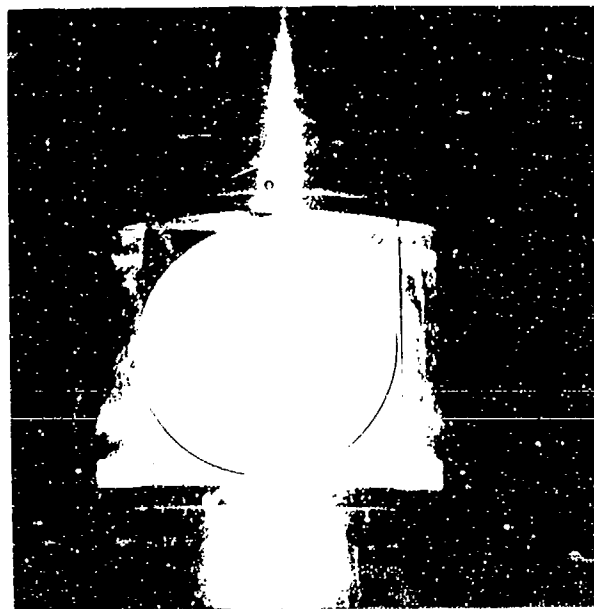


PHOTO 4, DEPTH 15mm

through 4. In this regard, since the axial ratio in the direction of attenuation of 10 dB comes to that right and left patterns have different values, two numerals have been entered.

Table 1 Measurement Result

Attached figure	Radiator depth	Directivity	10 dB beam width	Axial ratio		Absolute gain (Direction of 0°)
				Direction of 0°	Direction of 10 dB attenuation	
1	25 mm	Roll	160°	4 dB	5dB/7dB	6 dBi
2	"	Pitch	150°	3 dB	8dB/12dB	"
3	15 mm	Roll	178°	3 dB	4dB/ 7dB	"
4	"	Pitch	171°	3 dB	13dB/13dB	"
5	0 without G.P.	Roll/Pitch	196°	1.2dB	4dB/4dB	"

5.2 To receive the GPS satellite of more than 5° of angle of elevation, since it is required that the 10 dB beam width is more than 170°, the mounting of radiator cannot be satisfied at the depth of 25 mm from the shell plate, but made at 15 mm, and it is considered to be possible to carry out this.

5.3 The axial ratio is deteriorated in the direction of 90°, being maximum 13 dB in the direction of attenuation of 10 dB, and in this case, the receiving power comes to be the lower value by 3 dB than the peak value of pattern.

In this regard, the 10 dB beam width has been obtained including the portion of lowering by this.

6. Considerations

- 6.1 It is known from attached Figures 1 through 4 that the axial ratio of 15 mm of depth and 25 mm of depth has been deteriorated in comparison with the axial ratio of single antenna, and in this case the depth of the radiator is deep, the more the radiation level in the lateral (pitch) direction is lower, that is to say, the beam has come to be sharp. This is considered deriving from the fact that radiated waves from the radiator are scattered at edges of the shell plate and the shell plate forms cavities in a certain sense.
- 6.2 From attached Figures 1 through 4, in comparison with the direction of roll, for the directivity in the direction of pitch the ripple comes to remarkably appear. This is considered as an influence of scattered waves from both ends of aluminum cylinder

References

† : Engineering manager

2nd Defence Equipment Engineering Department

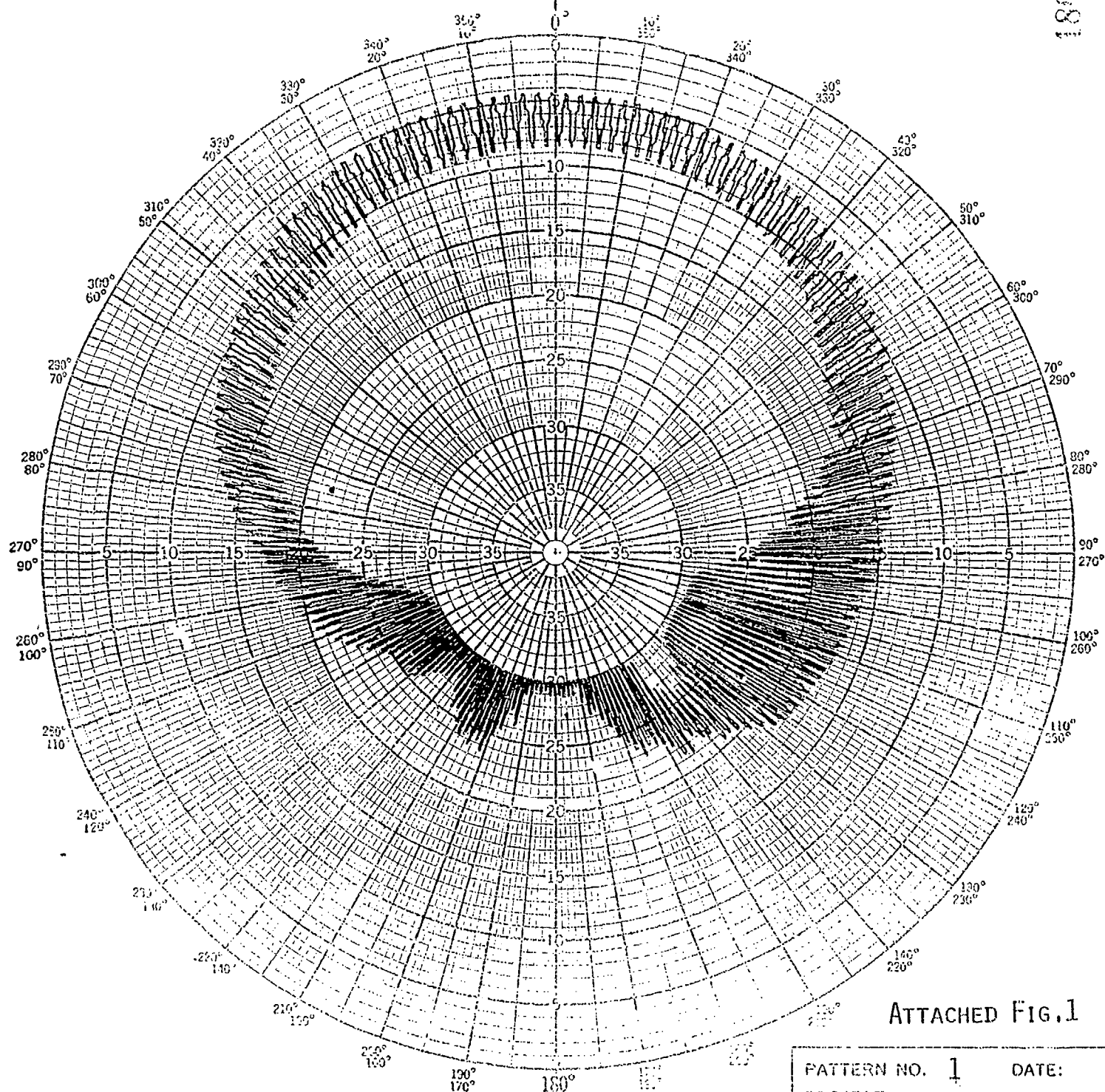
Mitaka Plant

Japan Radio Co., Ltd.

1-1 Shimorenjaku 5 Chome Mitaka city

Tokyo 181 Japan

183948



ATTACHED FIG.1

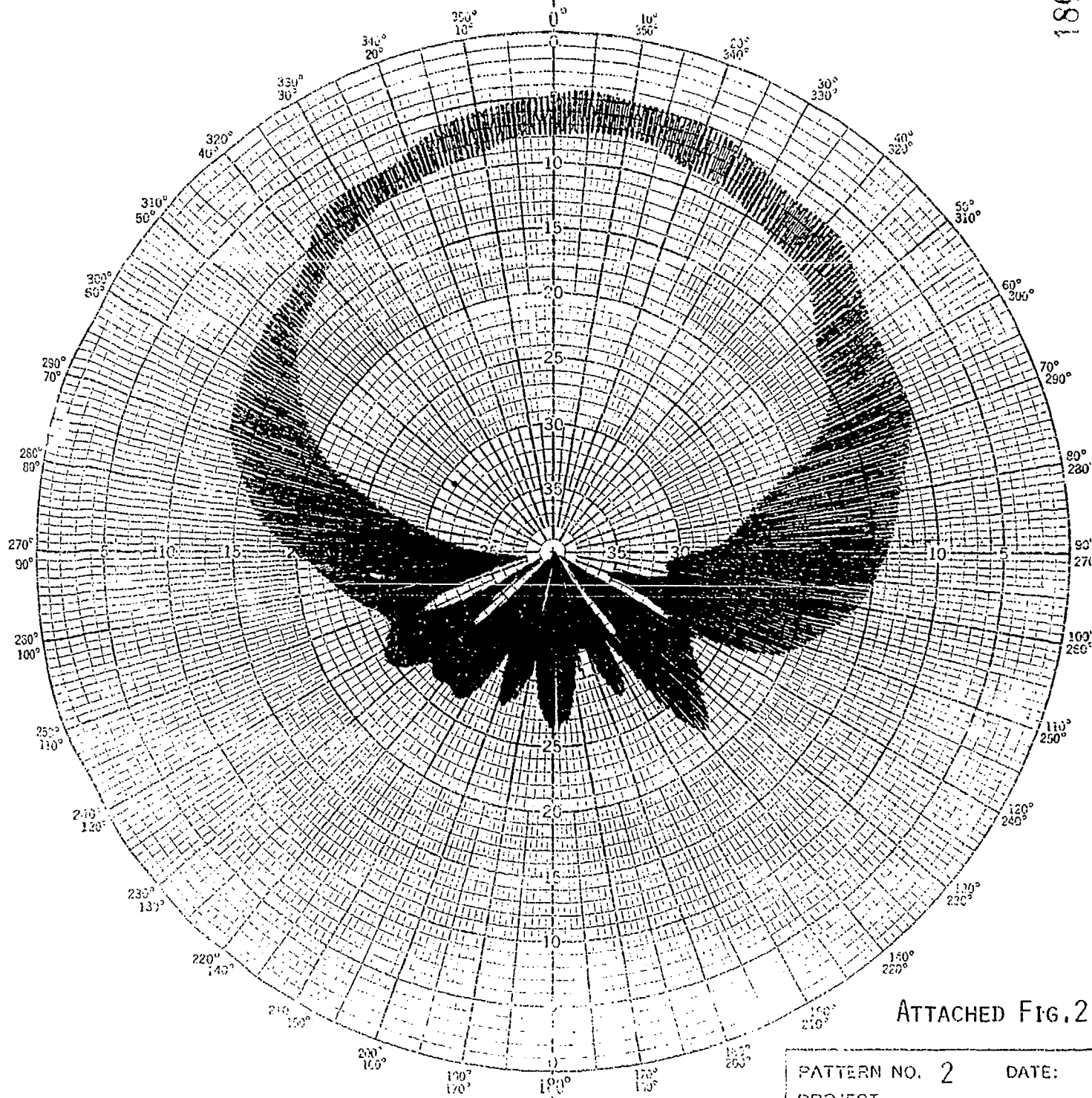
CHART NO. 220
SCIENTIFIC-ATLANTA, INC.
ATLANTA, GEORGIA

PATTERN NO. 1
PROJECT GPS
ENGRS.

DATE:

REMARKS DEPTH 25MM
ROLL DIRECTIVITY

189950



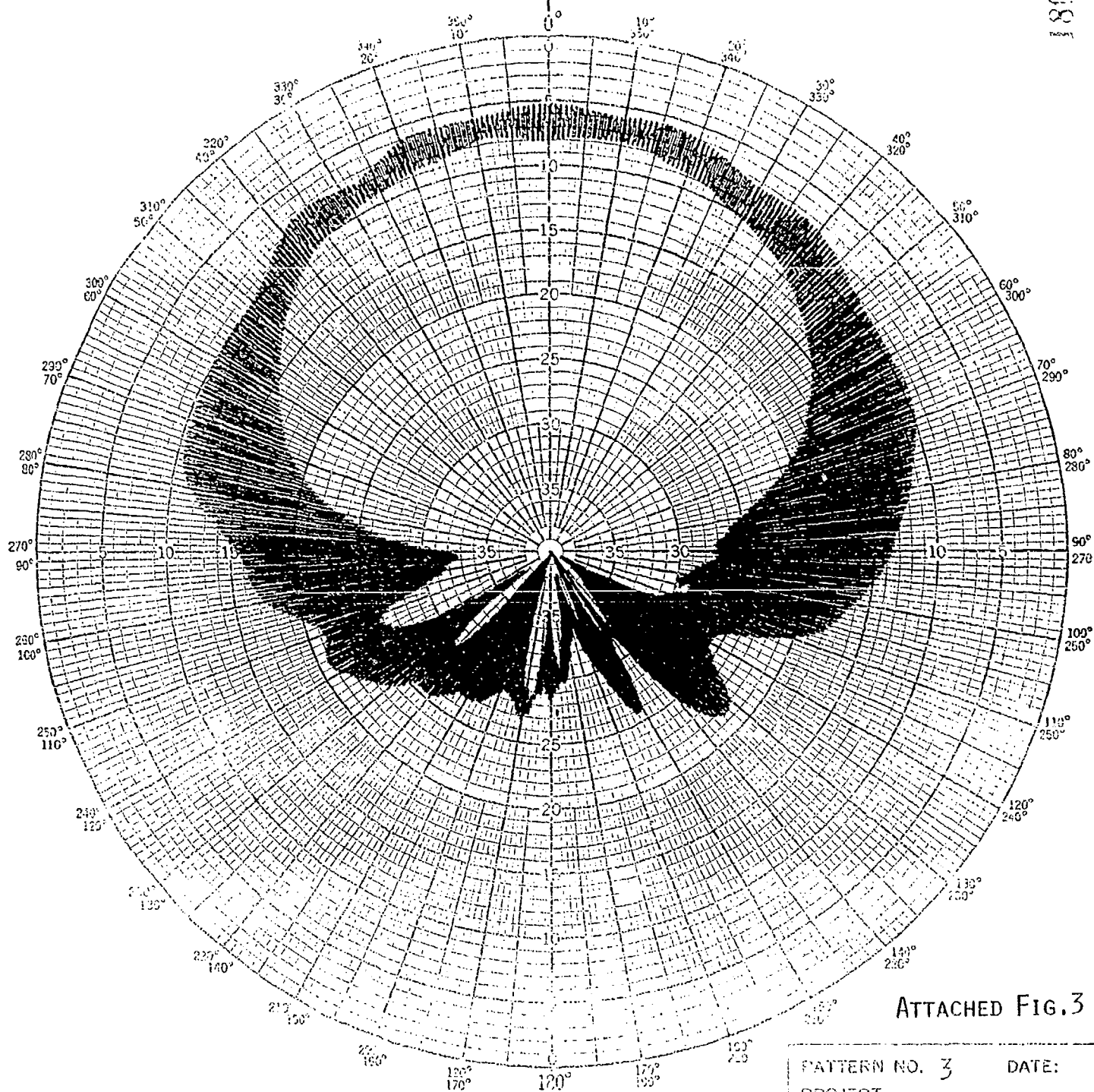
ATTACHED FIG.2

PATTERN NO. 2 DATE:
PROJECT GPS
ENGERS.

STIMULUS DEPTH 25MM
PITCH DIRECTIVITY

CHART NO. 230
NO. 1000-100-0000-0000

180952



ATTACHED FIG. 3

PATTERN NO. 3	DATE:
PROJECT	GPS
ENGERS.	
REMARKS	DEPTH 15MM
	ROLL DIRECTIVITY

180951

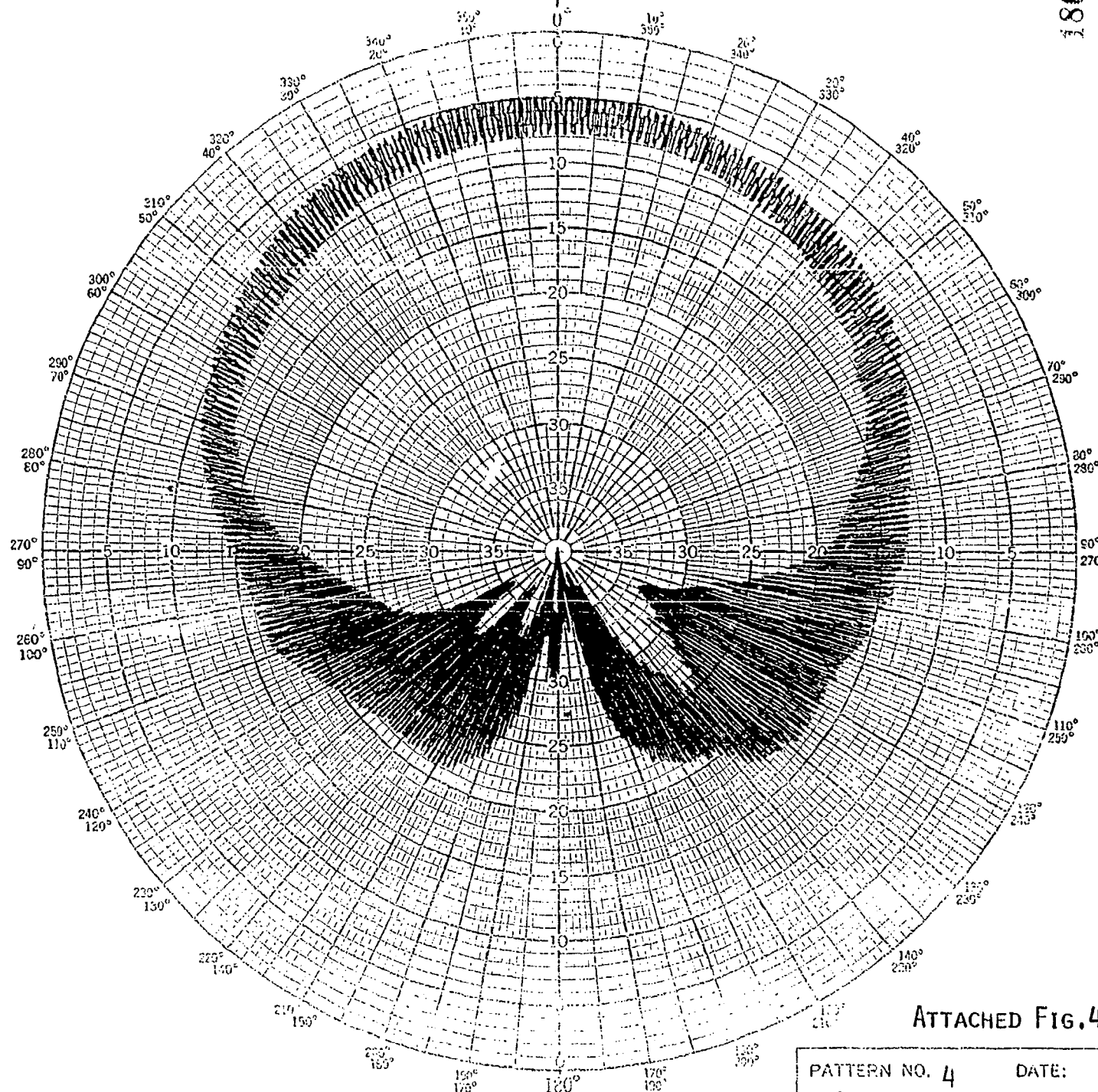


CHART NO. 220
SCIENTIFIC-ATLANTA, INC.
6 LEXINGTON AVENUE

PATTERN NO. 4 DATE:
PROJECT GPS
ENGERS.

REMARKS DEPTH 15MM
PITCH DIRECTIVITY

1

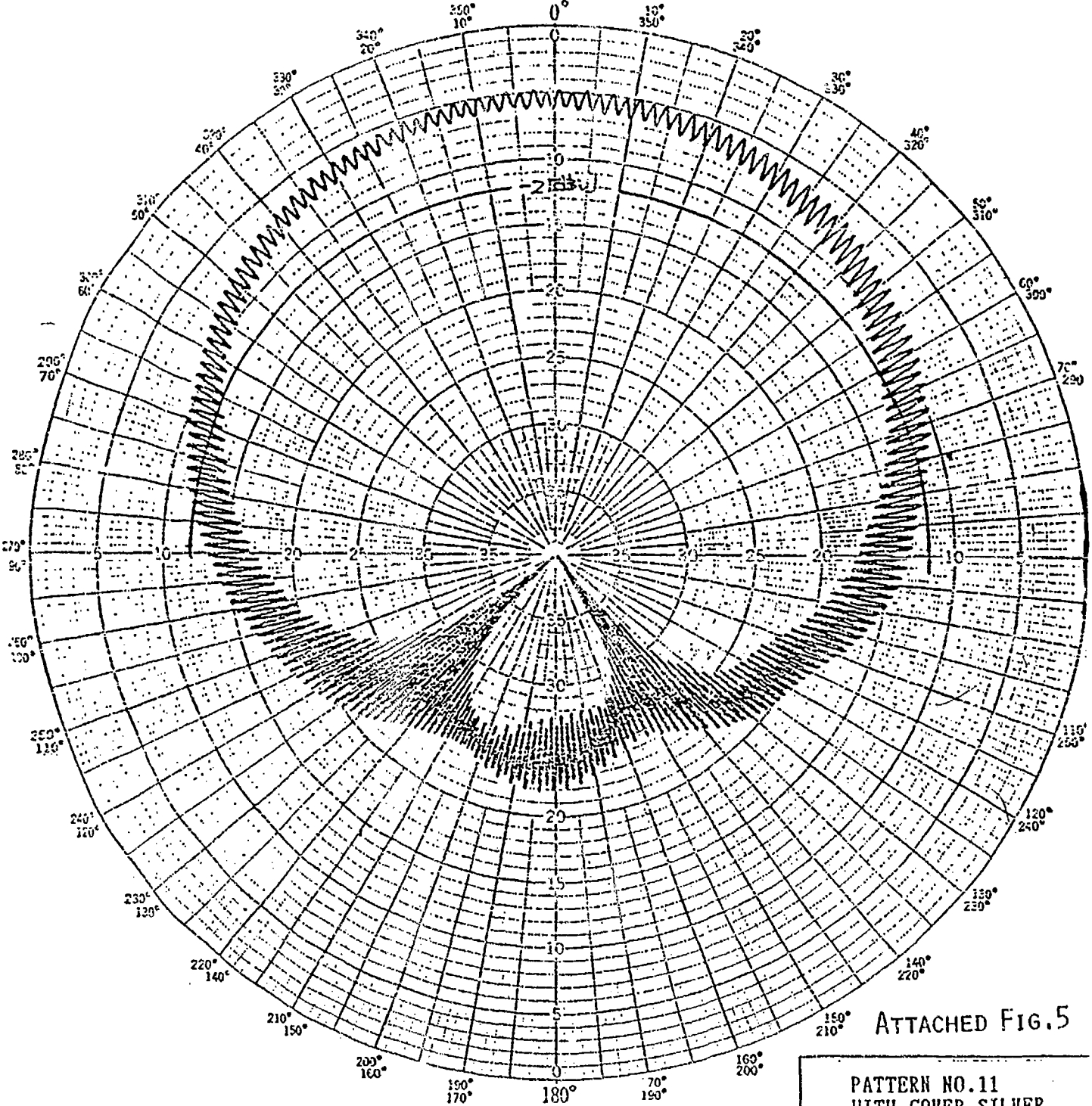


CHART NO. 220
SCIENTIFIC-ATLANTA, INC.
ATLANTA, GEORGIA

ATTACHED FIG. 5

PATTERN NO. 11
WITH COVER SILVER
F=1.5754 (GHZ)

REMARKS
DIRECTIVITY WITH-
OUT GROUND PLANE

**USE OF AIRCRAFT FACET MODELS
IN DETERMINING GPS SIGNAL AVAILABILITY**

Edward P. Bradley
YIER
Eglin AFB, FL

Steven N. Karels
TASC
Reading, MA

USE OF AIRCRAFT FACET MODELS IN DETERMINING GPS SIGNAL AVAILABILITY

ABSTRACT

TASC is supporting Eglin Air Force Base in the development of Air Combat Maneuvering Instrumentation (ACMI) system designs for the year 2000 and beyond. ACMI uses test pods which mount and have similar shape to an AIM-9 missile and they envision the use of GPS equipment within the pod for position determination. Since the ACMI pod is mounted under an aircraft wing, GPS signal availability is a major concern. An obscuration matrix software tool was developed and used to evaluate GPS signal availability using government-supplied aircraft facet models. The output of the obscuration matrix software program is an aircraft coordinate system-based obscuration matrix. This obscuration matrix was coupled with TASC's Test Range User Mission Planner (TRUMP) software and signal availability statistics were gathered. Relative measures of performance were collected for representative ACMI missions. This paper discusses the issues, facet models, and describes the software implementation employed in this study. Aircraft-induced blockage results are presented and discussed including various F-15 and F-16 obscuration plots and performance metrics.

INTRODUCTION

TASC is under contract with the ACMI 2000 program office located at Eglin Air Force Base, Florida to assist in the specification and development of ACMI training ranges. One of the key technologies to be used at future ACMI ranges will be the Global Positioning System (GPS). A similar development, also supported by TASC, is ongoing for the test range community through the Range Applications Joint Program

Office (RAJPO), also located at Eglin. While the RAJPO family of equipment can be employed either internally within the test vehicle (e.g., a high performance test aircraft) or on a wing-mounted pod, the ACMI training ranges envision the use of wing-mounted pods to carry time space position information (TSPI) equipment. In addition, the locations of the pods will be dictated by tactical/training needs (i.e., they need flexibility to position the pods anywhere on the airframe).

TASC was asked to investigate the effect of body (fuselage and wing) masking on GPS signal availability and resulting impacts on dilution of precision (DOP). If sufficient TSPI accuracy could not be established due to the effects of body masking, then consideration would be given to employment of ground transmitters (GTs) to provide additional signal sources and improved geometry. However, GTs are relatively expensive and there are certain operational impacts and constraints in their use. This study projected the expected level of body masking and the resultant effects upon navigation accuracy in order to make an informed decision on employing GTs.

BACKGROUND

The success of the Air Force and the Navy in the recent mideast air war was in part a reflection on the excellence of our air combat training ranges in the U.S. Pilots from both of the services gave high praise to our air combat training ranges in preparing them for their trial by fire. A movement is underway already to increase the utility of these ranges in both USAF and USN to take advantage of the lessons learned from this mideast conflict. Systems Operating Requirements Documents (SORDS) have been modified to reflect these findings and a top down systems conceptual study is currently underway to develop a system

specification for a Joint Air Combat Training System (JACTS) for the next generation training ranges. This single system specification for many ranges will ensure commonality and interoperability between them. Our pilots want to fly on other service ranges, they want increased precision, more indepth postflight debriefings and a large increase in the size of the training exercises both in terms of number of participants and the physical airspace used.

One of our national assets, the Global Positioning System (GPS) with its many satellites, has already been identified as a potential major contributor to greatly increased precision where time, space, and position information for a large number of aircraft is readily available. Additionally, a greatly increased size of the training ranges themselves can be easily accommodated by use of GPS. Secondary but equally important advantage to the use of GPS is the minimization of ground support equipment and radar altimeters for low altitude operations and the elimination of additional multilateration measurement sites with an increase in size of the ranges.

The JACTS conceptual study currently underway will address the application of GPS as a major component of the next generation air combat training systems for both the USAF and the USN. Capabilities for handling tactical and strategic aircraft as well as helicopter operations will be included. Upon completion of the study in early GFY92, work will commence on full scale development of systems for four Air Force and Navy ranges. The initial operating capability (IOC) for these system is in the mid 90's. Follow on efforts to upgrade additional ranges will then be initiated.

A key parameter in the utilization of the GPS system as the TSPI source on air combat training ranges is the ability of the participating aircraft to "see" the satellite constellation. For a three dimensional solution (and time), four satellites in good geometry are required to be in view. GPS signal availability can be degraded by fuse-

lage and wing masking effects either reducing the available satellite geometry or by lowering the available number of visible GPS satellites below the minimum of four needed for a solution. This will result in a degradation of accuracy. GPS user antenna location and masking of the GPS satellites by aircraft components, therefore, will have significant impact on how the design effort should proceed. If there is insufficient GPS signal availability from the GPS satellite constellation, the use of Ground Transmitters (GTs) to supplement the GPS constellation might be required. An analysis was therefore conducted to examine the extent of signal blockage due to aircraft components.

FACET MODELS

The selected approach was to consider the GPS signal to be not available if optical line of sight was obstructed from the phase center of the GPS antenna (assumed to be located within the nose cone of the ACMI 2000 instrumentation pod). A single isotropic GPS antenna was modeled with a stationary phase center located on axis within the pod. No consideration of multipath effects were included in the analysis and therefore fades and nulls were not addressed. Multipath from aircraft parts rapidly change as the geometry changes causing nulls and increased gains. Diffraction and aircraft movement will "average" the effects of gain variations. In many instances, the antenna will "see" the GPS signal source even when optically blocked due to diffraction and multipath effects. Therefore, the results should be more conservative than "real-life" signal availability on actual aircraft.

To minimize cost for the study, existing Air Force provided facet models were considered. Eglin Air Force Base provided two facet models; (1) an F-16, and (2) an F-15 aircraft model. The F-15 and F-16 aircraft were chosen as the most likely participants for an Air Force training range. The models were received on a nine-track

VAX-compatible tape and read and transferred to an IBM-equivalent personal computer (PC). A PC was chosen to minimize cost and for ease of portability to other PC stations. The two files were analyzed and converted into ASCII compatible files. The ASCII files were read by custom software developed by TASC to compute the upper and lower hemispheric visibilities as observed by a GPS antenna located at a user-defined location.

The Eglin-provided facet models consisted of a number of "parts" that together defined the surface structure of the aircraft. These "parts" referenced facets numbers and the facet numbers were assigned locations in three dimensional space. Table 1 defines the number of parts, points, and facets used to define the F-15 and F-16 aircraft models.

Table 1 Facet Model Structure

AIRCRAFT MODEL	NUMBER OF PARTS	NUMBER OF POINTS	NUMBER OF FACETS
F-15	154	2272	4534
F-16	60	1019	1932

Additional "parts" or collections of triangular facets were included to define store shapes and locations. Exhibit 1 shows the first part of the facet model file for the F-16 aircraft. The file describes the type of aircraft and the date the ASCII file was converted from the unformatted file received from Eglin AFB. The number of parts, points, and facets are listed for the model. The exhibit also shows the first 13 parts and the facet numbers included in the definition of each part.

Exhibit 2 shows the mapping of facet numbers to points defining the facet. Since these are triangular facets, three points define each facet.

The location of each point is defined within the file. Exhibit 3 illustrates a portion of the file for points 1 through 20. The three columns of

F16 converted on 1/02/91

* PARTS	POINTS	FACETS
60	1019	1932
* PART	START	END
1	1	16
2	17	48
3	49	80
4	81	112
5	113	144
6	145	176
7	177	208
8	209	218
9	219	228
10	229	253
11	254	278
12	279	298
13	299	316

Exhibit 1 Part Definition Portion of the F-16 Facet Model

* FACET	POINT	POINT	POINT
1	1	2	3
2	3	2	4
3	4	2	5
4	5	2	6
5	6	2	7
6	7	2	8
7	8	2	9
8	9	2	10
9	10	2	11

Exhibit 2 Facet Definition Structure

numbers are in scientific notation in the aircraft coordinate system. All units are in inches. From left to right, the columns represents the x, y, and z coordinates of a Cartesian system.

In this manner, the facets defining an aircraft model are constructed. A custom program reads the facet model and stores the part, point, and facet information for construction of the facet model and computation of visibility. An example of the F-16 model is shown in Fig. 1. As described above, the use of triangular facets to represent the surface of the aircraft model can readily be seen. Likewise, the stores mounted on the edge of the wing tip are similarly constructed from triangular facets. Our software makes no distinction of RF

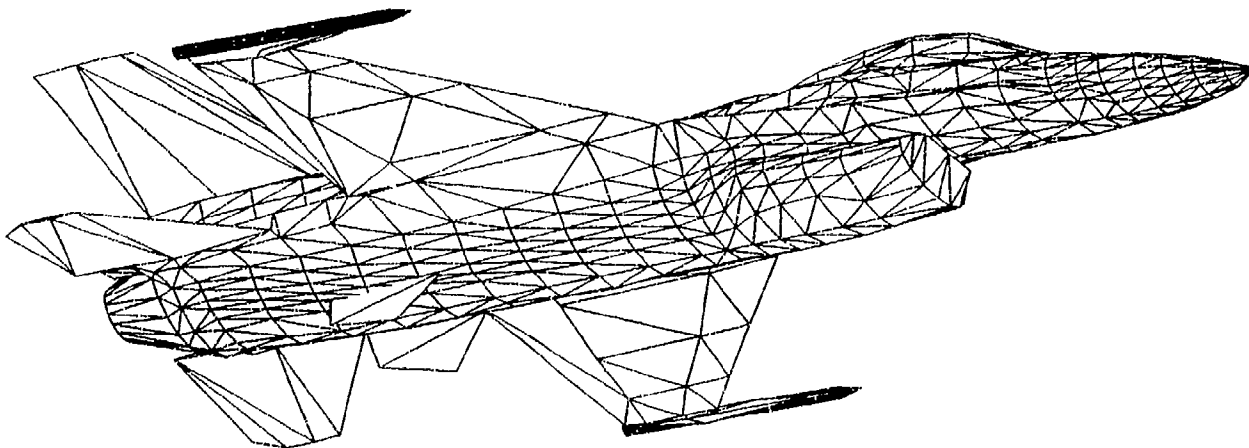


Figure 1 Hidden Line View of an F-16 Aircraft

1	-1.25000E+01	-6.55000E+00	8.45500E+01
2	0.00000E+00	0.00000E+00	8.51000E+01
3	-1.25000E+01	-5.57000E+00	8.76200E+01
4	-1.25000E+01	-4.08000E+00	8.90300E+01
5	-1.25000E+01	-2.04000E+00	8.99300E+01
6	-1.25000E+01	0.00000E+00	9.01800E+01
7	-1.25000E+01	2.04000E+00	8.99300E+01
8	-1.25000E+01	4.08000E+00	8.90300E+01
9	-1.25000E+01	5.57000E+00	8.76200E+01
10	-1.25000E+01	6.55000E+00	8.45500E+01
11	-1.25000E+01	6.34000E+00	8.31400E+01
12	-1.25000E+01	5.07000E+00	8.11100E+01
13	-1.25000E+01	3.33000E+00	7.99200E+01
14	-1.25000E+01	0.00000E+00	7.93000E+01
15	-1.25000E+01	-3.33000E+00	7.99200E+01
16	-1.25000E+01	-5.07000E+00	8.11100E+01
17	-1.25000E+01	-6.34000E+00	8.31400E+01
18	-2.50000E+01	-1.10500E+01	8.58100E+01
19	-2.50000E+01	-1.05900E+01	8.86000E+01
20	-2.50000E+01	-8.62000E+00	9.15900E+01

Exhibit 3 Facet Point Location Definition

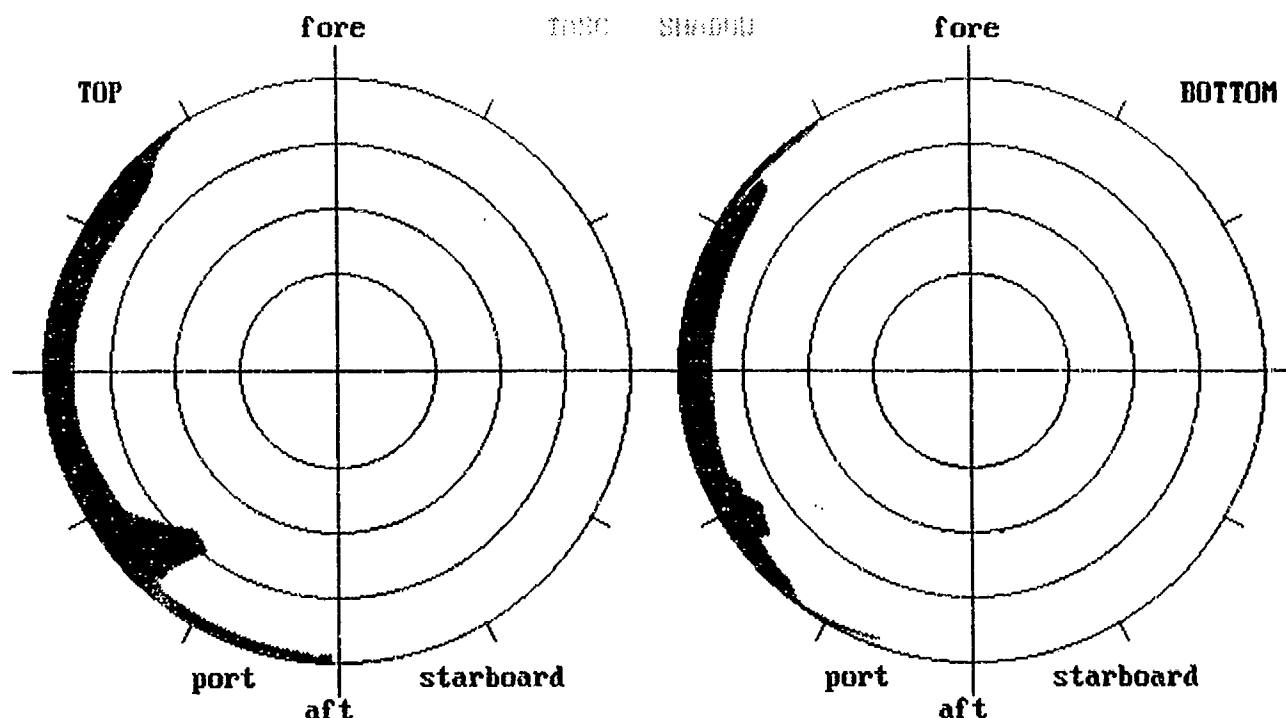
transparent surfaces (such as the canopy versus RF-opaque surfaces). This will not significantly alter the expected actual results.

The custom software program developed by TASC, called "Shadow," computes the line-of-sight visibility from a user specified point (in aircraft coordinates) for all azimuth and elevation angles consistent with VGA graphics resolution — about $1/2$ degree. The visibility results for an F-16 are shown in Fig. 2. Because the pod is located on the right wing tip, the visibility (as would be expected) is excellent. The F-16 aircraft was initially considered because the facet model con-

tained about $1/2$ the number of "parts" compared to the F-15 model. Also, because the wing tip mounting was known to produce excellent visibility, this airframe was selected to help validate the model and to gain confidence with the software tool.

After the success with the F-16 aircraft facet model, we considered the F-15 model. This model was more challenging because of the increased number of "parts" within the model. The higher number caused the program to exceed the DOS limitation of 640 Kbytes of memory access and the program was converted to run under a DOS extender. The F-15 model is important because of possible additional obscuration from pod mounting locations directly adjacent to the fuselage and under the wing. If sufficient GPS signal availability could not be obtained, then alternative mounting restrictions might be imposed or the use of GTs might be required. Figure 3 shows a hidden line presentation of the F-15 model.

Stores were defined for the mounting points on the aircraft model and added to the model. Shadow was run for eight pod mount locations and statistics were gathered for each pod location. Figure 4 shows the amount of upper hemispheric, lower hemispheric, and total (spheric) percent of visibility for each of the mounting locations. The



F16 converted on 1/02/91

-- y and z axes are inverted

reference point (x, y, z): -309.000 187.900 -90.000

percentage visibility: top 94.1, bottom 95.6, overall 94.9

Figure 2 F-16 Pod Visibility (Mounted on Right Wing Tip)

decrease in visibility as the pods are moved in-board are clearly seen.

Figure 5 shows a typical polar presentation for station number 8a on the F-15 aircraft. The shape of the F-15 and various stores can be seen, although in a highly distorted way.

SIGNAL AVAILABILITY

The effect of aircraft masking on GPS signal availability can be characterized by investigating its contribution to geometric dilution of precision (GDOP). One of the components of GDOP is PDOP or position dilution of precision. PDOP was selected as the metric because ACMI has a positional requirement of 25 feet in each dimension. An analysis was conducted to determine

the effect of various GPS pod mounting locations for an F-15 aircraft and their corresponding PDOPs. Because PDOP is a function of satellite location and launch schedule, certain approximations were made to characterize the problem. First, a nominal almanac (week 595) was used and the portion of the day was chosen when relatively good geometry was available. This was assumed to be representative of a typical day when the entire constellation would be in place. Second, because the orientation of the aircraft couples with the satellite geometry to determine signal availability, we modeled the "trajectory" of the F-15 aircraft as a stationary point in the Gulf of Mexico at 100 meters above sea level and rotation +6 degrees in azimuth in 5 seconds. This was repeated continuously during the majority of the day.

An azimuth and elevation matrix was generated from the SHADOW program and coupled

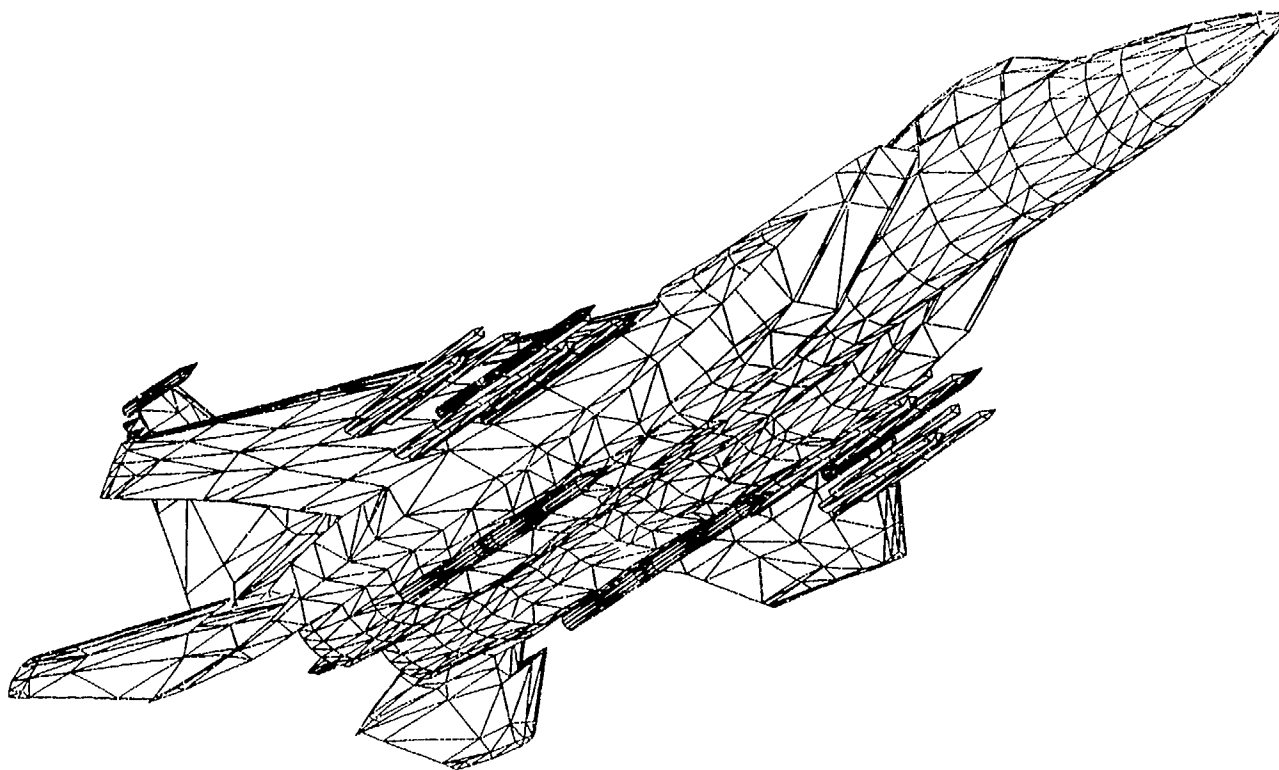


Figure 3 Hidden Line View of an F-15 Aircraft

with TASC's TRUMP GPS mission planner software. PDOP files were generated for each of the right side wing stations (8a through 9b) and also for the case of no aircraft masking. The left side was not considered because the visibility matrices are only a mirror image of those for the right side. The PDOP files were then examined and the means and standard deviations were computed. The results are shown in Table 2.

EFFECTS ON DOP

The effects on DOP are consistent with expectations — as the GPS pod is located closer to the fuselage center, PDOP becomes larger. The lack of effect of the outboard wing stations can be attributed to the GPS satellite masking angle of +5 degrees. Since we assumed a "level" flight, fuselage masking below a +5 degree angle would have no effect on the GPS receiver because it is as-

sumed to ignore satellites below the +5 degree masking angle. It was therefore concluded that ACMI could use GPS to meet their positional accuracy requirements without the need to incorporate ground transmitters. Either C/A-code or P-code sets may be used except at the inner wing station (i.e., station #8a), where P-code receivers would be needed to counter the increased PDOP while still meeting the ACMI positional accuracy requirements.

SUMMARY

The use of aircraft facet models to quantify GPS signal availability is a useful technique. Use of existing aircraft models saves valuable manpower and produces higher confidence results. The coupling of aircraft masking with GPS analysis tools provides an automated mechanism to explore GPS performance issues.

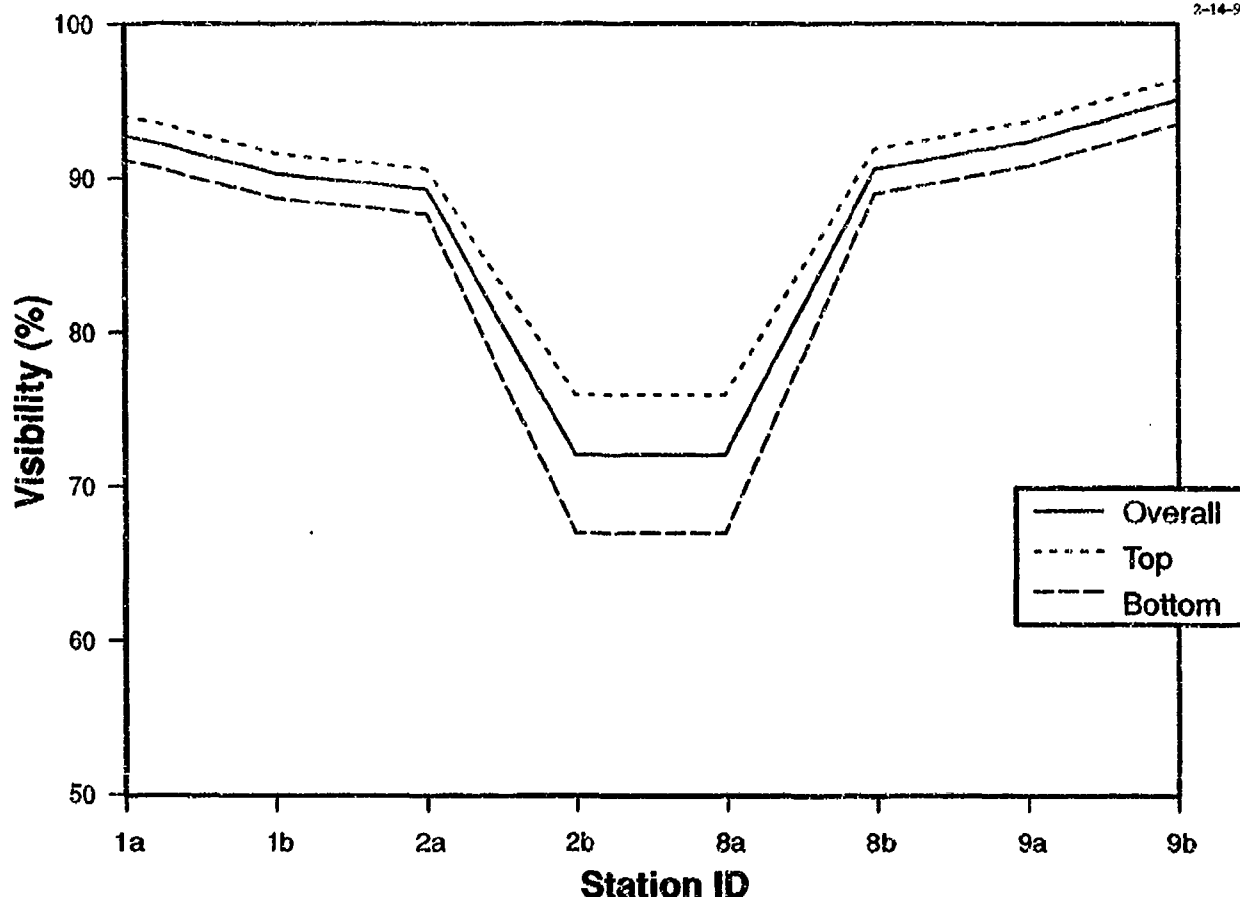


Figure 4 Visibility vs. Mounting Location

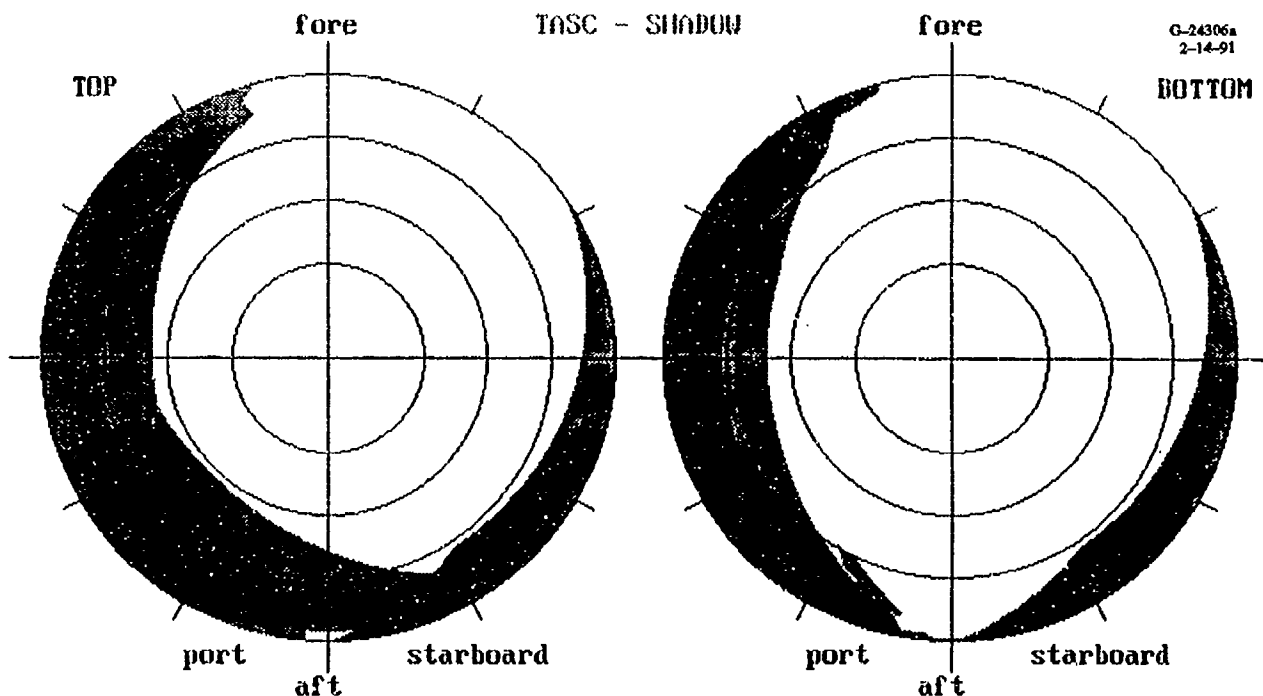
Future work might include incorporation of aircraft masking models with GPS mission planning tools to more accurately predict mission navigation performance. To properly accomplish this, a "library" of aircraft masking matrices would need to be developed and integrated with a GPS mission planning system such as TRUMP. Addition models, such as the A-10, B-1, and B-52 are also available.

AUTHORS BIOGRAPHY

Ed Bradley is the deputy director of engineering for USAF training range systems at Eglin AFB, Florida. He formerly was the chief engineer of the training range requirements directorate and

led the engineering team that developed the technical requirements for the Joint Air Combat Training System. A wealth of experience in the design and development of aircraft as well as weapons brings a background well suited to the development of next generation air combat training systems that will meet the mark of excellence.

Mr. Karels is the Manager of the Range Systems Section of TASC's Electromagnetic Systems Department. Mr. Karels is responsible for analysis and simulation of vehicle navigation issues involving integrated sensors such as Global Positioning System (GPS), inertial measurement devices, lasers, and radars. Mr. Karels has actively been supporting the GPS Range Applications Program Office (RAJPO) at Eglin Air Force Base,



'*** F15 MODEL CONVERTED ON 1/02/91 -- y and z axes are inverted
 reference point (x, y, z): -483.500 100.050 -116.220
 percentage visibility: top 68.3, bottom 76.2, overall 72.3

Figure 5 Pod Visibility from Station #8a, F-15 Aircraft

Table 2 PDOP Statistics vs. Wing Station

POD STATION	PDOP MEAN VALUE	PDOP STANDARD DEVIATION
None	3.50	1.77
9b	3.50	1.77
9a	3.53	1.77
8b	3.53	1.77
8a	3.99	2.37

Florida in the area of GPS simulations and test range integration issues.

Prior to joining TASC, Mr. Karels was the Time-Space-Position-Information (TSPI) expert at the Air Force Flight Test Center (AFFTC) at Edwards Air Force Base, California and the Utah

Test and Training Range (UTTR) at Hill Air Force Base, Utah. He was the Advanced Range Data System (ARDS) program manager and developed the requirements baseline and the system architecture which is still in effect today. The ARDS system is a combination of GPS (RAJPO) components and special high-accuracy augmentation components combined with a system of simultaneous Kalman filters to meet the TSPI requirements of the 1990's. He also developed instrumentation systems in such diverse areas as radar, laser systems, optical systems, timing systems, real time microprocessor interfaces, and coordinate transformation system interfaces. He is also familiar with telemetry systems and data processing associated with TSPI integration and data reduction. Mr. Karels also supported the Patriot missile program at White Sands Missile Range

(WSMR), New Mexico as a radar system analyst for the phased-array radar system.

Mr. Karels received a B.S. degree in Physics from California State Polytechnic at San Luis Obispo, California (1968), an M.S. in Electrical

Engineering (Communications Theory) from the University of Southern California (1974), and an Engineer's degree in Electrical Engineering (1976). He is currently working on his Doctorate's degree from Northeastern University. Mr. Karels is a member of IEEE.

REAL-TIME ATTITUDE DETERMINATION USING THE ASHTECH THREE-DIMENSIONAL DIRECTION FINDING SYSTEM

Mark Kuhl, Kendall Ferguson, Xinhua Qin, Sergei Gourevitch

**Ashtech, Inc.
390 Potrero Ave.
Sunnyvale, California 94086
(408) 737-2400**

Biography

Mark Kuhl is a graduate of Ohio University with both a Bachelor's and Master's Degree in Electrical Engineering. Throughout the last three years of his studies he was employed by Avionics Engineering Center at Ohio University where he worked on GPS projects to augment flight navigation. Mr. Kuhl is currently employed with Ashtech and is a member of the development team for the 3DF attitude determination system.

Abstract

A method for real-time, 3-dimensional attitude determination (heading, pitch, roll) has been developed using state-of-the-art GPS technology. This method is based on differential carrier phase measurements between four antennas which are connected to one 24-channel receiver. (The 24 channels are divided into four banks of six channels each.) Key advantages of this method over existing methods include the following: the initial phase ambiguity is determined with one epoch of data, the attitude is updated once per epoch, and cycle-slip detection and repair are achieved instantaneously.

The differential phase measurements are processed using double-differencing techniques, which have already been proven successful in real-time kinematic applications. The attitude angles calculated can be as accurate as one milliradian (3.5 arc-minutes) for antenna spacings on the order of one meter. Since such accurate attitude measurements may be achieved in real-time, numerous applications for the Ashtech Three-dimensional Direction Finding (3DF) system will arise. One obvious application is the integration of 3DF with an inertial measurement unit (IMU) for aircraft control and navigation.

In this paper, we describe the basic system architecture of the 3DF system, the initial relative antenna position calibration procedure, as well as a description of the phase ambiguity resolution technique used. Also shown are results illustrating the accuracy of the 3DF system in both static and dynamic conditions.

Introduction

The following is a quote from a paper presented by the U.S. Army Engineer Topographic Laboratories at a recent conference:

"The GPS Azimuth Determination System 'proof of technical feasibility' study resulted in a successful demonstration of the interferometric approach to azimuth determination. ...these contracts have led to the arrival of new receivers incorporating these concepts." [1]

One of these new receivers (not discussed in the paper) is the Ashtech Three-dimensional Direction Finding system (3DF). The Ashtech 3DF provides attitude information at a one second update rate using a single 24-channel receiver. The 24 channels are divided between four antennas (six channels for each antenna). The four antennas may be mounted anywhere on a vehicle or platform and as long as the relative antenna positions are known, attitude information is computed.

System Architecture

In the 3DF 4x6 configuration, there are four independent channel banks, each bank having six GPS L1 frequency channels and its own RF section. Figure 1 depicts a block diagram of the receiver hardware configuration.

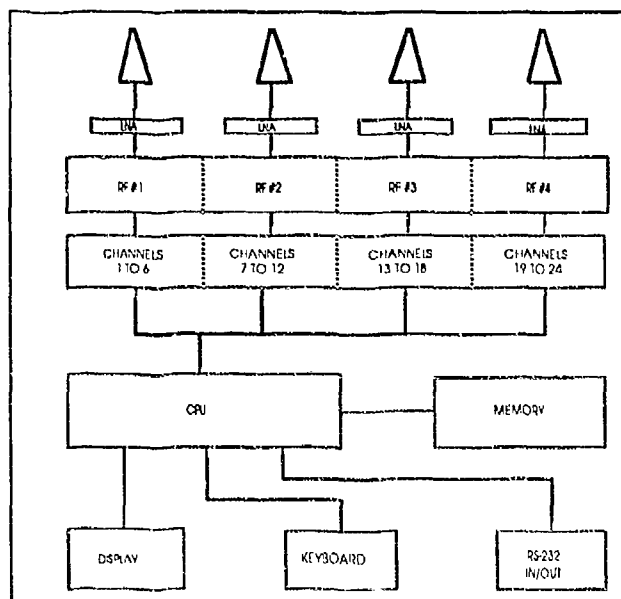


Figure 1. 3DF System Block Diagram

Proper layout of the 24-channel board and isolation of the four RF sections are required to prevent crosstalk between the four banks of channels. The RF section isolation is one of the keys to a successful implementation of the 3DF receiver, along with the software algorithm. The size, weight and power requirements of the receiver are 8.5" x 3.6" x 8", 9 pounds and 12 watts, respectively.

The first bank of six channels is designated as the "primary" bank - position and velocity are computed using this bank. The other three banks are designated as "secondary" banks and are used for attitude determination based on the differential phase measurements made relative to the primary bank.

The two RS-232 ports provide real-time data output at rates up to 115,200 BAUD. This feature is very useful for applications requiring integration of 3DF position and attitude information with other systems.

Relative Antenna Position Determination

After installation of the four antennas and prior to commencing attitude determination, an initial reference frame must be determined. This initial reference frame is defined by three vectors, $\vec{12}$, $\vec{13}$, $\vec{14}$, and their relationship to the Body-fixed ReferenceFrame, see Figure 2.

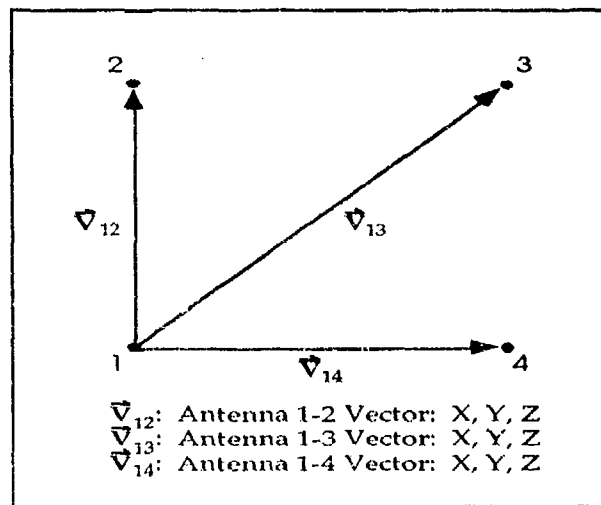


Figure 2. Definition of Relative Antenna Positions

The relative antenna positions can be determined while the vehicle is stationary or moving, so long as the antennas do not move with respect to each other. When the vehicle is stationary, the relative antenna positions can be determined by collecting about one hour of data from at least four satellites and using the Ashtech Geodectic Post-Processing Software (GPPS) package. For applications where it is not feasible to use the static technique, a "dynamic calibration" software package has been developed.

The dynamic calibration software requires at least 45 minutes of data from at least five satellites with good geometry (low PDOP). The data should be collected under normal vehicle motion. The calibration software will not work as well with data collected from stationary vehicles - motion actually helps the algorithm. On the other hand, high dynamic motion should be avoided as much as possible. This will help maintain lock on all the satellites visible.

The technique used by both static and dynamic methods is to first determine the differential phase ambiguities using the double-difference carrier phase. After these ambiguities are fixed, they are used along with the carrier phase measurements to determine the relative antenna positions.

Once the relative antenna positions have been found in the initial reference frame, their coordinates are rotated to a Body-fixed Reference Frame (BRF). The BRF is defined as the relative antenna positions when the vehicle's heading, pitch, and roll are 0.0. Since it may not be feasible to determine the relative antenna positions when the vehicle is at zero pitch and zero roll, offset angles need to be determined in order to rotate the computed vectors to the BRF. For a more detailed description, refer to [2].

For each 3DF installation, the relative antenna positions and offset angles need to be surveyed only once. These values are then provided to the 3DF software and are used in determining attitude.

Double-Difference Ambiguity Search Method

In order to compute attitude, the initial differential phase ambiguities must be resolved. This is accomplished using an integer search technique developed for the 3DF system. This integer search technique exploits double-differenced phase observables and the pre-surveyed spatial distances between the antennas.

Because the double-difference ambiguities are of an integer nature, each possible integer value forms a plane orthogonal to the double-difference range over short distances. Figure 3 shows a cross-section of three double-difference planes forming possible solutions for the antenna pair (1,2). The view shown is the intersection of one double-difference plane with the other two sets of double-difference planes. These other two sets of planes form the grid shown. Note that four different combinations exist which "fit" the correct solution in terms of vector $\vec{12}$ magnitude.

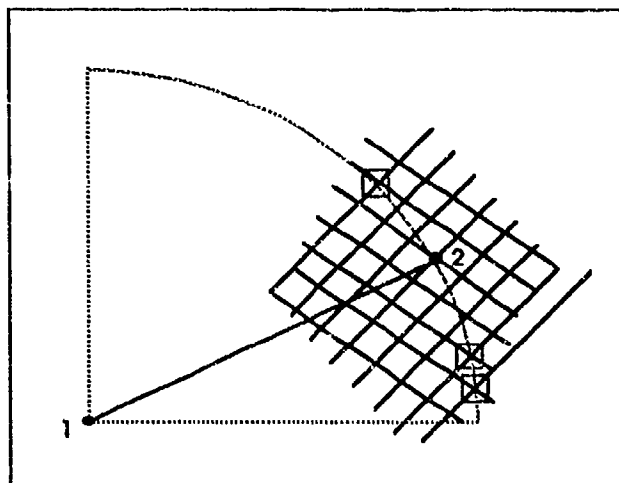


Figure 3. Double -Difference Plane Intersections

An ordered list of possible solutions is generated for each antenna pair. Each list of solutions can then be searched to find those solutions which match the entire platform, i.e., all four relative antenna positions. Additional satellites reduce the number of possible solutions. Also, note that only three antennas are needed for attitude determination. The fourth antenna is the key to fast ambiguity resolution. See reference [2] for a more complete description of the ambiguity resolution technique used.

For large antenna separations (greater than two meters), a codephase estimate of attitude is used to narrow down the ambiguity search region, see Figure 4. The codephase attitude estimate is arrived at by using smoothed, double-differenced codephase measurements as described in reference [3].

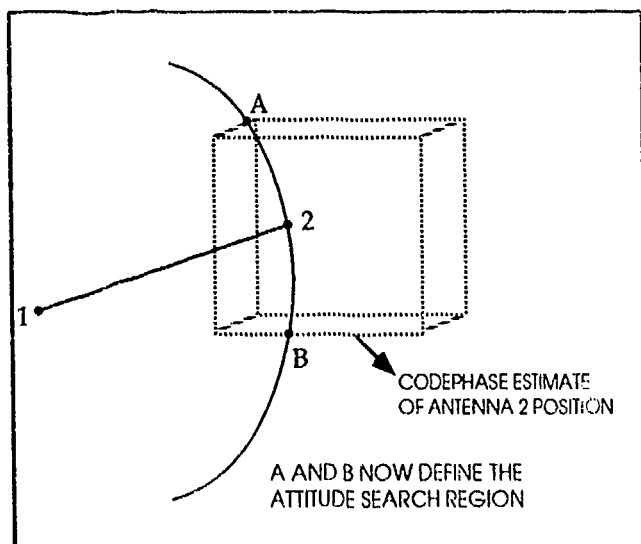


Figure 4. Long Baseline Attitude Determination

Three two-state Kalman filters have been implemented in the 3DF software to help predict an approximate attitude of the vehicle at the current epoch. They are a heading and heading rate filter; a pitch and pitch rate filter; and a roll and roll rate filter. The Kalman filter variables for heading, pitch, and roll are the system correlation time, τ , the system oscillation period, T_O , the process noise power spectral density matrix, Q , and the measurement noise scale factor, R . These variables may be adjusted to the characteristics of the vehicle dynamics (Kalman filter "tuning"). When set properly, the Kalman filters give a good overall estimate of attitude for the current epoch using both past and present codephase measurements and previous carrier phase measurements. This attitude estimate significantly narrows down the ambiguity search region.

Real-time solving of the ambiguities normally takes less than 1-2 seconds for antenna separations of 1-2 meters ("short baselines"). For larger antenna separations ("long baselines"), there is an initial Kalman filter "stabilizing period" before the initial ambiguities are resolved. Thereafter, whenever the ambiguities must be redetermined, it takes only 1-3 seconds.

Once the ambiguities have been determined, they are used to solve the antenna positions for each epoch until a cycle-slip occurs. As long as carrier lock is maintained on at least four satellites from epoch to epoch, cycle-slips can be detected and repaired. When a cycle-slip occurs such that the four-satellite criterion is not met, the phase ambiguities must be resolved. With the help of the Kalman filter prediction, this usually takes less than two seconds, when four satellites are reacquired a few seconds after a cycle-slip occurs.

Over the past several months, the 3DF has been tested in a number of different configurations in a wide range of environments. The next four sections describe both static and dynamic test results while tracking at least four satellites with PDOP at less than 6. Also, note that attitude information is computed every second.

Short Baseline Static Test Results

A one meter square antenna array, shown in Figure 5, has been designed to readily demonstrate the capabilities of the 3DF system on top of a ground vehicle such as a van.

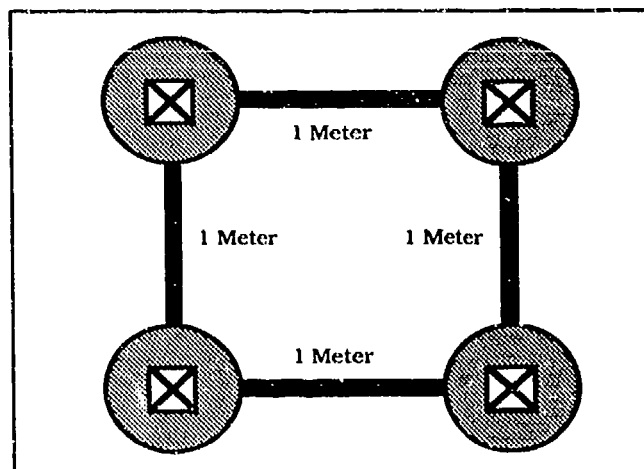


Figure 5. Antenna Array - 1 Meter Square

The heading, pitch, and roll of a parked van are shown in Figure 6 for a one hour period on Day 173 in Sunnyvale, CA. The slow oscillations in these plots, which were found to be the same for three straight days, show that multipath is the dominant error source. If multipath effects were eliminated from these plots, the standard deviations in heading, pitch, and roll would reduce to 0.08, 0.16 and 0.16 degrees, respectively.

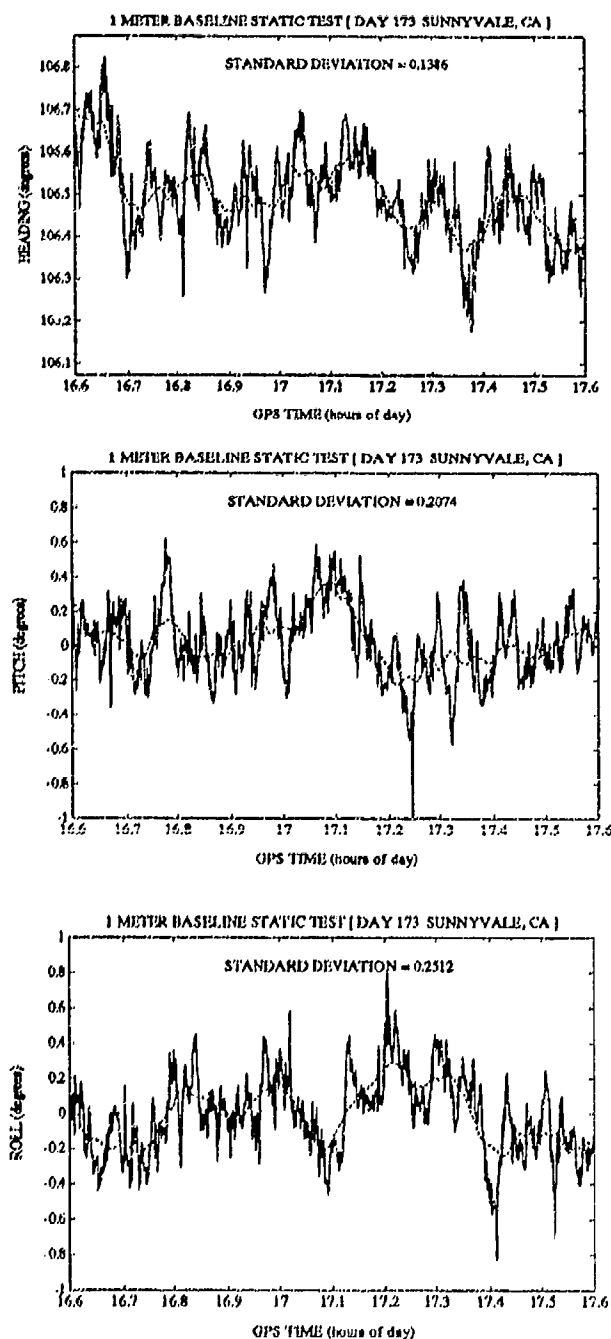


Figure 6. Day 173

Note that there are two curves in these figures. The solid curve is the "raw" attitude measurements that are output every second. The dashed curve is the smoothed attitude measurements using a 50-sample moving average window.

Long Baseline Static Test Results

If the antennas are separated a greater distance, more accurate attitude measurements are achieved. To show this, four antennas were mounted on the roof corners of Ashtech in Sunnyvale, CA. These antenna separations were on the order of 30 meters square. Figures 7 shows the results of heading, pitch, and roll for a one hour period on Day 123.

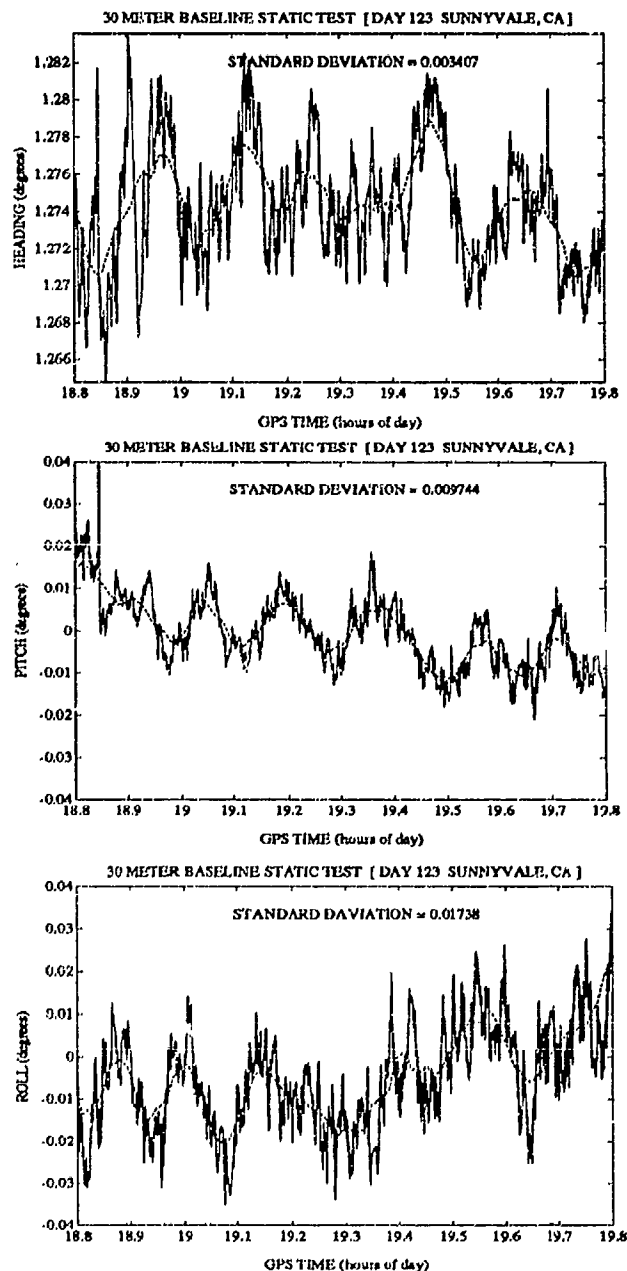


Figure 7. Day 123

The best attitude precision obtained so far has been with baseline lengths of 110 meters. The four antennas were placed in a square configuration at Shoreline Park in Mountain View, CA on Day 171. Figure 8 shows the attitude measurements collected for a one hour period.

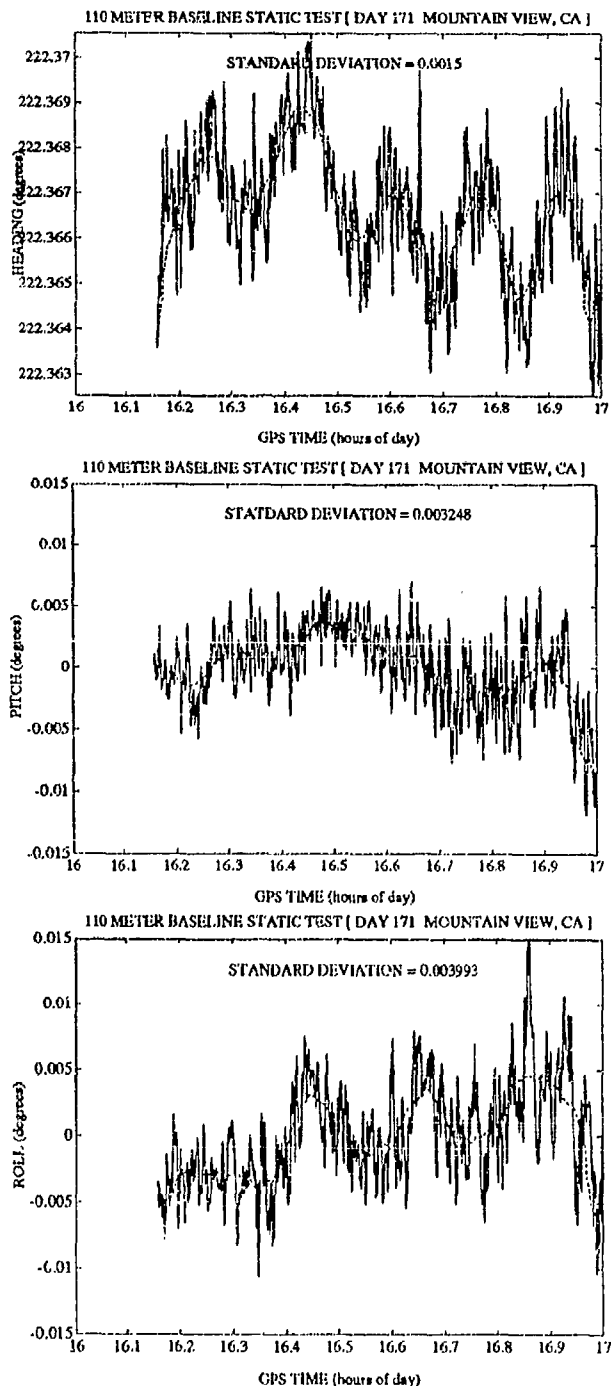


Figure 8. Day 171

Again, note the two curves in Figure 7 and 8. The solid curve represents the "raw" attitude computed and the dashed curve represents the smoothed attitude.

Attitude accuracy versus baseline length is depicted in Figure 9 below. This figure excludes multipath-type errors, which may be mitigated through proper antenna design and appropriate antenna location on the vehicle.

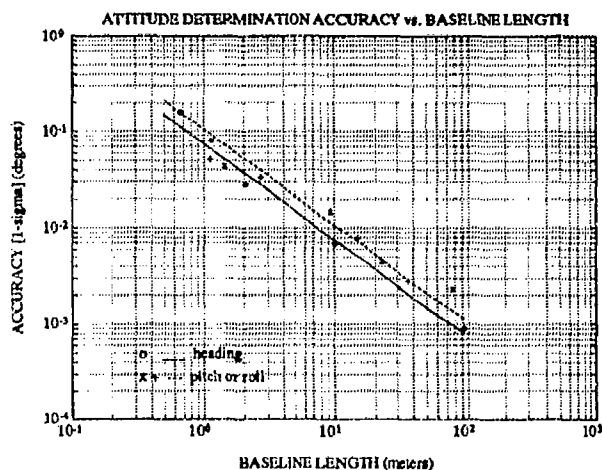
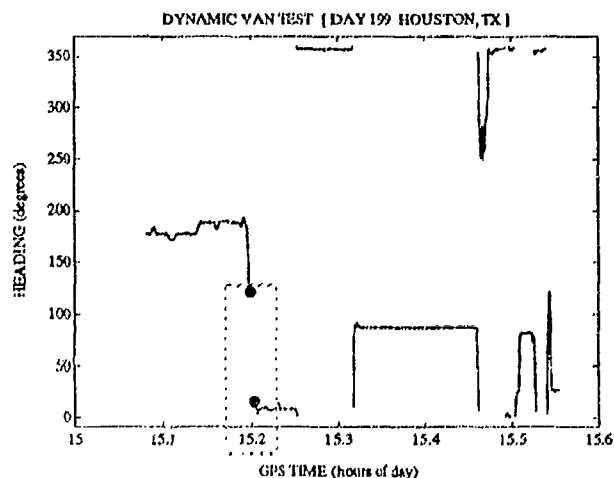


Figure 9. Attitude Accuracy vs. Baseline Length

Short Baseline Dynamic Test Results

Dynamic attitude results of the one meter square antenna array mounted on a van is shown in Figure 10. The data was collected on Day 199 in Houston, TX.



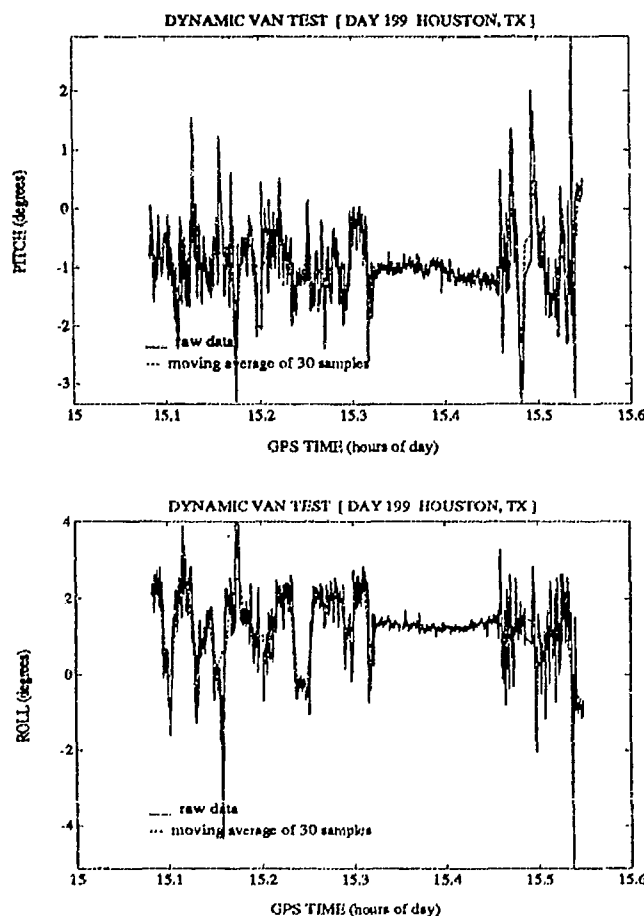


Figure 10. Day 199

Note the 15 second gap in the data during a turn at 15.2 hours. This gap was caused by the van travelling underneath a bridge for about 12 seconds. This part of the plot shows the quick recovery of attitude information after a complete cycle-slip occurs. For short antenna separations, attitude information is computed within one second of the first computed position - after at least four satellites have been reacquired. (This takes no more than three seconds). The other "gaps" in the plot are due to heading passing between 0 and 360 degrees.

Long Baseline Dynamic Test Results

(1) Motor Home Testing:

The four antennas of the 3DF system were placed at various locations on the roof of a 10-meter long motor home. Because none of the antennas could be mounted along the centerline

of the vehicle, a heading offset angle was computed. It was found to be 9.5 degrees for the motor home installation.

Figure 11 shows the vehicle attitude results while driving the same track repeatedly at Shoreline Park in Mountain View, CA on Day 170.

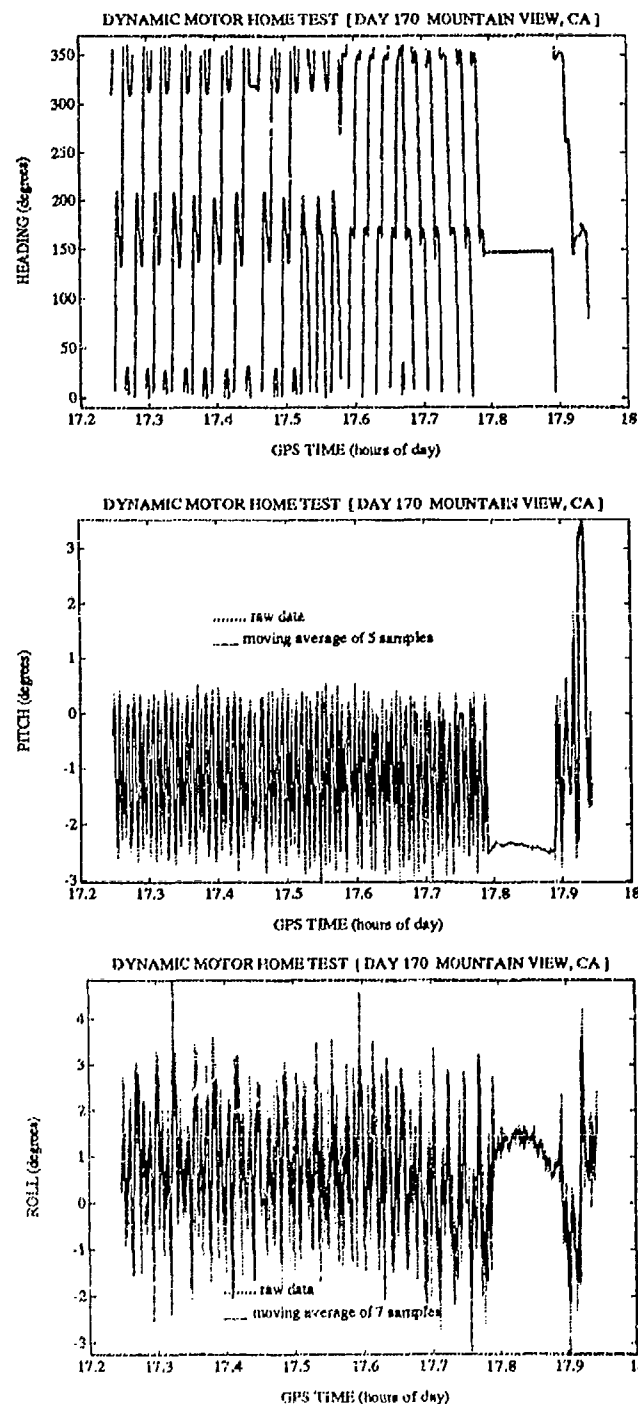


Figure 11. Day 170

In Figure 11 the dotted line is "raw" attitude data, the solid line is smoothed attitude data using a 5-sample or 7-sample moving average window.

(2) DC-3 Aircraft Testing:

Three flight tests were conducted with a DC-3 at Ohio University in Athens, OH. Antenna location was as follows: two antennas were mounted on the fuselage along the centerline of the vehicle about 7 meters apart and two antennas were mounted on each of the wing tips about 30 meters apart. One major problem for the 3DF attitude determination software is that the wings form a non-rigid platform (i.e., the wing tips move during flight). Therefore, two sets of input vectors have been determined - one set for aircraft taxiing and takeoff operations and one set for aircraft flying and landing operations. The ground input vectors were determined by a static survey and the air input vectors were determined by the dynamic calibration software.

Figure 12 shows the attitude results of the third flight test on Day 142. A more complete description of the flight test results is found in reference [3].

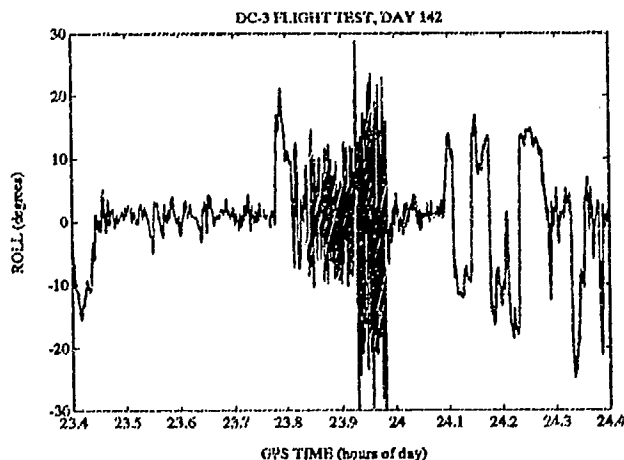
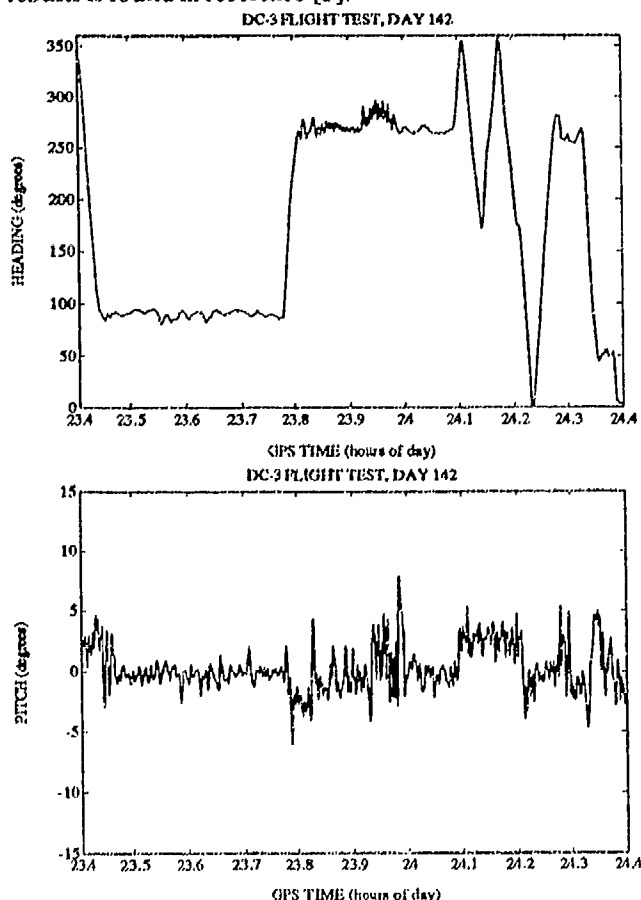
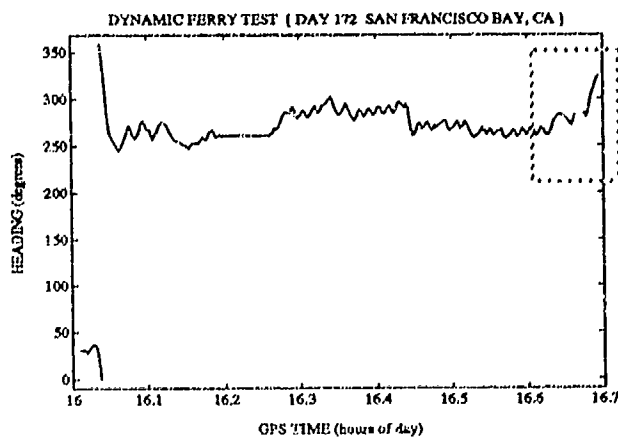


Figure 12. Day 142

(3) Blue and Gold Fleet Ferry Testing:

A two-hour test employing a ferry from the Blue and Gold Fleet was conducted on the San Francisco Bay on Day 172. In this test it was necessary to calibrate the antenna array in a dynamic environment. The test proceeded as follows:

The four antennas were mounted in a square configuration on the ferry about five meters apart along the railings. A 45-minute data set from six satellites was then recorded. In less than 30 minutes, the dynamic calibration software determined the relative antenna positions. Attitude was then successfully computed as shown in Figure 13. The gap at the end of the data set was due to the ferry passing underneath the Oakland Bay Bridge.



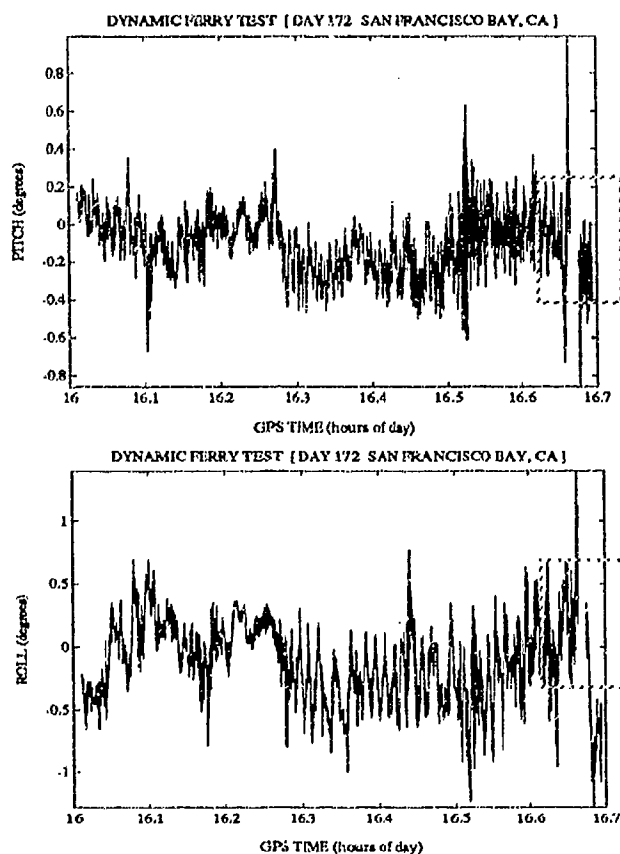


Figure 13. Day 172

Note that the whole procedure above took only two hours to complete. This shows how easily the 3DF is installed upon a moving vehicle.

(4) Ship Testing:

The 3DF system was tested aboard a 90-meter ship in the Gulf of Mexico on Days 202-204.

The four antennas were mounted as follows: one on the stern of the vessel, one atop a mast toward the bow, and two on the side railings of the ship's antenna farm. Much care was taken to ensure that the first two antennas were mounted along the centerline of the vessel. Dynamic calibration of the relative antennas positions was then performed. The antenna spacings were found to be approximately 50 meters between the first two antennas and 15 meters between the second two antennas. Since two antennas were on the vessel's centerline, a heading offset angle did not need to be calculated. The pitch and roll offset angles were determined to be -11.5 degrees and

-11.8 degrees, respectively.

Attitude data was collected by the 3DF receiver for three straight days and matched up with the ship's gyro data at the appropriate time tag. Because the current constellation of GPS satellites is not complete, attitude data was only collected for about 14 hours of each day. This was because four or more satellites were above a 10 degrees mask angle and PDOP was below 6 for only 14 hours of each day.

A part of a three-hour data set which was collected on Day 203 is shown in Figures 14 and 15. Figure 14 shows heading as computed by the 3DF and the ship's gyro. Note the offset between the two systems. This offset was measured to be -0.38 degrees. When the gyro was last calibrated at dockside, the gyro offset from truth was measured to be -0.34 degrees. Therefore, the difference in offsets measured for this particular data set was less than 0.05 degrees. Several other data sets were collected which confirmed this result.

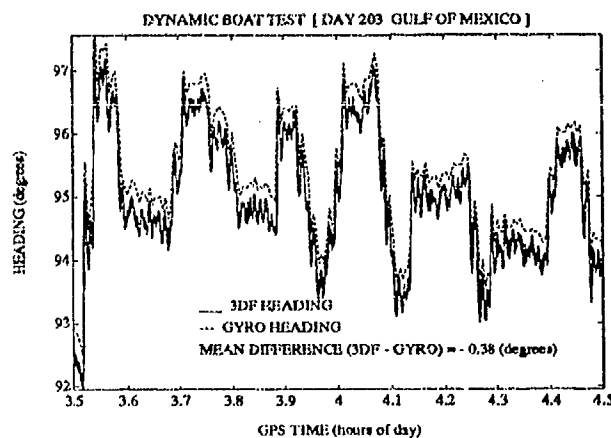


Figure 14. Day 203 - Heading

This test was an important verification of the absolute accuracy of the 3DF system. Comparison with the ship's gyro (which we called "truth") was within a milliradian (0.0573 degrees) for all data sets which were collected. Note that this result includes the effect of multipath.

An equally important result of the test was that on-the-fly gyro calibration can be achieved. Ships will no longer have to return to port for gyro calibration.

Future Applications

A significant future application of 3DF may be in aiding Inertial Navigation Systems (INS) to help speed initial calibration time and mitigate gyro drift rates.

Initially aligning the gyros to true north, using aiding from the 3DF will save critical time now spent by aircraft on the runway waiting - an unaided INS takes about 17 minutes to calibrate.

Integration of the 3DF with current INS will also provide dissimilar redundancy for attitude measurements. This will reduce the INS drift over time. Unaided, medium accuracy INS drift approximately 0.017 degrees/hour - high accuracy INS drift 0.004 degrees/hour but are cost prohibitive. For mission times on the order of a few hours, integrating 3DF with a medium accuracy INS could achieve the same accuracy as a high accuracy, high cost INS.

Because the future space station will go through much flexing as it orbits the earth, the 3DF system may be useful as an attitude control sensor due to its virtually unlimited antenna separation.

Testing of the 3DF on aircraft so far has been limited to a Douglas DC-3. In the future, vehicles which experience higher dynamics, such as tactical aircraft and missiles, need to be outfitted with a 3DF system and thoroughly tested. Also, more analysis of the 3DF attitude versus "truth" will be performed employing a high accuracy INS and a dynamic platform.

Conclusion

The Ashtech 3DF system, the "GPS gyro", is a complete three-dimensional attitude determination system which has now been tested in various dynamic conditions. In summary, key advantages of the 3DF are as follows. The whole system consists of four microstrip antennas and one small, ruggedized box which has an attitude and position update rate of once per second. The antennas may be mounted almost anywhere to meet user requirements and dynamic calibration of their positions is achievable. Finally, the initial phase ambiguity is resolved quickly and cycle-slip recovery is extremely fast.

Acknowledgments

The authors would like to acknowledge the significant contributions given by Dr. Frank van Graas and Michael Braasch of Ohio University and Skip Murphy of the San Francisco Blue and Gold Fleet.

References

- [1] Michael, Scott D., "Azimuth Determination from GPS Carrier Phase Measurements", ION National Technical Meeting, Williamsburg, VA, June 10-12, 1991.
- [2] Ferguson, Kendall, et.al., "Three Dimensional Attitude Determination with the Ashtech 3DF 24-Channel GPS Measurement System", ION National Technical Meeting, Phoenix, AZ, January 22-25, 1991.
- [3] Van Graas, Frank, Braasch, Michael, "Interferometric Attitude and Heading Determination: Initial Flight Test Results", ION National Technical Meeting, Williamsburg, PA,

SESSION VI-A
INERTIAL INSTRUMENTS

CHAIRMAN
DAVE ANDERSON
HONEYWELL, INC.

A Case of Flicker Noise

Reid G. Reynolds

TRW Guidance & Navigation Systems Department
One Space Park
Redondo Beach, CA 90278

Abstract - One type of noise which frequently degrades inertial instrument performance, the $1/f$ or flicker noise, which is often identified by the -1 decade per decade asymptotic slope which it produces on a log-log plot of the PSD, has been little understood and difficult to model. In this paper, a sample of oscillator noise producing the $1/f$ characteristic is demonstrated to be composed of two exponentially correlated noise processes using modern system identification techniques. These are simple, linear noise processes which may be modeled easily in a Kalman Filter, which may be used to great advantage in calibrating systems.

I. INTRODUCTION

In testing and evaluating inertial instrument performance, it is necessary to characterize and quantify noise levels. One type of noise which frequently degrades instrument performance, the $1/f$ or flicker noise, which is often identified by the -1 decade per decade asymptotic slope which it produces on a log-log plot of the PSD, has been little understood and difficult to model. Although several intricate models for the noise have been promoted at one time or another by various factions, few if any have been greeted with widespread enthusiasm, largely because the PSD result itself is not unique, and whether the given model describes the actual system under scrutiny or not is inconclusive without further tests.

In this paper, a sample of oscillator noise producing the $1/f$ characteristic is demonstrated to be composed of two exponentially correlated noise processes, using modern system identification techniques. These are simple, linear noise processes which may be modeled easily in a Kalman Filter, which may be used to great advantage in calibrating systems.

II. ANALYSIS

The data which is to be analyzed herein is frequency data collected from an oscillator circuit, and the deviation from its mean is plotted in Figure 1 below. The data has been scaled for the purposes of this presentation, and the magnitude of the fluctuations does not represent the performance of any actual instrument.

The Power Spectral Density (PSD) estimate for the data is depicted in Figure 2. For reference, the PSD is produced by smoothing the magnitude squared of the Fast Fourier Transform (FFT) of the data, and scaling it appropriately. Thus, if the data is represented by the set $Y = \{ y_k \mid k = 0, N-1 \}$, then the PSD estimate may be represented symbolically by

$$\hat{P}(f) = \frac{2T}{N} \text{smooth}(|\text{FFT}(Y)|^2) \quad (2.1)$$

where T is the sample period (8 seconds) and N is the number of data samples available for processing. Details on how this smoothing might be accomplished may be found in [5].

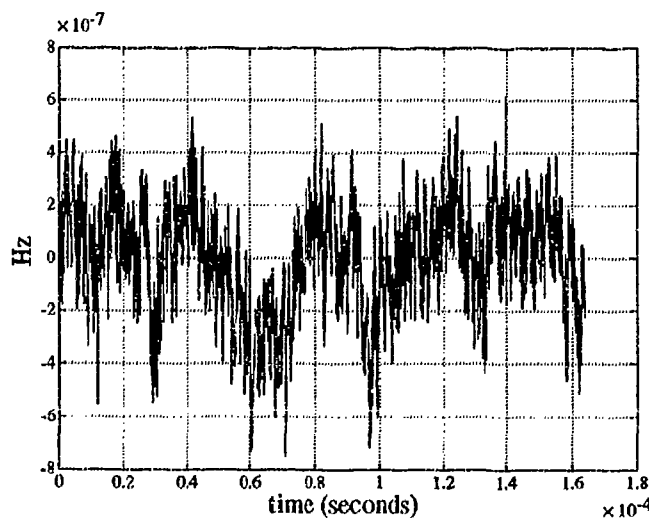


Figure 1. Oscillator Data

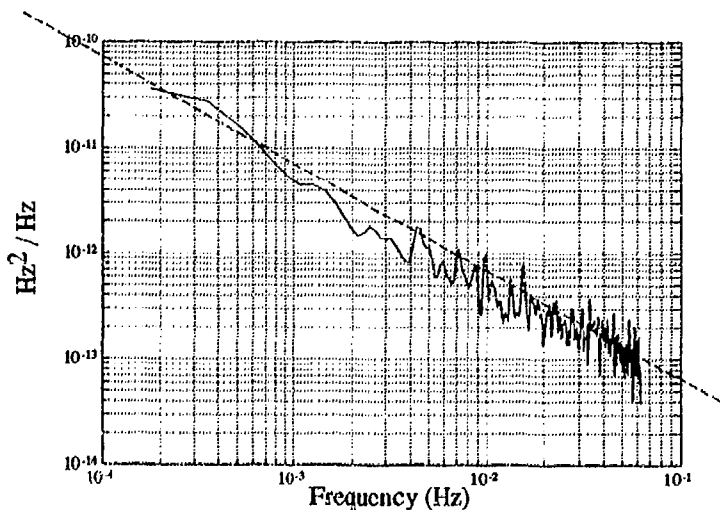


Figure 2. PSD Estimate for Oscillator Data

As may be observed, the PSD has a marked -1 decade per decade slope. Clues as to how this slope might have come about are provided by the autocorrelation estimate, shown in Figure 3. This intermediate step to estimating the PSD is often neglected but, in this case, it provides valuable insights.

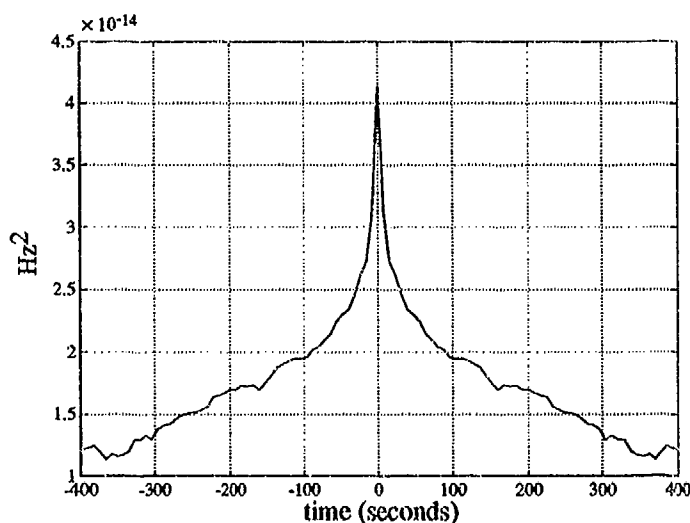


Figure 3. Autocorrelation Estimate for Oscillator Data

Here, an exponential correlation in the data is apparent, with a time constant of about ten seconds. The gradual decay of the autocorrelation estimate beyond the point where this first component damps out is indicative of a second exponential correlation in the data. These processes are also known as Ornstein-Uhlenbeck Diffusion processes[1,2].

From the above result, it is appropriate to hypothesize the following first order matrix stochastic differential and measurement equations as representative of the data.

$$\dot{\mathbf{x}}(t) = \begin{bmatrix} -\frac{1}{\tau_1} & 0 \\ 0 & -\frac{1}{\tau_2} \end{bmatrix} \mathbf{x}(t) + \mathbf{w}(t) \quad (2.2a)$$

$$\mathbf{y}(t) = \begin{bmatrix} 1 & 1 \end{bmatrix} \mathbf{x}(t) \quad (2.2b)$$

$$E \{ \mathbf{w}(t_1) \mathbf{w}^T(t_2) \} = \begin{bmatrix} q_1 & 0 \\ 0 & q_2 \end{bmatrix} \delta(t_1 - t_2) \quad (2.2c)$$

Here $\delta(t_1 - t_2)$ is the Dirac Delta function, and E is the expectation operator. The expected value of the single-sided PSD for data produced by such a system is

$$P(f) = \frac{2q_1}{(1/\tau_1)^2 + (2\pi f)^2} + \frac{2q_2}{(1/\tau_2)^2 + (2\pi f)^2} \quad (2.3)$$

Equation (2.3) may be expanded in powers of $1/f$, i.e., to first order

$$P(f) \approx P(f_0) + \left. \frac{\partial P(f)}{\partial (1/f)} \right|_{f=f_0} \left(\frac{1}{f} - \frac{1}{f_0} \right) \quad (2.4a)$$

$$\approx P(f_0) - \left. \frac{\partial P(f)}{\partial f} \right|_{f=f_0} f_0^2 \left(\frac{1}{f} - \frac{1}{f_0} \right) \quad (2.4b)$$

Expanding each term in equation (2.3) separately about its corner frequency and taking the arithmetic mean then yields

$$P(f) \approx \frac{1}{2} (q_1 \tau_1 + q_2 \tau_2) \cdot \frac{1}{2\pi f} \quad (2.5)$$

for f in the vicinity of the two corner frequencies, hence the approximately $1/f$ characteristic in the estimate of Figure 2 is produced.

Estimates of the time constants may be obtained by discretizing the model and applying the methods of [4]. The result of this operation is shown below in Figure 4. From this graph, it may be gathered that $\tau_1 \approx 12.3$ seconds, and $\tau_2 \approx 400$ seconds. Using these parameters, application of the RLSIC algorithm [6] yields the noise intensities

$$q_1 \approx 3.3 \times 10^{-15} \pm 1.2 \times 10^{-16} \text{ Hz}^2 / \text{sec}$$

$$q_2 \approx 7.7 \times 10^{-17} \pm 1.5 \times 10^{-17} \text{ Hz}^2 / \text{sec}$$

as depicted in Figure 5 Below. (From this graph, it may be observed that the estimate of q_2 is disturbed at about 2.5 hours, after having apparently converged to about $9.0 \times 10^{-17} \text{ Hz}^2 / \text{sec}$. Thus, a slight upward revision of this parameter is justified.)

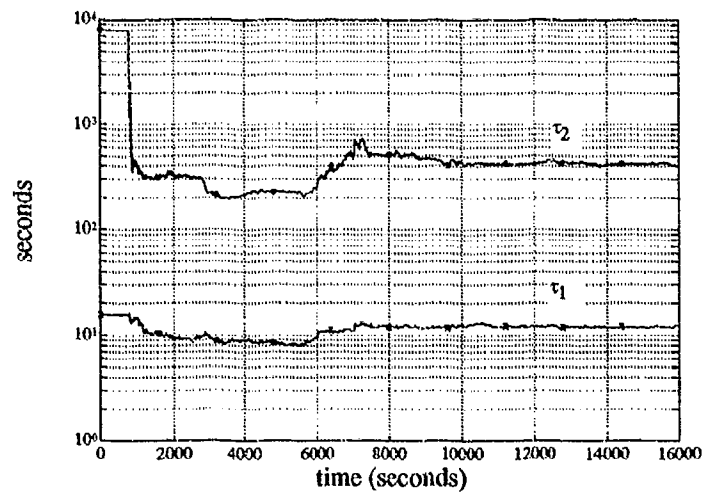


Figure 4. Estimates of Time Constants

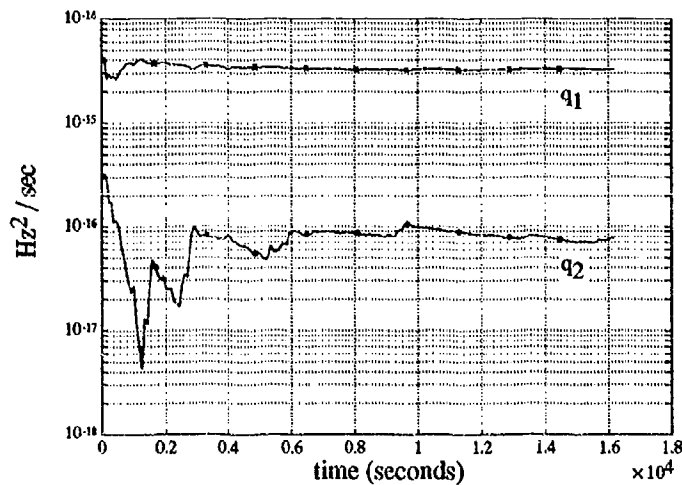


Figure 5. Estimates of Noise Intensities

III. SIMULATIONS

In order to confirm the accuracy of the above model for the data, the model was discretized, and a simulation was coded in the FORTRAN program listed below in an attempt to produce data with similar characteristics. Such discretization is discussed in [3]. The subroutine NORMAL produces approximately independent, unity variance, Gaussian random deviates. (The result of the simulation can be very sensitive to the quality of this process for generating random deviates.)

```
PROGRAM SIMULATE_FLICKER_NOISE
```

```
PARAMETER (N = 2048)
```

```
REAL A1, A2
```

```
REAL X1, X2, Z
```

```
REAL W1(N), W2(N), S1, S2, SEED
```

```
DATA A1, A2, S1, S2 / 0.52, 0.98, 1.2E-7, 2.7E-8 /
```

```
PRINT*, 'SEED?'
```

```
READ*, SEED
```

```
CALL NORMAL (W1, N, SEED)
```

```
CALL NORMAL (W2, N, SEED)
```

```
DO K = 1, N
```

```
    X1 = A1*X1 + S1*W1(K)
```

```
    X2 = A2*X2 + S2*W2(K)
```

```
    Z = X1 + X2
```

```
    WRITE (3,*) Z
```

```
END DO
```

```
END
```

FORTTRAN Program for Simulating 1/f Noise

Figure 6 contains the autocorrelation estimate of data produced by the program, which may be seen to be nearly identical to that of the real data in Figure 3. The PSD estimate of Figure 7 is equally similar to that of Figure 2, confirming that the equations (2.2) provide an accurate model for this set of oscillator data.

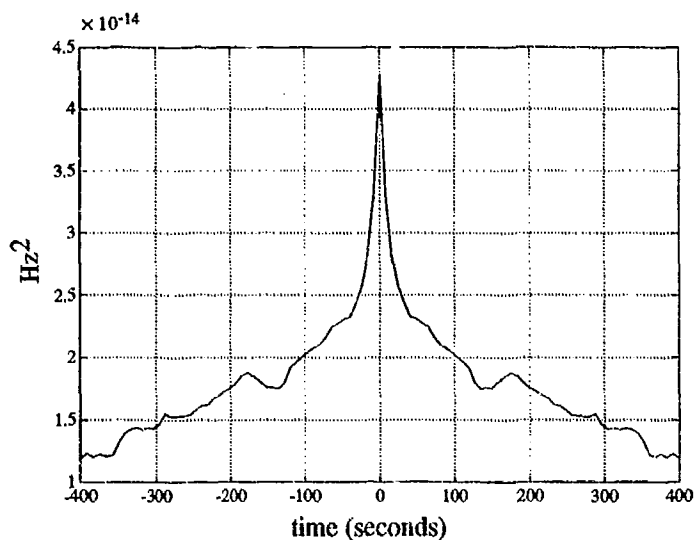


Figure 6. Autocorrelation Estimate for Simulated Data

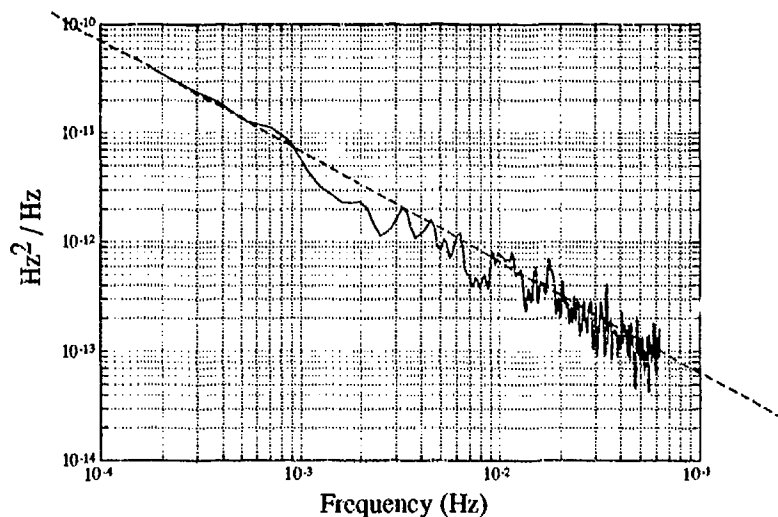


Figure 7. PSD Estimate for Simulated Data

IV. CONCLUSIONS

The $1/f$ characteristic of flicker noise may be produced by a variety of interacting noise processes, and data displaying such characteristics should be investigated on a case by case basis. The results of this analysis show that such data may be characterizable by a combination of relatively simple and commonly occurring processes.

Since it is important to know how the existence of such noise will affect navigation schemes, it may be worthwhile to mention that if a measurement of some quantity is contaminated by exponentially correlated noise such as examined here, averaging the data will produce little gain in accuracy until the cutoff frequency of the averaging filter reaches the break frequency of the PSD of the noise. After this point, the average may be improved by increasing the averaging time, assuming that other processes do not come into play.

V. REFERENCES

- [1] S. Karlin and H.M. Taylor, *A Second Course in Stochastic Processes*. San Diego, CA: Academic Press, 1981, pp. 170-173, 345-346
- [2] H.J. Larson and B.O. Shubert, *Probabilistic Models in Engineering Sciences*. New York: John Wiley & Sons, 1979, pp. 319-320
- [3] F.L. Lewis, *Optimal Estimation*. New York: John Wiley & Sons, 1986
- [4] L. Ljung and T. Soderstrom, *Theory and Practice of Recursive Identification*. Cambridge, MA: MIT Press, 1983
- [5] A.V. Oppenheim and R.W. Schaffer, *Digital Signal Processing*. Englewood Cliffs, N.J.: Prentice-Hall, 1975
- [6] R.G. Reynolds, "Robust Estimation of Covariance Matrices," *IEEE Transactions on Automatic Control*, vol. 35, pp. 1047-1051

Self Calibration of Q-FLEX[®] Sensor Head for Space Shuttle Microgravity Experiments

by

R. Anderson, R. Peters, B. Scott, C. Wilson
Sundstrand Data Control
Redmond, WA

ABSTRACT

The Space Acceleration Measurement System (SAMS) is being developed by NASA/Lewis Research Center to provide a microgravity acceleration measurement and recording system capable of supporting a wide variety of space experiments. SAMS is designed to measure microgravity acceleration levels on the Space Shuttle and Spacelab caused by events such as docking, crew motion, gravity gradient, and centrifuge.

The SAMS unit is comprised of several triaxial sensor heads attached to a central control and recording package. Each sensor head consists of either three Bell Model XI accelerometers or three Sundstrand Q-FLEX[®] accelerometers which provide stability to one micro-g over several hours under benign environmental conditions. The accelerometers are digitally modelled for bias, scale factor, and misalignment as a function of temperature over the range of -55 to +95°C. Programmable preamplifiers provide each acceleration channel with remotely commandable gain ranges from $\pm 0.5g$ to $\pm 0.0005g$ full scale.

Calibration and performance testing a microgravity sensor package in earth's one million micro-g field presents unique problems. Inputs accurate to ± 5 micro-g's require sensor head positioning relative to vertical to within one arc-second and precise compensation for sensor bias and axis misalignment must be provided. Calibrating three accelerometers at one time over multiple gain ranges dictates many data points and long thermal soak times. Automated testing with a two-axis test table minimizes technician involvement.

A test program was developed using a self calibrating procedure called g-squared testing. Twelve position tumbles are conducted in each of three orthogonal planes with each plane nominally parallel to the input axes of two accelerometers. Computer aided examination of the accelerometer outputs permits calibration of biases, scale factors, and misalignment angles without positioning to precisely known angles. Calibration data of the lowest gain range of each accelerometer is provided. Angle readouts on the dividing head are calibrated to an accuracy of three microradians one sigma. Calibrated position readings allow positioning the sensor head for calibration of the high gain ranges.

This paper presents a brief description of the theory of self calibrating tumble testing, describes the test hardware, and presents a flow plan of the data reduction process. It also presents estimates of the accuracy of the entire process and provides typical data to support these estimates.

INTRODUCTION

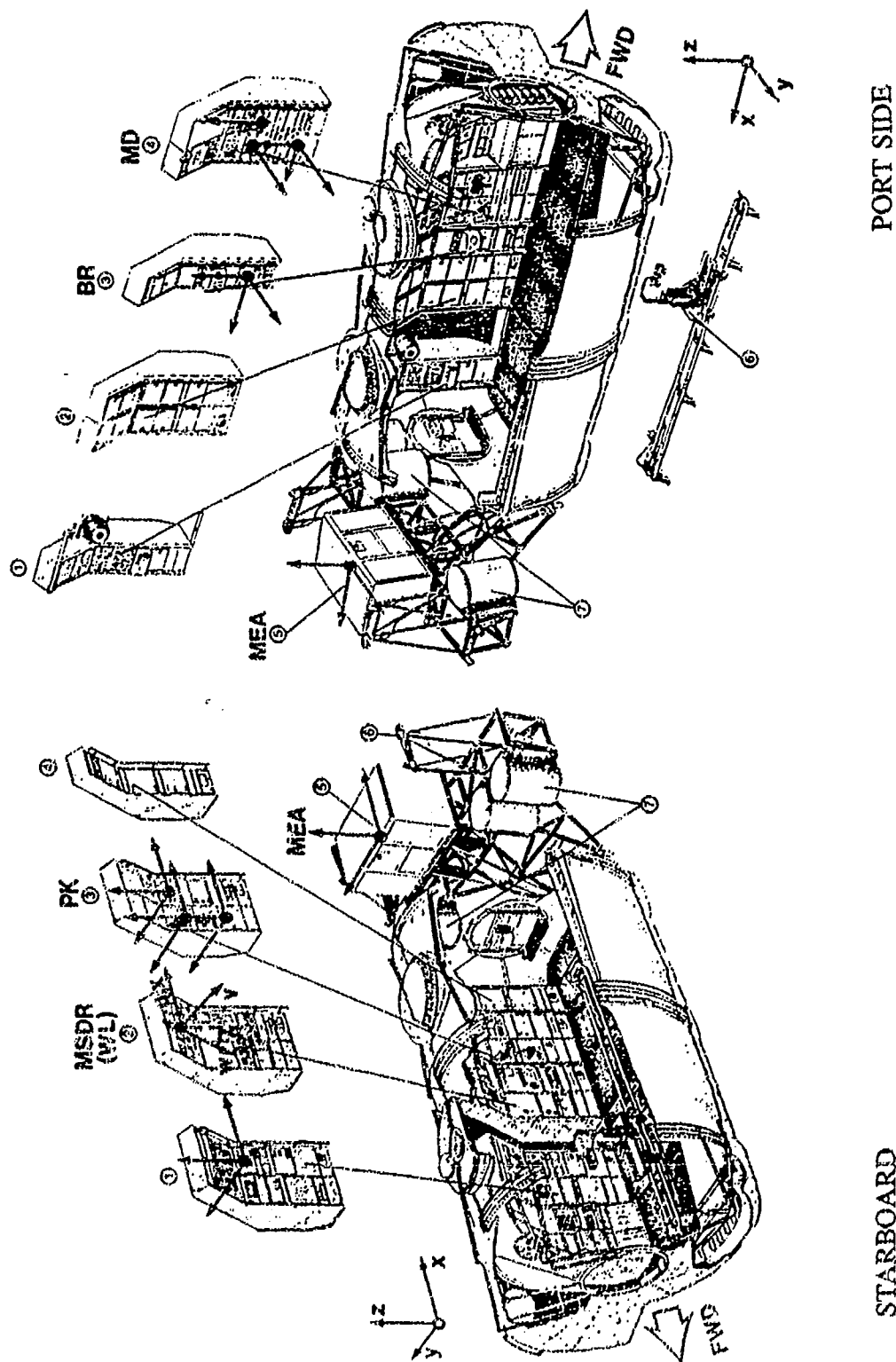
NASA has selected Sundstrand's Q-FLEX® Model QA-2000 pendulous quartz accelerometer as the primary sensor in this application for its unique combination of high performance, wide bandwidth, low power, high reliability and relatively low cost. The QA-2000 has traditionally been used in inertial guidance systems for military and commercial aircraft and missile systems. Hence, QA-2000's are usually delivered individually calibrated and modelled for scale factor, bias, and axis misalignment versus temperature. The unique performance goals of the SAMS demand a higher accuracy assembled triaxial sensor head calibration and temperature modelling technique be developed.

Standard individual four position tumble and coning measurements at various temperatures provide data for mathematical modelling of individual pendulous accelerometer error coefficients over temperature. However, because of measurement uncertainties such as mount to mount repeatability, thermal stability, dividing head runout, dividing head non-orthogonality, dividing head tilt, etc. it becomes extremely difficult to reliably model the individual accelerometers to the accuracy levels required.

A methodology for using the accelerometer triaxial sensor head combined with a two-axis dividing head with good short term repeatability as an inertially based system has been developed to meet the requirements of the NASA application. Multiposition equiangular testing of coplanar accelerometers mounted within the sensor head provides data for polynomial modelling of error coefficients over the -55°C to $+95^{\circ}\text{C}$ temperature range. A system of proven linear equations is utilized to reduce this multiposition accelerometer temperature-tumble data and calculate error coefficients. These equations are also used to calculate dividing head non-orthogonality and angle positioning errors for use in the high gain calibration measurements. Additional tumble positions and Fourier fits of the data are employed to increase the accuracy of the measurements.

Automated data collection and reduction is accomplished with the use of a Personal Computer. The software program commands the multi-channel voltmeter during data taking, the two axis station servoes for positioning, and also commands a cycling chamber to vary the full temperature range of the sensor head during test. The PC is programmed to automatically collect and reduce data at each temperature and position for both high and low gain testing. Data is summarized for each discrete temperature and includes the raw accelerometer output voltage at each position, the table angles, the accelerometer and mounting plate temperature, scale factor, bias, and two-axis misalignment of each accelerometer. The temperature coefficients of scale factor, bias, and two-axis misalignment are then calculated and fit to a 4th order polynomial error model for each accelerometer.

FIGURE 1: ESA SPACE CAPSULE

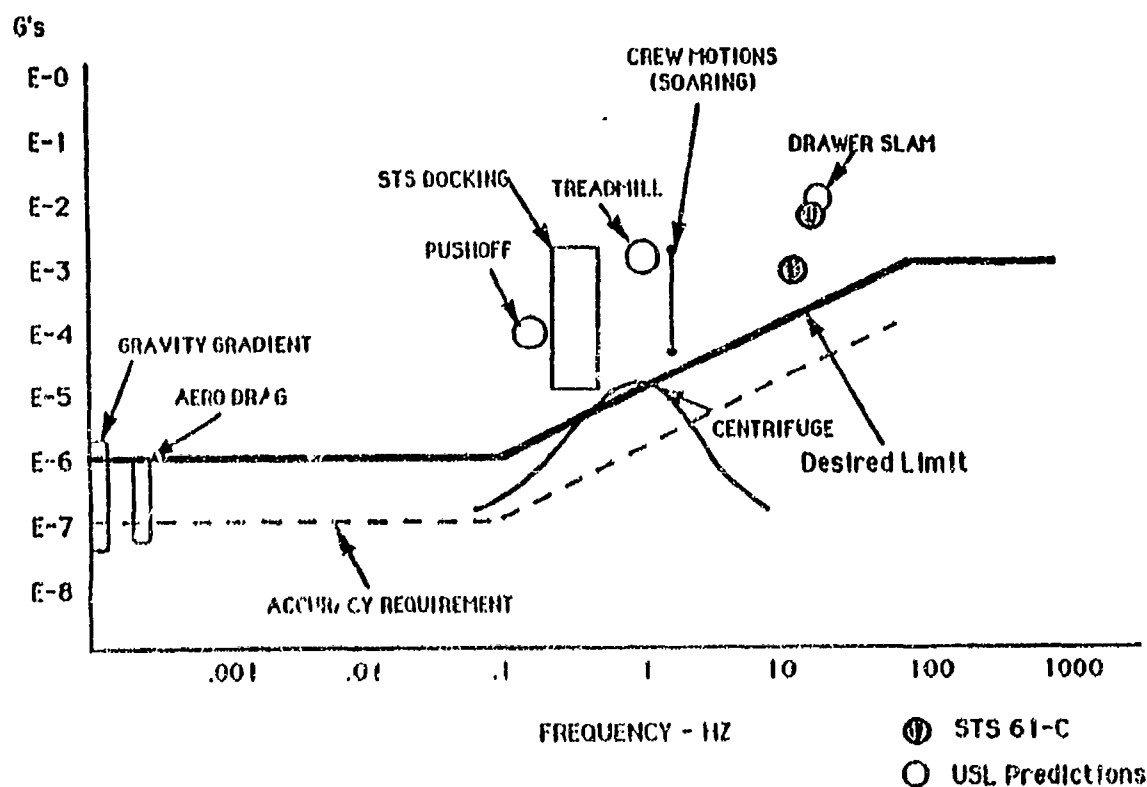


PROBLEM STATEMENT

The Space Acceleration Measurement System is being developed primarily to monitor acceleration levels applied to experimental packages carried aboard the Shuttle. An example is shown in Figure 1, which is a cutaway view of the European Space Agency Capsule. A single recorder and command package is cabled to several triaxial sensor heads, which can be positioned at the individual experiments.

The acceleration environment which is expected in flight is described in Figure 2. Benign environment stability testing on Earth has revealed that Q-FLEX[®] accelerometers are capable, under ideal conditions, of measuring acceleration less than $10^{-6}g$ over several orbital periods. But SAMS is designed primarily to measure the dynamic accelerations due to unpredictable Shuttle excitations at frequencies above 0.1 Hz, in areas of the Shuttle and its cargo which may not be temperature controlled. The accelerations of interest are all less than 1g, so calibration over temperature can be conveniently accomplished by orienting the sensor heads in earth's 1g field; but the presence of nearly a million micro-g cross axis when each sensor is positioned horizontally to have small accelerations along its input axis means that the positions must be determined very accurately.

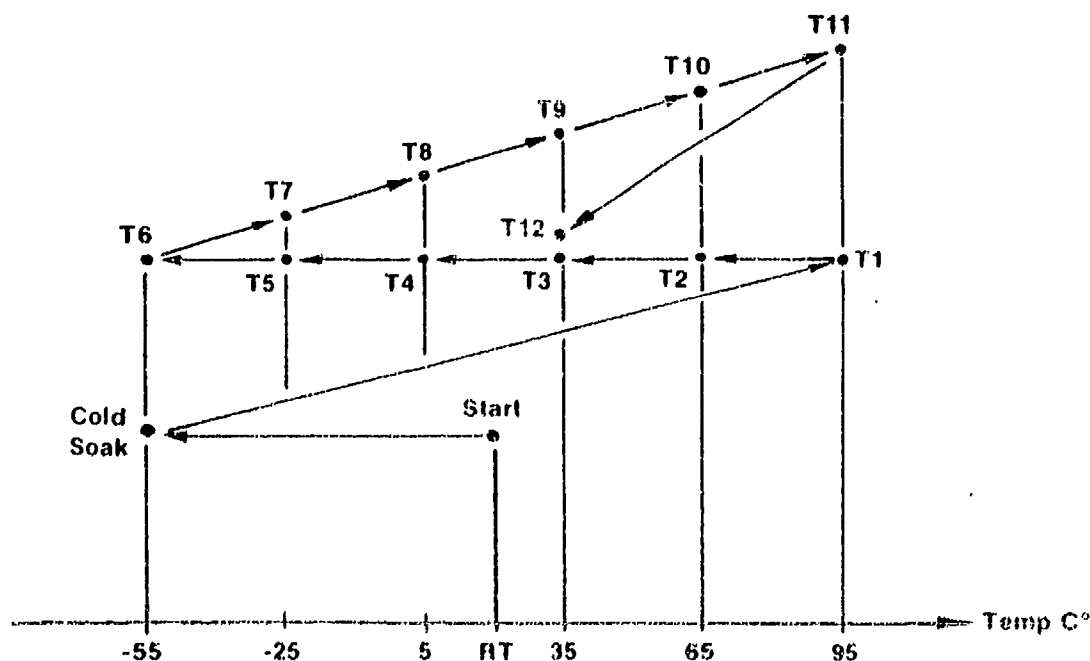
FIGURE 2: SAMS EXPECTED ACCELERATION ENVIRONMENT



The Specification Requirement to calibrate the SAMS sensor heads called for two optional test plans. Both of them required that the sensors be rotated to multiple positions with an accuracy of one arc-second or better, and both required testing at twelve different temperatures, as shown in Figure 3. Plan A was a minimal test in which each sensor was to be rotated to four positions in a vertical plane in 90° steps. It was intended to be used on approximately two-thirds of the heads calibrated to model bias and scale factor for the lowest gain range over temperature, and to provide a functional check of at least one of the higher gain ranges. With a few additional measurements at the positions called for, it would also provide misalignment information.

Test Plan B was much more ambitious. Its goal was to model against temperature the bias and scale factor of each of the three accelerometers in the sensor head at each of the four gain ranges, from 10volts/g to 10,000 volts/g, plus all six misalignment angles, plus indications of linearity and repeatability. To accomplish all of this, each of the accelerometers would be tested at the positions indicated in Table 1, at all of the temperatures of Figure 3.

FIGURE 3: TEMPERATURE CYCLE FOR TEST-A AND TEST-B



The temperature cycle calls for an initial cold soak at -55°C, to initialize any hysteretic effects, followed by twelve temperature points descending from +95°C to -55°C, rising again to +95°C and then closing at +35°C. Combined with the multiple positions and gains of Table 1, each calibration cycle would require approximately 3600 measurements. In addition, if a single axis head were used, the tumbles would require at least two runs through

the temperature profile, with each test unit removed and remounted between runs. With normal soak times each test cycle would require more than 48 hours, and the 153 triaxial heads proposed for the entire program could consume nearly a year of continuous testing.

TABLE 1: TEST PLAN B ACCELEROMETER
POSITION VS. GAIN RANGE

INPUTS		GAINS			
		1	10	100	1000
0°	<i>g</i>	X			
±60°	0.5 <i>g</i>	X			
±87° 8' 2"	0.05 <i>g</i>	X	X		
±89° 42' 49"	0.005 <i>g</i>	X	X	X	
±89° 58' 17"	0.0005 <i>g</i>	X	X	X	X
±90°	0 <i>g</i>	X	X	X	X
±90° 1' 43"	-0.0005 <i>g</i>	X	X	X	X
±90° 17' 11"	-0.005 <i>g</i>	X	X	X	
±92° 51' 58"	-0.05 <i>g</i>	X	X		
±120°	-0.5 <i>g</i>	X			
180°	-1 <i>g</i>	X			

A final complication lies in the setting of the small angles near the middle of Table 1. For simplicity, these angles were computed as they would be for accelerometers which had no bias and no misalignment angles. In actual fact, the accelerometers have significant biases, and their misalignment angles through accumulated tolerance build-ups could be as much as 3 milliradians. In space, where all accelerations are small, that much misalignment requires only a small, simple, software correction. On earth, it can result in partial or complete saturation of the highest gain ranges. It is thus necessary to use computed offsets from these angles, corrected for bias, misalignment, and all dividing head errors including angle readout errors, initial levelling errors, and base tilts. These offsets are different for each accelerometer and may vary from run to run.

The requirements of Test Plan B clearly call for automated testing, and preferably by means of a programmable two-axis head which would avoid the need for remounting. An almost suitable head was available at Sundstrand Data Control, with a temperature chamber big enough to accommodate four test packages per run. Its major shortcoming was that it was observed to produce errors in commanded position up to 12 arc-seconds with significant shifts from turn-on to turn-on.

In fact, the only test stations available at Sundstrand Data Control that consistently produce positioning errors smaller than one arc-second are the locally manufactured single

axis heads used for production calibration of QA-2000 accelerometers. These heads use computer commanded stepping motors to rotate to approximately the desired angle for each test point, and then determine the exact angle achieved by measuring the output currents of two Q-FLEX[®] accelerometers mounted on the rotating shaft, outside the temperature chamber. The most recent and most accurate version of these test stands is described in another paper at this symposium. The key to the accurate operation of these stands is that the reference accelerometers are continuously self-calibrated by adjusting their estimated biases, scale factors, and misalignment angles, so that the vector sum of the accelerations they indicate is always one g, to within a small error which is continuously minimized in a least squares sense. For pairs of accelerometers which are approximately orthogonal and approximately in a vertical plane, the software to do that is simple, robust, and well developed. This method, and its variations, have sometimes been referred to as " g^2 " testing, from its ideal state of $A_X^2 + A_Y^2 = 1$. The particular form developed at Sundstrand has the advantage of referring all orientations directly to the local gravity vector, so that test bed tilts produce no error. This is especially appealing in Redmond, Washington, where the prevailing glacial debris from the last ice age has been observed to shift several arc-seconds over several hours in response to intermittent ground-water pumping.

It is observed that each plane of rotation of Test Plan B can be arranged to include two accelerometers in a geometry suitable for g^2 testing, and that a small increase in test positions taken will allow each accelerometer to be tested as a member of two different pairs, with negligible effect on total test time. At the same time, the combination of tumbles produce enough information to permit two different estimates of each misalignment angle. When the details are worked out and the software written, the result is a calibration process which is self-calibrating, self-checking, and sufficiently efficient that Test Plan A has not been needed.

APPROACH

The g^2 technique is a variation on standard multipoint accelerometer tumble testing in earth's gravitational field. Standard multipoint testing depends on three fundamental assumptions:

1. That the gravity vector is constant in magnitude and direction for the duration of the test.
2. That the plane in which the input axis is rotated is vertical within the accuracy limits of the test, e.g. 3 milliradians or 1/6 degree for 5 ppm accuracy.
3. That the dividing head rotation scale is accurate and repeatable to within the accuracy limits of the test, e.g. 5 microradians for 1 arc-second alignment accuracy, or 5 μg input accuracy at low g.

The g^2 technique makes similar but much less restrictive assumptions:

1. That the gravity vector is constant in magnitude only, for the duration of the test.
2. That the plane of rotation is vertical as above.

Accuracy and repeatability of the dividing head rotation scale; e.g., to .05 degree for accuracy limits as above, are a convenience for some applications, but not a requirement. The method can be used with no means of angle read-out other than the accelerometers under test.

As outlined above, the essence of the technique is the observation that the indicated acceleration outputs of two or more accelerometers, having their input axes non-collinear but in a vertical plane, will always add to a vector with a magnitude of 1 local g , provided that they are correctly calibrated. By observing the difference between the indicated vector magnitude and $1g$ for a number of positions in earth's field, and adjusting the calibration coefficients of the accelerometers so as to minimize those differences in a least square sense, it is possible to calibrate the accelerometers without knowing in advance what the tumble positions might be. Then, with the optimal estimates of the calibration coefficients installed, it becomes possible to compute what the originally unknown positions were. This process results in a test station for accelerometers which is entirely self-calibrating.

The algorithms which describe the outputs of linear accelerometers in such tumbles are non-linear, and must be manipulated into locally linear approximations to permit solutions of the classic sets of least squares equations. Iteration of the solutions can be used to minimize the errors introduced by these approximations. The simplest and most robust version of the technique begins with two accelerometers which are nominally orthogonal, and which can be characterized by their two scale factors, two biases, and by the included angle between their input axes. The geometry of such a pair is illustrated in Figure 4. Expressing the non-orthogonality in terms of the two small angles δ provides solutions which are symmetric with respect to the two accelerometers.

If δ is of the order of a milliradian, the biases are of the order of a milli- g , and the initial guesses for scale factor are within 1000 ppm, accuracy to the order of 1 ppm can be achieved without iteration. The derivation of the operating algorithms for such an accelerometer pair begins with the model equations shown as Equation 1. [Eq. 1]

$$\frac{E_{1j}}{K_{11}(1 + \epsilon_1)} = B_1 + \sin(\Theta_j + \delta)$$

$$\frac{E_{2j}}{K_{12}(1 + \epsilon_2)} = B_2 + \cos(\Theta_j - \delta)$$

where:

E_{1j} (E_{2j}) is the output of accelerometer #1 (#2) at position Θ_j .

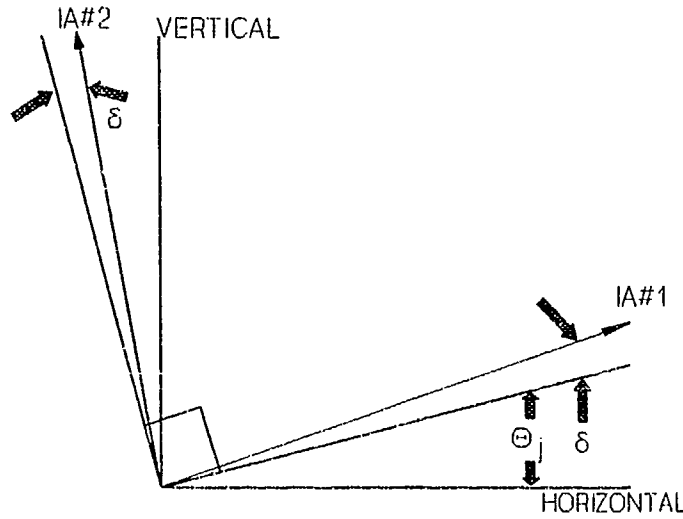
K_{11} (K_{12}) is an initial guess at the scale factor of accelerometer #1 (#2).

ϵ_1 (ϵ_2) is a small error in estimating K_{11} (K_{12}).

B_1 (B_2) is the unknown bias of accelerometer #1 (#2).

Θ_j is the rotation angle for position j , and δ is a misalignment angle as illustrated in Figure 4.

FIGURE 4: g^2 TEST COORDINATE AXES



Rearranging terms and discarding small quantities:

$$\sin \Theta_j \cong \frac{E_{1j}}{K_{11}} (1 - \epsilon_1) - B_1 - \delta \frac{E_{2j}}{K_{12}}$$

$$\cos \Theta_j \cong \frac{E_{2j}}{K_{12}} (1 - \epsilon_2) - B_2 - \delta \frac{E_{1j}}{K_{11}}$$

Since $\sin^2 \Theta_j + \cos^2 \Theta_j = 1$, a cost function for least squares minimization can be written as: [Eq. 2]

$$cost = \sum_{j=1}^{j=R} \left[1 - \left(\frac{E_{1j}}{K_{11}} (1 - \epsilon_1) - B_1 - \delta \frac{E_{2j}}{K_{12}} \right)^2 - \left(\frac{E_{2j}}{K_{12}} (1 - \epsilon_2) - B_2 - \delta \frac{E_{1j}}{K_{11}} \right)^2 \right]^2$$

Taking the partial derivatives of the cost function with respect to ϵ_1 , ϵ_2 , B_1 , B_2 , and δ , respectively, and setting them all equal to zero then produces the matrix equation, Equation 3.

$$\begin{vmatrix} S_{40} & S_{22} & S_{30} & S_{21} & S_{31} \\ S_{22} & S_{04} & S_{12} & S_{03} & S_{13} \\ S_{30} & S_{12} & S_{20} & S_{11} & S_{21} \\ S_{21} & S_{03} & S_{11} & S_{02} & S_{12} \\ S_{31} & S_{13} & S_{21} & S_{12} & S_{22} \end{vmatrix} \begin{vmatrix} \epsilon_1 \\ \epsilon_2 \\ B_1 \\ B_2 \\ 2\delta \end{vmatrix} = [1/2] \begin{vmatrix} S_{40} + S_{22} - S_{20} \\ S_{22} + S_{04} - S_{02} \\ S_{30} + S_{12} - S_{10} \\ S_{21} + S_{03} - S_{01} \\ S_{31} + S_{13} - S_{11} \end{vmatrix}$$

where

[Eq. 3]

$$S_{mn} = \sum_{j=1}^{j=R} \left(\frac{E_{1j}}{K_{11}} \right)^m \left(\frac{E_{2j}}{K_{12}} \right)^n$$

For angles which are evenly spaced through 360° within about ± 0.05 degrees, with R total readings, the matrix can be simplified to the form shown in Equation 4.

$$\begin{vmatrix} \frac{R}{8} & & & & & \\ & 6 & 2 & 0 & 0 & 0 \\ & 2 & 6 & 0 & 0 & 0 \\ & 0 & 0 & 8 & 0 & 0 \\ & 0 & 0 & 0 & 8 & 0 \\ & 0 & 0 & 0 & 0 & 2 \end{vmatrix} \begin{vmatrix} \epsilon_1 \\ \epsilon_2 \\ B_1 \\ B_2 \\ 2\delta \end{vmatrix} = \begin{vmatrix} S_{40} + S_{22} - S_{20} \\ S_{22} + S_{04} - S_{02} \\ S_{30} + S_{12} - S_{10} \\ S_{21} + S_{03} - S_{01} \\ S_{31} + S_{13} - S_{11} \end{vmatrix}$$

[Eq. 4]

Equation 4 is exactly analogous to the simplified version for the Fourier fit which arises with equally spaced angles, except that the angles themselves do not explicitly appear, and so they need not be accurately known in advance.

If ϵ_1 , or ϵ_2 is greater than 1000 ppm, the error can be quickly converged to nearly zero (depending on the measurement noise) by simply updating the estimates K_{11} and K_{12} and repeating the calculation. Similarly, large values for B_1 and B_2 can be subtracted from

the raw data before each iteration. Large values for δ add to the complexity of the terms in Equation 3 or Equation 4, but the method is exactly analogous and converges quickly to the noise limit of the data.

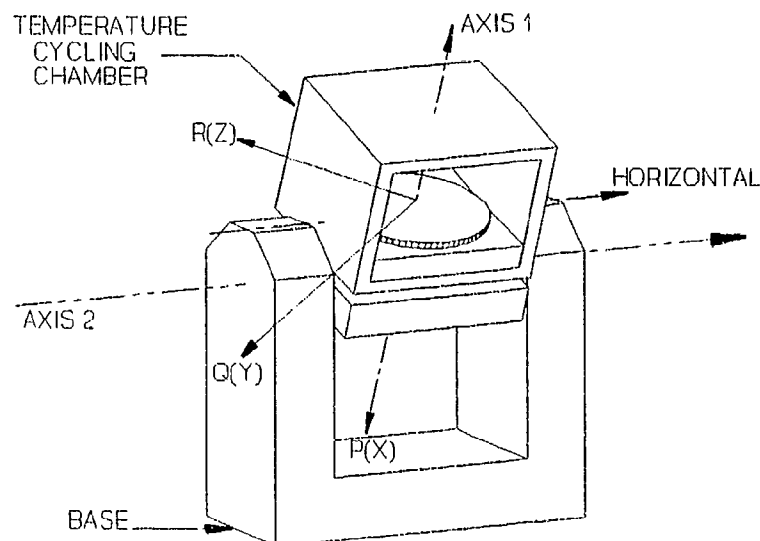
In any case, after the coefficients have been evaluated, angles can be calculated from Equation 5.

$$\tan \Theta_j = \frac{\frac{E_{1j}}{K_{11}(1+\epsilon_1)} - B_1 - \delta \frac{E_{2j}}{K_{12}}}{\frac{E_{2j}}{K_{12}(1+\epsilon_2)} - B_2 - \delta \frac{E_{1j}}{K_{11}}} \quad [\text{Eq. 5}]$$

An important feature of this last step is that it depends on a voltage ratio, and is unaffected by changes in the magnitude of gravity or by common mode scale factor drift (tidal effects, or the dominant effect of temperature).

For the calibration of the SAMS triaxial accelerometer heads, three of these g^2 tumbles are accomplished at each temperature using a two axis dividing head as diagrammed in Figure 5. Four SAMS heads at a time can be mounted on the inner gimbal table so that their X, Y, Z axes, shown in Figure 6a and 6b, correspond to the table P, Q, R axes, respectively. The first tumble starts with Θ_2 at 270° and Θ_1 at 90° , and calibrates the Y and Z accelerometers by stepping Θ_1 through 360° . The second tumble starts with Θ_1 at 0° and Θ_2 at 360° , and calibrates the X and Y axes by stepping Θ_2 back to 0° . The third tumble test sets Θ_1 to 90° and calibrates the X and Y axes by stepping Θ_2 forward to 360° .

FIGURE 5: SCHEMATIC DRAWING OF TEMPERATURE CONTROLLED TWO AXIS DIVIDING HEAD



An important feature of the SAMS calibration is determination of the change in misalignment angles as a function of temperature. The g^2 technique by itself is not sufficient to accomplish that, since the estimated angle, δ , does not change with common mode changes of alignment of the accelerometers being tumbled. While two accelerometers are undergoing a $1g$ tumble, however, the third is being rotated about an axis which is approximately parallel to its input reference axis. Four additional voltage measurements in each tumble provide enough information to calculate a set of mechanically based misalignment components which differ from the correct ones by the orthogonality errors of the two axis dividing head. These bring the total to about 3600 measurements over the full temperature range. When all of the data from three tumbles is combined there is enough information to provide two estimates of each bias and each scale factor, a mostly gravity based and a mostly mechanically based estimate of each of the six misalignment components (as shown in Figure 6b), and an estimate of the leveling and orthogonality of the axes of the two axis dividing head. The redundant coefficient estimates for the test accelerometers can be averaged for best noise rejection and differenced as a measure of test accuracy. In addition, since the orthogonality of the table axes is mechanically defined and should not change randomly with time, its variations provide a further indication of test accuracy, easily monitored day-to-day. It is an especially sensitive indicator, since its calculation depends on the effects of eight different angle estimates, four of them gravity based and four mechanically based.

FIGURE 6a: TWO AXIS
TABLE AXIS DEFINITION
VS. SAMS SENSOR HEADS

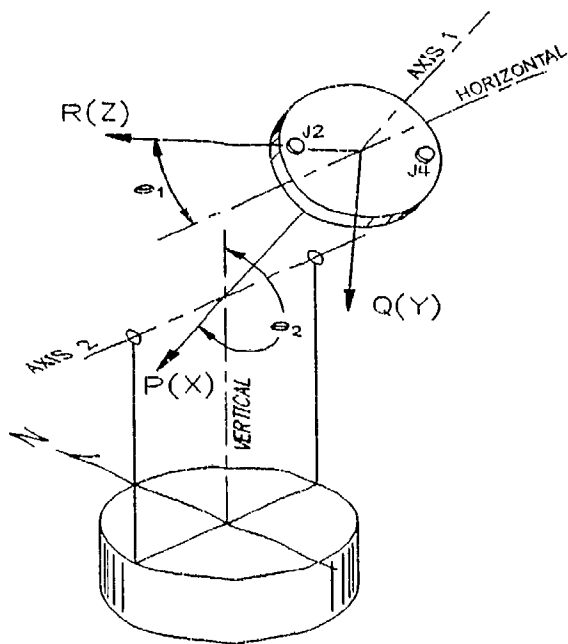
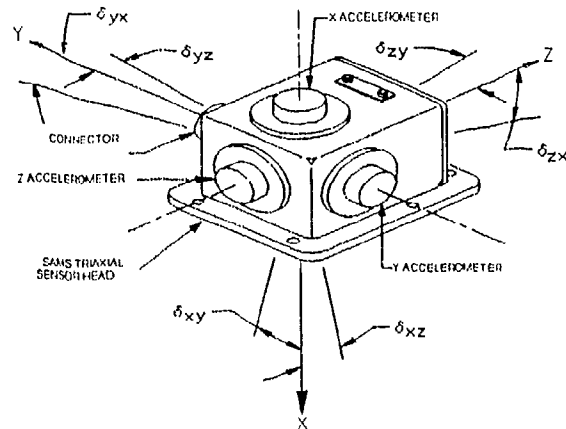


FIGURE 6b: AXIS AND MIS-
ALIGNMENT ANGLE DEFINITION
FOR SAMS SENSOR HEADS



SOME LIMITATIONS AND REFINEMENTS

Temperature testing typically involves a trade-off between time and accuracy, because of the long temperature soaks required to achieve low drift rates during the measurement period. g^2 testing is not more sensitive to thermal drifts than conventional Fourier analysis, but it does require reasonably stable coefficient values across a tumble. Alnico magnets characteristically exhibit scale factor temperature coefficients of about 100 ppm/°C, so to achieve tumble errors less than $\pm 5\mu g$ requires thermal drift less than 0.1°C across a tumble. With large test items and fixtures, the difference between 0.5°C and 0.05°C stability can easily add up to half a day of additional soak time over a multi-temperature run. In the SAMS calibration procedure, this tradeoff has been greatly reduced in sensitivity by use of iterative data reduction. A first pass treats all of the voltage readings at each temperature as though they had been taken at a single temperature, ignoring any drift present. The computer creates an approximate temperature model from these calculations, and then refits all of the data using the model to correct for temperature drifts. The process converges rapidly, typically in one cycle. Details are in the data analysis section.

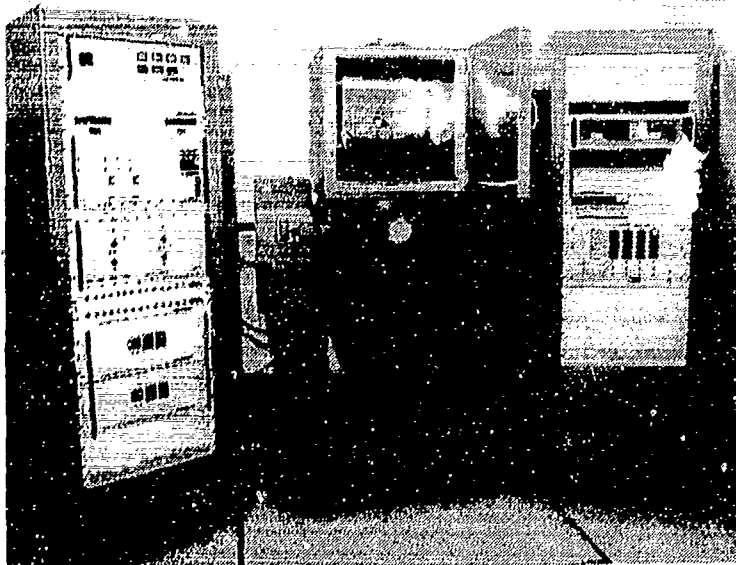
Some error has been accepted in this testing by neglecting the effect of non-linear coefficients, especially K_2 and K_{IP} . A straightforward extension of the theory described above works well for either K_{IP} or K_2 , but produces a nearly singular matrix when both coefficients are included. The partial derivatives give good results for the difference of these coefficients but appear to be nearly insensitive to their sum. Since values for either K_2 or K_{IP} are about $5\mu g/g^2$, one sigma for Q-FLEX accelerometers, there seems little point in adding either of these terms to the model unless both can be accommodated. A preliminary analysis indicates that the effect on computed Θ_j due to ignoring either of these coefficients is zero at the cardinal angles (0°, 90°, 180°, 270°) and reaches a maximum value of one quarter of the coefficient for angles midway between the cardinal angles. This result indicates a small error source for the SAMS application, but it is an area worthy of further development for future systems requiring higher absolute accuracy.

HARDWARE DESCRIPTION AND REQUIREMENTS

A precision biaxial station with temperature control capability is needed to meet the test objective. The test station selected for this test is the Contraves-Goerz Corporation Model 57CD/30H two-axis index table system with a Model 30H-MPACS controller. This station is capable of testing four SAMS accelerometers at one time. Vibrational noise during the test is required to be less than $100\mu g$'s from dc to 150 Hz. To accomplish this, the two-axis station is mounted to a 10,000 pound concrete block mass, which is isolated from the concrete floor. This method is found to reduce seismic disturbances from the floor and measurements demonstrate compliance with this requirement.

Figure 7 depicts the two-axis station (center), the controller (left), and the I/O Interface, Scanner and DMM (right). The environmental chamber is capable of producing an environment of -55° to +95°C by cycling either a heater element or a CO₂ solenoid valve.

FIGURE 7: SAMS SENSOR HEAD CALIBRATION HARDWARE



One problem that had to be overcome was to thermally isolate the SAMS units from the massive mounting head of the test chamber. Temperature cycling of the SAMS unit mounted directly to this head would expend considerable amounts of CO₂ and time. This problem was solved by fabricating a mounting fixture and isolating the fixture from the head by means of an array of spacers. In addition, a foam shroud was placed to reduce air thermal convection.

FIGURE 8: SAMS SENSOR HEAD MOUNTED ON TWO-AXIS STATION

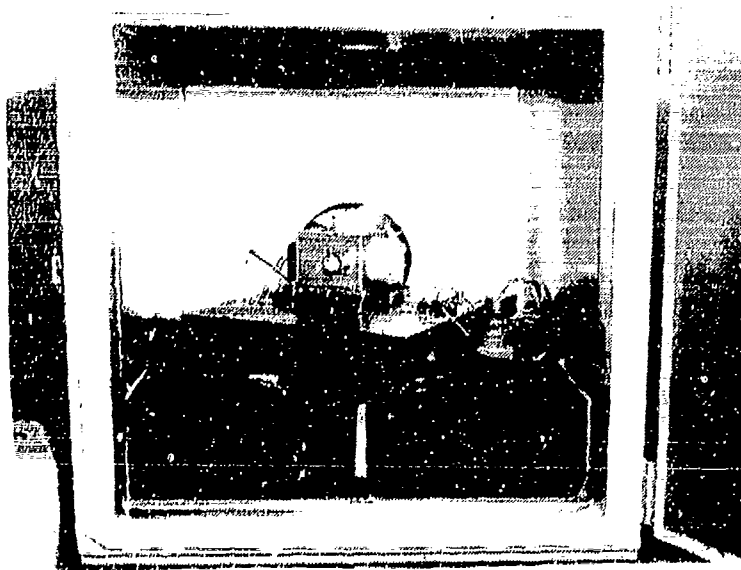
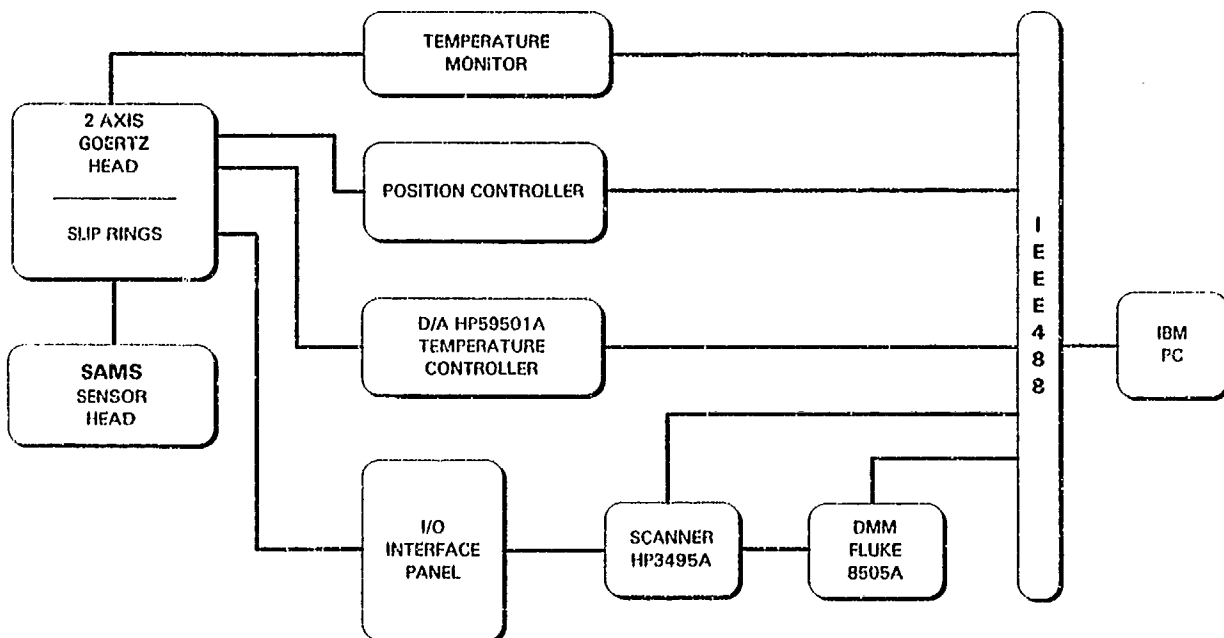


Figure 8 shows a SAMS accelerometer mounted to the test fixture inside the temperature chamber. Temperature is monitored using Analog Devices AD590 temperature sensors mounted to the mounting fixture. The AD590 temperature sensor, being a current output device, is not affected by cabling and slip ring resistances. The temperature sensor output is converted to a voltage (through a load resistor) near the scanner providing an accurate temperature signal.

All outputs are switched through an I/O interface panel and scanner. Switching, data collection and station operation are controlled by the IBM PC.

Figure 9 shows the station block diagram.

FIGURE 9: TEST STATION BLOCK DIAGRAM



TEMPERATURE TUMBLE TEST BACKGROUND

Since the introduction of temperature tumble testing (T3) for accelerometers, Sundstrand Data Control has emerged as one of the leaders in fully automated T3 stations. This technique has allowed the delivery of tens of thousands of Q-FLEX® accelerometers complete with fourth order models of bias, scale factor, and misalignment as well as predictable aging characteristics.

Sundstrand's T3 stations use PCs to control instruments via the IEEE-488 interface and positioning control via RS-232 with resolution and accuracies to the point where diurnal gravity fluctuations can be seen in the accelerometer data.

SAMS DATA ACQUISITION SOFTWARE

As stated earlier, each calibration cycle consumes 3600 data points per SAMS unit. Multiple testing of up to four units simultaneously creates a large bookkeeping problem. This problem is minimized with the use of multi-dimensioned arrays. Figure 10 shows the overall data acquisition flow chart.

A pre-run check performs a plus and minus 1g tumble confidence test for each X, Y and Z axis on each head that has been installed. The first unit then undergoes a series of three twelve point tumbles; one twelve point tumble for each orthogonal axis pair. A least mean square polynomial-fit is then performed for each pair. From this data, the actual angle versus the commanded angle offset is calculated. This data becomes the head calibration data, thus removing the zero order misalignment between the first head and the dividing head.

The test proceeds next to the first commanded temperature (-55°) which is used to condition the units. Data acquisition starts at the next temperature point ($+95^{\circ}$). After the test units have stabilized and soaked at temperature, three sets of twelve point tumbles are performed. One set of tumbles is performed for each orthogonal axis (Y-Z, Y-X and X-Z).

Using a least squared tumble fit, raw data is reduced. Resulting data is written to an ASCII file that is ready to print, and is also stored on disc for post processing.

The high gain test sequence is performed next, positioning each axis in the near zero g field. The high gain amplifiers are remotely actuated, and the applicable data is produced. Data is stored in a ready-to-print ASCII file, and is also stored on disc for post processing. This procedure is looped through each temperature, and data recorded accordingly.

THE DATA ACQUISITION MODULE

The plate that holds the four SAMS units is broken into four sections. Each section contains a packaged AD590 used for calibrating the internal AD590 in the SAMS units. Measuring the average plate temperature is the first action in the Data Acquisition module. Average plate temperature is recorded after each set of twelve point tumbles.

The test data is acquired conveniently within a nested I,J,K,L loop. 'I' represents the number of test angular positions (36); 'J' is the number of test heads (up to 4); 'K' is each sensor (XYZ); and 'L' is either the acceleration output or the AD590 output. Data is stored in a multi-dimensioned array with the same subscripts.

This data is processed to produce two independent estimates of bias, scale factor, and misalignment for each XYZ sensor. These values are averaged along with the average AD590 temperature sensor data, and stored for post processing. Two-axis dividing head errors are calculated and shown on the raw data sheet as an indication of data integrity. Figure 11 shows the high level flow diagram of the above process.

HIGH GAIN TEST SEQUENCE

The high gain test steps each sensor axis (XYZ) of each head through two sets of seven positions at approximately 180° apart. The center position of each of the seven positions is approximately zero volts output. The least squared tumble fit bias data, plus the zero order misalignment terms from the previous data acquisition module, plus the dividing head calibration data is used to 'zero' the accelerometer output.

At each of seven positions, each gain selection is made that does not cause the amplifier output to saturate. Data is taken at each of these non-saturating points.

After each of the seven points are tested, the two axes are rotated 180 degrees and the opposite *g* readings are taken.

This test is repeated for each sensor axis. After completion of each head, the data is stored into a data sheet in ASCII format so that it can be printed directly to a printer. Figure 12 shows the high gain test sequence flow diagram.

THE DATA REDUCTION SOFTWARE

After each temperature acquisition point, the average tumble fit data for each parameter is stored. When complete, data is retrieved for each temperature; and a fourth order polynomial model of scale factor and bias is computed.

Raw tumble data is retrieved and broken into twelve point sections, to match the data acquisition series. The center point of each of the twelve points is assumed to be the closest temperature to the average data used in the original tumble fit. All of the other points are then corrected for any temperature drift.

New tumble fit data for each twelve point series is computed. Data is reduced, and a new polynomial model for each parameter is obtained through an iterative process. This whole process could be repeated for more accurate models; however, after the first iteration, further correction amounts to less than 1 micro *g* bias change. Model hysteresis data is calculated, and is stored to data sheet files for the unity gain (10 volts/*g*) coefficients. The high gain data is then retrieved from disk, and the high amplifier data is converted to scale factors using the latest models. Amplifier zero intercepts are converted to micro *g*'s, and the amplifier gain sections are fit to the polynomial model. The final process is to write the High Gain data sheets to disk. Figure 13 shows the data reduction flow diagram.

FIGURE 10: SAMS DATA ACQUISITION SOFTWARE

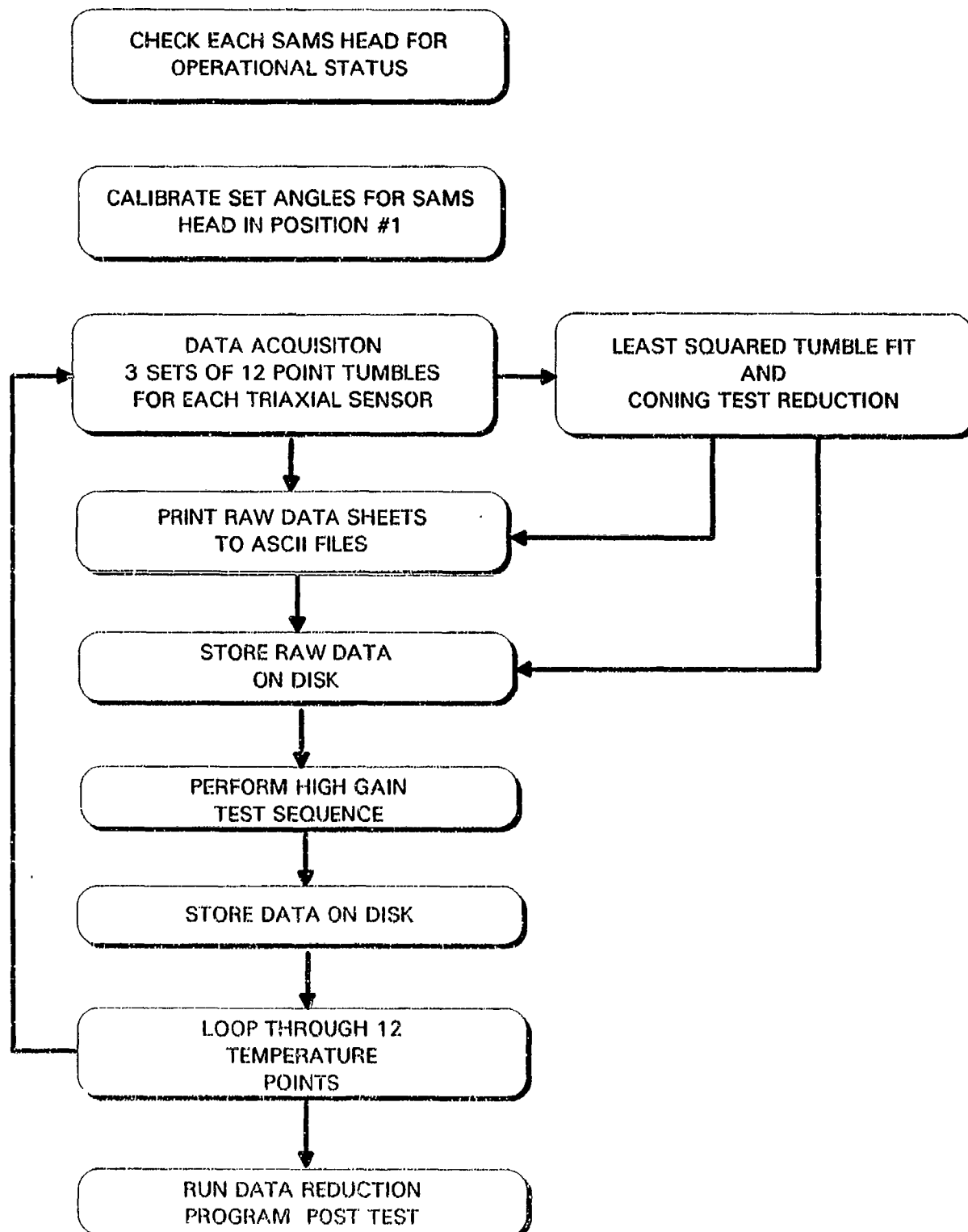


FIGURE 11: DATA ACQUISITION --
3 SETS OF 12 POINT TUMBLES

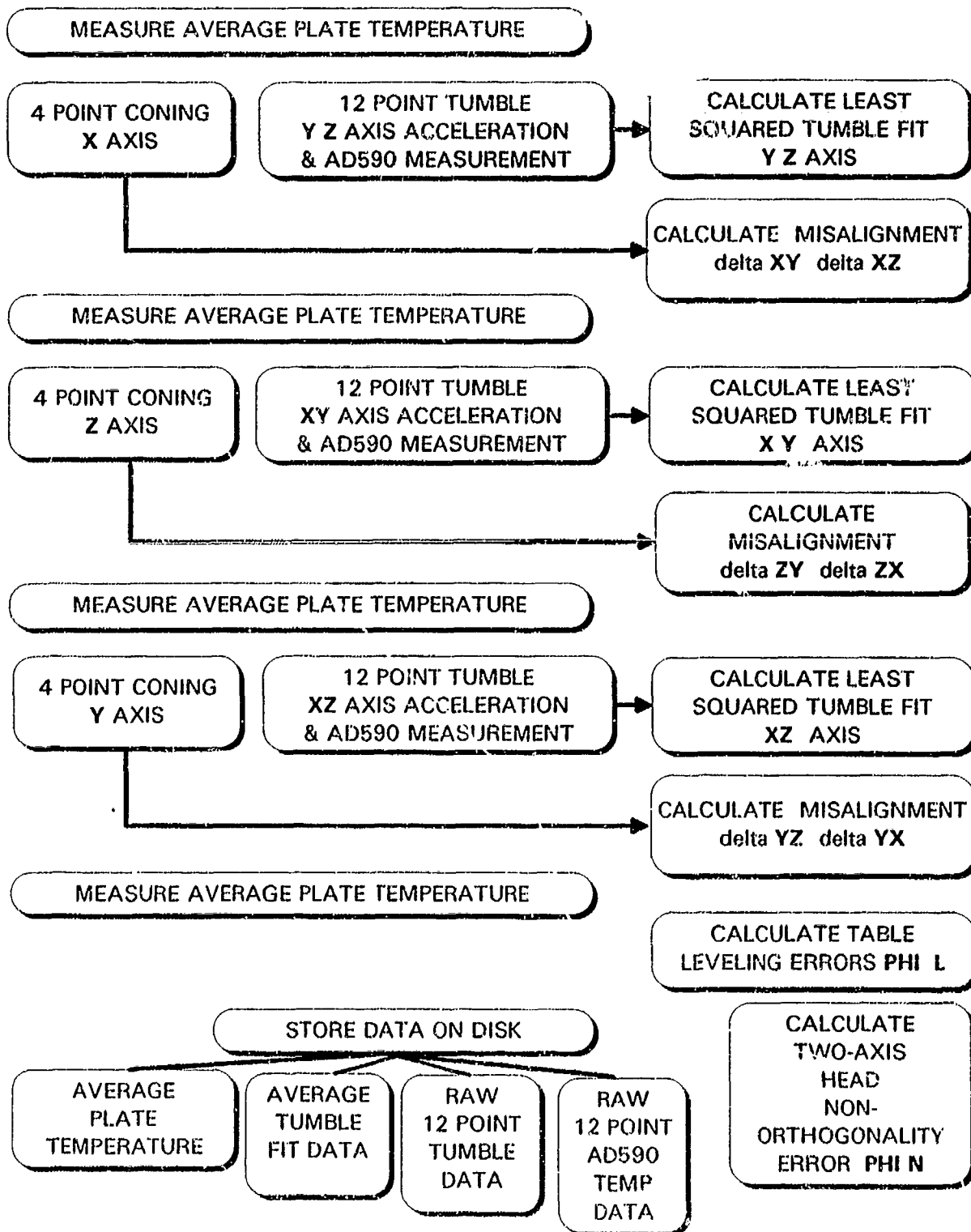


FIGURE 12: HIGH GAIN TEST SEQUENCE DATA DETAIL

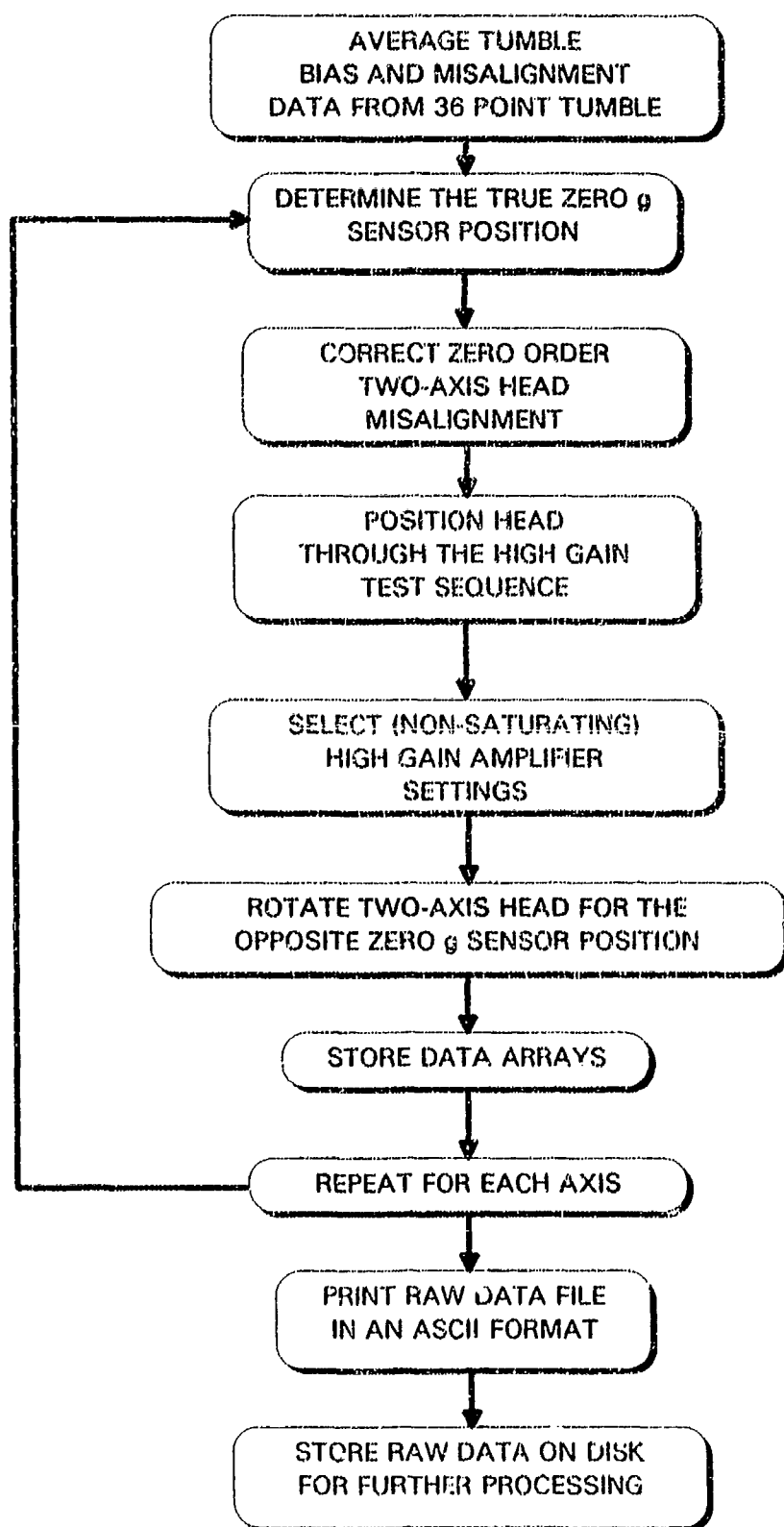
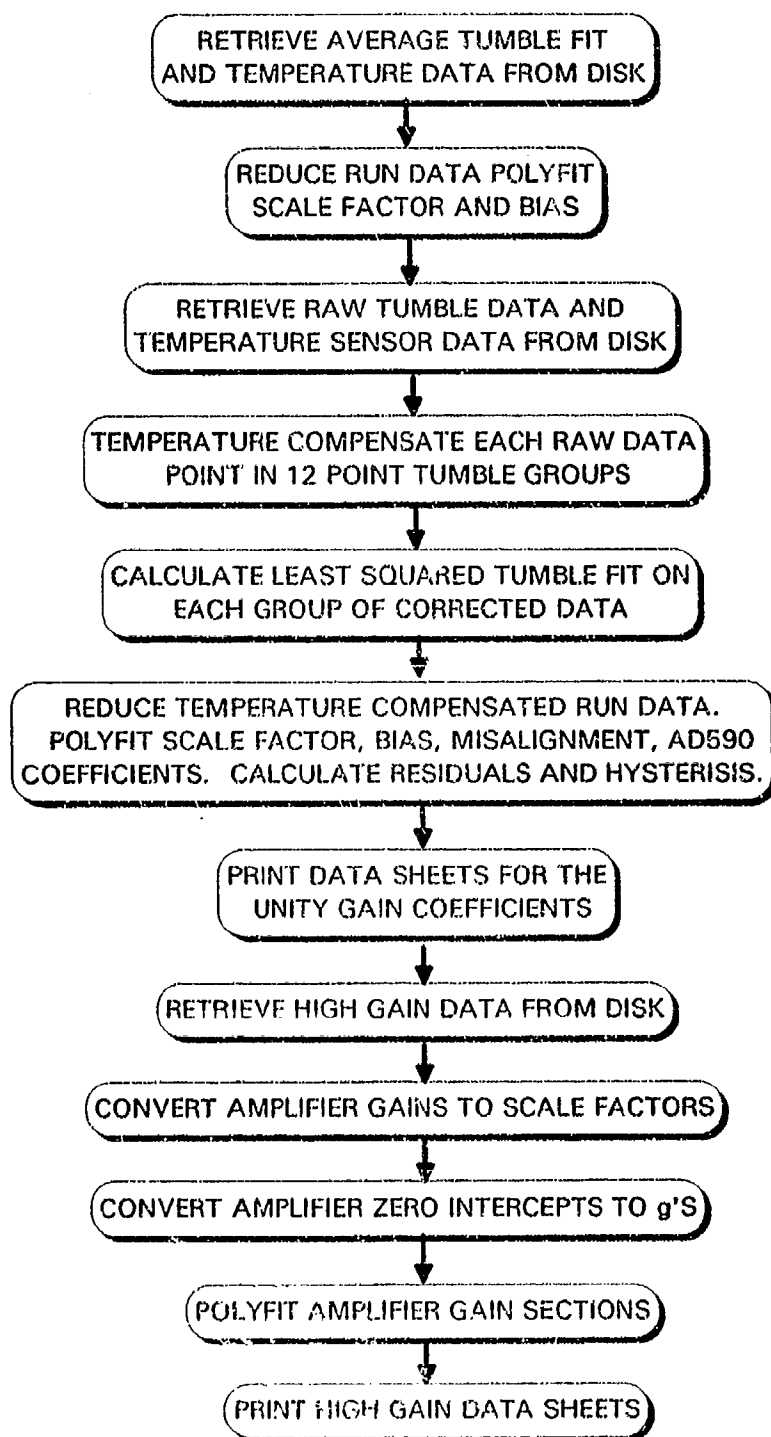


FIGURE 13: DATA REDUCTION SOFTWARE DETAIL



ESTIMATED ACCURACY

The elements that determine the overall accuracy of the SAMS calibration process are summarized in Table 2. Note that all of the entries in this table are three sigma estimates; i.e., essentially worst case. The top half of the table shows the error estimates for bias, scale factor, and misalignment for the basic calibration which is performed at a gain of 1, or nominally 10 volts/g. The lower part shows the factors which affect scale factor accuracy for the three higher gain ranges. The bias and misalignment estimates apply to all gain settings.

The worst case bias error is estimated to be 5.0 micro-g's, with the dominant error source being the neglected effect of square law nonlinearities. This is within the SAMS requirement, but represents an area worthy of further development.

Scale factor error is less than 12 parts per million, with the dominant error being voltmeter scaling. Temperature drift, even at 100 ppm/°C, is a minor contributor due to the use of iterative data reduction. Scale factor error is not a major concern in the SAMS applications because the measurements are almost exclusively at very low levels of acceleration. That fact is particularly evident in the high gain data, where the dominant error source is measurement noise. At the highest gain setting, Table 2 shows that the estimated scale factor error is 4200 ppm, primarily due to noise in the measurements. That seems to be a large scaling error; but at a gain setting that allows only 500 micro-g's full scale, its worst case contribution is only 2 micro-g's.

The estimates for Input Axis Misalignment (IAM) are based on non-repeatability only, since it is the variation over temperature that is being modeled. The initial alignment (the zero order term in the model) is determined inertially with respect to package axes at the time of installation in the experiment to be monitored. The dominant error source in this measurement is estimated to be fixture warping, which was not quantified in this setup; but has been the subject of earlier studies at Sundstrand. There are several test techniques for cancelling these effects. For SAMS, the test is judged sufficiently accurate without the added test time.

TABLE 2: SAMS Calibration Error Budget

Measurement System Errors (all 3 sigma)

I. Accelerometer Coefficients at Gain = 1 Error Source and Magnitude

	$\delta K0 \mu g$	$\delta K1/K1 \text{ ppm}$	IAM Non-repeatability in μ Radians		
			$\delta xy, xz$	$\delta yx, zx$	$\delta yz, zy$
Voltmeter bias	8uv	-	-	-	-
Voltmeter scaling	10ppm	10	-	-	-
Slip rings, connections, etc.	5uv	1	1	1	1
Sensor temperature drift (compensated)	1degC	3	2	2	2
AD 590 Measurement	0.03degC	3	1	1	1
Mechanical Noise (filtered)	2 μg	1	1	1	1
Electrical Noise (filtered)	1 μg	<1	<1	<1	<1
K1, KIP	16 $\mu g/g^2$	2	<1	1	1
Dividing head θ_1 run-out	2 μrad	-	2	2	2
Fixture warping	5 μrad	-	5	5	-
θ_1 Inductosyn non-repeatability	2 μrad	-	-	-	2
RSS	5.0 μg	11.2ppm	6.2 μrad	6.2 μrad	3.6 μrad

II. System Scale Factor at High Gain Error Source and Magnitude

 $\delta K1/K1, \text{ ppm}$

		$\delta K1/K1, \text{ ppm}$		
		GAIN = 10	GAIN = 100	GAIN = 1000
Voltmeter scaling	10ppm	10	10	10
Slip rings, connections, etc.	5 μv	1	1	1
Temperature drift	0.3degC	7	7	7
Mechanical and electrical noise	3 μg	42	420	4200
K2, KIP	16 $\mu g/g^2$	2	2	2
RSS		44ppm	420ppm	4200ppm

TYPICAL DATA

Figures 14 through 17 are data sheets typical of those printed by the SAMS software during each calibration run. Figures 14 and 15 show raw and partially processed data which are printed at each test temperature. The samples shown correspond to a nominal temperature of $+95^{\circ}\text{C}$. Figure 16 is one of six temperature model sheets printed for each triaxial head at the conclusion of a run, based on unity gain (10volts/g) data. Finally, Figure 17 is one of three temperature model sheets printed for each triaxial head based on a gain of 10, gain of 100, and gain of 1000 data.

Figure 14 shows the fundamental outputs of the system. The measured output of each of the three accelerometers in a single head is shown for each of 36 positions. Positions 1-12 correspond to the first tumble, about X. The angles listed correspond to theta 1, but are calculated from the accelerometer data rather than read directly from the Inductosyns. At the right are the coefficients that can be calculated from that tumble. Positions 13-24 represent the tumble about Z, and 25-36 the tumble about Y. At the bottom of the page are the misalignment angles calculated for the nominal temperature, with no correction for temperature drift. These are followed by the average temperature indications for each of the three tumbles.

Figure 15 shows the raw voltage measurements for all unsaturated gain settings for each of the three axes for the 42 positions of the high gain series. The positions are calculated for each accelerometer from the immediately preceding tumbles, still with no correction for temperature drift. With perfect data and no temperature changes, the middle A1 reading in each of the data blocks would ideally be zero. The observed scatter is about 10 microradians, 1 sigma, due to the combined effects of measurement noise, Inductosyn non-repeatability, and thermal and other drifts in bias, scale factor, and misalignment. The changing readings for the higher gain ranges show that the programmable amplifiers in the SAMS heads change bias as well as scaling when they are commanded to a different gain setting.

Figure 16 is a summary sheet for all temperatures tested showing the X axis misalignment angles at each temperature, and the coefficients of the 4th order polynomials which describe their variations with temperature. Printed residuals from the fitted curve include the effects of temperature hysteresis, and not merely scatter in the data. The program produces a similar sheet summarizing and modelling X-axis bias and scale factor as a function of temperature, and corresponding sheets for the other two axes. The data on these sheets are reduced iteratively and the individual readings which are used to calculate the modelled coefficients for each set of tumbles are normalized to the corresponding average temperature.

Figure 17 summarizes and models the X-axis high gain data. Again, there are corresponding sheets for the Y and Z axes, not shown.

FIGURE 14

DWG NO.

SH

REV

SAMS CALIBRATION TEST DATA TEST PLAN 8 TUMBLE DATA

P/N ENG_ S/N 01 CYCLE: 2 DATE 10-Mar-90 17:23

POS	X AXIS	Y AXIS	Z AXIS	ANGLES	TUMBLE FIT DATA		
1	0.024285	-9.634890	-0.023962	269.9989	Y sf=	9.612001	V/g
2		-8.346654	4.840996	299.9989	Y bias=	-2379	ug
3		-4.828056	8.402712	329.9982	Z sf=	9.729384	V/g
4	0.024998	-0.021748	9.706878	359.9989	Z bias=	-2307	ug
5		4.784176	8.404236	29.9992	2δ=	273	urad
6		8.302024	4.843546	59.9992	δYZg	117	urad
7	0.013613	9.589226	-0.020968	89.9991	δZYg	156	urad
8		8.300770	-4.885832	119.9990	δXY*	-565	urad
9		4.782232	-8.447584	149.9985	δXZ*	635	urad
10	0.013000	-0.024004	-9.751934	179.9989			
11		-4.829860	-8.449216	209.9986			
12		-8.347694	-4.888398	239.9992			
13	8.209846	-4.830536		329.9933	Y sf=	9.611938	V/g
14	4.750450	-8.347970		299.9942	Y bias=	-2381	ug
15	0.025090	-9.634842	-0.023941	269.9951	X sf=	9.450899	V/g
16	-4.700176	-8.346446		239.9965	X bias=	2664	ug
17	-8.159544	-4.827826		209.9968	2δ=	-151	urad
18	-9.425788	-0.021675	-0.014826	179.9971	δYXg	-169	urad
19	-8.159596	4.784248		149.9963	δXYg	17	urad
20	-4.700376	8.302052		119.9961	δZY*	240	urad
21	0.025019	9.589126	-0.019273	89.9966	δZX*	-691	urad
22	4.750516	8.300718		59.9967			
23	8.209958	4.781856		29.9956			
24	9.476050	-0.024507	-0.028279	359.9947			
25	9.476060	-0.017440	-0.023805	90.0040	X sf=	9.450674	V/g
26	8.209772		-4.887936	120.0029	X bias=	2673	ug
27	4.750934		-8.448528	150.0011	Z sf=	9.728971	V/g
28	0.025791	-0.022400	-9.751694	180.0000	Z bias=	-2320	ug
29	-4.699704		-8.447840	210.0005	2δ=	-113	urad
30	-8.159066		-4.886472	240.0008	δZXg	-100	urad
31	-9.425436	-0.026455	-0.021823	270.0012	δXZg	-13	urad
32	-8.159578		4.842634	300.0011	δYZ*	44	urad
33	-4.700446		8.403360	330.0009	δYX*	469	urad
34	0.025136	-0.021552	9.706372	0.0025			
35	4.750936		8.402314	30.0053			
36	8.210210		4.840348	60.0077			

g - Gravity δ angles
* - Coning δ angles

MISALIGNMENT ANGLES

δXY -565 urad δYX 525 urad δZX -635 urad δN -56 urad
 δXZ 635 urad δYZ 123 urad δZY 161 urad δL 79 urad
 δN - Table orthogonality δL - Table leveling

SENSOR TEMPERATURE OUTPUT (μA)

PLATE TEMPERATURE (°C)

POS	X AXIS	Y AXIS	Z AXIS	AVERAGE	DRIFT
1-12	367.923	368.921	369.126	93.42	-0.07
13-24	367.675	368.834	369.006	93.18	-0.41
25-36	367.477	368.865	368.830	92.92	-0.11

SIZE

A

FSCM NO.

97896

DWG NO.

REV

050-2257-001 REV A

SCALE: NONE

SHEET

SDCF-1475

FIGURE 15

DWG NO.		SH	REV			
SAMS CALIBRATION TEST DATA HIGH GAIN SEQUENCE DATA						
P/N ENG_		S/N 01	CYCLE: 2 DATE 10-Mar-90 17:43			
POS	A1	A10	A100	A1000	81	82
1	0.47266	4.70776			90.5933	272.6770
2	0.04733	0.45579	4.54252		90.5933	270.0975
3	0.00481	0.03056	0.29206	2.89459	90.5933	269.8396
4	0.00010	-0.01631	-0.17821	-1.79949	90.5933	269.8110
5	-0.00461	-0.06320	-0.64644	-6.48369	90.5933	269.7824
6	-0.04720	-0.48903	-4.90494		90.5933	269.5245
7	-0.47241	-4.73944			90.5933	266.9450
X AXIS						
8	0.47278	4.72530			90.5933	87.2578
9	0.04758	0.47450	4.74734		90.5933	89.8373
10	0.00507	0.04932	0.49574	4.95550	90.5933	90.0952
11	0.00033	0.00183	0.02127	0.21364	90.5933	90.1238
12	-0.00443	-0.04564	-0.45294	-4.53260	90.5933	90.1524
13	-0.04692	-0.47038	-4.70081		90.5933	90.4103
14	-0.47220	-4.72138			90.5933	92.9898
15	0.48077	4.79299			93.5890	269.9631
16	0.04828	0.46945	4.68312		91.0095	269.9631
17	0.00507	0.03751	0.36421	3.63786	90.7516	269.9631
18	0.00027	-0.01028	-0.11410	-1.13812	90.7230	269.9631
19	-0.00452	-0.05827	-0.59270	-5.92434	90.6944	269.9631
20	-0.04783	-0.49106	-4.91806		90.4365	269.9631
21	-0.48041	-4.81550			87.8570	269.9631
Y AXIS						
22	0.48036	4.80627			267.5848	269.9631
23	0.04784	0.48209	4.82890		270.1643	269.9631
24	0.00461	0.05003	0.50802	5.10553	270.4222	269.9631
25	-0.00016	0.00223	0.03038	0.32616	270.4508	269.9631
26	-0.00496	-0.04568	-0.44729	-4.45159	270.4794	269.9631
27	-0.04826	-0.47847	-4.77392		270.7373	269.9631
28	-0.48073	-4.80205			273.3168	269.9631
29	0.48662	4.86374			3.6013	269.9631
30	0.04894	0.48807	4.88614		1.0218	269.9631
31	0.00521	0.05080	0.51535	5.15361	0.7639	269.9631
32	0.00036	0.00238	0.03115	0.31343	0.7353	269.9631
33	-0.00450	-0.04605	-0.45459	-4.53206	0.7067	269.9631
34	-0.04835	-0.48406	-4.83466		0.4488	269.9631
35	-0.48615	-4.86042			357.8693	269.9631
Z AXIS						
36	0.48620	4.84368			177.6044	269.9631
37	0.04840	0.46743	4.65989		180.1839	269.9631
38	0.00469	0.03020	0.28740	2.86109	180.4418	269.9631
39	-0.00016	-0.01823	-0.19718	-1.97384	180.4704	269.9631
40	-0.00501	-0.05663	-0.68037	-6.80537	180.4990	269.9631
41	-0.04886	-0.50492	-5.06128		180.7569	269.9631
42	-0.48656	-4.88017			183.3364	269.9631

050-2257-001 REV A

SIZE

A

FSCM NO.

97896

DWG NO.

REV

SCALE: NONE

SHEET

SDCF-1475

FIGURE 16

P/N ENG_		S/N 01		DATE 12-Mar-90		LOCAL g - 980.708 cm/sec ²	
SAMS CALIBRATION TEST DATA X AXIS & MODEL DATA SHEET							
<u>TEMPERATURE</u> (°C)		<u>ΔXY</u> (μrad)		<u>ΔXZ</u> (μrad)		<u>TEMP. SENSOR</u> (μA)	
T 1	93.08	-565	635	367.576			
T 2	64.37	-595	587	338.347			
T 3	34.97	-614	562	308.768			
T 4	5.18	-637	555	279.124			
T 5	-25.00	-629	573	249.193			
T 6	-55.69	-606	558	219.194			
T 7	-26.22	-604	576	248.403			
T 8	4.46	-623	594	278.334			
T 9	34.61	-605	616	308.551			
T10	65.15	-609	655	339.084			
T11	94.38	-587	656	368.802			
T12	34.35	-623	564	308.242			
		<u>COEFFICIENTS</u> (@293μA)		<u>COEFFICIENTS</u> (@293μA)		<u>COEFFICIENTS</u> (@20°C)	
CONSTANT: D0=		-623	E0 =	573	A0 = 293.872		
1st ORDER: D1=		0.24	E1 =	0.38	A1 = 0.99673		
2nd ORDER: D2=		7.8E-03	E2 =	15.7E-03			
3rd ORDER: D3=		-10E-06	E3 =	41E-06			
4th ORDER: D4=		-35E-08	E4 =	-193E-08			
<u>TEMPERATURE</u> (°C)		<u>RESIDUALS</u> (μrad)		<u>RESIDUALS</u> (μrad)		<u>RESIDUALS</u> (μA)	
T 1	93.08	13	-11	0.08			
T 2	64.37	4	-31	-0.04			
T 3	34.97	3	-21	-0.06			
T 4	5.18	-12	-16	-0.00			
T 5	-25.00	-10	-4	-0.13			
T 6	-55.69	-1	1	-0.08			
T 7	-26.22	15	-0	0.28			
T 8	4.46	2	23	-0.08			
T 9	34.61	12	33	0.08			
T10	65.15	-10	36	-0.09			
T11	94.38	-11	10	-0.02			
T12	34.35	-5	-18	0.04			
SHIFT:		-8	3	0.10			
<u>HYSTERESIS(P-P):</u>							
TEMP= 64.76		-6	65	-0.14			
TEMP= 34.79		15	52	0.08			
TEMP= 4.82		17	38	-0.12			
TEMP=-25.61		27	3	0.39			
SIZE A		FSCM NO. 97896		DWG NO.		REV	
SCALE: NONE		SHEET					

050-2283-001 REV NEW

SDCF-1475

FIGURE 17

P/N ENG_		S/N 01	DATE 12-Mar-90	LCCAL g - 980.708 cm/sec ²	
SAMS CALIBRATION TEST DATA X AXIS HG MODEL DATA SHEET					
TEMPERATURE (°C)	A10 (V/g)	A100 (V/g)	A1000 (V/g)	TEMP SENSOR (µA)	
T 1	90.31	94.47310	944.7745	9491.482	367.515
T 2	63.62	94.10723	940.8511	9394.306	338.257
T 3	35.24	93.77775	937.5036	9389.997	308.549
T 4	6.04	93.49903	934.8557	9395.884	278.795
T 5	-23.47	93.28282	932.8151	9409.473	248.962
T 6	-52.86	93.14680	931.3767	9432.069	219.124
T 7	-25.19	93.27616	932.6002	9409.791	248.049
T 8	5.14	93.49497	934.7654	9457.043	278.355
T 9	34.32	93.77569	937.7579	9437.713	308.468
T10	63.70	94.11849	941.2000	9516.529	339.272
T11	92.25	94.49254	944.6995	9469.785	368.974
T12	34.74	93.77060	937.4518	9360.046	307.980
COEFFICIENTS (@293µA)					
CONSTANT: F0=	93.62446	G0=	936.0597	H0=	9402.597
1st ORDER: F1=	934.47E-05	G1=	931.29E-04	H1=	187.938E-03
2nd ORDER: F2=	3196.6E-08	G2=	3848.6E-07	H2=	18528.8E-06
3rd ORDER: F3=	-7764E-11	G3=	-7123E-10	H3=	33163E-09
4th ORDER: F4=	2292E-13	G4=	-6553E-12	H4=	-165546E-11
AMPLIFIER BIAS					
TEMPERATURE (°C)	A10 (µg)	A100 (µg)	A1000 (µg)	TEMP SE OR (µA)	
T 1	90.31	-98	-105	-106	367.515
T 2	63.62	-75	-80	-81	338.257
T 3	35.24	-55	-58	-58	308.549
T 4	6.04	-41	-42	-42	278.795
T 5	-23.47	-33	-34	-34	248.962
T 6	-52.86	-35	-36	-36	219.124
T 7	-25.19	-35	-35	-35	248.049
T 8	5.14	-43	-45	-45	278.355
T 9	34.32	-58	-61	-62	308.468
T10	63.70	-77	-82	-83	339.272
T11	92.25	-99	-106	-107	368.974
T12	34.74	-54	-57	-58	307.980

50-2283-001 REV NEW

SCALE: NONE

SIZE

A

FSCM NO.

97896

DWG NO.

REV

SHEET

SDCF-1475

CONCLUSION

The calibration requirements of the SAMS triaxial accelerometer heads are not particularly challenging in concept, but they have a number of features which, taken together, create a formidable task when approached by conventional means. They require a large number of data points taken at a large number of temperatures, and therefore require an extended period of time. They require that certain positions in a series of one g tumbles (the ones needed to calibrate the 100 Volts/ g , 1000 Volts/ g , and 10,000 Volts/ g scales) be computed in real time from measurements taken several minutes earlier. They require a two axis dividing head with a temperature chamber to avoid the need to remount the test units midway in the test, as remounting would increase several sources of test uncertainty and double the duration of the test. And they require an overall positioning accuracy of 5 microradians, a level of performance which is difficult to maintain in commercially available two axis dividing heads, even with no allowance for tilts and tidal effects; and equally as difficult to prove on a day-to-day basis. To meet these requirements economically, a software program has been created, based on g^2 testing, which takes advantage of the multiplicity of accelerometers to be tested and provides a test program with the following special features:

- Totally automated operation.
- Direct gravity reference; no tilt errors.
- Results independent of table accuracy.
- Needs only repeatability to calibrate accelerometers and table simultaneously.
- Iteration of temperature modeling speeds testing and improves model accuracy.
- Redundant data in bias, scale factor, and misalignment calculations provide greater accuracy, as well as continuous estimates of the accuracy of the measurement process, while providing table data which are not easily obtained by conventional means.

ACKNOWLEDGEMENTS

The authors wish to express their thanks to J. Curdy and T. Luxon for their support in the publication of this paper. Without their effort, dedication, and expertise this paper would not have been possible.

PROTOTYPE FIBER OPTIC GYRO PERFORMANCE
BY
DR. EDWARD KANEGSBERG
PRINCIPAL INVESTIGATOR, FIBER OPTIC GYRO DEVELOPMENT TEST
GUIDANCE AND CONTROL SYSTEMS DIVISION
LITTON SYSTEMS, INC.
5500 CANOGA AVE., WOODLAND HILLS, CA 91365

PROTOTYPE FIBER OPTIC GYRO PERFORMANCE

BY

DR. EDWARD KANEGSBERG

PRINCIPAL INVESTIGATOR, FIBER OPTIC GYRO DEVELOPMENT TEST
GUIDANCE AND CONTROL SYSTEMS DIVISION

LITTON SYSTEMS, INC.

5500 CANOGA AVE., WOODLAND HILLS, CA 91365

I. ABSTRACT

Litton Guidance and Control Systems Division has been developing an Interferometric Fiber Optic Gyro (IFOG) system to meet medium accuracy applications. Units of a prototype three-axis design are currently under test. They incorporate a proprietary solid state light source and additional features which enhance capabilities while minimizing size and cost. Testing is being done to demonstrate performance to specifications for particular applications such as AIWS, SCIT, and AMRAAM. Performance data is presented, including random walk, bias and scale factor stability, scale factor linearity and thermal sensitivities.

II. INTRODUCTION

The IFOG is an inexpensive alternative to spinning mass and ring laser gyros for many rotation sensing applications¹. Attitude and Heading Reference Systems (AHRS) for aircraft avionics and tactical missile guidance are the main near-term applications of these medium accuracy IMUs. Cost, in particular, is a driver of the architecture and manufacturing techniques of these units which must meet adequate performance over military environments. In this paper we present the current status of Litton's tactical missile-grade IFOGs, a prototype triax containing three orthogonal sensing gyros with a common light source. A earlier design consisting of three separately packaged IFOGs has previously been reported².

III. DESCRIPTION OF GYRO

The tests described were performed on two IFOG triaxes (units A and B) consisting of three fiber optic gyros with rate sensitive axes mutually orthogonal. Each gyro consists of a coupler, polarizer, splitter, phase modulator and fiber coil. Figure 1 shows a schematic of the architecture of each gyro. A common proprietary solid state light source is used to provide near-infrared light to the three gyros through additional couplers. The overall sensor unit is 4" x 4" x 2". Data from the first two of these Triax units will be presented.

IV. TESTING PROCEDURE

With the exception of the scale factor tests, the gyros were observed using an open-loop gyro demodulation method. A schematic of the test set-up for a single gyro is given in Figure 2. Using a commercial signal source, a square wave of frequency close to $1/2\tau$, where τ is the time of propagation of the light through the sensor coil, and amplitude sufficient to cause a phase shift of $\pi/2$ is applied to each gyro phase modulator. Output from each gyro detector is amplified and filtered, and input to a lock-in amplifier. The modulation square waves are also input to the lock-in amplifiers as a reference. The phase angle of the references are adjusted so that the output of the lock-in amplifiers are sensitive to input rates to the gyro. The outputs are calibrated by applying known (small) rates to the gyros along sensitive axes. Output signals from the lock-ins and other monitoring points (Eg. temperatures, optical power monitors, etc) are input to a data acquisition system.

The gyro triax was mounted in a thermal chamber for thermal sensitivity tests. All gyro components and preamplifiers are subject to the temperature; other electronic instrumentation is outside the chamber. Temperature ramps are applied under computer control.

Scale factor testing is done using a closed-loop demodulation method in which the signal being applied to the phase modulator is servoed to nullify the phase shift caused by input rate. The servo signal then becomes a measure of the input rate on the gyro. The gyro and the electronics are mounted on a rate table in the thermal chamber.

V. PERFORMANCE RESULTS

A. CONSTANT TEMPERATURE BIAS DRIFT TESTS

These tests generally consisted of segments of data at least four hours in length during which the test units were kept at constant temperature in the thermal chamber or under room ambient conditions (maximum thermal variation $< 3^\circ\text{C}$). An example of such a data run is shown by Figure 3. The data has been averaged to 100 sec.

B. ANGLE RANDOM WALK TESTS

Angle random walk is derived from constant temperature bias stability tests in which the data acquisition rate and bandwidth are sufficient to be sensitive to the short-term random fluctuations. A variance analysis can be used to separate the Angle Random Walk coefficient which varies as the

square root of the averaging time from long-term systematic variations. Figure 4 shows a variance analysis plot of some of the data shown in Figure 3.

C. BIAS SENSITIVITY TO TEMPERATURE TESTS

Triax unit A was built to operate over a limited temperature range about ambient; unit B was designed to operate over a full military range. Initial testing of these units has been over the range 12 to 32C for unit A and -55C to +80C for unit B. These tests expose variations due to birefringence caused non-reciprocity³ which is due to the mixing of the optical polarization modes in the gyro and which produces systematic variations of bias over temperature. An example of a run to measure thermal variation of bias is shown in Figure 5.

D. SCALE FACTOR TESTS

Prototype system electronics were connected to the triax unit A. Stability was measured over a 20 to 40C range at a rate of 50 °/sec and linearity was measured at 25°C over a rate range of ±200 °/sec. Examples of the linearity data are shown in Figure 6.

E. PERFORMANCE SUMMARY

Table I presents a summary of the performance of the Litton Prototype Triax IFOGs which have been tested to date.

VI. SUMMARY

Litton's IFOG approach is aimed toward minimum cost in production for systems which meet size, weight, and performance requirements of AHRS and tactical missile applications. The prototype units described here were designed to meet requirements for anticipated applications as well as being producible in a production environment. Although performance testing is not yet complete, test data on these and other Litton instruments continue to support the prediction that low production cost IFOG-based systems are capable of meeting the performance requirements of medium accuracy systems.

VII. ACKNOWLEDGEMENTS

The author wishes to thank E. Goldner, J. Hall, and C.A. Lee for their assistance in acquiring and preparing the data presented in this paper.

VIII. REFERENCES

1. S. Ezekial and H.J. Arditty, "Fiber Optic Rotation Sensors," presented at the First International Conference on Fiber Optic Rotation Sensors and Related Technologies, MIT

Cambridge, MA Nov. 1981, published in Fiber Optic Rotation Sensors and Related Technologies, Springer-Verlag, 2-26, 1982.

2. G.H. Chin, A. Cordova and E. Goldner, "Extended Environmental Performance of Attitude and Heading Reference Grade Fiber Optic Rotation Sensors", Fiber Optic and Laser Sensors VIII, Ramon P. DePaula, Eric Udd, Editors, Proceedings of the SPIE, vol 1367, 107-120 (1991).

3. H.C. Lefevre, J.P. Bettini, S. Vatoux and M. Papuchon, "Progress in Optical Fiber Gyroscopes Using Integrated Optics", AGARD/NATO Conference Report on Guided Optical Structures in the Military Environment, AGARD CCP-383, 9A/1-13(1985); also reprinted in "Selected Papers on Fiber Optic Gyroscopes", R. Smith, editor, SPIE Milestone Series Vol MS8 (1989).

TABLE 1
PROTOTYPE TRIAX PERFORMANCE SUMMARY

PARAMETER:	TRIAX A X-AXIS	TRIAX A Y-AXIS	TRIAX A Z-AXIS	TRIAX B X-AXIS	TRIAX B Y-AXIS	TRIAX B Z-AXIS
BIAS (DEG/HR) 1-Sigma (12 32°C) (-55 80C)	0.25	0.32	0.33	0.33	0.52	0.78
RANDOM WALK (DEG/RT-HR)	0.022	0.04	0.028	0.020	0.016	0.017
SCALE FACTOR NON-LINEARITY (PPM)	10	14	72	TBD	TBD	TBD
SCALE FACTOR STABILITY RESIDUAL (PPM)	6	12	14	TBD	TBD	TBD

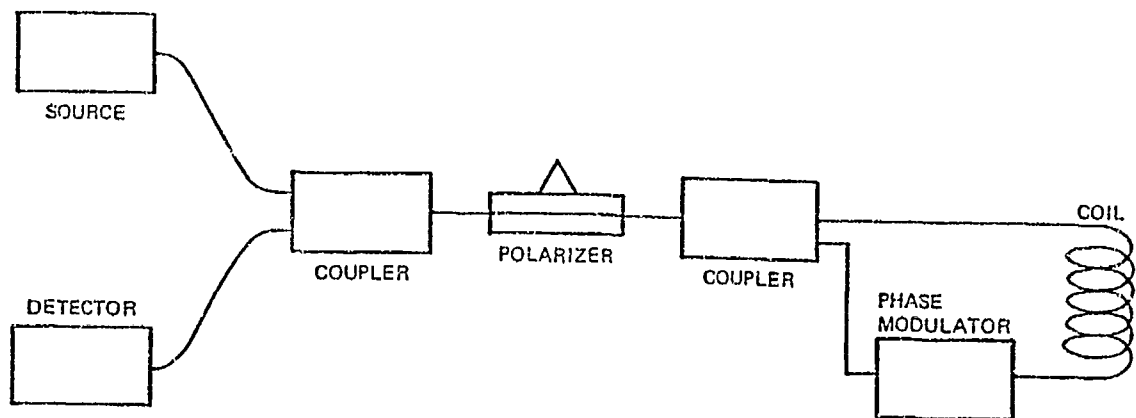


Figure 1. Optical configuration of a single-axis gyro in Litton's prototype triax.

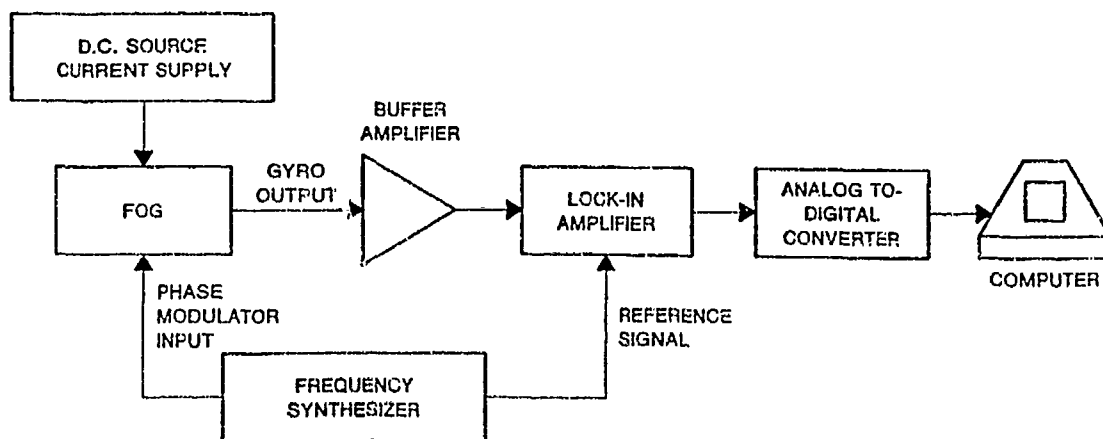


Figure 2. Open-loop measurement schematic.

Triax B Z-Axis

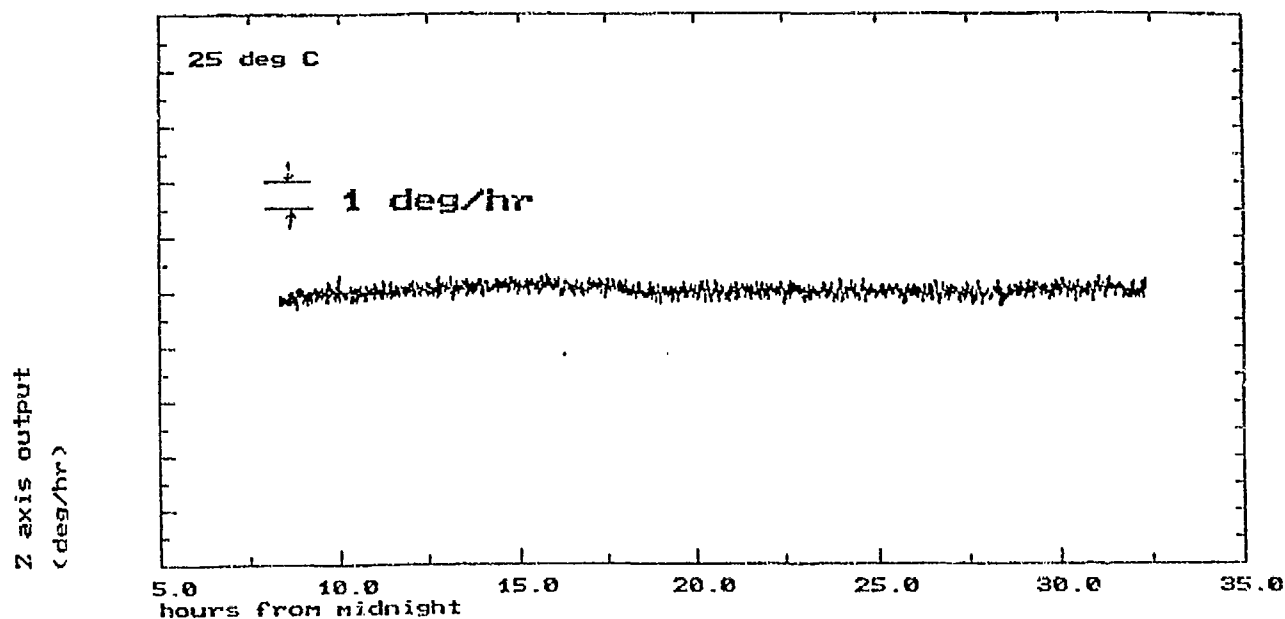


Figure 3. Triax B Z-Axis response at 25C
(100 sec averaged)

Triax B Z-Axis

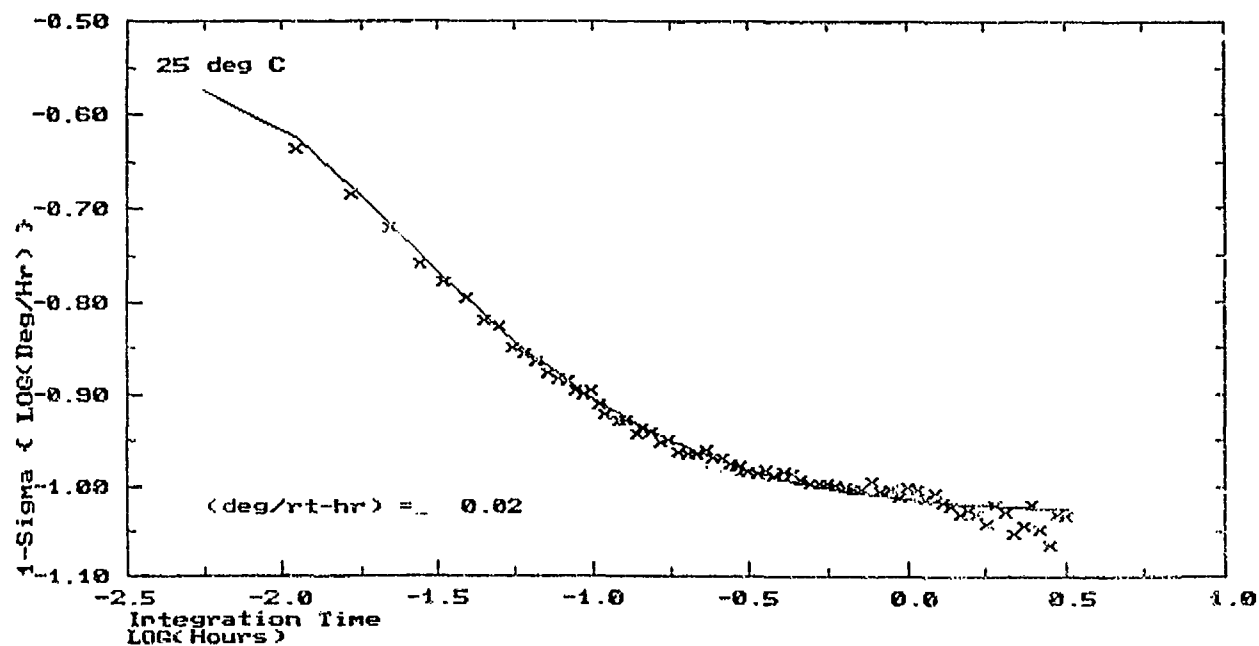


Figure 4. Variance plot of some of the data from Figure 3
with fit showing random walk coefficient.

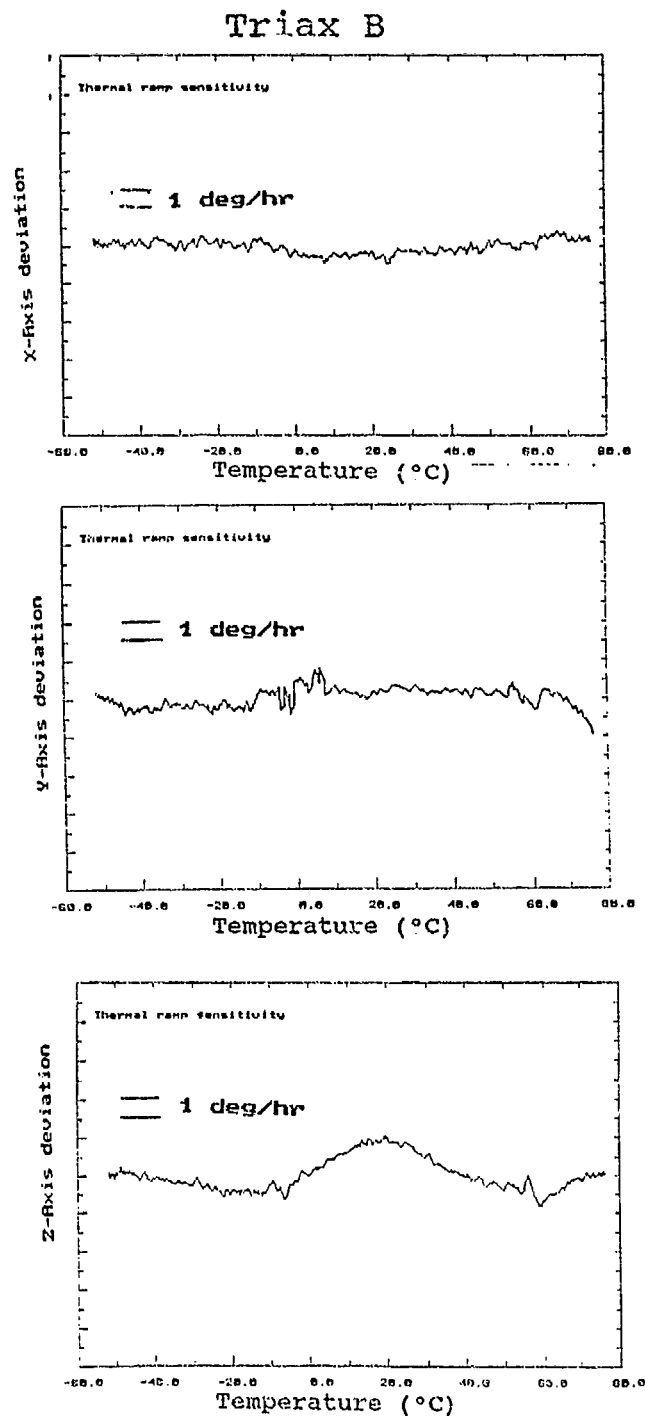


Figure 5. Triax B bias variation with temperature.
(5 minute average)
(Instrumental linear slope removed)

scale factor vs rate input

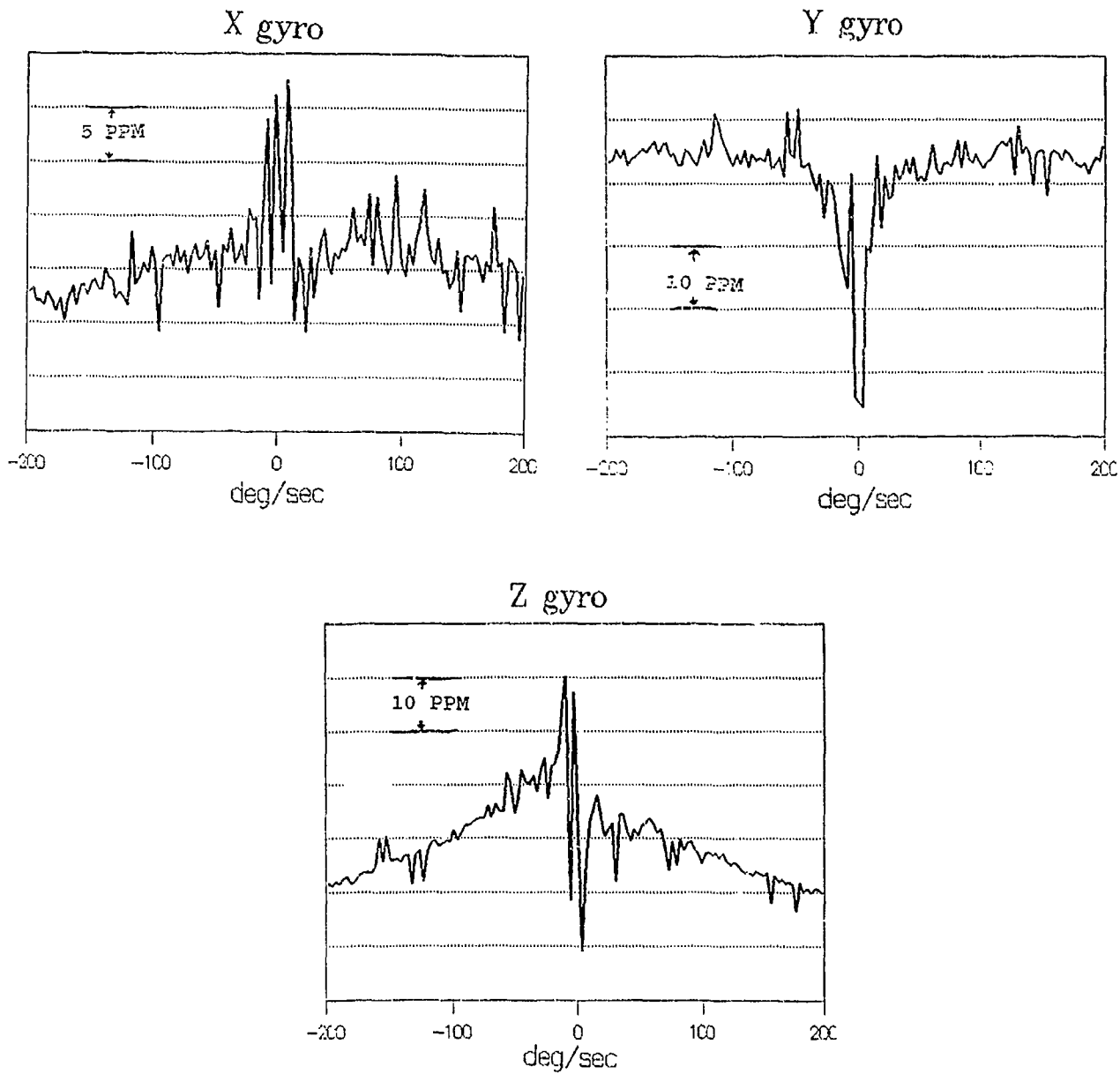


Figure 6. Triax A Scale Factor Linearity.
Deviation in parts per million (ppm)

SESSION VI-B
STELLAR GUIDANCE

CHAIRMAN
COLONEL ROBERT ALLEN, USAF
OUSDP/DTSA

Ultra-precise Azimuth Determination and Azimuth Transfer Using Stellar Optical Interferometry

by

James A. Hughes
and
Donald J. Hutter

both at the
U.S. Naval Observatory
Washington, D.C. 20392

Abstract

Classical direct imaging angle measuring telescopes appear to have reached a practical limit when used for the determination of azimuths. This is so despite the introduction of sophisticated electronic focal plane sensors. It is shown that improvements of an order of magnitude or better are possible using optical interferometric techniques. The U.S. Naval Observatory (USNO) is now in the design and prototyping phase of a program to provide instrumentation capable of making routine interferometric observations with very high levels of precision and accuracy. The development of this system is described, including a general discussion of astrometric interferometry, and it is pointed out that such a system, used with the proper observing strategies and data reduction techniques, can successfully solve three, related problems: 1) The rapid production of very high accuracy inertial positions for special lists of stars, 2) The determination of ultra-precise azimuths using such stellar positions, and 3) The transfer of known azimuth bearings to remote stations without significant loss of accuracy.

It is stressed that "proof-of-principle" and related "test bed" observations have already been carried out, and that the technique is now transitioning to an operational status.

Introduction

The application of interferometry to large angle astrometry has been a signal success in the radio domain, particularly for the determination of polar motion and UT1.¹ The extension of this technique to optical wavelengths is a relatively recent development. Although heterodyne detection is used at radio and infrared wavelengths, direct detection is necessary at optical wavelengths. The geometrical and optical principles however, are essentially identical in the two cases. A program has been initiated at the U.S. Naval Observatory (USNO)² which, building upon the experience gained with the MARK III interferometer³ at Mt. Wilson, is engaged in designing and building a dedicated, astrometric optical interferometer. This instrument is capable of producing inertial star positions at the level of a few milliarcseconds. Given a star catalog of such accuracy, the use of it to determine ultra-precise azimuths also requires the utilization of interferometric techniques.

Background

Every student of astronomy knows of the famous stellar diameter measurements made by Michelson using the 100-inch telescope at the Mt. Wilson Observatory in California.⁴ (Actually, the 100-inch was not used as a "telescope" but rather as a very sturdy mount for two mirrors whose separation could be varied.) It is particularly appropriate that at the present time, there resides at Mt. Wilson, within a stone's throw of the 100-inch, an optical interferometer which in many ways is a direct descendant of that original Michelson interferometer. This instrument is the MARK III, the development of which was a collaborative effort involving, the Smithsonian Astrophysical Observatory, the Massachusetts Institute of Technology, the Naval Research Laboratory and the U.S. Naval Observatory. This instrument is based upon earlier work by Shao and Staelin⁵, who successfully tracked the *white light fringe* from the star Polaris using a wide-band interferometer with the first operational *optical delay line*. It is essentially this feature which distinguishes current instrumentation from the Michelson interferometer and gives the MARK III capabilities well beyond those of the Michelson device. A general schematic of such an optical interferometer is shown in Figure 1.

The MARK III has produced star positions, indeed the instrument is unique in this achievement using interferometric techniques. Initial results were presented by Mozurkewich, et al.⁶, which showed that measurements at the level of 0".02 were possible using a single baseline, no metrology and observing in only one color. Subsequent observations, made in two colors using two baselines, and including determinations of the instrumental phase constant in real time, but still without metrology, have yielded results with precisions measured in a few milliarcseconds.⁷ (The significance of two color observations, metrology, the instrumental phase constant, etc. is discussed below.) There is little doubt that the full power of the method will be more nearly realized when laser metrology techniques are included in the USNO instrument.

Table 1, taken from [7], shows the average formal errors using various observing and reduction modes. In all these cases the solutions for the baseline(s) were based upon the FK5 positions of a standard set of stars, and therefore the derived corrections to the star positions are applicable within the FK5 system. Additionally, comparisons of observations made in successive years have shown that the results are repeatable to 0".008 or better.⁸ The USNO instrument, which includes metrology and other innovations, will undoubtedly improve this repeatability.

TABLE 1

MODE	Mean Error	
	α	δ
One-color	0".0198	0".0121
One-color + phase constant	0".0156	0".0095
Two-color + phase constant	0".0092	0".0056

The MARK III has baselines running North/South and East/South. The absence of an East/West baseline accounts to a great extent for the larger errors in α .

Operating Principles

The Michelson instrument observed *fringe visibility*⁹ which is defined as:

$$V = (I_{\max} - I_{\min}) / (I_{\max} + I_{\min}) \quad (1)$$

where I is the intensity of light observed.

For a particular kind of source, if one measures V as a function of the separation of the receivers (radio antennas or mirrors), then things may be inferred about the parameters describing the source. In Michelson's case, the source was assumed to be a uniformly illuminated disc and the separation of the mirrors corresponding to the first *minimum* of V allowed one to calculate the angular diameter of the source. The MARK III interferometer, and by extension, the coming USNO instrument, can make similar measurements¹⁰, including, for example, the measurement of the separations of spectroscopic binary stars some ten's of milliarcseconds apart. In the latter case fringe visibilities are also measured, but the theoretical dependence on separation is somewhat different than in the case of a disc.

However, the most significant feature of the type of instrument to be constructed by the USNO is the use of optical delay lines to directly measure the path length difference between pairs of interfering beams. As mentioned above, in the case of a wide band instrument, a white light fringe is formed, but only when the path length difference is zero. This can be arranged by inserting additional path length in the appropriate arm of an interferometer. A variable delay line is utilized for this purpose, as indicated in Figure 1. The realization of such a delay line has been accomplished by constructing a three-tiered servo. The first, coarse stage involves moving a cart along precision rails. The cart carries a cat's eye retroreflector. The second stage servo uses a voice coil to move the retroreflector as a unit, and the finest and last stage consists of a piezo stack moving the small flat secondary of the cat's eye with respect to the primary. For details of this and other features, see [3]. The path length introduced by a delay line is a measure of the optical path length difference between the beams from two receivers.

The vector joining the centers of two receivers is known as the *baseline vector* and is a fundamental characteristic of an interferometer. In Figure 1, the baseline vector joins the centers of mirrors A and B. The basic relationship describing an astrometric interferometer is given by the expression:

$$d = S \cdot B + c \quad (2)$$

where d is the delay, S is the unit vector towards the source, B is the baseline vector, and c is the instrumental phase constant. The latter is measured by pointing the mirrors back into the interferometer and finding the position of the delay lines necessary to generate a white light fringe. Assuming for the moment that B is known, a measurement of d allows one to calculate the angle between B and S , that is, make *large angle* astrometric measurements.¹¹

Atmospheric Effects

There is probably no type of ground-based astronomical observation that is not degraded to some extent by the Earth's atmosphere. An optical interferometer is no exception.¹² In some ways an interferometer is even more sensitive to the atmosphere than direct imaging instruments. On the other hand, an interferometer is not sensitive to some common atmospheric effects which plague classical astrometric instruments and methodologies. For example, an interferometer is not affected by the plane-parallel atmosphere component of astronomical refraction. In addition, by making observations in separate wavelength bands¹³, it is possible to annul the effects of the spherical atmosphere, synoptic wedges and isopycnic tilts by making use of the fact that the atmosphere is a dispersive medium.

The effects of atmospheric seeing can be reduced by these multi-color techniques, but not eliminated. The atmosphere, at any one site at any one time, may be characterized by the *Fried parameter*, r_0 , which is a measure of the average size of atmospheric turbulence cells. There is a relationship between seeing and r_0 , e.g., an r_0 of 10 cm in visible light corresponds to approximately 1"0 seeing (i.e., a stellar disc of 1" FWHM in the focal plane), 20 cm to about 0"5; thus r_0 's of 10 cm or greater are characteristic of a very good site. The formal definition of r_0 states that r_0 is the diameter of an aperture over which the atmospherically induced phase changes of an incoming optical wavefront are less than one radian. Obviously r_0 is a crucial parameter for an interferometer since it sets an upper limit on the size apertures one may use to collect the coherent light necessary to form a fringe. In addition to this spatial variation described by r_0 , there is a temporal variation depending upon the *atmospheric coherence time*, τ_0 . If one assumes that the relative motions of the turbulence elements are much less than the motion of the fluid as a whole, the so-called *frozen flow* hypothesis, then $\tau_0 = r_0/\text{windspeed}$. Typical values of τ_0 are of the order of ten milliseconds of time. The delay introduced by the atmosphere is a constant during an interval of τ_0 . The action of the atmosphere may be modeled as a Gaussian variation of the delay. This variation is superimposed upon the regular, calculable variation due to the Earth's rotation changing the aspect of the baseline with respect to the sky.

Fringe Tracking and Multi- r_0 Operation

As may be inferred from the foregoing section, active fringe tracking is possible only when using apertures of diameter r_0 or smaller. In addition, the time during which the position of the delay line is static, i.e., the delay difference is constant, is only of the order of τ_0 . Shao et al. addressed this problem by constructing a three-tiered servo system for the delay line as mentioned above. The actual tracking of the fringe is accomplished using synchronous detection. A path length dither of approximately one effective wavelength of the light observed is produced by introducing a movable relay mirror into the optical path. Using a piezo stack, this mirror is moved with respect to the beam it reflects. The movement is driven by a triangular waveform. The forward and back "sweeps" of the mirror are accomplished in a time $< \tau_0$ during which the fringe is fixed, and therefore an unambiguous fringe position is produced. Currently, on the MARK III, it is assumed that r_0 is 0"004 or larger.

Evidently, if for active fringe tracking one must use apertures of diameter r_0 or less, and can collect "coherent photons" only for a period τ_0 , a definite magnitude limit is inevitable. This limit appears to be about the ninth magnitude, perhaps a bit brighter, and is highly dependent upon the qualities of the site. If one wishes to observe fainter objects, an alternative to active fringe tracking must be found. One such alternative is the *dispersed fringe* technique (analogous to what radio astronomers call *band width synthesis*).

If the light from two large apertures, each containing many r_0 's, is combined, a complex fringe pattern is formed which is unsuitable for tracking. Suppose, however, that this pattern is imaged onto the input of a two-dimensional bundle of optical fibers. Further, suppose this bundle to be fanned out into a linear array and the light passed into a spectrometer, with each fiber corresponding to a single r_0 . The output of the spectrometer is then a two-dimensional array, one "coordinate" of which represents r_0 's and the other the wavelength of light, λ . Under these circumstances, it may be shown¹⁴ that the intensity of light, observed as a function of optical frequency, $\nu = 1/\lambda$, is proportional to:

$$V \sin(2\pi\nu d) \quad (3)$$

This expression is a constant only for an interval τ_0 , since the atmosphere is constantly changing the value of d , as indicated above. But it is the average value of d which is sought, and the Fourier transform of (3) for any single τ_0 , will provide a delta function corresponding to the then current value of d . If, for example, the atmosphere is Gaussian, then the envelope of the delta functions will be this Gaussian, and in particular, the value of d corresponding to the maximum of this envelope is the quantity sought, i.e., the effective average value of d . In actual practice a somewhat different approach will be used; that is, the autocorrelations of the photon distributions with respect to λ , over a coherence time τ_0 , for any one r_0 (an integration over τ_0 for an r_0 is called a *frame* of data), are averaged and then transformed directly into a power spectrum, which again gives the average value of d . This allows one to integrate without having to calculate a transform until the entire integration is complete, and more importantly, favors operation in the *photon starved mode*, where the average number of photons per r_0 per τ_0 is < 1 , i.e., some frames are empty.

A thermoelectrically cooled photomultiplier tube is suitable for active tracking, while a photon camera (PAPA)¹⁵ may be a good choice for detecting the two dimensional array produced in the multi- r_0 mode of operation. Avalanche photo diodes (APD's), with their much higher quantum efficiency, are being very seriously considered for both star and fringe tracking in the USNO instrument. Star (angle) tracking is required at the 0.1 level in order to avoid degraded visibility of the fringes due to misalignment of the interfering beams. An array of APD's, if available for a much reduced cost, could be a superior detector for multi- r_0 operation.

Metrology and Observing Programs

Earlier, it was assumed that the vector B was known. In practice, it will be necessary to assume positions for a selected list of stars and use these positions to solve for a provisional baseline vector. Then, in the case of producing a star catalog, a second solution may be made for corrections to star positions and the baseline. This procedure assumes that the baseline is fixed for the duration of the observations (say one night), and this is not likely to be the case at the level of stability ideally required for astrometric observations, which is to say, stability on the order of $0.1 \mu\text{m}$. The precision of the interferometer is proportional to $\Delta B/B$, where ΔB is the uncertainty in the baseline's length. A ΔB of $0.1 \mu\text{m}$ with $B = 20 \text{ m}$ corresponds to 0.001 . For this reason a rather elaborate *metrology system* will be incorporated into the USNO instrument.¹⁶ Using laser interferometers, this system will monitor changes in the baselines by using hemispherical *cat's eye* retroreflectors mounted on the flats of the siderostats. In addition, measurements will be made from siderostat to siderostat. At this time, the final reference for these measurements, which refers them to the Earth's crust, consists of so-called *optical anchors* sunk into bedrock. These are essentially vacuum pipes with retroreflectors rigidly mounted at the lower end. A "strawman" layout of the instrument is shown in Figure 2. Note that four siderostats are included. This will allow simultaneous observations on two orthogonal baselines which promotes the efficient determination of two coordinates on the sky. As indicated above, the constant, c , is determined by turning the siderostats to look back into the system.

Calculations show that using multi- r_0 techniques, with siderostats giving a working beam of the order of 1 m diameter, it is possible to reach approximately $m = 16$ with reasonable integration times, see [2]. In this case several dozen quasars will be accessible by the instrument. This is an extremely important consideration since observations of the quasars will help monitor the baselines with respect to the inertial frame defined by these objects, thus rendering the stellar positions directly inertial, without the need of other instruments or techniques. If, however, smaller siderostats become necessary initially due to cost considerations, possibilities exist for alternative methods of referring the star positions to an inertial frame. These methods include: using brighter *radio stars* previously referred to the VLBI radio frame, using somewhat brighter stars near enough to quasars of known position to permit differential position measurement using larger conventional telescopes and CCD's, and possibly, for a limited period of time, using the Hipparcos reference frame. It may also become possible to reach the quasars directly by incorporating advanced detectors with smaller siderostats. In addition, operation in the near-IR ($2.2 \mu\text{m}$) is possible and is planned for in the design of the USNO instrument. In any case, the interferometer will not be a "mass production" instrument. It will concentrate initially on perhaps a few thousand stars, and produce a catalog of superior accuracy for them. On the other hand, high accuracy, special purpose catalogs of a few hundred stars can be produced much more quickly and accurately than with classical methods. As time goes on, more and more stars will be added to the interferometric star catalog. The ultimate goal is to produce a reasonably dense optical reference frame as accurate as the radio VLBI frame.

Azimuth Determination

Historically, the determination of azimuth bearing has been a prime concern of DoD for many applications including: launch azimuths, gyro calibration and initialization, and certainly, test fixture orientations. The accuracies required for these unique uses vary widely. In many cases, errors of 10"0 are perfectly acceptable, while for other needs, errors of 0"1 or even less are unacceptable.

Azimuths have routinely been determined by observations of the star Polaris and associated angle turning using various high quality, surveying type instrumentation. Such methods usually produce accuracies on the order of perhaps 0"5 for single determinations, and precisions approaching 0"1 in the best cases by averaging over many observing sessions. Real-time determinations of azimuth at an accuracy level of 0"1 or even 0"25 are not possible using classical techniques, and further improvements in such methods are not likely to produce the necessary accuracies. The situation is entirely analogous to that in astronomy where classical astrometric transit circles have nearly reached their reasonable limits of accuracy. In addition, the use of a single star, Polaris, for azimuth determinations brings the positional error of the star into the process with full weight. What is needed is a highly accurate angle measuring device which can utilize many stars in determining azimuth. A stellar interferometer is undoubtedly the instrument of choice. One may envision a single baseline instrument with the baseline oriented nominally north-south in the horizontal plane, observing relatively bright stars in the fringe tracking mode, utilizing two small siderostats with the associated metrology.

Given an inertial, bright star catalog of sufficient areal density and accuracy, the determination of an azimuth bearing by such an instrument is straightforward. Adopting an orthogonal instrumental coordinate system with the z axis parallel to the Earth's axis, the y axis toward the east point on the horizon, and the x axis toward the intersection of the local meridian and the celestial equator, Equation 2 may be written:

$$B_x \cos \delta \cosh H - B_y \cos \delta \sinh H + B_z \sin \delta = d - c \quad (4)$$

Where, $H = t - \alpha$, the hour angle of a star at right ascension α at local sidereal time t , δ is the declination, and the B_i are the components of the baseline.

The quantities d and c are known positions of the delay line, hence their difference is a known length, while the declinations and right ascensions are known from the star catalog, updated to the times of observation. By observing several stars at various positions in the sky, values of the B_i may be derived from a least squares adjustment using Equation 4 as the observational equation. Alternatively, initial values of the baseline components may be adopted, and differential corrections may be derived from the observations.

A clockwise rotation of the coordinate system (counterclockwise rotation of the baseline vector) about the y axis of magnitude equal to the latitude ϕ , expresses the baseline vector in a horizon coordinate system, i.e.,

$$R_y(\phi) \cdot \begin{bmatrix} B_x \\ B_y \\ B_z \end{bmatrix} = \begin{bmatrix} L_x \\ L_y \\ L_z \end{bmatrix}$$

where,

$$R_y(\phi) = \begin{bmatrix} \cos\phi & 0 & -\sin\phi \\ 0 & 1 & 0 \\ \sin\phi & 0 & \cos\phi \end{bmatrix} \quad (5)$$

and,

$$\Delta a = \tan^{-1}[L_y/L_z]$$

Components in the horizon system are denoted by L_i , and Δa is the correction to the nominal zero azimuth of the baseline.

The metrology system monitors the motion of the baseline with respect to the Earth's crust, and the motions which are sensed can be used not only for improving the stellar observations, but in addition, for real-time updating of the azimuth of the baseline when not observing stars, e.g., during daylight hours.

Azimuth Transfer

Once the azimuth of the baseline of an interferometer is known, it can be used as a reference for determining other, differential azimuths. Various schemes may be considered for transferring the azimuth of the baseline to other locales. In order to maintain the accuracy inherent in the interferometric determination of azimuth, the most accurate transfer method is probably one involving interferometric length measurements.

One such method, which is schematically depicted in Figure 3, involves an extension of the method mentioned earlier for measuring the instrumental phase constant c . In the first part of this process, white light (from source WL via slide-in mirror S) is injected into the two arms of the interferometer at the beamsplitter/combiner (B). These beams are then retroreflected from the siderostat flats (ST) (in orientation "1") and the two delay lines are adjusted as necessary to observe a white light fringe at the detector (FT). Half of the difference in the delay line settings is the phase constant. The second step in transferring the baseline azimuth is accomplished by rotating the siderostat flats 45° from their retroreflecting position (to orientation "2") in order to project white light beams at right angles to the baseline. These beams are then reversed by suitable retroreflectors (R), rigidly mounted at the required distance, and the delay lines adjusted once again until the white light fringe is observed. The observed change in c is then just the difference in the distances of the two retroreflectors from their respective siderostats. Since the length of the baseline has been determined from stellar observations, and because the siderostats can be rotated to accurately project the beams to the retroreflectors at right angles to the baseline, the change in c can be used to solve for the azimuth of the line joining the retroreflectors (AZ).

A variation of the above scheme involves holding the delay lines fixed after the first step in the process, and then, in the second step, moving one of the retroreflectors parallel to its intercepted beam (as indicated by the double arrow in Figure 3), until the white light fringe is again detected. In this case AZ would have the same azimuth as the baseline.

In practice, these schemes will require careful measurements of and corrections for several sources of systematic error. First, due to both thermal and mechanical effects, the baseline is not fixed. For example, when the orientation of a siderostat is changed, the baseline is changed by bearing errors and by systematic errors in the mechanical construction, the latter arising principally from the non-intersection of the rotational axes and the offset of the plane of the front surface of the siderostat's mirror from the elevation axis. Compensation for such errors must be made for the stellar observations as well, thus the necessity to actively monitor the motion of the effective pivot points of the siderostats by laser metrology in order to determine changes in the instantaneous baseline vector. The system being developed for the USNO instrument should determine variations with an accuracy of approximately $0.1 \mu\text{m}$, corresponding to an azimuth uncertainty of 0.001 .

A second potential source of error is the accuracy with which the siderostats can be pointed to reflect light perpendicular to the baseline. The uncertainty of the pointing in this case produces an error in the measured distance to a retroreflector which is proportional to the pointing error squared multiplied by the optical path length through the system. If the pointing is accurate to 15 arcseconds, which is routinely achieved by the MARK III, and the separation between the baseline and (AZ) is ≤ 30 m, then no problem exists at the level of 0.01 accuracy in the azimuth.

A third source of error is the differential error in the optical path lengths between the siderostats and the retroreflectors due to differences in the temperatures of corresponding optical elements along the paths and to temperature, pressure and humidity differences of the air near the siderostats and retroreflectors. It should not be difficult to allow for these effects by using standard sensors at appropriate locations. In addition, these errors are much reduced by placing most of the path in vacuum.

Lastly, the geometric properties of the retroreflectors themselves must be understood and specified in order to define the "point" with respect to which the scheme outlined above is measuring the distance. Errors in the fabrication of any retroreflector causes the unit to depart from ideal behavior, however, it is possible by careful measurement of the unit's geometry to determine a point with respect to which the errors are minimized. These points can then be referenced to define the line AZ.

If the baseline of the interferometer is 20 m, the sum of the residual errors, after correcting for the above effects, must be $\leq 1 \mu\text{m}$ in order to achieve an azimuth transfer accurate to 0.01 . This is achievable.

Another scheme for transferring azimuth, especially applicable to the case where the line AZ must be rather short in comparison to the baseline, involves the measurement of absolute distances using two-color metrology techniques.¹⁷ As AZ decreases relative to the baseline length, the siderostat pointing requirements become more stringent and ultimately unrealizable. In such a case, a knowledge

of the absolute distance of each retroreflector from the siderostat pivots would allow the determination of the azimuth of the line AZ regardless of its length. On the other hand, as the distance between the baseline and AZ increases, absolute distance measurements become more difficult.

Evidently the exact method chosen for azimuth transfer depends upon the characteristics of the installation. However, it is undoubtedly true that in order to best achieve the accuracy possible and/or required, provision for the installation of the transfer device should be incorporated into the basic design of a facility. Retrofits are certainly not impossible, but maximum efficiency and accuracy are most likely to be possible with up-front designs.

Conclusion

In keeping with its activities over more than one and one-half centuries¹⁸, the U.S. Naval Observatory is now embarked upon the development of a most exciting new astrometric technique. The return from this effort will have profound effects upon many parts of astronomy. If one considers positions, proper motions and parallaxes with accuracies improved by more than one order of magnitude, spectroscopic binaries measured at the milliarcsecond level and many other similar developments, the potential gain in knowledge is impressive indeed. Applied astronomy, such as the determination of azimuths, will also benefit both operationally and conceptually through the use of new stellar data and the utilization of the associated instrumentation and techniques.

References

1. *International Earth Rotation Service Annual Report for 1988*, Prepared by the Central Bureau IERS, Paris Observatory, 1989.
2. J.A. Hughes and D.J. Hutter, "Description of the USNO Astrometric Interferometer," in *Amplitude and Intensity Spatial Interferometry*, SPIE Proceedings Series, 1237, p. 10, 1990.
3. M. Shao, M.M. Colavita, B.E. Hines, D.H. Staelin, D.J. Hutter, K.J. Johnston, D. Mozurkewich, R.S. Simon, J.L. Hershey, J.A. Hughes, and G.H. Kaplan, "The MARK III Stellar Interferometer," *Astron. Astrophys.*, 193, p. 357, 1988.
4. A.A. Michelson and F.G. Pease, *Ap.J.*, 53, p. 249, 1921.
5. M. Shao, D.H. Staelin, *Appl. Opt.*, 19, p. 1519, 1980.
6. D. Mozurkewich, D.J. Hutter, K.J. Johnston, R.S. Simon, M. Shao, M.M. Colavita, D.H. Staelin, B.E. Hines, J.L. Hershey, J.A. Hughes and G.H. Kaplan, "Preliminary Measurements of Star Positions with the MARK III Stellar Interferometer, *AJ*, 95, No.4, p. 1269, 1988.
7. M. Shao, M.M. Colavita, B.E. Hines, J.L. Hershey, J.A. Hughes, D.J. Hutter, G.H. Kaplan, K.J. Johnston, D. Mozurkewich, R.S. Simon and X.P. Pan, "Wide-Angle Astrometry with the MARK III Stellar Interferometer," *AJ*, 100, No. 5, p. 1701, 1990.
8. X.P. Pan, private communication, 1991.

9. *Principles of Optics*, M. Born and E. Wolf, 2nd Ed., The Macmillan Company, New York, 1964.
10. D.J. Hutter, K.J. Johnston, D. Mozurewich, R.S. Simon, M.M. Colavita, X.P. Pan, M. Shao, B.E. Hines, D.H. Staelin, J.L. Hershey, J.A. Hughes and G.H. Kaplan, "Angular Diameter Measurements of 24 Giant and Supergiant Stars from the MARK III Optical Interferometer," *Ap.J.*, 340, p. 1103, 1989.
11. J.A. Hughes and D.J. Hutter, "Astrometry with Optical Interferometers," in *Amplitude and Intensity Spatial Interferometry*, SPIE Proceedings Series 1237, p. 296, 1990.
12. F. Roddier, "The Effects of Atmospheric Turbulence in Optical Astronomy," *Progress in Optics*, 19, p. 281, 1981.
13. M.M. Colavita, M. Shao and D.H. Staelin, "Two-Color Method for Optical Astrometry: Theory and Preliminary Measurements with the MARK III Stellar Interferometer," *Applied Optics*, 26, p. 4113, 1987.
14. E.J. Kim, "Dispersed Fringe Group Delay Astrometry Using the MARK III Stellar Interferometer," M.S.E.E. thesis, Mass. Inst. of Technology, 1989.
15. C. Standley and P. Nisenson, "A Second Generation PAPA Detector," *Bull. Am. Astron. Soc.*, 21, p. 1072, 1989.
16. D.J. Hutter, "Siderostat/Site Metrology System for the USNO Astrometric Interferometer," JPL Workshop *Technologies for Space Interferometry*, 30 Apr. - 2 May 1990.
17. C.W. Gillard, and N.E. Buholz, "Progress in Absolute Distance Interferometry," in *Advanced Technology Optical Telescopes*, SPIE Proceedings Series, 332, p. 368, 1982.
18. J.A. Hughes, "The U.S. Naval Observatory and the Proposed Astrometric Program at Black Birch," *Southern Stars*, 29, No.8, September 1982.

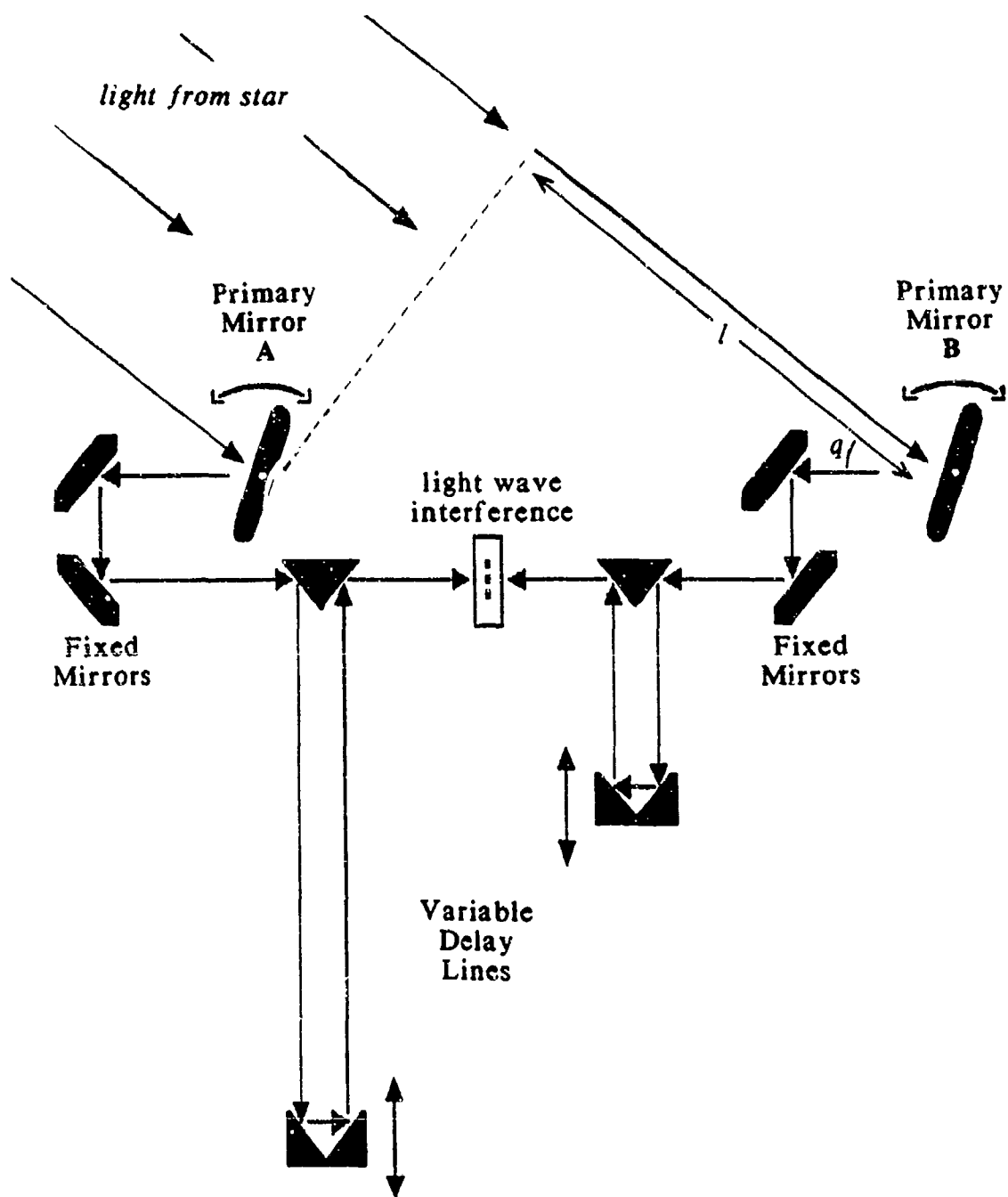
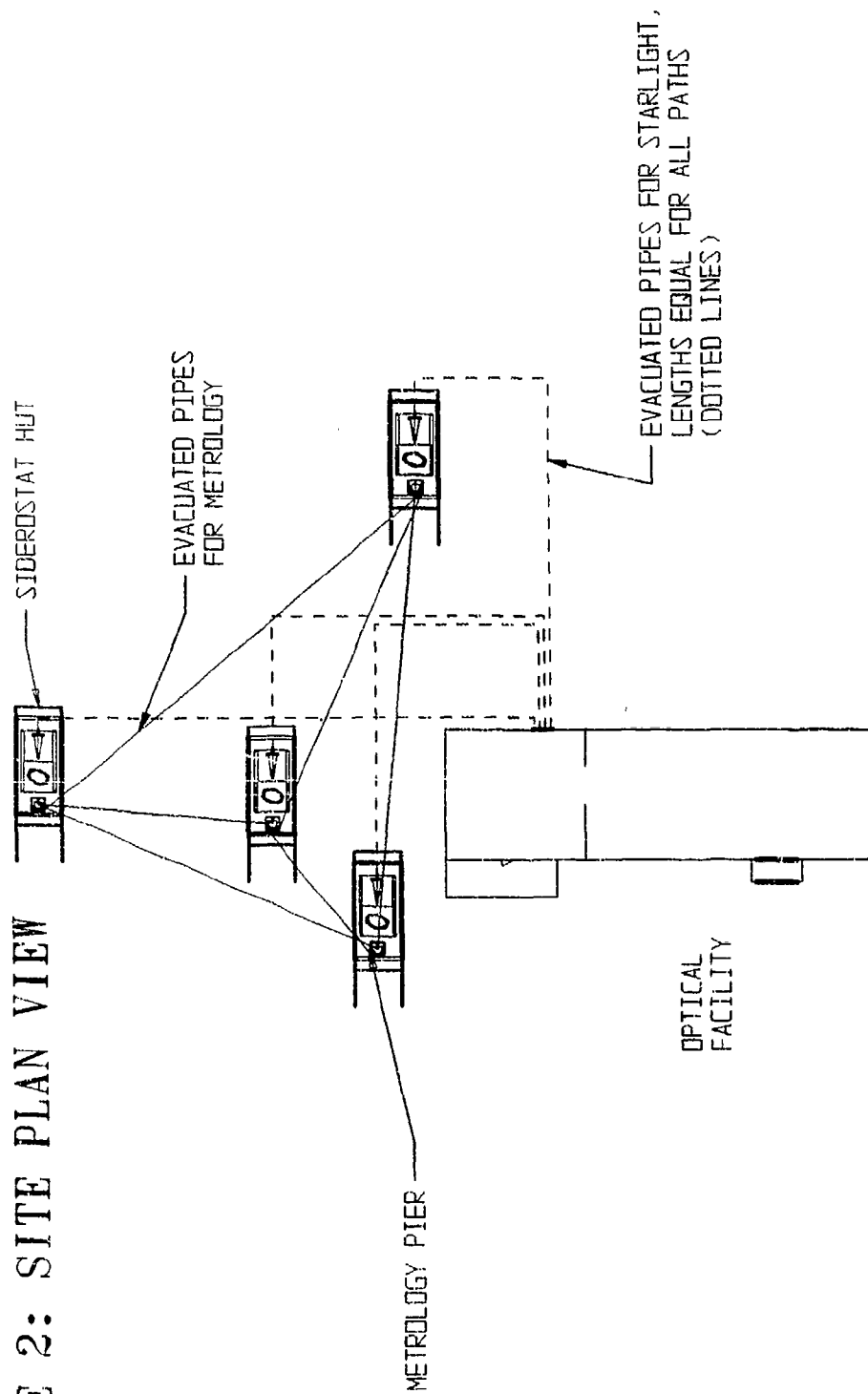
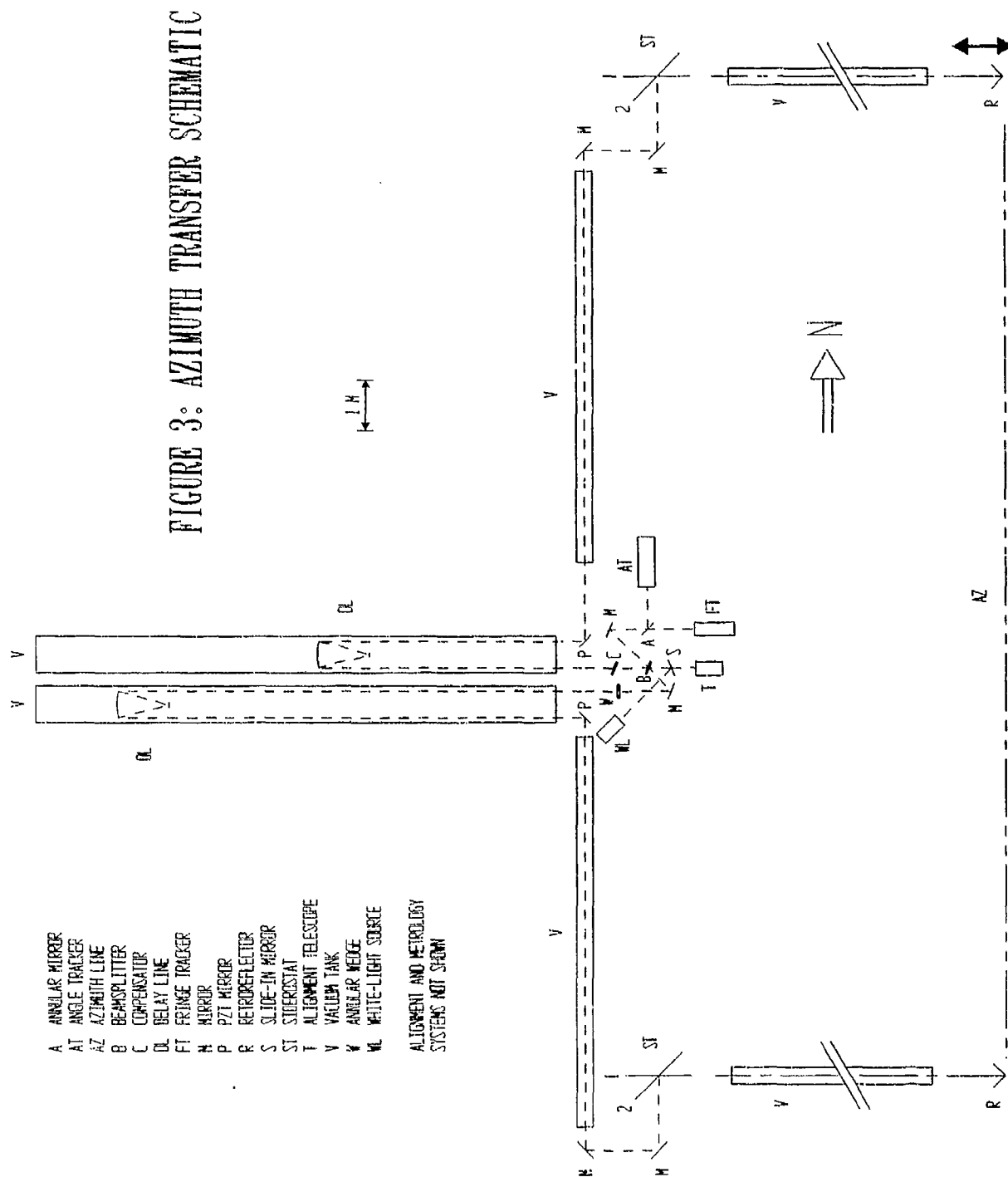


FIGURE 1: OPTICAL INTERFEROMETER SCHEMATIC

FIGURE 2: SITE PLAN VIEW





SESSION VII-B
TEST TECHNIQUES

CHAIRMAN
DOMINIC BRIENZA
NAVAL AVIONICS CENTER

**HIGH ACCURACY MEASUREMENT TECHNIQUES
FOR CHARACTERIZING AN ACCELEROMETER
CURRENT OUTPUT**

Prepared by:

D. E. Wentzel

**Sundstrand Data Control
15001 N.E. 36th Street
Redmond, Washington 98073
(206)885-8773**

ABSTRACT

In the first quarter of 1991, Sundstrand Data Control introduced an improved performance Q-FLEX® Accelerometer, Model QA3000, as a standard product. This paper describes test methodology improvements which have been employed in characterizing this improved performance.

A performance goal associated with the test equipment was to develop a test station capable of measuring the current output of the QA3000 with a one sigma uncertainty of less than one micro-G. To achieve this level of accuracy, Sundstrand joined with John Fluke Mfg. and the National Institute of Standards and Technology (formerly the National Bureau of Standards) in a Measurement Assurance Program which provides resistance and voltage standards supportive of the accuracy goal. This paper reports on the accuracies achieved to date with this program.

Another methodology improvement was to provide a test site provisioned with reference accelerometers. These reference accelerometers provide high accuracy test fixture attitude and heave data which provides compensation for environmental and seismic variances. This paper describes Sundstrand's computer-aided automatic tumble test approach, and reports on the effectiveness of reference accelerometer compensation in improving test station accuracy.

INTRODUCTION

In 1988 the need for a higher accuracy Temperature and Tumble Test Station was identified. This need was driven by the planned introduction of the QA3000 accelerometer which provided an improved performance unit intended for the 0.1 NM/hr. inertial navigator market. A summary of performance parameters is presented in Table 1.

• Bias modeling error	< 15 micro-G's
• Bias T.C.	< 10 micro-G's/°C
• Bias composite error	< 40 micro-G's
• S.F. modeling error	< 40 PPM
• S.F.T.C.	< 120 PPM/Deg C
• S.F. composite error	< 80 PPM
• Linearity	< 15 micro-G's/G ²

TABLE 1: QA3000 Performance Summary--Maximum Values

The bias data in Table 1 is very conservative. We have seen a significant percentage of units with bias modeling residuals less than 3 micro-G's over the full QFLEX temperature range. From this performance data, along with some pending performance improvements, it was concluded that a test capability which provided for measuring an accelerometer current output to an accuracy of 1.0 PPM, or 1.0 micro-G, was required.

The primary error elements driving accuracy were identified as follows:

- Digital Multimeter (DM) accuracy errors
- Load resistance accuracy
- Mounting Plate alignment
- Temperature instability
- Seismic/environmental noise

A strategy for addressing these errors was proposed which provided for ultra-precision metering of the output current. The strategy also provided for the addition of reference accelerometers on the test fixture which monitor the test fixture attitude. Additional reference accelerometers were employed to characterize the seismic noise induced accelerations. The final element in this strategy was the employment of a test fixture which provided thermal heat capacity and conductivity to reduce temperature instabilities and gradients.

This paper focuses on four of the five error elements, where temperature stability control is left as a separate topic in another paper.

DATA ACQUISITION SYSTEM DESCRIPTION

There are good news, bad news, aspects to working with a current scaled accelerometer output. The good news is that current is insensitive to lead resistance or thermal EMF's introduced by dissimilar metal electrical connections.

The bad news is that there is a national standard for voltage, based on the Josephson Cell. There is also a national standard for resistance, based on the Quantum Hall effect. However, the current standard is always a secondary standard, derived from a known voltage and resistance. Calibration laboratory transfer standards are then precision voltage sources and precision resistances traceable to the National Institute of Standards and Technology (NIST). For further detail on the theory of these standards refer to References 1 and 2.

Figure 1 provides a block diagram of Sundstrand Data Control's precision current measuring equipment. The general strategy for the functional interconnection of this equipment is the employment of the precision voltage standard and the precision resistance standard in a Wheatstone Bridge configuration to accurately quantify an accelerometer current output. In this configuration the DVM is used as a high performance null meter.

The precision voltage reference provides a 10 volt output known to within a few tenth's of a Part Per Million (PPM). The unit and its accuracy development is described in Reference 3.

A 10K ohm calibration laboratory standard was selected. The two calibration laboratory primary standards form the core of the intrinsic absolute accuracy inherent to the design of this station.

The precision reference voltage is fed to a high accuracy 10:1 voltage divider. In reference 4 the accuracy of this divider is evaluated and an accuracy of 0.075 PPM is derived. This level of accuracy is achieved by selecting ten very nearly equal valued resistors with a nominal 1000 ohm value. These resistors are also selected for minimal thermal sensitivity and they are enclosed in a thermal barrier for minimum temperature gradients across the bridge.

The key to attaining this level of accuracy in the voltage divider is the employment of a scanning switch unit designed for the calibration laboratory. The switching unit is designed to minimize thermal EMF voltages in the switching network. This is achieved by an output reversal feature which employs low thermal relays. Reference 5 describes the technical features of this switching unit in detail.

[illegible]

The final element in Figure 1 is an 8 1/2 digit DM. The DM selected has a reported linearity of 0.1 PPM. The DM, as configured in Figure 1, serves as a null meter reading the differential voltage between the 680 ohm load resistor (after filtering) and the 1.0 volt reference.

Alternatively, the DM can be used directly in measuring the voltage across the load resistor. The scale factor error of the DM can be neutralized by reading the 1.0 volt reference output. The bias errors resulting from thermal EMF's are neutralized by reading the voltage with the input leads reversed and the leads normally polarized.

Summarizing, the key elements in measuring current accurately are as follows:

- Characterize a precision load resistance using a calibration laboratory standard.
- Minimize DM bias errors and thermal EMF voltage cells by employing low thermal switching equipment.
- Minimize DM scale factor errors by employment of precision voltage source.
- Minimize linearity error with selection of a high quality DM and narrow span measurements.

To minimize the effects of tumble fixture alignment and seismic noise our tumble test station has been instrumented with reference accelerometers. The arrangement of these reference accelerometers is illustrated in Figure 2. There are two accelerometers located on the tumble plate outside the thermal chamber. These units are an orthogonal pair which measure and control the tumble fixture rotation.

Inside the thermal chamber there are provisions for five reference accelerometers. Three of these accelerometers monitor the fixture attitude in roll and pitch. The inclination angles derived from these reference accelerometers are applied to the Unit Under Test Accelerometer (UUT) data with appropriate coordinate transformation for optimum accuracy.

The remaining two accelerometers are oriented in the +1.0 G and -1.0 G planes to monitor seismic sourced heave micro-accelerations. The DM features an externally triggered voltage reading cycle which allows a setup as indicated in Figure 3. With this setup we are able to take a snapshot of acceleration data from several accelerometer sources. These two reference accelerometers record short term variations, normally the seismically induced, vertical accelerations.

Figure #2: Reference Accelerometer Deployment

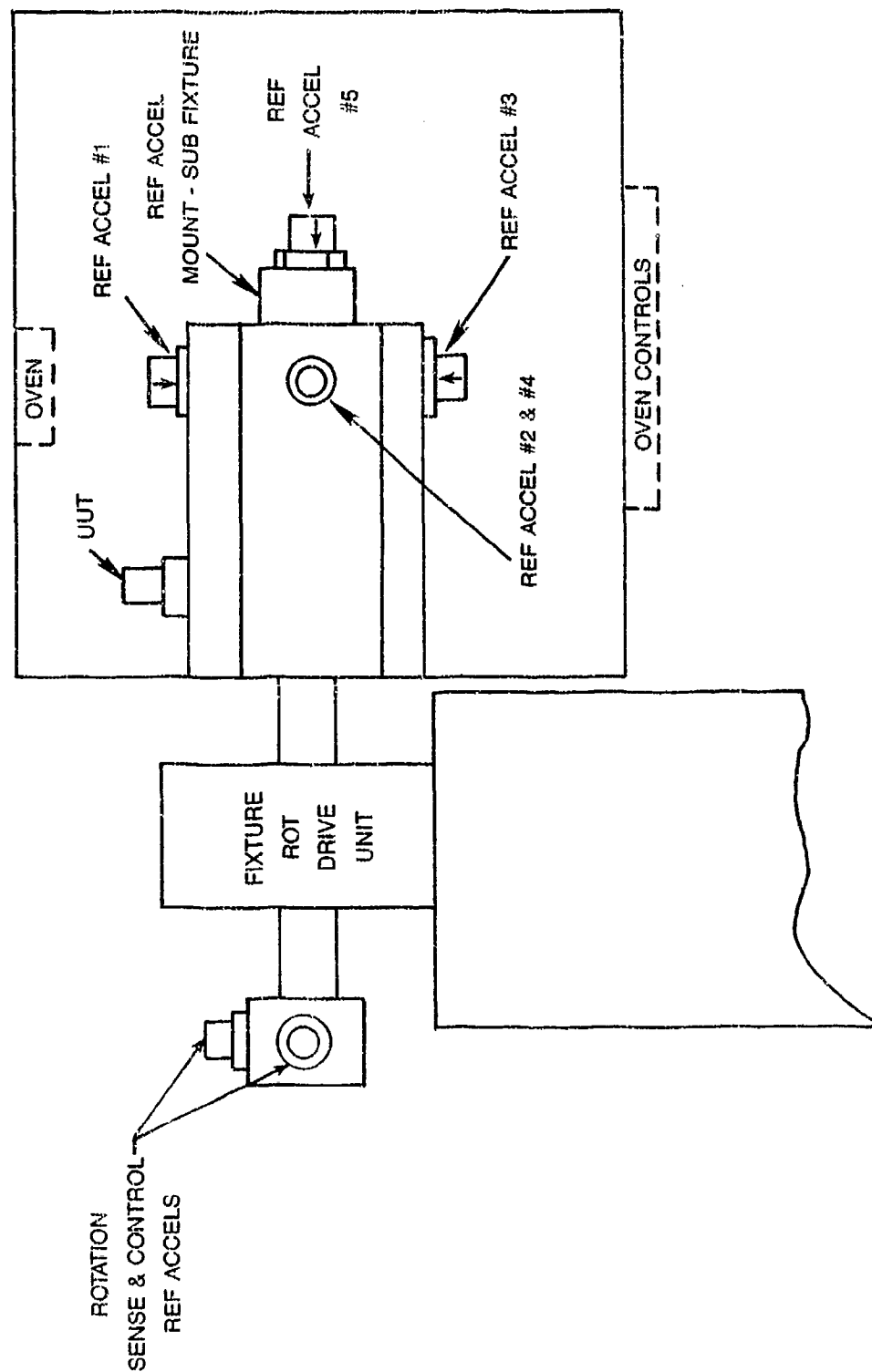
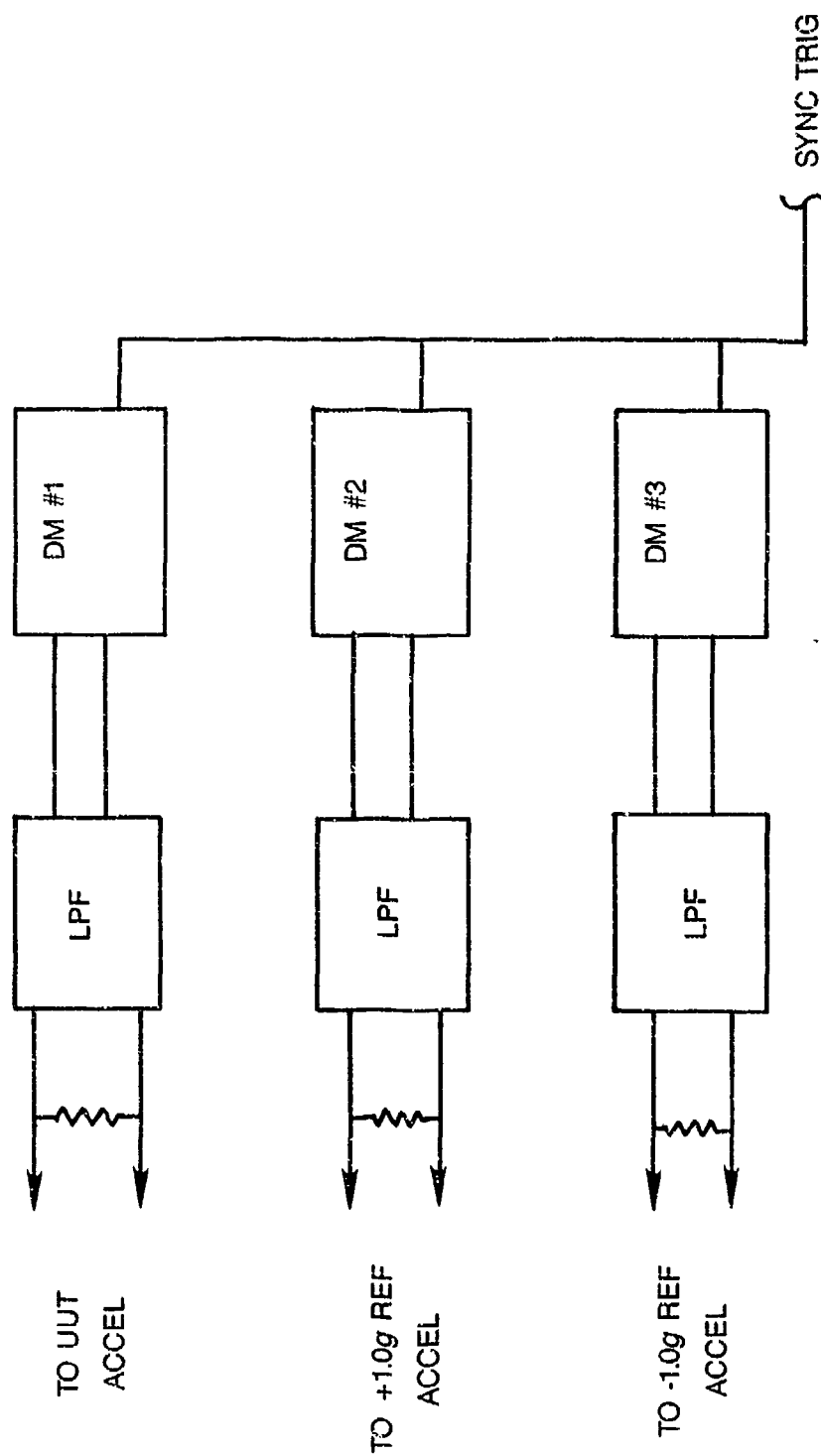


Figure #3: Multi-DM Setup



TEST STATION CALIBRATION PROCESS

The calibration of this equipment starts with the calibration of the voltage and resistance standards. The John Fluke Mfg. Company provides a calibration service which calibrates the 10 volt reference to an initial uncertainty of 0.5 PPM. This uncertainty level increases with time and after a 180 day period the uncertainty level increases to ± 0.66 PPM. This uncertainty includes an approximate 1.0 PPM/year modeled drift term.

To achieve an uncertainty of less than 1.0 PPM for our resistance standard we have joined with John Fluke in a shared Measurement Assurance Program. This calibration process starts with a set of NIST resistance standards sent from Gaithersburg, MD, to the Fluke Standards Laboratory in Metropolitan Seattle. These resistors are stabilized for approximately 15 days and then compared to the Fluke and Sundstrand resistance standards over a three to five week period. The NIST standards are returned to the NIST Gaithersburg primary standards lab and an error term associated with "traveling" these standards is derived. The resultant uncertainty of the Sundstrand 10k ohm standard is then reduced to ± 0.42 PPM.

Calibration of the 10:1 voltage divider follows a process described by Bruce Fields in Reference 4. Summarizing this process, the voltage drop across each 1000 ohm resistor is measured and the deviation from the 1.0 volt nominal value is recorded. In making these voltage measurements, bias and thermal EMF's errors are neutralized by reading each voltage with the meter leads reversed and then the source leads reversed. With the forward and reversed reading, bias terms can be derived which theoretically cancel these offset errors. Scale factor errors are neutralized by the fact that we are developing a ratio where the scale factor error appears in the numerator and denominator of the ratio determining equation. Linearity errors are minimized by the ultra narrow span of the measured voltages. A more detailed description of the data processing is provided in Appendix A. The error elements associated with this calibration are as follows:

•	DM linearity uncertainty	0.030 PPM
•	Voltage standard leakage currents	0.006 PPM
•	AC effects and random uncertainty	0.050 PPM
•	Scanner switch thermal EMF's	0.050 PPM
•	Uncorrected thermal variation	0.050 PPM

RSS total	<u>0.104 PPM</u>
-----------	------------------

The effects of environmental electrical noise are minimized in several ways. First the divider is enclosed in a grounded, highly conductive case. This package is then mounted in a relay rack which has been specially designed to minimize EMI/RFI penetration. Finally, the effects of EMI is reduced by averaging a series of voltage readings for each resistor in the divider. The average voltage readings are processed as described in Appendix A to develop a 1.0 volt reference value. Then a group of 1.0 reference values are averaged to derive the final value. This process of characterizing the 10:1 divider takes up to 24 hours of testing,

which is all controlled by a computer. Table 2 provides a typical data set for a group of ten derived one volt reference values.

TABLE 2: Typical 10:1 Voltage Divider Calibration Data

TEST #	1.0 VOLT REF	Δ PPM
1	0.99999214	+ 0.10
2	0.99999227	+ 0.03
3	0.99999221	- 0.03
4	0.99999227	+ 0.03
5	0.99999219	- 0.05
6	0.99999222	- 0.02
7	0.99999235	+ 0.11
8	0.99999230	+ 0.06
9	0.99999220	- 0.04
10	0.99999223	- 0.01

Mean = 0.99999224 VOLTS DC
 STD DEV = 0.053 Micro-volts

Calibration of the load resistance is accomplished by measuring the voltage drops across the resistor divider network illustrated in Appendix B. These voltages are determined by employing four terminal resistance elements and again each voltage reading is read in the forward and in the reversed direction such that EMF and bias offsets are neutralized. The value for the load resistance is derived using the formulas in Appendix B. In this derivation the most significant error term is the linearity of the DM. However, for this DM, the error term is less than 0.1 PPM. On the other hand, if the linearity error term is determined to be significant, the 10:1 divider provides a convenient tool for characterizing this error and thus transferring the intrinsic accuracy of the resistance standard to the load resistance without a significant error penalty.

Error elements associated with this calibration process are as follows:

- DM linearity uncertainty 0.10 PPM
- Reference resistor uncertainty 0.42 PPM
- AC effects and random uncertainty 0.15 PPM
- Scanner switch thermal EMF's 0.05 PPM
- Uncorrected thermal effects 0.40 PPM

RSS $\sqrt{0.10^2 + 0.42^2 + 0.15^2 + 0.05^2 + 0.40^2}$ 0.61 PPM

The final step in the calibration process of the current measuring equipment is to derive bias terms for the thermal EMF's imbedded in the low pass filters. These filters are necessarily a collection of capacitors and resistors soldered together and therefore represent a series of dissimilar metal EMF cells. Calibration consists of a series of voltage measurements of the input and the output of the filters. Two filters are employed, one for the reference and a second for the load resistance output. They are encased in an enclosure designed to provide EMI shielding and a dead air trap. Nevertheless, these filters are the largest variable and should be calibrated prior to each tumble test series.

Calibration of the reference accelerometers begins with calibration of the roll attitude sensing orthogonal pair. These units are calibrated for bias and scale factor at each test temperature with a 12 point tumble test. The bias and scale factor coefficients are derived employing a data reduction process outlined in Appendix C. This process is accurate (2-3 micro-radians) and minimally time consuming where a 5-7 minute time span is required to acquire and reduce the data.

A secondary calibration is performed where the difference angle between the orthogonal pair and the fixture UUT test surface is derived. In this case the roll angle from the two orthogonal reference accelerometer pairs on the fixture are compared against the orthogonal pair outside the test chamber to derived a roll angle correction value. This calibration is performed less frequently and a 24 point tumble to derive bias and scale factor terms is employed.

Calibration of the 1.0 G heave sensing accelerometers consists of a simple two point tumble at the normal QFLEX test temperatures. The key parameter is scale factor. Bias and mean 1.0 g levels are subtracted out to derive the effects of seismic variations and to some extent correlated uncompensated temperature effects.

Calibration of the pitch axis accelerometer requires a three step test process. The first test entails rotating the accelerometer, and its precisely square sub-fixture, 90 degrees such that the accelerometer is in a one gravity field for two of the cardinal axis. The accelerometer is then subjected to a standard two point tumble test at each of the standard Q-FLEX test temperatures. The accelerometer is then returned to its normal zero gravity test position where the coning error angles at the four cardinal angles are developed. The third test is a repeat of the previous coning test but the accelerometer mounting block is rotated 180 degrees; however, the accelerometer remains in the nominal zero G field.

With the data from these three tests, the reference accelerometer bias and axial misalignment terms are separated from the true fixture pitch misalignment angle. The theory of this process is outlined in Appendix D.

SUMMARY AND OBSERVATIONS

In this paper we have described a precision current measurement test setup. A summary of error elements is as follows:

• Precision Voltage Reference	0.66 PPM
• Precision 10:1 Divider	0.10 PPM
• Load Resistor	0.61 PPM
• DM errors	0.50 PPM

RSS Total	<u>1.03 PPM</u>
-----------	-----------------

It should be noted that standard metrology practice assumes a three sigma standard deviation whereas standard navigation practice normally works with a one sigma standard deviation.

In actual practice we have found that it is convenient to use the DM directly derived voltage as opposed to the differential bridge voltage measurement. However, the DM calibration is tested prior to a test cycle--employing the 10:1 Precision Divider derived one volt reference and adjusting with software the scale factor of the DM.

The employment of reference accelerometers to provide tumble fixture rotation angle data provides improved accuracy as compared to the index head. Both the leveling errors and absolute rotation angle errors of the index head are washed out. As a result, we believe the composite rotation angle error is less than 3 micro-radians. This estimate has been confirmed by comparing 12 and 24 point tumble data where the 24 point tumble data includes scale factor nonlinearity quantification.

The effects of seismic noise can be minimized by filtering and averaging output data with multiple measurements. The employment of reference accelerometers to extract seismic noise allows a faster data acquisition process without a significant sacrifice in accuracy, assuming significant resolution exists in the reference instrument.

The first step in minimizing seismic noise is the employment of a low pass filter with a several hertz cut-off frequency. The filtered accelerometer output is sampled once every second for a total of 16 samples. Seismic noise is extracted from this data employing the following algorithm:

$$a_{nsi} = a_{oi} - \frac{1}{16} \sum_{n=-8}^{n=+8} a_n$$

Essentially, the mean value of the 16 samples from a reference accelerometer output is subtracted from each of the individual 16 data points and the residual is assumed to be noise. This residual noise from both the +1.0 G and -1.0G reference accelerometers is

averaged and then subtracted from the accelerometer under test. Figure 5 as compared to Figure 4 illustrates the benefits derived from this process, which includes post process digital filtering with a one hour time constant. The results indicate less than $0.4\mu g$'s of uncompensated drift of the QA3000 accelerometer during the eight-hour observation period.

Future improvements in accuracy by utilizing reference accelerometers are expected with the implementation of software which provides multiple coordinate transformation capability. Here the true sensor coordinate system; i.e., the coordinate system aligned to the instrument axis alignment angles, is converted to an earth level coordinate system. In the process most cross-axis terms can be adjusted out of the accelerometer under test output, to provide higher accuracy multi-point tumble data.

Another planned improvement is the expansion of the algorithm employed to calibrate the bi-axial pair to account for the non-linearity coefficients, K_2 and K_{ip} . This will allow characterization of rotation angle with less than a 0.5 micro-radians uncertainty.

STABILITY RUN — S/N 00105 (QA3000-3)
Narrow Range T3 - Temp Comp

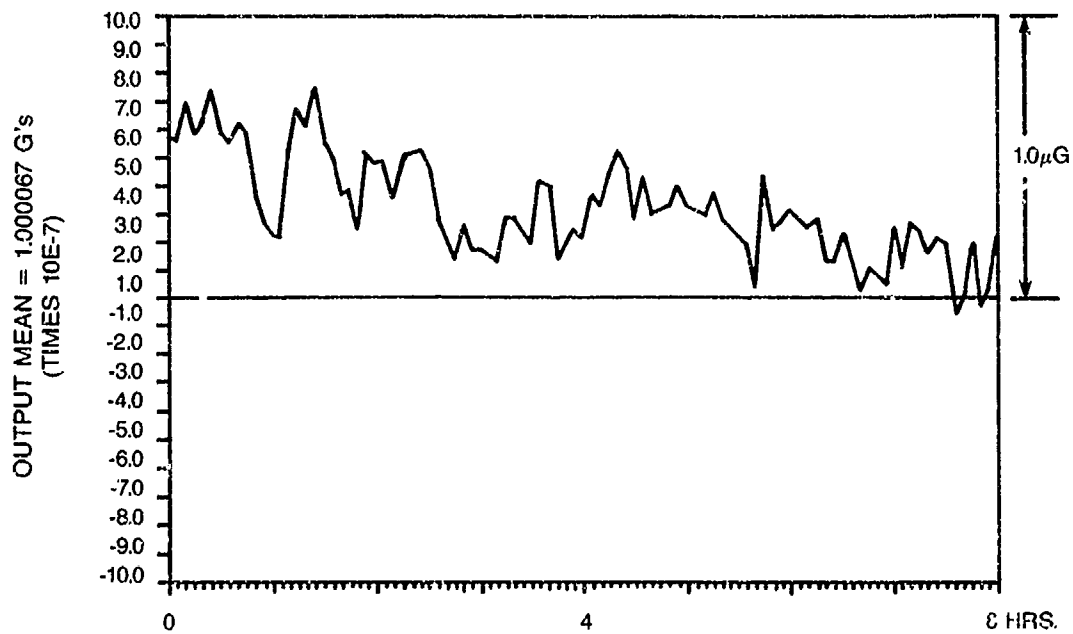


Figure #4: Accel Output Without Siesmic Noise Filter

STABILITY RUN - S/N 00105 (QA3000-3)
Narrow Range T3 - Temp Comp

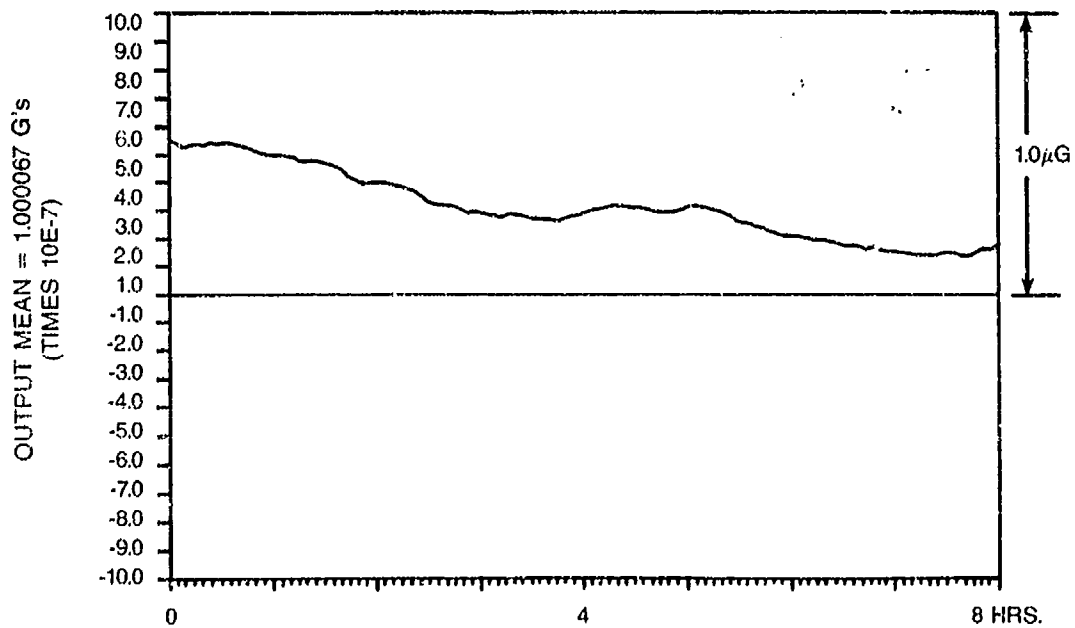


Figure #5: QA-3000 Output With Siesmic Noise Filter

APPENDIX A: PRECISION DIVIDER CONCEPTS

Apply Kelvin current loop to precision divider schematic in Figure A-1.

$$\begin{aligned} V_{FLK} &= V_{LD} + V_1 + V_2 + \dots + V_{10} \\ &= I_L R_{LD} + I_L R_1 + I_L R_2 + \dots + I_L R_{10} \end{aligned}$$

$$V_{FLK} - V_{LD} = I_L (R_1 + R_2 + \dots + R_{10})$$

$$V_{10} = I_L R_{10}$$

$$V_{FLK} - V_{LD} = \frac{V_{10}}{R_{10}} (R_1 + R_2 + \dots + R_{10})$$

$$V_{10} = \frac{(V_{FLK} - V_{LD}) R_{10}}{R_1 + R_2 + \dots + R_{10}}$$

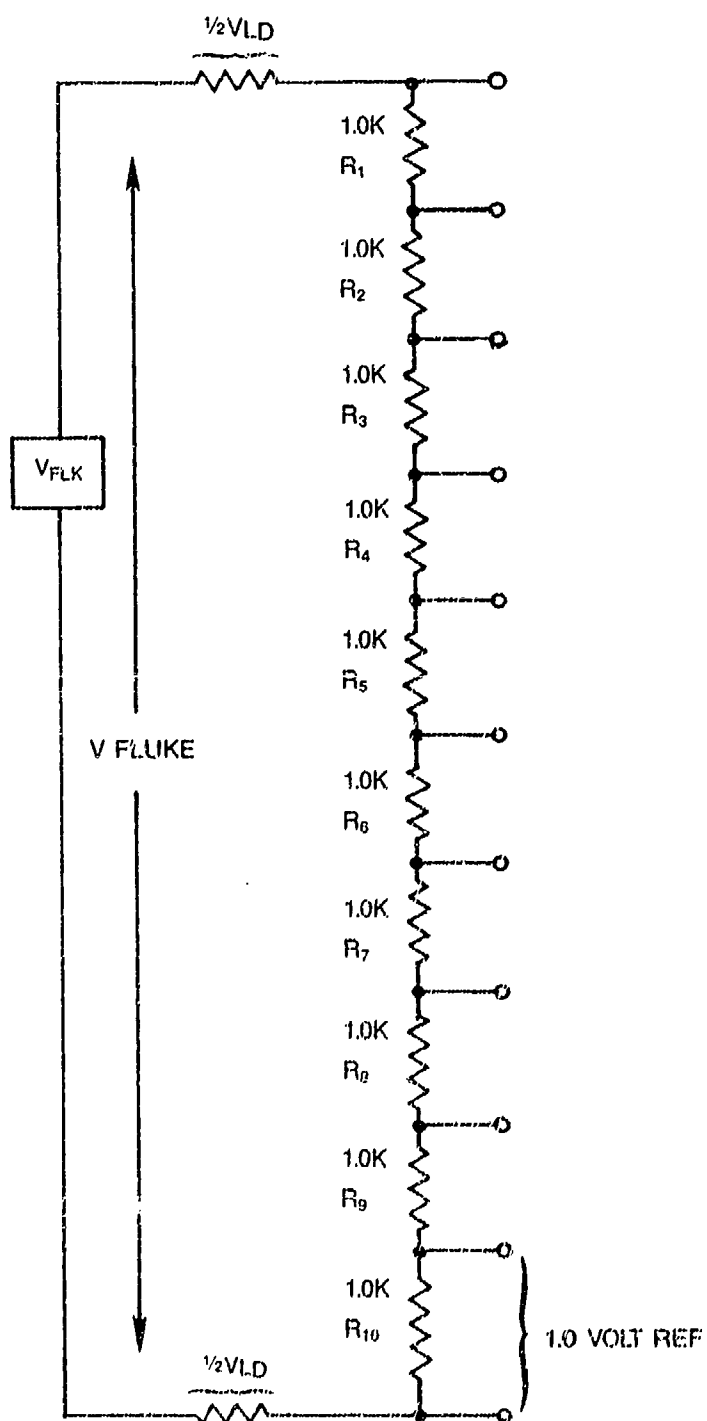
Multiplying numerator and denominator by I_L

$$= \frac{(V_{FLK} - V_{LD}) V_{10}}{V_1 + V_2 + \dots + V_{10}}$$

Then the ratio of the 1.0 volt reference to 10 volt FLUKE reference is given by

$$V_{1.0REF} = V_{10} = \frac{(V_{FLK} - V_{LD}) V_{10}}{V_1 + V_2 + \dots + V_{10}}$$

Figure A-1: Precision 10:1 Divider Circuit



Note that a DVM scaling error K_e does not affect the ratio

$$V_{1.0REF} = \frac{(V_{FLK} - V_{LD}) V_{10} K_e}{(V_1 + V_2 + \dots + V_{10}) K_e}$$

It is also convenient to use the algebra of small numbers

$$\text{let } V_i = 1.0 + \delta_i$$

$$V_{1.0REF} = \frac{(V_{FLK} - V_{LD}) (1 + \delta_{10})}{10 + \delta_1 + \delta_2 + \dots + \delta_{10}}$$

NOTE:

The linearity of the DVM minimally affects accuracy because of the narrow range of δ_i -- roughly ± 100 ppm from nominal 1.0 volt. Similarly the lead voltage drop is dependant on DVM linearity, but only over a ± 150 ppm from the nominal 10.0 volts.

APPENDIX B: LOAD RESISTOR CALIBRATION

Assume a test setup per Figure 1-B:

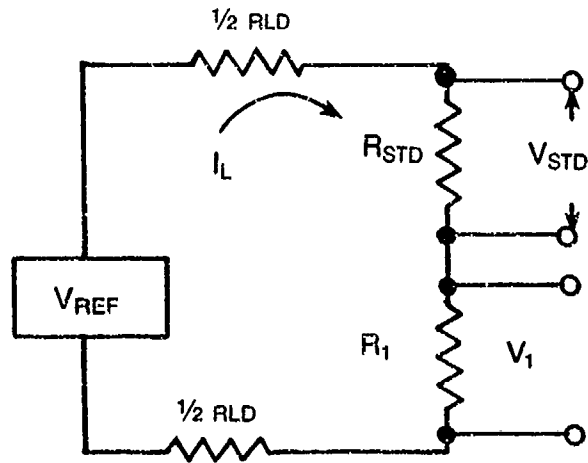


FIGURE 1-B: Calibration Circuit

Observe that
$$I_L = \frac{V_{STD}}{R_{STD}} \quad (1)$$

and
$$I_L = \frac{V_1}{R_1} \quad (2)$$

Equating (1) and (2)
$$R_1 = \frac{R_{STD} V_1}{V_{STD}}$$

Average twenty-five tests to minimize AC effects and random uncertainty

$$R_{1avg} = \frac{R_{STD}}{25} \sum_{i=1}^{i=25} \frac{V_{1i}}{V_{STD_i}}$$

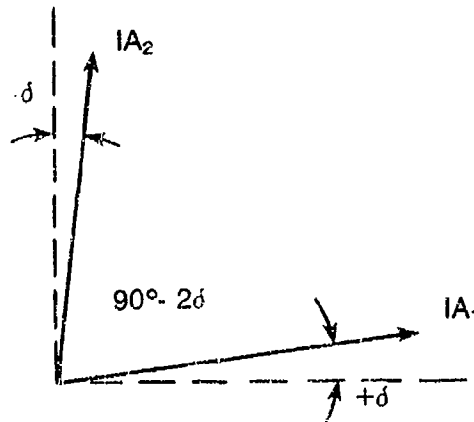
NOTE A: In making this measurement, each DVM voltage reading is measured once with leads in a standard connection and then reversed connection to provide DVM Bias and thermal EMF cancellation with the following equation:

$$V_{\text{FINAL}} = V_{\text{FWD}} - \frac{(V_{\text{FWD}} - V_{\text{REV}})}{2}$$

NOTE B: The derived value of resistance is independent of lead resistances and thermal EMF voltage associated with the voltage reference and test circuit. This results from quantifying the loop current with the resistance standard and DVM.

APPENDIX C: A METHOD OF MEASUREMENT OF SCALE FACTORS AND BIASES OF AN ACCELEROMETER BIAx

Consider the case of an instrument consisting of two orthogonally mounted linear accelerometers rotating in the uniform gravity field. The figure below illustrates the initial position of the accelerometer input axes, which are, due to misalignments, not exactly orthogonal, but rather form an angle of $90^\circ - 2\delta$ when projected on the vertical plane (δ is a small unknown angle)



If rotated by angle Θ_j in the mathematical position direction (counterclockwise), the accelerometer outputs will be

$$E_{1j} = K_1 (1 + \epsilon_1) B_1 + K_1 (1 + \epsilon_1) \sin (\Theta_j + \delta)$$

$$E_{2j} = K_2 (1 + \epsilon_2) B_2 + K_2 (1 + \epsilon_2) \cos (\Theta_j - \delta)$$

where

B_1 and B_2 are biases in g (unknown)

K_1 and K_2 scale factor estimates in V/g

ϵ_1 and ϵ_2 scale factor errors in ppm (unknown)

Assuming the unknown variables are small enough, e.g.

$$B_1, B_2 < 500 \mu g$$

$$\epsilon_1, \epsilon_2 < 500 \text{ ppm}$$

$$\delta < 500 \mu \text{rad}$$

the following set of approximations will hold true (within $< .2 \text{ ppm}$):

$$\sin (\theta_j + \delta) = \frac{E_{1j} - K_1 (1 + \epsilon_1) B_1}{K_1 (1 + \epsilon_1)} \approx \frac{E_{1j}}{K_1} (1 - \epsilon_1) - B_1.$$

$$\cos (\theta_j + \delta) = \frac{E_{2j} - K_2 (1 + \epsilon_2) B_2}{K_2 (1 + \epsilon_2)} \approx \frac{E_{2j}}{K_2} (1 - \epsilon_2) - B_2.$$

$$\begin{aligned} \sin_2 (\theta_j - \delta) + \cos^2 (\theta_j - \delta) &= \\ &= (\sin\theta \cos\delta + \cos\theta \sin\delta)^2 + (\cos\theta \cos\delta + \sin\theta \sin\delta)^2 = \\ &= \sin^2\theta \cos^2\delta + \cos^2\theta \sin^2\delta + \cos^2\theta \cos^2\delta + \sin^2\theta \sin^2\delta + 4 \sin\theta \cos\theta \sin\delta \cos\delta = \\ &= (\sin^2\theta + \cos^2\theta)(\sin^2\delta + \cos^2\delta) + 2 \sin\theta \cos\theta (\sin 2\delta) = \\ &= 1 + 2 \sin\theta \cos\theta (\sin 2\delta) \end{aligned}$$

Also:

$$\sin 2\delta \approx 2\delta \quad (\text{within } .0002);$$

$$\sin\theta \cos\theta = \left(\frac{E_{1j}}{K_1 (1 + \epsilon_1)} - B_1 - \delta \cos\theta \right) \left(\frac{E_{2j}}{K_2 (1 + \epsilon_2)} - B_2 - \delta \sin\theta \right)$$

$$\approx \frac{E_{1j}}{K_1} \cdot \frac{E_{2j}}{K_2} (1 - \epsilon_1 - \epsilon_2) - \frac{E_{1j}}{K_1} (B_2 + \delta \sin\theta) - \frac{E_{2j}}{K_2} (B_1 + \delta \cos\theta);$$

$$1 + 4\delta \sin\theta \cos\theta \approx 1 + 4 \frac{E_{1j} E_{2j}}{K_1 K_2} \cdot \delta$$

(within < 1ppm)

Ideally

$$\left(\frac{E_{1j}}{K_1} (1 - \epsilon_1) - B_1 \right)^2 + \left(\frac{E_{2j}}{K_2} (1 - \epsilon_2) - B_2 \right)^2 \approx 1 + 4 \frac{E_{1j} E_{2j}}{K_1 K_2} \delta$$

(with about 1ppm)

We, therefore, can define a cost function:

$$\text{cost} = \sum_{j=1}^n \left[\left(\frac{E_{1j}}{K_1} (1 - \epsilon_1) - B_1 \right)^2 + \left(\frac{E_{2j}}{K_2} (1 - \epsilon_2) - B_2 \right)^2 - 1 - 4 \frac{E_{1j} E_{2j}}{K_1 K_2} \delta \right]^2$$

Here Σ represents a sum of terms for a total of n positions, corresponding to n approximately equidistant angles θ_j .

Expanding and dropping terms less than 0.2ppm:

$$cost = \sum_j \left[\left(\frac{E_{1j}^2}{K_1} \right) (1 - 2\epsilon_1) - \frac{2E_{1j}}{K_1} B_1 + \left(\frac{E_{2j}^2}{K_2} \right) (1 - 2\epsilon_2) - \frac{2E_{2j}}{K_2} B_2 - 1 - \frac{4E_{1j}E_{2j}}{K_1 K_2} \delta \right]^2.$$

The kernel of the cost function is now a linear function of ϵ_1 , ϵ_2 , B_1 , B_2 and δ with known (i.e., measured) coefficients. It should, therefore, be possible to form a system of five linear equations with five unknowns by differentiating with respect to each of the variables, and find the precise correct values for two scale factors, two biases and angle between the sensor input axes. Then any required number of angles can be computed from:

$$\theta_j = W(E_{1j}, E_{2j}) \left[\sin^{-1} \left(\frac{E_{1j}}{K_1 (1 + \epsilon_1)} - B_1 \right) - \delta \right] +$$

$$W(E_{1j}, E_{2j}) \left[\cos^{-1} \left(\frac{E_{2j}}{K_2 (1 + \epsilon_2)} - B_2 \right) + \delta \right],$$

where $W(E_{1j}, E_{2j})$ is a weighting function which emphasizes the sensor which is not near $\pm 1g$.

The five equations obtained by partial differentiation are:

$$\frac{1}{2} \frac{\partial cost}{\partial \epsilon_1} = \sum (cost) \cdot \left(-2 \left(\frac{E_{1j}}{K_1} \right)^2 \right) = 0$$

$$\frac{1}{2} \frac{\partial cost}{\partial \epsilon_2} = \sum (cost) \cdot \left(-2 \left(\frac{E_{2j}}{K_2} \right)^2 \right) = 0$$

$$\frac{1}{2} \frac{\partial cost}{\partial B_1} = \sum (cost) \cdot \left(-2 \frac{E_{1j}}{K_1} \right) = 0$$

$$\frac{1}{2} \frac{\partial cost}{\partial B_2} = \sum (cost) \cdot \left(-2 \frac{E_{2j}}{K_2} \right) = 0$$

$$\frac{1}{2} \frac{\partial cost}{\partial \delta} = \sum (cost) \cdot \left(-4 \frac{E_{1j}E_{2j}}{K_1 K_2} \right) = 0$$

$$\begin{vmatrix} S_{40} & S_{22} & S_{39} & S_{21} & S_{31} \\ S_{22} & S_{04} & S_{122} & S_{03} & S_{13} \\ S_{30} & S_{12} & S_{20} & S_{11} & S_{21} \\ S_{21} & S_{03} & S_{11} & S_{02} & S_{12} \\ S_{31} & S_{13} & S_{21} & S_{12} & S_{22} \end{vmatrix} = \begin{vmatrix} \epsilon_1 \\ \epsilon_2 \\ B_1 \\ B_2 \\ 2\delta \end{vmatrix} = \begin{vmatrix} S_{40} + S_{22} - S_{20} \\ S_{22} + S_{04} - S_{02} \\ S_{30} + S_{12} - S_{10} \\ S_{21} + S_{03} - S_{01} \\ S_{31} + S_{13} - S_{11} \end{vmatrix}$$

where

$$S_{mn} = \sum_j \left(\frac{E_{1j}}{K_{11}} \right)^m \left(\frac{E_{2j}}{K_{12}} \right)^n$$

To determine an expression for rotation angles Θ_j , we use the approximate equations:

$$E_{1j} = K_1(1+\epsilon_1) B_1 + K_1(1+\epsilon_1) \cdot \sin(\Theta_j + \delta) \approx K_1(1+\epsilon_1) B_1 + K_1(1+\epsilon_1) \sin \Theta_j + K_1(1+\epsilon_1) \cdot \delta \cdot \cos \Theta_j$$

$$E_{2j} = K_2(1+\epsilon_2) B_2 + K_2(1+\epsilon_2) \cdot \cos(\Theta_j - \delta) \approx K_2(1+\epsilon_2) B_2 + K_2(1+\epsilon_2) \cos \Theta_j + K_2(1+\epsilon_2) \cdot \delta \cdot \cos \Theta_j$$

To a good approximation:

$$\frac{E_{1j}}{K_1(1+\epsilon_1)} = B_1 + \sin \Theta_j + \delta \frac{E_{2j}}{K_2(1+\epsilon_2)}$$

$$\frac{E_{2j}}{K_2(1+\epsilon_2)} = B_2 + \cos \Theta_j + \delta \frac{E_{1j}}{K_1(1+\epsilon_1)}$$

$$\theta_j = \tan^{-1} \left(\frac{\frac{E_{1j}}{K_1(1+\epsilon_1)} - B_1 - \delta \frac{E_{2j}}{K_2(1+\epsilon_2)}}{\frac{E_{2j}}{K_2(1+\epsilon_2)} - B_2 - \delta \frac{E_{1j}}{K_1(1+\epsilon_1)}} \right) + (-1)^p \cdot \pi$$

where

$$p = \frac{1}{2} \left[\operatorname{sgn} \left(\frac{E_{2j}}{K_2(1+\epsilon_2)} - B_2 - \delta \frac{E_{1j}}{K_1(1+\epsilon_1)} \right) - 1 \right]$$

$j = 1, \dots, n$

APPENDIX D: CALIBRATION OF THE Z-AXIS REFERENCE ACCELEROMETER

Given accelerometer conical misalignments δ_x and δ_y where

$$\delta_x = \frac{A_{0^\circ} - A_{180^\circ}}{2 \times S.F.} = \text{Pendulous axis misalignment}$$

$$\delta_y = \frac{A_{90^\circ} - A_{270^\circ}}{2 (S.F.)} = \text{Hinge axis misalignment}$$

The above equations are defined in Reference 6, Paragraph 10.3.4. These misalignment angles are illustrated by solid lines in Figure D-1.

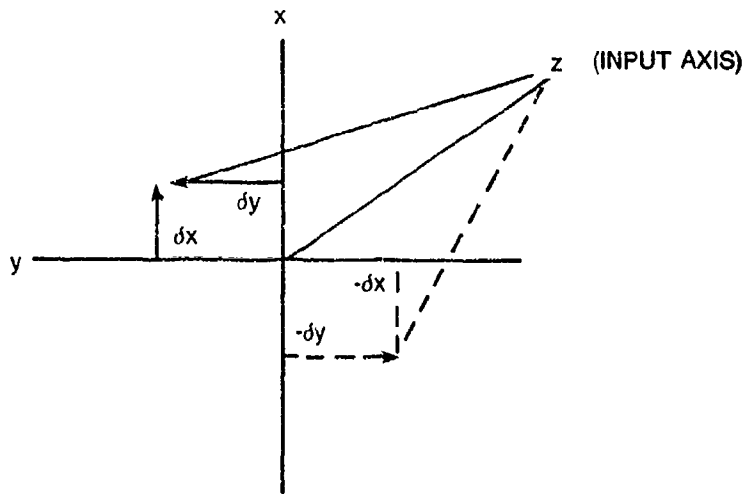


FIGURE D-1: Accelerometer Axial Misalignment

Assuming a perfectly level mounting fixture and rotating the accelerometer 180° about the input axis results in the δ_x and δ_y terms changing sign, but maintain equal magnitude as indicated by dashed lines in Figure D-1. Note the algebraic sum equals zero.

On the other hand, if there is misalignment angles ϵ_x and ϵ_y associated with the test fixture, then we have a situation as illustrated in Figure D-2.

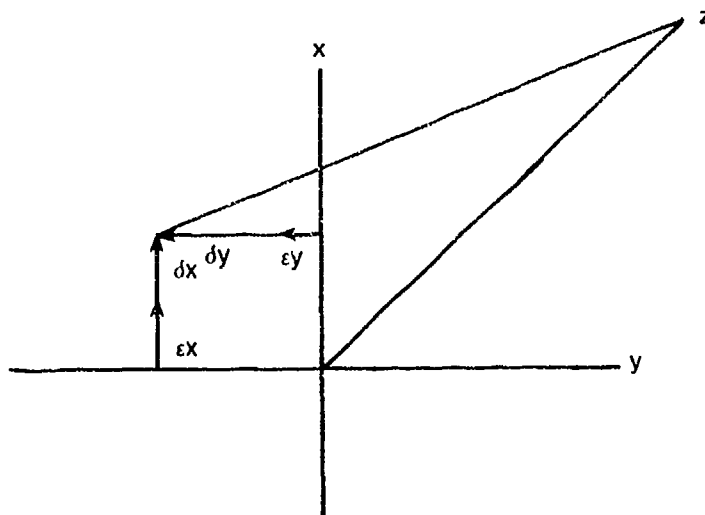


FIGURE D-2: Combined Fixture and Accelerometer Axial Misalignments

Next, rotate the accelerometer, but not the fixture, 180° , and then repeat the misalignment test. Summing the misalignment terms for both axis yields:

$$(\delta_{x1} + \epsilon_x) + (-\delta_{x1} + \epsilon_x) = 2\epsilon_x$$

$$(\delta_{y1} + \epsilon_y) + (-\delta_{y2} + \epsilon_y) = 2\epsilon_y$$

There are some error elements which remain unquantified. These include bearing eccentricity and the surface flatness associated with the sub-fixture mounting surface. These error elements are estimated to be on the order of 50 micro-radians.

In measuring the accelerometer misalignment terms, we can also account for bias by adding them up as follows:

$$A_{BIAS} = \frac{A_0 + A_{90} + A_{180} + A_{270}}{4}$$

This fixture pitch attitude angle deviation is derived by

$$\Theta_{p \text{ rad}} = \frac{(A_0 ma - A_{BIAS} ma)}{K_1} - \delta_{xc}$$

where Θ_p is assumed a very small pitch angle, and the small angle approximation $\Theta_{rad} = \sin\Theta$ applies with K_1 the two-point tumble derived scale factor, and the δ_{xc} term is the reference accelerometer misalignment angle after correcting for fixture misalignment ϵ_x .

ACKNOWLEDGEMENTS

A special thanks to Les Huntley of John Fluke Mfg., Inc., for his willingness to share his experience in voltage references, and work with us in the MAP calibration of our resistance standards.

A special thanks to Rex Peters for his contribution of the Biaxial Pair Accelerometer Calibration Technique outlined in Appendix C.

A special thanks to Dr. Graeme Blake for his contribution of the Fixture Leveling Calibration Technique outlined in Appendix D.

REFERENCES

- 1.) C. Hamilton, R. Koutz, F. Loyd, R. Steinper and B. Field, "NBS Josephson Array Voltage Standard"; IEEE Transaction Instrument and Measurement, " VOL. IM-36, 258, June 1987.
- 2.) M. Cage, R. Dziuba, B. Field, T. Kiess and C. VanDegrift, "Monitoring the U.S. Legal Unit of Resistance Via the Quantum Hall Effect"; IEEE Transaction Instrument and Measurement, VOL. IM-36, 222, June 1987.
- 3.) L. E. Huntley, "A Primary Standard of Voltage Maintained in Solid State References;" IMT Conference, 1987.
- 4.) B. F. Field, "A Sub-PPM Automated One To Ten Volt DC Measuring System"; IEEE Transaction Instrumentation and Measurement, VOL. IM-34, NO.2, June 1985, pp. 327-330.
- 5.) J. Marshall, "A 32 Channel Scanner System With 50 Nanovolt Thermals for Standard Cell Measurements"; MSC Proceedings, 1984, pp. 206-213.
- 6.) IEEE Standard 337, "Standard Specification Format Guide and Test Procedure for Linear, Single-axis, Pendulous Analog Torque Balance Accelerometer"; Nov 10, 1972.

**METHODS FOR MINIMIZING THE INTERACTION BETWEEN
COUPLED PARALLEL CONTROL SYSTEMS**

**John P. Blackburn
Applied Technology Associates, Inc.**

ABSTRACT

One of the most challenging problems encountered in the design of multi-axis active stabilization systems is the minimization of the interaction or coupling between the controlled axes of motion of the system. If a multi-axis stabilization system is coupled, it will exhibit non-zero responses in two or more axes of motion when excited in a single axis. The result is that commands to actuators which are intended to stabilize the motion of the system in one axis will cause undesirable motion in other axes.

This paper is a discussion of several methods which can be used to minimize such coupling. The methods presented are specific to systems which employ independent classical control loops to stabilize each axis of motion separately. The advantages and limitations of each method are discussed, and results are supported by the appropriate simulated or real data.

INTRODUCTION

Modern and optimal control techniques can be employed in the control of some multi-input/multi-output (MIMO) systems (Ref. 1). Several methods have been developed for decoupling the axes of motion, or "modes" of systems described in this form (Refs. 1 and 2). However, most multi-axis stabilization systems are designed so that each mode is controlled by an independent "classical" control loop. This is because unmodeled or time-varying poles in the plant model can cause modern and optimal controllers to become unstable. Furthermore, when a modern or optimal controller is found to be unstable or inadequate, it is not always intuitively obvious how the controller should be adjusted in order to correct the problem. The coupling problems associated with the implementation of parallel classical control loops have not been fully addressed.

The Seismically Stable Platform (SSP)¹ is a three-axis active stabilization system which employs three independent classical control loops. Coupling between the three axes of motion reduces the values of the loop gains which can be tolerated without causing instability, and thus limits the performance of the system. Several methods for minimizing the coupling in this system have been investigated over the course of the project. Iteration and improvement has resulted in an automated procedure which effectively reduces the coupling with a reasonable expenditure of time.

SYSTEM COUPLING AND ITS IMPACT ON PARALLEL CONTROL SYSTEMS

Consider a linear system having two inputs, U_1 and U_2 , and two outputs, Y_1 and Y_2 . The relationships between the inputs and outputs of the system can be written in matrix form as follows.

$$\begin{bmatrix} Y_1 \\ Y_2 \end{bmatrix} = \begin{bmatrix} H_{11} & H_{12} \\ H_{21} & H_{22} \end{bmatrix} \begin{bmatrix} U_1 \\ U_2 \end{bmatrix} \quad (1)$$

In the frequency domain (the domain in which most stabilization analysis is performed) the H_{ij} in equation (1) are the transfer functions from input to output for the system. If this system is decoupled, a single input will affect only a single output. If it is desired to influence only Y_1 when U_1 is changed, and to influence only Y_2 when U_2 is changed, then the transfer functions H_{12} and H_{21} are required to be zero-valued for all frequencies.

¹ The Seismically Stable Platform is located in the Advanced Inertial Test Laboratory (AITL) on Holloman Air Force Base in Alamogordo, New Mexico.

Figure 1 shows the signal-flow diagram for two parallel feedback control loops, operating simultaneously when H_{12} and H_{21} are non-zero. These loops are intended to control the quantities Y_1 and Y_2 . Both of the loop outputs are functions of both inputs.

$$\begin{aligned} Y_1 &= \frac{[(1 + H_{22})H_{11} - H_{12}H_{21}]U_1 + H_{12}U_2}{(1 + H_{11})(1 + H_{22}) - H_{21}H_{12}} \\ Y_2 &= \frac{H_{21}U_1 + [(1 + H_{11})H_{22} - H_{21}H_{12}]U_2}{(1 + H_{11})(1 + H_{22}) - H_{21}H_{12}} \end{aligned} \quad (2)$$

The response of a MIMO linear system to one of the multiple inputs to that system is the response of the system to that input with all other inputs set to zero. The off-diagonal transfer functions H_{12} and H_{21} in equation (1) can be derived from equation (2) by setting the appropriate inputs equal to zero and solving for the ratios Y_1/U_2 and Y_2/U_1 , but it is more instructive to employ Mason's Gain Rule.

Figure 2 is much like Figure 1, except that two paths through the network are traced by the dashed line and the solid thinner line. The dashed line traces the forward path gain from U_1 to Y_2 , and the thinner line outlines the loop gain from U_1 to Y_2 , and then back to U_1 again. By Mason's Gain Rule the closed-loop transfer function from U_1 to Y_2 is given by the ratio:

$$G_{cl} = \frac{\text{forward path gain}}{1 \pm \text{loop gain}} \quad (3)$$

The sign in the denominator depends on the sign of the feedback. This exercise is actually not intended to explore all the means available for obtaining the transfer function Y_2/U_1 . What is important to recognize is that in tracing the loop gain path (the thinner line in Figure 2), the algebraic sign of the signal returning to the U_1 summing junction is positive. The signal has passed through two successive minus signs. This is positive feedback. Positive feedback implies instability. In fact, coupling between system modes has a destabilizing effect on parallel control systems which are intended to control those modes.

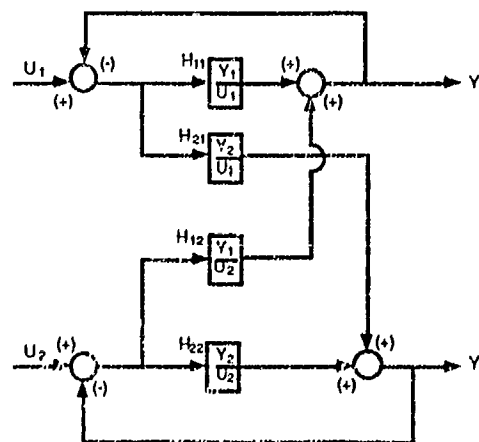


Figure 1. Signal-Flow Diagram for Two Parallel Control Systems

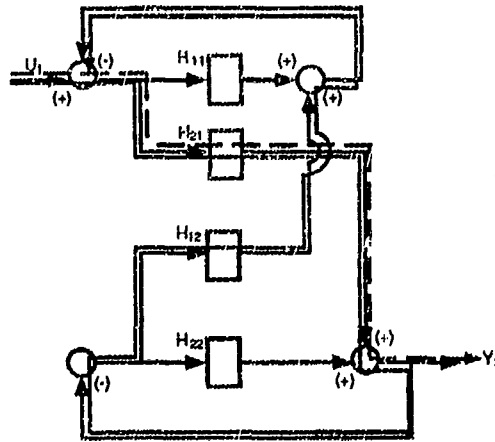


Figure 2. Forward Path and Loop Gain Trace for the System Shown in Figure 1

It should be noted that a real system has the ability to tolerate a certain amount of coupling without going unstable. However, it is important to minimize the magnitude of coupling terms such as H_{12} and H_{21} in the above discussion, in order to achieve the best possible system performance.

SSP SYSTEM MATRIX DESCRIPTION

The relationships between the system inputs and the system outputs for the SSP can be described by an equation similar to equation (1). The three inputs to the system include the vertical force input F_z , and the x- and y-axis moment inputs M_x and M_y . The three system outputs are the vertical acceleration of the primary mass, and the angular rotations of the primary mass about the x- and y-axes.

$$\begin{bmatrix} \frac{d^2(Z)}{dt^2} \\ \Theta_x \\ \Theta_y \end{bmatrix} = \begin{bmatrix} H_{11} & H_{12} & H_{13} \\ H_{21} & H_{22} & H_{23} \\ H_{31} & H_{32} & H_{33} \end{bmatrix} \begin{bmatrix} F_z \\ M_x \\ M_y \end{bmatrix} \quad (4)$$

In this system there are a total of six off-diagonal terms which we desire to minimize.

In the following sections several methods to minimize these terms, which have been investigated over the course of the SSP effort, are presented.

DECOUPLING IN SOFTWARE

One of the more innovative approaches investigated was a method by which the coupling in the system was taken out "in software." Consider the block diagram in Figure 3. In this figure, the matrix $[H]$ is the same as the matrix $[H]$ in equation (4). It is the 3x3 matrix of transfer

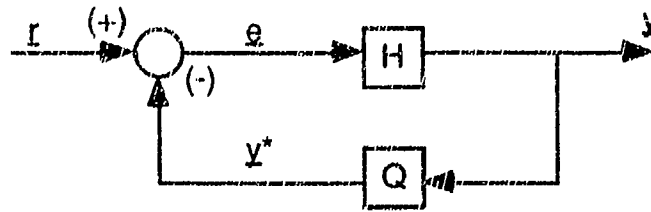


Figure 3. Block Diagram for the Decoupling in Software Method

functions, and it is measured on the real system. It therefore exists as two sets of nine data files. The first set is vectors of magnitude data, and the second set is vectors of phase data.

The matrix $[Q]$ will also be composed of nine magnitude data files and nine phase data files. This matrix must be calculated such that the following relation is true.

$$y/r = [H_d] \quad (5)$$

In equation (5), $[H_d]$ is the dynamics matrix $[H]$ as the designer would like it to appear. It can be anything the designer pleases, but most sensibly it is a diagonal matrix having on its diagonal the diagonal elements of the matrix $[H]$. After some matrix algebra has been performed, it turns out that equation (5) is true when:

$$[Q] = [H_d]^{-1} - [H]^{-1} \quad (6)$$

Since $[H_d]$ is chosen by the designer, it is known. It must be made available in the same "data file format" in which the matrix $[H]$ was stored (i.e., nine magnitude data files and nine phase data files). The matrix $[Q]$ is calculated point-by-point using equation (6).

The matrix $[Q]$ will indeed decouple the system perfectly if implemented as it is shown in Figure 3. Unfortunately, data files are in themselves difficult to implement digitally. There are no mathematical expressions which describe the data in these files as explicit functions of frequency. To circumvent, the magnitude vectors are curve-fitted in the frequency domain. It is usually the case that when the magnitude vectors are fitted correctly in this manner, the resulting (curve-fitted) phase vectors closely approximate the actual phase vectors as well (and vice versa). Figures 4 and 5 show plots of the "actual" magnitude and phase vectors of the entry Q_{23} as calculated by equation (6). Overlaid on the "actual" data are curve-fitted approximations of the data.

The dynamics matrix $[H]$ must also be curve-fitted so that functional relationships are available to describe the data making up its magnitude and phase entries. The curve-fitted version of this matrix will be denoted $[H^*]$.

Once all 18 filters (curve-fitted versions of H^*_{ij} and Q_{ij}) have been obtained, they are mapped to the z (discrete) domain so that they can be implemented digitally. The implementation of the matrices of filters $[H^*]$ and $[Q]$ is yet another issue. Let the vector of inputs \underline{r} and the vector of outputs \underline{y} be represented as follows.

$$\begin{aligned} \underline{r} &= [r_1 \ r_2 \ r_3] \\ \underline{y} &= [y_1 \ y_2 \ y_3] \end{aligned} \quad (7)$$

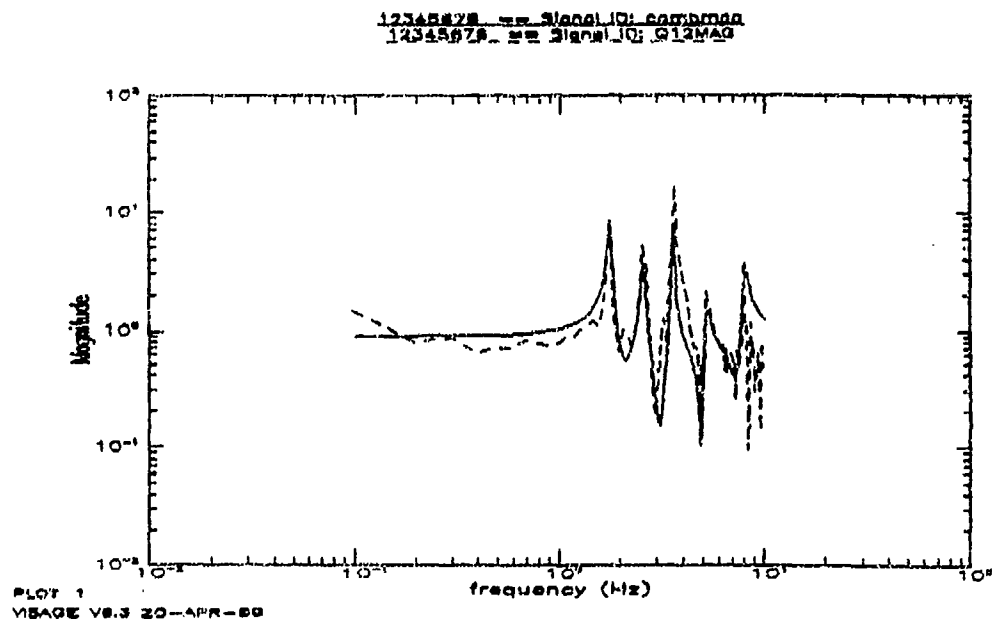


Figure 4. Matrix Entry Q12, Actual and Curve-fitted Magnitude

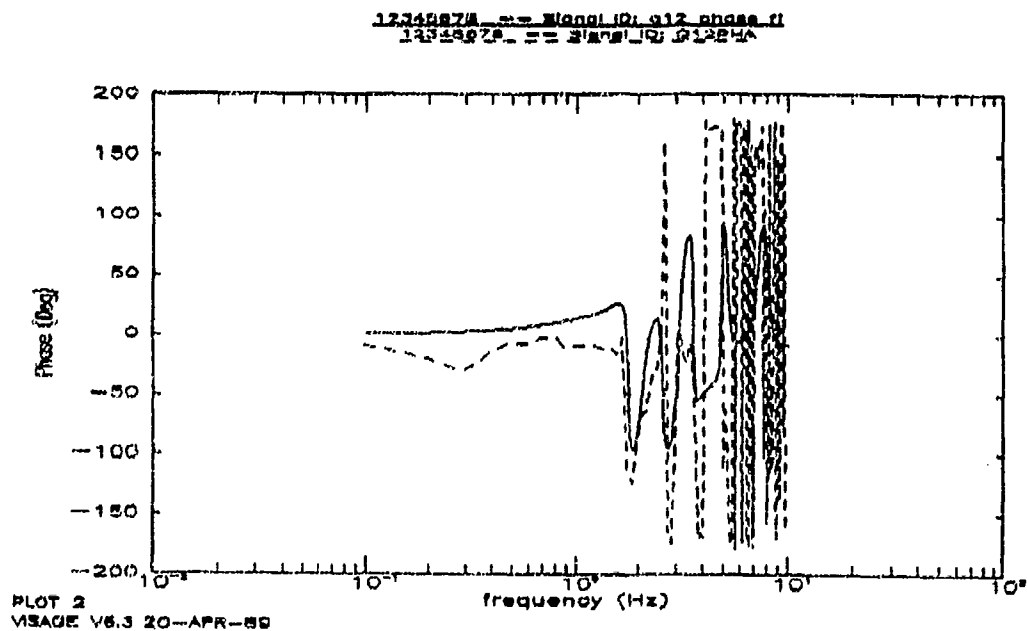


Figure 5. Matrix Entry Q12, Actual and Curve-fitted Phase

The vector \mathbf{y} is given by:

$$\mathbf{y} = \mathbf{e}[\mathbf{H}^*] \quad (8)$$

Suppose that the output of the matrix $[\mathbf{Q}]$ in Figure 3 is the vector \mathbf{y}^* . The vector of error signals \mathbf{e} is then given by:

$$\mathbf{e} = \mathbf{r} - \mathbf{y}^* \quad (9)$$

In typical stabilization applications the reference input \mathbf{r} is zero, since the desired output is zero. The vector of error signals \mathbf{e} , which become the commands to the actuators, are simply negative feedback of the output¹. The vector of voltage signals sent to the actuators is then:

$$\mathbf{e} = -\mathbf{y}^* \quad (10)$$

Each of the elements of \mathbf{y}^* are functions of all three error voltages e_i , and the filters Q_{ij} and H^*_{ij} . For example, the command voltage to the vertical axis controller is given by:

$$\begin{aligned} (e_1)_{k+1} = & -((e_1)_k H^*_{11} + (e_2)_k H^*_{21} + (e_3)_k H^*_{31})Q_{11} \\ & -((e_1)_k H^*_{12} + (e_2)_k H^*_{22} + (e_3)_k H^*_{32})Q_{21} \\ & -((e_1)_k H^*_{13} + (e_2)_k H^*_{23} + (e_3)_k H^*_{33})Q_{31} \end{aligned} \quad (11)$$

While this method is interesting from an academic standpoint, it has serious shortcomings. Not only are there 18 filters that must be implemented digitally (H^*_{ij} and Q_{ij}), but the filters are relatively complicated. For example, the curve-fitted filter shown in Figures 4 and 5 is 10th-order. The method is computationally expensive.

But there is yet another problem with this method. The dynamics of the plant change daily. This means that every time the plant changes significantly, the matrix $[\mathbf{H}]$ must be measured again, and the digital filters H^*_{ij} and Q_{ij} must be generated again. The modified filters must then be mapped to the discrete domain once again for implementation. This task requires a sizeable expenditure of time.

DECOUPLING BY TRIAL-AND-ERROR

While the title of this method suggests a cumbersome process, this method has afforded some of the best coupling performance in the history of the SSP project. In this method, the magnitude functions of the off-diagonal responses are observed using a spectrum analyzer as various system parameters are adjusted. If the magnitudes of these undesirable responses drop with a certain adjustment, then that adjustment had a beneficial impact on the system coupling.

This method differs fundamentally from the last in that it seeks to improve the dynamics of the system rather than accepting them, and then compensating for the imbalances inherent in the

¹ Such systems are often called regulators because, unlike servo systems in which the desired system behavior is commanded as a reference input, these systems appear to have no reference input. Technically speaking, a stabilization system intended to suppress motion does have a reference input, but the input is always zero.

existing dynamics. Before proceeding with the discussion of the trial-and-error method, the physical parameters which contribute to the coupling must be identified.

Although many factors, both electrical and mechanical, contribute to the coupling in the SSP system, there are only a few sets of parameters which are adjusted easily in software. The parameters which are optimized in the decoupling methods hereafter are listed below.

- (1) Electromagnetic (EM) actuator scale factor bias gains;
- (2) Linear Variable Differential Transformer (LVDT) position sensor bias voltages.

The EM actuator scale factors are known to vary from one actuator to another. In addition, one cannot be certain that the actuators are aligned to any specific accuracy. Variations in the scale factors and alignment of the actuators introduce coupling into the system.

The LVDT sensors measure the relative displacement between the primary and secondary masses, and between the secondary mass and the base. The masses are raised pneumatically by closing a low frequency proportional-integral (PI) control loop around the LVDT readings. The control law seeks to obtain a desired voltage output from the LVDT sensors. By adding or subtracting from the volume of air enclosed by the pneumatic isolators, the primary and secondary masses can be raised or lowered. When the desired LVDT readings are obtained, the masses are in the desired position.

The pneumatic isolators have associated with them spring constants which are a measure of the force that a given isolator imparts on the masses, as a function of the distance by which the isolator is compressed. A given isolator spring constant can be affected by adjustment of the amount of air enclosed by the isolator. These spring constants dictate much of the dynamics of the system and when imbalanced introduce significant coupling.

Eight system parameters which are adjusted in the following discussion are identified above. They include four EM actuator biases and four LVDT sensor biases. Clearly, a sensible, systematic means of optimizing all eight parameters is required because a parametric study of the effects of varying each parameter separately would be formidable.

The EM actuator bias gains and the LVDT sensor bias voltages are iterated in pairs. Consider the configuration shown in Figure 6. The ends of the rigid rod are labeled N for north and S for south. Forces F_N and F_S act on the north and south ends of the rod, respectively. If F_N and F_S are equal, the rod will translate and no rotation will occur. However, if the two forces are not exactly equal, the rod will rotate as well as translate. The translational and rotational modes of this system are coupled in this case.

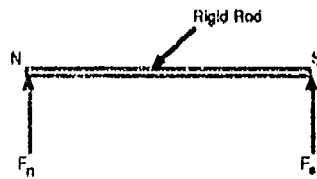


Figure 6. North-South Force/Reaction Diagram

The force imparted by an electromagnetic actuator is directly proportional to the current in the coils. If it is assumed that the current amplifier used to provide the current in the coils is perfect, such that it provides a current that is directly proportional to the input voltage, then the force

generated by the actuator can be assumed to be directly proportional to the current amplifier input voltage. The scale factors of electromagnetic actuators vary from one actuator to the next, so that two seemingly identical actuators may produce different forces, given the same current amplifier input voltage. Such imbalances can be compensated for by adding a bias gain, k^* , to the scale factor of the "weaker" actuator, and by adding the negative of this gain to the scale factor of the "stronger" actuator.

$$\begin{aligned} F_n &= (k_n + k^*) V_n \\ F_s &= (k_s - k^*) V_s \end{aligned} \quad (12)$$

In equation (12), k_n is the scale factor of the north actuator (lbf/V), and V_n is the voltage command to the current amp that drives this actuator. On the SSP, equations like (12) are written for the east-west pair as well. The pair of biases (k^* , $-k^*$) is referred to in this analysis as an "EM-delta," and distinction is made between the north-south EM-delta, NS_EM_DELTA, and the east-west EM-delta, EW_EM_DELTA. These "deltas" are iterated by trial-and-error, over a range of negative as well as positive values, and the effects on the system coupling are observed. The optimal values for the two deltas are obtained. It should be noted that differences in the alignment of the actuators are also reflected in the optimal values of the deltas obtained.

The spring constants associated with the pneumatic isolators, k_i , are directly related to the volume of air enclosed by the isolators, v .

$$k_i = \sigma v \quad (13)$$

For small movements of the primary and secondary masses, the forces imparted on the masses by the isolators, F_i , are directly proportional to the isolator spring constants, k_i .

$$F_i = \beta k_i \quad (14)$$

The output voltages of the LVDT sensors, V , are related by a similar relation to the volumes of air, V enclosed by the isolators.

$$V = \sigma v \quad (15)$$

Combining equations (13), (14), and (15) results in a linear relationship between the forces imparted on the masses by the isolators and the voltage outputs of the LVDT sensors. By introducing biases to the voltages, an equation similar to the biases in equation (12) can be written for the LVDT sensors.

$$\begin{aligned} F_n &= k_n(V + V^*) \\ F_s &= k_s(V - V^*) \end{aligned} \quad (16)$$

In equation (16), k_n is the sensitivity of the north LVDT sensor (V/in), and F_n is the force imparted on the mass by the north isolator. The PI controllers employed to raise the masses will now attempt to satisfy the relations

$$\begin{aligned} V_{DES} &= V \pm V^* \\ V_{DES} - V_{ACT} &= 0 \end{aligned} \quad (17)$$

In equation (17), V_{DES} is the desired voltage output from the LVDT sensors, and V_{ACT} is the actual voltage output from the LVDT. As was done for the EM actuator iterations, deltas are defined to denote the voltage pairs (V^* , $-V^*$). The north-south and east-west deltas pertaining to the LVDT sensor biases are denoted NS_LVDT_DELTA and EW_LVDT_DELTA , respectively. These deltas are iterated by trial-and-error, through a range of values until optimal values have been obtained.

The upper and lower-bounds on NS_EM_DELTA and EW_EM_LVDT are set by the maximum voltage inputs that the current amplifiers can tolerate before blowing fuses. Limits on NS_LVDT_DELTA and EW_LVDT_DELTA are fixed by the geometry of the platform. If the PI controller attempts to raise the platform with an excessively large value of say NS_LVDT_DELTA , then the separation between the two sections of the LVDT (core and housing) becomes too large and out of the linear range of the sensor. In this situation there is also a risk of damage to the sensors when the masses are returned to the stops.

The trial-and-error method is an ongoing process, since the optimization of NS_EM_DELTA and EW_EM_DELTA cause the optimum values of NS_LVDT_DELTA and EW_LVDT_DELTA to change and vice versa. Fortunately, the process converges and the overall system coupling is reduced through successive iterations of the LVDT and EM bias voltages.

In theory, there is nothing wrong with the trial-and-error method. The method has proven to be effective. But in practice the process is very time consuming. Each time an adjustment is made, plots of the six off-diagonal transfer function magnitude functions must be obtained with a spectrum analyzer. An assessment of the current coupling in the system must then be made based on these plots. The decoupling process must be performed at regular intervals because the dynamics of the system change over time. A more efficient method must be developed.

DECOUPLING BY MINIMIZATION

In the trial-and-error method of decoupling, the relative amplitudes of the magnitude functions are used to assess the overall system coupling. Obtaining frequency response information requires data acquisition capability, signal processing software, and time to acquire the necessary data. When only the relative amplitudes of the responses are required, a faster, simpler method can be used to obtain the needed information. The time histories of the three system outputs are collected for each of the three system inputs and are manipulated as they are collected to form a "coupling error." The coupling error is just a number which is large when the coupling is large and small when the coupling is small.

The coupling error is formed by obtaining the time histories of the outputs of the vertical, x-tilt, and y-tilt loops for each of the three input commands. Recall that the three input commands are the vertical force command and the x- and y-axis moment commands. The standard deviation of the i th output time history, due to the j th input, is calculated as follows.

$$\sigma_{ij} = \left[(1/N) \sum_{k=1}^N (V_k - \mu_{ij})^2 \right]^{1/2} \quad (18)$$

where:

$$\mu_{ij} = (1/N) \sum_{m=1}^N V_m \quad (19)$$

The standard deviation of the input signal σ_0 (which is, in general, a band-limited white noise sent to one of the three input commands) is also calculated using a set of relations similar to (1) and (2). A matrix equation involving the relative magnitude terms G_{ij} is the result.

$$\begin{bmatrix} d^2(Z) \\ dt^2 \\ \Theta_x \\ \Theta_y \end{bmatrix} = \begin{bmatrix} G_{11} & G_{12} & G_{13} \\ G_{21} & G_{22} & G_{23} \\ G_{31} & G_{32} & G_{33} \end{bmatrix} \begin{bmatrix} F_z \\ M_x \\ M_y \end{bmatrix} \quad (20)$$

where:

$$G_{ij} = \frac{\sigma_{ij}}{\sigma_0} \quad (21)$$

The coupling error is then a function involving the G_{ij} .

$$\text{err} = \left[\frac{G_{12}G_{21}}{G_{11}G_{22}} + \frac{G_{13}G_{31}}{G_{11}G_{33}} + \frac{G_{23}G_{32}}{G_{22}G_{33}} \right]^2 \quad (22)$$

The function is squared so that the change in the function is more pronounced as the three constituent ratios change.

A minimization algorithm is employed to seek out those values of the parameters NS_EM_DELTA, EW_EM_DELTA, NS_LVDT_DELTA, and EW_LVDT_DELTA which result in the lowest obtainable value of the coupling error. The algorithm used in the minimization described in this paper is the Nedler-Mead "Amoeba" routine (Ref. 3).

The minimization algorithm searches for the optimal values of the parameters through successive iterations. Figure 7 is a plot of the coupling error versus the iteration number. In this plot, the parameters being optimized are NS_EM_DELTA and EW_EM_DELTA. Notice that the optimization converges rapidly and then ceases to improve.

The problem with this method is that the coupling error to which the algorithm converges is not small enough. The values of NS_EM_DELTA and EW_EM_DELTA corresponding to the convergent coupling error yield coupling performance which is only slightly better than that obtained with both parameters set to zero. The reason for this is that the repeatability of the rms measurements used to calculate the coupling error is poor. Two successive measurements of the same G_{ij} will differ by as much as 20%. Increasing the time duration over which the rms is

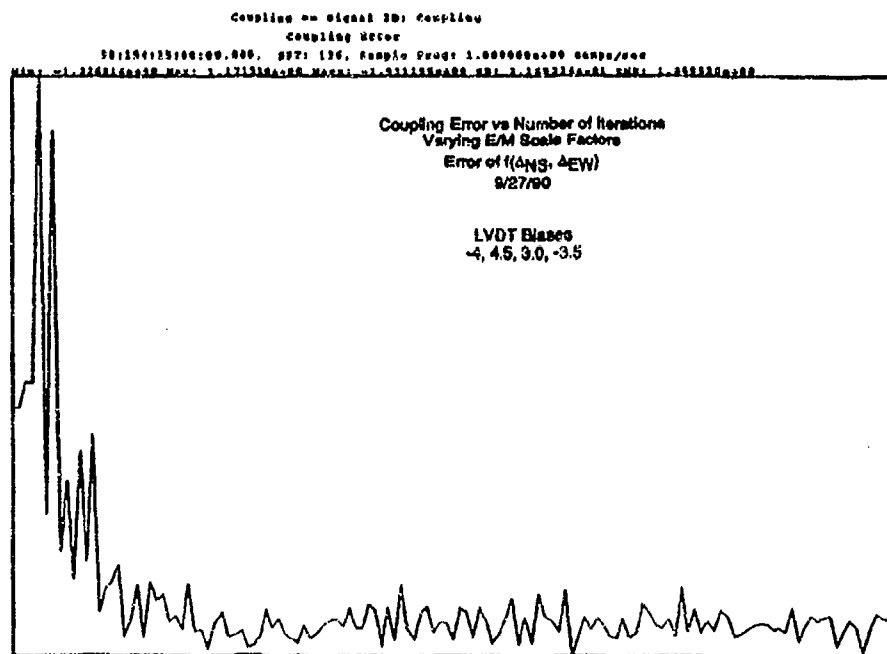


Figure 7. Plot of Coupling Error versus Iteration Number by Minimization Method

calculated improves the repeatability, but significant improvement requires prohibitively long time histories. It has been determined that most of the repeatability problem can be attributed to noise corruption of very low and very high frequency measurements, so a digital bandpass filter has been implemented to isolate only the frequency band containing the system resonances. But even with this modification, the minimization code does not converge to an acceptable coupling error. Apparently, even the slightest noise in the measurement of the coupling error degrades the performance of the minimization algorithm.

MODIFIED GRID SEARCH METHOD

The trial-and-error method yielded good coupling performance. The heights of the off-diagonal resonant peaks were reduced by as much as 15 dB using this method. A similar method can now be employed in which the acquisition of the six frequency response plots is replaced by the calculation of the coupling error.

Software is written to automatically produce plots of the coupling error versus NS_EM_DELTA and EW_EM_DELTA. Examples of these plots are shown in Figures 8 and 9. The minima in these plots are well pronounced. The EM actuator bias voltages are set to the values implied by the minima in Figures 8 and 9, and similar plots are obtained of the coupling error versus NS_LVDT_DELTA and EW_LVDT_DELTA. These plots are shown in Figures 10 and 11. The minima are not as well pronounced as they were in the EM delta plots, but they are still discernible. The LVDT bias voltages are set to the values implied by the minima in this set of plots. However, in searching for the optimal LVDT bias voltages, the optimal EM actuator bias voltages have likely changed. They must be iterated again, but iterating these values affects the

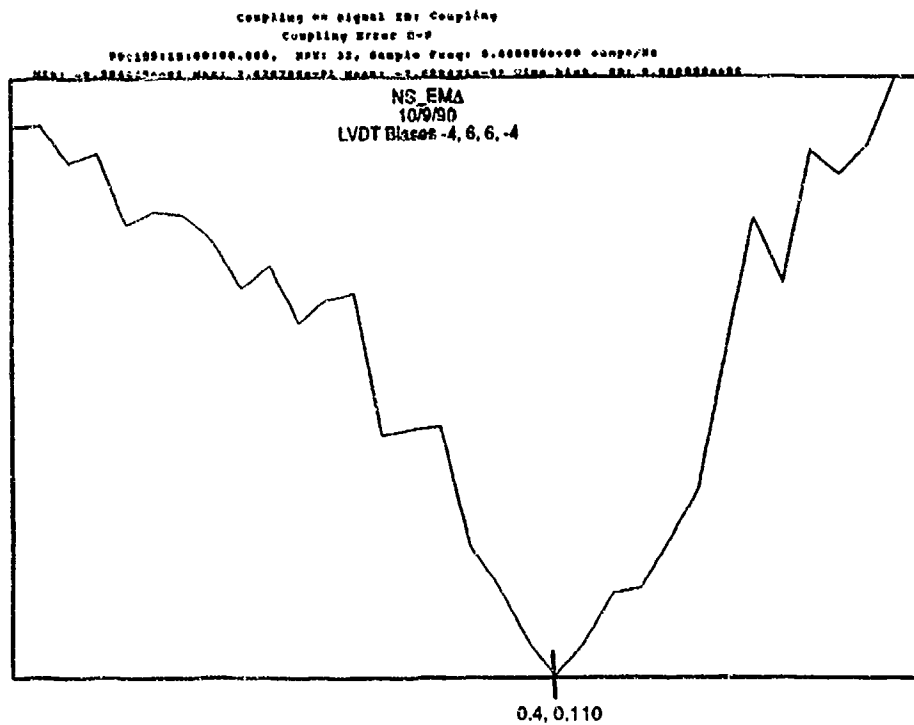


Figure 8. Coupling Error versus NS_EM_DELTA

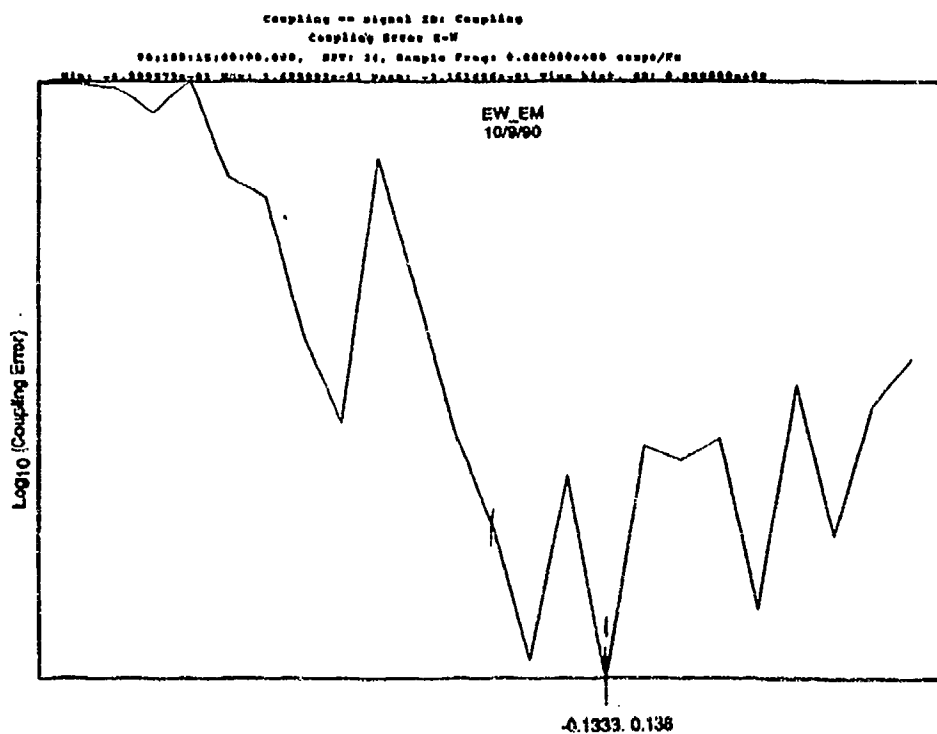


Figure 9. Coupling Error versus EW_EM_DELTA

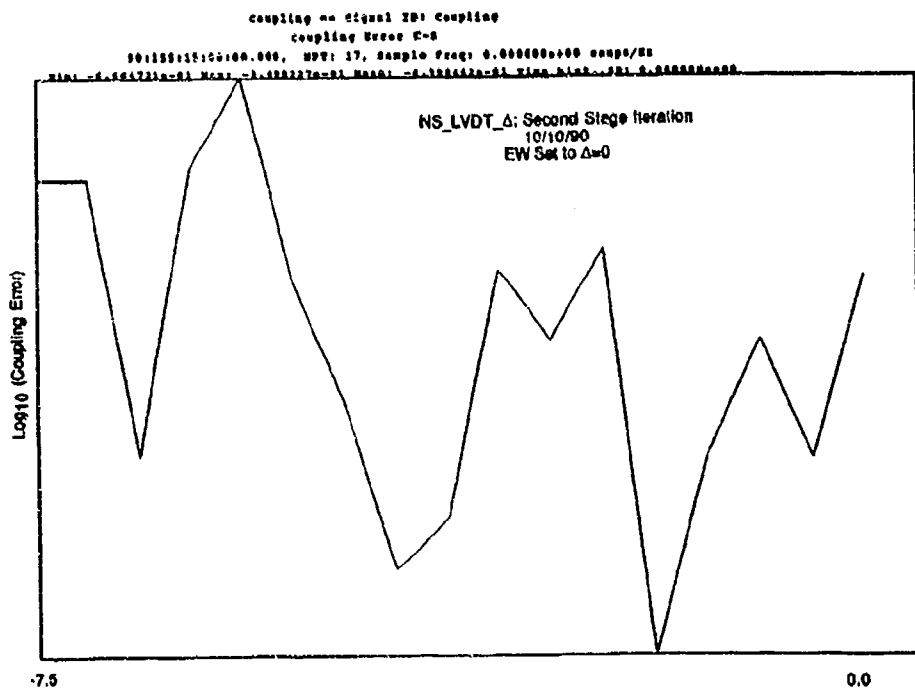


Figure 10. Coupling Error versus NS_LVDT_DELTA

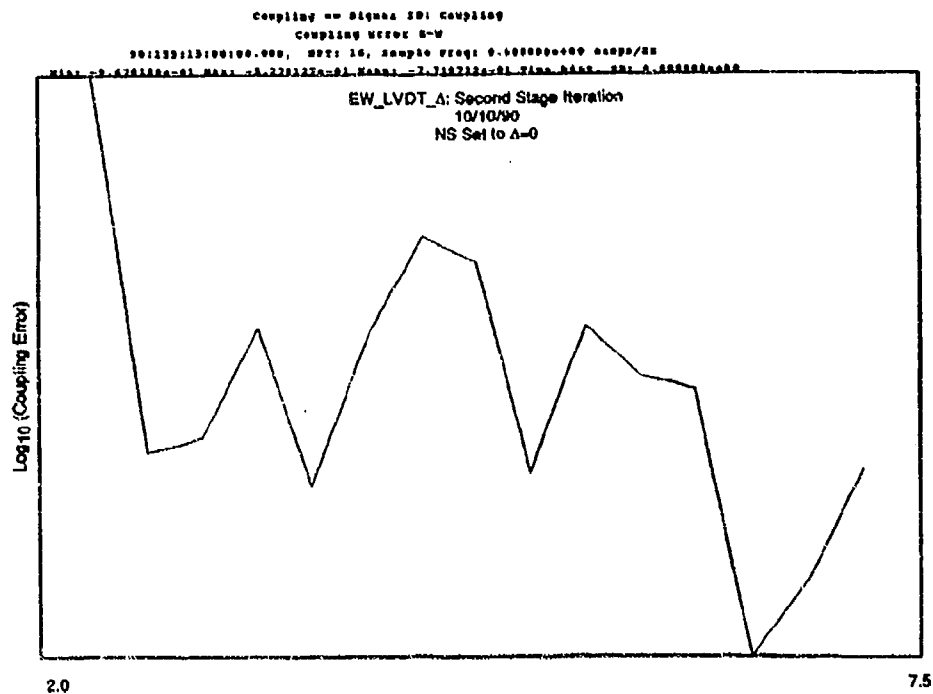


Figure 11. Coupling Error versus EW_LVDT_DELTA

LVDT biases, and so on. As in the trial-and-error method, the process is repetitive and must be carried out through convergence.

Figure 12 shows three iterations of the EW_EM_DELTA. Improvement can be seen with each iteration. However, the coupling error by itself is not a particularly meaningful number. The true measure of the worth of the decoupling is the effect that it has on the cross-axis transfer functions. Figures 13, 14, and 15 are magnitude functions of the following cross-axis transfer functions before and after the optimization process.

$$\frac{d^2(Z)/dt^2}{M_x}, \frac{\Theta_y}{F_z}, \text{ and } \frac{\Theta_y}{M_x}$$

The process had not quite finished converging when these plots were obtained, but it is believed that these responses show approximately the best decoupling performance available using this method. The modified grid search method is the method now used to decouple the SSP.

CONCLUSIONS

The development of a decoupling algorithm for the Seismically Stable Platform (SSP) has been an iterative process. Concepts introduced in the Trial-and-Error method were employed in the Minimization method. The calculation of the coupling error developed in the Minimization method was incorporated into the Modified Grid Search method. The Modified Grid Search method was found to be the most effective in reducing the coupling in the SSP system. This method makes good intuitive sense, and is easily implemented.

Figures 13, 14, and 15 show that the off-diagonal terms of the transfer function matrix can be reduced by as much as 20 dB at certain frequencies using the Modified Grid Search method. Also evident in these figures is that the coupling cannot be eliminated completely by varying only the EM actuator scale factors and the LVDT bias voltages. There are apparently other factors which contribute a great deal to the overall system coupling. Unfortunately, many of the contributors such as geometric and dynamic imbalances cannot be altered easily in software. Minimization of these coupling effects must be addressed by some other means.

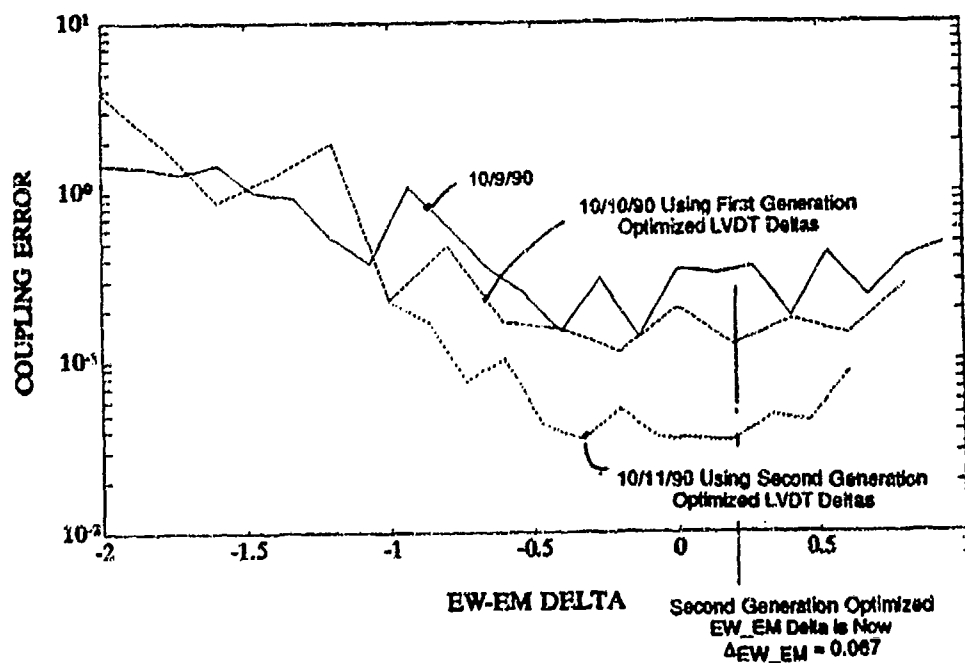


Figure 12. Coupling Error versus EW_EM_DELTA: Three Sets of Data

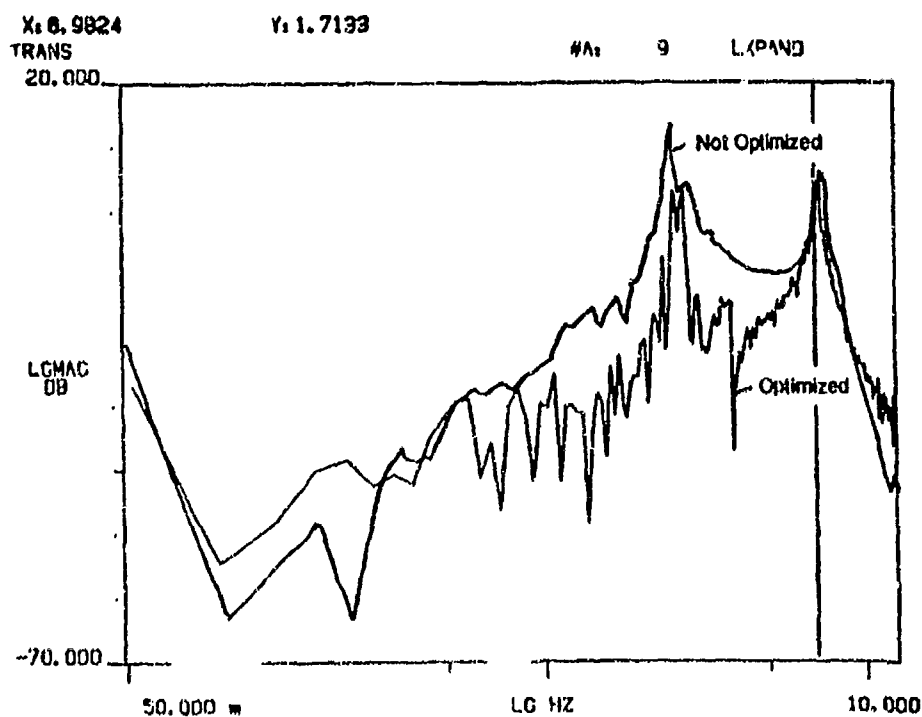


Figure 13. Matrix Entry G_{12} Before and After Decoupling

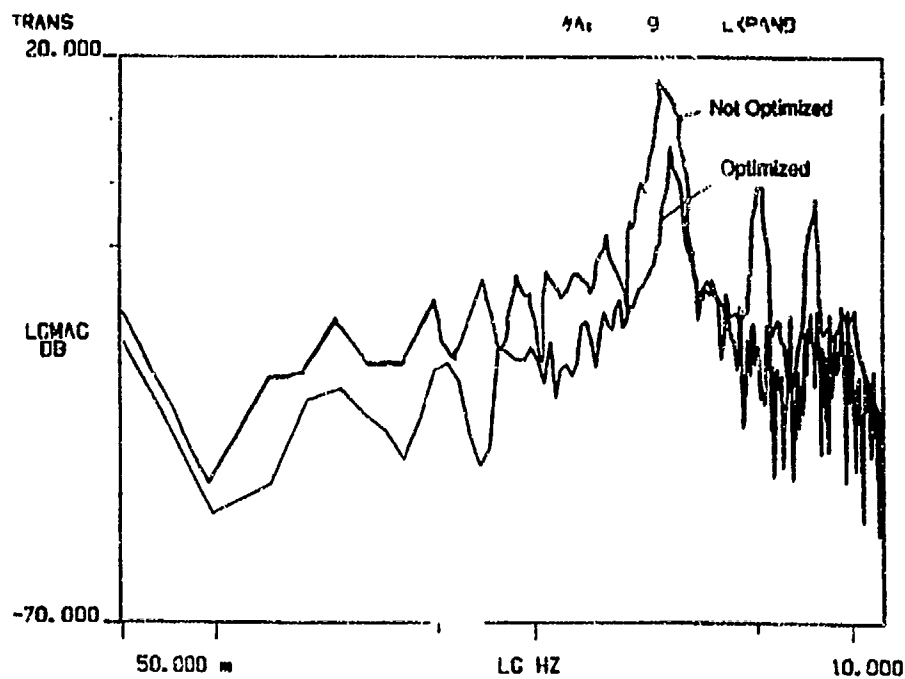


Figure 14. Matrix Entry G_{31} Before and After Decoupling

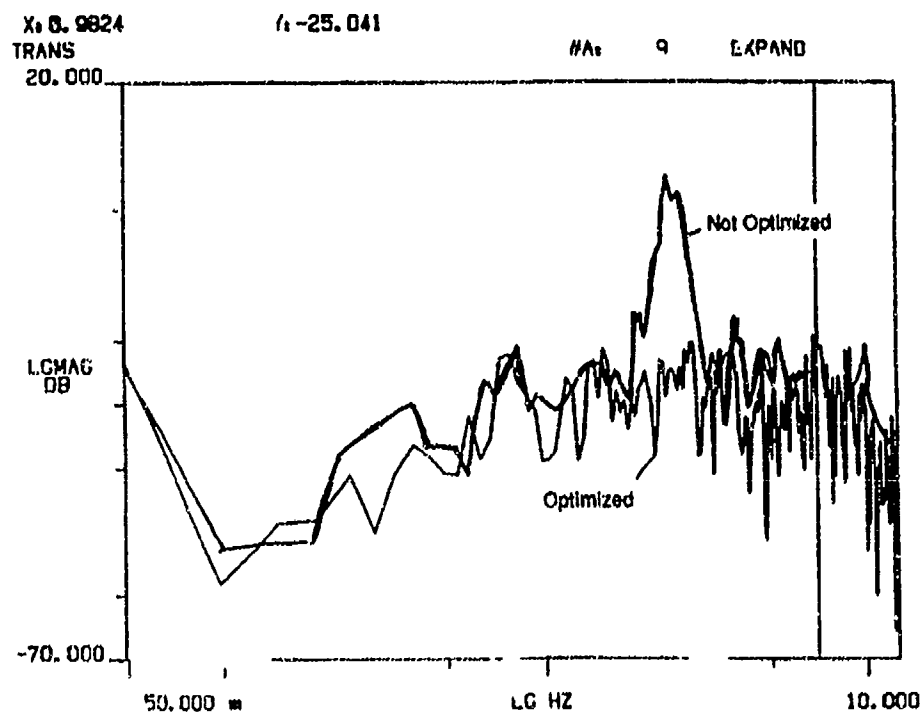


Figure 15. Matrix Entry G_{32} Before and After Decoupling

REFERENCES

1. Gene F. Franklin, J. David Powell, Digital Control of Dynamic Systems, Addison-Wesley, 1980.
2. A. Stephen Morse, W. M. Wonham, Status of Noninteracting Control, technical paper published in IEEE Transactions On Automatic Control, Vol. AC-16, No. 6, December 1971.
3. William H. Press, Brian P. Flannery, Saul A. Teukolsky, William T. Vetterling, Numerical Recipes In C, Cambridge University Press, 1988.

**FIFTEENTH BIENNIAL
GUIDANCE TEST
SYMPOSIUM**

**FEASIBILITY OF
CORRECTING
GYRO BIAS ERRORS
WHILE TAXIING**

**Robert Buchler
Robert Grethel
John Diesel**

Litton

Aero Products

6101 Condor Drive, Moorpark, California 93021 USA TEL: 805-378-2000 TWX: 910-494-2780 TLX: 662619

PRINTED IN USA

ABSTRACT

TAXICAL is a software mechanization which corrects initial turn-on gyro bias errors. In particular, it corrects the initial east gyro bias error and its associated azimuth error. These are by far the principal sources of navigation error in a strapdown IRS, since north gyro bias error is corrected during initial or extended alignment. It corrects these errors while the aircraft is taxiing and does not require the aircraft to stop. These corrections also make the Z gyro bias more observable at the end of the flight.

This paper presents the results of a feasibility study on TAXICAL. The principal conclusion is that TAXICAL is feasible. It can correct initial east gyro bias errors and will not degrade normal IRS performance. The TAXICAL mechanization will be tested in the Boeing Advanced Avionics Test Bed (AATB) aircraft starting August 1, 1991. Test results will be available by mid September for presentation at the Fifteenth Biennial Guidance Test Symposium, September 1991.

INTRODUCTION

The TAXICAL mechanization was first described in Reference 1, where it was proposed as a means of achieving minimum velocity error. This paper considers a different application in a transport-type aircraft where it is desired to achieve an accuracy of only 2 nautical mile/hr., 95 percent.

The paper consists of these sections:

- I. TAXICAL Cross-Heading Model
- II. TAXICAL Cross-Heading Simulation
- III. Conclusions

In Section I, the theory of TAXICAL Cross-Heading observations is described. In Section II, the mechanization is analyzed and it is shown that very large east gyro bias errors can be corrected, and that normal IRS performance would not be degraded. In Section III, it is concluded that TAXICAL is feasible, and recommended mechanization equations are presented. The definitions and error model for Section III are derived in Reference 2.

Reference 1. J.W. Diesel, "Calibration of a Ring Laser Gyro Inertial Navigation System for Minimum Velocity Error." Proceedings, Fourteenth Biennial Guidance Test Symposium, CIGTF, Holloman AFB, New Mexico, Oct. 3, 4, 5, 1989.

Reference 2. J.W. Diesel, "GPS/INS Integration for Civil Aviation." IEEE National Telesystems Conference Proceedings, Atlanta, Georgia, March 26, 27, 1991.

I. TAXICAL CROSS-HEADING MODEL

I.1 Cross Body Zero Velocity Observation

During aircraft taxi, the initial east component of gyro-bias error and the associated azimuth error will be estimated. These are by far the principal sources of navigation error for a strapdown system during the first few hours of flight, since the north component of gyro bias error will be estimated during initial alignment or extended duration alignment. The Z-gyro bias error is only significant after many hours of flight with no intermediate stops, since the TAXICAL Filter 4 mode would correct errors during intermediate stops. Even for long flights without stops, the Z-gyro bias will be more observable post-flight because of TAXICAL.

Observation of velocity error requires a velocity reference so that it may be compared with the erroneous IMU inertial velocity. Since velocity is a vector, 3 components of velocity reference are needed. When stopped, all 3 components of velocity are zero (and known to be zero if it is known the aircraft is indeed stopped). When taxiing, the forward velocity is clearly not zero, but the up-body and cross-body velocity at a specific point on the aircraft will always remain zero. We will exploit the zero cross-body velocity, as explained next.

The wheel structure of most large aircraft results in motion which can, to first order, be approximated as that due to a tricycle (Figure I.1). In this simplification, there are two main landing gears, which do not steer, and one nose wheel which steers. With such a model, all three wheels of the tricycle experience pure rolling motion (no slide-slip at any wheel) whether taxiing straight or while turning (in heading) as shown in Figure I.1.

Figure I.1 shows the wheels in a turn during taxi. The velocity vectors are drawn in length proportional to the vehicle speed at the point of the vector tail. Clearly, different points on the vehicle experience different velocities, but the

total velocity at each wheel points in a direction in which that wheel is rolling. The normals to each wheel intersect at point C, the instantaneous center of rotation.

The first equation in Figure I.1 is the well known vector equation relating the velocity at two points on a rigid body experiencing simultaneous translation and (planar) rotation. Point R is a point in the body halfway between the rear wheels. The second point is the IMU located at lever arm L from R. The second and third equation of Figure I.1 give the y and x components of the first equation. The y-component equation is of no use because the forward velocity of point R is unknown. However, if we assume point R has zero velocity in the x direction, (which, to first order, seems reasonable since non-zero velocity of R in the x direction would require the rear wheels to side-slip instead of roll), then all quantities on the right side of the third equation of Figure I.1 are known: The x velocity component of point R is zero, the y component of the lever arm can be pre-measured and is thus known, and the turn rate can be measured by the IMU gyros. Thus, a reference for the cross-body velocity of the IMU has been obtained. This reference is compared with the erroneous inertial system cross-body velocity, the error passed to an error controller (Kalman filter), with resulting correction to system velocity, level axis gyro bias errors and azimuth.

The third equation in Figure I.1 can also be used by the Kalman filter in the reverse direction: If the left side is known, then the right side can be estimated. For example, upon start of taxi, immediately following initial IMU alignment with the aircraft stationary, the inertial system velocities have small error. Thus the left side of the third equation is known, and the y lever arm appearing on the right side may be found.

Small errors due to tire flexure, structure bending, etc. will cause the y lever arm to vary slightly under different conditions of taxi. The nominal y lever arm itself will vary with different aircraft installations. Thus, we are motivated to

THIS PAGE INTENTIONALLY LEFT BLANK.

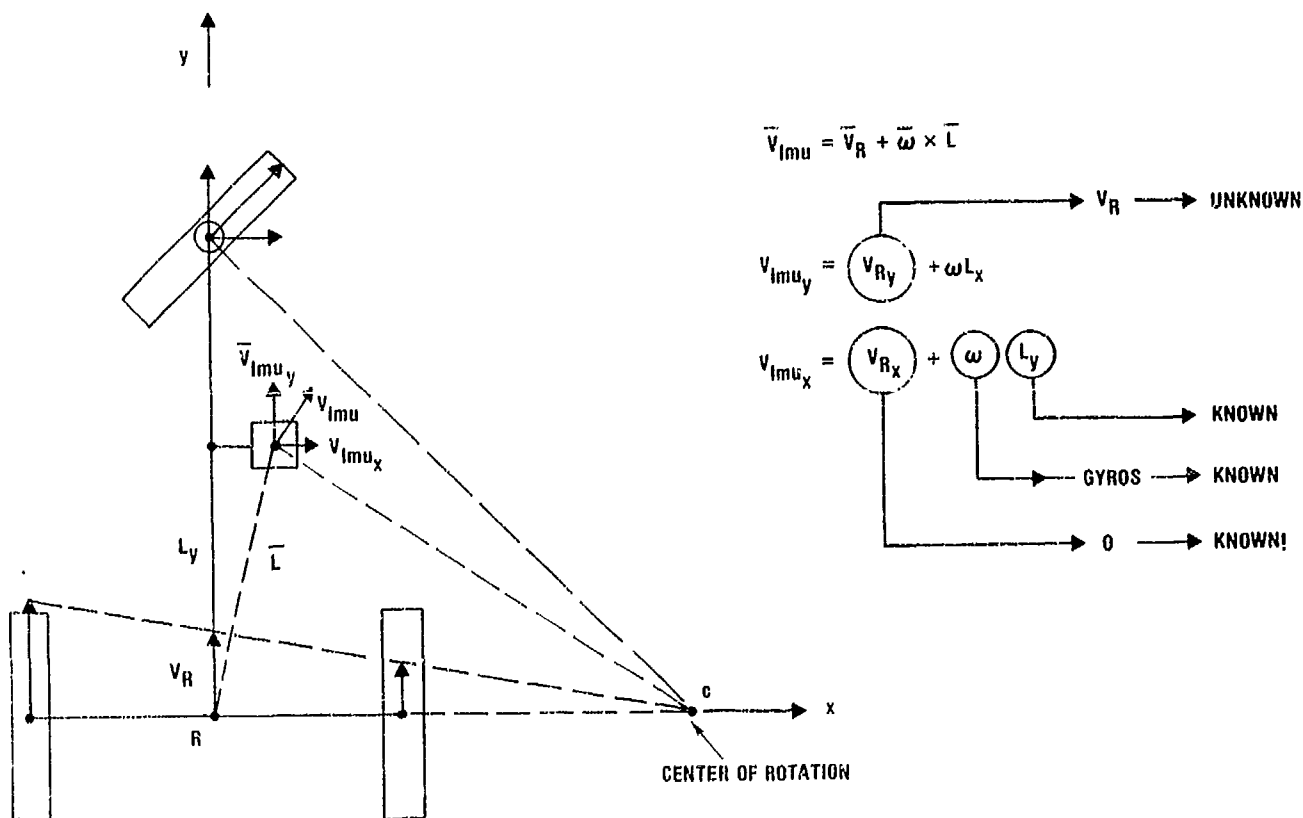
include a bias and correlated bias y lever arm error states in the Kalman filter.

The vehicle body may not line-up with the rear axle (discussed in the next section) or the IMU may be mounted in error in azimuth. Both of these effects may be lumped into a taxi "crab" angle. The crab angle will vary slightly under different taxi conditions. Thus, we are motivated to add bias and correlated bias crab

angle states in the Kalman filter.

Finally, with the IMU located in the vehicle at significant height above the ground, a vertical lever arm correction, used when rolling, is required. To avoid pre-measuring this lever arm, a vertical lever arm bias state is added to the Kalman filter.

The next sections discuss the crab angle in more detail.



910042-1

Figure I.1. Tricycle Model

1.2 Crab Angle Model

The Taxical mechanization corrects the on-board Inertial Measurement Unit (IMU) velocity errors before take-off by exploiting the fact that, when the aircraft is taxiing or under tow, the aircraft main wheels tend not to sideslip. Therefore, during straight taxi, the IMU should experience zero "crab" angle. Any crab angle actually measured by the IMU is therefore a measure of IMU crosstrack velocity error, which can then be corrected.

During turns, while taxiing or under tow, the IMU will experience a non-zero crab angle since the IMU is mounted at some distance from the main wheels, but this crab angle at the IMU can be accounted for by a lever-arm compensation. Any residual crab angle is again a measure of IMU crosstrack velocity error, which can again be corrected.

Any errors in the assumption for a zero crab angle at the main wheels will degrade the correction capability. The following addresses some of the mechanisms that could produce a non-zero crab angle during straight taxi, turning taxi and towing.

1.2.1 Crab Angle β_0 During Nominally Straight Taxi, Trimmed, No Wind

Figure 1.2 shows the aircraft taxiing in a straight line (zero turn rate) along the taxiway centerline. The aircraft is trimmed and there is zero wind. The direction of motion of the aircraft (velocity vector) is along the taxiway centerline with all wheels purely rolling (no wheel side-slip). The axis of rotation for rolling of the nose-wheel and the axis of rotation for rolling of the main wheels are thus perpendicular to the direction of aircraft velocity.

Due to manufacturing tolerances, the airframe centerline will not be exactly normal to the axis of rotation of the wheels. This misalignment angle, which we have called β_0 , is shown (greatly exaggerated) in Figure 1.2. The IMU would be mounted parallel to the airframe centerline. Thus, under normal straight taxi, the IMU will be crabbing at the angle β_0 . This is modeled as a bias term in the taxical mechanization.

1.2.2 Crab Angle β_1 During Nominally Straight Taxi, with Cross-Wind

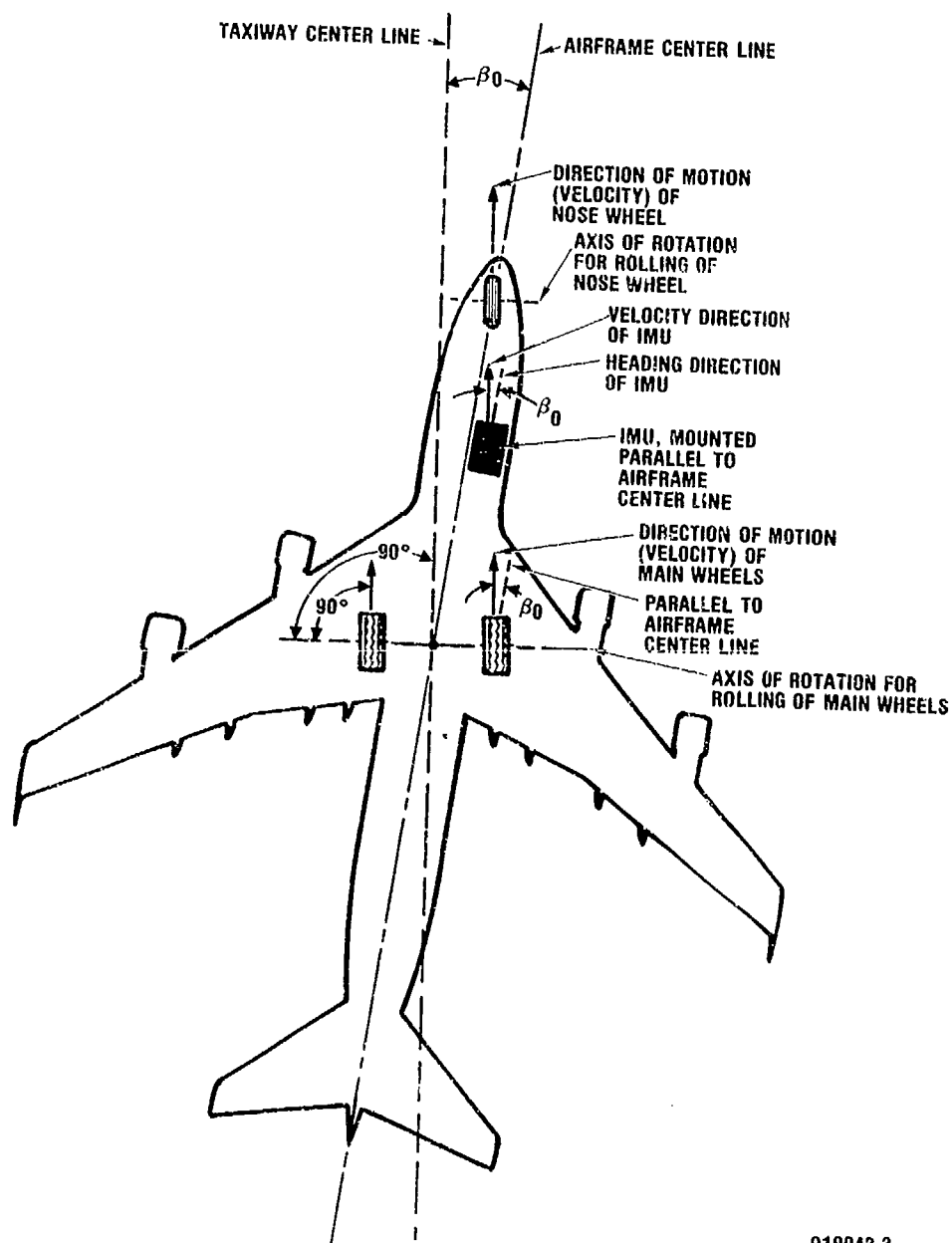
Figure 1.3 shows the aircraft taxiing straight (zero turn rate) along the taxiway centerline. The direction of motion of the aircraft (velocity vector) is along this line. The velocity of each wheel is also parallel to this line but the main wheels are side-slipping by the angle $\Delta\beta$, required due to the cross-wind blowing from starboard.

The aircraft centerline is shown rotated from the direction of motion by the angle $\beta_1 > \beta_0$ where β_0 is the original crab angle of Figure 1.2 (with no wind). Thus, the crab angle has changed due to crosswind by $\Delta\beta = \beta_1 - \beta_0 > 0$. This is modeled as a correlated noise source in the taxical mechanization.

1.2.3 Other Wheel Configurations and Effects of Turning and Being Towed

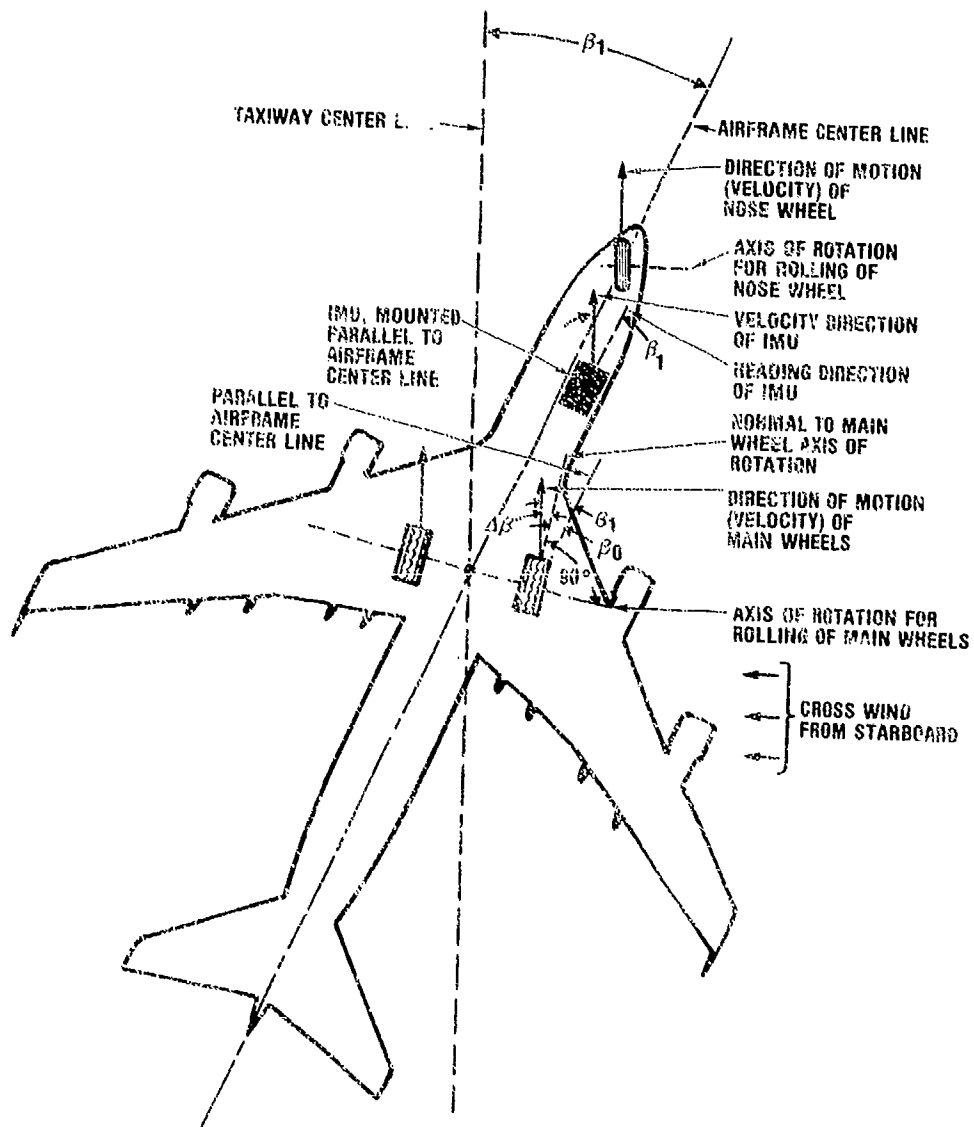
Figure 1.4 shows configurations for other wheels that are being considered in the taxical analysis.

Figure 1.5 displays an aircraft in a circular turn. Effects of a small turn radius, slippage of wheels and varying turn radius that may impact the lever arm and β are being analyzed. Effects while being towed (Figure 1.6) are also being studied.



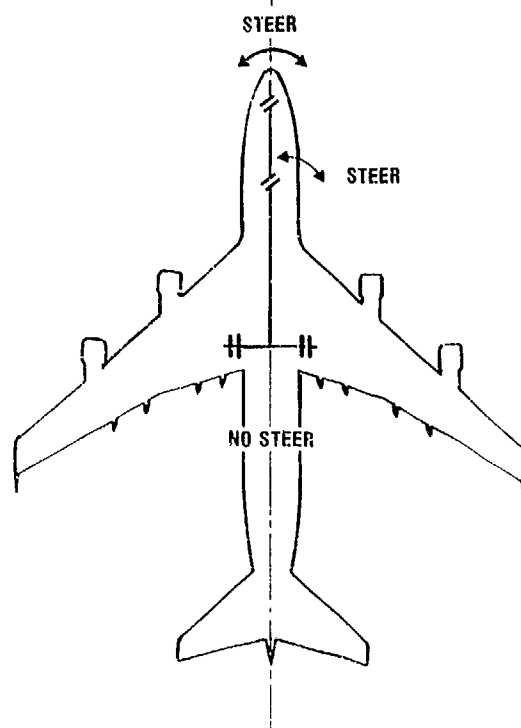
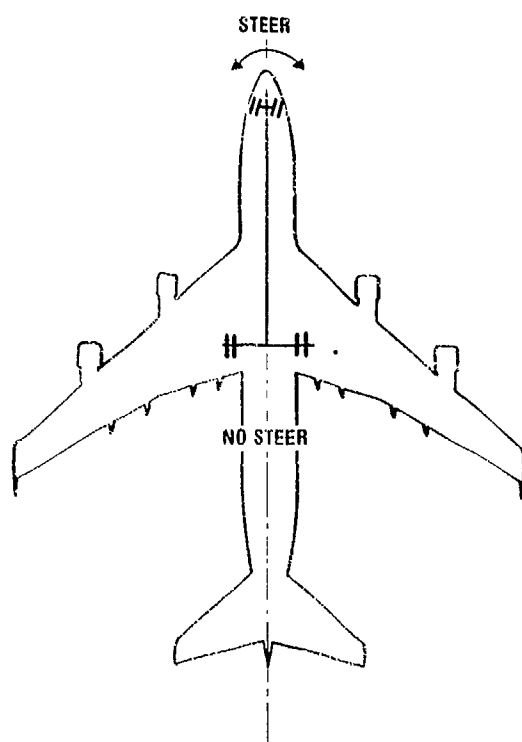
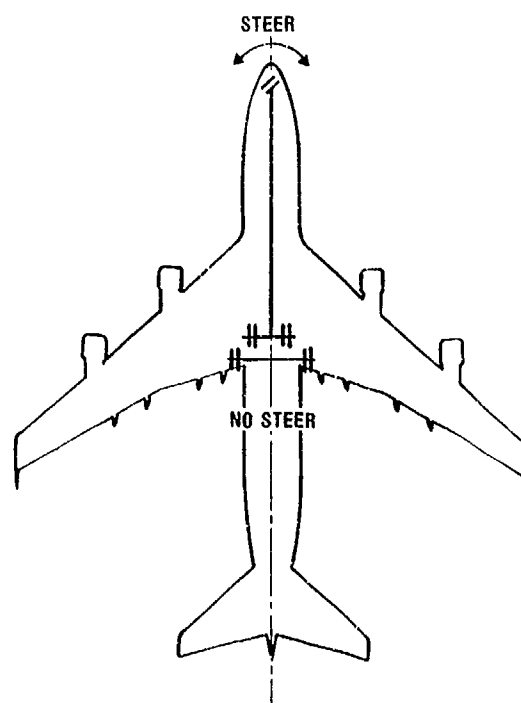
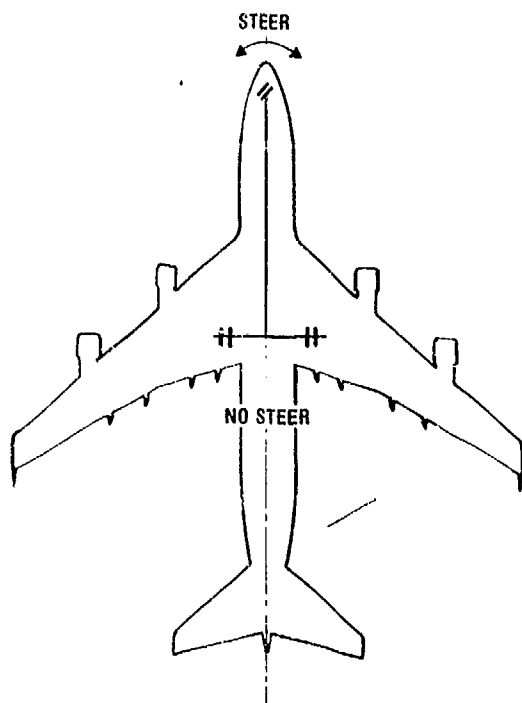
910042-3

Figure I.2. Crab Angle β_0 During Straight Taxi, Trimmed, No Wind



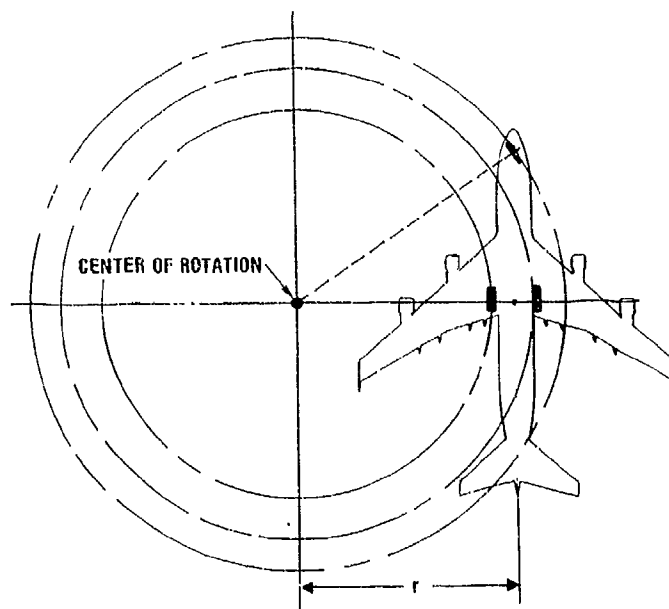
910042-4

Figure I.3. Crab Angle β_1 During Straight Taxi with Cross-Wind



910042-5

Figure I.4. Wheel Configurations



910042-5

Figure I.5. Turn Radius r

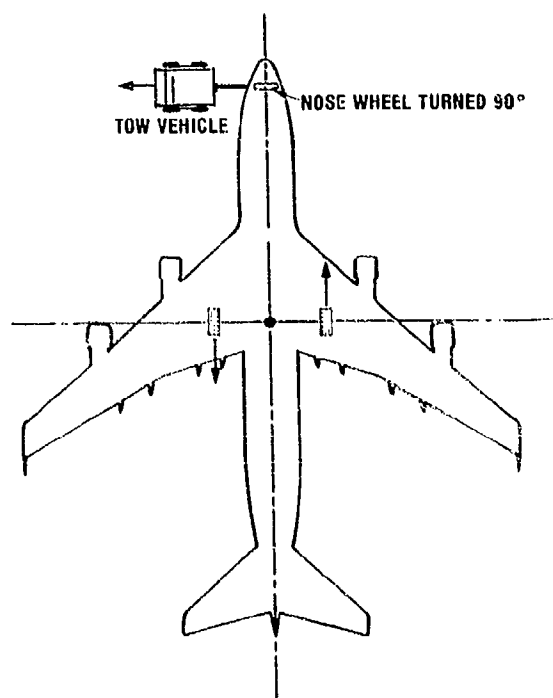


Figure I.6. Towing

II. TAXICAL CROSS-HEADING SIMULATION

A simulation to verify the feasibility of the taxical mechanization when the aircraft is taxiing was performed using the RAIDES program. RAIDES is a complex Monte Carlo simulation program that has been used at Litton Guidance and Control Division for proposals and studies for more than 20 years.

Figure II.1 displays the two taxi profiles (A1 and B1), that were simulated. The aircraft aligns at a north heading for 20 minutes then proceeds for 4 minutes to the take-off runway without stopping. The simulation ends when take-off velocity reaches 20 kts. These profiles are conservative in that typically there is a longer taxi time, frequently the aircraft stops again on the runway, and the simulated profiles contain a minimum number of turns. As discussed below, longer taxi time, more stops, or more turns will improve the error estimates.

Figure II.2 lists the 16 Kalman filter states that were simulated and their initial covariances. Figure II.3 shows the cross track velocity error observation mechanized in the filter. Note that x and y velocity errors, crab-angle error, and lever arm errors are observable. The latter two errors have bias and correlated noise components as listed in Figure II.2.

Fifty-two system errors were simulated with the 16 state Kalman filter. The error budget is shown in Figure II.4. A turn-on gyro bias of 0.01 deg/hr, which represents the expected error after a 10 hour flight from an error in trend of 0.025 deg/hr/day, was used to model the gyro bias in the Kalman filter. In the system, to reflect a pessimistic gyro bias and to determine if the mechanization can handle a large gyro bias created by gyro trend over a longer

period of time, 0.05 deg/hr was used in the system for gyro bias.

The calibrated system errors are generally larger than the Kalman filter covariance because more errors are modeled at the system than in the filter to reflect all known and significant real world errors. Figure II.5 shows the sensitivity from all the modeled errors to accelerometer bias and gyro bias. The major contributions to accelerometer bias are accelerometer correlated noise, accelerometer misalignments, x gyro bias, and gyro misalignments. The major contributions to y gyro bias are y gyro bias itself, gyro white noise, and gyro correlated noise. The x gyro is not as well calibrated because it is not as observable as the y gyro, but still is reduced to about 0.02 deg/hr which is equivalent to a 2 nm/hr error.

The system responses to the 52 errors for trajectory B1 are similar to the results obtained from trajectory A1. Figure II.6 shows the sensitivity to accelerometer bias and gyro bias. Figures II.5 and II.6 also show that if the crab angle and lever arm errors are pessimistically increased 2 to 3 times that which has been simulated, little effect will be observed on the final calibrated values.

Previous simulations have shown that if, during taxi, the aircraft stops a second time and aligns at a different heading, alignment and calibration benefits obtained while updating during taxi are negligible. However, if this second stop does not occur, taxical cross heading updating does enhance calibration. The gyro biases and accelerometer biases get calibrated, shifts in turn-on bias and trends can be observed and removed, and improvements can be made on the calibration parameters estimated during post flight updating.

Simulated Kalman Filter

<u>Error State</u>	<u>Covariance</u>
1. X Position	(100 ft) ²
2. Y Position	(100 ft) ²
3. X Velocity	(0.3 ft/s) ²
4. Y Velocity	(0.3 ft/s) ²
5. X Tilt	(0.017 deg) ²
6. Y Tilt	(0.017 deg) ²
7. Azimuth	(2 deg) ²
8. X Gyro Bias	(0.01 deg/hr) ²
9. Y Gyro Bias	(0.01 deg/hr) ²
10. Z Gyro Bias	(0.01 deg/hr) ²
11. X Accelerometer Bias	(40 micro-g) ²
12. Y Accelerometer Bias	(40 micro-g) ²
13. Lever Arm Bias	(10 ft) ²
14. Lever Arm Correlated Bias	(0.5 ft) ²
15. Crab Angle Bias	(10 mrad) ²
16. Crab Angle Correlated Bias	(0.5 mrad) ²

Figure II.2. Simulated Kalman Filter

Kalman Filter Observation

OBS = Cross Track Velocity Error

$$= \delta V_X \cos \psi - \delta V_Y \sin \psi - V \delta \beta - \dot{\psi} \delta R$$

Where:

δV = Velocity Error

ψ = Heading

V = Velocity

$\delta \beta$ = Crab Angle Error

δR = Lever Arm Error

Figure II.3. Kalman Filter Observation

Simulated Error Budget

<u>Error Parameter</u>	<u>Units</u>	<u>Budget</u>
Gyro		
Bias	deg/hr	0.01*
Scale Factor	PPM	5.0
Misalignments	arcsec	1.5
Compliance	arcsec/g	0.25
White Noise	deg/√hr	0.0015
Correlated Noise	deg/hr	0.03 (30 min. CT)
Thermal Transients	deg/hr	0.008 (80 sec. TC)
Accelerometer		
Bias	μg	40
Scale Factor	PPM	120
Asymmetry	PPM	20
Misalignments	arcsec	2
Non-linear Scale Factor	PPM	10
White Noise	μg/√hz	10
Correlated Noise	μg	10 (1.5 hr CT)
Thermal Transients	μg	10 (3 min TC)
Initial Tilt	deg	0.017
Initial Azimuth	deg	2.0
Null Velocity Reference	ft/sec	0.01
Gravity Disturbance	arcsec	5.0
Gravity Anomaly	μg	25.0
Errors During Taxi Updates		
Lever Arm		
Bias	feet	10.0
Correlated Noise	feet	0.5 (60 sec CT)
Crab Angle		
Bias	mrاد	10.0
Correlated Noise	mrاد	0.5 (60 sec CT)
Velocity Reference	ft/sec	0.01

* Example: 0.025 deg/hr/day trend causes 0.01 deg/hr change on a 10 hr flight

Figure II.4. Simulated Error Budget

Error Sensitivity for Trajectory A1

Error	Y - Accel (Micro-g)	X - Accel (Micro-g)	Y - Gyro Deg/Hr.	X - Gyro Deg/Hr.
Accel Misalignment	9.5	9.6	0.0	0.0
Accel Correlated Noise	15.6	13.9	.0014	.0017
Accel Thermal Transient	0.4	0.3	.0012	.0005
Y Gyro Bias	0.9	0.2	.0034	.0008
X Gyro Bias	8.7	0.4	.0008	.0222
Gyro Misalignment	7.1	7.2	0.0	.0002
Gyro White Noise	2.2	2.9	.0020	.0025
Gyro Correlated Noise	0.7	0.6	.0022	.0015
Reference Velocity Error				
Stopped	1.6	1.0	.0005	.0017
Taxi	1.8	1.1	.0001	.0018
Gravity Disturbance	1.2	1.0	.0002	.0027
Lever Arm CN	0.8	0.5	.0003	.0013
Crab Arm CN	1.8	0.6	.0002	.0021
Others	1.6	0.0	.0004	.0021
RSS	21.9	18.7	.0050	.0230

Figure II.5. Error Sensitivity for Trajectory A1

Error Sensitivity for Trajectory B1

Error	Y - Accel (Micro-g)	X - Accel (Micro-g)	Y - Gyro (Deg/Hr.)	X - Gyro (Deg/Hr.)
Accel Misalignment	9.5	9.6	0.0	0.0
Accel Correlated Noise	15.5	13.8	.0015	.0011
Y Gyro Bias	0.4	0.0	.0034	.0003
X Gyro Bias	5.8	1.2	.0003	.0203
Gyro Misalignment	7.1	7.2	0.0	0.0
Gyro White Noise	2.1	2.3	.0020	.0020
Gyro Correlated Noise	0.5	0.2	.0022	.0014
Gravity Disturbance	0.8	1.3	.0002	.0022
Lever Arm CN	0.9	0.6	.0002	.0035
Crab Arm CN	1.2	0.5	.0002	.0015
Others	2.5	1.6	.0011	.0025
RSS	20.7	18.6	.0049	.0211

Figure II.6. Error Sensitivity for Trajectory B1

III. CONCLUSIONS

The parameters used in the Kalman filter were selected to ensure that the mechanization could not degrade the IRS performance, and could only improve it. This was done by using error values for crab angle and lever arm effects which are larger than can reasonably be expected, based on discussions with pilots and with Boeing Aircraft Co., which is the world's leading supplier of transport aircraft. Also, the bias errors assumed in the Kalman filter were selected to be smaller than the expected values for the IRS, to ensure that the Kalman filter would not degrade the IRS per-

formance. Because of these assumptions and the results of the simulations, it is concluded that the TAXICAL mechanization is feasible.

The recommended mechanization for the TAXICAL Kalman filter is summarized in Figure III-1, and Tables III-1 through III-5, which are self-explanatory. However, the parameters given here are preliminary, and it is assumed that these parameters will be fine-tuned during at least 6 months of taxi and flight tests for data collection and analysis.

	0	1	2	3	4	5	6	7	8	9	10	11	12	13	14
	$\delta\theta_z$	$\delta\theta_y$	δh	$\delta V'_x$	$\delta V'_y$	$\delta V'_z$	ϕ_x	ϕ_y	ϕ_z	ϵ_x	ϵ_y	ϵ_z	∇_x	∇_y	∇_z
$\dot{\delta\theta}_x$			$-\frac{Q_x}{R}$		$\frac{1}{-R}$										
$\dot{\delta\theta}_y$			$-\frac{Q_y}{R}$	$\frac{1}{+R}$											
$\dot{\delta h}$						1									
$\dot{\delta V}'_x$								$-A_z$	$+A_y$				C_{xx}	C_{xy}	C_{xz}
$\dot{\delta V}'_y$									$-A_x$				C_{yx}	C_{yy}	C_{yz}
$\dot{\delta V}'_z$			$+\frac{2g}{R}$				$-A_y$	$+A_x$					C_{zx}	C_{zy}	C_{zz}
$\dot{\phi}_x$		$-\Omega_z$	$-\frac{Q_x}{R}$		$\frac{1}{-R}$			$+ \omega_z - \omega_y$	$- \omega_x$	C_{xx}	C_{xy}	C_{xz}			
$\dot{\phi}_y$	$+ \Omega_z$		$-\frac{Q_y}{R}$	$\frac{1}{+R}$			$- \omega_z$		$+ \omega_x$	C_{yx}	C_{yy}	C_{yz}			
$\dot{\phi}_z$	$- \Omega_y$	$+ \Omega_x$					$+ \omega_y$	$- \omega_x$		C_{zx}	C_{zy}	C_{zz}			

Figure III-1. Dynamics Matrix for IRS States

Table III-1. Basic IRS Error States and Initial Variance

State No.	Symbol	Square Root Initial Variance	Definition of Error State
0	$\delta\theta_x$	$1.0e^{-4}$ rad	Position about x
1	$\delta\theta_y$	$1.0e^{-4}$ rad	Position about y
2	δh	100 meters	Altitude
3	δV_x	0.1 m/s	X velocity
4	δV_y	0.1 m/s	Y velocity
5	δV_z	0.1 m/s	Z velocity
6	ϕ_x	1 m rad	X tilt
7	ϕ_y	1 m rad	Y tilt
8	ϕ_z	10 m rad	Azimuth
9	ϵ_x	0.01 deg/hr.	X Gyro bias
10	ϵ_y	0.01 deg/hr.	Y Gyro bias
11	ϵ_z	0.01 deg/hr.	Z Gyro bias
12	∇_x	40 micro-g	X Accel bias
13	∇_y	40 micro-g	Y Accel bias
14	∇_z	40 micro-g	Z Accel bias

Table III-2. Taxical Cross-Heading Error States and Initial Variance

State No.	Symbol	Square Root Initial Variance	Definition of Error State
15	β_o	10 m rad	Fixed crab angle
16	β_c τ_β	0.5 m rad (60 sec.)	Variable crab angle (correlation time)
17	R_{y_o}	10 ft.	Fixed longitudinal lever arm
18	R_{y_c} τ_{R_y}	0.5 ft. (60 sec.)	Variable longitudinal lever arm (correlation time)
19	R_{z_o}	10 ft.	Fixed vertical lever arm
20	R_{z_c} τ_{R_z}	0.5 ft. (60 sec.)	Variable vertical lever arm (correlation time)

Table III-3. Taxical Cross-Heading Observation Matrix

State No.	Symbol	Observation Matrix Element
3	δV_x	$\cos \psi$
4	δV_y	$-\sin \psi$
15	β_o	$-V_o$
16	β_c	$-V_o$
17	R_{y_o}	$-\dot{\psi}$
18	R_{y_c}	$-\dot{\psi}$
19	R_{z_o}	$-\dot{\phi}$
20	R_{z_c}	$-\dot{\phi}$

Table III-4. Coefficients of Dynamics Matrix and Observation Matrix

x, y, z (subscripts)	Local level wander azimuth coordinates (reference axes)
R	Earth radius, m
A_x, A_y, A_z	Non-gravitational acceleration, m/s ²
Q_x, Q_y, Q_z	Craft rate, rad./sec.
$\Omega_x, \Omega_y, \Omega_z$	Earth rate, rad./sec.
$\omega_x, \omega_y, \omega_z$	Spatial rate, rad./sec.
C_{ij}	Direction cosines of body axes with respect to (w.r.t.) reference axes
ψ	Heading w.r.t. reference axes
ϕ	Roll w.r.t. reference axes
V_G	Ground speed

Table III-5. IRS Plant Noise and Taxical Observation Noise

$$Q_3 = 1.0e^{-7} \text{ (m/s)}^2/8s$$

$$Q_4 = 1.0e^{-7} \text{ (m/s)}^2/8s$$

$$Q_5 = 1.0e^{-7} \text{ (m/s)}^2/8s$$

$$Q_6 = 1.0e^{-14} \text{ (rad/s)}^2/8s$$

$$Q_7 = 1.0e^{-14} \text{ (rad/s)}^2/8s$$

$$Q_8 = 1.0e^{-14} \text{ (rad/s)}^2/8s$$

$$R_{dvc} = (0.01 \text{ F/S})^2s$$

SESSION VIII-B
GPS SIMULATION-INS

CHAIRMAN
FRED NADEAU
WRDC/AAAN

Honeywell's GG1308 Ring Laser Gyro Inertial Measurement Systems — Test Results

Michael G. Secord
John G. Messler
Leroy O. Thielman

Honeywell Inc.
Military Avionics Division

ABSTRACT

Honeywell's family of low-cost GG1308 Ring Laser Gyro Inertial Measurement Systems are designed to provide inertial guidance, mid-course navigation, and vehicle stabilization functions for tactical missiles, standoff weapons, torpedoes, Unmanned Aerial Vehicles (UAVs), and manned aircraft. Two members of this family are a stand-alone Inertial Measurement Unit (IMU), and an Inertial Measurement Module (IMM) configured as a line replaceable subsystem installed in Honeywell's Integrated Vehicle Management Unit (IVMU). This paper presents results of testing to date which shows that the demonstrated performance of these packages makes them ideal candidates for these applications. A brief description of the functional design of these two systems, as well as the special test equipment and procedures used to test them are also presented.

INERTIAL MEASUREMENT SYSTEM OVERVIEW

Honeywell's family of GG1308 Ring Laser Gyro Inertial Measurement Systems provide fully compensated incremental angles and incremental velocities with very small errors, fast reaction times, and high rate capabilities. These features are offered with standard RS-422 serial output formats in small volume, light weight, low-cost packages. Two members of this family are a standalone Inertial Measurement Unit (IMU), and an Inertial Measurement Module (IMM) configured as a line replaceable subsystem installed in Honeywell's Integrated Vehicle Management Unit (IVMU). The HG1500 IMU (Figure 1) is a self-contained unit providing fully compensated incremental angle and incremental velocity with a single power input of 28 volts. The HG1108 IMM (Figure 2) is a line replaceable module providing the identical output as the IMU, but deriving the low voltage conditioned power required for operation from a power supply in the host system. From both a form factor and performance perspective, each of these devices is well suited for most tactical missile standoff weapon, torpedo, Unmanned Aerial Vehicle (UAV), and manned aircraft applications.



Figure 1. HG1500 Inertial Measurement Unit (IMU) is less than 125 cubic inches in volume and weighs less than 6.0 lbs.

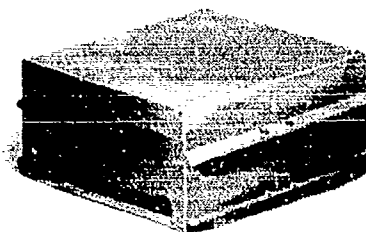


Figure 2. HG1108 Inertial Measurement Module (IMM) is less than 110 cubic inches in volume and weighs less than 5.5 lbs.

An extensive market survey was performed focusing on applications for which these products would be best suited. From this survey, a set of design requirements was established for each device. Although form factors between the two units are slightly different, the performance requirements defined by the market were identical. Key package performance characteristics are shown in Table 1.

Table 1. Key IMU/IMM Characteristics

Volume	<110*/125** in ³
Weight	< 5.5*/6.5** lbs
Power	<15*/20** Watts
Angular Rate Range	± 1000 deg/sec
Angular Rate Bias	1 deg/hr (1σ)
Angular Rate Scale Factor	100 ppm (1σ)
Angular Random Walk	< 0.125 deg/√hr
Angular Rate Misalignment	100 μRad (1σ)
Acceleration Range	± 30 g
Acceleration Bias	1.0 mg (1σ)
Acceleration Scale Factor	1000 ppm (1σ)
Accelerometer SF Asymmetry	300 ppm(1σ)
Acceleration Axis Misalignment	500 μRad (1σ)

* IMM requirement

** IMU requirement

Along with increased performance over that currently available, these packages are designed to meet the low-cost requirements of their applications. The IMU and IMM were developed using a common module approach to achieve low cost. Commonality helps to achieve low cost through manufacturing economies of scale, reduced development duplication, reduced production tooling and capital equipment, reduced configuration management, and simplified logistics and support requirements. Commonality between the IMU and IMM is maintained at the highest level: the Inertial Cluster Assembly (ICA) and the Sensor Support Electronics (SSE). The IMU also includes a Low Voltage Power Supply (LVPS) module to convert 28 volt input power to the low voltages required for operation. These basic modules are the same building blocks used for several members of Honeywell's GG1308 Inertial System family.¹

¹ For a more complete description of Honeywell's low-cost common module approach to the GG1308 RLG Inertial Measurement Systems, see J. M. Oelschlaeger & L. O. Thielman, "The GG1308 Ring Laser Gyro Inertial Measurement Systems - Honeywell's Low-Cost Solution for Tactical Applications," *IEEE 1990 Position and Navigation Symposium*, p. 528-36, March 1990.

IMU/IMM TEST RESULTS

Many IMUs and IMM's have been built and evaluated against the requirements of Table 1 through both laboratory and field testing. The data presented herein is the result of extensive laboratory testing evaluating both performance and environmental capabilities. The IMU/IMM design has also undergone many successful field and flight tests as part of Honeywell's Integrated Vehicle Management Unit (IVMU).² The following results demonstrate that Honeywell's low-cost GG1308 IMU/IMM designs deliver performance which consistently meets or exceeds most tactical missile requirements.

Performance Data

The charts of Figures 3 and 4 compare GG1308 Angular Random Walk (ARW) and bias stability of a sample of gyros built in 1990 as measured during the gyro Acceptance Test Procedure (ATP) and IMU test. These charts show the close correlation between the individual sensor and IMU performance. This permits the use of sensor measured coefficients for IMU compensation, thereby further reducing the costs associated with IMU calibration. Figures 3 and 4 also show the steady improvement in GG1308 performance, as increasing channel number also represents increasing time. The average ARW for the first eight gyros in the sample is 0.105°/√hr, compared to 0.085°/√hr for the last eight. The bias stability shows a similar trend toward improved performance. The average bias stability of the first eight gyros is 0.74°/hr, compared to 0.47°/hr for the last eight in the sample.

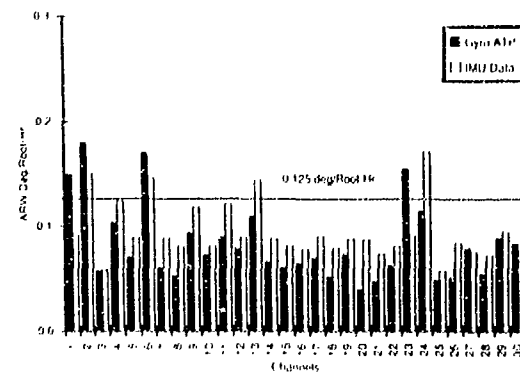


Figure 3. GG1308 Gyro and IMU ARW correlate very well. 26 out of a sample of 30 IMU channels satisfy the 0.125°/√hr ARW specification.

² Data from field and flight testing of the IMU/IMM design is being presented in Douglas O. Hoppe, "Field Tests of the Miniature RLG Integrated Vehicle Management Unit," *IEEE Digital Avionics Systems Conference*, October 1991.

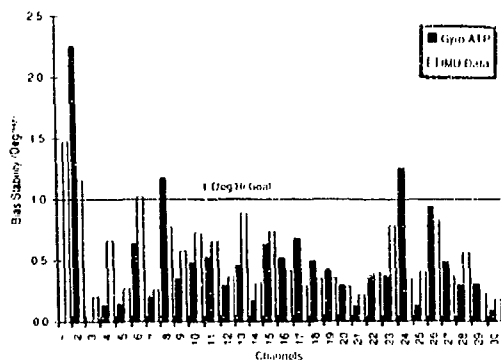


Figure 4. GG1308 Gyro and IMU bias stability correlate very well. 27 of a sample of 30 IMU channels satisfy the 1°/hr bias stability specification.

IMU/IMM Channel Performance

Throughout design verification testing, the IMU/IMMs have typically performed better than their design specification. The four key performance characteristics are presented in histogram form in Figures 5-8 for the gyro channels and Figures 9-12 for the accelerometer channels. A multi-position tumble test was used to extract each of these errors through addition and subtraction of velocity and rotation vectors. In all cases, except for gyro ARW, the data represents the standard deviation of each channel's performance parameter over temperature. Channels that exceed self-imposed requirements were typically from earlier vintage IMUs or IMMs. Data from more recent devices has consistently met requirements, the result of build process maturity. The distribution of these histograms shows the margin against the IMM/IMU requirement necessary for high yields and therefore lower unit cost.

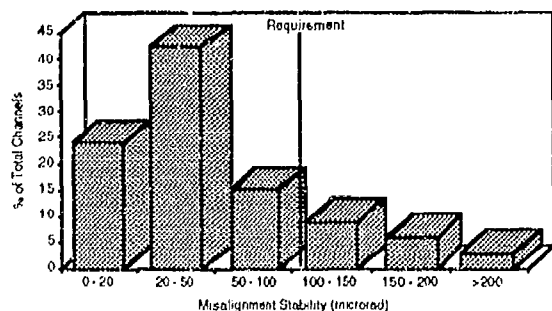


Figure 5. Eighty percent of the gyro channels meet the misalignment stability requirement.

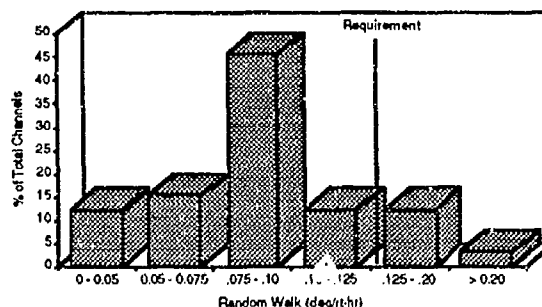


Figure 6. The later GG1308 RLGs exhibited consistent angular random walk in the 0.075-0.10°/hr range.

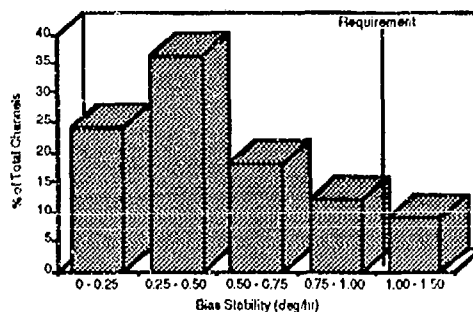


Figure 7. Ninety percent of all gyro channels, including early units, meet the gyro bias stability requirement.

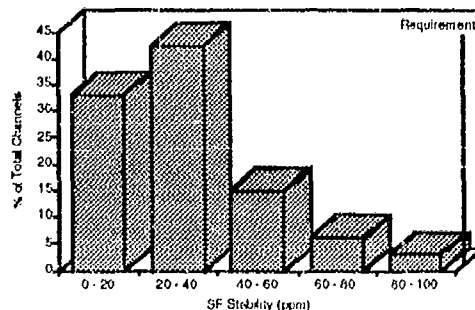


Figure 8. All gyro channels meet the scale factor stability requirement.

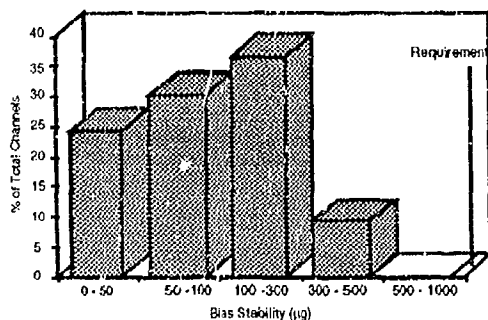


Figure 9. The accelerometer bias stability of all channels is less than half the requirement.

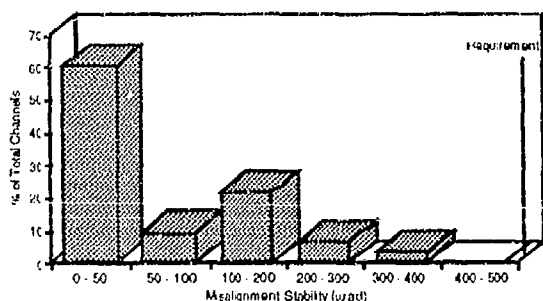


Figure 10. Accelerometer misalignment stability of all channels meet the requirement – the majority are under 50 micro-radians.

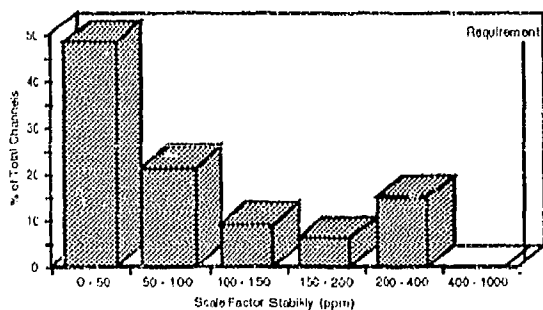


Figure 11. The scale factor stability of all accelerometer channels is less than half the requirement.

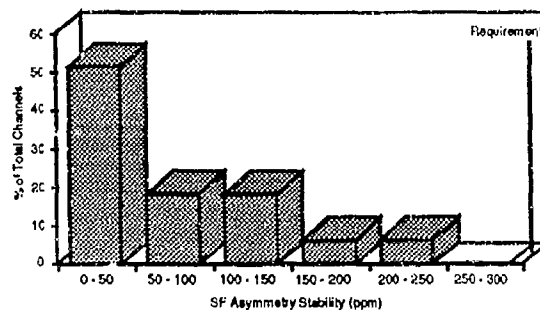


Figure 12. Ninety percent of all accelerometer channels show scale factor asymmetry stability at less than half the requirement.

These IMU/IMM performance parameters, with the exception of gyro ARW, are compensated using simple first or second-order temperature compensation algorithms. Applications that require lower performance than that specified in Table 1 will realize even lower costs. This is because generic sensor family compensation terms can be used in the IMU/IMM, reducing required sensor testing in addition to the IMU/IMM calibration cost.

GG1308 RLG Turn-on Transient Data

The well-behaved turn-on transient characteristics of the gyro channel performance is shown in the turn-on transient plot of bias pictured in Figure 13. This data was taken during the first five minutes after power was applied to the IMU and after a one-day dormancy. The U, V, and W channels were oriented East, North and Down, respectively. The data was taken at Honeywell's Inertial Instruments Operation in Minneapolis, Minnesota. This facility is located at 45 degrees latitude which accounts for the 10.6°/hour symmetrical offset from zero on the V and W channels. The trend of the gyro turn-on bias transient is typically less than 0.1°/hr/min over the first five-minute period.

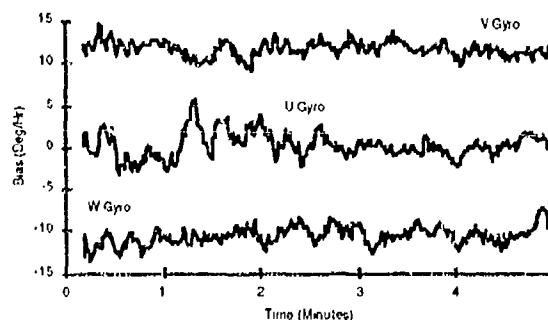


Figure 13. GG1308 gyro channel turn-on transients are nearly imperceptible.

GG1308 RLG Scale Factor Range and Linearity

As was demonstrated by the histogram of Figure 8, the GG1308 RLG has excellent scale factor characteristics. The device is capable of operating well beyond 2,000°/s and its scale factor linearity is excellent. Figure 14 shows uncompensated scale factor linearity out to 2,500°/s. Figure 15 shows thermally compensated scale factor. Again the performance is excellent. Scale factor accuracy and dynamic range are inherent characteristics of the RLG. Competing technologies typically fall far short of these performance levels.

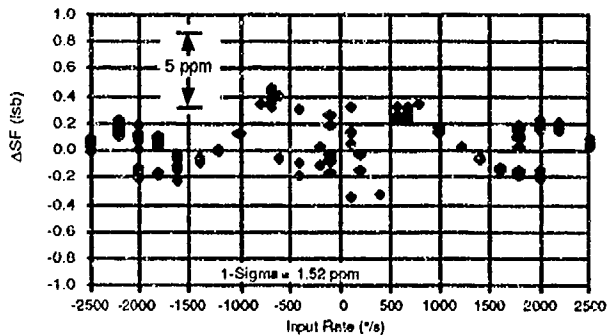


Figure 14. GG1308 scale factor linearity to 2,500°/s easily meets 100 ppm requirement.

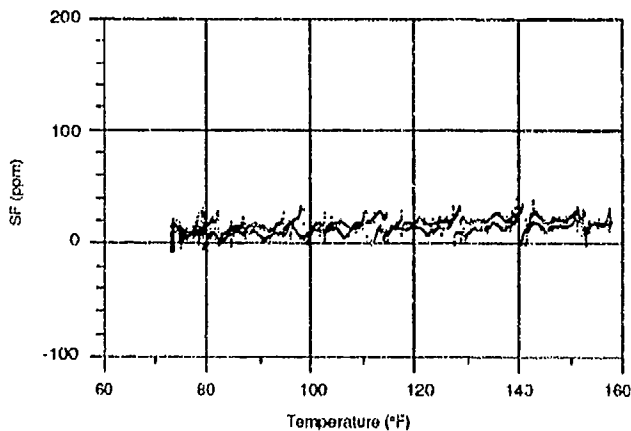


Figure 15. GG1308 compensated scale factor thermal sensitivity is consistent with 100 ppm requirement.

Environmental Data

Temperature

The IMU/IMM design is fully capable of operating over the entire Military Specification temperature range. Figure 16 shows data from a gyro channel as temperature is varied from 20°C to +85°C to -55°C and back to 20°C in two cycles. The angular random walk during this entire

run was 0.065°/hr. The gyro bias stability for this run was 0.29°/hr. The specifications for these two parameters are 0.125°/hr for angular random walk and 1.0°/hr for bias stability.

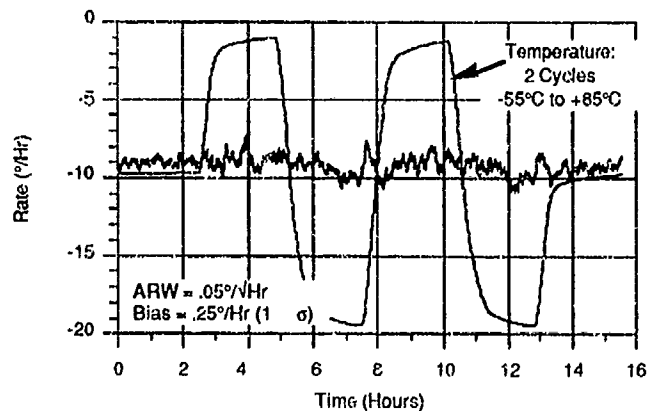


Figure 16. Outstanding uncompensated GG1308 RLG channel performance over -55°C to +85°C thermal environment.

Vibration

The operational random vibration requirement for the IMU/IMM is 15 grms in a spectrum ranging from 20 Hz to 2000 Hz. Figure 17 shows a gyro channel output as the vibration machine was repeatedly switched on and off. That is, during each 15-minute on period, the vibration machine is applying 15 grms random vibration; and during each 15-minute off period, there is no vibration input. As can be noted in the figure, there is no perceptible difference in gyro channel bias or angular random walk between on and off periods.

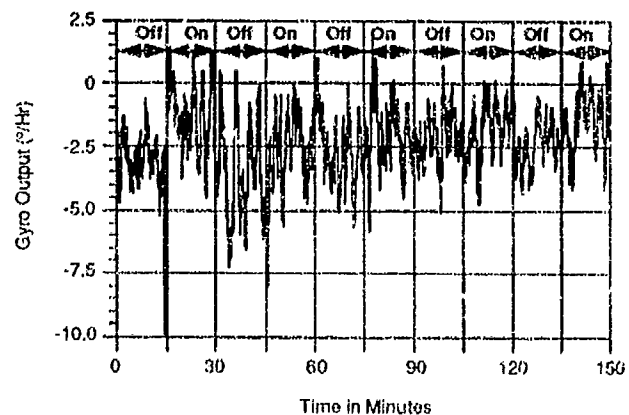


Figure 17. No perceptible change in GG1308 RLG channel output during repeated on/off cycling of 15 grms random vibration environment.

Shock

The shock requirement for IMU/IMM is a composite shock response spectrum combining the effects of a 250 g, 1 msec shock and a 200 g, 6 msec shock. The spectrum is shown in Figure 18. This spectrum was applied three times in each of three axes using a vibration machine. Five minutes of data were recorded prior to the shock application and five minutes were recorded after. Table 2 shows the change in bias of two gyro channels after shock application in each axis. As can be seen, there is no appreciable bias shift as a result of the shocks.

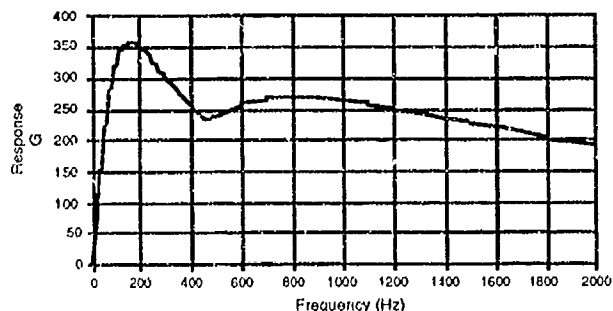


Figure 18. Shock response spectrum, composite of 250 g, 1 msec shock and 200 g, 5 msec shock.

Table 2. No appreciable GG1308 RLG bias change after shock exposure.

	Channel A Δ Bias	Channel B Δ Bias
Input Axis	0.18	-0.018
Long Axis	0.01	0.44
Cross Axis	-0.03	-0.07

TEST EQUIPMENT AND PROCEDURES

The low-cost theme in the development of the IMU and IMM was pervasive. The test equipment and test procedures were developed with the same goal in mind: off-the-shelf test hardware and software would be used wherever possible. By following this philosophy, test equipment development costs were kept to a minimum and, more importantly, recurring costs associated with replicating test stations were minimized. The IMU/IMM test station, called the Data Acquisition and Calibration Station (DACS), is based on the power of the common Personal Computer (PC). By utilizing the vast number of interface circuit boards and software programs available for

the PC, Honeywell has been able to effectively implement the off-the-shelf test philosophy to yield inexpensive, yet extremely capable test equipment for the GG1308 Inertial Systems product family.

The DACS takes advantage of the flexibility that has been designed into the IMU/IMM to allow for extensive testing, calibration, and troubleshooting to be performed through the serial data bus without having to disassemble the unit. Standard serial communication interface boards are used to communicate with the IMU/IMM via their RS-422 serial bus. This interface not only allows the collection of data from the individual inertial devices, but also provides access to internal IMU/IMM program memory to load executable code and calibration coefficients and to interrogate internal variables not normally available in the standard data output format. Embedded software development efficiency is also enhanced with this capability, since adjustments to the code can be quickly downloaded and evaluated in a fully assembled unit.

Test procedures are also consistent with the low-cost theme. A simple fifteen-point tumble test performed on a two axis position table was designed to measure all the significant IMU/IMM error sources such as sensor bias, scale factor, and misalignment. The tumble test is used both for the calculation of calibration coefficients used for compensation within the IMU/IMM and for determining performance of a calibrated unit by measuring residual errors. This test consists of a combination of static and dynamic test points in which data is collected by the DACS for a fixed period of time while the unit is subjected to static inertial inputs and angular rotations over temperature. Once the data is collected, the DACS post-processes the data and calculates compensation coefficients scaled appropriately for the unit. These coefficients consist of scale factor, bias, and misalignment error terms for both the gyro and accelerometer channels. The coefficients are then ported into the unit through the serial bus and are stored in the appropriate EEPROM locations. Once calibration is completed, additional tumble tests are performed to determine the performance of the unit. The DACS has been designed such that this entire sequence can be automated, thereby reducing operator interaction and, ultimately, unit cost.

Throughout the evaluation testing of the IMU/IMM, several other capabilities of the DACS were exploited. Commercially available analog-to-digital and digital-to-analog conversion boards and discrete input-output boards were integrated into the DACS environment to collect special interest data. For example, extensive vibration testing was performed to evaluate structural resonances within the designs. During these tests, several miniature accelerometers were secured to various components within the units and were monitored by the DACS analog-to-

digital inputs at rates sufficient to resolve resonant frequencies up to 2kHz. A similar technique was used to monitor the IMU/IMM response to mechanical shock inputs. Collecting the data in this manner permitted it to be conveniently analyzed within the same environment as all other IMM/IMU data, utilizing commercially available software. These are but two of the many cases where the flexibility of the DACS was exploited to collect and analyze specialized data over and above that required by the normal calibration and performance evaluation procedures.

CONCLUSION

Two designs in Honeywell's family of low-cost GG1308 Ring Laser Gyro Inertial Measurement Systems have demonstrated performance which consistently meets or exceeds most tactical missile requirements. The designs are also capable of performing through the severe

environments characteristic of mission scenarios applicable to these devices. Both the HG1500 Inertial Measurement Unit and the HG1108 Inertial Measurement Module designs have been extensively tested to support these claims. The performance margins demonstrated in these tests clearly show a cost advantage. The generous margins not only ensure high yields, but also reduce calibration and test costs of the products by the ability to use sensor family compensation terms, simple first-order compensation coefficients, or no compensation terms at all. Combining these advantages with the low-cost test equipment and procedures approach has resulted in economies over and above those realized by the common module design philosophy. The result is inertial measurement units which meet both the cost and performance requirements of tactical applications of the 1990's and beyond.

CSDL-P-3091

**APPROACH FOR THE EVALUATION OF
ALTERNATIVE CLEANING SOLVENTS AND
TECHNIQUES TO REPLACE THE USE OF
OZONE DEPLETING SOLVENTS IN
INERTIAL INSTRUMENT PRODUCTION**

by

**John W. Agopovich
Ann L. Hynes**

July 1991

Presented at

**CIGTF 15th Biennial Guidance Test Symposium
Holloman AFB, New Mexico
24-26 September 1991**

**Approved for public release;
distribution unlimited.**

BMO 11/4/91



**The Charles Stark Draper Laboratory, Inc.
555 Technology Square, Cambridge, Massachusetts 02139-3563**



Approach for the Evaluation of Alternative Cleaning Solvents and Techniques to Replace the use of Ozone Depleting Solvents in Inertial Instrument Production

John W. Agopovich and Ann L. Hynes

Abstract

The ozone depletion issue is well publicized and various directives have been mandated to phase out ozone depleting chemicals before the end of this century. These directives include the Montreal protocol, (shown in table 1) US EPA guidelines, the US Clean Air Act, DOD Directive 6050.9 and Air Force Regulation 19-15. In the precision cleaning required for the production of inertial instruments, solvents such as Freon®-113 and to a lesser degree 1,1,1-trichloroethane are used. Both solvents are scheduled for phaseout per above directives. To date no universal replacement solvent or cleaning process has been developed or proposed to supplant the use of ozone depleting CFCs (Chlorofluorocarbons) such as Freon-113 and 1,1,1-trichloroethane. This presents a serious problem in the inertial instrument production because Freon-113 is widely used. The stringent cleaning needs for inertial instruments require subsequent verification testing to introduce any change in the manufacturing process. The upcoming deadlines for phaseout of these solvents dictate that this problem be addressed immediately.

The approach taken to solve this problem was to propose implementation of a three phase study to eliminate the use of Freon-113 and 1,1,1-trichloroethane usage on Air Force programs. The specific programs include the Peacekeeper accelerometer and gyroscope. This problem is not going to be completely solved by the chemical companies therefore the various Air Force contractors must work together to address this issue. The first phase of this program includes a survey, review, and experimental evaluation of the current and emerging cleaning fluids and processes. The application of alternative methodologies to instrument assembly starting at the subcomponent level, and an evaluation of options for the manufacturing operations would be addressed in the second phase of the program. Verification by instrument build with the proposed changes, would be validated in the final phase. It was proposed that this approach would be taken by Draper as the coordinating agency. Draper would work with the inertial instrument manufacturers, the industrial producers of the cleaning agents and equipment, and the Air Force to evaluate alternatives and place them into the production facilities as quickly as possible.

The use of Freon-113 cleaning operations inertial instruments is separated into three types of operations: 1) power spray cleaning of parts, fixturing, etc. during the assembly process for particle removal, 2) power spraying of instrument hardware in teardowns for fluid and particle removal and 3) areas where lesser quantities are used such as Freon-113 ultrasonics, wipes, scrubbing, soaking, etc. It was estimated that 75-80% of Freon-113 volume used in inertial instrument manufacture is tied directly to power spraying in the first two applications mentioned above.

Due to the many desirable properties of Freon-113, it will be difficult if not impossible to find one drop in replacement. These properties of Freon-113 include

availability of high purity grades, high density, low surface tension, nontoxic and nonflammable, solvent for gyro fluids and high volatility. This paper will discuss the following alternatives to Freon -113 shown below:

Alternative solvents

- 1) FCs (Fluorocarbons)
- 2) HCFCs (Hydrochlorofluorocarbons) and a mixture of HCFCs and other solvents
- 3) Aqueous Systems
- 4) Semi aqueous systems

Alternative cleaning methods

- 1) SCF (Supercritical fluid extraction)
- 2) U/S and tuneable ultrasonics with alternative solvents
- 3) Plasma and UV ozone cleaning

This paper will outline the details of alternative solvents and cleaning techniques that are available to the gyro community and how these are implemented in a coordinated plan. The application and advantages/disadvantages of each alternative cleaning technique will be discussed in relation to instrument build processes.

Introduction

The destruction of the ozone layer by CFCs was suspected for several years. Due to the high stability of these class of chemicals, the CFCs are not broken down in the troposphere. CFCs eventually make their way up to the stratosphere where UV radiation causes the breakage of carbon-chlorine bonds to yield reactive chlorine radicals. The chlorine then reacts with ozone to produce oxygen and chlorine monoxide. The simplified chemical reaction is shown below using Freon-12 as an example:



This process is even more damaging than appears because the reaction of the chlorine and ozone is catalytic. One molecule of chlorine can destroy several orders of magnitude more molecules of ozone. The presence of "reactive" chlorine has been proven by the measurement of the increase ClO with a corresponding decrease in ozone¹. The effects of bromine containing CFCs are even more damaging. The global impact of the depletion of the ozone layer is obvious and extensive. The effect on the human population as far as increased exposure the UV radiation will eventually lead to a higher amount of skin cancers.

¹ Chemical and Engineering News, May 30, 1988 pages 16-25.

A list of ozone depleting substances commonly used on Air Force programs taken from Air Force regulation 19-15 is shown below:

SUBSTANCE	ABBREVIATED NAME	CHEMICAL STR.	ODP
Trichlorofluoromethane	CFC-11	CFCl_3	1.0
Dichlorodifluoromethane	CFC-12	CF_2Cl_2	1.0
1,1,2-Trichloro-1,2,2-trifluoroethane	CFC-113	$\text{CF}_2\text{ClCFCl}_2$	0.8
1,2-Dichlorotetrafluoroethane	CFC-114	$\text{CF}_2\text{ClCF}_2\text{Cl}$	1.0
Chloropentafluorocethane	CFC-115	$\text{CF}_3\text{CF}_2\text{Cl}$	0.6
Bromochlorodifluoromethane	Halon 1211	CF_2BrCl	3.0
Bromotrifluoromethane	Halon 1301	CF_3Br	10.0
1,2-Dibromotetrafluoroethane	Halon 2402	$\text{CF}_2\text{BrCF}_2\text{Br}$	6.0
1,1,1-Trichloroethane	TCA	CCl_3CH_3	0.11
Tetrachloromethane	Carbon tetrachloride	CCl_4	1.11

CFC-113 and TCA are the substances of concern as far as precision cleaning in inertial instrument manufacture. Later discussions will involve proposing alternatives to replace these two solvents.

Background

Freon-113 has been by far the major solvent used in cleaning required for the assembly of precision inertial instruments. Freon-113 has unique properties that make it ideal for this application. These desirable properties include:

1) High purity grades are available at low cost. (i.e. Freon PCA from Du Pont) The Freon-113 is not only is pure chemically but is available in grades that contain very low non-volatile residues. (<1 ppm by weight). This low nonvolatile residue requirement is crucial when large quantities of solvent are used in precision cleaning of instrument parts.

2) Freon-113 is nontoxic and nonflammable. This is important as large quantities are used in some power spray cleaning applications and hazards to personnel must be minimized.

3) Freon-113 has a high density, low surface tension and low boiling point making it ideal for removal of particles from instrument parts, hardware assemblies, gyro and PIG fill stations, etc.

4) Freon-113 is a solvent for T-17-2 (TGG damping fluid), BTFE (SFIR and Mod G damping fluid), FC43 (SFIR and Mod G fill fluid) and L-11512 (proposed FC 43 replacement fluid). Freon-113 solvent properties are especially critical for the FC43 and L-11512 fluids as few solvents adequately dissolve these fluorinated fluids. The Freon-113 cleaning for fluid removal from hardware is critical for instrument disassembly.

The use of Freon-113 cleaning operations inertial instruments consists of three types of operations:

- 1) Power spray cleaning of parts and fixturing during the assembly process for particle removal
- 2) Freon-113 cleaning involving ultrasonics, soaking, etc. for soil removal

- 3) Freon power spray cleaning and power spray for fluid removal.

TECHNICAL PLAN FOR THE EVALUATION OF FREON ALTERNATIVES IN THE PRODUCTION OF INERTIAL INSTRUMENTS

PHASE I

Approach

This proposed study will focus on three major areas, 1) the evaluation of alternative solvents to replace Freon-113 as it is used in inertial instruments and 2) the evaluation of alternative cleaning methods and 3) a combination of 1) and 2)

Alternative solvents to be studied include the following:

- 1) Fluorocarbons (FC72 and Vertrel™ 245)
- 2) HCFC's blends (Allied's Genesolv 2000 series, Dupont Vertrel 400 series)
- 3) Aqueous Systems
- 4) Semi aqueous systems

Alternative cleaning methods include the following:

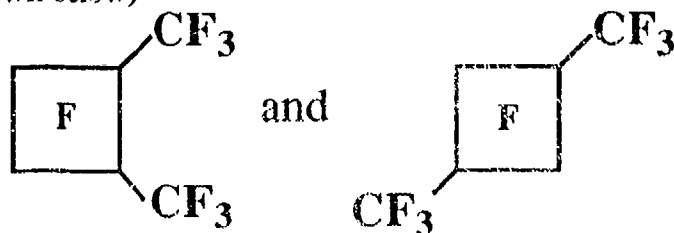
- 1) SCF (CO₂)
- 2) U/S and tuneable ultrasonics with alternative solvents
- 3) Plasma and UV ozone cleaning

There are various considerations for choosing alternative solvents/techniques. A summary of technical and nontechnical issues are shown in table 2.

ALTERNATIVE CLEANING SOLVENTS

Fluorocarbon Candidates

The use of Freon-113 in of inertial instruments is unique from other industrial applications of this solvent in that most of the solvent usage is for particle removal from hardware and tooling. Because the particle removal is one of the critical requirements of the use of Freon-113, fluorocarbon solvents, that is species containing only carbon and fluorine could be adequate replacements due to their low surface tension and high density. These materials are also solvents for the gyro and fill fluids therefore fluorocarbons will be proposed replacements for power spraying and may solve ≈ 75-80% of the Freon-113 elimination problem. Two fluorocarbon solvents are currently available to evaluate as replacements for Freon-113. These include an experimental Du Pont solvent, Vertrel 245 (structures shown below)



This material is a mixture of the 1,2 and 1,3 perfluorodimethylcyclobutane isomers. The other candidate is FC 72 (perfluorohexane) which is commercially available from 3M. 3M is currently evaluating a "cheaper grade" of FC72 that has the 3M product designation PF-5060. These solvents should be adequate replacements for Freon-113 in many areas of inertial instrument manufacture.

Comparison of Properties of FC72 and Vertrel 245 to Freon-113

Solvent	Freon-113	Vertrel 245	FC 72
Property			
Boiling Point °C	48	45	59
Surface tension	17.3	11.6	12.0
Density	1.57	1.67	1.68
Cost	≈ \$4/lb.	≈ \$20/lb.	≈ \$20/lb.

Fluorocarbons have advantages as replacement solvents because of some of their similarities of physical properties to Freon-113.

- 1) The absence of chlorine atoms in these compounds results in a zero ODP (ozone depletion potential)
- 2) Low toxicity and nonflammability
- 3) Solvents for FC43, T-17-2, BTFE and L-11512
- 4) Volatile, low surface tension and high density (advantageous for the removal of particles)
- 5) Inert, Not likely to have compatibility problems

Disadvantages

- 1) Cost is high - can be reduced by containment and recycling
- 2) Not as good solvent as Freon-113 (may be an advantage sometimes, disadvantage other times) In general, fluorocarbons are poor solvents thus they are not good candidates for the removal of oils, greases, hydrocarbon contaminants, etc. This property will not lead to compatibility problems however.
- 3) May have a global warming problem because they don't breakdown in the atmosphere

HCFCs as cleaning solvents in inertial instruments

HCFCs are chlorofluorocarbon compounds similar to the CFCs with hydrogen atom(s) present in the molecule. The effect of hydrogen in these compounds are many. First, these are attractive solvents in that the ozone depletion potential (ODP) is less than the CFCs on the near term phaseout list. These compounds breakdown lower in the atmosphere before they reach altitudes where chlorine radicals are generated as with the high ODP CFCs. Because these are hydrogen containing materials, the solvent character of HCFCs will be better Freon-113 and much better than the fluorocarbons discussed earlier. This may be advantageous in removal of machining oils, flux, etc. HCFCs have higher volatilities as compared to Freon-113. Also the cost of the HCFCs will likely be lower than the fluorocarbon candidates mentioned earlier.

Examples of HCFCs under consideration include HCFC-141b (CCl_2FCH_3) and HCFC-123 (CCl_2HCF_3). Both Du Pont and Allied Signal supply these materials, but recent information revealed that Du Pont may no longer be a source of HCFC-141b due to

new analyses that yielded higher ODP values. Also recent toxicity studies with HCFC-123 found the formation of benign tumors in rats. These results may limit the availability of these materials in the future.

Du Pont and Allied have marketed Freon replacements that are mixtures of the above two materials. Du Pont's Vertrel 400 series materials are cleaning agents containing various blends of HCFC-123 and HCFC-141b. Allied's Genosolv 2000 series are also blends of HCFC-123 and HCFC-141b. Some HCFC blends contain small amounts of methanol and stabilizers.

Specific examples of HCFC blends are as follows:

Vertrel 400 series (Dupont)

Vertrel 434 (62% HCFC-141b, 35% HCFC-123, 3% MeOH)

Genesolv 2000 series (Allied)

2004 - (96% HCFC-141b, 0.1% nitromethane, 3.9% MeOH)

2010 - (86% HCFC-141b, 10% HCFC-123, 0.3% nitromethane, 3.7 % MeOH)

2020 - (80% HCFC-141b, 20% HCFC-123)

Unfortunately, the presence of hydrogen in chlorofluorocarbons give these compounds properties that are undesirable. These properties include:

- 1) Toxicity problems, long term availability unknown
- 2) May be flammable
- 3) Phase out scheduled in \approx 30 years, only temporary fix
- 4) Good solvents may lead to compatibility problems

Aqueous Solvents

Aqueous systems such as high purity water with detergents or surfactants will be evaluated. These may be especially useful in the gas bearing assembly area.

Semi Aqueous Systems

Semi aqueous solvent blends such as Du Pont's Axarel™ 32, 38 and 52 will be studied. The Axarels are complex mixtures of polar and nonpolar components. These include aliphatic hydrocarbons, aliphatic esters, a surfactant and aliphatic alcohols. This cleaning blend is especially proficient in removal of solder fluxes. This material forms an emulsion with water so a final water rinse is used as a part of the final cleaning process to remove traces of ionic impurities left from soldering processes. The use of this material has several advantages:

- 1) The material is commercially available from Du Pont
- 2) Low toxicity, low vapor pressure, low flammability, odor levels are lower than terpenes
- 3) Water is used in the final rinsing process

Approach for the evaluation of alternative solvents as Freon-113 replacements

A) Evaluation of solvent purities, recycling and recovery methods and long term availability

Significant vendor interaction will be required to ensure grades of solvents produced meet the requirements of precision cleaning. Specific areas of concern are the presence of nonvolatile residues such as plasticizers and silicones. The presence of these in cleaning solvents must be kept to an absolute minimum. Other general impurities such as hydrogen containing species must be controlled. Particle content of the solvents is obviously critical and methods must be developed at either the vendor or the instrument manufacturer or both to make sure the solvent is free of particles.

The immediate and long term availability of these solvents needs to be established. Also issues as far as containment/recycle of the expensive fluorocarbon solvents must be addressed. The containment question can be addressed by the use of various contained power spray apparatus available.

B) Compatibility Verification

It is not expected that fluorocarbons and instrument hardware will be incompatible but these still must be evaluated. The HCFC's and the aqueous or semi aqueous alternatives require closer scrutiny. Exposure of the solvent(s) and instrument part for a given period at room and elevated temperatures must be performed. After exposure the following analysis must be done:

- 1) Inspection of parts first with an optical microscope and then surface evaluation using FTIR and SEM/EDAX.
- 2) Analysis of fluid for changes in composition and extractables from the respective instrument hardware.

C) Power Spray Cleaning/Particle Removal

Instrument parts will be spray cleaned with the fluorocarbon or other replacement solvents at each subassembly/component step and the process will be subsequently evaluated by Tyndall and surface analysis of the parts.

D) Fluid Removal/Teardowns

As mentioned earlier, a significant quantity of solvent is used in teardown of instruments. Instruments parts (can use scrap parts) will be exposed to the various fluids were applicable and cleaned with the replacement solvents. A surface analysis technique such as FTIR is very sensitive in detecting the presence of trace levels of organic species on a surface. The cleaning efficiency will be evaluated whether the fill fluids (FC43 or L-11512) and damping fluids (T-17-2 and BTFE) remain on the part surface after cleaning.

ALTERNATIVE CLEANING TECHNIQUES

The several non-solvent techniques that are available are attractive options to solvent cleaning. Often where trace contaminants are not satisfactorily removed, these techniques can complete the task left unfinished by solvent cleaning. Ultraviolet (UV)/ozone and plasma cleaning are two "dry" processing techniques that are used for the removal of organic contamination from surfaces. Limited use has been made in the build of inertial instruments. These approaches are used in the processing of optics and semi-conductors. To date, there is no application of SCF extraction cleaning in inertial instrument production. Preliminary studies show that this technique may be particularly useful where removal of damping fluid is required. These three techniques have the

capability for batch processing, reduction in the individual handling of piece parts, and greater control of the process.

Plasma Cleaning

Plasma cleaning is a dry processing technique in which a gas is excited in an electrical field forming free radicals, ions, and other reactive species. These excited species react with organic surface films breaking chemical bonds and forming smaller molecules that are removed in the flowing gas phase. Oxygen, argon, and fluorine/oxygen mixes are the gases most frequently used in cleaning applications. This technique has found wide application in the optics, electronics, and semiconductor fields where surface cleanliness is important. The process is applied to Air Force inertial instrument programs in the preparation of surfaces prior to bonding, the removal of excess epoxy on laminations and limited use for removal of contaminants from the surface of gas bearings. Auger/ESCA analysis of gas bearing surfaces before and after plasma cleaning has shown a reduction in surface contamination. As with UV/Ozone cleaning, plasma cleaning is effective for removal of organic contaminants only, and generally requires removal of gross contamination by a prior process using wet (solvent) cleaning. The process is used on Air Force build programs in the preparation of surfaces prior to bonding, for the removal of excess epoxy on laminations, and limited application for removal of contaminants from gas bearing surfaces. The effectiveness of plasma cleaning was established by Auger/ESCA analysis. As with any process, the interaction of the cleaning agent and build materials must be compatible. There is sufficient experience among the agencies and in literature references, to guide selective use of reactive gases such as oxygen and CF_4 .

Ultraviolet (UV)/Ozone Cleaning

UV cleaning is a simple process that is inexpensive to set up and operate, and is easy to use. The cleaning mechanism is a photosensitized process initiated with the absorption of UV radiation. The absorption of UV (below 300 nm) radiation is responsible for producing photochemical changes necessary for the removal of absorbed species. Molecular oxygen in air, dissociated by short wave radiation, ~185 nm, leads to the generation of oxygen radicals that combine with oxygen to form ozone. Ozone is dissociated by radiation at a higher wavelength, at 254 nm to produce atomic oxygen which is strong oxidizing species. UV radiation at 254 nm also breaks the chemical bonds of surface species creating free radicals that are readily oxidized by the atomic oxygen to volatile species such as water and carbon dioxide. The efficacy of this process has been evaluated by surface analysis such as Auger/ESCA and is documented in the literature. Limited inhouse studies on the cleaning of gas bearing surfaces, compared favorably with the literature evaluations of the process. UV cleaning does have some limiting aspects. It cannot remove gross contaminants, and requires some precleaning (solvents, detergents, etc.) of the surface to remove bulk contamination for the procedure to work reliably. UV cleaning would be considered a final cleaning step. A chamber could be interfaced with an automated assembly station.

Supercritical Fluid (SCF) Extraction

When a gas is subjected to pressures and temperatures above its critical point, a highly compressed gas, referred to as a supercritical fluid is formed. Supercritical fluids have properties that are intermediate to ordinary liquids and gases having gas-like diffusivities and liquid-like densities. With high diffusivity and low viscosities, supercritical fluids have been established to be particularly effective for removal of materials such as machining coolants, damping fluids, and oils from components of complex configuration. Solubility studies performed by HI and Draper (through Phasex corp.) have established that SCF carbon dioxide, an environmentally acceptable

solvent, can dissolve many materials. These include halocarbon and triazine damping fluids, Krytox fluids, silicone oils, and many other materials indigenous to the inertial instruments, as well as processing aids and contaminants. SCF extraction is a particularly attractive approach for the processing of rebuilds which currently requires high volumes of solvents to remove damping fluid, because of the ability of SCF CO₂ to remove damping fluid from micro-clearance interstitial regions and pores of gyro parts. This approach would eliminate the time consuming bake out procedure required due to solvent absorption. A drawback with respect to SCF is personnel safety and the integrity of instrument hardware. There are defined regulations for high pressure operations to minimize personnel hazards. The integrity of the hardware to high pressure exposure would have to be established. Limited evaluation of SCF extraction was successful in removing damping fluid from a gyro with minimum disassembly with no precleaning and no obvious damage.

Equipment for Alternative Cleaning Techniques

Facilities for plasma cleaning, UV/ozone cleaning and SCF extraction already exist among the agencies although some may be adequate for only research studies and not for production application. An assessment of scale-up requirements for production, and associated capital expenditure required would be done. Safety issues such UV/ozone exposure, gases, and high pressures operations would be reviewed. These techniques are directed to batch processing with reduced handling and greater control than is experienced with current individual piece part/operator subjectivity. The points in instrument build where these techniques can be introduced will be identified.

Compatibility Verification for Alternative Cleaning Techniques

As with the alternative solvents, the compatibility of materials with UV radiation and plasma gases must be established. These techniques are generally applied only to surface cleaning. The following areas of compatibility must be evaluated.

- 1) Reactivity of the substrate with the active gas species
i.e. is the surface oxidized?
- 2) Etching of the surface
- 3) Effect on organics

With respect to SCF extraction, the effect of exposure to high pressure must be evaluated. Areas to be evaluated include the following:

- 1) Physical integrity of laminations
- 2) Stability of the electronics
- 3) Adhesive bonds
- 4) Effect on urethanes, epoxies, elastomers

Cleanliness testing

The requirements for cleanliness must be defined. It is intended that comparison testing will be the basis for establishing whether alternative methods are equal to current methods using Freon-

113. Test pieces will be doped with processing contaminants such as machining coolants, solvent and water-based lapping compounds, grit blast compounds, lubricants, and damping fluids. Plasma and UV cleaning techniques will be used on test pieces with subsequent evaluation for surface cleanliness. Parameters for time, gases and power for plasma, and distance for UV cleaning will be established. Temperatures and pressures of SCF, required for effective removal of organics will be established.

The following tests will be among those used to establish relative cleanliness levels:

Inspection - white light and UV light

Water break test

Extraction with NVR, GC/MS or FTIR testing

Ionic cleanliness

SEM. <

Surface analysis

Hardness and expansion tests for organics/elastomers

PHASE II

Those alternatives that successfully tested with the controlled samples, will be applied to the cleaning of subcomponents and assemblies to establish the most effective cleaning sequence with the alternatives. Test methods established in the evaluation of the alternative fluids and the cleaning of test samples, would be used in evaluating the processing of the instrument hardware. Processes will be redefined at this stage, if required, to minimize any fluctuations of the process and to ensure duplication of the processing in future operations. An assessment of the options for the production lines, would be considered. Criteria will be established for the cleanliness standards for each component or level of build. Performance testing would be conducted on individual components, such as the gas bearing, to verify the processes at the subassembly stage.

Examples of assembled subcomponents:

Gas bearings

Ball bearings

Slip ring Assemblies

Gyro fill stations

Glassware/tooling

PHASE III

Validation of the Freon-113 free procedure considered to be the most optimum by instrument build, will be addressed in this phase. This would be done as a qualification effort. An assessment would be done to determine the requirements for transfer of the processes to the production. Some issues to be considered for production implementation are as follows:

New equipment required for alternative processes

Lead time to incorporate changes

Adaptation of production facilities

Safety requirements

Organic vapor proofing

DI water systems

Energy requirements

Availability

Cost

Installation

Personnel training

AF Documentation changes

Some of the above mentioned issues will be partially addressed in phase 1 and phase 2.

Conclusions

Alternative solvents and/or methods must be found for the use in all industrial applications including the production of inertial instruments. Because of the large usage of Freon-113, the replacement of the use of Freon-113 will require detailed studies to validate that alternatives do not compromise the quality of the precision instruments. It will not be possible to find one direct replacement for Freon-113.

The elimination of Freon-113, the single most widely used solvent on the Air Force programs, will require a concerted and coordinated effort to achieve any degree of success. Although the program proposed to achieve this is presented as defined stages, the preparation for the changes must begin from the start. Assuming development of Freon-free processes, it must be recognized that there will be no operator experience base. More quality control testing will be required to ensure that implementation of the new process does not compromise the product.

Table 1

MONTREAL PROTOCOL*

solvent	1993	1995	1997	2000	2005	2020
CFC-113	20%	50%	85%	100%		
1,1,1-trichl.		30%	70%		100%	
HCFC-123						100%
HCFC-141b						100%

*Also have Clean Air Act, EPA, USAF regulation 19-15 per DOD dir. 6050.9 with their respective phaseout dates/protocols

Table 2

FACTORS/CRITERIA CHART OF REPLACEMENT SOLVENTS

Technical	Non-technical
requirements (purity and particles)	cost
reproducibility of material	toxicity, vapor pressure, flash point
compatibility issues	available commercially
density	# of sources
viscosity	storage requirements
surface tension	long term availability (corporate)
new equipment purchase required	long term availability (phase out)
volatility, heat of vaporization	global warming
solvency	universal or limited applications
stability vs. time	waste disposal
how can it be recycled	can it be recycled

DISTRIBUTION LIST

DRAPER:

J. Agopovich (4)
N. Barbour
V. Assarian
J. DiSorbo
L. Eichinger (Draper @ LI)
W. Fitzgerald
J. Hand
A. Hynes (4)
J. Kane
J. Kauppinen
J. McClain
K. McColl (Draper @ HIF)
J. Ricker
R. Riley
J. Schmidt
J. Shearer
J. Stemniski
J. Williams
R. Williams
TIC

BMO/MVEG

Captain S. Henderson

HONEYWELL/FL.

R. Woodwell
F. Strother

LITTON G+CS (Woodland Hills, Ca.)

S. Cleary
E. Alber

LITTON G+CS (Salt Lake City, Ut.)

R. Prior

SESSION IX-A
PEACEKEEPER INSTRUMENTS

CHAIRMAN
RICHARD HOLDEMAN
TRW

LITTON'S SECOND GENERATION LASER GYROSCOPE

Charles H. Volk
Ian Longstaff
John M. Canfield
Steven C. Gillespie

Litton Guidance and Control Systems Division
5500 Canoga Avenue
Woodland Hills, CA 91367

ABSTRACT

The design and performance of Litton's second generation aircraft navigator grade multioscillator ring laser gyroscope, the Zero-lock Laser Gyro™ (ZLG), is described. The S18-4 ZLG is intended to meet the size, weight, and volume constraints expected for next generation aircraft and helicopter inertial navigation systems. The ZLG, a non-mechanically dithered ring laser gyro, offers advantages for strapdown navigation system applications.

The theory of operation of a ZLG is briefly described, gyro readout and control functions are described, design tradeoffs are discussed, and instrument and system level performance data are summarized relative to required performance for a 0.8 nmph inertial system. More than 300 instruments have been fabricated and tested during the last six years of intensive company-funded development effort.

INTRODUCTION

Litton Guidance and Control Systems has been developing a second generation ring laser gyroscope (RLG) capable of aircraft navigator grade performance using a ditherless multioscillator RLG. Development of this instrument, the Zero-lock Laser Gyro (ZLG), has been underway at Litton since 1975. An accelerated development program was begun in 1984 when the Raytheon multioscillator technology was purchased by Litton.

Since that time, four generations of ZLGs have been designed and fabricated. The S18-4 ZLG is a fourth-generation, 18-cm pathlength instrument currently in production to support Litton Aero Products Division's Flagship Global Positioning Air Data Inertial Reference System (GPADIRS) pro-

gram and Guidance and Controls' LN-100 System for the LH program and the Apache helicopter guidance system update. More than 100 S18-4 prototypes have been fabricated in engineering with pre-production units currently in fabrication in the factory.

THEORY OF OPERATION

The cavity modes in a planar ring resonator are four-fold frequency degenerate. The fourfold degeneracy is removed by use of a reciprocal (nondirection dependent) rotator and a nonreciprocal (direction dependent) rotator. Figure 1 shows the elements of a ZLG. The reciprocal frequency splitting is achieved by use of a nonplanar ring resonator which removes the degeneracy between the right circular polarized (RCP) eigenmode and left circular polarized (LCP) eigenmode (circular polarization modes are required in a nonplanar ring resonator to ensure cavity resonance). Frequency splitting is determined by the image rotation which is dependent on the out-of-planeness. Since each polarization can oscillate as a ccw or a cw traveling wave, the possibility of four-frequency operation is open. Typical reciprocal splitting is hundreds of MHz.

A nonreciprocal rotator is also required. The nonreciprocal rotation is supplied through the Faraday effect which introduces a directionally dependent phase shift. Figure 2 shows the resulting four frequencies. Typical Faraday bias is of the order of 1 MHz.

Removing the direction dependent frequency degeneracy by the Faraday effect creates two opposite biased two-frequency gyros (RCP and LCP) in one cavity. Application of a rate increases the frequency splitting of one gyro while the other gyros' frequency splitting is decreased. A differential gyro

is achieved by taking the difference between the two two-frequency gyros

$$F = (f_4 - f_3) - (f_2 - f_1)$$

With differential output, the fluctuations in the optical bias are common moded out while twice the rate sensitivity is achieved. Lock-in problems are avoided because the Faraday splitting is larger than the typical Sagnac splitting even at rates of 400 degrees/second.

READOUT AND CONTROL FUNCTIONS

Figure 3 is a block diagram for the ZLG. The main functions are gain media excitation and control, pathlength control, gain media dispersion equalization control, and gyro readout. Temperature sensor outputs are provided for system level thermal compensation.

The ZLG utilizes a split dc discharge He-Ne plasma to provide laser gain. A high voltage power supply (HVPS) is required along with plasma current regulators to provide constant current operation in each of the two discharge legs. A split discharge is utilized to mitigate bias caused by gain media motion relative to the gyro body as in an RLG.

Since the geometry of the ring resonator determines the conversion factor between gyro output and rotation pathlength control is required. The ring resonator is made from an ultralow thermal expansion material. Diaphragm mirrors, in conjunction with piezoelectric transducers, maintain pathlength control over the range of environmental conditions expected for a military aircraft. An error signal is required as a discriminant such that feedback is provided to the piezoelectric transducers when environmental effects cause cavity length changes. By ac modulating the cavity length, an amplitude modulated reciprocal splitting frequency signal is obtained on the uncombined output beam. This is a very sharp discriminant—the RF power at the reciprocal splitting frequency falls rapidly as the cavity is detuned away from equal intensity.

Gain media dispersion control is required in the ZLG. Mode pulling affects will create a ZLG bias in the absence of dispersion equalization control. The frequency shift of each of the four frequencies, due

to mode pulling, is proportional to their distance from the center of the gain curve and their loss. This affect will create a ZLG bias in general and a sensitivity to cavity detuning. A longitudinal magnetic field on the gain media will shift the gain curve for LCPcw and RCP ccw opposite to the gain curve for the LCPccw and RCPcw relative to the zero magnetic field gain curve center. This will cause a ZLG bias and a sensitivity to magnetic fields in general. A technique may be employed, called dispersion equalization, in which a longitudinal magnetic field is applied to the gain media and a pathlength control offset is selected which will desensitize the ZLG to magnetic field or pathlength offset variations. The dispersion equalization parameters are determined during calibration.

The gyro readout method employed is to use a combining prism in conjunction with a dual spot photodiode and electronic signal processing. The photodiode outputs are double sideband suppressed carrier signals which can be electronically processed to obtain the two difference frequencies. The two frequencies are counted—the multioscillator output is the difference between the two frequencies.

DESIGN TRADEOFFS

Design of the S18-4 ZLG was primarily driven by system performance, system size and weight constraints, and cost. The 18-cm pathlength ZLG selected is the minimum pathlength instrument still expected to be able to meet the requirements of a medium accuracy aircraft navigator system. The S18-4 ZLG weighs about 1.5 pounds and dissipates about 1.5 watts of power in an envelope 3.92 inches in diameter and 2.05 inches high. The instruments are designed to be nested together on a sensor block; the three instruments mutually orthogonal to each other. Figure 4 is a photograph of the S18-4 ZLG.

A ZLG-based navigation system has the advantage of reduced coning and sculling errors relative to a dithered RLG navigation system. Low angle random walk makes fast alignment times possible. High bandwidth is achievable if required. Increased angular resolution is possible due to the fact that the ZLG is not mechanically dithered.

Cost and reliability were estimated to be closely comparable for RLG and ZLG technology. Marketability of the ZLG was judged to be superior;

applicability of the ZLG was also judged to be wider ranging particularly in pointing and tracking applications. Opportunity for further performance improvement exists.

INSTRUMENT PERFORMANCE RESULTS

More than 100 S18-4 ZLGs have been fabricated. The data base from these instruments provides a good indication of the expected system level performance. Typical aircraft navigators require bias residuals of less than 0.01 deg/hr, 5-ppm scale factor stability and linearity, and angle random walk of about $0.0015 \text{ deg}/\sqrt{\text{hr}}$ for fast alignment time.

Figure 5 shows the distribution of angle random walk data collected on prototype S18-4 ZLGs. The angle random walk is determined from triangularly filtered high-speed gyro data. The mean angle random walk of the gyros built to date is $0.0013 \text{ deg}/\sqrt{\text{hr}}$, with more than 80% of the population less than $0.0015 \text{ deg}/\sqrt{\text{hr}}$. The numbers agree well with angle random walk predicted from calculations.

Scale factor linearity of ZLGs is excellent. Linearity from 0-400 deg/sec is always well under 1 ppm. Scale factor thermal sensitivity is less than 0.2 ppm/°C. Table 1 shows scale factor linearity and temperature sensitivity for a number of S18-4 prototype ZLGs along with the scale factor thermal residual after a simple linear temperature model ($SF=A+BT$) is applied. Residuals of less than 1.1 ppm are observed.

Bias turn-on to turn-on stability was evaluated by making six drift runs of one hour each at laboratory ambient temperature. The gyro is off for 15 minutes between each test. The average bias of each one-hour run and the standard deviation of the six biases are computed. A histogram of bias turn-on stability for 20 ZLGs is shown in Figure 6.

SYSTEM PERFORMANCE RESULTS

Figure 7 is a photograph of the LN-100 preproduction prototype system. Table 2 is a summary of

Litton ZLG-based systems flights. The average radial error for these 11 flights is 0.42 nmph. Flight 11 is of particular interest as it was a long distance, cross-country flight of six and one-half hours, from Lambert Field, St. Louis, to Van Nuys Airport, Los Angeles. For this flight, a high accuracy Litton LN-94 RLG navigation system was used as a reference system and allowed to warmup for 20 minutes before being aligned for 10 minutes, in parallel with the LN-100 navigation system. The terminal radial error of the LN-94 navigation system was less than 0.6 nm and the velocity errors less than 1 ft/sec so it was decided to difference the two systems outputs to get an indication of LN-100 inflight performance. The differenced radial and velocity errors are shown in Figure 8. Radial error of about 0.5 nmph CEP with velocity errors of less than 2.5 ft/sec rms overall are observed. In fact, for the first two hours the errors are more like 0.2 nmph CEP and 1.5 ft/sec rms.

One advantage of a ZLG-based strapdown inertial navigation system is low inherent noise which makes gyrocompassing faster and smoother. A series of alignments were performed in the lab to investigate LN-100 gyrocompassing capability. The first gyrocompass was from cold turn-on, the rest were done with various off periods ranging from 10 minutes to an hour. Results are shown in Figure 9. As can be seen, the heading comes in smoothly, and is below a milliradian 1σ even at two minutes. Four-minute alignments to less than 0.05 degree were readily achievable and even faster alignment may be possible due to the low angle random walk of the ZLG.

SUMMARY

The theory of operation and performance of Litton's second generation gyroscope, the ZLG, has been reviewed. Instrument and system level data supporting the instruments capability to fulfill the requirements of a medium accuracy aircraft strapdown navigation system have been presented.

TABLE 1. SCALE FACTOR DATA ON S18-4 PROTOTYPE ZLGS
(RATE RANGE $0 \pm 400^\circ/\text{SEC}$)

S/N	Scale Factor Thermal Residual (ppm)	Scale Factor Thermal Sensitivity (ppm/ $^\circ\text{C}$)	Scale Factor Linearity			Scale Factor Asymmetry		
			@ 25 $^\circ\text{C}$ (ppm)	@ 0 $^\circ\text{C}$ (ppm)	@ 50 $^\circ\text{C}$ (ppm)	@ 25 $^\circ\text{C}$ (ppm)	@ 0 $^\circ\text{C}$ (ppm)	@ 50 $^\circ\text{C}$ (ppm)
1003	0.12	-0.07	0.11	0.17	0.13	0.15	0.18	0.13
1008	0.16	0.09	0.07	0.06	0.07	0.03	0.06	0.07
1050	0.18	0.08	0.10	0.11	0.05	0.12	0.16	0.15
1052	0.47	0.12	0.32	0.30	0.14	0.34	0.18	0.19
1055	0.12	-0.01	0.11	0.16	0.11	0.13	0.18	0.14
1056	0.11	0.02	0.10	0.17	0.13	0.12	0.21	0.15
1058	1.08	-0.07	0.33	0.40	0.38	0.41	0.59	0.57
1077	0.24	0.01	0.29	0.28	0.29	0.31	0.33	0.29
1078	0.30	-0.04	0.21	0.20	0.32	0.23	0.19	0.30
1080	0.40	0.17	0.19	0.21	0.25	0.08	0.19	0.15
1202	1.01	-0.12	0.19	0.28	0.41	0.29	0.30	0.44
1214	0.39	-0.03	0.13	0.27	0.09	0.11	0.21	0.10
1215	0.50	0.00	0.12	0.14	0.19	0.17	0.18	0.20
1217	0.28	0.01	0.05	0.06	0.07	0.06	0.07	0.08
1219	0.13	0.20	0.19	0.29	0.16	0.14	0.25	0.18
1230	0.24	0.07	0.28	0.30	0.27	0.26	0.38	0.30
1233	0.37	0.08	0.10	0.06	0.10	0.10	0.06	0.11
1242	0.47	-0.09	0.28	0.22	0.27	0.26	0.12	0.22
1248	0.18	0.00	0.16	0.32	0.18	0.12	0.34	0.20
1249	0.64	-0.04	0.41	0.48	0.35	0.53	0.66	0.55
1005	0.24	-0.03	0.37	0.34	0.47	0.38	0.51	0.41
1017	0.21	-0.00	0.34	0.46	0.31	0.52	0.72	0.50
MEAN	0.359	0.052*	0.202	0.240	0.216	0.221	0.276	0.248
1 σ	0.257	0.080	0.104	0.118	0.120	0.141	0.185	0.150
*Average of absolute value								

TABLE 2. LN-100 FLIGHT TEST RESULTS

Flight No.	Date	Performance, nm/hr CEP	Duration, hrs min
1	5/10/90	0.3 nm/hr	2 hr
2	5/11/90	0.5 nm/hr	1 hr, 25 min
3	5/11/90	0.3 nm/hr	1 hr, 20 min
4	5/14/90	0.7 nm/hr	1 hr, 20 min
5	5/14/90	0.3 nm/hr	2 hr, 15 min
6	8/7/90	0.3 nm/hr	1 hr, 20 min
7	8/8/90	0.4 nm/hr	1 hr, 20 min
8	8/8/90	0.6 nm/hr	1 hr, 40 min
9	10/22/90	0.5 nm/hr	1 hr, 25 min
10	10/24/90	0.3 nm/hr	1 hr, 45 min
11	10/25/90	0.5 nm/hr	6 hr, 30 min

REFERENCES

1. W. W. Chow, et al, "The Ring Laser Gyro," Reviews of Modern Physics, 57, 1, pp 61-104 (1985).
2. W. W. Chow, J. B. Hamberne, T. J. Hutchings, V. Sanders, M. Sargent, and M.O. Scully, "Multioscillator Laser Gyros," IEEE Journal of Quantum Electronics, Vol QE-16, No. 9, pp 918-936 (1980).
3. D. Grant, J. Hamberne, T. Hutchings, V. Sanders, M. Scully, "A Multioscillator (Four-Mode) Ring Laser Gyro Report," Proceedings of the National Aerospace and Electronics Conference (NAECON), pp 1029-1032 (1977).
4. I.W. Smith and T.A. Dorschner, "Biassing the Raytheon Four-Frequency Ring Laser Gyroscope," Laser Inertial Rotation Sensors, SPIE Vol 157, pp 21-29 (1978).
5. H. Statz, T. A. Dorschner, M. Holtz, and I.W. Smith, "The Multioscillator Ring Laser Gyroscope," Laser Handbook, Vol 4, North Holland Press, pp 229-332 (1985).

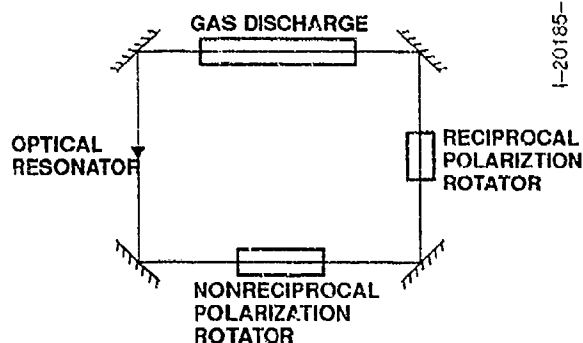


Figure 1. Elements of a Multioscillator Laser Gyroscope. In the ZLG, the reciprocal polarization is supplied by a nonplanar geometry while the nonreciprocal polarization rotation is supplied by a Faraday element

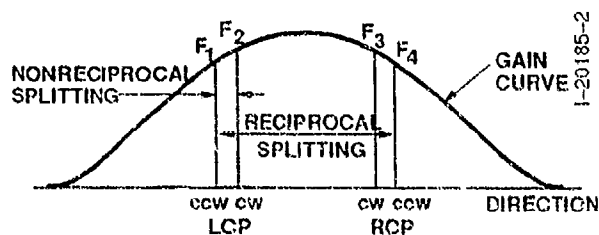


Figure 2. Modes of a Four-Frequency Laser

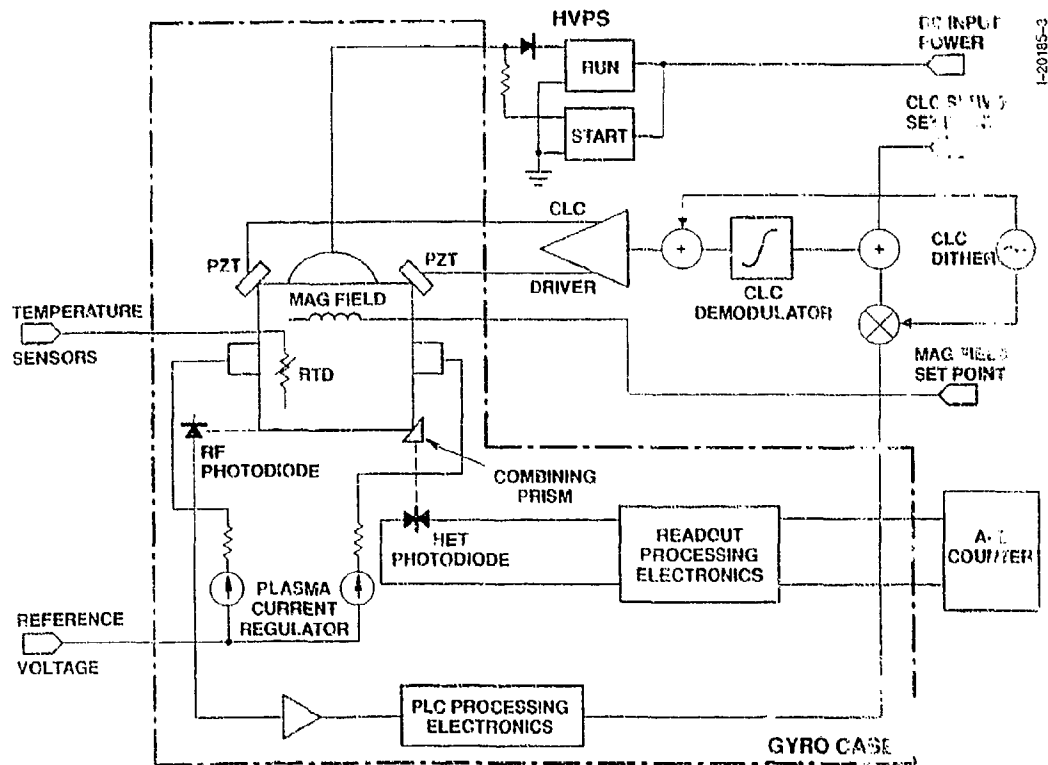


Figure 3. Block Diagram of ZLG

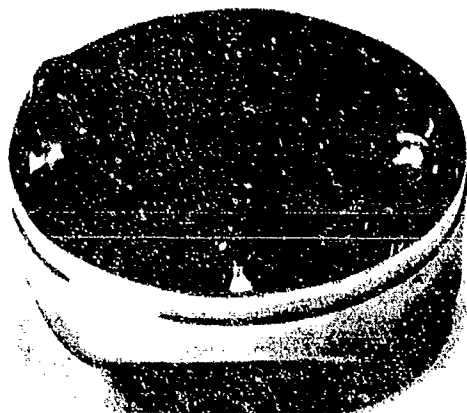


Figure 4. S18-4 ZLG

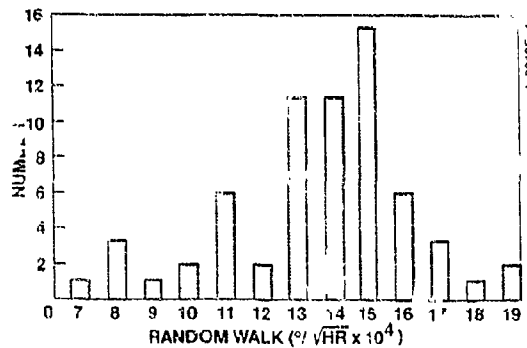


Figure 5. Histogram of Angle Random Walk on Prototype S18-4 ZLGs

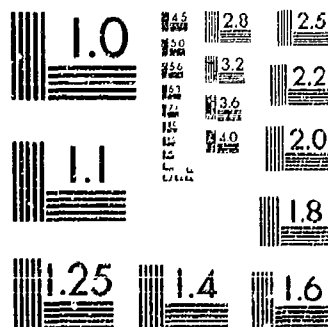
The gyro readout is referenced to the fixed stars since the readout loop is mechanically coupled to the telescope pointed at the guide star Rigel (the readout loop plane is aligned parallel to the telescope axis) and to a star blipper looking approximately normal to the telescope axis. The spacecraft together with the readout loop rolls about the line-of-sight to the star Rigel with a roll period of 10 minutes. The SQUID output is modulated at the 1.67 mHz roll frequency. The amplitude of the 1.67 mHz output is proportional to the angle between the gyro spin axis and the roll axis, and its phase is related to the position of the stars in the field of the star blipper.

Misalignment between the roll axis and the line of-sight to Rigel can be subtracted from the SQUID output using the two-axis telescope readout signals, finally yielding an overall gyro readout.

The opening of the dewar is a necktube where the vacuum probe for the quartz block housing containing the gyroscopes is emplaced. The design of the vacuum probe and necktube represent a formidable physics and engineering challenge. First the assembly must survive launch loads. In addition it must meet the following abbreviated list of requirements: (1) Maintain stable quartz block temperatures of 1.8 °K, (2) Remove spin-up gas rapidly to prevent electrical breakdown, (3) Create an operating vacuum of better than 10^{-11} torr (gyro spin-down time constant is 4000 years), (4) Reduce the magnetic field to 10^{-14} gauss, (5) Minimize the heat leaks into the payload so the superfluid helium lasts 1 to 2 years, (6) Allow "rapid" assembly and disassembly, and (7) support all the interconnecting electrical cabling for the instruments of the stable quartz block assembly, readouts, heaters, thermometers, and other instrumentation (approximately 400 wires):

The evolved design supports the Quartz-Block load with a cantilevered aluminum cylinder. This is within the vacuum shell, both of which are attached at the base of the neck tube assembly. The neck-tube is wound of alumina fibers and bonded with epoxy. This composite material has particularly high thermal resistance combined with high strength over the entire temperature range.

In order to spin up the gyroscopes a system supplying each gyroscope with low temperature (5° - 7°K) helium gas through an in line class 100 articulate filter. Exhaust lines then vent most of the spin up gas to an external thrust nullifier located on the spacecraft. Five heat-exchanger stations allow the warm gyro spin-up gas to be efficiently cooled by the exhaust gas. Leakage gas is pumped out of the neck tube. A large gate valve on the front of the probe is open during spin up to vent to space a residual gas leaking into the probe. After spin-up the probe gate valve is closed and



MICROCOPY RESOLUTION TEST CHART
NATIONAL BUREAU OF STANDARDS-1963-A

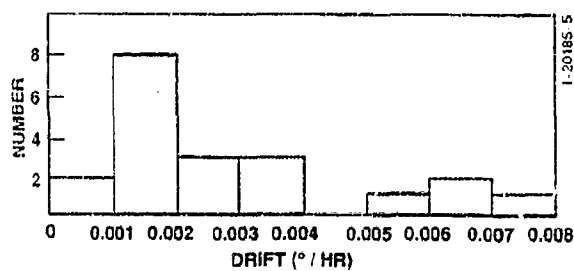


Figure 6. Histogram of Bias Repeatability

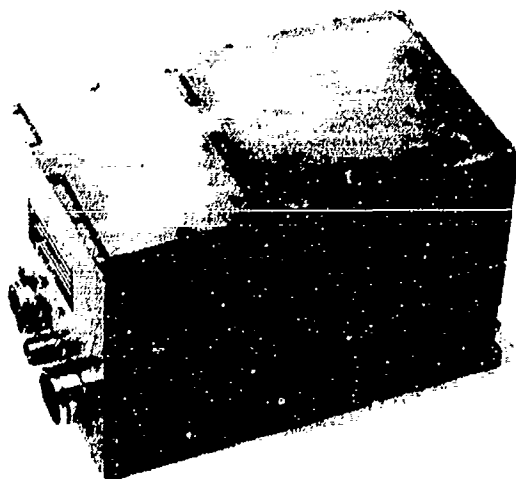


Figure 7. LN-100 Prototype Preproduction Navigation System

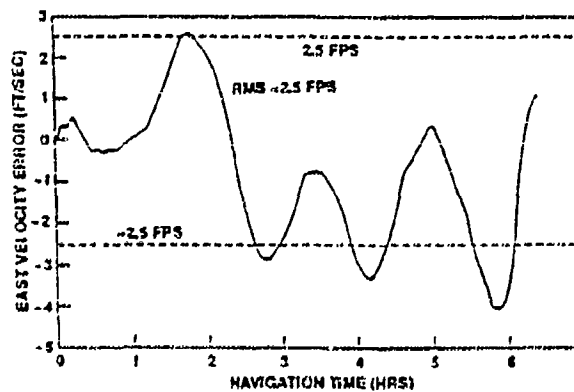
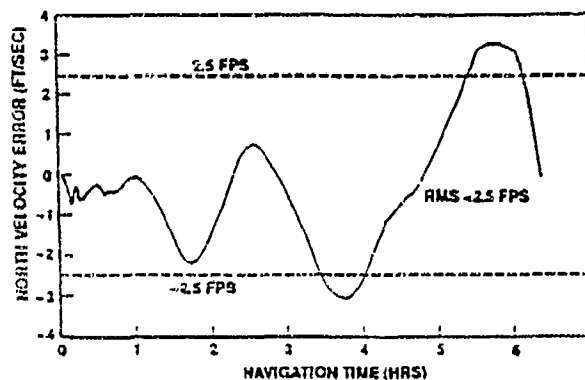
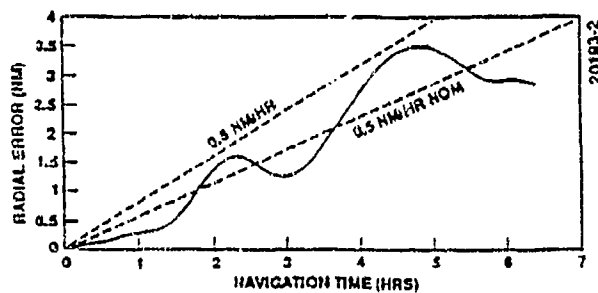


Figure 8. LN-100 Flight Test from St. Louis to Van Nuys

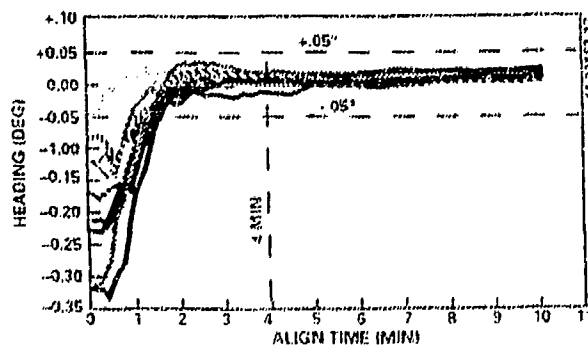


Figure 9. LN-100 Alignment Response Time

SESSION IX-B
GPS USES - TERRAIN SYSTEMS

CHAIRMAN
SAM GEORGE
OC-ALC/MMIRN

ASICs AND BIT/TESTABILITY IN NAVIGATION SYSTEMS

by Jacques A. Tazartes
Litton Systems Inc.
Guidance & Control Systems Division
5500 Canoga Avenue
Woodland Hills, CA 91367-6698

ABSTRACT

Embedding effective BIT and Testability in Navigation Systems could require significant added hardware in discrete circuitry. But ASICs, together with the IEEE P1149 Test bus, have opened new opportunities for BIT and Testability with very little hardware penalty. This paper examines the inherent advantages of BIT/Testability in digital ASICs, and the techniques used. A hurdle to be overcome is the lack of familiarity by many ASIC designers with the P 1149 Bus. A method for designer education is described, as well as the types of trade-offs performed, for the BIT definition and assessment process. Some guidelines are also provided. The problem of BIT and Testability in highly integrated circuits is addressed, because of the high circuit density and the need for numerous test points, then BIT and IEEE P 1149 serial Test Bus concepts are reviewed. A Test controller (TAP) inside the ASIC will reconfigure long counters in small registers which can be tested much faster. It will create some loops to rapidly test the ASIC. Trade-offs on the Boundary Scan technique are performed. The use of a digital ASIC as a board level BIT and Testability controller is then discussed. Circuitry needed to form external test loops is included in the ASIC, BIT effectiveness is evaluated, and guidelines are presented.

INTRODUCTION

Designing Testability and Built-in-Test (BIT) in a system or on a board could bring out the best (or the worst) in a Concurrent Engineering team. The Electronic designer is trying to minimize the additional BIT circuits and Test Points, the Reliability and ESD protection engineers might be cheering him on to minimize the impact on Reliability and ESD. On the other hand, the Testability engineer is presenting a list, reduced to the bare minimum, of 350 Test Points. The BIT and Systems engineers are pushing for a "wall-to-wall" BIT which will automatically test everything and eliminate Test Points, but which requires another dozen chips and the design of a sophisticated additional controller. The Mechanical and EMC engineers are siding with the "minimum test point" group, because of the serious (if not impossible) layout and crosstalk burden brought about by the additional hundreds of traces for those test points and Test connector. Somewhere in the middle is the Manufacturing engineer who is campaigning for In-Circuit Test (ICT) pads. Those pads will eliminate the need for the Test point traces. But the Mechanical engineer senses a new threat to the extremely valuable real-estate available for the Surface Mounted devices (SMD). The Logistics and Maintainability engineers get preoccupied with the fact that those pads may be coated or somewhat unavailable in Field Repair! and so on.

On the face of it, this could be a recipe for internal warfare within the Concurrent Engineering team. And yet, at Litton G/CS, harmony and cooperation manage to emerge from all those conflicting requirements. While making good use of undeniable diplomatic skills, this group has discovered a near-magic potion to spread contentment in the Testability camp: ASICs, Scan testing and Test busses.

The above scenario describes the daily challenge in designing modern military electronic systems and reflects the multiple conflicts to be resolved while designing-in BIT and Testability. These conflicts are being amply documented in the trade literature and in many Design-for-Testability and BIT conferences and workshops. This paper does not intend to retrace the same ground, but focuses on practical solutions used in today's avionics.

PRESENT BIT AND TESTABILITY CHALLENGES

To start with, BIT Fault Detection and Isolation, Testability and Diagnostics performance requirements have been steadily rising to the point of near perfection. Performance requirements of 98%, 99% and even 100% are commonly encountered. As a consequence, BIT and Testability design features have to be more elaborate and have a greater impact on the structure and design of the hardware. In previous generation electronics, with many ICs and components on a single board, a few analog and digital multiplexing chips strategically located on the board provided a major portion of the BIT wraparound test circuits. Similarly, a good solution to Testability was the use of hundreds of Test Points and one or more large Test connectors on a board. With moderate clock speeds and 0.1 or 0.05 inch pitch (component pin center spacing on board), the cross-talk or noise problems were manageable. This is not the case with the present densely packed boards, with Surface Mount Devices (SMDs), 0.02 inch pitch and clock speeds nearing the microwave frequencies. An inch long open test point trace could be a noise antenna! What is the Testability Engineer to do? First solution: In-Circuit test, which applies hundreds of delicate probes ("Bed of nails" fixtures) to the board, with no long traces going to Test Points. But SMDs and 0.02 inch pitch make those fixtures very costly. In addition, pads have to be placed near every component pin being probed, because SMDs cannot be directly probed. Second solution: let the board test itself through BIST (Built-in Self-Test). Such solution is appealing, since it eliminates test points. But additional test circuits, paths, controls, test vector generators must be added, through added components. Cost, Reliability and weight will probably be adversely affected and one should abandon this solution, *unless all added circuitry is housed in one chip: an ASIC*. Better yet, the ASIC which has replaced dozens of ICs, Processors, RAMS, etc. on the board, radically reduces the number of nodes on the board, since many of them have been moved inside the single ASIC. *The ASIC can then be the test controller on the board*, the test vector generator and the component under test. It can even perform feats of near magic: it can modify the circuit to shorten the test process then it can restore it to its operational configuration. But how can the Test engineer, with just a handful of test pins, completely test the whole board? Use a P 1149.1 (JTAG) test bus to introduce in a serial fashion as many test vectors as needed, and configure each IC with Boundary Scan cells.

It should be noted that, similarly to the Testability evolution, BIT faces the never ending challenge of increasing circuit density. In the recent past, it was sufficient for each board to include a few BIT lines allowing an external Maintenance Processor board to remotely run BIT tests (wraparounds, Test words, "canned" operations). Presently, with the considerable increase in gate and transistor density afforded by Very Large Scale Integration, such BIT processes would be either too slow or too superficial. For example, to test to a high degree of confidence a 50,000 gate ASIC, an *external BIT processor*, would be nearly *100 times slower* than an internal test structure using ASIC reconfiguration (because of the greater number of test vectors). It should also be noted that the considerable advantage provided by internal *digital* ASIC reconfiguration is not presently available to the *analog* devices.

With the ASIC, test points are considerably reduced, cross-talk is minimized, BIT performance is much faster and more thorough, board real-estate is saved. Where is the catch? Test Busses, such as the 4-line serial bus described in IEEE Standard P 1149.1, must be introduced, Boundary and Set Scan circuits and cells must be designed in ASICs. Additional silicon must therefore be added inside the ICs to accommodate the test circuitry. Structural changes must be introduced, the impact of the embedded test circuitry on performance must be considered. Additional design effort is required too. Semiconductor manufacturers must acquire a new test philosophy. Additional training is required in all the user and design disciplines.

BIT AND TESTABILITY DESIGN FLOW

MIL-STD-2165 specifies the approach needed to design BIT and Testability into a system. A similar discipline has been in place for many years at Litton G/CS (later formalized in the BIT and Testability sections of the Litton G/CS Best Practices manual). A dedicated Testability Engineering group exists, which is the focal point of all related activities. One of the important features of the BIT/Testability design process is the establishment, from the proposal stage, of a *Testability Team*. A very condensed version of the BIT/Testability design flow is provided in Table 1.

TABLE 1
BIT AND TESTABILITY DESIGN FLOW

- **FORM TESTABILITY TEAM**
- **ISSUE BIT/TESTABILITY DESIGN GUIDELINES PER CUSTOMER REQUIREMENTS**
- **TRAIN DESIGN ENGINEERS IN LATEST TESTABILITY TECHNIQUES (TEST BUS, SCAN, ETC.)**
- **PERFORM TRADE-OFFS AT EVERY STEP OF THE MANUFACTURING AND FIELD FLOW**
- **ESTABLISH TEST AND BIT PHILOSOPHY AND CRITERIA AT EACH STEP OF THE MANUFACTURING AND FIELD FLOW**
- **DESIGN BIT ARCHITECTURE AND TEST FEATURES IN HARDWARE AND SOFTWARE**
- **PERFORM BIT/TESTABILITY ANALYSES TO VERIFY REQUIREMENTS COMPLIANCE**
- **VERIFY BIT AND TESTABILITY PERFORMANCE (TEST)**

TESTABILITY TEAM

Because of their present sophistication and wide application levels, BIT and Testability cannot be confined to a single discipline. They require a Concurrent Engineering process from the proposal stage. This is why a dedicated Testability Team is formed at Litton G/CS for each major project. It is headed by the Testability Engineer and includes, among others: the Systems, Electrical, Mechanical, Maintainability, Test Equipment, Manufacturing, Reliability, Factory Test and Logistics engineers. The team has the specific mission to provide in real time all the requirements and guidance needed at all stages of Hardware and Software design and Verification. The team reports directly to the Project Technical Director.

TEST AND MAINTENANCE CONCEPT DEFINITION AT EACH STEP OF THE LIFE CYCLE FLOW

One of the first Testability Team tasks is the definition, at each step of the Life Cycle flow, from component procurement to Field maintenance, of the Test and Maintenance concepts. They are the source of the BIT and Testability design architecture, partitioning, test point vs BIST distribution, Test busses, ASIC characteristics, etc. Some examples of the considerable importance of such definitions are provided in Table 2.

TABLE 2
EXAMPLES OF TEST CONCEPT INFLUENCE
ON BIT AND TESTABILITY DESIGN

Repairable vs throwaway module: Isolation to the piece part level may or may not be required. This may considerably reduce the need for test points, BIST, or other test overhead.

Best point in the flow for testing a particular feature. An examination of failure modes, yield, cost, etc., may lead to the addition of a particular test during the assembly flow. This may require additional stimuli at the lower level, but may eliminate the need for test points at the higher assembly.

In-Circuit test application: possibility of ICT may reduce the need for additional BIST features.

Speed and/or thoroughness of Power-Up BIT: If very fast, very thorough BIT is required at Power-Up, an internally reconfigurable ASIC may provide an elegant solution.

If emphasis is on In-Flight Fault Detection, ASIC reconfiguration is not a priority. Long wraparound loops within the system are a better solution.

TYPICAL BIT AND TESTABILITY DESIGN TRADE-OFFS

In any carefully designed product, a considerable amount of design trade-offs must be performed for BIT and Testability. Examples of parameters considered are given in Table 3.

SOME SCAN AND TEST BUS STRUCTURES

Hundreds of papers and many volumes have been written on the Scan Path, Boundary Scan, Test Busses, Linear Feedback Shift Registers, Parallel Signature Analyzer, the JTAG and the IEEE P 1149 Test Bus standards. A very brief bibliography is given at the end of this paper. An attempt is made here to place those test structures in the context of this paper.

TEST CONCEPTS

EXHAUSTIVE TESTING: For any type of complex device, this type of test is impractical, as it requires 2^n test vectors, where n is the total combined number of input signals and internal states

FUNCTIONAL TESTING (OR GO-NO GO): It generally exercises the equipment along its functional GO paths. It is often not sufficiently thorough. An exhaustive functional test requires a considerable amount of test vectors and is generally quite expensive.

FAULT GRADING: It is an analytical technique, implemented in CAE, and designed to measure the effectiveness of test vectors in functionally testing a circuit. The grade, which can reach 100%, is the ratio of faults detected to the total number of faults modeled.

IN-CIRCUIT (OR "BED-OF-NAILS") TESTING (ICT): This technique applies to Printed Wiring boards (PCB) only. It uses an elaborate fixture carrying hundreds of delicate probes which inject local stimuli at the pins of each piece part. This method is limited by access problems in high density, small pitch PCBs. This is one example of the "Divide-and-Conquer" concept implemented by the Scan techniques.

SCAN PATH TESTING: It is a serial partitioning method which allows control, stimulus and observation of a circuit along the scan path. A major reason for its success is the economy in test pins and test vectors and its modularity, which allows the test vectors to be reused at several levels. It has a drawback, however: it is slower than the other conventional methods.

BOUNDARY SCAN TESTING: It is a particular application of the Scan Path testing, where each IC I/O pin is equipped with a Scan cell. The latter allows multiplexing of a Test Input stimulus with the normal signal at that pin. This test is particularly advantageous for isolation to the failed component with a minimum number of test points.

TABLE 3

EXAMPLES OF TRADE-OFF PARAMETERS FOR BIT AND TESTABILITY DESIGN

NUMBER OF SYSTEMS PRODUCED:

For a small system quantity, elaborate isolation to the component level or the SRU level may not be needed.

BOARD DENSITY:

Low board density, and/or use of DIPs might favor ICT over Scan methods

APPLICATION:

An I/O intensive board may already have sufficient test points provided by the I/O signals, while a Processor or a Power Supply board may require many internal test points.

ASIC PACKAGE LIMITATIONS:

The internal test-related gates added to the ASIC may cause it to go to the next size, which may be too large to fit or is not available.

ASIC RECURRING/NON RECURRING COST VS SAVINGS:

Cost of designing-in the Scan cells, TAP and test vectors (although the vectors are usually automatically generated) must be traded for the recurring and non-recurring cost savings (Savings in next level Test vectors, in ATE test vectors, test point design, etc.)

THE "DIVIDE AND CONQUER" APPROACH TO ASICS (INTERNAL RECONFIGURATION)

Reference(1) cites the following general rule of thumb to estimate the cost of ATPG and Fault Grading:

$$(1) \text{ Circuit Size}^2 < \text{Fault Grading} + \text{ATPG Costs} < \text{Circuit Size}^3$$

If one applies the above formula to a 10,000 gate ASIC, a 60,000 gate ASIC and a 120,000 gate board (which includes the 60,000 gate ASIC), and assumes that 30,000 test vectors provide at least 95 % Fault Grading to the 10,000 gate ASIC, then the number of test vectors needed to arrive at the 95 % level, for each of the three cases, is listed in Table 4. The right-hand column of the table also lists the estimated number of test vectors which would be required if the ASIC or board were partitioned in 10 or 100 subgroups. Conservative estimates based on formula (1) were used.

TABLE 4
INFLUENCE OF RECONFIGURATION
ON NUMBER OF TEST VECTORS

DEVICE/GATE NUMBER	GATE VECTORS NEEDED	VECTORS NEEDED IF PARTITIONED IN 10/100 SUBGROUPS
Small ASIC/10,000 gates	30,000 vectors	2000/1000 vectors
Large ASIC/60,000 gates	2,700,000 vectors	90,000/9000 vectors
Board/120,000 gates	15,000,000 vectors	500,000/50,000 vectors

P 1149.1, BOUNDARY SCAN, SCAN CELLS, TEST ACCESS PORT (TAP)

A breakthrough in High Density logic PC boards testability was achieved when the Joint Test Action Group (JTAG) and the IEEE P 1149 committees established the present JTAG or P 1149.1 Standard. It defined a 4-line test bus and structure which would essentially multiplex hundreds of parallel test points and dozens of control lines within a PC board into a 4-line bus. It would also allow testing at various levels with the same reusable serial vectors. This enormous economy in test points and more efficient usage of test vectors come at the expense of slower test and additional silicon overhead in each of the logic ICs involved. The merits of such a concept have been widely discussed. This paper will briefly describe the bus elements.

SCAN CELL

It is illustrated in Figure 1 and provides the basic mechanization of the P 1149.1 bus. The Scan Cell multiplexes the Input between the normal functional signal (Normal Data Input, or *NDI*) and the test signal (Test Data Input or *TDI*) It also simultaneously multiplexes the Output between the normal functional signal (Normal Data Output, or *NDO*) and the resulting test signal (Test Data Output or *TDO*) Note that Figure 1 shows a Boundary Scan Cell (BSC) at an Input pin and another at an Output pin. Every pin including in the scan path requires such a BSC. Each IC involved must also include a Test Clock (*TCK*) and a Test Mode Select (*TMS*) pin.

BOUNDARY SCAN ARCHITECTURE

Boundary Scan allows the introduction of Test vectors at any input pin, and the examination of a test output at any output pin. Figure 2 illustrates a typical ASIC Boundary Scan architecture. The test input stimulus is introduced by exercising the Test Clock (*TCK*) and the Test Mode Select (*TMS*), which control the Test Access Port (*TAP*). The latter, in conjunction with the contents of the Instruction Registers (*IR*) embedded in the ASIC, route the serial test vectors injected in the *TDI* through an internal path, which can be as complex and as extensive as the designer wishes. The complete ASIC can therefore be covered by the serial test vectors. Internal reconfiguration is also affected by the *TAP*, which partitions the IC in small groups much more amenable to rapid test with few vectors. Use of Linear Feedback Shift Registers (*LSFR*), and other signature readout methods, among other methods, enable thorough ASIC BIST testing. In fact, it is as if the ASIC contained its internal tester. Since a large ASIC virtually participates in all board activities, it is possible that a series of serial test vectors stored in its ROM or even an external PROM (located on the same board) will perform a set of board level tests, involving the great majority of its components. The ASIC can then essentially test the complete board. In addition, some internal instructions or additional ASIC test pins might place all the ASIC outputs in a High Z state, allowing a microprocessor on that board to run component isolation tests.

It is therefore incumbent upon the Testability/BIST and Electrical design engineers to carefully map the specific ASIC-embedded test circuits (Scan cells, *TAP*, Instruction and Data registers, internal partitioning, fault detection schemes, such as signature analysis or other).

Some disadvantages are listed below:

- The added design effort, which is substantial
- The added training required
- The added silicon (increased chip size, but not necessarily package size)
- The added small increase in ASIC failure rate
- The added 4 bus pins
- The generation of the serial test vectors
- The additional small delay associated with the Boundary Scan pin. For a 1 micron process, it is approximately 0.5 nanosecond per pin. In designs where propagation delays can be in the order of 20 nanoseconds, this will require an additional 5% timing margin. The designer has of course the prerogative to forego testing at pins which are in the timing critical path, which will slightly degrade Testability.

But the following advantages more than compensate for those drawbacks:

- Major ASIC vendors now provide "turnkey" scan cells
- Major ASIC vendors provide design assistance for *TAP* and other testability features
- Major ASIC vendors provide tools for Automatic Test Program Generation (*ATPG*) which greatly simplify vector generation
- The vectors generated at ASIC level, used for ASIC validation, can immediately be reused at board level, thereby reducing the considerable effort of Board level test generation.
- Reliability is virtually not affected by the added test circuits.
- ASIC test and isolation are much more thorough.
- To achieve the same level of BIST at board level, many additional ICs would need to be added, together with many test points.
- Lower Life Cycle cost is achieved through simplification of the Test process

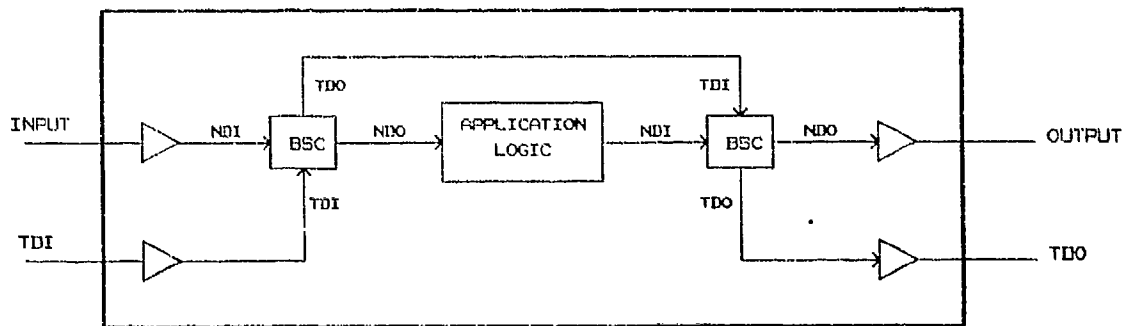


FIGURE 1 - BOUNDARY SCAN EXAMPLE

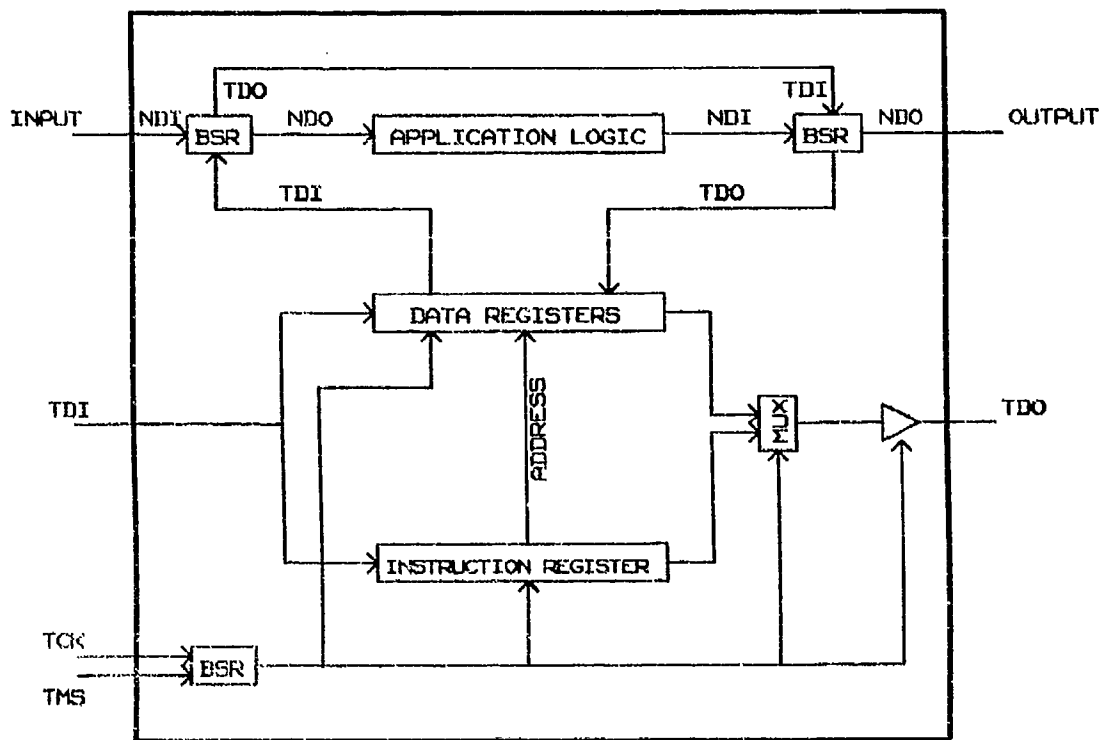
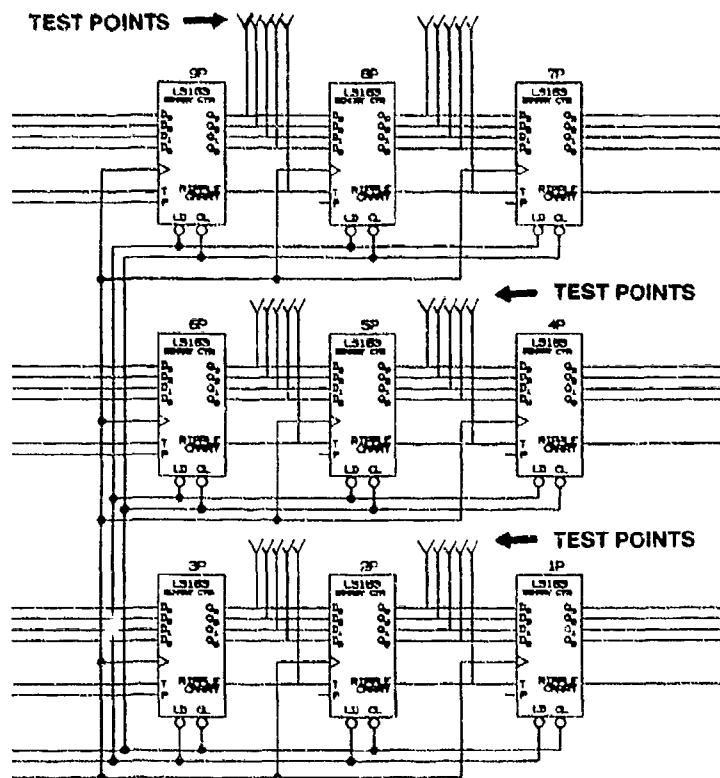
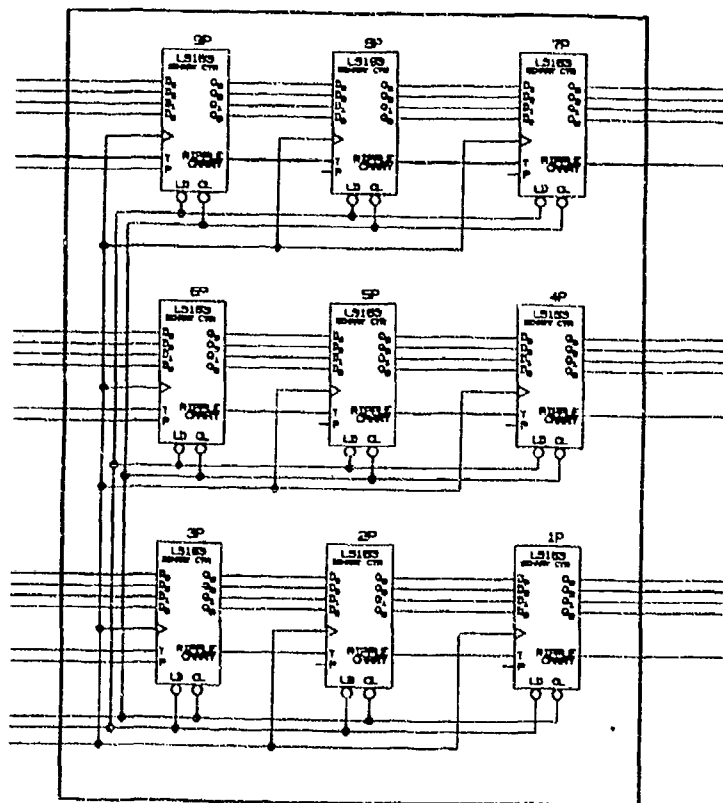


FIGURE 2 - STANDARD ASIC BOUNDARY SCAN ARCHITECTURE

**FIGURE 3A -
NON ASIC BOARD
TEST POINT
REQUIREMENTS**



**FIGURE 3B -
ASIC BOARD
TEST POINT
REQUIREMENTS**



A COMPARATIVE REVIEW OF ASIC AND NON-ASIC TESTABILITY SOLUTIONS

NUMBER OF TEST POINTS

A very simplistic version of the savings afforded is illustrated in Figures 3A and 3B. In Figure 3A, a sample of logic is presented, with intermediate test points required to observe the internal connections between ICs. In Figure 3B, those test points have disappeared, since they are now inside the ASIC. It is no longer necessary to observe them, since no isolation within the ASIC is required. Controllability is of course still required. This is where internal Scan paths provide small partitions which can be controlled with few test vectors.

THE FAILURE RATE DILEMMA

Consider a **50,000 gate digital ASIC**. To obtain a very high level of testability, according to Industry estimates, the Test "overhead" in the ASIC ranges from 10% to 20%. Litton experience confirms that a 10% to 15% overhead is more than adequate. The classic questions are then:

Are the 5000 to 7500 gates added to this ASIC going to significantly degrade the system Reliability?

If Testability is not embedded in the ASIC but scattered among 10 external LSI chips, will Reliability be more or less impacted?

To answer this question, a PC board example was selected, with a 50,000 gate ASIC, as described below, and the conclusions are presented in Table 5. The ASIC Failure rate is calculated under a typical Airborne Inertial Navigation System environment. The simplifying assumptions are indicated in the Table. The conclusion is striking and not surprising: *the testability added to the ASIC has an insignificant effect on system Reliability. By contrast, use of multiple external chips clearly degrades Reliability (5%, in last line of Table 5).*

TABLE 5

COMPARATIVE TESTABILITY FAILURE RATE IMPACT OF ASIC EMBEDDED AND NON-EMBEDDED BIST

ASIC GATES ADDED FOR TESTABILITY	ASIC FAIL. RATE (FPMH)	ASIC % FAIL. RATE INCREASE	BOARD FAIL. RATE (FPMH)	BOARD % FAIL RATE INCREASE
0	2	0%	20	0%
2500 (5% overhead)	2.022	1.1%	20.022	0.10%
5000 (10% overhead)	2.042	2.1%	20.042	0.21%
7500 (15% overhead)	2.064	3.2%	20.064	0.32%
0 ASIC gates 10 external ICs added (1.0 FPMH total added)	2	0%	21.0	5.0%

LIFE CYCLE COST IMPACT OF SCAN/ATPG ASICS VS NON-SCAN/NON-ATPG ASICS

As indicated in Table 4, small ASICs can be adequately tested in conventional ways, without scanning, TAPs or dedicated embedded bus features. Internal ad hoc BIST still needs to be included. But for larger ASICs (i.e. 50,000 gates or more), it is highly advantageous to structure BIST in Scan and TAP format, with extended internal reconfiguration possibilities. Some of the cost trade-off elements involved in the decision are listed in Table 6

TABLE 6
SOME COST TRADE-OFF ELEMENTS IN ASIC
SCAN/TAP USAGE

RECURRING/ NON RECURRING COST	SCAN/TAP/ATPG SOLUTION	CONVENTIONAL SOLUTION
Non-Recurring Cost	Design or purchase of Scan cells	None
Non-Recurring Cost	Design or Purchase of TAP and other ASIC test logic	None
Non-Recurring Cost	Purchase of ATPG CAE tool	None
Non-Recurring Cost	ATPG generation of test vectors	Conventional generation of test vectors
Non-Recurring Cost	Reduced test program cost at PCB because of test vector reuse	PCB test program independent of ASIC vectors
Non-Recurring Cost	Designer training	None
Recurring Cost	Individual ASIC test using the serial test bus.	Individual ASIC test using numerous conventional parallel vectors
Recurring Cost	Small loss in System or Field due to escapes of defective ASICs	Greater losses in System or Field due to escapes of defective ASICs
Recurring Cost	Simplified Isolation test to defective part on PCB	Complex, less efficient Isolation test of defective part on PCB

The following comments apply to Table 6:

Due to the great number of gates in the ASIC, the number of conventional "parallel" test vectors, particularly if they are not generated with some automatic tool, becomes prohibitively large for a 95% confidence level. This probably results in a compromised test effectiveness and greater subsequent cost to correct escapes. Such a cost might become too great if high production rates are involved.

Reuse at PCB and system level of most of the serial vectors generated for the ASIC is a major cost saving, and it probably enhances component isolation performance.

Figure 4 illustrates a qualitative assessment of the influence of ASIC testability philosophy on Life Cycle cost, for a 10,000 and a 60,000 gate ASIC, versus number of systems built. For a 10,000 gate ASIC, the Scan Cell architecture may not be significantly superior, but for a 60,000 gate ASIC, the Scan structure is an economic necessity.

INFLUENCE OF ASIC DESIGN ON SYSTEM BIT CHARACTERISTICS

Table 7 considers the various System and other user requirements and provides a summary of the design solution for an ASIC and a non-ASIC configuration.

TABLE 7

ASIC VS NON-ASIC TESTABILITY FEATURE COMPARISON

PARAMETER	NON ASIC SOLUTION	ASIC SOLUTION
On-Aircraft Fault Detection in Flight	<ul style="list-style-type: none"> o Additional ICs (Wraparounds, Multiplexing). o BIT Failure rate : 2% to 5% 	<ul style="list-style-type: none"> o No additional ICs (Wraparound loops embedded in ASIC). o BIT Failure rate: 1% to 3%
On-Aircraft Fault Detection at Turn-on	<ul style="list-style-type: none"> o On-board Test Vector storage. o Slower self-test (no reconfiguration): Seconds 	<ul style="list-style-type: none"> o Reduced number of Test Vectors o Storage in ASIC o ASIC reconfiguration allows very fast self-test: Milliseconds
On-Aircraft LRU isolation	<ul style="list-style-type: none"> o No significant ASIC impact 	<ul style="list-style-type: none"> o No significant ASIC impact
Off-Aircraft Fault Detection	<ul style="list-style-type: none"> o Major effort required to generate ATE Test Vectors 	<ul style="list-style-type: none"> o Use of P 1149.1 ASIC Test Vectors may reduce Test Vector effort
Board level Fault Detection	<ul style="list-style-type: none"> o In-Circuit (ICT) and Functional tests are satisfactory o Test Vector generation is major task 	<ul style="list-style-type: none"> o Boundary Scan is partial substitute for ICT o ASIC P 1149.1 Test Vectors may be reused (reduces cost)
Board level Fault Isolation to piece-part	<ul style="list-style-type: none"> o Test Connectors and Hundreds of Test Points o Significant Test Vector generation effort 	<ul style="list-style-type: none"> o ASIC Boundary and Level Scan sharply reduce Test Point count o P 1149.1 Test Vectors reused to isolate ASIC
Component level test	<ul style="list-style-type: none"> o Standard tests performed at the Component Vendor. No Cost impact. 	<ul style="list-style-type: none"> o Additional cost to design Scan cells, Test Access Port (TAP) circuits and serial Test Vectors for ASIC.

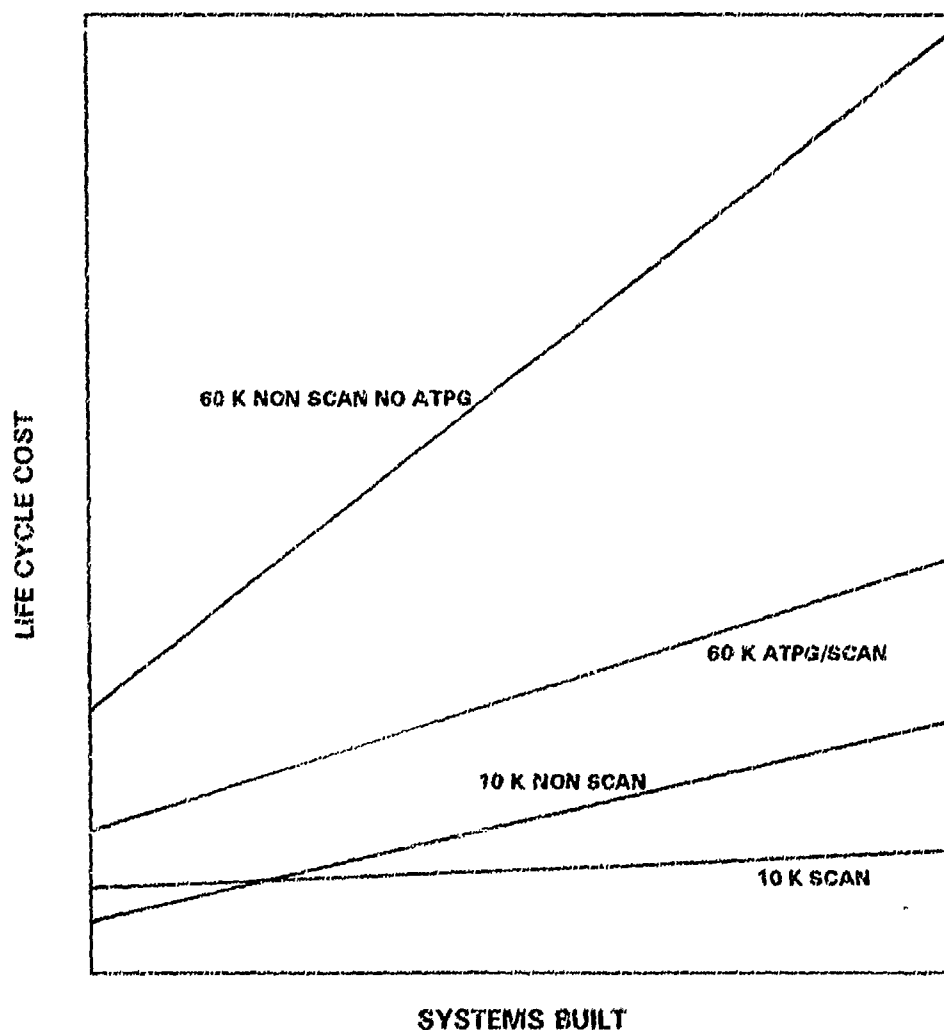


FIGURE 4 - INFLUENCE OF ASIC TEST PHILOSOPHY ON LIFE CYCLE COST

OPTIMIZATION AND ENHANCEMENT OF TEST BUSSES

There are surely more efficient *dedicated* alternatives to the P 1149.1 Test Bus: for example, with a couple of additional *MODE* pins, various *predetermined self-test configurations* can be attained, without the slow process of loading the P 1149.1 Instruction register in a serial fashion, and without some of the additional burden placed on the TAP to reconfigure the whole ASIC. Another very *substantial* way to speed up the ASIC test is to use many of the functional control and address, or even data bus lines, to load *in parallel* (much faster operation) the Test addresses, vectors or controls. Those lines already exist and generally number in the hundreds for a very complex ASIC. But the above very powerful enhancement and speed-up techniques come at the expense of standardization, since the resultant mechanization does not meet the P 1149.1 standard (i.e. the Test Clock, Data In and Out must be completely independent of the functional circuits. That is, when the P 1149.1 *MODE (TMS)* pin is set in the Test position, no functional pin or clock can influence the test).

The question is then: In a highly dedicated and specialized application where a single ASIC is used on a special purpose board, what advantage does the P 1149.1 standard provide? This is where the initial Testability Team ground work becomes crucial, in the definition of the Life Cycle Test concept. If in this concept the opportunity of P 1149.1 use is minimal, then it is advantageous both for the Contractor and the Customer that an enhanced test configuration be used.

TRAINING THE DESIGNER

Most Systems and Electrical design engineers have been exposed to the classic test concepts of test points and some BIT, but they are somewhat uncomfortable with the latest concepts of BIST and of Testability designed in ASICs. The Test bus and Scan techniques are a field in themselves and need to be learned. This would happen, given enough time. But the need is immediate, and the process must be "jumpstarted". Litton G/CS created a "P 1149 Team" composed of a selected set of representatives of different disciplines. The results were extremely good: beside a detailed understanding of the P 1149 standard, this group is enthusiastically propagating the Testability concepts in ASICs. It also serves as a panel of experts which are called upon during the Testability design reviews.

BIT AND TESTABILITY EFFECTIVENESS EVALUATION

The BIT and Testability evaluation methods are important for complex ASICs, since their size is too extensive for a completely manual assessment. New CAE tools are starting to appear, to supplement the ones already in use. The following is an overview of the BIT and Testability assessment techniques:

Fault Grading: This is a standard method by which ASIC test effectiveness is measured, and is routinely used at Litton G/CS. For a given set of test vectors, it inserts faults in the ASIC model and declares detection if any of the output conditions has changed. But several drawbacks make this method less than satisfactory for accurate determination of BIT/Testability performance.

This process is dependent on the test vectors selected. The ones used for stand-alone ASIC test are completely inappropriate for simulation of Flight conditions. Actual In-Flight vectors must be used, which are often a small subset of the Component test vectors, and will probably yield a poor detection. Is this result credible? Certainly not, because the system test vectors are the only ones that matter In-Flight. The first conclusion is that, the *In-Flight Fault Detection Ratio (FDR) must be normalized to its test vectors only.* But another objection can be made: to determine Fault Detection performance, the CAE model verifies, for each fault inserted, if any change appears at the outputs. But the system BIT may not be looking at all the changes, and may therefore miss some. System BIT design and behavior must therefore be accounted for. And yet another problem appears: *Not all faults are created equal.* A least significant bit in a data word with 4 bit accuracy is essentially irrelevant from a Fault Detection viewpoint, since no system performance is lost. A Fault Grading assessment is therefore too pessimistic here. As it is by now apparent, a more System oriented approach is required.

System oriented BIT analysis: A System oriented BIT analysis conducted in an FMECA fashion is desirable, but is not practical on an ASIC, because of the high device complexity. A combination of Fault Grading and System oriented BIT analysis can be conducted on a random sample of faults. For each fault, a system level analysis will be conducted to determine the System and BIT responses. This is a tedious but achievable task.

Mixed level/Mixed signal System Fault Simulation: There is presently no practical Mixed Signal/Mixed level Fault Simulation which can accurately simulate an Inertial Navigation system. It is conceivable that in the near future a combination of System High level language modeling and ASIC level Fault Simulation will be achieved. This will provide the most accurate assessment.

CONCLUSION

The advent of high density packaging and high gate count ASICs have precipitated a series of technical solutions and innovations in the areas of BIT and Testability, which in turn have favored even higher densities. The JTAG and the IEEE P 1149 committees have defined effective solutions to the ever spiraling test point problem. They include: use of highly testable and reconfigurable structures within the ASIC, providing the device with a 4-pin serial Test bus, with embedded Test Access Port, Scan cells and other test functions, and reusable test vectors. The significant problem of educating the designer in the advanced testability concepts was successfully resolved by creation of a team. It is accurate to state that such solutions are presently the best path towards highly testable and BIT capable Inertial Navigation systems.

GLOSSARY

ASIC	Application Specific Integrated Circuit
ATE	Automatic Test Equipment
ATPG	Automated Test Pattern Generation
BIST	Built-In-Self-Test
BIT	Built-In-Test
CAE	Computer Aided Electronic design
EMC	Electromagnetic Compatibility
ESD	Electrostatic Discharge
ICT	In-Circuit-Test (Often called "Bed-of-Nails")
PCB	Printed Wiring board, Printed Circuit board
P 1149.1	IEEE Standard for a 4-line serial bus
SMD	Surface Mounted Device
TAP	Test Access Port

REFERENCES

- 1- Texas Instruments, "Testability: Test and Evaluation" Primer SSYA002, 1989
- 2- McClean, Don and Romeu, Javier, "Design for Testability with JTAG Test Methods", *Electronic Design*, June 8, 1989, pp. 67-71
- 3- Kinnucan, Paul, "Boundary Scan Makes an Impact on Military ATE", *Military and Aerospace Electronics*, Sept 1990, pp. 37-40.
- 4- Fasang, Patrick P., "Boundary scan addresses parametric test issues", *ASIC Technology and News*, Oct. 1990, pp. 22-23.
- 5- JTAG Boundary-Scan Architecture Standard Proposal, Version 2.0, *Technical Subcommittee of the Joint Test Action Group*, 30 March 1988.
- 6- Texas Instruments, SCOPE Testability Products, Applications Guide, 1990

Honeywell



**INS AND GPS
COMPETITIVE OR SYNERGISTIC?
~ AN OVERVIEW ~**

BY

**MICHAEL J. HADFIELD
GLENN R. QUASIUS**

**HONEYWELL MILITARY AVIONICS
CLEARWATER, FLORIDA**

Honeywell



GPS/INS APPLICATIONS

- **Missions**
 - Aircraft Navigators
 - Land Survey Systems
 - Land Vehicle Navigators
 - Tactical Missiles/RPVs
- **Inertial Navigator Types**
 - Strapdown
 - Gimbaled
- **GPS Types**
 - C/A Code to P-Code
 - Single to Multi-Channel

Honeywell



DEGREES OF GPS/INS INTEGRATION

Simplest —————> **Complex**

Hardware

**Separate INS/GPS
Simple Antennas**



**Integrated or
Combined Boxes**



**Integrated
Control,
Displays,
Steerable
Antennas**

Functions

GPS Provides Position

INS Provides Velocity and Attitude

Bootstrap Velocity

Integrated But Separate Filters

Aided Acquisition

Aided Tracking

Adaptive Tracking

Antenna Control

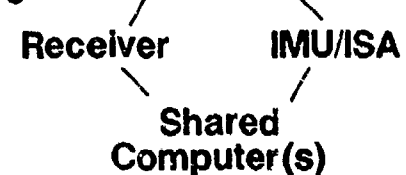
GPS/INS SYNERGISM ISSUES

- **Errors of Integrated or Combined System Better Than Either on a "Stand-Alone" Basis**

"Combined" GPS/INS



"Integrated" GPS/INS



- **INS Aids GPS and Reduces:**
 - Jamming Effectiveness
 - Vehicle Maneuver Sensitivity
 - Velocity Errors
- **GPS Aids INS in Longer Term Navigation Performance Even If GPS Only Intermittent**
 - Good Kalman Filtering
 - INS Error Source Trimming
- **GPS Improves INS Airborne Align Time and Accuracy**
- **INS Can Improve Pointing of Narrow Beam GPS Antennas (Especially a Strapdown INS)**
- **INS Speeds Up Acquisition or Re-Acquisition of GPS Signals**

Honeywell



INS ADVANTAGES

- **Totally Self-Contained, Autonomous Operation**
- **Autopilot Functions With Strapdown INS**
- **Three Axis Attitude Outputs**
- **Fast Reaction Time (Particularly With Ring Laser Gyro Systems)**
- **Continuous, High Frequency Data**
- **Insensitive to Vehicle Maneuvers and Environments**
- **Faster, More Productive Land Survey — Positioning and Pointing**

INS DISADVANTAGES

- **Error Growth vs Time and Distance Traveled**
 - **Position**
 - **Velocity**
 - **Attitude**
- **Needs Initialization (Starting Coordinates and Alignment Technique)**
- **Accuracy vs Cost Sensitivity**
- **Generally Higher Cost Per Unit Than GPS User Equipment (At Least On a Projected Future Cost Basis)**

Honeywell



GPS ADVANTAGES

- **Bounded High Accuracy Position**
- **Velocity Data Available**
- **Relatively Lower Cost for User Equipment**
- **Anticipated High Equipment Reliability**
- **Can Establish Land Positioning/Survey Control Data Where None Otherwise Available (vs INS Function as Basically an Interpolator or Extrapolator)**

GPS DISADVANTAGES

- **Fade-Outs or Blackouts**
 - **Urban Areas**
 - **Mountainous Terrain**
 - **Heavy Forests and Jungles**
 - **Some Geographical Areas**
 - **Antenna/Satellite LOS Shading With Vehicle Maneuvers**
 - **Deep Sub-Surface Operation**
- **Attitude/Attitude Rate Measurement Limitations**
- **Vulnerability — Dependence Upon Satellite Availability**
- **Jammable — From Signal Deterioration to Complete Loss Is Possible**
- **Can Stand Alone in Benign Environment But Needs Help in a Dynamic and/or Noisy One**
- **Relatively Low Information Rates**
- **Limited Availability of Military Channel (P-Code)**

FACTORS IN GPS/INS INTEGRATION

- **Stand-Alone Fallback Capability**
- **Time Tagging and/or Synchronization**
- **Sensor, Data and Algorithm Resolutions**
- **Update Rate vs Navigation Filter States**
- **Functional Partitioning**
- **Inertial Sensor Technology and Mechanization**
- **Single vs Multiple Channel GPS**

Honeywell



NAV PRECISION/GPS TRADES

- **GPS With High Precision (0.1 NMPH) INS**
 - **INS Performance Monitoring**
 - **Intermittent Use Practical**
 - **In Flight Upgrading/Trimming**
 - **“Bootstrap” — Aiding of GPS Code Loops**
 - **Land Survey Implications**
 - **GPS Primary Control**
 - **INS Densification or Secondary Control**



NAV PRECISION/GPS TRADES (Continued)

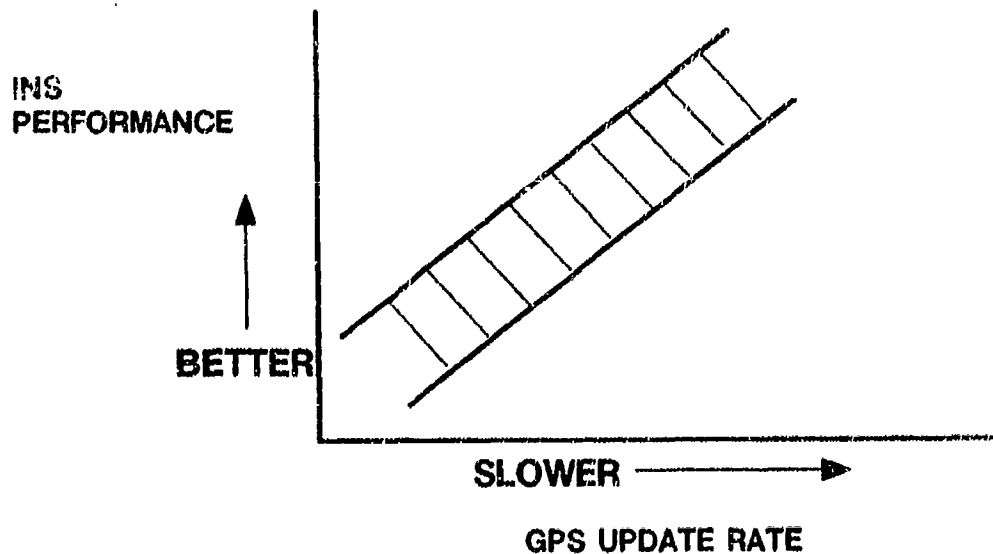
- **GPS With Moderate Accuracy (<1.0 NMPH) INS**
 - **Aircraft Nav Accuracy vs Weapon Delivery Accuracy, Complexity, Seekers**
 - **Operations With Adverse Jamming Conditions**
- **GPS With Low Accuracy (10 + NMPH) INS**
 - **Trim Nav Accuracy vs Terminal Seeker Basket Size/Complexity**
 - **Operations With Adverse Jamming Conditions**



GPS/INS USE IN TACTICAL MISSILES (10 TO 300 NMPH INS'S)

- **Characteristics**
 - Short Flights — A Few Minutes
 - Fast GPS Acquisition Is Critical
 - Small Size — Low Weight
 - Often Have Terminal Seekers
 - INS Used For Guidance, Nav, Flt Control
- **GPS Aiding Allows:**
 - Bounding Position Error
 - May Eliminate Terminal Seeker or Significantly Reduce Its Complexity/Acquisition Basket Size
 - Trim of INS Errors/Calibration/Alignment
 - Use of Far Less Precise INS For Lower Overall Avionics Cost

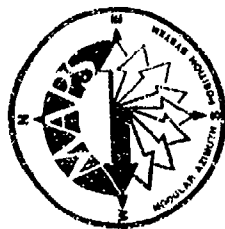
INS VERSUS GPS UPDATE RATE



For INS Position Error Clamping

- Low GPS Update Rates
- P-Code Improves Trimming/Damping
- Single Channel GPS More Usable If An INS Is Available

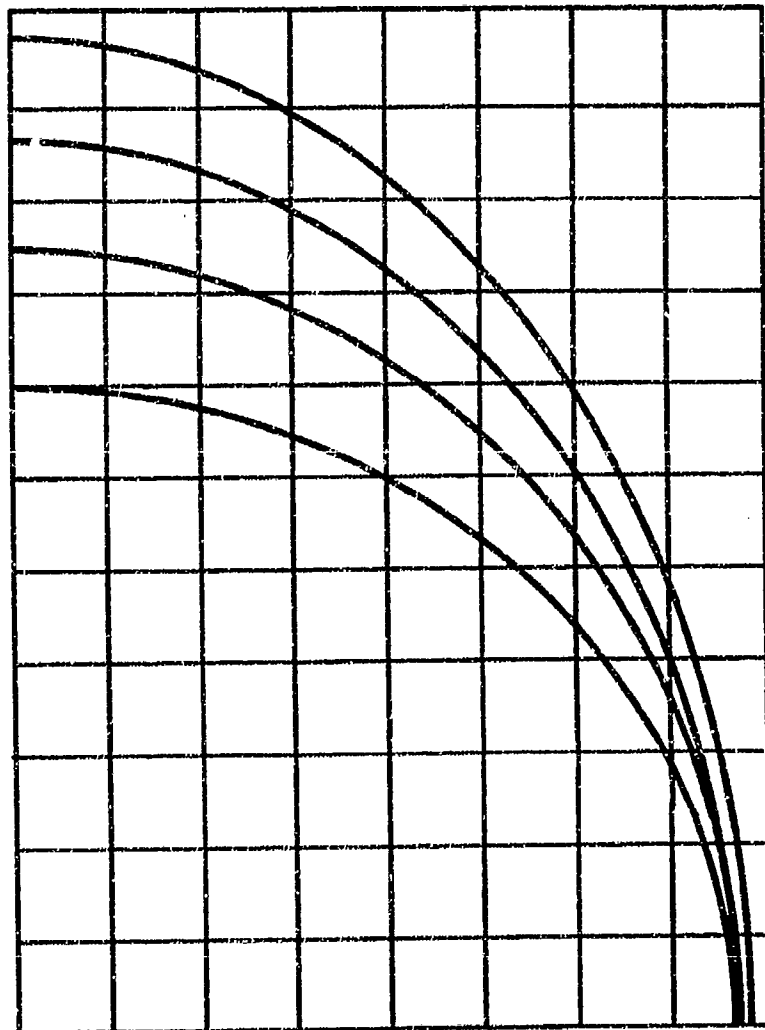
Good Velocity Needs More GPS Channels



SYSTEM PERFORMANCE AFTER GPS LOSS CRUISE PROFILE WITH AIRBORNE ALIGN/TRIM

moneywell

N52763



POSITION ERROR

TIME AFTER GPS LOSS

COMBINED GPS/INS SYSTEM ADVANTAGES

INS AIDS GPS AND REDUCES:

- **JAMMING EFFECTIVENESS**
- **VEHICLE MANEUVER SENSITIVITY**
- **VELOCITY ERRORS**

GPS AIDS IN LONGER TERM NAVIGATION PERFORMANCE

- **GPS INTERMITTENT**
- **GOOD KALMAN FILTERING**
- **RLS ERROR SOURCE TRIMMING**

GPS IMPROVES INS AIRBORNE ALIGN TIME AND ACCURACY



SUMMARY

- **INS And GPS Are Synergistic Not Competitive, (Each Can Compensate the Other's Shortcomings)**
- **The Specific Application Drives the Complexity, Degree, and Cost of Integration or Combination**
- **Need for Autonomous Operation and High Speed Continuous Data Are Key INS Advantages**
- **Low Cost, High Accuracy Positioning Is the Key GPS Advantage**

FLIGHT TESTING A TERRAIN REFERENCED NAVIGATION SYSTEM

Roger Blasius
6510 Test Wing/DORN
Air Force Flight Test Center
Edwards AFB, California 93523

INTRODUCTION

This paper discusses the testing techniques and challenges involved in flight testing Terrain Referenced Navigation (TRN) systems for tactical aircraft. There are many algorithms in existence which utilize a radar altimeter, inertial navigation unit, and a digital terrain data base to perform a terrain profile correlation for a navigational position estimation. The most well known algorithms are Sandia Inertial Terrain-Aided Navigation (SITAN), Stock Pot Algorithm for Terrain Aided Navigation (SPARTAN), and Terrain Profile Matching (TERPROM). The Advanced Fighter Technology Integration (AFTI)/F-16 has flight tested two of these systems, SITAN and SPARTAN, and will be testing an Enhanced SITAN (ESITAN) within the next year. This paper focuses on the knowledge gained on TRN systems and some of the problems encountered in flight testing these types of systems. This paper also discusses the future testing techniques for ESITAN and TRN systems in general.

The primary goal of these TRN algorithms is to provide autonomous and accurate navigation for terrain following and/or target acquisition. These systems allow the aircraft to traverse the data base in any direction. The algorithm must also be robust and capable of handling the performance envelope of modern tactical fighter aircraft.

Although, many papers have been written on these TRN systems and studies have been conducted in the simulators, actual flight tests on these systems has been limited. The AFTI/F-16 program has produced a large part of the flight test data on these systems.

In general, each system is based on one or more Kalman filters which compare the measured terrain profile from the radar altimeter with a digital terrain elevation data base. Each system somewhat differs in acquisition logic and the parameters which are used by the Kalman filter. See References 1, 2, and 3 for a detailed description of each algorithm.

HISTORY

The AFTI/F-16 program tested the SITAN algorithm which was hosted by the Harris Digital

Terrain Management and Display System (DTMDS) and the SPARTAN algorithm hosted by the GEC Digital Terrain System (DTS).

The AFTI/F-16 program conducted a limited evaluation of the SITAN algorithm during the Automated Maneuvering Attack System (AMAS) phase from 31 July 1984 to 2 April 1987. The SITAN flight testing was not the primary objective, but data was collected on parts of six flights totalling about 2 hours of usable data. At the conclusion of the AMAS phase, the DTMDS and SITAN were immature and experienced many integration problems. The results from the AMAS phase were documented in the AFTI/F-16 AMAS Avionics Evaluation and System Integration Technical Report (Reference 4) and the AFTI/SITAN Final Report (Reference 5).

The AFTI/F-16 Close Air Support (CAS) 1 phase began 15 January 1988 and built upon the AFTI/F-16 AMAS design. The overall objective of the AFTI/F-16 CAS flight test program was to examine, develop, and demonstrate individual technologies and integrated systems for the CAS mission. The Harris DTMDS and SITAN continued to be utilized during the CAS phase. Some effort was made to fix the integration problems with SITAN and the DTMDS, although it was minimal. All of the SITAN data collected during the CAS 1 phase was to investigate the integration problems.

Testing of the GEC DTS with the SPARTAN algorithm began with the CAS 1A phase in December 1988. The test program consisted of 45 flights that were conducted between 14 December 1988 and 12 December 1989. The major objectives of these tests were to evaluate the TRN and terrain following (TF) performance and the color map display. The results from these flight tests were documented in AFTI/F-16 CAS Block 1A DTS Evaluation (Reference 6) which contained about 2 hours of TRN data.

Some data for a follow-on SITAN evaluation were also collected during the CAS 1A phase, although the results were still corrupted by the integration problems. The flight tests for SITAN were oriented towards research and development, whereas the SPARTAN flight tests were an evaluation of a complete system. The SITAN and the DTMDS did not support a TF function.

FLIGHT TEST TECHNIQUE

The flight testing of SITAN and SPARTAN began with evaluating the tracking accuracy over different terrain types. The TRN navigational accuracy was considered the overall performance measure and was evaluated by comparing the TRN position to radar time, space, and position information (TSPI) data. The TSPI data was accurate ground based radar or optical tracking of the aircraft position correlated with time for post flight analysis with the onboard aircraft parameters. The available radar TSPI tracking was extremely limited for most low-level routes.

The TRN, TSPI and inertial navigation unit (INU) positions were converted to the same geodetic coordinate system. The respective errors in degrees latitude and longitude were converted to feet. The INU errors were useful in identifying poor TSPI tracking. The INU error should have resembled a Schuler cycle and any sharp deviations from a smooth curve were identified as possible TSPI drop outs. The time slices of TSPI drop outs were removed from analysis. Runs with repeated drop outs were not used.

GENERAL PERFORMANCE CHARACTERISTICS

Terrain Variation

Neither SITAN nor SPARTAN operated satisfactorily in the flat terrain in the immediate Edwards AFB area. Each system had the ability to coast while traversing flat terrain, but this was only possible once a track had been established over moderate or rough terrain. Extended periods of time over flat terrain severely degraded the accuracy and even caused the systems to reinitialize because they lost track. Neither system could acquire track if reinitialized and flown over only flat terrain due to the ambiguities in the comparison of the measured terrain profile to the stored data base. The flat terrain in the Edwards area was usually much less than 2 percent, and there were no transitional terrain types, such as gently rolling hills, between the extremely flat and moderate terrain profiles. Terrain types such as gently rolling hills need to be tested. Different terrain types, especially in the smooth to moderate range, may be one of the areas in which the different algorithms might exhibit different performance characteristics in transitioning to satisfactory tracking.

Altitude Effects

The height above ground level (AGL) of the aircraft was important to the performance of each system. As the aircraft altitude increased, the radar

altimeter footprint became larger. The radar altimeter gave the closest return within the footprint, which may not have been directly beneath the aircraft. The higher altitudes caused a degraded ground profile as measured by the radar altimeter and consequently degraded the TRN algorithm's performance.

One of the TRN algorithms was mechanized to not accept AGL altitudes above 2000 feet, so the algorithm did not update above 2000 feet AGL. The algorithm always performed satisfactory below 2000 feet AGL over moderate and rough terrain. An interesting result was the average accuracy at 1000 feet AGL and below was fairly consistent (141 feet), but the average tracking accuracy at 2000 feet AGL was over twice as much (325 feet). This AGL altitude effect was a function of the AGL altitude sensor (radar altimeter). A narrow beam AGL altitude sensor could improve this performance and perhaps offer a medium altitude capability.

Tracking Convergence

A TRN algorithm must converge quickly to a tracking solution to be operationally useful. The tracking convergence time is an aspect in which TRN algorithms may differ, because of the different acquisition approaches and logic. There may also be a trade off of how quick the algorithm converges to a tracking solution and the chance that it may be the wrong solution or false track. This aspect of a TRN system was probably one of the most noticeable system characteristics and had the greatest chance of potential mission impact.

The SPARTAN algorithm usually converged to an accurate tracking solution in about 30 seconds over moderate and rough terrain. This convergence time was acceptable for most CAS scenarios, although the pilot had to manually fly the airplane without the help of the TF system until high confidence in the tracking solution was reached. The TF system did not provide TF cues until TRN high confidence was reached. The SITAN tracking convergence was not specifically tested.

Confidence Factor

The SPARTAN TRN algorithm also supported a TF function with an estimation of the accuracy of the TRN position. Tracking convergence as discussed in the previous paragraphs was characterized by a horizontal TRN confidence factor below 426 feet (130 meters). The confidence factors were computed as a linear distance and meant the TRN algorithm was 90 percent sure that the TRN horizontal and vertical

positions were less than their respective confidence factors. The SPARTAN computed a horizontal and a vertical confidence factor for the TRN horizontal position and TRN altitude estimation.

The confidence factors were almost as important as the accuracy itself. False fixing or high confidence in a bad position estimate was considered poor performance and may have produced a catastrophic effect during TF. The TRN horizontal confidence factor and accuracy were evaluated and verified before TF testing was started. The SPARTAN TRN confidence factors satisfactorily supported the TF function. Figure 1 shows the SPARTAN tracking accuracy and confidence factor during tracking convergence.

TECHNICAL CHALLENGES

Evaluating The TRN Altitude

Both SITAN and SPARTAN also computed a TRN corrected mean sea level (MSL) altitude to correct the pressure altitude for nonstandard day conditions. The following is a simplified description of the principles involved in calculating a TRN altitude. In general, the pressure altitude was sufficient to generate a ground profile with the radar altimeter. However, once the TRN horizontal position was established, the height AGL from the radar altimeter may be added to the data base elevation at the TRN position to generate a corrected TRN MSL altitude. The TRN altitude was one of the parameters used to generate the TF command in the SPARTAN algorithm. Poor performance of the TRN altitude would have had a direct impact on TF performance.

Accurately evaluating the TRN altitude was difficult at the AFFTC. The TSPI radar was not accurate enough to evaluate the TRN altitude, and the accuracy required was only available over flat terrain with cinetheodolite (optical) TSPI. None of the SITAN altitude testing was performed with cinetheodolite TSPI. The SITAN altitude data that was collected with the radar TSPI indicated the SITAN altitude error was less than or equal to the order of magnitude of the error of the TSPI radar (approximately 25 feet).

Figure 2 shows the TRN vertical accuracy of the SPARTAN algorithm with cinetheodolite TSPI over the Haystack Butte route which was flat terrain with an isolated obstacle. The vertical accuracy was satisfactory under these flight conditions, although this was only a small portion of the all possible combinations of terrain types and aircraft flight conditions.

The TRN vertical confidence and accuracy was not adversely affected by flat terrain. Even with poor horizontal confidence and accuracy over flat terrain, the TRN altitude was accurate because the flat terrain generated a relatively constant terrain elevation.

There were many factors that could have influenced the accuracy of the TRN altitude (data base accuracy, pressure altitude, radar altimeter characteristics). The effects of these factors individually or in combinations will be extremely important if the TRN altitude estimation is used for digital data base TF.

Characterizing the Digital Terrain Data Base

Both SITAN and SPARTAN used the Defense Mapping Agency (DMA) Level I Digital Terrain Elevation Data base (DTED). The Level I DTED was the least accurate elevation data base, but it had the most complete area coverage. Level I DTED was designed to be used on simulators and mission planning stations. The DTED Level I incorporated data from many sources from cartographic (digitized paper maps) to more modern methods. The DTED Level I is updated quarterly as more accurate data becomes available. More detailed information on Level I DTED may be found in DMA Digital Data Information Sheet for DTED Level I (Reference 7).

The Level I DTED has been suitable for proof of concept testing of these TRN algorithms. However, direct comparisons between the algorithms may not be valid, because each algorithm was tested with a different release of the DTED. Also, the operational capability and performance of these algorithms cannot be evaluated unless operational type data is used for the flight test. The need for a new DTED standard or a change to the Level I standards is even more evident considering that the data bases are also used for a TF function. The TRN and TF algorithms must be developed in parallel with data bases that they will use.

Data Base Manipulation

The DTED contained 1.44 million elevation posts in a 1 by 1 degree cell of latitude and longitude. The data bases used by SITAN and SPARTAN were roughly 2 degrees of latitude by 3 degrees of longitude.

The SITAN algorithm was designed to work in a Transverse Mercator grid coordinate system instead of a geodetic system. This required the 3 arc-second DTED to be interpolated to a 100 meter Transverse Mercator grid. The data was then compressed through a software algorithm and loaded onto two cartridge tapes. Figure 3 shows the SITAN data flow including

AFTI/F-16
SPARTAN TERRAIN REFERENCED NAVIGATION
SALTDAL E LOW LEVEL ROUTE
360 KGS/500 FT AGL

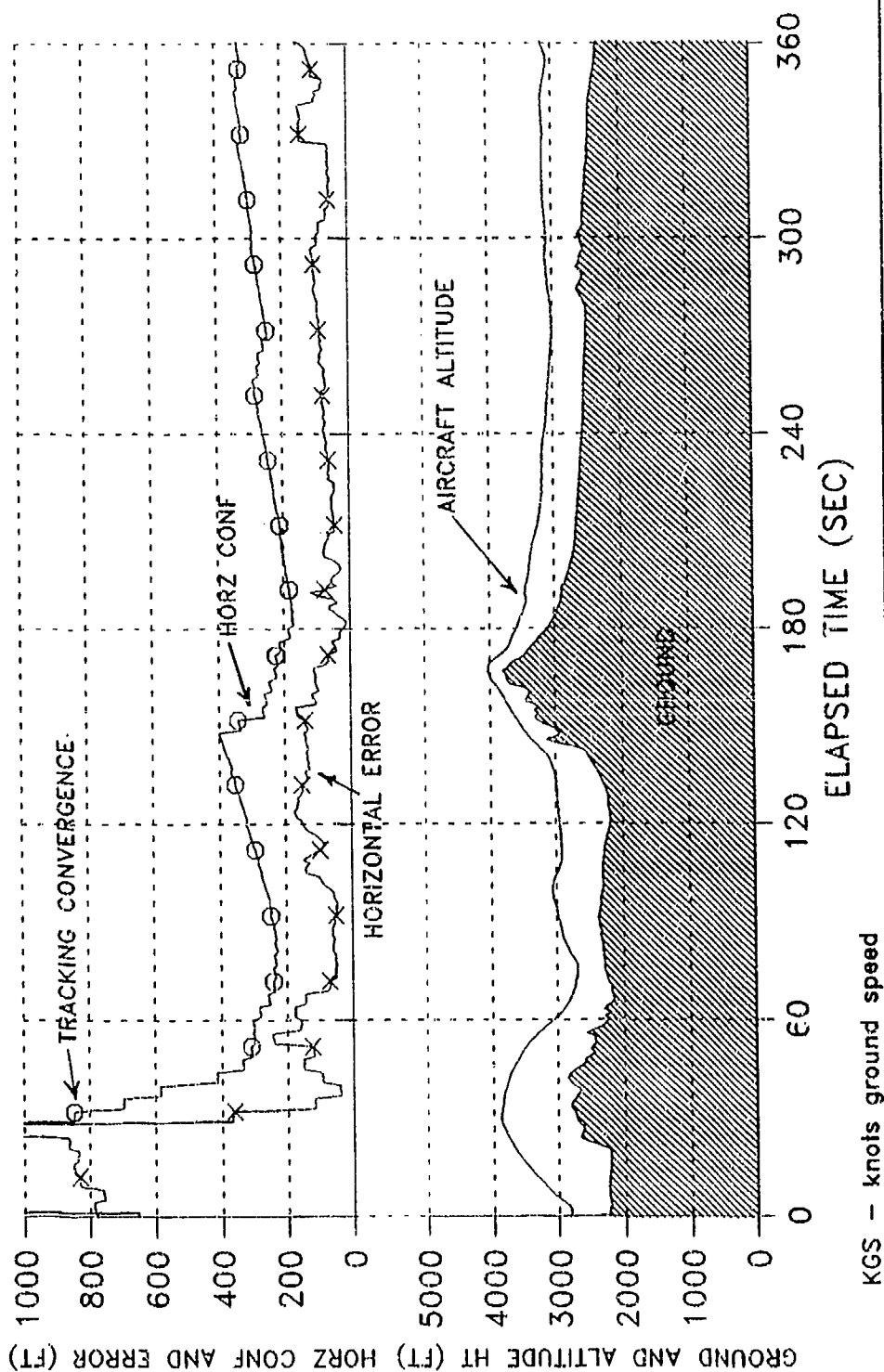
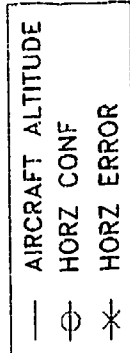


Figure 1 - SPARTAN Moderate Terrain TRN Performance

AFTI/F-16
SPARTAN TERRAIN REFERENCED NAVIGATION
VERTICAL ACCURACY FLAT TERRAIN
500 FT AGL

— AIRCRAFT ALTITUDE
 □ VERT CONF
 ○ HEIGHT ERROR (FT)

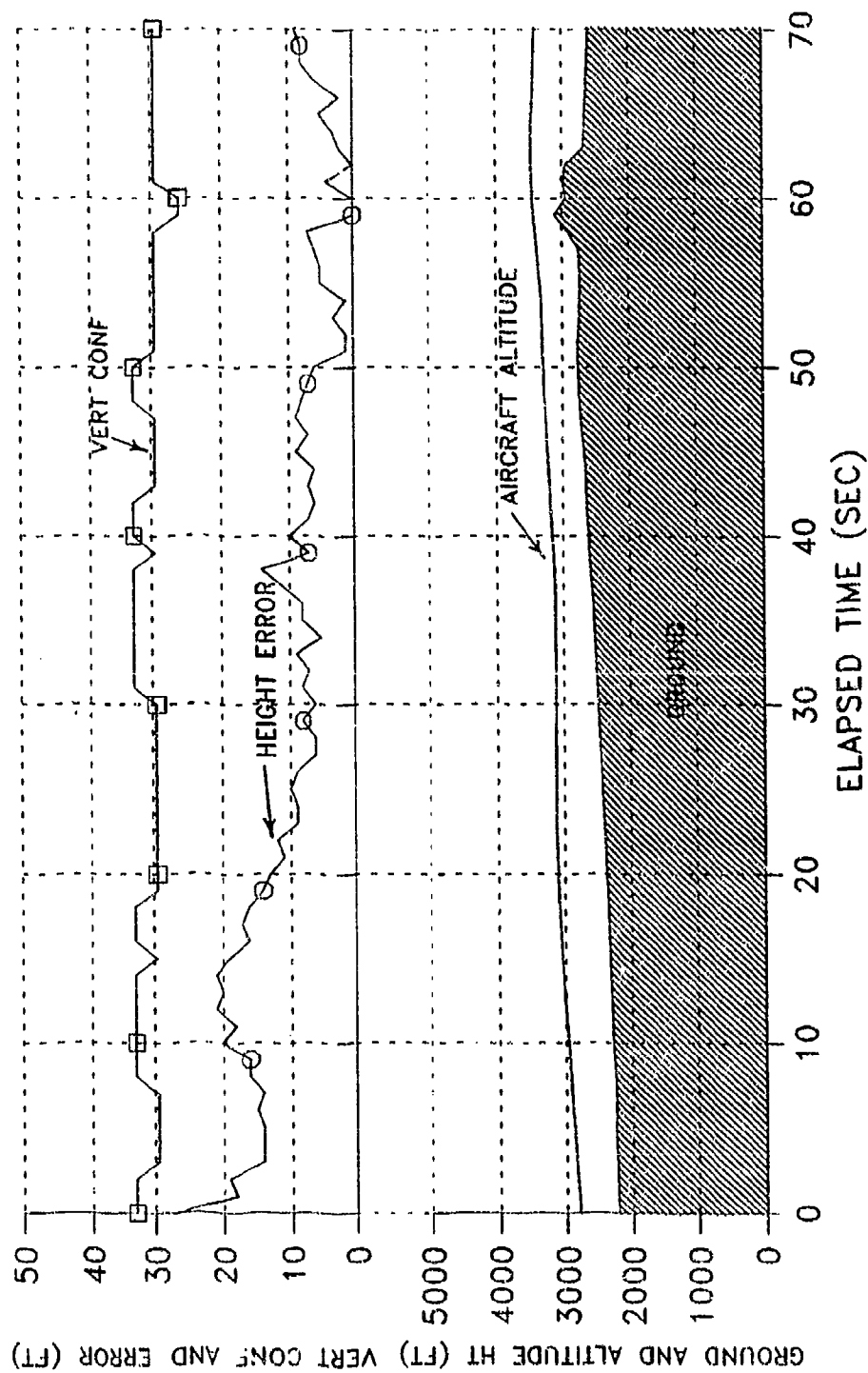
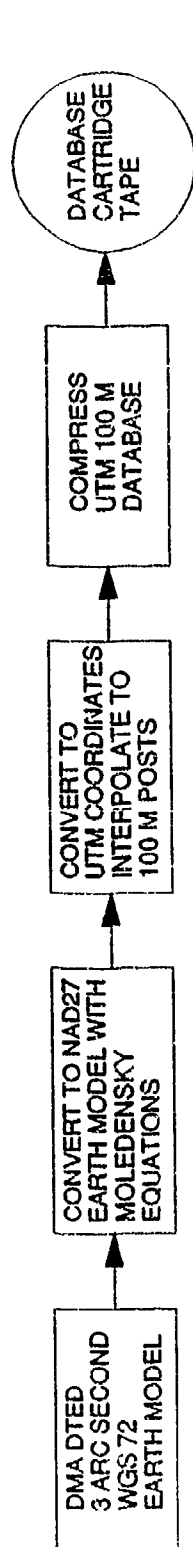


Figure 2 - SPARTAN Vertical TRN Accuracy

DATABASE CARTRIDGE TAPE PREPARATION



ONBOARD AIRCRAFT

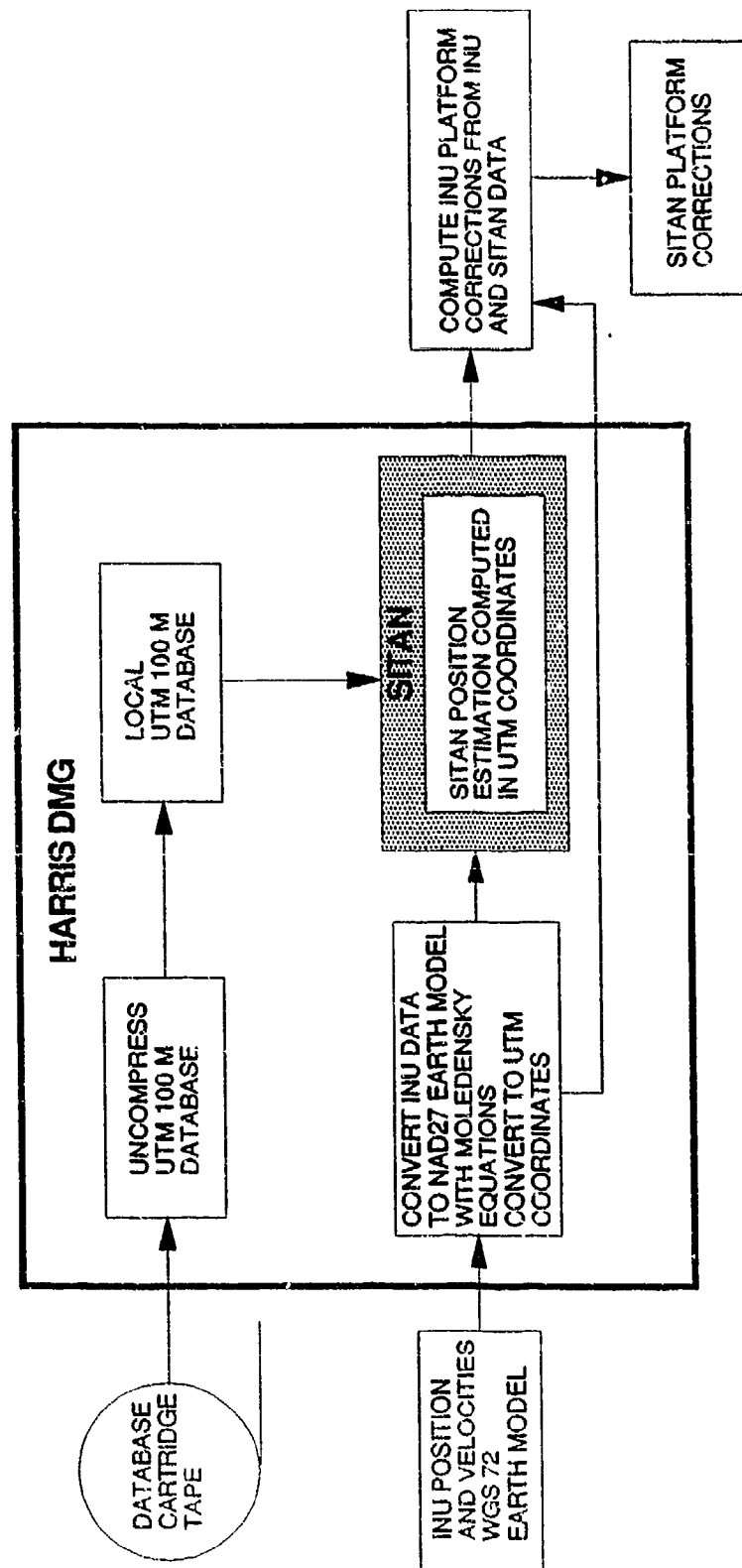


Figure 3 - Sitan Data Flow

the data manipulation and the conversion of the on board parameters for SITAN operation. These data base compressions, coordinate systems and earth model conversions may have introduced errors into the data base. An apparent bias was evident in all SITAN results, and it was probably caused by an error in the data base manipulation. The process was so complicated that tracing down the source of the error was extremely difficult, and the source of the bias was not identified.

The SPARTAN elevation data base was stored on solid state memory. This greatly increased the speed of the data retrieval over a tape storage method. The TRN algorithms by themselves did not require a fast data base retrieval, but TF and map display functions did have a time critical requirement. The GEC DTS data base handling and manipulation steps were proprietary. All GEC DTS data handling was satisfactory.

FUTURE TECHNIQUES

We will be testing ESITAN with the Advanced Range Data System (ARDS) which is a differential Global Positioning System (GPS) TSPI source. The ARDS pod is shaped like an AIM-9 missile body and contains a 5-channel GPS receiver, an inertial reference, a solid state recorder, and a telemetry package. The accuracy of the ARDS TSPI information using differential GPS should be 3 to 5 meters. This capability will allow us to test the TRN system over a much wider variety of terrain and flight conditions. The quality of the TSPI data should also be much better, because there will not be multiple radar drop outs normally experienced during low level flying.

The ARDS pod will enable an almost unlimited coverage of TSPI data over any type of terrain. Testing in the rough terrain of remote areas will now be possible. Of particular interest will be the testing of the altitude accuracy with dynamic maneuvering in the rough terrain. The continuous coverage will enable an indepth examination of the long term transitioning characteristics between the different terrain types. As a result, there will be orders of magnitude more data collected than previously acquired which will lend much more statistical significance to the test results.

We are also developing new methods to characterize terrain types to correlate to TRN system performance. In the past, testing was performed on specific TF routes which were designated rough, moderate, or smooth depending on the standard deviation of terrain slope on the route. One of the most promising new methods is to characterize the terrain by the power spectral density of terrain slopes. This method should allow a much better characterization of the terrain.

CONCLUDING REMARKS

Prototype TRN systems for tactical fighter aircraft have been around for a long time, although they are still relatively unknown and untested. The testing that has been accomplished has not produced conclusive results and has only scratched the surface as far as determining the full potential of these systems. These types of systems offer advantages and capabilities that other systems and sensors cannot provide, so research and development efforts should continue to exploit the full potential of TRN systems.

All three systems (SITAN, SPARTAN, and TERPROM) should be thoroughly tested under the same conditions (data base, INU, Ralt, central air data computer) to investigate the advantages and disadvantages of each approach. This would be best accomplished by flight testing all three systems on the same aircraft at the same time. If the systems are not flown at the same time, a large amount of data would have to be collected on each system to make the results statistically significant and comparable.

The TRN algorithms should be tested to determine:

1. Navigational accuracy.
2. Time to acquire or tracking convergence
3. Coasting performance over flat terrain
4. Reacquisition and recovery from data base errors
5. Vulnerability to false track
6. Terrain content requirements for satisfactory performance between flat and moderate terrain

The TRN algorithms must perform well (or at least consistently) in each category in order for them to be satisfactory during operational usage. Research and development of TRN systems should continue in flight test. Simulations have not been able to accurately model the radar altimeter characteristics over varying terrain profiles or properly characterize the errors in the elevation data base. Flight test is the only way to adequately test TRN systems.

REFERENCES

1. Henley, A.J., "Navigation and Guidance Using a Terrain Data base", in the *RAeS Symposium Guidance and Control Systems for Tactical Weapons*, April 1988
2. Grey, D.M., "Recent Developments in TERPROM", in *AGARD Conference Proceeding No. 455*, May 1989.
3. Boozer, D. D., et. al., *SITAN Design for Low-Level Attack Aircraft*, SAND84-2059, Sandia Labs, Albuquerque, NM, May 1985.
4. Reuter, A. L., *AFTI/F-16 AMAS Avionics Evaluation and System Integration*, AFFTC-TR-87-13, AFFTC, Edwards AFB, CA, September 1987.
5. Fellerhoff, R. J., *AFTI/SITAN Final Report*, SAND88-7325, Sandia Labs, Albuquerque, NM, November 1988.
6. Blasius, R. P., *AFTI/F-16 Close Air Support Block 1A Digital Terrain System Evaluation*, AFFTC-TR-90-04, AFFTC, Edwards AFB, Ca, April 1990.
7. Defense Mapping Agency Digital Data Information Sheet, *Digital Terrain Elevation Data - Level I*, DMA Combat Support Center, Washington, DC, September 1987.

UNCLASSIFIED/UNLIMITED/OPEN

LOW COST NAVIGATION

AND

BATTLEFIELD INFORMATION

FORWARD SYSTEMS (BIFFS)

CHRIS COLES
UK RESEARCH AND DEVELOPMENT LIMITED
23 CLIFTON ROAD
SALISBURY
WILTS
ENGLAND
SP2 7BP

TEL (0722) 331484
FAX (0722) 331313

SUMMARY

The drive to reduce the unit cost of the basic electronic package which forms the foundation of GPS navigation systems has now been joined by similar volume and cost reductions in combined video camera and radio transmission systems. This will have a dramatic effect upon the cost of and thus uses for military navigation systems. More fundamentally, they will have a dramatic effect upon the availability of smart, passive devices in the battle field. We are now entering the age where the prospect of a rock, a bamboo shoot, or other camouflaged small object having both eyes and ears and the ability to tell you where it is, becomes reality. Battlefield Information Forward Systems (BIFFS) have arrived.

None of you will need reminding how rapidly the physical size and purchase cost of satellite navigation electronic systems have been decreasing. A system previously costing \$80,000 and filling several suitcases can now be placed in the palm of the hand for a few hundred dollars. There is every reason to expect that this process will continue to the point where the technology to define the location of any object is going to reduce in cost at least one order of magnitude further.

Some of you by now will have become aware of the development of my own patented ideas for the GPNS navigation system and for my video fax security system.

With both of these ideas, state of the art experts believed in 1989 that neither would be physically possible within a reasonable time scale, to make it worth while proceeding. Both of these assumptions have been shown to be wrong and have proven my personal belief in the power of the free individual to innovate.

With GPNS (Global Portable Navigation System) we show you how you can have a conventional printed map display, with all the attendant advantages, while at the same time enjoying much, if not all of the features of a modern electronic navigation system, at a price, moreover, perhaps 90 times less than the comparable CD disc driven LCD display.

It is important that you understand that we are talking about the display of a conventional map image.

We propose that the chart, map or road atlas is printed upon a suitable thin plastic film held between two rollers and encased within a sealed plastic cassette; the cassette dimensions being any suitable size to suit the needs of the user. The operation is simple. Reeling the map from side to side under a single line marked down the centre of the cassette gives you longitude. Making the longitude line a piece of thread with a mark upon it and reeling that up and down gives you latitude.

A lot of people went that far with their thinking years ago. What we proposed next was considered impossible just three years ago. We put the entire electronic guidance system as a standard removable module, or "box" between the rollers in the cassette, complete with two stepper motors to drive the map and the indicator line. In addition, we added electronic storage in the cassette and as it turned out, more crucially, outlined how the map and indicator line had to interact with the integral navigation system. The system must know where the map and indicator line are relative to each other and be able to adjust these relationships accordingly.

The GPNS cassette creates a global standard display system giving the highest quality visual display in a form with which the user is fully familiar, the printed map. In addition the GPNS cassette can hold both electronic and printed display information, the electronic information being displayed on the LCD screen on the navigation system "box". With the normal commercial product, the GPNS cassette forms the foundation for a very large publishing market. Tourist maps will now, for example not only display where the user is, but all the local places of interest, times of opening, price of entry. But, most importantly of all, the user's navigation system thus stays with the user. The GPNS road atlas cassette stays in the vehicle but the navigation system "box" stays with the user who may carry the GPNS system box anywhere, walking, riding a horse, sailing a boat, flying an aircraft, anywhere using the appropriate GPNS map cassette.

GPNS HIGHLIGHTS

- familiar, high quality printed map.
- global standard system.
- pocket sized portable.
- creates a new advertising medium.
- addresses existing road atlas market.
- wide tourist market potential.

You may all well ask why should I give you information about a cheap consumer product?

The answer is quite simple. I believe that GPNS suitably modified for military requirements will be seen as an indispensable tool in the battlefield. For a start, you will be able to consider providing a navigation system for every individual in the field. That system will provide a high quality map display which shows each individual where they are in real time. In addition, significant local terrain information, for example, can be pre programmed into the cassette's electronic storage. A pilot brought down in enemy territory could be provided with information on known military installations to help him evade capture. An inviting open door may not be so attractive if your personal navigation system tells you it is the front door to Saddam Hussein's palace guard barracks. Perhaps more importantly still, we must remember that under intense fire the ordinary soldier frequently becomes disorientated. Having his own navigation system in his pocket will improve matters immensely.

These developments will become possible economically due to the vast volume manufacturing requirement for this product as a consumer product - we expect to be selling between two and ten million units per annum from product launch - and can expect to deliver the basic navigation system "box" for perhaps \$500 or less each. The map cassettes may well come out at something around \$5 or \$10.

The size and shape of a GPNS Navigation System will make it extremely useful as, in its smallest version, it will fit inside the pocket of a conventional jacket.

The basic navigation system "box" will also drive larger cassettes. Not only will this make an economical navigation system for troops, it also opens up a whole host of uses which need a low cost historical copy of position.

The question - "Where have you been for the last two hours airman?" becomes for example, "Show me on your GPNS where you were when you were fired upon."

I am sure your own imaginations will conjure up numerous other uses. But remember, the system will display the map even if the batteries are flat or the electronics are damaged.

I turn now towards my other idea, The Video Fax Security System, again, originally considered physically impossible. By physically I mean it was considered impossible to put the electronics into a small enough package at a low enough cost.

In essence I proposed a PORTABLE (perhaps pocket sized or less) unit combining a video camera, a transmission system such as a radio telephone and a GPS Navigation System.

The technology to place a video camera, and radio telephone communications electronics all on one single chip have now been announced and this, combined with the very low cost navigation receivers, opens up an enormous range of options for both military and civilian use.

The civilian use is primarily targeted towards individuals carrying a module which will fax a photograph of any impending dangerous situation - I leave you to exercise your own imaginations as to what that might be - direct to a local franchised security monitoring service who would receive a photograph of your problem. However, because we integrate cheap satellite navigation into the system, the security monitor knows exactly where the user is and because of the manner of

transmission it means they may also have immediate real time direct verbal communication with the user.
I know everybody says it - so the guy shoots your user dead!!!

Well, for the first time you have something you never had before, which is a photograph of the guy pulling the trigger.

I am not going to elaborate any further on the commercial uses but I will now give some ideas I have personally for military use that go beyond the obvious civilian/military applications.

Once you have a small electronic unit that can take a photograph and transmit that photograph over long distances, where the receiver knows exactly where the transmitter is, then the applications become really quite interesting. You give the opportunity for a battle field commander to drop what I call BIFFS (Battlefield Information Forward Systems), in whatever pattern or form he feels appropriate over a proposed battle field area. He will get a photograph of what is in the surrounding area now. He can organise the electronics to give him updates as and when he wishes. The device can be as small as you would reasonably wish. A potato shaped rock for example. Or it could be encased in a plastic spear that once imbedded in the ground would look like a blade of grass or bamboo shoot or an old fence post giving you just some examples of your opportunities. At the start of a battle if you have these devices available you can place one at every military crossroad, at every hilltop promontory, in any area where you would like to know what was going on. It would be rather handy for example to leave one in amongst a bombload on a runway perhaps outside the hangars to find out exactly what happens after your attacking force leave. Do personnel come out and from where? An hourly watch on some particularly interesting prospective locations for mobile rocket launchers, for example would give you immense opportunities to redefine the whole concept of war in the modern battle field.

I have to assume that everyone will recognise that the potential capability to fax a single frame photograph out of a battlefield presents some interesting technological challenges, not the least from the point of view of integrating with existing battlefield communications systems. The old adage, if you can see it you can hit it, if you can hit it you can destroy it, takes on a whole new meaning when you can place a device onto the battlefield which will not only tell you where it is but show you what lies around it and be cheap enough to be considered as expendable as a round of ammunition.

The day of the intelligent allseeing cow pat has arrived and I intend to supply it.

SESSION X
TEST CAPABILITIES

CHAIRMAN
LEN R. SUGERMAN
PHYSICAL SCIENCE LABORATORY

**STATE-OF-THE-ART VIBRATION MEASUREMENTS
FOR SPACECRAFT APPLICATIONS**

**Joel Anspach, Paul Sydney, and Henry Sebesta
Applied Technology Associates, Inc.**

**Gregg Hendry
Ball Aerospace Systems Group**

ABSTRACT

The Wideband Angular Vibration Experiment (WAVE) was flown to measure vibrations and their influence on pointing and tracking functions in the Relay Mirror Experiment (RME). The technology exploited in the WAVE instrument provides 6-DOF vibration measurements on an orbiting spacecraft at unprecedented levels of accuracy. The broadband (1-1,000 Hz) measurement noise for the WAVE is less than 0.1 microradian RMS in each angular axis and less than 25 micro-g RMS in linear acceleration. Amplitudes of individual angular vibration frequencies can be measured to levels of a few nanoradians. The instrument includes 16 individual sensors: three angular displacement sensors, six magnetohydrodynamic (MHD) angular rate sensors, and seven linear accelerometers. The WAVE instrument was mounted on the optical bench and supporting structure to which a laser beacon tracking assembly and mirror pointing servo subsystems were attached. By performing coherence analysis between the vibration data and the residual tracking errors, one can obtain a quantitative measure of how base motion influences the performance of the system. Results during self-check modes of operation show that base motion is the dominant disturbance to tracking subsystem performance. Active attitude control system elements, specifically the horizon sensors and the reaction wheel, excite the structural vibrations of the optical bench and result in residual tracking errors. After a year of on-orbit operation, the WAVE instrument continues to provide 6-DOF vibration data for correlation with RME tracking performance.

INTRODUCTION

In 1985, a program to conduct space pointing and tracking experiments (TPE) in support of the Strategic Defense Initiative (SDI) was initiated. After a period of development and rigorous ground test verifications, two TPE experiment payloads were carried into orbit by a Delta expendable launch vehicle on February 14, 1990. Since launch, the Relay Mirror Experiment (RME) has performed successfully its two essential functions: 1) electro-optical tracking of a pair of cooperative beacons; and 2) stabilization of a mirror to accomplish relay of a laser beam between a source site and a scoring site (Ref. 1). RME provides an on-orbit research system to explore technology issues critical to strategic defense directed energy concepts. Associated with the RME is a second experiment, the Wideband Angular Vibration Experiment (WAVE). It functions to measure the vibrations of the structure to which RME trackers and stabilization components are attached. It also validates performance and operation of the MHD angular rate sensor in a space environment. This paper focuses on the results from the WAVE by reporting on three issues:

- 1) The ability of the WAVE system to measure base angular motion of the RME tracking system with measurement noise of 100 nanoradians RMS or less over the frequency range 1-1000 Hertz;
- 2) The verification of MHD sensor technology for precision vibration measurements in space applications;
- 3) The determination of quantitative influences of base motions on the RME beacon tracker performance while in the self-check mode.

The WAVE system provides measures of vibrations on the RME spacecraft in six degrees of freedom at levels of precision and range of frequency heretofore unavailable. The reader will find additional information on the RME and WAVE in technical presentations given at the 1991 SPIE Symposium on Optical Engineering and Photonics in Aerospace Sensing (Ref. 2).

WIDEBAND ANGULAR VIBRATION EXPERIMENT

The WAVE was developed in response to the TPE program announcement on the premise that base motion constitutes a significant disturbance in most precision tracking and pointing experiments. The ability to measure angular motions to levels of 100 nanoradians or less had been recognized as significant requirements for a variety of SDI systems and applications. Suitable instrument packages and sensors to resolve low level angular motions did not exist and the main focus of the WAVE was to address this gap.

Key motivations for proposing and flying WAVE were rooted to the history of problems caused by base motions during previous experiments to demonstrate pointing and tracking functions to levels required in laser airborne defense scenarios. The Air Force funded a program to develop an advanced angular sensor (AAS) for utilization in airborne laser pointing and tracking systems. Shortly before the TPE program was solicited, a technical breakthrough emerged from the AAS effort in which it was demonstrated that angular motions of a few nanoradians could be measured (Ref. 3). The new inertial rate sensor operated in a broad frequency range and employed the magnetohydrodynamic (MHD) principle to sense angular rate. The two objectives of WAVE are to provide base motion measurements of the RME beacon tracker optical assembly and to verify performance of the MHD angular rate sensor in a space environment. The RME spacecraft houses optical trackers whose purpose are to acquire and track two ground based laser beacons. The beacons originate from two ground sites, separated by about 20 kilometers, on the island of Maui. The 60 cm relay mirror is positioned by the optical tracker to bisect the angle between the beacons, allowing the relay of a third laser from one ground site to the other. WAVE sensors provide information on how the vibrations on the spacecraft affect performance of the beacon trackers and the ability to perform a beam relay. A drawing of the RME beacon tracker with the WAVE sensor is shown in Figure 1.

The WAVE hardware is comprised of two elements: the sensor package, which houses all motion sensors and their preamplifier electronics, and an encoder package which provides the functions of power supply, signal amplification, anti-alias filtering, time stamping, digitization, and interface to the spacecraft's telemetry system. The sensor package is designed to measure vibration in six rotational and translational degrees of freedom over a frequency band of 1 to 1,000 Hz. The sensor suite consists of seven linear accelerometers, three angular displacement sensors (ADSs), and six MHD angular rate sensors.

Sensor position and orientation in the package are indicated in Figure 2. The package itself was designed so that the first structural mode of the sensor box occurs at 1,800 Hz. Below this frequency, the sensor package can be considered as a rigid body.

The MHD transducer was specifically designed for applications, such as the RME, in which angular vibration measurements on space-based precision optical pointing and tracking systems are required. The sensor measures angular rate by employing an MHD generator (Ref. 4). A permanent magnet near a constrained annulus of conductive fluid produces a constant magnetic field with flux lines perpendicular to the fluid annulus (see Figure 3). As the sensor moves, the fixed permanent magnet moves with the case. The fluid will tend to remain inertially stable about its rotational sensitive axis but to move with the sensor in all other directions in both translation and cross-axis rotation. A rotation of the sensor about its sensitive axis results in a velocity difference \bar{U} between the fluid and the applied magnetic field density \bar{B} . This induces an electric field \bar{E} that is radial in direction and proportional in amplitude to \bar{U} and \bar{B} :

$$\bar{E} = \bar{U} \times \bar{B}$$

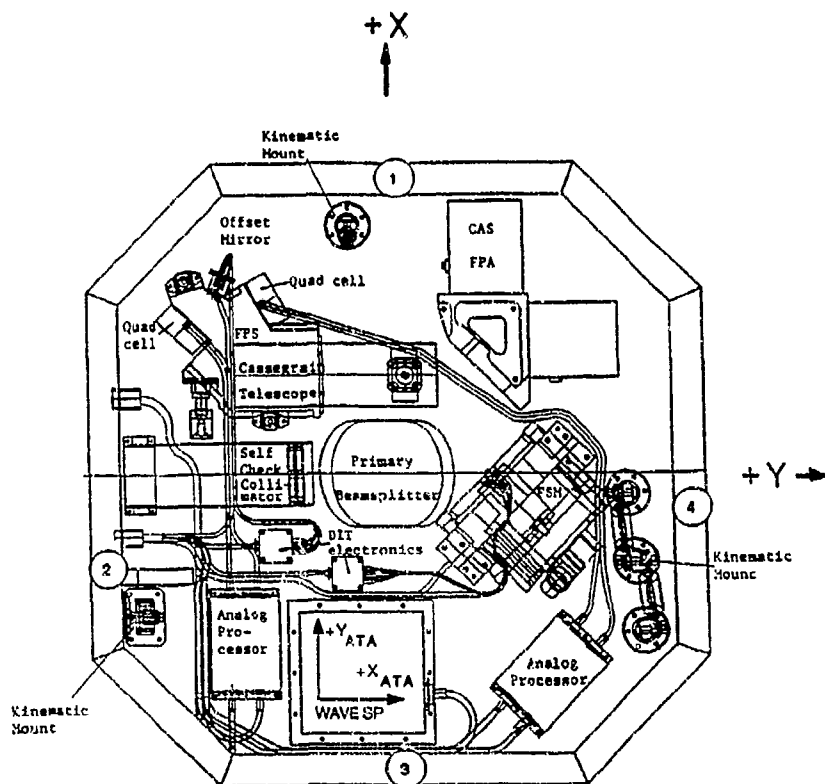


Figure 1. PEP Optical Bench/WAVE Configuration

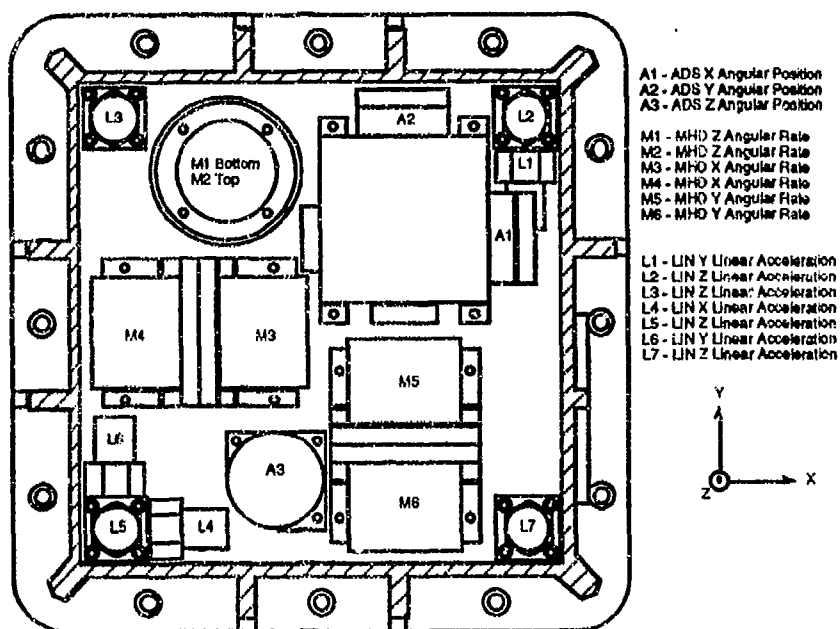


Figure 2. WAVE Sensor Package

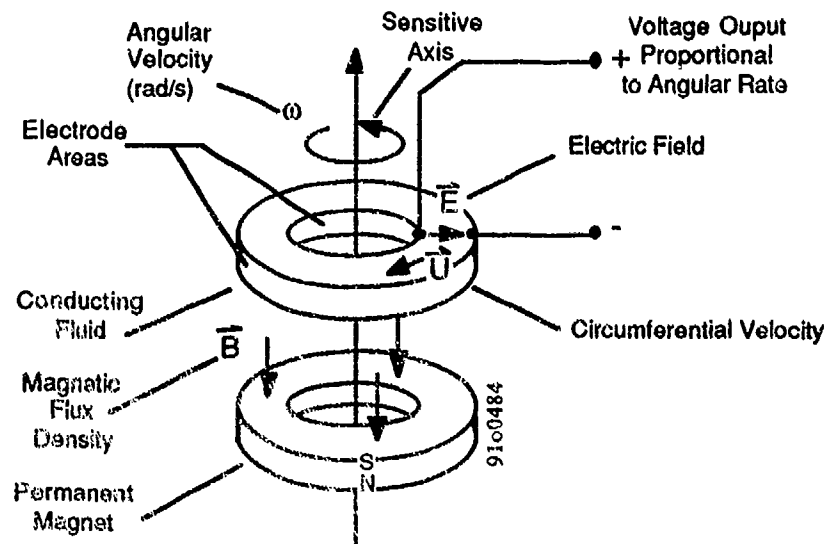


Figure 3. In a magnetohydrodynamic angular motion sensor, the magnetic field moves with the angular vibration of its housing. A relative velocity between fluid and magnetic flux density creates a voltage across the fluid and the electrodes. The relative velocity is proportional to the input angular velocity and the radius of the fluid annulus.

where:

\vec{E} = electric field (V/m) produced in the radial direction

\vec{U} = circumferential velocity (m/s) of fluid relative to the magnetic field

\vec{B} = magnetic flux density perpendicular to fluid annulus acting along the Z direction

The circumferential velocity is determined by

$$\vec{U} = r\vec{\omega}$$

where:

r = root mean square radius of the channel (in meters)

$\vec{\omega}$ = input angular velocity of the sensor (rad/s)

The voltage generated radially across the annulus of fluid is the integration of the induced electric field over the width of the fluid channel. The MHD sensors, flown in WAVE, have a scale factor of 100 V/rad/s.

In order to evaluate WAVE performance, the spacecraft was configured for the quietest possible base motion environment. The spacecraft was on orbit number 476.5 at about 450 km altitude, in a nadir pointing attitude and performing no specific maneuvers (Ref. 5). The attitude control magnetic torque rods were disabled during this time; however, the reaction wheel was actively maintaining attitude control in pitch.

In this quiet environment it can be shown that residual vibrations in the spacecraft were greater than the sensor noise floor. Parallel sensor techniques were employed to extract the noise floor spectra from that of the spacecraft base motion (Ref. 6). Sensor performance can be effectively evaluated using a parallel sensor approach which assumes equal input noise to two sensors subjected to the same angular motion.

The parallel sensor technique can be used to estimate autospectra of the noise equivalent angle for each sensor in the package. The noise autospectra are generally broadband with increasing amplitudes at lower frequencies and a root mean square (RMS) level at approximately 100 nanoradians between 3 and 1,000 Hz. Figure 4 illustrates the character of the MHD angular rate sensor noise spectra derived from measurements taken during a typical on-orbit experiment. This is typical for this model of the MHD sensor and is comparable with measurements taken during ground testing (Ref. 7). The ADS shows lower noise levels than either MHD sensor or differenced linear accelerometers in the 1-10 Hz band. The best measurements were achieved by blending measurements from the three types of sensors - ADS measurements in the 1-10 Hz frequency band, measurements from MHD angular rate sensors in the 10-100 Hz band, and measurements derived from differenced outputs of linear accelerometers in the 100 - 1000 Hz band. By processing the simultaneous, parallel measurements, the noise floors listed in Table 1 were derived.

<u>Frequency Band,</u> <u>Hz</u>	<u>Noise Floor,</u> <u>nanorad RMS</u>	<u>Sensors Processed</u>
1-10	29	ADS and MHD Rate Sensors
10-100	8	MHD Rate Sensors and ADS
100-1000	4	Differenced Accelerometers & MHD
Rate Sensors		

Table 1. Estimates of WAVE Sensor Package Noise Floors

A best estimate for angular motion of the WAVE package during this data interval is obtained, again taking advantage of parallel sensors processes to separate motion measurements from noise. The composite beacon tracker angular displacement autospectra in the x-axis is shown in Figure 5. The estimate comprises the ADS between 1 and 10 Hz, the MHD sensors between 10 and 100 Hz, and the differenced linear accelerometers between 100 and 1,000 Hz. These are the bands over which each group of sensors has the least noise. The total RMS angular motion is about 200 nanoradians over the 1 to 1,000 Hz band and shows discrete frequency components that above the measurement noise spectra. This level is typical for the RME spacecraft while maintaining a nadir pointing cruise attitude.

SPACECRAFT BASE MOTION SOURCES

RME spacecraft mechanical systems, specifically attitude control systems (ACS), are the principal sources of base motion to the beacon tracker optical bench. ACS mechanical systems include two horizon scanners and an angular momentum wheel. The beacon tracker employs three movable mirrors, a fast steering mirror, a relay mirror, and an offset mirror, to stabilize beacon images on the tracking sensors.

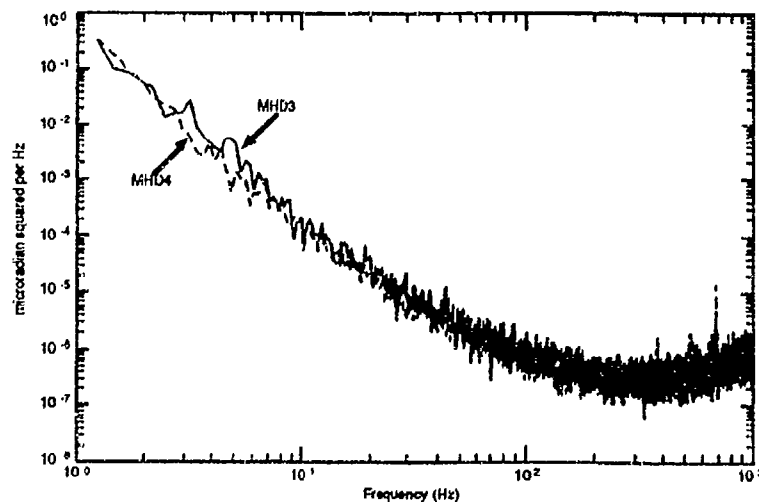


Figure 4. MHD X-Axis Equal Input Noise Autospectra

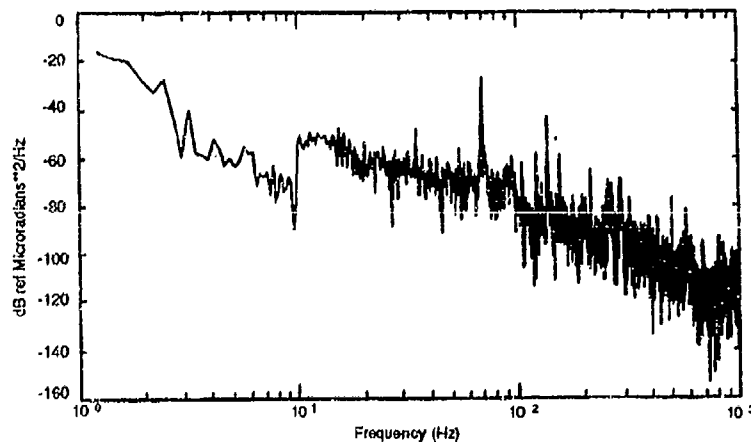


Figure 5. Combined X-Axis WAVE Sensor Package Base Motion

Spacecraft attitude is controlled by two different classes of angular actuation: 1) magnetic torque rods for three-axis, low authority control; and 2) one angular momentum wheel for high authority pitch control. The ACS is digitally implemented by an Intel 8086 based on-board computer. It uses data from various sensors to derive spacecraft position information. Two earth horizon scanners determine spacecraft pitch and roll. A magnetometer that measures magnitude and direction of the earth's geomagnetic field vector contributes to yaw determination.

The two infrared horizon scanners are located on either side of the roll axis of the spacecraft. Each has a small rotating mirror which conically scans the field of view across the detector looking for the cord and phase of the earth's limb. Both scanning mirrors rotate at a constant rate of 4 Hz. The horizon scanners run continuously.

The momentum wheel provides the ability to perform a pitch maneuver, rapidly rotating the spacecraft in the pitch axis, keeping the relay mirror's normal vector pointing to a fixed spot on the ground as the beacon tracker engages the ground sites. Operating range for the momentum wheel is typically between 1,700 and 2,500 revolutions per minute. When the spacecraft is in cruise mode, the ACS is maintaining a nadir pointing attitude. In this mode the momentum wheel maintains a fixed angular rate. When the ACS is performing a pitch maneuver the momentum wheel ramps through a range of speeds, rotating the spacecraft by exchanging angular momentum between the wheel and spacecraft body. Wheel imbalance and bearing rumble are sources of base motion to the beacon tracker. In addition the ACS is digitally commanding momentum wheel electronics with updates at a 4 Hz rate. This results in torque updates to the wheel at the 4 Hz rate, the same as the horizon scanner rotation rate.

Autospectral density functions calculated from orbit number 476.5 data reveal the effects of angular vibrations generated by the momentum wheel. Figures 6 through 8 show angular displacement autospectra from the MHD sensors in all three axes for this data interval. These autospectra have been processed with the parallel sensor techniques in order to remove incoherent sensor noise from the coherent angular motion signal. Dominant frequencies are noted at 35, 70, and 140 Hz. The 35 Hz disturbance is believed to be generated by the momentum wheel spinning at 2,100 RPM, and the 70 and 140 Hz oscillations are present as harmonics of the fundamental frequency. Note that these spikes appear in all three axes.

STRUCTURAL INTERACTION

Primary structural resonances of the beacon tracker and relay mirror assemblies were measured in vibration tests during ground characterization of the spacecraft. Results of these measurements are tabulated in Table 2. In the previous figures the magnitude of the first harmonic of the momentum wheel at 70 Hz seen is larger than the fundamental 35 Hz frequency. This may be attributable to the 70 Hz support plate resonance listed in Table 2.

<u>Primary Mode</u>	<u>Frequency (Hz)</u>	<u>Description</u>
1	42	Y-Axis, Beacon Tracker
2	48	Z-Axis, Relay Mirror
		Y-Y Rotation, Fast Steering Mirror
		Z-Z Rotation, Relay Mirror
3	70	Z-Axis, Support Plate
4	77	Z-Axis, Beacon Tracker
5	87	Y-Axis, Relay Mirror
6	88	X-Axis, Relay Mirror
7	170	Z-Axis, BT and Support Plate
		Z-Axis, BT Plate Mode

Table 2. Primary Resonance of the Beacon Tracker and Relay Mirror

The ADS in each axis registers base motion similar to the MHDs for this interval. Figure 9 through 11 show the characteristic 35, 70, and 140 Hz spikes measured by the ADS. The dotted lines in the plots are the integrated power in the autospectral density functions. Two additional features are revealed in these plots. The x-axis ADS is dominated by low frequency motion from 1-3 Hz which is not present in the other two axes. This axis corresponds to the pitch axis of the spacecraft, in which the momentum wheel has authority. This low frequency motion results from

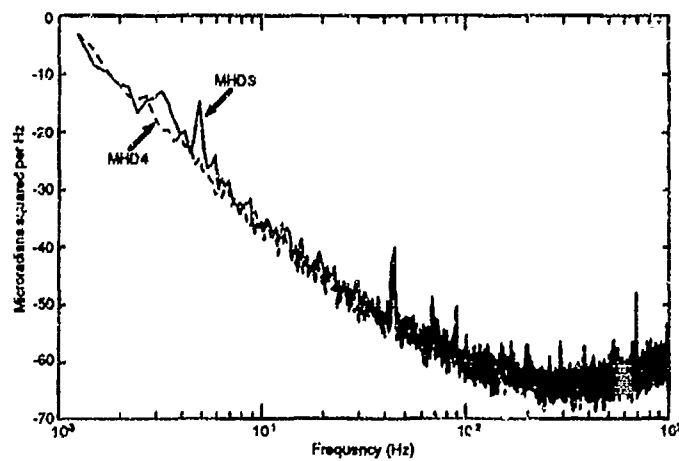


Figure 6. MHD 3 and 4 X-Axis Autospectra

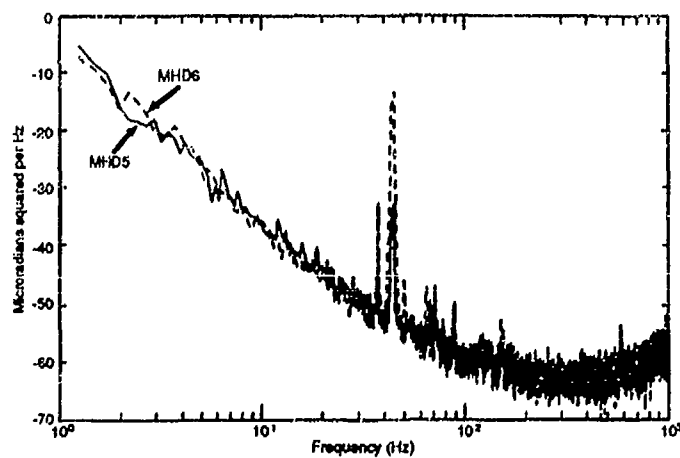


Figure 7. MHD 5 and 6 Y-Axis Autospectra

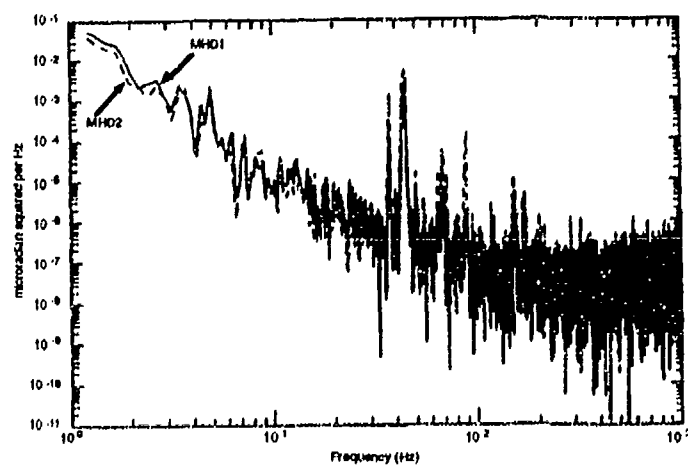


Figure 8. MHD Z-Axis Autospectra

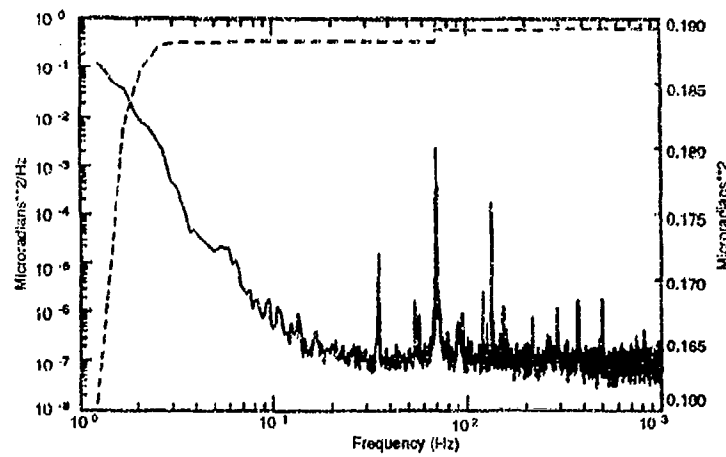


Figure 9. ADS X-Axis Auto Spectral Density

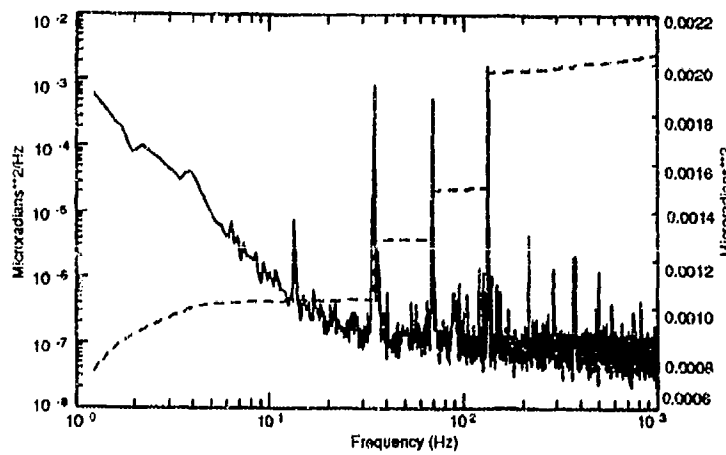


Figure 10. ADS Y-Axis Auto Spectral Density

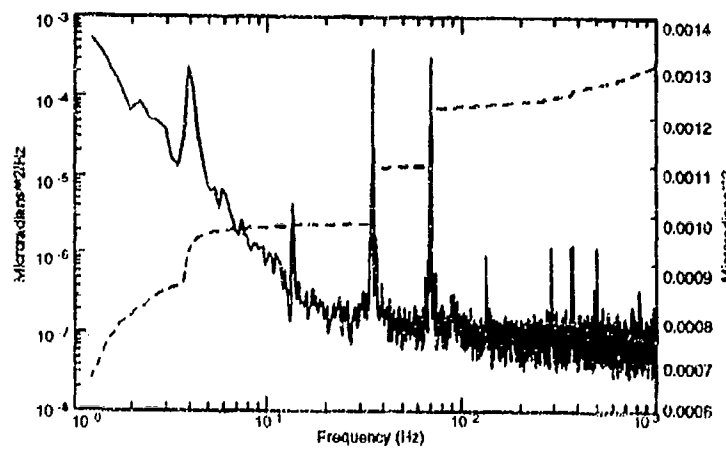


Figure 11. ADS Z-Axis Auto Spectral Density

the spacecraft ACS pitch errors coupling angular momentum between the momentum wheel and the body of the spacecraft. Also of notice is a spike with significant power at 4 Hz in the z-axis autospectra. This frequency correlates with that of the horizon sensor scan and momentum wheel update rates. It is interesting to note that there is no significant power at this frequency in the other axes. The z-axis corresponds to the yaw axis of the spacecraft.

TRACKING PERFORMANCE DURING SELF-CHECK

The beacon tracker employs a self-check collimator and laser diode which simulate both ground beacons to test functional operation of the system. In the self-check mode, the beacon tracker acquires and tracks the internal diode. The relay mirror is positioned off to one side; it does not participate in the tracking of the diode beacon. The beacon images are acquired by the coarse acquisition sensors, then control is handed off to the fine pointing sensors which are Silicon quadrant detectors. Fine track is maintained until the self-check is terminated.

A self-check was performed on orbit number 294.5. The spacecraft was in cruise mode with ACS torque rods disabled. The effects of base motion on beacon tracking performance during self-check is analyzed for this interval. Fine pointing sensor residual errors are examined to determine their sources. It is expected that in self-check mode, quadrant detector noise and optical bench base motion will dominate residual track error.

For this analysis, only the source pitch channel of the fine point sensors is presented. Figure 12 shows the auto spectra and integrated power of the residual source pitch track error in arbitrary units. The plot indicates that the dominant power is in the 70-200 Hz band. Figures 13 and 14 are autospectra from ADSs in pitch and roll axes over the same time interval. Note that the low frequency power below 10 Hz seen in the pitch axis ADS does not appear in the residual track error. At these frequencies, the beacon tracker acts as a rigid body; there is no relative motion between diode source and track sensor at these frequencies and thus, no contribution to track error.

It is desirable to know what fraction, if any, of the source pitch track errors are due to unrejected base motion. Multiple and partial coherence functions can help quantitatively evaluate this (Ref. 8). Two-input, single-output coherence analysis was performed with the x and y ADSs as inputs and source pitch track sensor error as output. Figure 15 shows the resulting multiple and partial coherence functions. The first plot is the partial coherence between the track error and the x-axis ADS. The coherence is high in the frequency band of 60 to 170 Hz, indicating that a large fraction of the unrejected track error can be attributed to bench base motion in the pitch axis. The second plot is the partial coherence function of the track error and the y-axis ADS with the linear contribution of the x-axis ADS removed. It shows additional contribution around 70 Hz and significant coherence at 200 Hz. Both of these frequencies can be identified as structural modes of the beacon tracker and relay mirror assemblies. The last plot in the figure is the coherent contribution of both pitch and roll ADS signals with the track error indicating that a majority of that signal between 60 and 200 Hz can be accounted for by base motion disturbances. Figure 16 reinforces this conclusion in the form of integrated autospectra. The solid curve is the unprocessed source pitch track error. It represents the unrejected error before any base motion effects are removed. The long dashed curve, third from the top, is the residual track error after the effects of pitch and roll base motion have been removed. The result is significantly less power than the raw signal, indicating that beacon tracker performance in the self-check mode is limited by non-rigid body optical bench base motion.

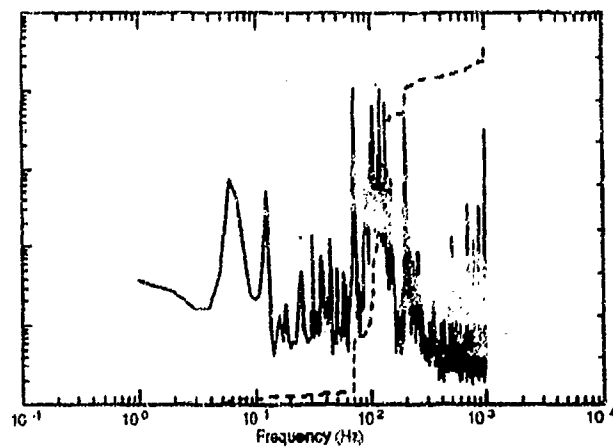


Figure 12. Source Pitch Auto Spectral Density

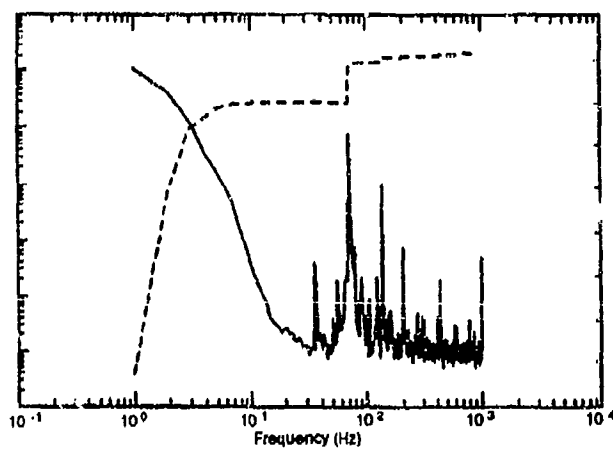


Figure 13. X-Axis Angular Displacement Auto Spectral Density

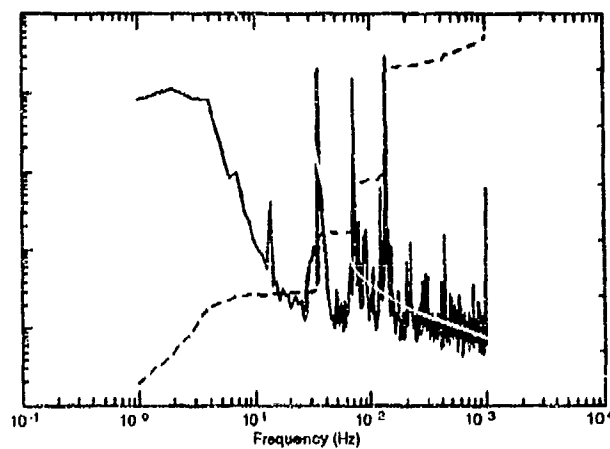


Figure 14. Y-Axis Angular Displacement Auto Spectral Density

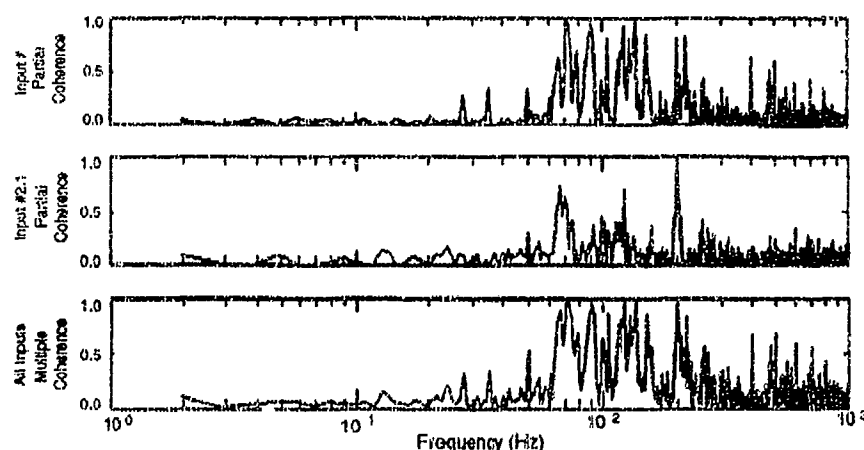


Figure 15. Partial and Multiple Coherence Functions

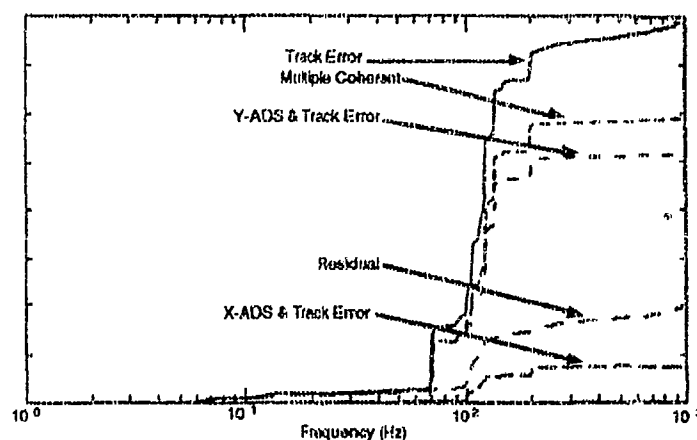


Figure 16. Integrated Multiple and Partial Autospectra

CONCLUSIONS

The WAVE provided on-orbit vibrational environment of the RME beacon tracker from 1-1000 Hz from sixteen WAVE sensors. A new inertial sensor for precision angular vibration measurements based on the MHD principle was flown for the first time. The MHD sensor performs as designed in the space environment and operated reliably for over 12 months during the data collection phase of the RME. WAVE measured optical bench motion in two typical and distinct vibrational environments: a nadir pointing spacecraft with no beacon tracker activity and the beacon tracker performing a self-check. In the first situation, measured bench vibration signatures have been correlated with the fundamental speed of the momentum wheel, horizon sensor scan rate and wheel command update rate, and structural resonance modes of the beacon tracker and relay mirror assemblies. In self-check mode, multiple and partial coherence methods were used to show that unrejected beacon tracking error was dominated by base motion whose frequencies correlated to known resonance modes of the beacon tracker and relay mirror assemblies. The capability of

WAVE to provide accurate, broadband measurements of angular vibrations to levels less than 100 nanoradians was demonstrated with considerable margin.

ACKNOWLEDGEMENTS

The Strategic Defense Initiative Organization (SDIO) has provided the support for the RME and WAVE programs under contracts with Ball Space Systems Division and Applied Technology Associates, Inc. The Phillips Laboratory (PL), Kirtland AFB, NM, manages and actively participates in the work to accomplish the experiments. Many individuals at PL, BSSD, and ATA have contributed to the hardware, software, and test results described. The authors gratefully acknowledge the efforts of the many participants.

REFERENCES

1. Scott, William B., "RME Spacecraft Demonstrates Precision Tracking and Pointing", Aviation Week & Space Technology, p. 204, June, 17, 1991.
2. Dierks, J. S., et. al., Acquisition, Tracking and Pointing V, Proceedings of Technical Conference 1482, Papers 1482-15 through 1482-21, Sponsored by the International Society for Optical Engineering (SPIE) and American Institute of Aeronautics and Astronautics (AIAA), Orlando, FL, April, 1991.
3. Laughlin, Darren, "MHD Angular Sensor Design and Evaluation", Report ATA-R-49, Prepared for Contract F29601-83-C-0016, Air Force Weapons Laboratory, Kirtland AFB, July, 1985.
4. Laughlin, Darren, "Testing Crash Dummies with an Angular Motion Sensor," pp. 32-40, Sensors, the Journal of Machine Perception, September 1989, Vol. 6, No. 9.
5. Anspach, Joel E. and Paul Sydney, "WAVE Sensor Quicklook Report #2," ATA Memo WAVE-0226, July, 1990.
6. Morgan, Felix E. and Randy O. Goucher, "Alternate Techniques for Determining Sensor Noise in High Signal-to-Noise Parallel Tests," presented at 30th International Instrumentation Symposium, May 1984.
7. Anspach, J., et al, "Final Ground Test Report," ATA Memo WAVE-0201, February, 1990.
8. Sebesta, Henry, et al, "Advanced Testing Methods for Acquisition, Tracking, and Pointing," paper presented at SPIE 1990 Technical Symposium on Optical Engineering and Photonics in Aerospace Sensing, April 1990.

PROBLEMS SPECIFYING PRECISION INS IN THE 90'S

by
Regan C. Lowrey

Honeywell
MILITARY AVIONICS DIVISION
ST. PETERSBURG, FLORIDA

ABSTRACT

Over the last 20 to 30 years, the performance of free-inertial airborne navigation systems has progressed from 10 miles per hour (mph) to 1 mph and now to 0.8, 0.5, 0.2 and even 0.1 mph in position drift. This progress can be largely attributed to advances in gyroscope technology since the main limitation in Inertial Navigation System (INS) performance has always been gyro drift performance. The old days of "degree an hour" platform-stabilized iron wheel gyros have given way to strapped-down ring laser gyros that are 200 times more stable (i.e., 0.005 degree per hour bias stability). Gyros are so good today that now accelerometer error sources are becoming more prominent in inertial navigation performance. Specific force measurement errors result in average position errors rather than the average position error *rates* that result from gyro drift. Thus it is becoming much less meaningful to specify free-inertial performance as simply 0.8 mph.

Further complicating this issue is the widely held misconception in the industry about the statistical measure of Circular Error Probable (CEP). Many INS users, and in fact many INS producers, are perplexed, for example, when presented with the fact that a system could be off by 0.9 mile after one hour, yet meet a specification requiring 0.8 mph CEP performance.

In the last ten years, sub-mile-per-hour (e.g., < 0.2) airborne systems have been deployed in the field and many controversies have arisen in attempting to certify compliance with specifications. Statements such as "We can meet the 0.2 nmi/hr spec *after* the first hour, but we can only do 0.3 in the first hour," have circulated around many conference tables. Attempts to resolve the controversy have lead to breaking the specification up into different time phases using different numbers for each phase. While helpful, this approach fails to address position error at the source: inertial measurement error.

In 1984, the Air Standardization Coordinating Committee in Washington, D.C., drafted several international agreements, which fifteen Army, Navy, and Air Force departments of five western countries ratified. These agreements provided a standard method of performance evaluation, but while the methods are sound, they provide little direction as to how to specify system performance.

Given knowledge of inertial navigation error sources and a standard method to evaluate performance, a systematic approach to INS performance specification can be put forth. This paper presents one such approach in an effort to convince the users and producers of inertial systems of the need for a standardized specification. This interface between customer and supplier is critical if there is to be confidence that the end-item system will be supplied an inertial unit that satisfies its needs.

THE PROBLEMS

Problem #1 CEP IS WIDELY MISUNDERSTOOD

It seems that many people in the industry believe that "CEP performance" for a free-inertial system means an average *rate* (so many mph) by which the INS position drifts. Strictly speaking, this is incorrect. By standard definition, CEP performance is a *position* (not rate) performance measure. Without correct understanding of this principle, it is possible, and even likely, that degraded performance systems could be mistakenly certified as compliant and fielded for operation. So for the user as well the producer, a thorough understanding of this principle and its governing standards is crucial if there is to be confidence that the end-item user will be delivered a system that meets the top-level requirements. The following briefly outlines this principle and its governing standards.

Given a bullseye plot of position errors, a circle can be drawn around the reference point which encloses half of the observed errors. The other half of the plotted observations will fall outside this circle. Thus the radius of the circle becomes the 50 percentile radial position error (RPE). This principle is illustrated in Figure 1.

SIMULATED TERMINAL POSITION ERRORS FOR 60 FLIGHTS

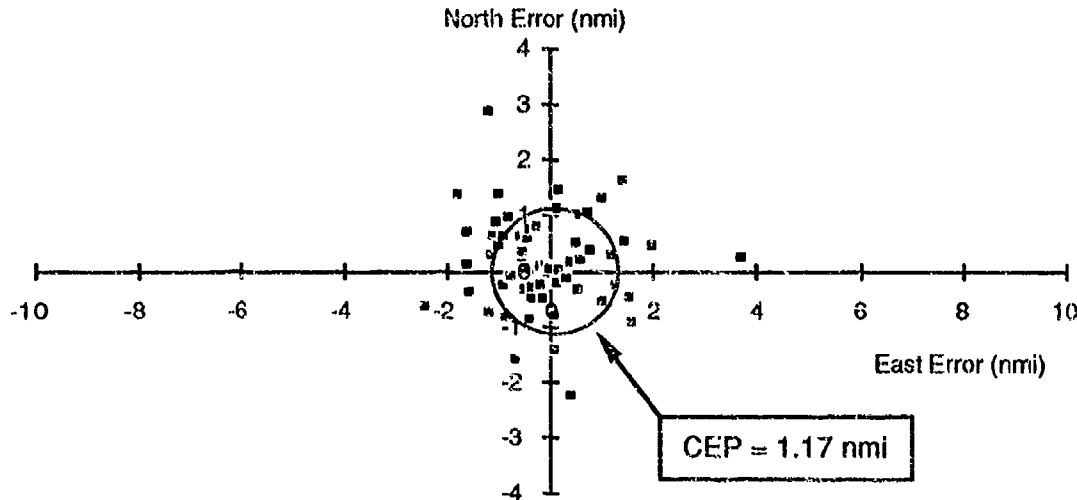


Figure 1. Sample Bullseye Plot of RPE

If the inertial navigator (IN) in this example had been specified to provide terminal position accuracy to 2.0 nautical miles (nmi) CEP, 1.17 nmi would have easily passed. Note however, that even though this system passed the 2.0 nmi CEP specification, there were several flights that exceeded 2.0 and

one at nearly 4.0 nmi. So for a typical system that operates at about "half spec," occasional measurements above the CEP specification number are not only allowed, but expected.

This is why an IN, allowed a CEP error of 0.8 nmi after 1 hour, can be off by 0.9 nmi at that time and still be an "in-spec" navigator. As a matter of fact, it can be shown mathematically that the probability is better than 50% that the system really is within specification. The cause for this scatter in position performance is traced to the statistical nature of the normal day-to-day and random variations in the inertial instruments. The actual number-crunching methods used to compute CEP have long ago been worked out and are well defined in an international agreement to which the United States is a signatory.

In 1984, the Air Standardization Coordinating Committee (ASCC) in Washington, D.C., drafted several international agreements, which fifteen Army, Navy, and Air Force departments of five western countries ratified. One such agreement that is often cited in USAF specifications is the ASCC AIR STD 53/16, "The Specification for Evaluation of the Accuracy of Hybrid Navigation Systems," dated 24 October 1984. This is the spec that requires that data from a minimum of six flights be collected in order to compute CEP. Further, it requires that data be sampled no less frequently than every 12 minutes.

Thus there is a new CEP data point (time, distance) computed every ten minutes or so during the mission, and therefore there must be a corresponding CEP limit specified for each point in time. The collection of those specified points is called "the limit curve" in ASCC AIR STD 53/11B which further declares, "The user will specify the values d_1 and t_1 governing the initial error limit and will define the remainder of the curve which in the simplest case will be a straight line of specified slope through the point (t_1, d_1) ." See Figure 2 for a reproduction of the Figure 2 in that ASCC Air Standard.

The "specified slope" mentioned above is the x *mile/hr* parameter that we are all so used to hearing about. However, the point (t_1, d_1) is rarely mentioned. It is sometimes described in specifications by saying that the line of specified slope should be forced through the zero intercept at time zero (0,0). Being the origin of the graph, the point (t_1, d_1) is easily neglected in conversation and over the years has virtually disappeared from the vocabulary of the INS community. New people coming into the field thus never become aware of its existence, much less that it is a requirement.

Problem #2 **CEP PERFORMANCE IS COMMONLY TIME AVERAGED**

CEP time averaging is not only a direct violation of international agreement, but is a practice which can result in degraded performance systems being accepted and fielded for operation.

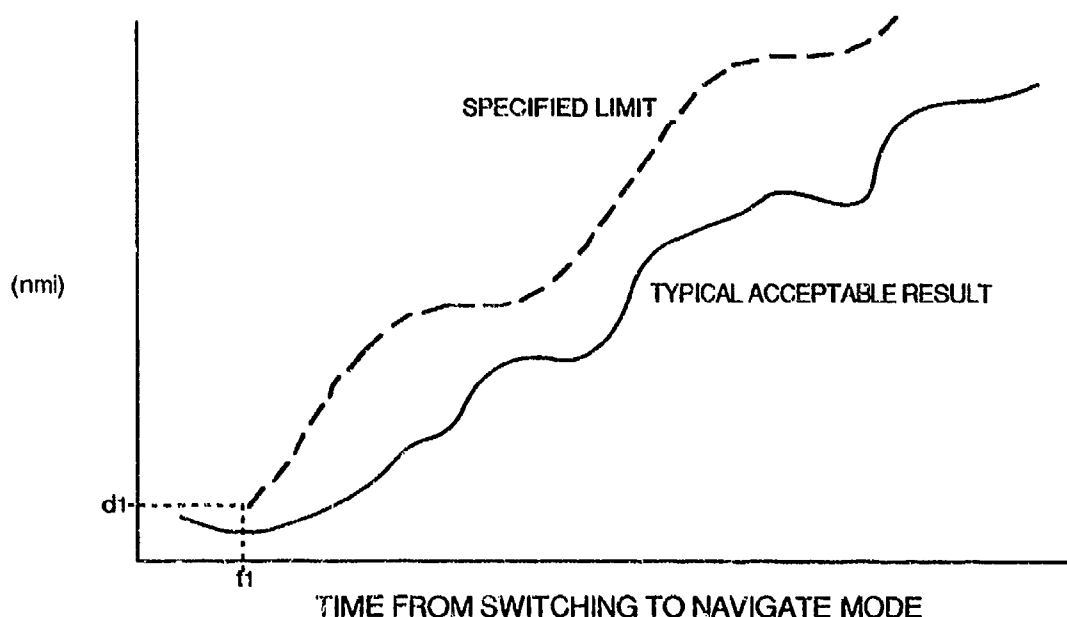


Figure 2. ASCC AIR STD 53/11B Figure 2, Error Limits

Oftentimes we see CEP data collected and plotted correctly in accordance with ASCC AIR STD 53/16, but then a time-average is obtained by drawing a best-fit line through the plotted data and this line is forced through the origin. The numerical value of the slope of this best-fit line is compared with the numerical value of the slope specified for the limit curve and compliance is pronounced based on this comparison alone.

This time-averaging scheme is explicitly prohibited by ASCC AIR STD 53/16, unless it can be demonstrated that "there is no time-dependent or distance-traveled-dependent trend in [the CEP data]." In other words, time averaging is permitted only if there is no correlation between CEP and time; and that is rarely, if ever, the case for free-inertial systems. Hybrid or aided systems are a different story and are beyond the scope of this paper.

The origin of the practice of time averaging probably comes from the following equation commonly used to describe single-axis position drift over time, given a constant level-axis gyro drift:

$$s = R\delta_{gb} \left[t - \frac{\sin(\omega t)}{\omega} \right] \quad (1)$$

where,

s = position error (nmi)
 R = Earth radius (nmi)
 δ_{gb} = gyro bias error (rad/hr)
 t = time (hours)
 ω = Schuler frequency (rad/hr)

This equation describes a straight line, of specific slope, added to a small sinusoid as illustrated in Figure 3. The slope of the "average s" line is simply $R\delta_{gb}$ (Earth radius times gyro drift rate). The dimensions of this slope are nmi/hr. Since the 50 percentile gyro drift rate is one of the characteristics of an INS, it is easy for people to make the mistake of just scaling that number by the Earth radius and giving out the resultant as the INS characteristic for position drift, the so-called *Radial-Error-Rate* (RER). The fallacy here is that Equation (1) comes with several assumptions not always valid in practice. These assumptions include:

- 1) Zero azimuth drift
- 2) Zero specific-force measurement error
- 3) No 24-hour effects (which can come into play after approximately 4 hours)

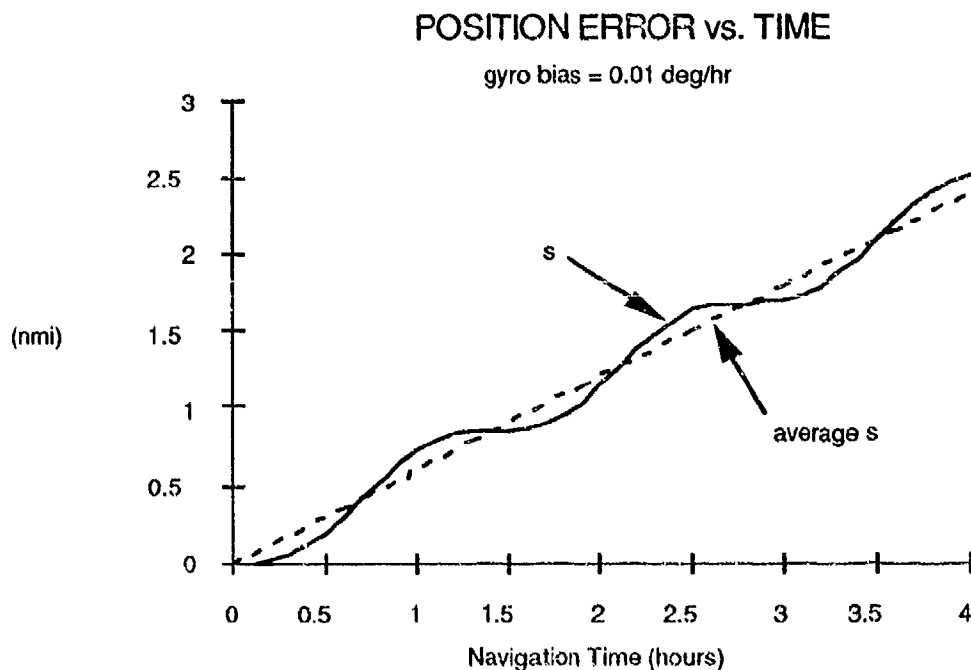


Figure 3. Single-Axis Position Drift with Constant Gyro Drift

While this approach to CEP data analysis does produce roughly correct results under these three assumptions, it ends with significant error in the case of an azimuth control problem. It has been long studied and is now a well-understood fact that a constant gyro drift in the azimuth channel causes average position error to grow proportional to time squared for the first few hours and proportional to approximately time quadrupled in the first hour. Some systems are specified for slightly higher performance in the first hour than in subsequent hours, so often in the name of cost-

effective test, CEP is measured only in the first hour using the time-averaging scheme and then it is assumed that if it passes this more stringent initial requirement, it must be able to pass the subsequent and less stringent requirements. Figure 4 illustrates the problem in the first hour.

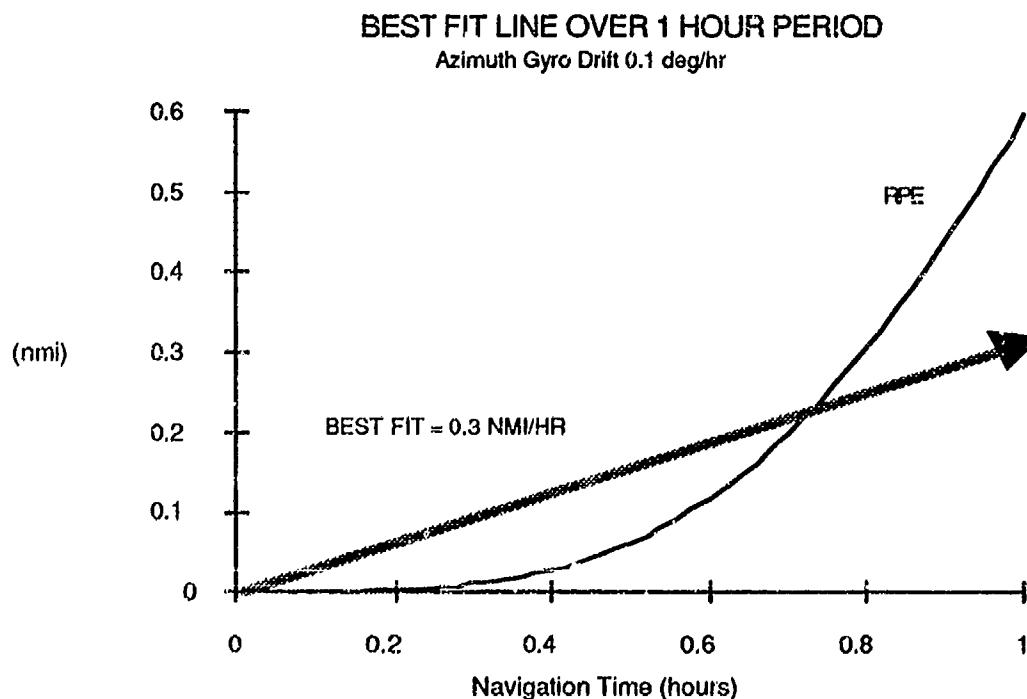


Figure 4. Problem of Best-Fit Lines in the First Hour

If a user required an IN good to 0.3 nmi/hr CEP for one hour, the system represented in Figure 4 would pass using the best-fit line scheme since that came out to approximately 0.3 nmi/hr. But in the field the user would find position errors at the 1 hour point exceeding 0.6 nmi for half the time period. That would be twice the specified limit and the performance of the user's next-higher system would be significantly degraded.

Further, the position performance degrades more dramatically and more quickly over the next three hours as shown in Figure 5.

RPE grows to nearly 12 nmi after 4 hours which would just barely be contained by a 3.0 nmi/hr limit curve passing through the origin. This is one full order of magnitude greater than the 0.3 nmi/hr requirement; however, the system could have passed using the best-fit line scheme in the first hour.

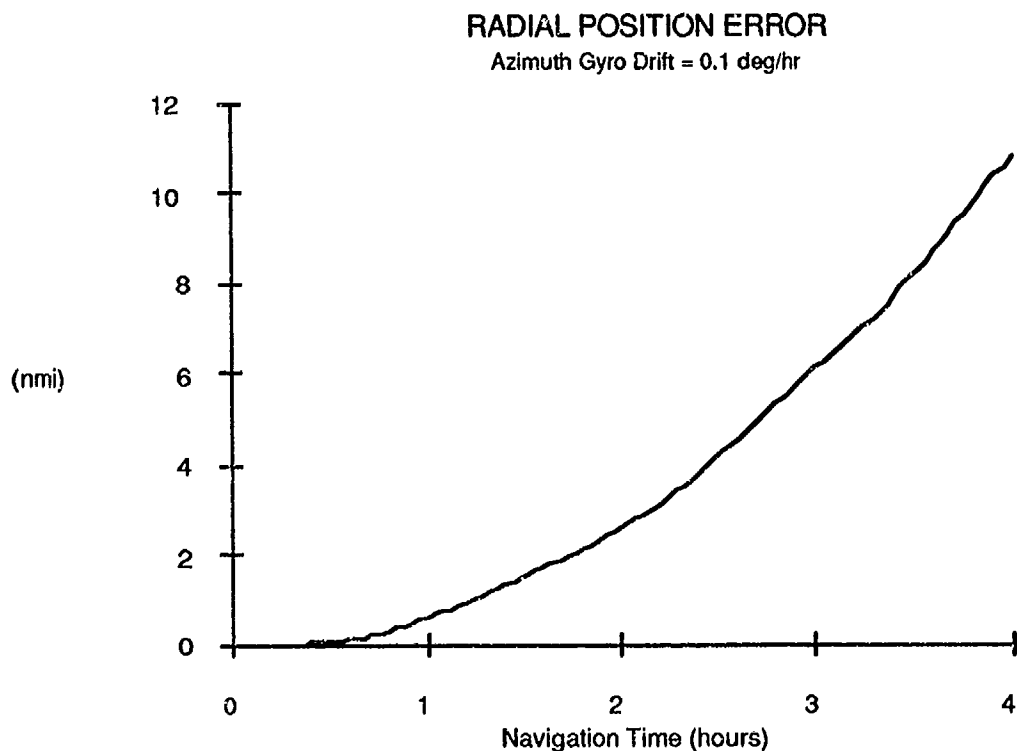


Figure 5. Radial Position Error Over Four-Hour Period

Problem #3 ***CEP SPECIFICATION CURVES ARE RARELY DRAWN***

In a typical specification, we see words like, "0.8 nmi CEP *per hour* of navigation time." So the all-important position error specification for an INS is not a *constant* number, but the number varies as a function of time and, in the general case, is not necessarily linear with respect to time. This is probably the single most commonly misunderstood concept among INS users, purchasers, and even the vendors themselves.

Although a position error specification *can* be given in words only, a picture is really essential if the specification is to gain wide understanding by the variety of specialists whose work is involved with the INS. As an example, Figure 6 illustrates the words found in typical medium-accuracy military INS performance specifications.

The picture is quite complex. It is broken up into three time phases, mixes 50 and 95 percentile parameters, and mixes radial errors with along-track and cross-track errors. However, by collecting and plotting the data in accordance with AIR STD 53/16, the average reader needn't have a full engineering background in order to quickly assess system compliance. As an example, Figure 7 shows hypothetical INS performance, 95 percentile, against a 2 nmi/hr, 95 percentile zero-intercept specification. The curve

POSITION ACCURACY SPECIFICATION

GC ALIGN, minimum 6 flights required for evaluation

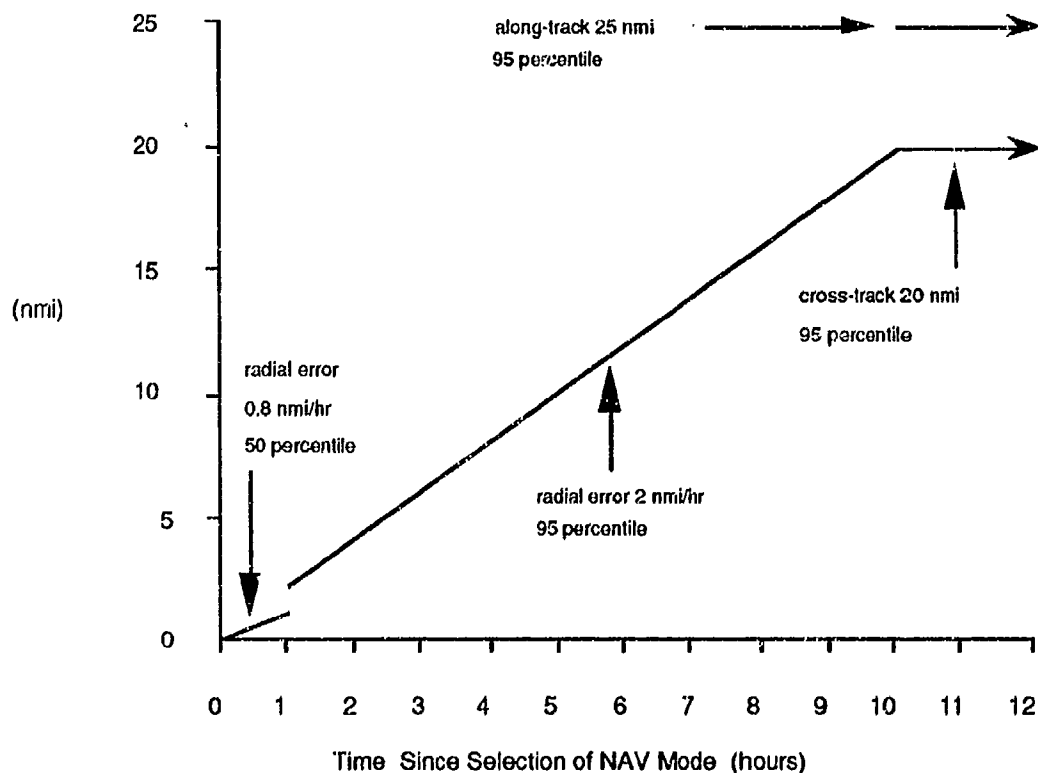


Figure 6. Graphic Representation of Position Accuracy

Specification accurately represents what the six-flight 95 percentile performance would be for an ideal INS with a constant azimuth gyro drift error. Just prior to the five-hour point, the INS performance curve crosses the dotted 2 nmi/hr "limit curve." It is at this point that the INS is declared failed. Failure is not based on a best-fit line. It should be noted that even if the INS performance curve had exceeded the limit curve only briefly and then fallen below the limit curve for the remainder of the time, the INS must still be declared as failed in accordance with ASCC Air Standards.

Problem #4

STRAPDOWN INS CEP IS A FUNCTION OF FLIGHT PROFILE

Systems in the 90's will consist almost entirely of strapdown instead of gimballed platforms. However, the added reliability gained by removing the gimbals comes not without penalties. Not only are the strapdown systems typically less accurate, but analyzing, measuring, and predicting strapdown performance is no longer the simple pad-and-pencil operation enjoyed by

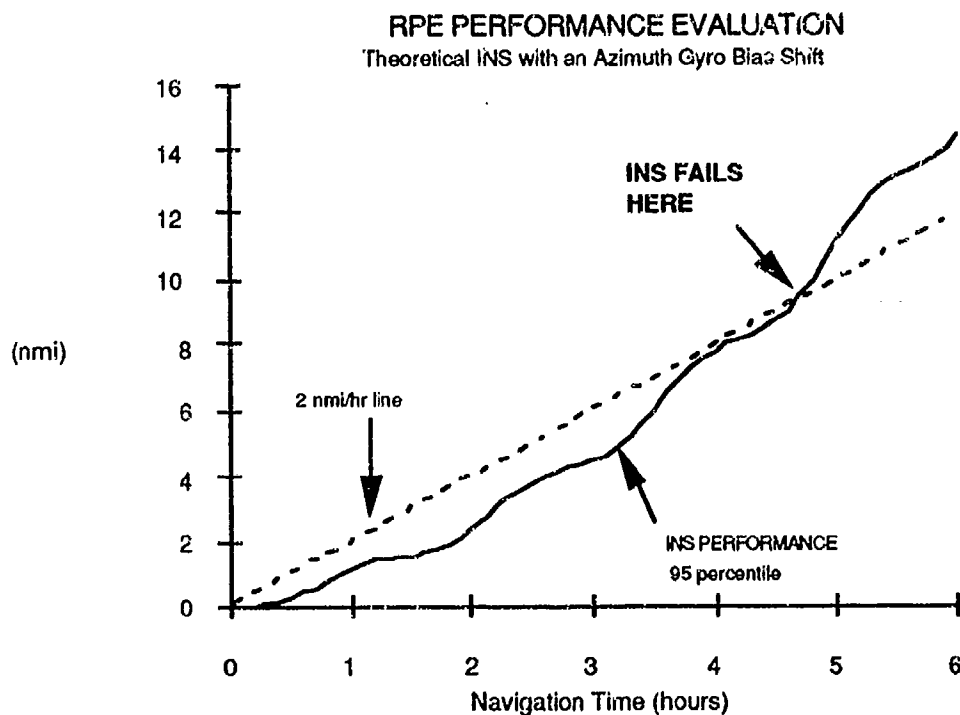


Figure 7. Hypothetical INS Performance

gimballed platform users of the past.

For the local-level wander-azimuth platform systems, the gyros and accelerometers remain approximately fixed in space (always pointing along local-vertical) for slow-moving vehicles no matter what rocking and rolling the vehicle might execute. Thus it is a simple matter to predict position performance based on known sensor performance. And the reverse is true as well. Given measurements of performance and the assurance of sensor stability in space, relatively simple analytical techniques can be used to derive (and troubleshoot) sensor performance.

For the strapdown IN, where the inertial sensors are essentially "strapped down" to the vehicle frame, only in the case of constant vehicle attitude (e.g., parked) can those simple techniques be applied. As the vehicle pitches and rolls and yaws, the sensors are pointed in varying directions and errors measured in a particular direction will be composed of errors from different sensors at different times. This makes for a very difficult task of decomposing position performance data into sensor performance or predicting navigation performance given sensor performance.

Let's take a look at a very simple example to illustrate this principle: A strapdown IN, with a typical level-axis gyro bias error of 0.01 deg/hr pointed east, is flown north for 84 minutes, a quick U-turn is made, then it

returns south for another 84 minutes. In theory, the position error at the end of this flight scenario is exactly zero. Figure 8, however, represents what really happens during the flight.

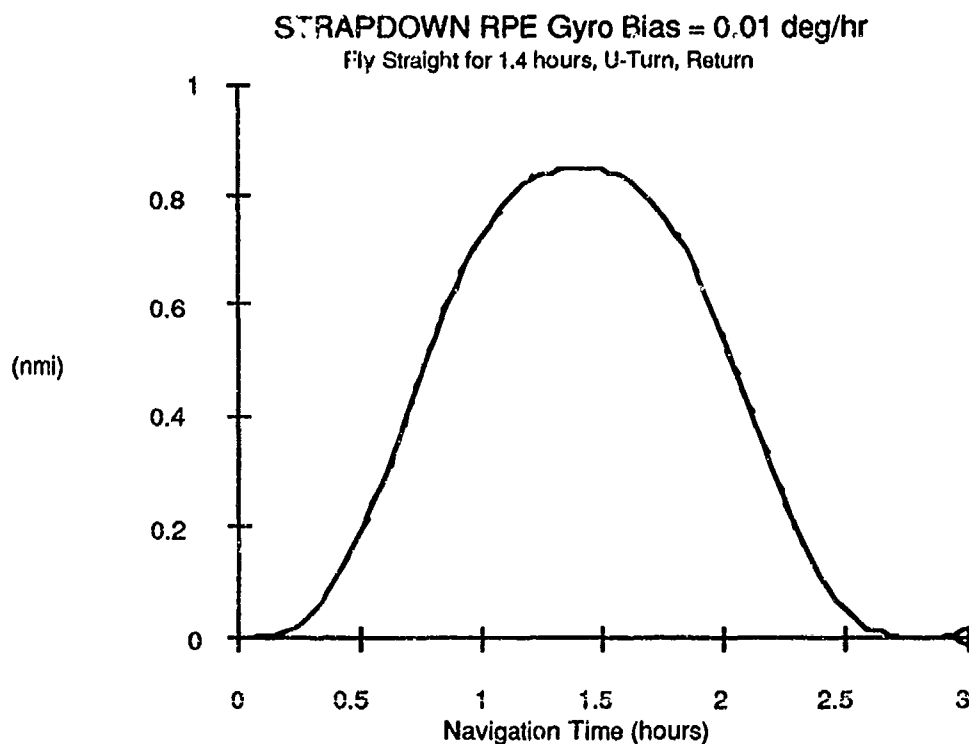


Figure 8. Strapdown CEP Sensitivity to Flight Profile

Position error builds north in accordance with Equation (1) as expected during the first 1.4 hours. Then, because the offending gyro is strapped down to the aircraft frame, the U-turn causes effective gyro bias in the navigation frame to reverse from pointing east to pointing west. Now position error builds in a southerly direction which opposes the northerly error built up during the first leg of the flight.

In this example, position error varies on average at 0.6 nmi/hr ($R\delta_{gb}$). But if the best-fit line scheme were applied here, a slope of only about 0.3 nmi/hr would be obtained. Again, a good example of why the ASCC Air Standards prohibit that practice.

Problem #5 **STRAPDOWN INS CEP CAN DEPEND UPON MOUNTING ORIENTATION**

If a particular gyro is going to spend most of its time aligned vertically with

respect to local-level, INS designers can allow slightly less stable gyros to be installed in that slot. This is true of gimballed platform as well as strapdown systems. The rationale is sound, that position performance is significantly less sensitive to vertical-axis gyro drift than to level-axis gyro drift. The incentive for the designer is in cost savings.

The problem arises when an IN is performing well in one aircraft but is installed in another aircraft requiring a different mounting orientation such that the normally vertical gyro is flying in the level plane. Now, position performance might be significantly degraded.

Problem #6

HYBRID INS USERS ARE CONCERNED WITH SHORT-TERM PERFORMANCE

Global Positioning System (GPS) aided navigation systems are sure to become prominent in the 90's. And with position fixes coming in as frequently as every second, free-inertial performance "by the hour" is of little interest. The GPS/INS designers are more interested in what happens during a 3-4 minute loss of signal (LOS) from the satellite when the navigation system will be dependent upon the free-inertial performance of the IN.

Equations are available to describe position performance over time for a variety of error sources such as accelerometer bias, gyro random walk, and heading error. Given the system error budget for the INS, standard deviation position performance can be predicted as a function of time. Figure 9 shows free-inertial position uncertainty for a representative medium-accuracy IN over a period of four minutes.

This curve is far from linear with respect to time; in fact, it is predominantly parabolic in shape driven by specific force measurement error. The GPS/INS hybrids in the 90's will be measuring accuracies in the centimeters in a time frame based in seconds. So it is apparent that it will be insufficient to specify position performance as *linear* with respect to time (i.e., x nmi/hr) as was the case in days gone by when INS performance was viewed on an hourly basis and gyro drift was the dominant error source. Position specifications will have, at the very least, to be quadratic with respect to time (e.g., ft/s^2) in the short-term. These dimensions are those of specific force measurement error, so we find ourselves getting to the very basic core of INS performance analysis - inertial measurements.

THE SOLUTIONS

This paper makes no attempt to provide all the answers or even all the problems. In fact it is hoped that others will be inspired to write about the

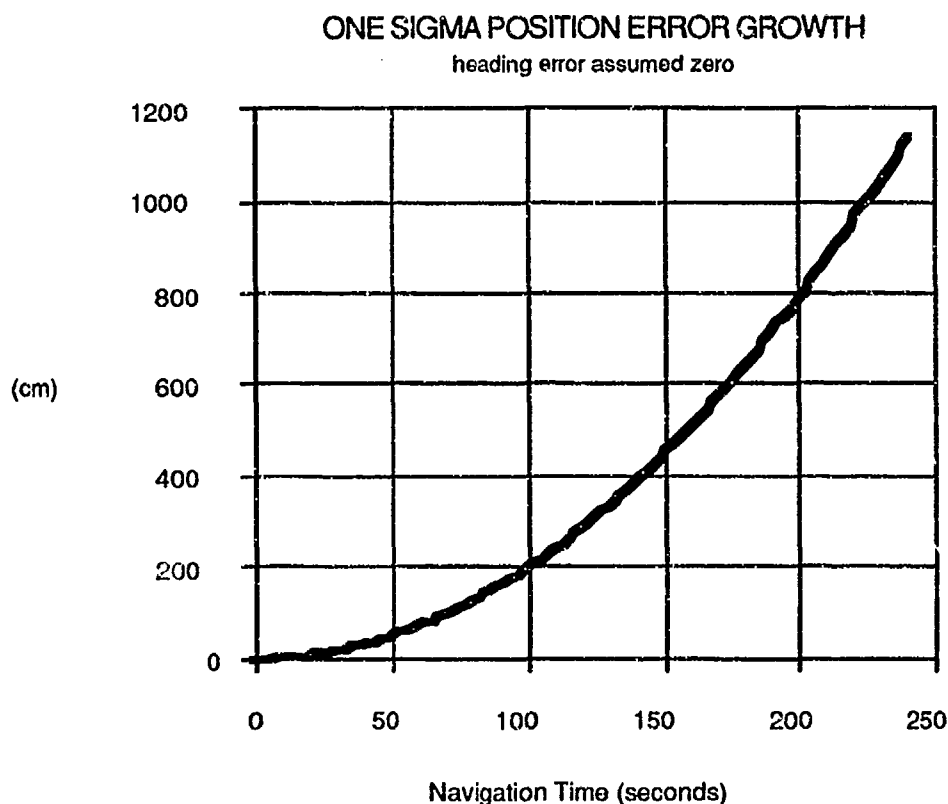


Figure 9. Short-Term Free-Inertial Position Performance

problems they have encountered and offer their ideas for solutions. Perhaps in the near future ASCC will convene to draft a standard that will provide the same leadership in INS specification that AIR STD 53/16 and 53/11B are providing in INS evaluation.

Define Performance Evaluation Conditions: The end-item user's mission profile need not necessarily be invoked to evaluate performance, especially if it is long and complex. Relatively simple and short flight maneuvers can be used effectively instead. For example, multiple S-turns can be used to quickly evaluate gyro misalignment accuracy. Straight and level flight for an hour and a half, a U-turn, then another hour and a half of straight and level flight can isolate gyro bias, heading, and accelerometer bias error sources. Specialized laboratory test equipment can simulate temperature/altitude/vibration environments encountered in the mission profile.

In the case of gimballed platform systems, evaluation conditions such as a flight profile are not so critical. But the INS of the 90's will most certainly be predominantly strapdown and thus this point must be stressed.

Draw Limit Curves: Using the *apparent* system-level sensor performance parameters derived from the mission profile and the

evaluation conditions defined, expected position performance can be projected and drawn on a graph against time. Evaluation data assessment is greatly simplified and compliance with international agreements is preserved.

The user should be careful to include expanded limit curves for time intervals of specific interest. For example, the GPS/INS user will want to be able to view the limit curve in fine detail in the 3-4 minute time frame. Such detail might not be discernable in a graph covering the 24-hour time frame. Perhaps three views of the limit curve might be in order. These would include:

- 1) short-term (3-4 minutes)
- 2) cross-country (1-4 hours)
- 3) long-term (24+ hours)

Where,

short-term views would expose accelerometer-based errors
cross-country views would expose gyro bias errors
long-term views would expose gyro random-walk and azimuth
gyro drift errors

CONCLUSION

The advent of the strapdown IN brings with it the need for a more disciplined approach to INS specification and evaluation. Research into these areas uncovers standards that already exist to provide direction in INS evaluation, but many in the INS community are apparently unaware of their existence or the requirements that they impose through international agreement.

Diligent study and education of the INS community could certainly provide one path to improvement in the INS procurement process which stands to benefit all parties involved. It is hoped that this paper can provide one step in that direction.

AERIAL CABLE TEST CAPABILITY
PRECISION TESTING IN A CONTROLLED ENVIRONMENT

Robert E. Green

Instrumentation Directorate
White Sands Missile Range, New Mexico

Aerial Cable Test Capability
Precision Testing in a Controlled Environment

INTRODUCTION

The Sandia National Laboratories (SNL) began the use of aerial cables as a testing device in 1968. The original installation was a steel cable stretched across a canyon. It was used to support items that were dropped for test purposes. The technique proved to be a cost effective testing method. The Sandia Facility has evolved since the initial cable erection. A location that permitted a longer span and greater ground clearance was identified and a cable erected. The new facility provided improved drop testing capability but was limited to the velocities that could be achieved by gravity from an altitude of 800 feet. A rocket sled was added to the facility in order to achieve greater downward velocities. This was accomplished by attaching a line to the test object suspended on the overhead cable. This line was threaded through a pulley anchored to the ground and then attached to a rocket sled. Simultaneous release of the test object from the overhead cable and ignition of the rocket sled permits achieving a desired impact velocity. This velocity can be varied by altitude of the overhead cable and the impulse of the rockets used on the sled. Methods of propelling a trolley along an overhead cable were also developed. Propulsion by rockets and gravity have been used successfully by SNL. This aerial cable facility was developed by Sandia for the testing of nuclear material containers as a part of their mission for the Department of Energy (DOE).

Various elements of the Department of Defense (DOD) have made use of the aerial cable facility at SNL. A wide variety of drop tests ranging from submunitions to fuel-air explosives have utilized these overhead cables as a drop platform. Short range air defense missiles have used targets moving along the cable to perform inexpensive developmental tests. The cables have also been used as a platform for countermeasures testing. Initial tests of new Unmanned Aerial Vehicle (UAV) concepts have also been conducted on the cable facility by elements of DOD. All three Services within DOD have made extensive use of the SNL aerial cable facility at Albuquerque, New Mexico.

Continued frequent use of the SNL facility by various elements of the DOD has created congestion among the various customers. It has caused some interference in completing the DOE mission for which the facility was developed. The facility is near the Albuquerque International Airport which has raised questions about the safety of conducting short range air defense

missile tests there. The canyon utilized for the Sandia aerial cable facility is narrow and deep and therefore presents only one engagement angle for air defense missile firings. After reviewing the status of the SNL aerial cable facility, the Deputy Director of Defense Research and Engineering for Test and Evaluation (DDDRE(T&E)) made the decision in 1988 to develop an aerial cable test capability for the DOD. SNL was tasked by DOD to survey the areas of land controlled by the Department and recommend the three most favorable sites for an expanded aerial cable testing facility. The three most favorable sites identified were all located on White Sands Missile Range (WSMR). As a result, in August of 1989 the Instrumentation Directorate at WSMR was assigned the responsibility for the development of a DOD Aerial Cable Test Capability (ACTC).

AN AERIAL CABLE RANGE (ACR) CONCEPT

The experience of the SNL cable testing personnel was used to identify the desired parameters for the new DOD cable facility. The new facility needed expanded capabilities over the Albuquerque facility in order to meet the needs of DOD testers. The need for these expanded capabilities had been identified by interaction with DOD customers at the SNL cable facility. Based on the available information, the sites selected will accommodate a cable span of approximately three miles. This cable is expected to support moving loads of up to 20,000 pounds at velocities up to 550 knots. The sites chosen provide a wide range of variation in target aspect angle with both sky and cluttered backgrounds. In addition, it was desired that cable heights of 1000 feet be provided if a suitable location could be found.

The sites that were identified will permit the development of an Aerial Cable Range (ACR) that meets these requirements. Only one site was located that would provide the 1000 feet of ground clearance. The ACP concept has been developed based on the concepts outlined by SNL. A 2 1/2 inch diameter KEVLAR cable spanning an unsupported distance of 15,500 feet is planned. The cable is expected to have a breaking strength of 450,000 pounds. This cable is expected to be the longest unsupported cable span in the world. Tension in the cable will be varied to change the height of the cable. Maximum tension is not expected to exceed 140,000 pounds. The KEVLAR cable may be jacketed to protect the KEVLAR from heat, abrasion, and ultra violet exposure and the reduce sliding friction on the surface. Motorized equipment to control cable tension will be used for quickly raising and lowering the cable.

Supporting facilities will be constructed to make the ACR a fully functional self-contained testing facility. Service areas will be provided at each end of the cable and at the low point of the cable span. The service area at the low point of the cable will be used for installing trolleys or targets onto the cable. The service areas at either end of the cable will be used to service objects that are already installed on the cable for conducting specific tests. Installing rockets, instrumentation, and control equipment are examples of services that might be performed at the ends of the cable. Manual arming of rockets and other pyrotechnics may also be functions performed at these service areas. A control bunker will be constructed that will be used for housing personnel conducting tests. It will be hardened to provide protection from test objects that may go astray. Cable target control, tracking instrument control, test sequencing, countdown, and test management are functions planned to be housed in the control bunker. A target/trolley assembly building will be located near the control bunker. This building will provide shop facilities for servicing targets and trolleys that are used on the cable. It will also include office space for personnel managing and servicing the ACTC. Explosive storage and explosive assembly buildings will be located at a safe distance away from the rest of this area. Rocket motors, missiles, and other pyrotechnics will be stored in approved explosive storage bunkers. Equipment using these components will be assembled in the explosive assembly building and then transported to the cable target/trolley or launch site for testing. A metal hangar building is included in the ACTC plans. It will be used to house trolleys and targets when not in use. Roads, power, and communications will be installed to permit the ACTC to be a functional test facility.

An aerial cable can be used to support a wide variety of targets and trolleys. The simplest example is a fixture that hangs on the cable used to suspend objects above the ground. Trolleys that move along the cable add another dimension to the testing possibilities. A simple box carrying instrumentation and/or sensors provides an inexpensive testing platform for a variety of applications. Past examples have included electro optical countermeasures, miss distance measurement systems, captive carry seeker tests, and decoy evaluation systems. High speed rocket powered trolleys provide a further expansion of the types of tests that can be performed at the ACR. Prototypes of bombs and rockets that would normally be dropped from aircraft can be tested. UAV concepts can be verified using this high speed capability. Captive carry of seekers and sensors can be carried out economically and repeatability. Air-to-ground munitions tests can be conducted under highly controlled conditions to aid in verifying proper function. In addition to

these types of trolleys, mockups of full-sized, fixed, and rotary winged aircraft may be used on the cable. These cable craft may be used for targets in short range air defense missile testing. These vehicles must be light weight and cannot use standard aircraft engines. This means that it is practical to fabricate the cable targets to be threat realistic in both shape and signature. It is expected that these targets will be repairable and therefore reusable making them very cost effective in short range air defense missile testing. Mockups of U.S. aircraft are planned for use in the study of separation dynamics for a wide variety of aircraft stores. Repeated tests under the same conditions make this an attractive ACR application. High precision remotely controlled instrumentation will provide high quality test data that cannot be achieved using current testing methods.

A dedicated suite of instrumentation is being proposed for the ACR. The limited range for tests conducted using the cable permits instruments to be located optimally for highly accurate measurements. The plan is to collect Time, Space, Position Information (TSPI), miss distance, and telemetry from an array of remotely controlled tracking mounts. Each tracking mount will be equipped with infrared and video image trackers, laser range finders, and telemetry receiving antennas. The present proposal is to acquire three mounts so equipped. It is planned that these tracking mounts will be networked to the control bunker using a fiber optics system. This will permit real-time utilization of the TSPI, imaging, and telemetry data for immediate test evaluation results. A real-time three dimensional image processing system is also proposed. It will provide three dimensional views of both target and interceptor from a vantage point chosen by the customer. TSPI, attitude and associated rates, and miss distance will be computed and displayed in real-time. Playback at reduced speeds and from other vantage points will be available at the conclusion of each test. A real-time distributed computing system is part of the same proposal to provide final test reports at the conclusion of each test.

PRECISION TESTING APPLICATIONS

The ACR configuration will provide the opportunity to conduct testing programs in an efficient and cost effective manner. A testing program will be able to use this compact range with less interface expense and time as compared to using the regular WSMR test documentation process. This will permit a customer to come to the ACR, conduct a test, and receive test results without experiencing the delays that WSMR Users normally experience;

unless extensive post mission processing and data reduction are necessary. The following paragraphs illustrate the types of testing programs that are expected to utilize the ACR.

Short range air defense missile testing has made effective use of the SNL cable facility. This was demonstrated over several test programs even though the facility could accommodate only a single firing azimuth. The WSMR facility will provide greater flexibility in firing azimuths, target backgrounds, target altitude, target dynamics, and target variety. The ACR will permit short range air defense systems to fire at threat realistic targets moving at expected combat speeds. These targets will display signatures that replicate the threat. Cable mounted targets are expected to survive most hits, be easily repairable, and provide a very low life cycle cost. The quality of test data expected to be available at the ACR for testing short range air defense missiles is shown in Table 1 below.

Table 1

Short Range Air Defense Test Data Quality

Measurement Type	Accuracy Tolerances
TSPI	Pos: ± 1 ft, Vel: ± 1 ft/sec, Acc: ± 2 ft/sec ²
Miss Distance	Range: ± 0.5 ft Dir: ± 5 deg
Target Attitude	± 2 deg
Missile Attitude	± 5 deg

Data of the quality shown is expected to be available in real-time. Most of the testing requirements are expected to be satisfied without further data processing. The ability to view the missile-target intercept from any required viewing location is expected to provide a powerful diagnostic tool assessment of test results.

The ACTC provides an opportunity to perform drop/separation tests. These test types include submunition drop tests, weapons systems component drop tests, and stores certification. The use of the cable permits the tester to choose the release point

accurately. The same release point can be repeated very accurately for each test. This reduces the number of variables in the test; permitting the isolation of the test parameters of interest. The cable facility allows developmental objects to be dropped without incurring the time and expense of aircraft modification and certification. The use of the ACR for stores certification permits the collection of very accurate test data under repeatable conditions. It provides an opportunity to perform these tests without the danger to personnel that is attendant when using manned aircraft. The quality of test data that is expected for drop/separation tests is the same as shown in Table 1 for short range air defense tests.

An aerial cable range provides the opportunity to perform a wide variety of other types of tests in a cost effective manner. Examples include captive carry tests, countermeasures tests, seeker function tests, and signature measurements. Each of these applications benefits from the attributes of repeatable test conditions, high quality measurement data, and reduced cost by eliminating the use of manned aircraft. The use of a non-metallic cable is particularly attractive for signature measurements due to its minimal interference at the frequencies of interest.

TECHNOLOGY DEVELOPMENTS

The development of the ACTC at WSMR requires the application of new technology in several scientific disciplines. A steel cable cannot be used for this application due to insufficient tensile strength. This means that a synthetic cable must be utilized. Synthetic cables have not been used for this type of application. The ACTC application requires a cable that has high tensile strength, light weight, heat resistance, abrasion resistance, and weather resistance. There do not appear to be any currently manufactured synthetic cables that possess all of the characteristics. An investigation of large diameter synthetic cables has identified some limitations that the use of a synthetic cable will impose on the ACTC. The investigations have considered KEVLAR (aramid fiber) as the most promising candidate material. Various types of jacketing material are being considered. Trade offs to be made include abrasion resistance, coefficient of friction, and heat resistance. Polyester fiber, extruded polyester, and ceramic fibers have been suggested as potential candidates for jacketing materials. KEVLAR cables have been shown to fail when exposed to a short bending radius. This means that objects must be supported on such a cable with large radius sliders or sheaves.

The low abrasion resistance of synthetic cables will require the development of new methods of cable erection. The method must permit moving a 2 1/2 inch diameter cable across a three mile span without touching the ground at any point. The preferred site includes some rugged terrain between the end points. This makes the erection of the cable an even greater challenge.

One of the planned uses of the ACR is to present aerial targets for use in testing short range air defense weapons systems. An advantage of using the cable system is that the targets are recoverable, easily repairable, and reusable. Since cable targets of the type described are not available, a cable target technology development has been initiated. The program was designed to determine the feasibility of constructing lightweight, easily repairable, threat realistic targets that are flight worthy to speeds of 550 knots. Two target development efforts have been completed. The first was a theoretical feasibility study to determine the practicality of constructing a full sized composite model of a threat realistic aircraft. The study identified achievable weight and speed, propulsion and braking methods, and control surface requirements. It appears that a composite aircraft using surplus rockets for propulsion and braking can be fabricated at a weight of approximately 10,000 pounds. It also appears that aerodynamic control surfaces will such as ailerons, flaps, rudder, and elevators will be required to prevent the aircraft from exerting excessive pressure on the cable. Speeds of approximately 700 ft/sec at mid-cable appear to be achievable. The study also indicated that UV, IR, and radar signatures can be matched within reasonable limits. The cost of such a target appears to be competitive with the cost of converting obsolete U.S. aircraft for drone use. Droned aircraft are normally destroyed when hit by air defense missiles and therefore are not reusable.

The second target development effort was to construct a 1/4 scale model of a candidate target aircraft to be used for concept testing on the SNL cable. The model was constructed of composite materials. Three 5 inch rocket tubes were installed underneath the tail to provide propulsion. The cable carriage was installed inside the vehicle with the cable entering thru the wind screen and exiting below the vertical stabilizer. The top of the model is removable for cable installation and service. The scale model is supported on the cable at the front by a steel slider and by a 12 inch aluminum pulley at the rear. The model was mounted on the 1 1/4 inch standard steel cable at the SNL. Rockets used to propel the model included 2.75 inch and the HVAR, Zuni, and Super Zuni 5 inch rockets. The model was propelled along the cable at speeds from 80 feet per second to 380 feet per

second using the various types of rockets. The model exhibited stable flight without dynamic control at all of the speeds achieved. This was true in the presence of wind gusts as high as 25 knots. The 1/4 scale model sustained major damage when the brakes failed due to vibration on the highest speed run. However, inspection of the model showed that repair could be effected for approximately 1/3 of its original cost. This experience demonstrated effectively that composite structures can be repaired after sustaining significant damage. The viability of the concept of reusable targets was established by this unplanned test.

PROJECT STATUS

The first action in the development of the WSMR ACTC was to initiate the completion of an Environmental Impact Statement (EIS). All of the field surveys for the EIS have been completed. The Draft EIS has been completed and staffed through Army channels to Headquarters, Department of Army. The current plan predicts a Record of Decision on the EIS early in 1992. Final design of the ACTC cannot be completed until the Record of Decision has been signed.

The SNL has been tasked to design the cable, the cable erection system, and the cable tensioning system for the ACTC. This task will provide the complete design for the cable and all of the supporting equipment. This will include end supports, anchors, and tensioning equipment. The tensioning equipment are the devices that are used to raise and lower the cable. The design for this part of the ACTC is expected to be complete in the fall of 1991.

The U.S. Army Corps of Engineers has been tasked to design the remainder of the ACTC. This will include the required roads, buildings, power lines, anchors, and supports. Preliminary design work is underway but final design cannot commence until the EIS Record of Decision has been signed. Buildings planned for the ACTC include a control building, an assembly building, explosive storage, and explosive assembly. A hangar building to house targets will be constructed if funding permits. Current schedules call for completing construction late in 1993. Initial operating capability is planned for mid 1994. Continued emphasis at very high levels will be required to execute the ACTC Project according to the schedule indicated.

SUMMARY

The Aerial Cable Test Capability is a miniature test range being developed at White Sands Missile Range at the request of DDDRE(T&E). It is a scaled-up version of the aerial cable testing facility at the Sandia National Laboratories, Albuquerque, New Mexico. The Aerial Cable Range provides an opportunity to perform high precision developmental testing in a controlled environment. Test conditions can be replicated as many times as necessary to permit effective diagnostic evaluation. Threat realistic targets can be presented in a cost effective manner by using easily repairable targets that are suspended on the cable and can be reused. The test arena is limited in size permitting the collection of highly accurate test data. On site image and data processing capabilities will permit immediate evaluation of test results.

Cable and target technology are being developed as a part of the acquisition of the ACTC. New designs for synthetic cables are being considered that will be optimized for the aerial cable application. Studies and technology demonstrations have been completed to establish the feasibility of using full sized threat representative targets on an aerial cable. These investigations have demonstrated the durability and repairability of composite aircraft targets for cable operation.

The ACTC Project is currently funded and in progress. The Environmental Impact Statement has been drafted and is being staffed. The design of the cable system is underway and should be completed in the Fall of 1991. Final design of the remainder of the Facility will begin as soon as the EIS Record of Decision is signed. The planned facility Initial Operating Capability is mid 1994.

The ACTC truly represents a flexible, low cost method of precision testing in a controlled environment. It has the additional advantage that high speed threat realistic targets can be utilized. All of this capability will be available in a compact, cost effective test facility.

**Measuring Inertial Space
Gravity Probe B**

by

G. Green, C.W.F. Everitt, B. Parkinson

J. Turneare, D. Bardas

and the Stanford Relativity Gyroscope Team

Submitted to

Fifteenth Biennial Guidance Test Symposium

Hq 6585 Test Group (AFSC)

Holloman AFB, NM 88330-5000

ABSTRACT

The Gravity Probe B Relativity Gyroscope Experiment (GP-B) will provide a precise and controlled test of Einstein's General Theory of Relativity by observations of the precession of nearly perfect gyroscopes in Earth orbit. For a 650 km polar orbit the two effects predicted by the theory, known as the geodetic and frame-dragging precessions, are orthogonal with calculated rates of 6.6 arc-s/yr and 0.042 arc-s/yr respectively. The goal of the experiment is to measure the geodetic effect to better than 0.01% and the frame-dragging effect to better than 1%.

INTRODUCTION

The development of the Stanford Relativity Gyroscope Experiment has proceeded since 1964 following a proposal by L.I. Schiff for a new test of the General Theory of Relativity (Reference 1). The *geodetic* and *frame-dragging* precession rates, 6.6 arc-s/yr and 0.042 arc-s/yr respectively, will be measured with respect to the line-of-sight to a suitable guide star (Rigel), corrected for the star's proper motion and the difference between its apparent and actual positions. By fabricating the gyroscope to exacting standards, and by careful control of its environment, an absolute Newtonian drift rate (due to all known non-relativistic disturbance torques) of ≤ 0.3 milliarc-s/yr is achievable. Combining this with a similar error expected in the readout-chain yields a total measurement error in the relativistic drift rate (excluding proper motion of the guide star) of ≤ 0.43 milliarc-s/yr as shown in figure 1. In fact, the error is expected to be lower than this and thus the primary experiment objective, that of measuring the geodetic effect to $\leq 0.01\%$ and the frame-dragging effect to $\leq 1\%$, seems achievable with margin. Other experiment objectives and a comprehensive discussion of other aspects of GP-B are described in a number of papers. (References 2-4)

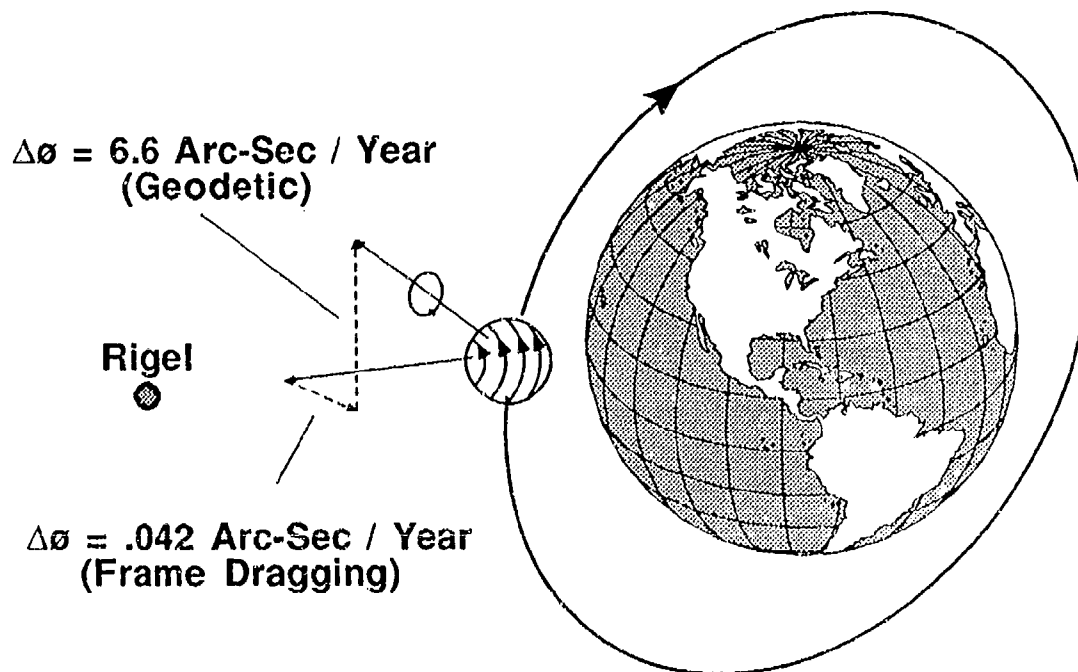


Figure 1 - The GP-B Experiment will use gyroscopes to measure the effects of relativity (curvature and rotation of inertial space) in the vicinity of earth.

THE GYROSCOPE AND EXPERIMENT PAYLOAD

The unique gyroscope design and fabrication is now complete. Error terms are controlled by the manufacturing process and environmental control. The laboratory test program of these devices is ongoing before commencing with the final fabrication followed by a shuttle flight test program followed by the satellite mission. The total integrated absolute Newtonian drift error expected of these instruments after a one year uninterrupted science mission is expected to be .0003 arc seconds.

The gyroscope rotors are made from jewel-like spheres of solid fused quartz, roughly the size of ping-pong balls (1.5-inch diameter), each coated with a very thin (15 nanometer), very uniform, chemically pure, mechanically robust, electrically stable layer of the metal niobium. The rotor spheres achieve "near zero" extremes of homogeneity, mechanical sphericity, and electrical sphericity.

Homogeneity is achieved through the choice of material. Quartz is stable, has good inherent uniformity and shrinks uniformly on cooling; being transparent it can also be optically selected to near-perfection. Density variations in these quartz spheres will be minute, parts in ten million, thousands of times less than in typical metal spheres. Equally severe constraints apply to the uniformity of the niobium coatings. To yield a uniform coating, the rotor is moved to 32 orientations corresponding to the faces and vertices of a regular icosahedron with an equal amount of niobium deposited for each orientation. Typical density homogeneity of the quartz rotor to better than $2 \times 10^{-6} \Delta \rho / \rho$ is achieved.

Mechanically, the 1.5-inch diameter rotors are within 40 atomic layers (0.8 millionth-inch) of a perfect sphere, rounder than anything within many light-years distance from us. If the Earth were smoothed to a proportionate sphericity, then the corresponding radial span, from towering mountain top to deep ocean trench, would be 20 feet. Only neutron stars are rounder.

Electrical sphericity, more subtly, requires that a quantity known as the electric dipole moment, fixed by the rotor's surface properties, be vanishingly small. Its value, scaled against the maximum allowable charge on the rotor, must be held to parts in ten million.

Attaining this triad of manufacturing extremes has demanded the invention of new methods for lapping, polishing and coating the spheres, and of new instruments for selecting the material and measuring the rotor's diameter, sphericity and surface properties. (References 5-7)

Each rotor spins inside a stator quartz housing, made in two halves to form a spherical cavity with clearances to the rotor of barely one thousandth of an inch. The matched housing halves are fabricated from the fused-quartz blanks into their final shape by ultrasonic machining, diamond grinding, lapping, and polishing. The stator surface is required to be spherical within 250 nanometers peak-to-valley. To achieve this requirement, approximate hemispheres are formed in the two halves by ultrasonic machining and hand lapping, the halves are precisely joined with tapered fused-quartz pins, and the assembled pair is tumble lapped. Tumble lapping is a process in which a weighted lapping element and slurry of grinding compound and water are located in the spherical cavity formed by the assembled housing, then the housing is randomly rotated about the lapping element.

To build a gyro absolutely accurate, early in the program four fundamental issues had to be resolved:

- 1) *Suspension*: How could the gyro rotors be suspended in mid-air (or mid-vacuum) without disturbance?
- 2) *Spin-up*: How could the rotors be set spinning and be kept spinning isolation for many years without disturbance?
- 3) *Readout*: Most baffling, how could the spin direction of a perfect unmarked sphere be observed and read out without disturbance?
- 4) *Environmental Control*: How could the environment be controlled sufficiently so that no torques effect the rotating member?

In part, the answers lay in a separation of functions—electrical suspension, gas spin-up, and magnetic readout. In part, they lay in exploiting phenomena of superconductivity. And in part, they lay in precision control of gravity, magnetic and thermal environments.

Levitation is electrical with voltages applied to three pairs of saucer-shaped electrodes inside the spherical cavities, and the rotor stays centered to a few millionths of an inch while spinning at 10,000 rpm. To lift the rotor in a one g field takes 1,000 volts and resultant suspension torques. Mass-unbalance disturbance torques (where the mass unbalance is measured by the difference between the rotor center of support and center of mass) and the other disturbance torques coming from the suspension electrode voltages need to be further reduced. However if the gyroscopes are place

in a controlled orbiting satellite, only micro-g levitation is required and only a fraction of a volt is needed for suspension.

Spin-up is by a scheme much like an old-fashioned water-wheel. A stream of helium gas is pumped past the ball at nearly the speed of sound, through a channel of sophisticated design cut in the inner surface of the stator housing. Full rotor speed is reached in half an hour. Again if this is accomplished in an orbiting satellite, evacuation to space is easy and the gas can be diminished to a pressure lower even than that of the space around the satellite, and the rotor coasts freely in vacuum. The subtleties lie in preventing electrical arcing during the spin-up cycle from the suspension system and in reaching final pressure—a pressure so low (10^{-11} torr or $1/100,000,000,000,000$ of an atmosphere) that in 1,000 years the gyroscope will barely lose 1% of its starting speed. (Reference 8)

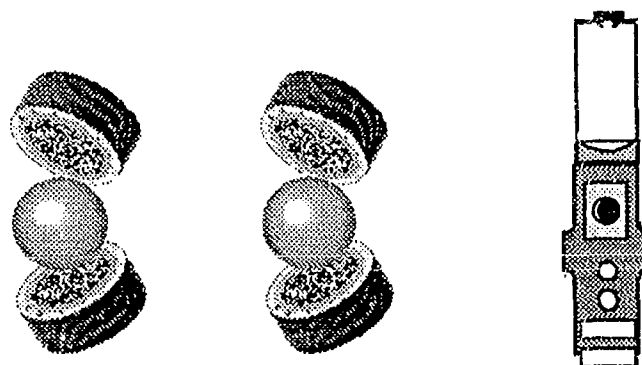


Figure 2 - Four quartz gyroscopes as shown above left are housed in a quartz block shown above right.

For a readout, the problem is to measure—to 1 milliarc-second—the direction of spin of a perfect unmarked sphere, and do so without disturbing it?

The answer comes through superconductivity, a phenomenon first seen in metals at low temperatures by the Dutch physicist H. Kamerlingh Onnes in 1911, and now known in some ceramic materials at higher temperatures.

Superconductivity provides a spin pointer—one that is neither optical nor mechanical as in conventional gyroscopes but magnetic. It requires a sensitive noninterfering instrument, the SQUID (Superconducting Quantum Interference Device), to read the pointer. It also provides a region of very low and stable magnetic field for the gyroscope to minimize any magnetic error sources.

One property of superconductors is that when cooled below a specific "transition temperature" they completely lose their electrical resistance. Hence their name; they become not just "great" conductors, but for steady currents, perfect ones; currents have been shown to persist for many years absolutely unchanged.

Another phenomenon, equally surprising, is that when a superconductor—niobium, for example—spins, it generates a magnetic field effect known, after physicist Fritz London, as the London moment. Picture the niobium coating on the quartz gyro rotor as a crystalline lattice of positively charged atoms containing a sea of infinitely slippery electrons or to be more exact, electron-pairs. As the rotor starts turning, the niobium atoms move with it, but not the electron-pairs—not at first anyway.

Each circling positive charge, like a small electric current, generates a magnetic field parallel to the rotation axis. The total field thus produced would be very large, were it not that the paired electrons themselves respond to it. Nearly all are forced to keep up with the lattice, generating a cancelling field of their own except in a shallow surface layer about 100 atoms thick. In this layer they lag slightly behind the charged lattice leaving a small difference field—the London moment—proportional to spin speed and exactly aligned with the spin axis. Here is our pointer for the readout. Readout of gyroscope is accomplished by detecting changes in the direction of the London magnetic dipole moment which is co-aligned with the spin vector of the gyroscope. It results because the surface of the spinning rotor has a superconducting coating (~ 2.5 mm Nb, $T_c = 9.2$ K).

To measure the spin direction, the rotor is encircled with a thin superconducting loop connected to a SQUID. As the gyro rotor tilts relative to the case (stator), the London moment tilts with it, changing minutely the magnetic field through the loop. So sensitive is the SQUID that a field change of 5×10^{-14} gauss (1/10,000,000,000,000 of the Earth's magnetic field), corresponding to a gyro tilt of 1 milliarc-second, is detectable within a few days of data collection.

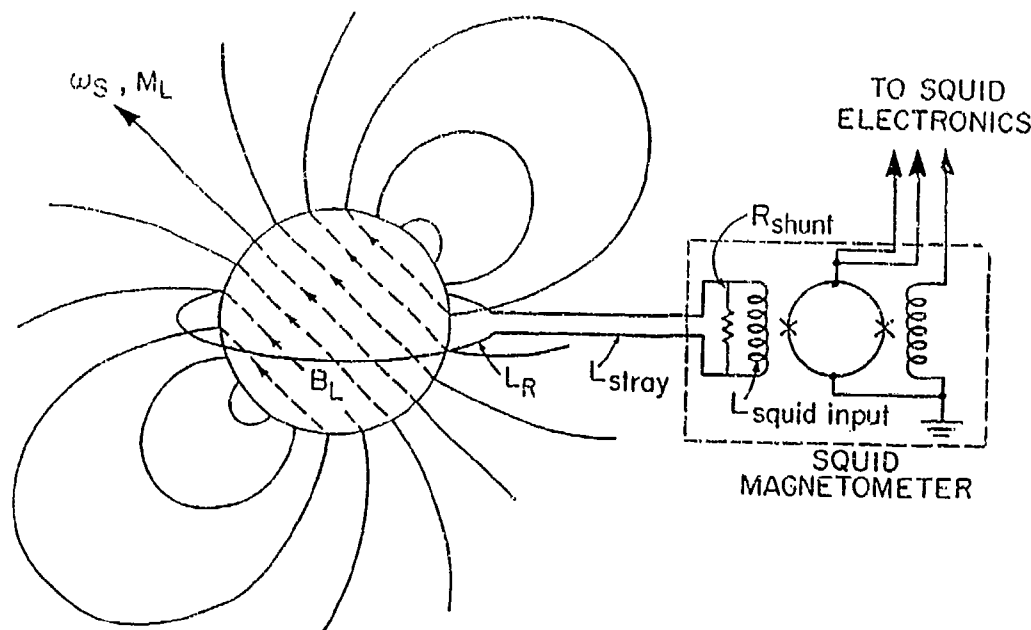


Figure 3 - The sensitive Squid measures the gyro spin axis by using the London Moment

The suspension, spin-up and readout stator housing features are produced by sputter deposition. These include the six suspension electrodes, the support lands around the electrodes, the spin-up land, and the gyro readout loop. The first three coatings are all thin copper films with a titanium bonding layer. The electrodes are about 3.5 mm thick and the lands are 13 mm thick. The readout loop is produced by depositing a 400 nm thick niobium layer overcoated with a 20 nm gold layer to assist in bonding wires and then by patterning the loop using either photolithographic or laser milling techniques. All of these coatings have successfully undergone multiple thermal cycles between room temperature and 4°K. (Reference 8)

The exquisite sensitivity of the SQUID plus other constraints require that the gyroscope be operated in a magnetic field that is both very low and very stable. The field trapped in the rotor when it goes superconducting has to be practically zero; effects from the Earth's field varying from a spacecraft roll has to be attenuated by a factor of 10,000,000,000,000 before reaching the gyroscope.

One property of superconductors is that a closed superconducting shell cannot be penetrated by external magnetic fields. Long lead bags are used for shielding—the “balloons”—are applied first to pump magnetic fields out of the space containing the scientific instrument and then to keep them out. Four folded bags, known as lead balloons, are successively inserted each into the one before, cooled to superconducting temperatures and expanded. Each expansion lowers the field. Already large bags, containing operating gyroscopes, have been made with the lowest stable magnetic fields ever produced.

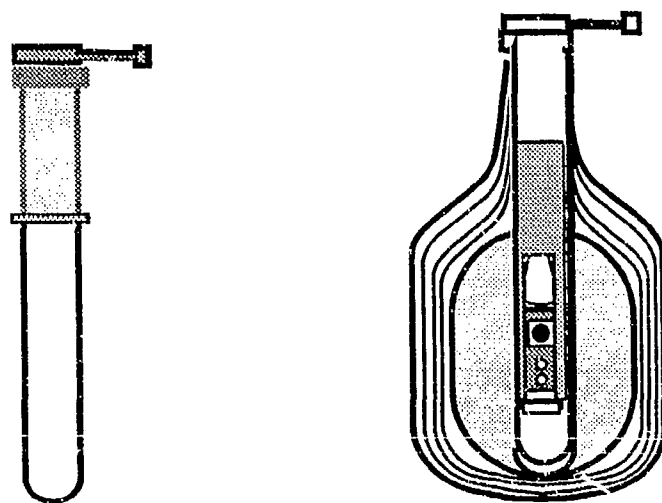


Figure 4 - Magnetic shielding is provided by superconducting lead bag enclosure of the gyroscope

Attenuating the magnetic fluctuations by 10^{-12} for the SQUID readout takes, in addition to the lead bag, an outer shield of special iron alloy, local superconducting shields around each gyroscope, and finally the self-shielding action of the superconducting rotor within its own readout loop.

The Science Instrument Assembly consists of a block of fused quartz, 21 inches long, bonded to a quartz telescope and containing within it four gyroscopes plus a drag-free proof mass. This gyro-telescope structure is kept at vacuum within a nine foot-long cigar-shaped chamber (“the probe”), which is inserted into a large dewar vessel filled initially with 400 gallons of superfluid helium. The dewar maintains the instruments at a temperature of 1.8°K above absolute zero.

The drag free proof mass housed in the quartz block is a 1.5 inch quartz sphere in a slightly larger spherical cavity than that of the gyroscope. The proof mass, being shielded from external accelerations, tends to follow an

ideal gravitational orbit; and by sensing its position and applying thrust forces to make the spacecraft chase after it, the satellite can be made drag-free. The Helium gas boiling off from the dewar is expelled thru thrusters to maintain the proof mass at the center of the cavity. Because the mean acceleration on the gyroscopes is thus reduced to 10^{-11} g's by controlling to the proof mass, the gyroscope performance improves by a factor of 1,000. The drag free concept was developed at Stanford and demonstrated in 1972 by flight on the U.S. Navy's Triad Transit navigation satellite.

CHARACTERISTICS

- **USES HELIUM BOIL OFF**
 - Mass flow ~ 1 mg sec
 - Force ~ 1 millinewton
 - Reynold's number < 100
- **PROPORTIONAL**
 - Electromagnetic Actuator
 - Restrictor
- **NOZZLE FEATURES**
 - Exit Cone = 20 deg
 - Area Expansion Ratio = 4
 - Knudson Number > 1
 - * Free molecular Flow
 - * Slip Flow

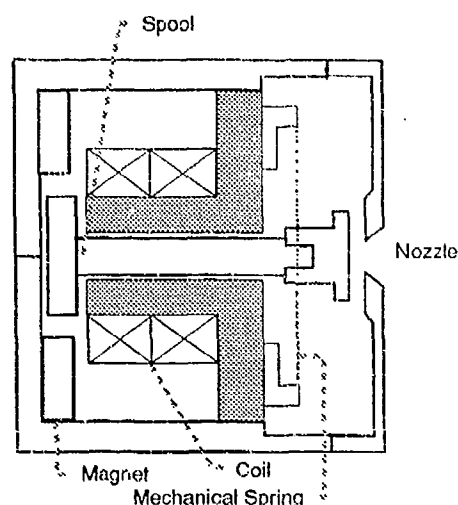


Figure 5 - The GP-B spacecraft proportional thrusters use the dewar exhaust gas to maintain attitude and drag free control of the spacecraft.

The flight telescope is used as sensor for the spacecraft attitude control system and for the measurement of the total gyro drift. The telescope provides the signal to maintain the satellite's roll axis pointing in the direction of the guide star to milliarc-seconds. Any small deviation in pointing is compared with the gyroscope readout signal to determine the spin-axis direction of the gyroscopes relative to the reference. The telescope is also fabricated from fused quartz and is operated at a nominal 1.8°K. It has a physical length of 14 inches and a focal length of 150 inches. It's precision is 0.1 milliarc-second over a linear range of 70 milliarc-seconds. The total acquisition range is 2 arc-minutes. The readout of star direction is rigidly attached to the gyro readouts through the quartz block.

The gyro readout is referenced to the fixed stars since the readout loop is mechanically coupled to the telescope pointed at the guide star Rigel (the readout loop plane is aligned parallel to the telescope axis) and to a star blipper looking approximately normal to the telescope axis. The spacecraft together with the readout loop rolls about the line-of-sight to the star Rigel with a roll period of 10 minutes. The SQUID output is modulated at the 1.67 mHz roll frequency. The amplitude of the 1.67 mHz output is proportional to the angle between the gyro spin axis and the roll axis, and its phase is related to the position of the stars in the field of the star blipper. Misalignment between the roll axis and the line of-sight to Rigel can be subtracted from the SQUID output using the two-axis telescope readout signals, finally yielding an overall gyro readout.

The opening of the dewar is a necktube where the vacuum probe for the quartz block housing containing the gyroscopes is emplaced. The design of the vacuum probe and necktube represent a formidable physics and engineering challenge. First the assembly must survive launch loads. In addition it must meet the following abbreviated list of requirements: (1) Maintain stable quartz block temperatures of 1.8 °K, (2) Remove spin-up gas rapidly to prevent electrical breakdown, (3) Create an operating vacuum of better than 10^{-11} torr (gyro spin-down time constant is 4000 years), (4) Reduce the magnetic field to 10^{-14} gauss, (5) Minimize the heat leaks into the payload so the superfluid helium lasts 1 to 2 years, (6) Allow "rapid" assembly and disassembly, and (7) support all the interconnecting electrical cabling for the instruments of the stable quartz block assembly, readouts, heaters, thermometers, and other instrumentation (approximately 400 wires).

The evolved design supports the Quartz-Block load with a cantilevered aluminum cylinder. This is within the vacuum shell, both of which are attached at the base of the neck tube assembly. The neck-tube is wound of alumina fibers and bonded with epoxy. This composite material has particularly high thermal resistance combined with high strength over the entire temperature range.

In order to spin up the gyroscopes a system supplying an gyroscope with low temperature (5° - 7°K) helium gas through an in line class 100 articulate filter. Exhaust lines then vent most of the spin up gas to an external thrust nullifier located on the spacecraft. Five heat-exchanger stations allow the warm gyro spin-up gas to be efficiently cooled by the exhaust gas. Leakage gas is pumped out of the neck tube. A large gate valve on the front of the probe is open during spin up to vent to space a residual gas leaking into the probe. After spin-up the probe gate valve is closed and

an innovative "bake out" scheme is used to attain the operating vacuum. To mount and demount the probe, a quick disconnect mechanism called an axial-lock is used. Gold-coated windows and radiation baffles further restrict the amount of stray heat that is admitted to the payload.

The helium dewar maintains the space telescope/quartz block assembly at a low temperature of less than 2 °K for 16 1/2 months. The helium boil off gas is used as a propellant by the spacecraft force and torque system to maintain the 10^{-11} g's on the science gyroscopes.

The dewar is a toroidal, 1580 Liter SFHe tank made from 6061-T6 aluminum. Its neck-tube section is also constructed of alumina-epoxy. In addition to the main tank a special guard-tank with 63 liters of normal helium is used to simplify launch pad operations by intercepting heat before it reaches the main superfluid helium. This avoids the necessity of complex helium transfer or pumping operations while on the launch pad. Insulation is provided by four vapor-cooled shields, multilayer insulation and 12 Passive Orbital Disconnect Struts (PODS) which offer high resistance heat paths in space, but stiff and strong capacities when placed under launch loads. The piping allows the normal filling, venting and burst relief through a system of remotely actuated valves.

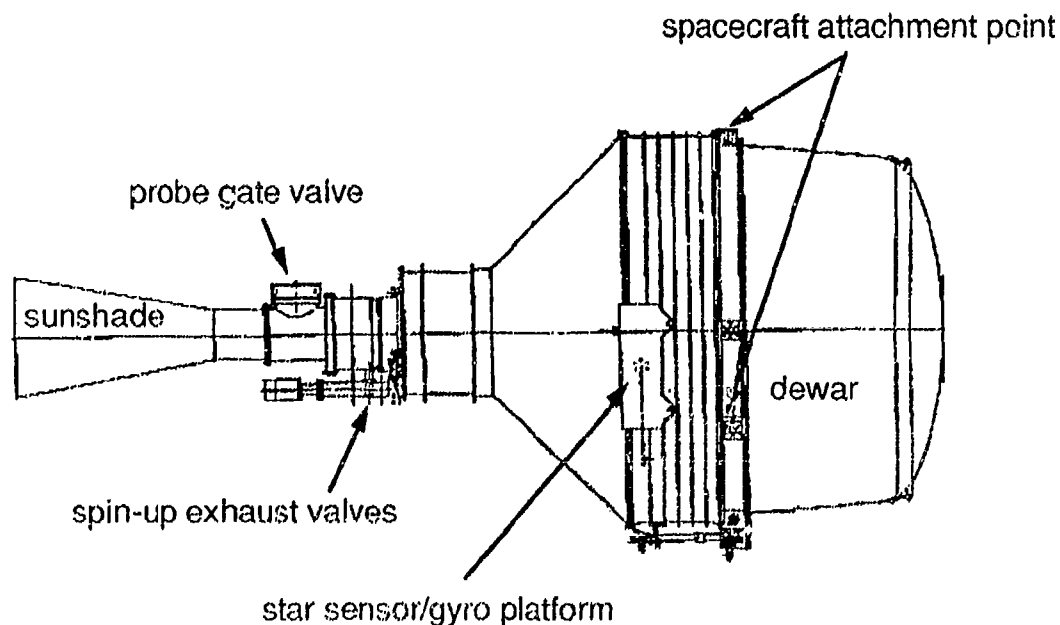


Figure 6 - The dewar contains the liquid helium for the Science Mission. The dewar and contained components weighs approximately 4500 lbs.

Table 1. Key GP-B technologies.

1. ELECTROSTATICALLY SUSPENDED GYROS
USING GAS SPIN-UP SYSTEM
– *Precision quartz housings, rotors, and thin film coatings*
2. GYROS IN NEAR-ZERO AVERAGE
ACCELERATION ($\leq 10^{-11}$ g);
– *Satellite controlled by proportional thrusters to follow "proof mass"*
3. ULTRAHIGH VACUUM ($< 10^{-11}$ torr); DIFFERENTIAL
DAMPING NEGLIGIBLE
– *Low temperature "bake" at $\sim 7^\circ\text{K}$; incorporate cryopump into probe*
4. "AVERAGING OUT" OF RESIDUAL TORQUES ON
THE GYRO
– *Satellite rolled with ~ 10 minute period around line of sight to star*
5. ULTRASTABLE MECHANICAL ENVIRONMENT
(GYROS, QBA, TELESCOPE)
– *All quartz construction at $\sim 2^\circ\text{K}$ within superfluid helium dewar*
6. LONDON MOMENT READOUT OF GYRO
PRECESSION USING DC SQUIDS;
– *~ 5 hr integration time to achieve 1 milliarc-s resolution*
7. SUPERCONDUCTING MAGNETIC SHIELDING OF
GYROS AND READOUT
– *Lead bag surrounding probe plus local Nb shields around each gyro*
8. INTEGRATION OF WARM PROBE INTO
CRYOGENIC DEWAR
– *Thermal/mechanical coupling via indium coated links at heat exchangers*

THE SHUTTLE TEST UNIT (STU)

Shown in Figure 8, is the Shuttle Test Unit (STU) consisting of the STU Vacuum Assembly (SVA) "probe", containing a scaled down quartz block with two operational gyroscopes, together with caging and spin-up gas management assemblies (GMAs) and a complement of suspension and

control electronics. These will be mounted on two plates which attach to the top and side of the Microgravity Program Experiment Support Structure (MPRESS). Insulation and heaters will control the thermal environment of STU to approximately room temperature. Two flights of essentially the same payload are presently planned for 1995 and 1996.

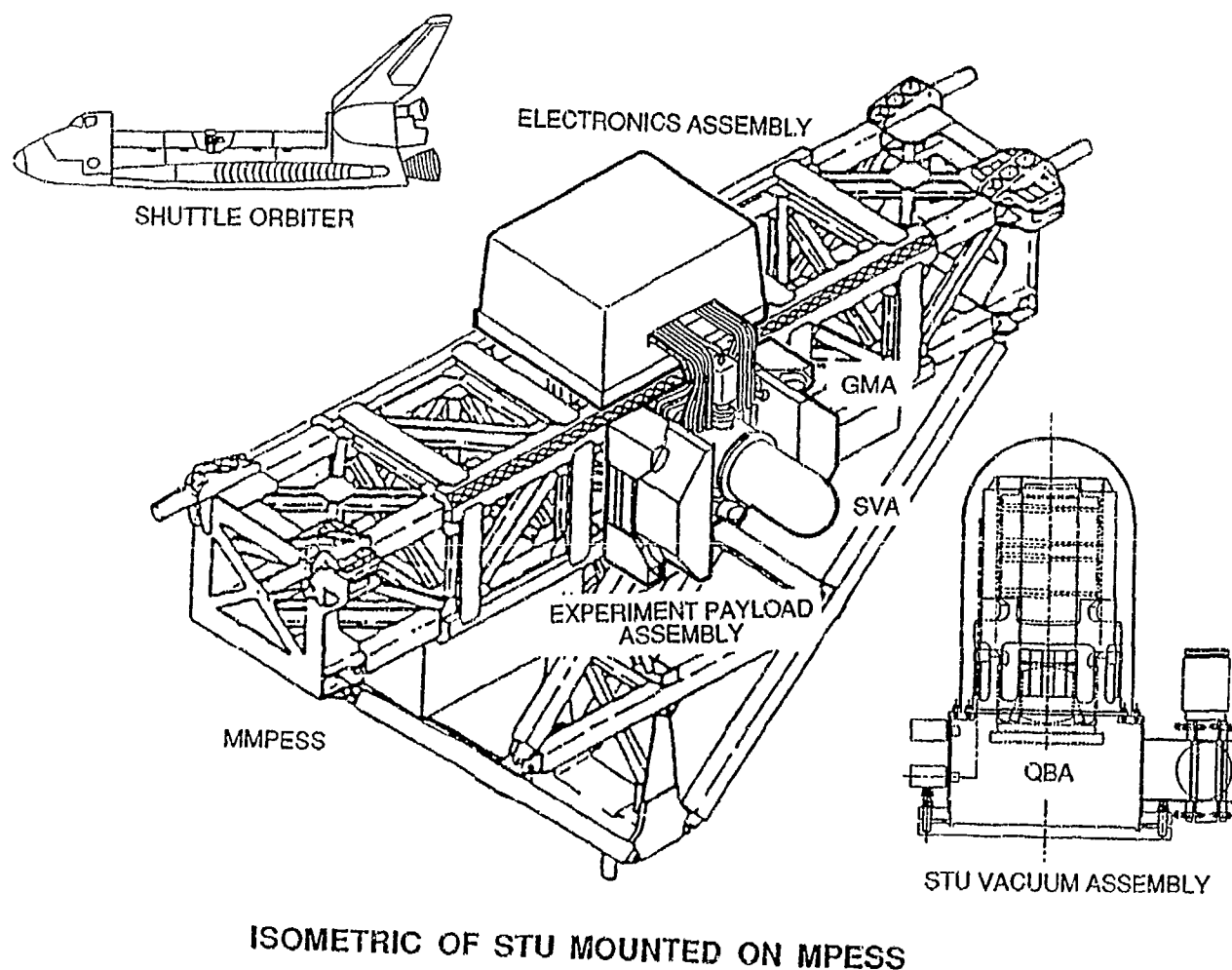


Figure 7. The Shuttle Test Unit mounted on the MPRESS. This experiment will test non-cryogenic gyroscopes in low-acceleration and provides valuable experience applicable to the GP-B Science Mission.

The purpose of the STU missions are to verify (in a low-acceleration environment): (i) gyroscope suspension system performance, (ii) gyroscope spin-up methodology, (iii) high vacuum gyroscope spin-down performance, (iv) prototype data acquisition performance and (v) physical integrity of the quartz block assembly through the various space mission environments.

The basic mission operations time-line will consist of: (a) uncaging and suspension of the two gyroscopes, (b) spin up of both gyroscopes to ~50 Hz in mission 1 (~170 Hz in mission 2) for ~2 hr, (c) spin down of both gyroscopes to ~1 Hz and pump out to high vacuum, (d) collection of gyroscope spin data for 5 to 10 days, including measurement of the response to shuttle-induced accelerations and (e) final spin down, de-suspension and caging for the return trip to Earth.

Many key GP-B team members are working on both STU and the Science Mission payload development. This provides a number of benefits including: (1) simplification of the design and fabrication process resulting from the adaptation of equivalent parts of existing probe technology, (2) natural cross-fertilization of solutions to technical problems- in-common, and (3) valuable flight program experience for the Science Mission team.

THE SCIENCE MISSION

Currently two contractors are performing definition studies on the spacecraft for the Science Mission with a selection of a single contractor planned during 1992.

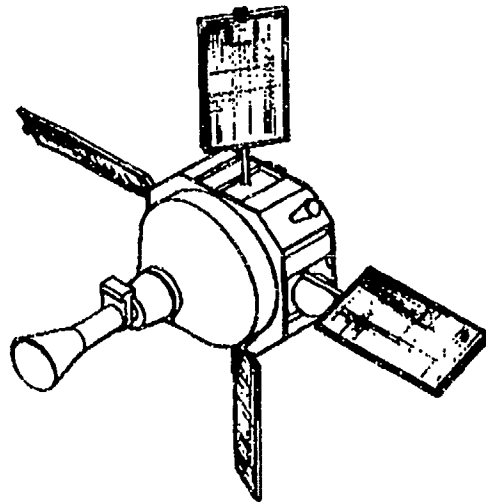


Figure 8 - Generic spacecraft design planned to be launched in 1988 for the Gravity Probe B Science Mission.

To accomplish this a GPS Receiver provides the high precision required. The GPS will determine the position of the satellite to 5 meters and velocity to better than 0.1 meters per second. It also allows timing synchronization to better than 20 nanoseconds for all of the science data. NASA is sponsoring the project for a flight in 1998.

THE ERROR BUDGET

By controlling the gravity forces to 10^{-11} , all mass and balance and compliance terms are reduced to near zero. By controlling the magnetic field to 10^{-14} gauss, magnetic terms approach zero. By controlling the dewar temperature very accurately and adding micro temperature controllers where required, and keeping all heat from the passively rotating gyroscope, these thermal terms approach zero. With precision manufacturing, many bearing terms approach zero. All bias terms are roll averaged to zero by a .1 revolution per minute of the experiment. The gyroscope is analyzed accurate to 10^{-11} degree per hour in inertial space. Because the gyroscope can not be tested to the necessary accuracy on the ground before the flight test, in-flight calibrations are used to ensure the accuracies are attained.

Unbalance effects. The effects of linear accelerations on the mass-unbalance of the gyroscopes shall be measured by applying "large", known translational accelerations along various axes of the satellite before and after the main science experiment. The accelerations will be applied in two different modes, in body fixed coordinates and in inertial coordinates.

Gyroscope Suspension test. The performance of the gyroscope rotor suspension system shall be verified by applying known translational accelerations along various axes of the satellite. The applied acceleration levels will be compared with the estimated levels determined by the suspension system.

A known translational acceleration level at the gyroscopes may be set up by establishing angular dither. The amplitude of the dither is controlled by the gyro. The center of rotation shall be the Proof Mass (PM), as the result of drag-free operation. With known angular dither and known radii of rotation, the linear accelerations at the gyroscopes are known. An acceleration level of $10^{-6}g$ is set up at 0.2 m from the PM by sinusoidally dithering at a rate of 1 rad/sec and an amplitude of 10 arcsec. The dither frequently must be sufficiently lower than the bandwidth of the drag free control system so that the radius of rotation indeed approaches the known

center of the PM. Care must be taken not to subject the gyroscopes to an excessive acceleration regime during calibration.

Gyro (SQUID) calibration. The precise calibration of the SQUID outputs is an essential issue. The calibration shall be based on known basic physical processes, such as the aberration and the bending of starlight. The movement of the satellite tracking the precisely known apparent motions of the guide star serves as the input against which the SQUID outputs are calibrated. The telescope signals provide the pointing errors, which are used as a correction term in the calibration.

The aberration and bending of starlight have characteristic, distinct, known spectral signatures. As the earth orbits the sun, there is a ± 20.408 arcsec variation in the apparent position of the guide star. As the satellite orbits the earth, there is a ± 5.5 arcsec variation in the apparent position of the guide star. The directions, amplitudes and dynamics of the variations are well known. JPL ephemerides gives annual aberration to 0.07 milliarcsec, or 3 parts in 10^6 . Orbital aberration is known from tracking data to about the same precision. The deflection of light has an amplitude of 14.4 milliarcsec. (Reference 9)

Parallax is ± 7 marsec 90 deg out of phase with annual aberration.

Roll reference calibration. The well defined inertial direction of the aberration of starlight processes permits the calibration of the Roll reference system will be used because of its relatively fast dynamics.

ACKNOWLEDGEMENTS

This work was supported by NASA Contract NAS8-36125 from the NASA George C. Marshall Space Flight Center. We thank the following persons for their support: R. Ise, R. Potter, R. Decher, S. Davis, and E. Urban of the NASA Marshall Space Flight Center; and the Gravity Probe B personnel of Stanford University and the Lockheed Missiles and Space Company, Inc.

REFERENCES

1. L. I. Schiff, *Proc. Nat. Acad. Sci.* **46**, 871 (1960).
2. Everitt, *Proceedings of MG6*, Kyoto 1991 (World Scientific, to be published).
3. D. Bardas, M. A. Taber, S. Buchman, D. B. Debra, C.W.F. Everitt, . Gill, G. Green, G. Gutt, N. J. Kasdin, G. M. Keiser, J. A. Lipa, J. M. Lockhart, B. Muhlfelder, B. W. Parkinson, J. P. Turneure, R. A. Van Patten, Y. Xiao, P. Zhou, *Gravity Probe B: II. Hardware Development; Progress toward the Flight Instrument*, *Proceedings of MG6*, Kyoto 1991 (World Scientific, to be published).
4. C. W. F. Everitt and B. W. Parkinson, Gravity Probe B, Program Brochure (1989)
5. G. Dunbar, Measurement of optical homogeneity of fused silica, M.Sc. Thesis, University of Aberdeen, Aberdeen, Scotland, U.K. (1981)
- 6 W. Angele, Finishing high precision quartz balls, *Prec. Eng.* **2**, 119 (1980)
- 7 D.G. Chetwynd and G.J. Siddall, Improving the accuracy of roundness measurement, *Phys. E: Sci. Instrum.* **9**, 537 (1976)
- 8 J.P. Turneure, C.W. F. Everitt, B.W. Parkinson, J.T. Anderson, D.Bardas, W.S. Cheung, D.B. DeBra, W.M. Fairbank, R.A. Farnsworth, D. Gill, R. Hacker, G.M. Keiser, J.A. Lipa, J.M. Lockhart, R.A. Van Patten, R.T. Parmley, R.H. Vassar, and L.S. Young, The Gravity-Probe-B Relativity Gyroscope Experiment: Approach to a Flight Mission, in: *Proc. of the Fourth Marcel Grossmann Meeting on General Relativity*, ed. R. Ruffini, North-Holland, Amsterdam, 1986, p. 411
- 9 J.T. Anderson and C.W.F. Everitt, Limits on the measurement of proper motion and the implications for the relativity gyroscope experiment, GP-B Document No. S0020, W.W. Hansen Laboratories of Physics, Stanford University.

FIFTEENTH BIENNIAL GUIDANCE TEST SYMPOSIUM
ATTENDANCE LIST

AANERUD	KEN	SYNETICS	LAGUNA HILLS	CA
ABBY	DARWIN G	INTERMETRIC	HOLLOMAN AFB	NM
ABDELOADER	SHAFIE Y.	U.S. ARMY	WHITE SANDS MISSILE	NM
ADAM	WALLACE B.	DYN CORP	HOLLOMAN AFB	NM
AGOPOVICH	JOHN W.	C. S. DRAPER LABORAT	CAMBRIDGE	MA
AIRTH	WALTER E.	MAGNAVOX	TORRANCE	CA
ALANIS	ARNIE	BMO/MVEG	NORTON AFB	CA
ALLEN	ALFRED L.	HONEYWELL, INC.	ST. PETERSBURG	FL
ALLEN	ROBERT G.	OSD/D TSA	ARLINGTON	VA
ANDERSON	DAVE	HONEYWELL, INC.	ST. PETERSBURG	FL
ANDERSON	GARY	6585TH TEST GROUP/GD	HOLLOMAN AFB	NM
ANDERSON	GERALD M.	AGMC/CN	NEWARD AFB	OH
ARONOWITZ	FRED	ROCKWELL INTERNATIONAL	ANAHEIM	CA
AWALT	BRUCE	NORTHROP CORP	HAWTHORNE	CA
BABIN	RICHARD G.	6585TH TEST GROUP/GD	HOLLOMAN AFB	NM
BAILEY	HAROLD C.	U.S. NAVY	LAYTONSVILLE	MD
BAKER	HOWARD W.	C.S. DRAPER LABORATO	CAMBRIDGE	MA
BAKER	JAMES B.	HONEYWELL, INC.	CLEARWATER	FL
BALDASTI	WALTER J.	LITTON GCS	WOODLAND HILLS	CA
BANKE	NEIL R.	WL/AAAN	KETTERING	OH
BARKER	CLEON	6585TH TEST GROUP/GD	HOLLOMAN AFB	NM
BASS	CHARLES A.	NAVAL OCEAN SYSTEMS	SAN DIEGO	CA
BAUER	DAVID A.	DELCO ELECTRONICS	GOLETA	CA
BEAL	SONJE F.	ASD/AEMR	WRIGHT-PATTERSON AFB	OH
BEALE	ROBERT E.	COLONEL USAF (RET)	ALBUQUERQUE	NM
BEALS	DAVID C.	NASA LANGLEY RESEARC	HAMPTON	VA
BEAUPIED	DAN	A.A. GAGE, INC.	FERNDALE	MI
BEDELL	COLE	DYN CORP/EPG	FT. HUACHUCA	AZ
BENNETT	SID	ANDREW CORPORATION	ORLAND PARK	IL
BERARDUCCI	MIKE	WL/AAAN-2	WRIGHT PATTERSON AFB	OH
BERRIE	DAVID	6585TH TEST GROUP/CA	HOLLOMAN AFB	NM
BEYER	ROBERT	NAVAL AIR SYSTEMS CO	WASHINGTON	DC
BEYERS	RON	6585TH TEST GROUP/GD	HOLLOMAN AFB	NM
BINKLEY	BRAD J.	HQ FTD/SDJEA	WRIGHT-PATTERSON AFB	OH
BLACKBURN	JOHN	APPLIED TECHNOLOGY A	ALBUQUERQUE	NM
BLASIUS	ROGER	AFFTC 6510 TESTW/DOR	EDWARDS AFB	CA
BLASNEK	CECIL M.	TRW/BMO	SAN BERNADINO	CA
BLIZZARD	ROBERT C.	HONEYWELL, INC.	CLEARWATER	FL
BOIVIN	RICHARD	NORTHROP CORP	HAWTHORNE	CA
BONGIOVANNI	STEPHEN A.	HONEYWELL SASSO	CLEARWATER	FL
BOYKIN	LARRY W.	6585TH TEST GROUP/GD	HOLLOMAN AFB	NM
BRADLEY	EDWARD P.	USAF, ASD/YIES	EGLIN AFB	FL
BREWER	JAMES	6585TH TEST GROUP/GD	HOLLOMAN AFB	NM
BRIENZA	DOMENICO	NAVAL AVIONICS CENTE	INDIANAPOLIS	IN
BROCKSTEIN	ALLAN J.	LITTON GUIDANCE & CO	WOODLAND HILLS	CA
BROGREN	JAN EDVIN	DEFENSE MATERIEL ADM	STOCKHOLM	SW
BROHAUGH	TERRY G.	NORTHROP COPR. ESD	HAWTHORNE	CA
BROWNE	JOSEPH F.	NAVAL AIR TEST CENTE	PATUXENT RIVER	MD
BUCK	ROBERT	6585TH TEST GROUP/GD	HOLLOMAN AFB	NM
BURGESS	ALAN	SPACE SYSTEMS DIVISI	PALOS VERDES EST	CA
BURROUGHS	GEORGE	NAVAL AVIONICS CENTE	INDIANAPOLIS	IN
BURZLAFF	B. H.	LTV AEROSPACE & DEFE	BURLESON	TX
BYERS	THOMAS E.	6585TH TEST GROUP/GD	HOLLOMAN AFB	NM
CADWALLADER	CURT B.	6585TH TEST GROUP/GD	HOLLOMAN AFB	NM
CALDWELL	ROGER R.	LITTON SYSTEMS	WOODLAND HILLS	CA

CALLAGHAN	TIMOTHY	HONEYWELL SRC	MINNEAPOLIS	MN
CAMPBELL	A. T.	RETIRED	DOWNEY	CA
CARR	DONALD S.	MANTECH INTERNATIONAL	ARLINGTON	VA
CARTER	JOHN M.	CARCO ELECTRONICS	MENLO PARK	CA
CARTER	TERRY H.	6585TH TEST GROUP/GD	HOLLOMAN AFB	NM
CARVIL	JOHN	NAVAL SEA COMBAT SYS	NORFOLK	VA
CHASKO	ANDREW	INTERMETRICS	ALAMOGORDO	NM
CHRISTIENSEN	ROBERT G.	ROCKWELL INTERNATIONAL	ANAHEIM	CA
CLARK	RICHARD E.	TASC	MIDWEST CITY	OK
CLOUD	DAVE	USAF ACADEMY	COLORADO SPRINGS	CO
COCCOLI	JOSEPH D.	C. S. DRAPER LABORAT	CAMBRIDGE	MA
COFFMAN	CURTIS	6585 TESTG/GDOS	HOLLOMAN AFB	NM
COLE	JOHN C.	AFOTEC/OL-BC	VANDENBURG AFB	CA
COMALLIE	LEO	6585TH TEST GROUP/GD	HOLLOMAN AFB	NM
CONROY	JOHN	SMITHS INDUSTRIES AE	GRAND RAPIDS	MI
COSENTINO	BARBARA A.	6585TH TEST GROUP/GD	HOLLOMAN AFB	NM
COSENTINO	DENNIS L.	6585TH TEST GROUP/GD	HOLLOMAN AFB	NM
COULTER	JOE E.	NORTHROP AND	HAWTHORNE	CA
COX	RONALD F.	LITTON GUIDANCE & CO	WOODLAND HILLS	CA
CROUCH	DAN S.	6585TH TEST GROUP/GD	HOLLOMAN AFB	NM
DANCE	SCOTT	INTERMETRICS, INC.	HOLLOMAN AFB	NM
DARR	STEVE	SUNDSTRAND INSTRUMEN	REDMOND	WA
DE ARAUJO	PETER	6585TH TEST GROUP/GD	HOLLOMAN AFB	NM
DE BRABANDER	EDWARD T.	FWATD/MT	PATUXENT RIVER	MD
DE DOSE	DIRK	INTERMETRICS, INC	HUNTINGTON BEACH	CA
DE GRANDCOURT	ROBERT F.	ROCKWELL INTERNATIONAL	ANAHEIM	CA
DE TORRES	DON	INTERMETRICS, INC.	HOLLOMAN AFB	NM
DELLON	FRANKLIN	JOHNS HOPKINS UNIV/A	LAUREL	MD
DENHARD	WILLIAM G.	JSDE	READING	MA
DENNIS	RONALD W.	WL/AAAN-1	WRIGHT-PATTERSON AFB	OH
DIAZ	JOSE LUIS	6585TH TEST GROUP/GD	HOLLOMAN AFB	NM
DOBSON	TOMMY L.	6585TH TEST GROUP/GD	HOLLOMAN AFB	NM
DODDS	LARRY	6585TH TEST GROUP/GD	HOLLOMAN AFB	NM
DODDS	MARIE	6505TH TEST GROUP/GD	HOLLOMAN AFB	NM
DOUGHERTY	JOHN J.	TRW, INC.	SAN BERNADINO	CA
DOVE	LYLE L.	6585TH TEST GROUP/GD	HOLLOMAN AFB	NM
DOW	PAUL C.	C. S. DRAPER LABS	CAMBRIDGE	MA
DOYLE	SEAN M.	6585TH TEST GROUP/GD	HOLLOMAN AFB	NM
DREXLER	RONALD	6585TH TEST GROUP/GD	HOLLOMAN AFB	NM
DURBIN	DUANE	TRW/BMO	SAN BERNARDINO	CA
DURIEUX	PATRICK L.	SAGEM	FRANCE	
EBNER	ROBERT	LITTON SYSTEMS	WOODLAND HILLS	CA
EDMONDSON	GREG	LTV AEROSPACE MISSIL	NORWOOD	MA
EICHNER	RICHARD D.	NORTHROP, ESD	NORWOOD	MA
ELDER	JIM	HONEYWELL, INC.	SAN BERNARDINO	CA
ELLS	STEVE	LITTON GUIDANCE & CO	WOODLAND HILLS	CA
ENGELHART	MICHELLE	GALAXY SCIENTIFIC CO	WARMINSTER	PA
ETTL	SUSAN	TRW	SAN BERNARDINO	CA
EVANS	ROGER J.	USAF BMO	NORTON AFB	CA
EVENSON	RONALD	479 FG/SEF	HOLLOMAN AFB	NM
FAY	CHARLES L.	STC COMPONENTS, INC.	SCHAUMBURG	IL
FEDER	EARL	U.S. ARMY AVIONICS R	FT. MONMOUTH	NJ
FELDMAN	JULIUS	C.S. DRAPER LABORATO	CAMBRIDGE	MA
FERNANDEZ	RONALD	C. S. DRAPER LABORAT	CAMBRIDGE	MA
FERRARIS	AL	NORTHROP	HAWTHORNE	CA

FIELKE	GARY	DEFENSE SCIENCE & TE	SALISBURY SOUTH	AU
FILIATREAU	THOMAS R.	6585TH TEST GROUP/GD	HOLLOMAN AFB	NM
FINLEY	TOM	NASA LANGLEY RESEARC	HAMPTON	VA
FISCHER	RAY	NORTHROP CORP., ESD	HAWTHORNE	CA
FISHER	STANLEY R.	DELCO ELECTRONICS	GOLETA	CA
FITZGERALD	WARREN J.	C. S. DRAPER LABORAT	CAMBRIDGE	MA
FITZPATRICK	WILLIAM J.	LOGICON, INC.	SAN PEDRO	CA
FLAHIVE	MARTIN M.	KEARFOTT GUIDANCE &	DALLAS	TX
FLEENOR	MIKE	6585TH TEST GROUP/GD	HOLLOMAN AFB	NM
FLORES	MATT	6585TH TEST GROUP/GD	HOLLOMAN AFB	NM
FRALEY	ERNIE	DELCO SYSTEMS OPERAT	GOLETA	CA
FRAME	LARRY A.	LITTON GUIDANCE & CO	WOODLAND HILLS	CA
FRANKLIN	JAMES H.	CARCO ELECTRONICS	MENLO PARK	CA
FRIESEN	CAARK D.	SUNDSTRAND DATA CONT	REDMOND	WA
GALLOWAY	JOHN	ASD/AEEA	WRIGHT-PATTERSON AFB	OH
GARCIA	FRANK H.	6585TH TEST GROUP/GD	HOLLOMAN AFB	NM
GAUTHIER	ROBERT J.	C. S. DRAPER LABORAT	CAMBRIDGE	MA
GEORGE	SAM	ALC/LIIRN	HARRAH	OK
GILBERT	STEPHEN	INTERMETRICS, INC	HUNTINGTON BEACH	CA
GILLESPIE	GAYLE H.	HONEYWELL, INC.	CLEARWATER	FL
GILMORE	JEROLD P.	C. S. DRPAER LABORAT	CAMBRIDGE	MA
GLASCOE	WILLIAM O.	6585TH TEST GROUP/GD	HOLLOMAN AFB	NM
GLEASON	DAVID	PHILLIPS LABORATORY/	HANSCOM AFB	MA
GOODALL	DAVID A.	LOCKHEED ADVNANCED D	SUNLAND	CA
GREEN	GAYLORD	STANFORD UNIVERSITY	LOS GATOS	CA
GREEN	JOHN J.	6585TH TEST GROUP/GD	HOLLOMAN AFB	CA
GREEN	ROBERT E.	STEWES-ID-P	WHITE SANDS MISSILE	NM
GREENSPAN	RICHARD	C. S. DRAPER LABORAT	CAMBRIDGE	MA
GREIG	JOY Y.	NAVAL COASTAL SYSTEM	PANAMA CITY	FL
GRIEBLER	JERRY	HONEYWELL, INC.	ST PETERSBURG	FL
GRIMES	KEVIN	NAVAL AVIONICS CENTE	INDIANAPOLIS	IN
GRONES	ROYCE G.	RETIRED	MELBOURNE	FL
HADFIELD	MICHAEL J.	HONEYWELL MILITARY A	ST. PETERSBURG	FL
HAGSTEDT	BENGT ANDERS	DEFENSE MATERIEL ADM	STOCKHOLM	SW
HAGUE	LARRY	VSR CORPORATION	PHOENIX	AZ
HALE	GARY C.	HONEYWELL GSM	OGDEN	UT
HAND	JAMES A.	C. S. DRAPER LABORAT	CAMBRIDGE	MA
HANDZEL	JIM	LITTON GUIDANCE & CO	WOODLAND HILLS	CA
HANIGAN	JOHN L.	WL/FIGZ	WRIGHT-PATTERSON AFB	OH
HANSEN	ROBERT A.	NORTHROP CORPORATION	NORWOOD	MA
HARDY	DON	AEROSPACE GUIDANCE &	NEWARK AFB	OH
HARRIS	RICHARD L.	6585TH TEST GROUP/GD	HOLLOMAN AFB	NM
HARTMAN	DWIGHT	NAVLA AVIONICS CENTE	INDIANAPOLIS	IN
HATFIELD	DAVID N.	6585TH TEST GROUP/GD	HOLLOMAN AFB	NM
HAUGE	LEE	GENERAL ELECTRIC DEF	PITTSFIELD	MA
HAYTER	JOHN M.	NAVAL AIR SYSTEMS CO	ARLINGTON	VA
HEAD	ROGER C.	EX-COMMANDER	ALTO	NM
HEATH	ROY L.	STEWES-NR-A	WHITE SANDS MISSILE	NM
HEILMAN	ROGER D.	SUNDSTRAND DATA CONT	REDMOND	WA
HELLINGS	FRAZIER J.	DOUGLAS AIRCRAFT COM	FOUNTAIN VALLEY	CA
HENDERSON	FRANKLIN R.	6585TH TEST GROUP/GD	HOLLOMAN AFB	NM
HENDRIX	DAVE	HEWLETT PACKARD	EL PASO	TX
HENLEY	ANTHONY J. M.	GEC AVIONICS, LTD.	ROCHESTER, KENT	UK
HENSON	LARRY	CARCO ELECTRONICS	MENLO PARK	CA
HEYBL	JACK E.	DELCO SYSTEMS OPERAT	GOLETA	CA

HIRNING	JAMES L.	6585TH TEST GROUP/GD	HOLLOMAN AFB	NM
HOEFENER	CARL	INTERSTATE ELECTRONI	ANAHEIM	CA
HOENIGMAN	JOHN	DELCO SYSTEM OPERATI	GOLETA	CA
HOHMAN	DAVID S.	TRW, INC.	SAN BERNADINO	CA
HOLDEMAN	RICHARD E.	TRW	OGDEN	UT
HOLLAND	KENNETH R.	6585TH TEST GROUP/GD	HOLLOMAN AFB	NM
HOLM	SELMER R.	NORTHROP OPERATIONS	HAWTHORNE	CA
HOLMES	DONALD W.	ROCKWELL	ANAHEIM	CA
HOLSAPPLE	BOYD E.	WRIGHT LABORATORY/AA	WRIGHT-PATTERSON AFB	OH
HOMER	WILLIAM C.	NAVAL OCEAN SYSTEMS	SAN DIEGO	CA
HOOK	JOHN C.	NAVAL AIR SYSTEMS CO	WASHINGTON	DC
HOOSER	MIKE	6585TH TEST GROUP/GD	HOLLOMAN AFB	NM
HUGHES	JAMES A.	U.S. NAVAL OBSERVATO	WASHINGTON	DC
HUNEYCUTT	JAMES E.	JOHNS HOPKINS UNIVER	LAUREL	MD
HUNT	COY	6585TH TEST GROUP/GD	HOLLOMAN AFB	NM
INGOLD	NORMAN L.	6585TH TEST GROUP/SC	HOLLOMAN AFB	NM
JACOBS	PAUL L.	AMSMI-RD-GC	REDSOFT ARSENAL	AL
JAENKE	MARTIN G.	RETIRED DIGTF	ALAMOGORDO	NM
JANKOVITZ	JACK	NAVAL AIR DEVELOPMEN	WARMINSTER	PA
JEFFRIES	JULIE	6585TH TEST GROUP/GD	HOLLOMAN AFB	NM
JENSEN	DAVID	SUNDSTRAND DATA CONT	REDMOND	WA
JENSEN	RICK	6585TH TEST GROUP/PR	HOLLOMAN AFB	NM
JOBO	RON	6585TH TEST GROUP/GD	HOLLOMAN AFB	NM
JOHNSON	GREG	6585TH TEST GROUP/GD	HOLLOMAN AFB	NM
JONES	DAVID L.	MICOM - INERTIAL, RE	REDSTONE ARSENAL	AL
JONES	MALCOLM E.	NASA/JSC	HOUSTON	TX
JONES	THOMAS W.	ANALEX CORPORATION	LITTLETON	CO
JURGENS	RICHARD	ADROIT SYSTEMS	ALEXANDRIA	VA
KALKWARF	DAVID	INTERMETRICS, INC.	HOLLOMAN AFB	NM
KANEGSBERG	EDWARD	LITTON GUIDANCE & CO	WOODLAND HILLS	CA
KANYUCK	ALLEN	INTERSTATE ELECTRONI	ANAHEIM	CA
KARELS	STEVEN N.	TASC	READING	MA
KELHER	ROBERT	6585TH TEST GROUP/GD	HOLLOMAN AFB	NM
KELLEY	GILBERT F.	DYN CORP	HOLLOMAN AFB	NM
KERCHNER	WILLIAM	SEMCO	FAIRBORN	OH
KERRIGAN	PAUL R.	C. S. DRAPER LABORAT	CAMBRIDGE	MA
KLEIN	A. DAVID	LITTON SYSTEMS, INC.	WOODLAND HILLS	CA
KOCH	ROBERT C.	LITTON GUIDANCE & CO	WOODLAND HILLS	CA
KOCHAKIAN	CHARLES R.	C. S. DRAPER LABORAT	CAMBRIDGE	MA
KONDO	NOBORU	LITTON GUIDANCE & CO	WOODLAND HILLS	CA
KONIK	EDWARD H.	LITTON GCS	WOODLAND HILLS	CA
KROEPFEL	WAYNE	HONEYWELL, INC.	CLEARWATER	FL
KROHN	ALICE	6585TH TEST GROUP/GD	HOLLOMAN AFB	NM
KUHL	MARK	ASHTech, INC.	SUNNYVALE	CA
KUHN	FRED	RETIRED CIGTF	ALAMOGORDO	NM
KURKOWSKI	JEROME J.	DEFENSE MAPPING AGEN	F. E. WARREN AFB	WY
LACKEY	ROY	DYN CORP	HOLLOMAN AFB	NM
LADEMANN	ERNEST	BENDIX FIELD ENGINEE	TETERBORO	NJ
LANDERS	A. JACK	6585TH TEST GROUP/GD	HOLLOMAN AFB	NM
LARNEY	JOHN L.	HONEYWELL, INC.	PHOENIX	AZ
LAWER	ALAN	SSD/MZUT	LOS ANGELES	CA
LAWRENCE	ROBERT	6585TH TEST GROUP/GD	HOLLOMAN AFB	NM
LEAR	THOMAS C.	JET PROPULSION LABS	PASADENA	CA
LECHER	JAMES M.	LOCKHEED	HOUSTON	TX
LENZO	JIM	6585TH TEST GROUP/GD	HOLLOMAN AFB	NM

LETTIERE	CHRIS A.	6585TH TEST GROUP/GD	HOLLOMAN AFB	NM
LEVINE	SY	NORTHROP ESD	HAWTHORNE	CA
LEVY	LARRY J.	JOHNS HOPKINS UNIV -	LAUREL	MD
LEVY	ROBERT E.	APPLIED TECHNOLOGIES	SAN MARINO	CA
LI	DR. T. C.	LITTON GUIDANCE & CO	WOODLAND HILLS	CA
LIEB	JOHN E.	COMPREHENSIVE ENGINE	SAN DEIGO	CA
LIMA	BRYAN	6585TH TEST GROUP/GD	HOLLOMAN AFB	NM
LOWREY	REGAN	HONEYWELL, INC.	ST. PETERSBURG	FL
LOWREY	REGAN	HONEYWELL MILITARY A	ST PETERSBURG	FL
LUKE	ROBERT	AEROSPACE CORPORATIO	ALBUQUERQUE	NM
LUKESH	JOHN	NORTHROP ELECTRONICS	HAWTHORNE	CA
LUNDSTROM	EVA ANNIKA	DEFENSE MATERIEL ADM	STOCKHOLM	SW
LYDAY	CARL V.	6585TH TEST GROUP/CC	HOLLOMAN AFB	NM
MACAGNONE	MIKE	HQ SAC	OFFIT AFB	NE
MACPHERSON	D. G.	6585TH TEST GROUP/GD	HOLLOMAN AFB	NM
MADL	JAMES	STEWES-NR-AR	WHITE SANDS MISSILE	NM
MALZAHN	RICHARD F.	HONEYWELL	CLEARWATER	FL
MAROTTA	A. CHARLES	AVRADA	FORT MONMOUTH	NJ
MARQUESS	R.D. SAM	APPLIED MOTION TECHN	CONCORD	CA
MARX	RON	HQ SAC	OFFIT AFB	NE
MATTE	PERRY R.	ASD/AEEA	WRIGHT-PATTERSON AFB	OH
MATTHEWS	RICHARD	ALAMOGORDO PUBLIC SC	ALAMOGORDO	NM
MAY	NANCY	6585TH TEST GROUP/GD	HOLLOMAN AFB	NM
MCADORY	ROBERT W.	GEC-MARCONI ELECTRON	DAYTON	OH
MCHALE	JOHN P.	INSTITUTE FOR DEFENS	ALEXANDRIA	MA
MCPHERSON	KEITH W.	SSD/MZUF	LOS ANGELES AFB	CA
MELINE	MIKE	HUGHES AIRCRAFT COMP	ALBUQUERQUE	NM
MENAPACE	JEFF	6585TH TEST GROUP/GD	HOLLOMAN AFB	NM
MENEFEE	LYNN	6585TH TEST GROU1/GD	HOLLOMAN AFB	NM
MEVERS	JULIE	HONEYWELL, INC	ST PETERSBURG	FL
MICHAEL	SCOTT D.	U.S. ARMY ENGINEER T	FORT BELVOIR	VA
MILLER	CHARLES E.	ASD/AEEA	WRIGHT-PATTERSON AFB	OH
MILLER	MIKEL M.	6585TH TEST GROUP/GD	HOLLOMAN AFB	NM
MILLER	RICHARD G.	WL/MNSI	EGLIN AFB	FL
MIOLA	JOE	C. S. DRAPER LABORAT	CAMBRIDGE	MA
MITCHELL	HARVEY A.	NORTHROP ESD	HAWTHORNE	CA
MITCHELL	STEVEN J.	6585TH TEST GROUP/OL	MELBORNE	FL
MITCHELL	WILLIAM J.	ALLIED-SIGNAL AEROSP	TETERBORO	NJ
MOLNAR	LAWRENCE B.	C. S. DRAPER LABORAT	SAN BERNADINO	CA
MOODY	R. B.	LITTON GCSD	WOODLAND HILLS	CA
MOORE	JAMES MATTHEW	WL/MNAG,	EGLIN AFB	FL
MOORE	JOHN	NAVAL SEA COMBAT SYS	NORFOLD	VA
MORGAN	MARJORIE	6585TH TEST GROUP/GD	HOLLOMAN AFB	NM
MORTON	JACK L.	6585TH TEST GROUP/GD	HOLLOMAN AFB	NM
MOZER	JERRY	RETIRED CIGTF	ALAMOGORDO	NM
MURPHY	DANIEL J.	HONEYWELL, INC.	ST. LOUIS PARK	MN
MURPHY	JAMES	C. S. DRAPER LABORAT	CAMBRIDGE	MA
MURPHY	ROBERT C.	US NAVAL OCEANOGRAPH	STENNIS SPACE CENTER	MS
NADEAU	FREDRIC R.	WL/AAAN	WRIGHT-PATTERSON AFB	OH
NEEL	LEROY K.	2-7 BN COMMANDER	FT BLISS	TX
NIBLETT	BARBARA J.	WL/AAAN-2	WRIGHT-PATTERSON AFB	OH
NICHOLSON	GRADY	6585TH TEST GROUP/GD	HOLLOMAN AFB	NM
NIEMELA	JOHN	U. S. ARMY AVIONICS	FORT MONMOUTH	NJ
NIX	ROY W.	GE AEROSPACE	SAN BERNADINO	CA
OLIVER	ROBERT E.	DELCO SYSTEMS OPERAT	GOLETA	CA

OLSON	PAUL	AVRADA	FORT MONMOUTH	NJ
OMDALEN	CARL W.	DELCO SYSTEMS - GMHE	GOLETA	CA
OTT	PAUL W.	APPLIED TECHNOLOGIES	SAN MARINO	CA
PALMER	RICHARD H.	MCDONNELL AIRCRAFT	SAINT LOUIS	MO
PAYNE	DEAN A.	JOHNS HOPKINS UNIVER	LAUREL	MD
PERLMUTTER	MICHAEL S.	NORTHROP CORPORATION	NORWOOD	CA
PERRY	RONALD B.	BMO/MYEG	NORTON AFB	CA
PETERS	REX B.	SUNDSTRAND DATA CONT	REDMOND	WA
PIECZULEWSKI	DAN	A.G. DAVIS GAGE & EN	HAZEL PARK	MI
PORDY	SHELDON H.	ROCKWELL INTERNATION	ANAHEIM	CA
PORTER	DAVID, DR.	COLEMAN RESEARCH	LAUREL	MD
PORTNEY	JOSEPH N.	LITTON GUIDANCE & CO	TARZANA	CA
POTH	TIMOTHY R.	WL/MNSI	EGLIN AFB	FL
PRICE	JOSEPH K.	HARRY DIAMOND LABORA	ADELPHI	MD
PUBLICOVER	JOSEPH	C.S. DRAPER LABORATO	CAMBRIDGE	MA
QUEEN	PHILLIP D.	LITTON GUIDNACE & CO	WOODLAND HILLS	CA
QUIGLEY	JACK	6585TH TEST GROUP/GD	HOLLOMAN AFB	NM
RAMIREZ	DONALD M.	TRW	SAN BERNADINO	CA
RAMIREZ	FRANCISCO J.	6585TH TEST GROUP/GD	HOLLOMAN AFB	NM
RANDALL	JACK	BENDIX FIELD ENGINEE	MESILLA	NM
RAQUET	JOHN F.	6585TH TEST GROUP/GD	HOLLOMAN AFB	NM
RATER	LONNIE M.	MC DONNELL-DOUGLAS	HOUSTON	TX
REDMAN	WILLIAM A.	SMITHS INDUSTRIES	GRAND RAPIDS	MI
REED	TOM	R.G. BROWN ASSOCIATE	CHIRLTON	MA
REID	CHRISTOPHER C.	6585TH TEST GROUP/GD	HOLLOMAN AFB	NM
RETA	MARIA L.	6585TH TEST GROUP/GD	HOLLOMAN AFB	NM
REYNOLDS	REID G.	TRW	CARSON	CA
RICE	ROBERT	6585TH TEST GROUP/GD	HOLLOMAN AFB	NM
RICHARDSON	LOREN W.	LOCKHEED MISSILES &	SUNNYVALE	CA
RIGG	KENNETH W.	BOEING MILITARY AIRP	SEATTLE	WA
RIGGINS	ROBERT N.	AFIT/ENG	WRIGHT-PATTERSON AFB	OH
RITTER	JOHN W.	TELEDYNE SYSTEMS COM	NORTHBRIDGE	CA
RITTER	WILLIAM T.	6585TH TEST GROUP/GD	HOLLOMAN AFB	NM
ROBERTS	PAUL J.	CARCO ELECTRONICS	MENLO PARK	CA
RODGERS	CHARLES	ADROIT SYSTEMS	ALEXANDRIA	VA
RODRIGUEZ	JESUS A.	6585TH TEST GROUP/GD	HOLLOMAN AFB	NM
ROHRS	DICK	HONEYWELL, INC.	ST. PETERSBURG	FL
ROSS	CHRISTOPHER C.	WL/MNAG,	EGLIN AFB	FL
ROSSO	PAUL G., DR.	NAVAL WEAPONS CENTER	CHINA LAKE	CA
RUFF	DENNIS	6585TH TEST GROUP/GD	HOLLOMAN AFB	NM
RUFF	DEREK A.	6585TH TEST GROUP/GD	HOLLOMAN AFB	NM
RYBAK	FRANK J.	DELCO SYSTEM OPERATI	GOLETA	CA
SANTANA	MELCHOR A.	COLSA, INC.	EL PASO	TX
SARVADI	ROD	NR-AR-A	WHITE SANDS MISSILE	NM
SCHAUER	S. TONY	6585TH TEST GROUP/GD	HOLLOMAN AFB	NM
SCHREIBER	FRED	6585TH TEST GROUP/GD	HOLLOMAN AFB	NM
SCHWEITZER	ALAN R.	DELCO ELECTRONICS	GOLETA	CA
SEBESTA	HENRY	APPLIED TECHNOLOGY A	ALBUQUERQUE	NM
SECORD	MICHAEL G.	HONEYWELL MAVD	MINNEAPOLIS	MN
SELLERS	MARK D.	TRW/BMO	SAN BERNADINO	CA
SHARP	H. C. TED	NORTHROP, ESD	HAWTHORNE	CA
SHAW	GERALD L.	PHILLIPS LAB/LW	HANSCOM AFB	MA
SHEARD	KEITH	BRITISH AEROSPACE SY	PLYMOUTH, DEVON	UK
SHIINOKI	CARL Y.	BMO/MVEG	NORTON AFB	CA
SHOOK	BRIAN J.	AFOTEC/OL-BC	VANDENBERG AFB	CA

SHU	JULIUS C.	LOGICON, INC.	SAN PEDRO	CA
SIMPSON	PHILIP	6585TH TEST GROUP/GD	HOLLOMAN AFB	NM
SINHA	PRASUN	INTERMETRICS, INC.	HUNTINGTON BEACH	CA
SIROKA	MURRAY	NORTHROP	HAWTHORNE	CA
SITOMER	JAMES	C.S. DRAPER LABORATO	CAMBRIDGE	MA
SMITH	ARNOLD J.	CS DRAPER	ARLINGTON	MA
SMITH	BRAD	6510TH TEST WING/DOR	EDWARDS AFB	CA
SNODGRASS	F. BRITT	6585TH TEST GROUP/GD	HOLLOMAN AFB	NM
SOKOL, CAPT	CHARLES W.	BMO/MVEG	LOMA LINDA	CA
SPAULDING	SCOTT	6585TH TEST GROUP/GD	HOLLOMAN AFB	NM
SPEISER	MARIO	TRW	SAN BERNADINO	CA
SPICER	BENNY R.	NAVAL AVIONICS CENTE	INDIANAPOLIS	IN
STACEY, CAPT	RICHARD	6585TH TEST GROUP/GD	HOLLOMAN AFB	NM
STAFFORD	D.E.	CATERPILLAR, INC.	DUNLAP	IL
STANLEY	TIM	6585TH TEST GROUP/GD	HOLLOMAN AFB	NM
STARKEY	O.D.	TELEDYNE GEOTECH	GARLAND	TX
STONEKING	DON	6585TH TEST GROUP/GD	HOLLOMAN AFB	NM
STRATING	JOEL W.	BMO/MVEG	NORTON AFB	CA
STROUD	ROBERT A.	6585TH TEST GROUP/GD	HOLLOMAN AFB	NM
STURDEVANT	REESE C.	6585TH TEST GROUP/GD	HOLLOMAN AFB	NM
SUGERMAN	LEN	PHYSICAL SCIENCE LAB	LAS CRUCES	NM
TADDER	DAVID A.	HONEYWELL, INC.	ST. PETERSBURG	FL
TAMBARA	CHARLENE J.	LOGICON, INC.	SAN PEDRO	CA
TAN	H. HENRY	LOGICON, INC.	SAN PEDRO	CA
TAZARTES	JACQUES A.	LITTON SYSTEMS, INC.	WOODLAND HILLS	CA
TEITT	ROBERT	LITTON INDUSTRIES	SALT LAKE CITY	UT
THOMPSON, JR.	CLAY	HONEYWELL, INC.	ST. PETERSBURG	FL
THORVALDSEN	TOM	C.S. DRAPER LABORATO	CAMBRIDGE	MA
TIPPS	BEN	LITTON GUIDANCE & CO	WOODLAND HILLS	CA
TOUCHBERRY	ALAN	HONEYWELL SRC	MINNEAPOLIS	MN
TREROTOLA	RON	CUBIC CORPORATION	SAN DIEGO	CA
TRUNCALE	ANGELO	ROCKWELL INTERNATION	ANAHEIM	CA
TRUNZO	ANGELO	6585TH TEST GROUP/GD	HOLLOMAN AFB	NM
TWEEDY	MICHAEL J.	LITTON GUIDANCE & CO	WOODLAND HILLS	CA
VESTGARD	BERIT KATARINA	DEFENSE MATERIEL ADM	STOCKHOLM	SW
VOLK	CHARLES H.	LITTON GUIDANCE & CO	WOODLAND HILLS	CA
VOROS	ARTHUR R.	DELCO SYSTEMS - GMHE	GOLETA	CA
WALDIE	HOWARD	LOCKHEED	WHITE SANDS MISSILE	NM
WARD	PHILLIP W.	TEXAS INSTRUMENTS, I	PLANO	TX
WASKIEWICZ	LEO Y	6585TH TEST GROUP/DO	HOLLOMAN AFB	NM
WATANABE	YASUHIRO	JAPAN RADIO CO., LTD	HUDSON	NH
WELLS	RANDY L.	SCIENCE APPLICATIONS	SHALIMAR	FL
WENTZEL	DAVE	SUNDSTRAND	REDMOND	WA
WERNLE	KENNETH R.	6585TH TEST GROUP/GD	HOLLOMAN AFB	NM
WHEELER	RAIMIE	INTERMETRICS, INC.	HOLLOMAN AFB	NM
WILKINSON	BILL	CIGTF	HOLLOMAN AFB	NM
WING	KEVIN	6585TH TEST GROUP/GD	HOLLOMAN AFB	NM
WINGLER	RANDY L.	PHILLIPS LABORATORY/	KIRTLAND AFB	NM
WISE	JOHN P.	WL/MNAG	EGLIN AFB	FL
WISSLER	RICHARD J.	BMO/MYEP	NORTON AFB	CA
YAMAMOTO	AKIYOSHI	JAPAN RADIO CO., LTD	MITAKA-SHI, TOKYO	JA
ZAGONE	PETER V.	RETIRED	ALAMOGORDO	NM
ZELTNER	RUSSELL J.	CONTRAVES USA, INC.	PITTSBURG	PA

SUPPLEMENTARY

INFORMATION



DEPARTMENT OF THE AIR FORCE
HEADQUARTERS 8585TH TEST GROUP (AFSC)
HOLLOMAN AIR FORCE BASE, NEW MEXICO 88330-5000

B 164 018

ERRATA

REPLY TO
ATTN OF: GD

1 April 1992

SUBJECT: Volume I of Proceedings for Fifteenth Biennial Guidance
Test Symposium

TO: TO ALL RECIPIENTS OF VOLUME I

Per the attached letter, please cross out the distribution
statement on page 183 of AFDTC-TR-91-06 proceedings and
replace with the following statement:

"Public release is approved.
AFDTC/PA 92-094."

Please staple/affix the attached letter to inside the back
cover of the document.

K R Holland

K. R. HOLLAND
Technical Director
Guidance Test Division

1 Atch
AFDTC/PA Ltr dtd 25 Mar 92

ERRATA B 164 018

ERRATA

B 164 018

151.20/14